VNiVERSiDAD D SALAMANCA

CAMPUS OF INTERNATIONAL EXCELLENCE

Thermodynamic optimisation of thermosolar hybrid Brayton cycle plants

Optimización termodinámica de plantas termosolares híbridas de ciclo Brayton

Rosa Pilar Merchán Corral

Doctoral thesis / Tesis doctoral

Supervisors: Dr. Alejandro Medina Domínguez and Dr. María Jesús Santos Sánchez

UNIVERSITY OF SALAMANCA / UNIVERSIDAD DE SALAMANCA

Department of Applied Physics / Departamento de Física Aplicada

Salamanca (Spain), September 2020

VNiVERSiDAD D SALAMANCA

CAMPUS OF INTERNATIONAL EXCELLENCE

Thermodynamic optimisation of thermosolar hybrid Brayton cycle plants

Optimización termodinámica de plantas termosolares híbridas de ciclo Brayton

Departamento de Física Aplicada

Tesis doctoral presentada para optar al título de
Doctora por la Universidad de Salamanca con Mención Internacional,
bajo el Programa de Doctorado en Física Aplicada y Tecnología

Author:

ROSA PILAR MERCHÁN CORRAL

Supervisors:

Alejandro Medina Domínguez

María Jesús Santos Sánchez

September, 2020

MEMORIA que presenta Rosa Pilar Merchán Corral,

Para optar al título de

Doctora por la Universidad de Salamanca con Mención Internacional,

bajo el Programa de Doctorado en Física Aplicada y Tecnología

Salamanca, España, septiembre 2020

Abstract

Current anthropogenic intensification of climate change together with fossil fuel exhaustion have made imperative the necessity of a new energy generation paradigm looking for increasing generated power, but from cleaner sources that reduce associated pollutant emissions. Among the different renewable energy sources, Concentrated Solar Power (CSP) technology constitutes a very interesting option that employ solar radiation as main energy source. This technology stands out thanks to its ability to produce reliable, safe, efficient and clean power reducing, or even fully removing, pollutant greenhouse effect emissions associated with conventional fuel combustion. In Concentrated Solar Power systems, direct solar radiation is concentrated in order to obtain high temperature thermal energy that is transformed into electrical energy by means of a thermodynamic cycle and an electric generator. Main advantage of Concentrated Solar Power technology is its potential for hybridisation and its potential to store solar energy as heat, both in order to produce electric energy when desired and to complete and to rectify the inherently variable solar contribution.

This doctoral thesis is devoted to study, from the thermodynamic point of view, a Concentrated Solar Power plant, in particular a Solar Power Tower coupled to a hybrid Brayton cycle. In this way, the plant is considered to be set up by a heliostat field pointing to a solar receiver, where solar radiation is absorbed. Afterwards, solar heat is exchanged to a working fluid that develops a Brayton cycle. Above all else, the plant is aimed to work as baseload; in other words, to produce, and to deliver to the grid, a constant net power independent of solar radiation. As a consequence, the gas turbine is hybridised in series by means of a combustion chamber that ensures a constant turbine inlet temperature, and so, desired power output. When solar heat is not enough to reach imposed turbine inlet temperature, the combustion chamber burns natural gas completing and rectifying the solar heat.

There exists a significant lack of studies focusing on integrating all subsystems and analysing their inter-relationships and how they affect the global plant. In this way, the objectives of the thesis comprise the development of a theoretical model and its implementation in an own code for performing on-design and dynamic simulations that can offer valuable information of energy losses and configurations that lead to better output records.

According to the plant scale and to the heliostat field symmetry, two different sorts of systems are analysed in this doctoral thesis. First, a *SOLUGAS*-like plant with a power scale of about 5 MW and a polar field is evaluated. Alternatively, a larger power scale of around 20 MW and a surround field are examined too. In this case, *GEMASOLAR* plant is employed for parameters dimensioning. Nevertheless, a Brayton cycle is simulated instead of the Rankine power unit from *GEMASOLAR*. Following this trend, the comparison of two different power units (gas turbine and steam turbine) with similar power scales and solar subsystem size is one

of the goals of this study.

Moreover, model predictions are validated by means of commercial software packages and by employing literature data. Apart from this validation, a comparison and a simple contextualization are also conducted for the different subsystem models output records.

Real meteorological data, such as solar direct normal irradiance and ambient temperature, are implemented in the code for the considered location. Additionally, other input parameters are taken into account in the solar subsystem like tower height, receiver size, heliostats reflectivity or mirrors area. Pressure ratio, turbine inlet temperature, working fluid mass flow, turbine and compressor efficiencies and heat release and heat absorption pressure decays are the main heat engine parameters for the plant modelling.

Some of the analysed output parameters are related to different kind of efficiencies: overall thermal efficiency, optical heliostat field efficiency, solar subsystem efficiency and heat engine efficiency. All cycle temperatures and heat rates are also computed. And other variables as fuel conversion rate, solar share, power output, specific fuel consumption and its associated greenhouse effect emissions are surveyed. From the thermo-economic perspective, net energy, Levelised Cost of Electricity and its components are evaluated.

In order to analyse different working fluids performance, a closed cycle with heat exchangers is simulated. Thus, dry air, nitrogen, carbon dioxide and helium are tested. Additionally, the number of compression and expansion stages is also surveyed. Moreover, a pre-optimisation process is carried out looking for optimum pressure ratio configurations that lead to improved output variables.

Daily simulations show that the objective of producing a stable power output is accomplished. On the other hand, seasonal behaviour is translated into the width and into the height of output variables daily evolution curves, such as efficiencies and temperatures. A key outcome from off-design annual simulations is that heat engine improvements could lead to the largest enhancements of analysed overall plant output records.

Moreover, the recuperator influence is researched and concluded to be positive from both thermodynamic and thermo-economic viewpoints. Likewise, plant location is varied in order to evaluate its effect on plant records. Furthermore, sensitivity analyses allow to demonstrate that Levelised Cost of Electricity still presents potential for reduction regarding pressure ratio.

Besides those particular outcomes, this doctoral thesis reveals the importance of designing the Solar Power Tower hybrid gas turbine system as a whole, taking into account subsystems interactions. Therefore, this doctoral thesis can be useful in an initial step of the design of future Solar Power Tower systems developing hybrid Brayton cycles.

Keywords: Solar Power Tower, gas turbine, hybridisation, overall plant pre-optimisation, solar field efficiency, pressure ratio, on- and off-design analyses, Levelised Cost of Electricity.

Resumen

La actual intensificación antropogénica del cambio climático junto con el agotamiento de los combustibles fósiles han impuesto un nuevo paradigma energético en el que destaca la necesidad de generar más potencia eléctrica, pero a partir de fuentes de energía más limpias y que reduzcan las emisiones contaminantes asociadas. La energía solar de concentración (*Concentrated Solar Power*, *CSP*), que emplea la radiación solar como principal fuente de energía, es una de las opciones más interesantes entre las diferentes energías renovables. En los sistemas que emplean esta tecnología, se concentra la radiación solar normal para obtener energía térmica a altas temperaturas y, a continuación, esta energía se transforma en energía eléctrica mediante un ciclo termodinámico y un generador eléctrico. De este modo, la energía termosolar de concentración permite producir energía de forma fiable, estable, segura, eficiente y limpia puesto que reduce, o incluso elimina por completo, las emisiones contaminantes de efecto invernadero asociadas con los combustibles convencionales y los problemas derivados de ellas. Una de las principales ventajas de los sistemas de energía termosolar de concentración radica en su potencial para ser hibridados con otras fuentes de energía y para almacenar energía solar en forma de calor, de modo que se pueda producir energía eléctrica cuando se desee y que se complete y rectifique el aporte de calor solar, que es intrínsecamente variable.

Esta tesis doctoral está dedicada a estudiar una planta de concentración termosolar (*CSP*) desde el punto de vista termodinámico; en concreto, una planta solar de torre central (*Solar Power Tower*, *SPT*) acoplada a un ciclo Brayton híbrido. La planta en estudio está formada por un campo de heliostatos que apuntan hacia un receptor solar, donde se absorbe la radiación solar. A continuación, se intercambia este calor solar concentrado con un fluido de trabajo que lo absorbe y desarrolla un ciclo Brayton. El objetivo de la planta es funcionar como planta de generación de carga base (*baseload*), es decir, producir y entregar a la red eléctrica una potencia neta constante e independiente de la radiación solar. Para ello, se hibrida la turbina de gas en serie con una cámara de combustión, lo cual asegura una temperatura de entrada a la turbina constante y, como consecuencia, una potencia de salida constante. Si el aporte de calor solar no es suficiente para alcanzar la temperatura de entrada a la turbina impuesta, entonces la cámara de combustión quema gas natural completando y rectificando así la entrada de calor solar.

Respecto al estado de la cuestión, existe una escasez significativa de estudios que se centren en integrar todos los subsistemas y en analizar sus inter-relaciones y cómo afectan estas a la planta global. Por consiguiente, los objetivos de la tesis comprenden el desarrollo de un modelo teórico y su implementación en un código propio para realizar simulaciones, tanto en el punto de diseño como dinámicas, que puedan ofrecer información valiosa sobre las pérdidas de energía y sobre las configuraciones que traen consigo mejores registros de salida.

En esta tesis doctoral se analizan dos tipos de sistemas diferentes teniendo en cuenta el tamaño de la planta y la simetría del campo de heliostatos. Primero se evalúa una planta similar a *SOLUGAS* con una potencia de alredor de 5 MW y un campo polar. En segundo lugar, se examina una planta más grande, de aproximadamente 20 MW, y con un campo circundante. En este caso, para el dimensionamiento de los parámetros se emplea la planta *GEMASOLAR*, aunque se simula un ciclo Brayton en vez del ciclo Rankine propio de *GEMASOLAR*. Asimismo, otro objetivo de este estudio es la comparación de dos unidades de potencia diferentes (turbina de gas y turbina de vapor), pero con potencias similares, y con dimensiones del subsistema solar también similares.

Por otro lado, se validan las predicciones del modelo mediante varios paquetes de *software* comerciales y utilizando datos de la literatura. Además de esta validación, también se realizan una comparación y una simple contextualización de las variables de salida de los modelos de los diferentes subsistemas.

En el código se implementan datos meteorológicos reales de la localización específica, tales como irradiancia solar directa normal (*Direct Normal Irradiance*, *DNI*) y temperatura ambiente. Asimismo, en el subsistema solar se tienen en cuenta otros parámetros de entrada como la altura de la torre, el tamaño del receptor, la reflectividad de los heliostatos o el área de los espejos. Los principales parámetros de la máquina térmica incluidos para la modelización de la planta son la relación de presiones, la temperatura de entrada a la turbina, el flujo de masa del fluido de trabajo, las eficiencias de la turbina y el compresor y las caídas de presión asociadas con la cesión y absorción de calor.

De entre los parámetros de salida analizados, varios están relacionados con diferentes eficiencias: eficiencia térmica global, eficiencia óptica del campo de heliostatos, eficiencia del subsistema solar y eficiencia de la máquina térmica. Igualmente, se calculan todas las temperaturas y todos los flujos de calor del ciclo. Al mismo tiempo, se estudian otras variables como la fracción solar o *solar share*, la potencia de salida, el consumo específico de combustible y las emisiones de efecto invernadero correspondientes. Desde la perspectiva termo-económica, se evalúan la energía neta, el Coste Normalizado de la Electricidad (*Levelised Cost of Electricity*, *LCoE*) y sus componentes.

Con el objetivo de analizar el comportamiento de diferentes fluidos de trabajo, se simula un ciclo cerrado mediante intercambiadores de calor. Así, se estudian aire seco, nitrógeno, dióxido de carbono y helio. También se examina la influencia del número de etapas de compresión y expansión. Por otro lado, se lleva a cabo un proceso de pre-optimización buscando configuraciones óptimas para la relación de presiones que impliquen mejores valores de las variables de salida.

Las simulaciones diarias confirman que se ha cumplido el objetivo de generar una potencia

de salida estable. Por otro lado, el comportamiento estacional se traslada directamente a la anchura y a la altura de las curvas de evolución diaria de variables de salida tales como eficiencias y temperaturas. Una conclusión clave de las simulaciones anuales fuera de diseño es que, entre todos los subsistemas, la máquina térmica se asocia potencialmente con la mejora más significativa de los registros de salida analizados.

Asimismo, se investiga la influencia del recuperador en el esquema de la planta y se ha demostrado que su presencia es positiva tanto desde el punto de vista termodinámico como termo-económico. Igualmente, también se varía la localización de la planta para evaluar su efecto en las variables del modelo. Finalmente, los análisis de sensibilidad llevados a cabo permiten demostrar que, respecto de la relación de presiones, el Coste Normalizado de la Electricidad presenta todavía potencial para su reducción.

Aparte de estos resultados concretos, la tesis doctoral revela la importancia de diseñar como un todo los sistemas solares de torre central acoplados a una turbina de gas híbrida, teniendo en cuenta la interacción entre los diferentes subsistemas. Por tanto, esta tesis doctoral puede ser útil en una etapa inicial de diseño de futuros sistemas solares de concentración de torre central que realicen ciclos Brayton híbridos.

Palabras clave: torre solar central, turbina de gas, hibridación, pre-optimización de la planta global, eficiencia del campo solar, relación de presiones, análisis en punto de diseño y fuera de diseño, Coste Normalizado de la Electricidad.

Lista de las publicaciones incorporadas

La tesis corresponde a un compendio de trabajos previamente publicados o aceptados para publicación. Se incluyen siete artículos (enumeración numérica), de los cuales seis han sido ya publicados y uno ha sido enviado para publicación; dos capítulos de libro publicados (enumeración alfabética) y un proceeding publicado (enumeración alfabética griega).

1. M.J. Santos, **R.P. Merchán**, A. Medina, A. Calvo Hernández. "Seasonal thermodynamic prediction of the performance of a hybrid solar gas-turbine power plant". *Energy Conversion and Management*, 115: 89−102, 2016.
   DOI: http://dx.doi.org/10.1016/j.enconman.2016.02.019
2. **R.P. Merchán**, M.J. Santos, I. Reyes-Ramírez, A. Medina, A. Calvo Hernández. "Modeling hybrid solar gas-turbine power plants: Thermodynamic projection of annual performance and emissions". *Energy Conversion and Management*, 134: 314−326, 2017.
   DOI: http://dx.doi.org/10.1016/j.enconman.2016.12.044
3. **R.P. Merchán**, M.J. Santos, A. Medina, A. Calvo Hernández. "Thermodynamic model of a hybrid Brayton thermosolar plant". *Renewable Energy*, 128: 473-483, 2018.
   DOI: http://dx.doi.org/10.1016/j.renene.2017.05.081
4. M.J. Santos, C. Miguel-Barbero, **R.P. Merchán**, A. Medina, A. Calvo Hernández. "Roads to improve the performance of hybrid thermosolar gas turbine power plants: Working fluids and multi-stage configurations". *Energy Conversion and Management*, 165: 578−592, 2018.
   DOI: https://doi.org/10.1016/j.enconman.2018.03.084
5. **R.P. Merchán**, M.J. Santos, I. Heras, J. González-Ayala, A. Medina, A. Calvo Hernández. "On-design pre-optimization and off-design analysis of hybrid Brayton thermosolar tower power plants for different fluids and plant configurations". *Renewable and Sustainable Energy Reviews*, 119: 109590, 2020.
   DOI: https://doi.org/10.1016/j.rser.2019.109590
6. **R.P. Merchán**, M.J. Santos, A. Medina, A. Calvo Hernández. "On- and off-design thermodynamic analysis of a hybrid polar solar thermal tower power plant". *International Journal of Energy Research*, 1-17, 2020.
   DOI: https://onlinelibrary.wiley.com/doi/full/10.1002/er.5854
7. **R.P. Merchán**, M.J. Santos, J. García-Ferrero, A. Medina, A. Calvo Hernández. "Thermoeconomic analysis of a central tower hybrid Brayton thermo-solar plant: sensitivity of LCoE to main design parameters". Submitted to *Applied Thermal Engineering*, 2020.

A. Santos Sánchez, María Jesús; **Merchán Corral, Rosa Pilar**; Medina Domínguez, Alejandro; Calvo Hernández, Antonio. "Simulación termodinámica de una planta

termosolar híbrida tipo Brayton". *Current Trends in Energy and Sustainability. 2015 Edition*, Chapter XVII: 267-284, 2015
ISBN: 978-84-608-5438-8

B. **R.P. Merchán**, M.J. Santos, A. Medina, A. Calvo Hernández. "Hybrid Brayton thermosolar systems: thermodynamic prediction of annual efficiencies and emissions". *Current Trends in Energy and Sustainability. 2017 Edition*, Chapter IV: 47-60, 2017.
ISBN: 978-84-0903541-0

α. **Rosa P. Merchán**, Alejandro Medina, María Jesús Santos, Irene Heras, José Miguel M. Roco, and Antonio Calvo Hernández. "Towards a more efficient generation of central tower hybrid thermosolar gas turbine power plants". *AIP Conference Proceedings (SolarPACES2018)*, 2126: 140004, 2019.
DOI: `https://doi.org/10.1063/1.5117652`

Se expone a continuación el nombre y la afiliación completa actual de cada uno de los autores, por orden de aparición:

- Rosa Pilar Merchán Corral: *rpmerchan@usal.es*.
  Departamento de Física Aplicada, Universidad de Salamanca.
  Instituto Universitario de Física Fundamental y Matemáticas (IUFFYM), Universidad de Salamanca.
  Plaza de la Merced, s/n, 37008, Salamanca, España.
- María Jesús Santos Sánchez: *smjesus@usal.es*.
  Departamento de Física Aplicada, Universidad de Salamanca.
  Instituto Universitario de Física Fundamental y Matemáticas (IUFFYM), Universidad de Salamanca.
  Plaza de la Merced, s/n, 37008, Salamanca, España.
- Alejandro Medina Domínguez: *amd385@usal.es* .
  Departamento de Física Aplicada, Universidad de Salamanca.
  Instituto Universitario de Física Fundamental y Matemáticas (IUFFYM), Universidad de Salamanca.
  Plaza de la Merced, s/n, 37008, Salamanca, España.
- Antonio Calvo Hernández: *anca@usal.es*.
  Departamento de Física Aplicada, Universidad de Salamanca.
  Instituto Universitario de Física Fundamental y Matemáticas (IUFFYM), Universidad de Salamanca.
  Plaza de la Merced, s/n, 37008, Salamanca, España.
- Israel Reyes Ramírez: *ireyesram@hotmail.com*.

Unidad Profesional Interdisciplinaria en Ingeniería y Tecnologías Avanzadas (UPIITA), Instituto Politécnico Nacional (IPN).
Av. Instituto Politécnico Nacional 2580, La Laguna Ticoman, Gustavo A. Madero, 07340, México D.F., México.

- César Miguel Barbero: *cesar.miguel.barbero@gmail.com*.
  Minsait (Indra).
  Avenida de Bruselas, 35, 28108, Alcobendas, Madrid, España.
- Irene Heras Pérez: *iheras@catec.aero*.
  Centro Avanzado de Tecnologías Aeroespaciales (CATEC).
  Parque Tecnológico y Aeronáutico de Andalucía, C/ Wilbur y Orville Wright 17-19-21, 41309, La Rinconada, Sevilla, España.
- Julián González Ayala: *jgonzalezayala@usal.es*.
  Departamento de Física Aplicada, Universidad de Salamanca.
  Instituto Universitario de Física Fundamental y Matemáticas (IUFFYM), Universidad de Salamanca.
  Plaza de la Merced, s/n, 37008, Salamanca, España.
- Judit García Ferrero: *jgferrero@usal.es*.
  Departamento de Física Aplicada, Universidad de Salamanca.
  Instituto Universitario de Física Fundamental y Matemáticas (IUFFYM), Universidad de Salamanca.
  Plaza de la Merced, s/n, 37008, Salamanca, España.
- José Miguel Mateos Roco: *roco@usal.es*.
  Departamento de Física Aplicada, Universidad de Salamanca.
  Instituto Universitario de Física Fundamental y Matemáticas (IUFFYM), Universidad de Salamanca.
  Plaza de la Merced, s/n, 37008, Salamanca, España.

Dr. D. Alejandro Medina Domínguez, Catedrático del Departamento de Física Aplicada de la Universidad de Salamanca, y **Dra. Dña. María Jesús Santos Sánchez**, Profesora Contratada Doctora Básica del Departamento de Física Aplicada de la Universidad de Salamanca,

CERTIFICAN:

que la tesis doctoral titulada "Optimización termodinámica de plantas termosolares híbridas de ciclo Brayton" (*"Thermodynamic optimisation of thermosolar hybrid Brayton cycle plants"*) ha sido realizada por **Dña. Rosa Pilar Merchán Corral** para optar al título de Doctora por la Universidad de Salamanca con Mención Internacional y desarrollada en el marco del Programa de Doctorado en Física Aplicada y Tecnología bajo su dirección, por lo que autorizan su presentación, mediante compendio de publicaciones.

MEDINA DOMINGUEZ ALEJANDRO - 07865245G
Firmado digitalmente por MEDINA DOMINGUEZ ALEJANDRO - 07865245G
Fecha: 2020.09.29 16:50:01 +02'00'

Fdo.:
Dr. D. Alejandro Medina Domínguez

SANTOS SANCHEZ MARIA JESUS - 07864423X
Firmado digitalmente por SANTOS SANCHEZ MARIA JESUS - 07864423X
Fecha: 2020.09.29 19:16:20 +02'00'

Fdo.:
Dra. Dña. María Jesús Santos Sánchez

En Salamanca, a 29 de septiembre de 2020.

Agradecimientos / Acknowledgments

En primer lugar quiero agradecer inmensamente a mis dos directores de tesis, Alejandro Medina Domínguez y María Jesús Santos Sánchez, todo su trabajo, su apoyo constante y sus ánimos durante todos estos años, por ser tan generosos y haber compartido tantas cosas conmigo, por la tranquilidad y por saberme guiar tan bien. Muchas gracias por transmitirme cada día vuestro entusiasmo por todo lo que hacéis y vuestras ganas de enseñar. Quiero que sepáis que he aprendido mucho de vosotros en todos los sentidos y ámbitos. Sin vosotros esta tesis no tendría ningún sentido. Quiero agradecerles también tanto a ellos como al resto de miembros del Área de Física Aplicada de Salamanca haberme acogido tan bien desde el primer día, con tanto cariño, en un ambiente distendido, y haberme hecho sentir una más del grupo desde el principio. A Antonio Calvo, que tanto se ha preocupado de esta tesis; a Julián, que me ha acompañado durante todo este tiempo; a Antonio González, siempre solucionando todos los problemas técnicos; a Roco por facilitarme siempre todo y porque siempre encuentra un hueco para un chiste; a Juan Antonio por los consejos técnicos; a Javi por todo su cariño y a Santi por sus ganas constantes de innovar. Gracias a todos ellos porque son los mejores maestros que se puede tener y porque me siento muy afortunada de haber podido realizar esta tesis con ellos cerca. A Judit, que es la siguiente en esta etapa. A César por su sentido del humor, a Irene, a Juncheng, a Wanli, a Gabriel y a todas las personas que de un modo u otro han pasado por aquí en estos años porque todos me habéis ayudado mucho y todos formáis parte de este gran equipo.

I want to acknowledge all the people from KTH Royal Institute of Technology at Stockholm, who welcomed me and treated me so well during my three months internship. Rafael Guédez and Silvia Trevisan for helping me so much and for having always a smile on their faces, Wujun Wang, Jorge Garrido, all the people that I met there, Adriana Zurita for sharing this experience with me, and the rest of the *Division of Heat and Power Technology* and the *Concentrating Solar Power and Techno-Economic Analysis Group*, who made from my internship a wonderful experience. In addition, I would also like to thank Peter King and the *Concentrating Solar Power group* at Cranfield University, who allowed me to visit their facilities and who welcomed me with open arms. A Susana Sánchez Orgaz y a todas las demás personas de la Universidad Politécnica de Madrid que me enseñaron y me acogieron durante aquella semana. A Pilar Vélez por dedicarme su tiempo y por todos los consejos. A la gente increíble que conocí en Adventia, que me trataron, y me siguen tratando, con tanto cariño. A los alumnos que tuve la oportunidad de conocer allí, y de los que tanto aprendí, porque fueron mi primera experiencia docente y me dieron ganas de continuar. A todos los alumnos que durante estos años me han permitido acompañarles y aprender juntos durante sus TFGs o TFMs.

A mis compañeras de Grado, que tienen ya para siempre un huequito en mi corazón, por haber compartido tantas cosas y también la física. A Carmen por caminar juntas desde el instituto; a Alba, que lleva una gran artista dentro; a Paz por seguir juntas hasta el doctorado; y a Thaís porque ni la distancia hace que nuestra amistad sea menos especial. A los sucedáneos de física por los consejos de futuro y, por supuesto, por los juegos: a Julián, Carlos, Rocío, Felipe, José y a todos los demás. A Víctor.

A toda la gente que he conocido gracias al desarrollo de esta tesis y que me he cruzado en este maravilloso camino porque de cada uno he aprendido y todos me habéis aportado algo.

A Dani Martín y a Baleo por poner banda sonora a mi vida. A Villavieja de Yeltes por ser raíz y refugio. A todos mis amigos de Guguel S.L. porque hemos crecido juntos y porque también son mi familia: a Carlos, a Javi, a Alba, que son los que comparten mis días; a Omar, mi vecino lejano; a Raquel por compartir una pasión y a todos los demás que integran esta gran peña.

A toda mi gran y extensa familia por lo afortunada que me siento de tenerlos cerca. ¡Os quiero mucho! A los que están y a los que, por desgracia, ya no están y me faltan cada día. Con mucho cariño a mis abuelos a los que echo mucho de menos, Antonio y Pilar, y a los que todavía puedo disfrutar, Angelines y Pedro. A mi abuelo Antonio por regalarme el mejor hogar posible. A mi abuela Pilar por su carácter y por darme hasta su nombre. A mi abuelo Pedro por su original punto de vista del mundo. A mi abuela Angelines por quererme tanto, por transmitirme el vocabulario charro y, por supuesto, por las perronillas, las rosquillas y los buñuelos. A todos mis tíos y todos mis primos porque todos ellos forman la mejor familia posible, de la que me siento increíblemente orgullosa. Dedicatoria especial a Hugo, René y Manuel por ser luz y sacarme las sonrisas más verdaderas. ¡Sofía, estoy deseando conocerte!

A mi hermano Andrés por poner siempre mis pies en la tierra, por su sinceridad y por todo lo que hemos compartido y nos queda por compartir. Brenda, gracias por cuidar tan bien a mi hermano y ¡bienvenida a la familia! A Álvaro por ser la mejor compañía posible, por aportarme tantas cosas (incluida su familia), por saber estar a mi lado durante todo este tiempo, por conocerme mejor que yo misma, por sus sonrisas diarias y por nuestro futuro juntos. A mi madre por ser todo en mi vida, por la paciencia infinita, por estar siempre a mi lado y, por supuesto, por el amor incondicional. Pero especialmente me gustaría agradecer esta tesis a mi padre por la complicidad, porque echo mucho de menos su sonrisa, por mostrarme el camino de la felicidad, por ser fuente de vida constante y porque estoy segura de que su orgullo en este momento sería indescriptible.

A mi padre,
que hubiera disfrutado como un niño tocando este papel.

Preface

This doctoral thesis has been performed at the *Research Group on Energy Optimization, Thermodynamics and Statistical Physics* within the Department of Applied Physics at the University of Salamanca. The Group has devoted a research line to the model and optimisation of several energy converters since mid nineties. Particularly, several models for gas turbines (GT) were developed [1]. The research group experience on Concentrated Solar Power (CSP) started as an application of a simple and theoretical gas turbine model to a generic solar plant [2]. However, that model did not contain any detail of real plants. The model was so general that no particular CSP type was even been selected [3, 4, 5, 6]. Then, a further approach was carried out by adapting the model to a central tower plant just at design conditions [7]. Afterwards, the author of this thesis began her contribution to the research on the coupling of gas turbines with central tower CSP plants. The results of this research project are compiled in this doctoral work.

The author would like to acknowledge that this doctoral thesis has been specifically funded by *Banco de Santander* and University of Salamanca. Though, throughout it, other fundings by *MINECO of Spain* (Spanish Economy and Competitiveness Ministry), *Junta de Castilla y León* and General Foundation of the University of Salamanca have been also received and are acknowledged.

Contents

Chapter 1. Introduction

In this Chapter, doctoral thesis topic is introduced first by explaining key antecedents of Concentrated Solar Power (CSP) at Section 1.1. Then, real plants (both prototypes and commercial) and research projects are distinguished. In this way, Section 1.2 deals with CSP technology and current plants. Thereafter, the Introduction is focused on the specific CSP type that is the subject area of this doctoral thesis: Solar Power Towers (SPT). Section 1.3 broadens this information with present and future commercial SPT plants and prototypes. On the other hand, the state of the art of those plants from research perspective is addressed at Section 1.4. Finally, a summary of current investigation challenges (Section 1.5) and the doctoral thesis objectives (Section 1.6) are displayed.

1.1 Antecedents

One of the first prototypes for obtaining usable energy from concentrating solar radiation was developed by Augustin Mouchot, who presented it at the Universal Exhibition in Paris in 1878. More than one hundred years later, in the 1980s, Concentrated Solar Power (CSP) started its commercial development thanks to the construction of nine operational plants in California [8]. US continued leading the CSP market until 2010, when Spanish installed capacity overtook US one [9]. Since then, a very fast development both at a commmercial and at a research stage of CSP has been performed. Actually, CSP has been proposed by the International Energy Agency (IEA) as key for the future of power generation [10]. Nowadays, other countries are making big efforts in order to increase their CSP installed capacity, especially China, India, UAE, Morocco and South Africa [9].

1.2 CSP plant types and present real plants

Sun radiation that reaches the Earth is denominated global radiation. It has two components: direct and diffuse solar radiation. Direct Normal Irradiance (DNI) is the only important component for solar concentrating energy generation and it accounts for the amount of solar irradiance that reaches a normal or perpendicular area. Therefore, best places in the Earth for CSP generation are those with higher DNIs levels, namely, regions approximately between 15º and 40º both north and south latitudes and also places with higher elevations. As a result, regions like Chile, Peru, north of Mexico and south west of USA in America; western Australian areas; south and north Africa, Middle East; or north west of India and western China in Asia have a big potential for CSP [11, 12].

The working principle of Concentrated Solar Power is very simple: direct solar radiation is concentrated in order to obtain high temperature thermal energy that is transformed into electrical energy [13]. Although there exist different geometries, CSP systems are basically formed by the same elements [14]:

- a solar reflector, which gathers and concentrates the Sun radiation;
- a solar receiver, where the solar radiation is concentrated and absorbed;
- a power conversion system, which turns the concentrated solar heat into mechanical energy;
- and an electric generator, which transforms that mechanical energy into electricity.

The key advantage of CSP against other renewable energies like photovoltaic (PV) energy or wind power is its ability to store heat for producing electric energy when desired. Hence, CSP can be coupled with Thermal Energy Storage (TES), but also with a combustion chamber burning some conventional fuel or some biogas constituting hybrid plants [8]. Nowadays other hybridisation schemes are being investigated, as the coupling with photovoltaic systems. Both these hybrid and TES systems allow for high dispatchability. Therefore, the generation can be shifted to non-Sun shining times, as cloudly periods or even nighttime [15]. In this way, CSP plants can be designed for covering baseload or demand peaks, conversely to what happens in PV or wind facilities.

Currently, four broadly accepted types of Concentrated Solar Power systems can be distinguished. They are differentiated by the way of concentrating the Sun radiation onto the receiver, as it can be observed in Table 1.1 [13].

- Parabolic Trough Collectors (PTC) are made up of a parabolic mirror which concentrates the Sun radiation on a focal line.
- Linear Fresnel Reflectors (LFR) focus sunlight on a linear receiver too, but, in this case, through an array of linear mirrors, behaving as a Fresnel lens.
- Parabolic Dish Collectors (PDC) consist of a parabolic mirror which reflects and con-

	Continuous reflector	**Discrete reflector**
Line focus collector	Parabolic Trough Collector (PTC) 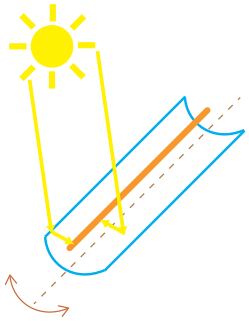	Linear Fresnel Reflector (LFR) 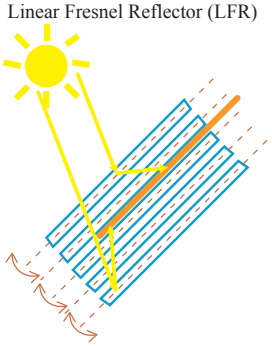
Point focus collector	Parabolic Dish Collector (PDC) 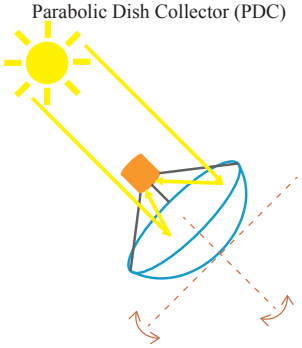	Solar Power Tower (SPT) 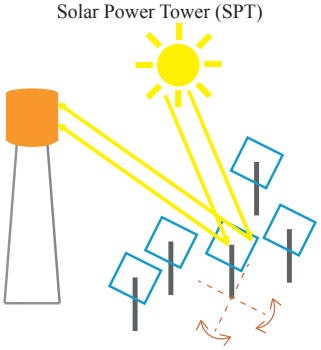

Table 1.1: Classification by reflector geometry of the commonly accepted CSP systems. Yellow arrows represent Sun radiation, orange structures symbolise solar receivers, blue structures correspond to solar reflectors and brown arrows with dashed lines show reflectors rotation axis.

centrates the Sun heat on the focal point of the dish.

- Solar Power Towers (SPT) or Central Receiver Systems (CRS) are set up by a heliostats field which reflects solar radiation into a central receiver located atop a tower. These heliostats track the Sun in two axis [16]. They are also considered as point focus collectors.

Overall installed capacity of CSP worldwide reached 6.3 GW in 2019 [16]. Regarding concentration ratio, PDC can achieve the highest values, in the range of 1000-3000 and SPT intermediate ones (300-1000) [17], while PTC and LFR present relatively lower values: between 60 and 80 [14]. Right now, Parabolic Dishes are the only technology recommended

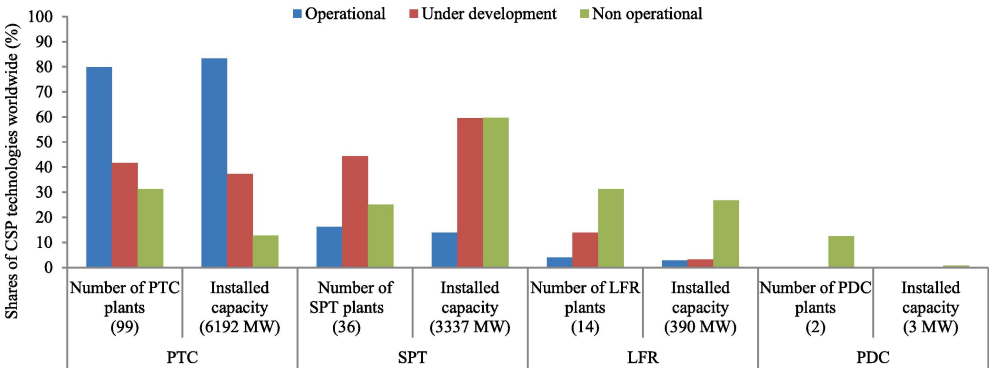

Figure 1.1: Shares of worldwide CSP plants by technology, as they were in 2020, by Achkari and El Fadar [9]. Number of plants and their installed capacity are detailed in accumulated terms.

for small scale generation, in the range [0.01-0.4] MW, whereas the other three systems are preferred for medium or high scale generation ([10-200] MW) [17].

Currently, most mature technologies are Parabolic Trough Collectors, which constitute 80% of operational plants [9], as it can be observed in Fig. 1.1. Since the development of *Andasol* plants at Spain in 2011, which have significant TES, and of *Solana* plant at US in 2013, other interesting projects have been recently carried out worldwide and some are under development. Among already operating commercial plants, *Noor II* at Morocco (2018), *Shouhang Dunhuang 100 MW Phase II* at China (2018) and *Kathu Solar Park* at South Africa (2019) stand out thanks to their installed capacity and innovative concepts.

Solar Power Towers, which constitute about 15% of operational plants [9] (see Fig. 1.1), are the second most mature technology. Further details about real SPT plants are gathered at Section 1.3. Linear Fresnel Reflectors and Parabolic Dish Collectors represent just a very small percentage of installed capacity. Regarding LFR, *Puerto Errado 2* in Spain (2012) and *Dhursar* in India (2014) are among the few commercial plants and *Zhangjiakou* project is presently under development in China. Finally, two Parabolic Dishes were built in the US, *Maricopa* in 2010 and *Tooele Army Depot* in 2013, but currently they are non-operational [18].

However, this trend is already changing since the amount of under development SPT plants (45%) and their installed capacity (60%) are higher than those of PTC [9], as illustrated by Fig. 1.1. The reason of that growth is the capacity of SPT to achieve higher temperatures in comparison to PTC [9] and, thus, greater solar to electric efficiencies [17].

1.3 Current Central Tower plants: working and R&D projects. Thermo-economic data

1.3.1 Solar Power Towers sorts

Depending on the characteristics of each component, there exists a big variety of Solar Power Tower plants both at a commercial and at a research stage. As it was previously mentioned, Solar Power Towers, also denominated Central Receiver Systems, are composed of a heliostat field, in which a varying number of heliostats reflect and concentrate solar radiation. Regarding heliostat field symmetry, there are basically two types of commercial plants: surround and polar fields. In surround fields, heliostats are placed around a central tower in a nearly circular shape, covering 360° or almost. On the other hand, polar fields are set up by heliostats placed occupying just a sector of a circle, thus the field has a wedge shape. In low latitudes, close to the equator, a surround field is the best option for reducing land use as well as tower height. As latitude increases, a field more concentrated to the polar side of the tower becomes better in order to improve performance. Therefore, in higher latitudes, a north / south field depending on the hemisphere is preferred. In the case of a north field, all heliostats are placed in the north side of the tower since the Sun is towards the south during all the year [11, 19, 20, 21].

In the top of the tower, concentrated solar radiation reaches solar receiver. Nowadays, according to their geometry, receivers can be external or have a cavity aperture. External receivers are suitable both for surround fields, in case they have a cylindrical shape, or for polar fields, if they are made up by a flat-plate panel. Alternatively, cavity receivers present a small aperture through which concentrated solar radiation enters. Due to its constrained geometry, they are normally employed for polar fields [19, 20]. Therefore, heliostat field depends also on the receiver type [21].

This solar receiver acts as a solar radiation absorber too. At a commercial stage, most of the absorbers are made by tubes that can be placed to form a cylindrical or a billboard absorber, hence they are denominated tubular absorbers [19, 22]. Thus, both external and cavity receivers could employ tubular absorbers [23]. In volumetric absorbers, solar heat enters within the structure or volume, where it is absorbed by a porous material, though currently they are not mature enough to be fully commercial [19, 24]. As a general rule, tubular receivers are employed for high temperatures or high pressures, but not both at the same time; meanwhile, volumetric concepts are adequate for higher temperatures with limited pressures [19]. Most employed materials for the receivers are ceramics and metals stable at high temperatures [25].

Then, in that solar absorber, a Heat Transfer Fluid (HTF) absorbs that concentrated solar heat and it can either transmit it to the thermodynamic cycle working fluid (through some type of heat exchanger) or it can act itself as this working fluid. The function of the Heat Transfer

Fluid can be performed presently by water/steam or by molten salts. Moreover, the use of air as HTF is being researched nowadays [25]. Maximum operating temperature of HTF is a very important parameter for receivers, clearly conditioning their design [8].

Therefore, high temperature heat is achieved and employed for running directly a power block or indirectly by storing this energy in advance. All commercial and operational Central Receiver plants employ steam for running a Rankine cycle; although some research projects about air as working fluid running a gas turbine are being conducted, as this doctoral thesis. With respect to Thermal Energy Storage, right now, almost all commercial plants accumulate energy through two tanks of molten salts. Most of current commercial SPT plants employ two working fluids: molten salts as HTF and for TES, and superheated steam for the Rankine cycle [13].

In 2018, worldwide and operational Solar Power Tower gross installed capacity was 618.42 MW and, in the following years, it will finish achieving 995 MW [25]. The overall capacity of under construction and development Solar Power Towers reached around 5383 MWh_e in 2019, with an average power capacity of 207 MWh_e [8].

1.3.2 Current Solar Power Tower plants

Spanish *PS10* plant, the first purely commercial solar power tower system providing electricity to the grid in the world, started operation in 2007 and the same in 2009 for the very similar *PS20* plant [18, 25]. Both of them employ a cavity receiver, a saturated steam turbine and a pressurised water thermal storage with 1 hour of capacity as main technology systems [21, 31]. Then, in 2011, *GEMASOLAR* plant [32], which utilizes a 19.9 MW steam turbine, was already working in Spain too. This plant is pioneer due to an innovative up to 15 hours storage system, which uses molten salts as the Heat Transfer Fluid (HTF) and storage medium [21].

After that Spanish SPT boost, United States of America began its contribution thanks to the construction of three key Central Receiver plants which were operative in 2009, *Sierra*, 2014, *Ivanpah*, and in 2015, *Crescent Dunes* (Tonopah). *Ivanpah* project, with a net turbine capacity of 377 MW, was at that moment the largest solar thermal power tower system in the world [18, 25]. *Crescent Dunes* plant used an external cylindrical receiver with molten salts as HTF and incorporated a 10 hours storage. Nevertheless, it is not currently operational because of some ongoing issues [33, 34]. Along the same lines, *Sierra Tower*, which employed water as HTF and is made up by two towers and, thus, two receivers (a dual cavity receiver and an external rectangular one), is currently non-operational [18, 21].

China constitutes another major SPT driver with several operational plants in the last years. From 2013, when *SUPCON 10 MW* plant started operation at that country, passing through the

Country	Non-operational	Operational	UC / UD
Australia	*Lake Cargelligo** (2011)	*Solar Field (1+2)** (2010) / *Sundrop* (2016) / *Jemalong** (2017)	*Aurora* (UD)
Chile			*Cerro Dominador* (Atacama) (UC) / *Copiapó*, *Likana*, *Tamarugal* (UD)
China	*Huanghe Qinghai Delingha* (2017) / *Yumen 100 MW** (-)	*Dahan** (*Yanqing*), *Badaling** (2012) / *SUPCON 10 MW* (2013) / *Shouhang Dunhuang I* (2016) / *Shouhang Dunhuang II*, *SUPCON 50 MW* (2018) / *Hami*, *Luneng Haixi*, *Qinghai Gonghe* (2019)	*Golmud*, *Yumen 50 MW** (UC) / *Golden*, *Shangyi* (UD)
Germany		*Jülich** (2008)	
Greece			*MINOS** (UD)
India		*ACME** (2011)	
Israel		*Ashalim Plot B* (2019)	
Italy			*Mazara* (UD)
Morocco		*NOOR III* (2018)	
South Africa		*Khi Solar One* (2016) / *Redstone* (2018)	
Spain	*SOLUGAS** (2012)	*PS10* (2007) / *PS20* (2009) / *GEMASOLAR* (2011)	
Tunisia			*TuNur* (UD)
Turkey		*Greenway Mersin** (2012)	
UAE			*DEWA Tower* (UC)
USA	*Sierra* (2009) / *Coalinga** (2011) / *Crescent Dunes* (Tonopah) (2015)	*Ivanpah* (2014)	*Rice* (Mojave), *Palen*, *Hidden Hills* (UD)

Table 1.2: Current (operational and non-operational) and Under Construction (UC) / Under Development (UD) Solar Power Tower plants in the world by country according to [8, 9, 14, 18, 21, 25, 26, 27, 28, 29, 30]. In brackets the commissioned start year of the plant for the operational, currently non-operational plants, and - if not available. * R&D, pilot and demonstration plants.

development of *Shouhang Dunhuang I* in 2016, up to the last two years, when those growth has been intensified due to the development of five Chinese operative plants: *SUPCON 50 MW* and *Shouhang Dunhuang II* in 2018 and *Qinghai Gonghe*, *Hami* and *Luneng Haixi* in 2019 [9, 18].

Three years before, in 2016, South African *Khi Solar One* plant began to operate its 50 MW Rankine turbine. The same year, *Sundrop* project commenced heating greenhouses, desalinating seawater and running a steam turbine in Australia. Apart from that project, other two Australian non-commercial plants have been set up. In 2011, the demonstration *Lake Cargelligo* project, currently non-operational, tested a very interesting graphite solar receiver, which acts also as a boiler and storage system. Moreover, pilot *Jemalong* plant has been operational since 2017 [18].

Other region thas has promoted this sector is the so-called Middle East and North Africa (MENA) area with different projects. From a research perspective, Turkey built the demonstration *Greenway Mersin* plant in 2012. On the other hand, the commercial *NOOR III* plant, located in Morocco in the Ouarzazate complex, was launched in 2018, with 7 hours of storage capacity. While *Ashalim Plot B* project, with the tallest tower worldwide (240 m) [30], started operation in 2019 at Israel [18].

All these commercial plants and other current pilot and demonstration projects are gathered in Table 1.2. In addition, in the same table, some of the most important SPT plants under construction and development (following Subsection) are collected.

1.3.3 Under construction and under development Solar Power Tower plants

One of the best locations regarding solar radiation in the world is sited on Chilean deserts. As a consequence, Chile is trying to take advantage of its natural resources and stands out as one of the most promising countries regarding SPT according to their four planned plants. *Cerro Dominador* project is already being constructed [18]. It will have more than 10600 heliostats and 17.5 hours of storage capacity for producing 110 MW [35]. Additionally, *Copiapó*, *Likana* and *Tamarugal* are being developed right now, 2020. Another key country for the future of Central Receiver Systems is China, where *Golmud 200 MW* plant is currently being constructed and other two plants are under a development process (*Golden* and *Shangyi*) [9, 18]. Other three projects are right now under development in USA: *Rice* (Mojave) with 150 MW of capacity, *Palen* and *Hidden Hills*, both with 500 MW planned capacity [8].

Furthermore, the construction of *DEWA Tower* has already started in United Arab Emirates and other plants are currently under development worldwide as *Redstone* in South Africa, *MINOS* in Greece, *Aurora* in Australia, and *TuNur* in Tunisia, which stands out due to their 2000 MW of capacity [18]. Although, *Aurora* project has recently (December, 2019)

changed to a fully different kind of project and now it will be supossed to be a photovoltaic facility [36, 37].

1.3.4 Solar Power Tower thermo-economic data

Regarding efficiency values and as a general overview, it can be highlighted that thermal efficiency is estimated between 30% and 40% for Solar Power Towers. This kind of systems presents overall plant peak efficiency values in the interval of [23-35]%, while its annual solar to electric efficiency varies from 20% to 35% [25]. In the case of *PS10*, a real plant that has been operational for 13 years, the total annual efficiency is about 15.4% [20].

Apart from efficiency, other interesting parameter is capacity factor, which is defined as the ratio between the actual output of a power plant and its maximum over a year (including nights) [9]. If capacity factor is higher than 50%, this means a significant amount of storage is employed [8]. For instance, the annual capacity factor for a tower plant with 10 h of TES is around 55% [25]. Hence, among the others CSP systems, tower plants present the highest capacity factor [25].

A quite employed economic indicator is the Power Purchase Agreement (PPA). A PPA is a deal between a seller and a purchaser of electricity, in which all the commercial terms are defined [8]. Table 1.3 and Fig. 1.2 gather information about a few commercial tower projects with their PPA data [18]. PPA data are taken from [18] and currency changes to USA dollars (USD) according to start year have been applied in order to unify units. Highest tariff rates correspond to the earliest plants: *PS10* and *PS20* in Spain. On the other hand, *Aurora*'s project was associated with the lowest signed PPA among the analysed plants, although, as it was previously mentioned, the project type has recently changed to a photovoltaic facility [36, 37] . *DEWA* project has also a very low tariff rate for a duration of 35 years [16] and all considered PPAs signed in China are related to almost the same electricity prices. Therefore, tariff prices have decreased with time, as it can be observed in Fig. 1.2 [8]. This trend indicates that, nowadays, Solar Power Towers electricity production costs are more competitive regarding other energy generation sources, which proves the maturity growth of those systems [8].

Another key economic indicator is the Levelised Cost of Electricity (LCoE). It illustrates the ratio between income and generated energy that is necessary for recovering the initial investment and the yearly costs of the plant for an estimated period of operation [39]. Thus, it is employed in order to analyse the economic profitability of a power plant [9]. This Levelised Cost of Electricity depends on TES capacity. If no storage is assumed, estimated LCoE in 2020 is around 145 USD/MWh. When 6-7.5 h of TES are considered, LCoE drops until 118-129 USD/MWh. And a further reduction is achieved when bigger TES is implemented (12-15 h TES): 112-121 USD/MWh [9].

Project	Heliostat Field	Receiver	Net Turbine Capacity	TES	Commiss. Year	PPA/Tariff Rate (USD/MWh)
PS10 (Spain)	Polar	Cavity	11 MW	4 tanks (SS), 1 h	2007	352
PS20 (Spain)	Polar	Cavity	20 MW	4 tanks (SS), 1 h	2009	377
SUPCON I (China)	Surround	External	10 MW	2-tank direct (MS), 2 h	2013	193
Crescent Dunes (USA)	Surround	External	110 MW	2-tank direct, salt, 10 h	2015	135
Huanghe Qinghai (China)	Surround	External	135 MW	2-tank indirect (MS), 3.7 h	2017	166
Shouhang Dunhuang II (China)	Surround	External	100 MW	2-tank direct (MS), 11 h	2018	177
SUPCON II (China)	Surround	External	50 MW	2-tank direct (MS), 7 h	2018	177
NOOR III (Morocco)	Surround	External	134 MW	2-tank direct (MS), 7 h	2018	156
Redstone (South Africa)	Surround	External	100 MW	2-tank direct (MS), 12 h	2018	124
Hami (China)	Surround	External	50 MW	2-tank direct (MS), 8 h	2019	167
Luneng Haixi (China)	Surround	External	50 MW	2-tank direct (MS), 12 h	2019	167
Qinghai Gonghe (China)	Surround	External	50 MW	2-tank direct (MS), 6 h	2019	167
Ashalim Plot B (Israel)	Surround	External	121 MW	None	2019	212
DEWA Tower (UAE)	Surround	External	100 MW	2-tank direct (MS), 15 h	UC	73.0
Aurora (Australia)	Surround	External	135 MW	2-tank direct (MS), 8 h	UD	54.9
MINOS (Greece)	Surround	External	52 MW	2-tank indirect, 5 h	UD	312

Table 1.3: A few Solar Power Tower Projects, some of their features and their PPA data [18, 20, 26, 38].PPA data are taken from [18] and currency changes to USA dollars (USD) according to start year have been applied in order to unify units. Commiss. corresponds to Commissioned, SS means saturated steam, MS, Molten Salt, UC stands for Under Construction and UD, Under Development.

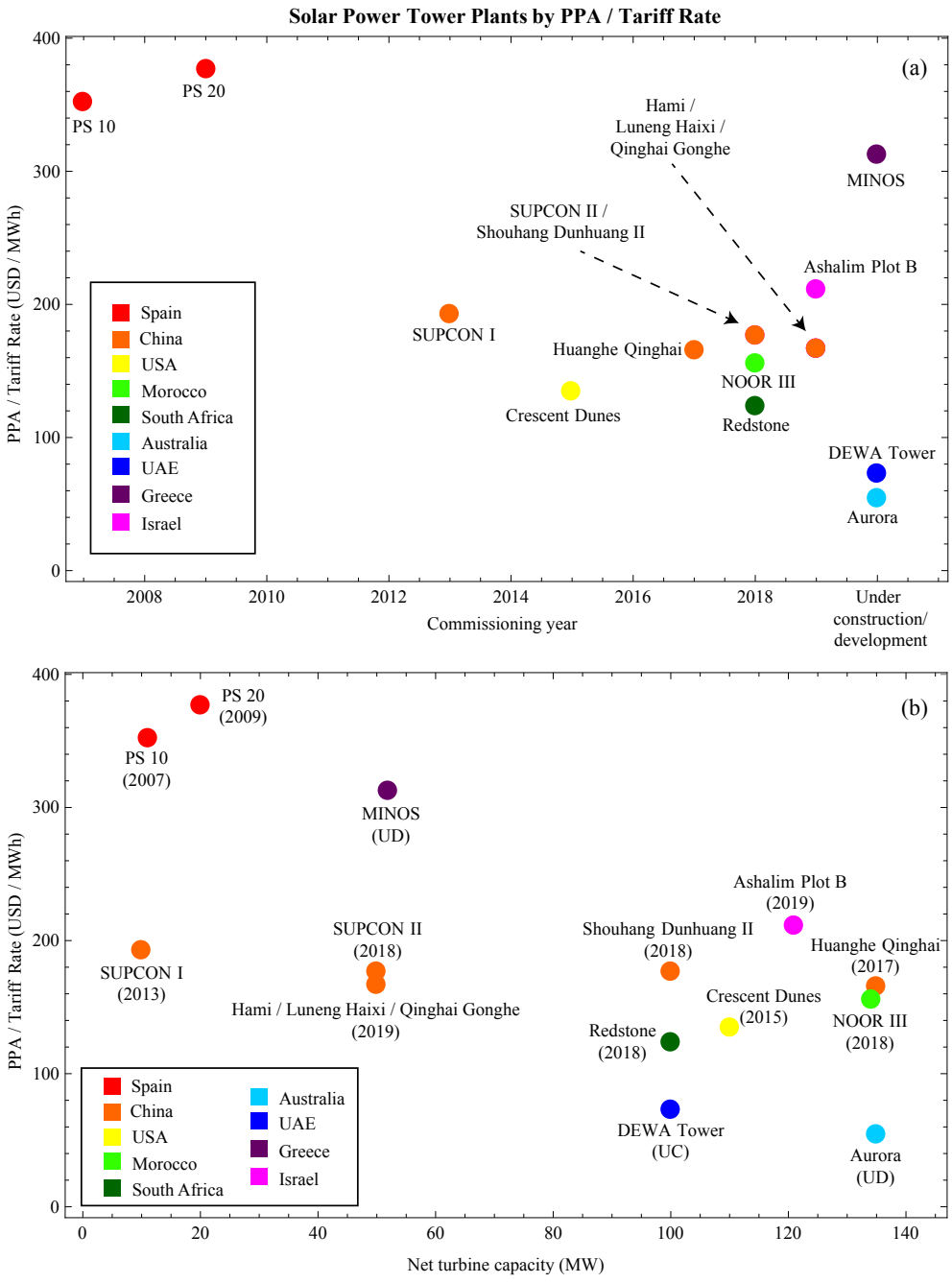

Figure 1.2: PPA data, commissioning year (a) and net turbine capacity (b) of a few SPT plants. Colours make reference to location country. PPA data are subjected to currency changes to USA dollars (USD) according to start year have been applied in order to unify units [18].

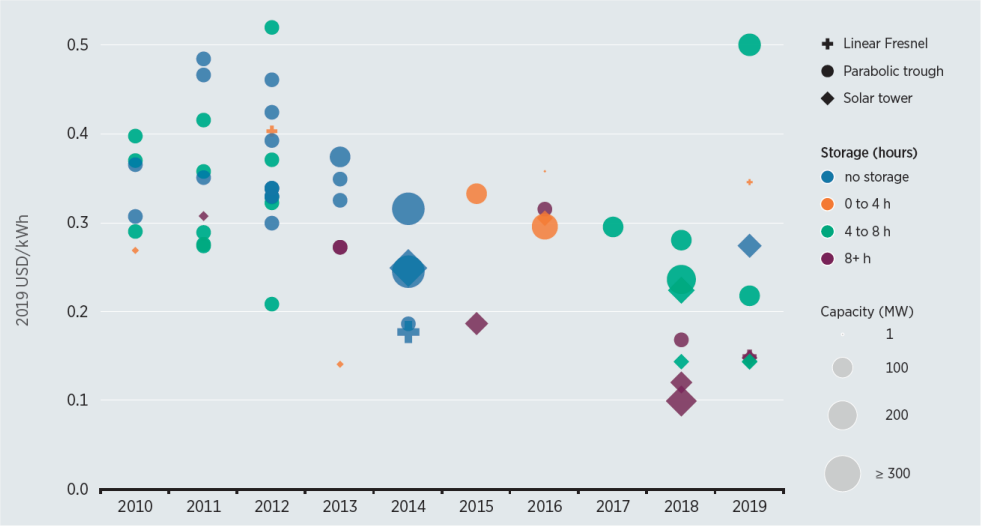

Figure 1.3: Levelised Cost of Electricity (LCoE) versus year of commissioning of a few CSP plants. Figure from IRENA ©IRENA2020 [16].

Moving back to all CSP technologies and looking at Fig. 1.3, it is clear that CSP levelised costs have suffered a decrease process, mainly and likely motivated by the higher levels of irradiance of recent plant locations [15] and by the lower total installed costs and by the higher capacity factors [16]. In the same way, those higher DNIs and higher storage capacities have been also definitive for the observed increment of CSP capacity factor [16]. Regarding future plants, average PPA tariff rate for CSP commissioned projects in 2020 and 2021 ranges between 75 and 94 USD/MWh, according to IRENA [16]. Comparing CSP technologies, from Fig. 1.3, it stands out the fact that, in 2018 and 2019, Solar Power Towers give the lowest LCoE [16, 40]. SPT plants have a bigger potential for cost decrease and a better performance when employing TES, room for improvement is higher and there are more under construction and development plants than the rest of CSP technologies, due to their technical advantages [9, 25]. In this way, among the four CSP types and for large scale generation, SPT are expected to lead the market and to be the most developed ones in the near future [11, 14, 26, 30, 41, 42, 43].

1.4 Solar Power Towers subsystems state of the art

In this Subsection a brief summary of the state of the art for research of the main subsystems that constitute solar power towers is accomplished.

1.4.1 Heliostat fields

Heliostat field accounts for around 40-50% of the total SPT plant cost and can be responsible for up to 40% of energy losses, so lot of efforts have been made for designing and optimizing it in such a way that costs could be reduced and efficiency could be improved [44, 45].

Currently, commercial heliostat units have decreased their costs until 100 USD/m^2 and a target of 75 USD/m^2 is expected for the following years [44]. Lot of different designs are under a development or test process with the objective of obtaining low cost heliostat concepts, as the STAGE-STE European project or the Heliostat Cost Down Scoping Study from Australian Solar Thermal Research Initiative (ASTRI). Several issues related to heliostat units are currently being adressed like the study of wind loads, the dimensioning, components and designs of heliostats, the canting, the manufacturing and assembly, the qualification or the heliostat cleaning [44]. Regarding heliostat materials, nowadays the most adequate option for reflectors are mirrored glasses and reflective films [46]. The optimal size of a heliostat is currently an open research subject, compromising both optical and cost issues [29, 44, 47, 48, 49]. Small heliostats have the advantage of high optical quality, lower shading and blocking in the field, feasible mass production, easily handling and installation and they are associated with smaller wind loads [21, 29]. Conversely, large heliostats can raise concentration ratio, while decreasing their number and control requirements. Nevertheless, they have to suffer very often higher wind loads [21].

Among current commercial heliostats, some designs can be mentioned like the CSIRO one which is a small heliostat made by a single facet; the Stellio heliostat, with a pentagonal shape for reducing shadowing and blocking; or designs from SENER, eSolar and Abengoa [44]. Other designs that are being researched nowadays comprise a rim drive and a carousel heliostat from DLR, a pitch/roll heliostat at Amrita University, a small sized EASY heliostat from IK4-TEKNIKER and CENER, and other two design from US National Renewable Energy Laboratory (NREL) and Stellenbosch University. All of these and possibly others constitute the next generation heliostats [44].

Placing those heliostats in a field is not trivial, therefore current research is also focused on looking for optimum optical efficiencies in heliostat fields layouts [50]. Nowadays, two different types of field layouts are being researched in SPTs: radial staggered and biomimetic, but some other configurations are also possible [50]. In radial staggered fields, the most common ones, heliostats are placed in circles with some offset with respect to the heliostat immediately in front [21, 50]. Nevertheless, cornfield configurations, where heliostats are placed one just directly behind the other, were also tested, like in *Sierra* and *Jülich* projects [21]. More recently, biomimetic layouts have been proposed by Noone *et al.* [51], in which heliostats

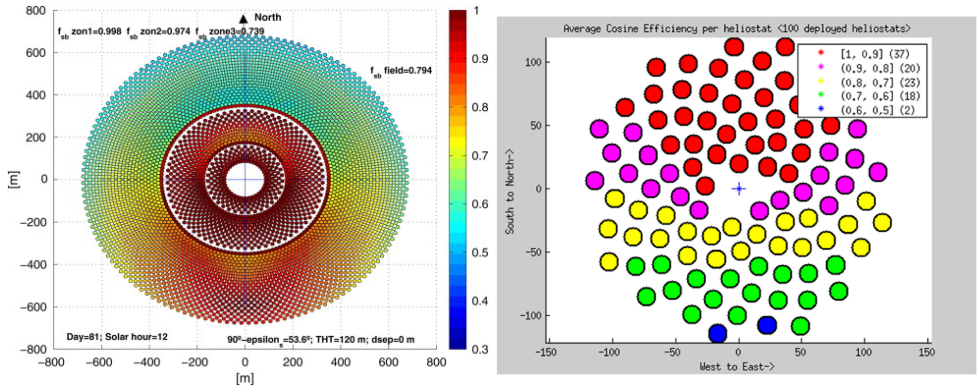

Figure 1.4: Examples of a dense radial staggered layout from *campo* code by Collado *et al.* [52] (left) and of a biomimetic heliostat field from Biomimetic software by Cruz *et al.* [45] (right).

follow a spiral pattern. An example of a radial staggered and a biomimetic layout is shown in Fig. 1.4.

A major conclusion from Barberena *et al.* [50] is that similar heliostat field efficiencies are found for different layout generation algorithms if they are optimised, but a further analysis should be done in order to check if this behaviour is kept when wider conditions are studied. However, for North fields, Zhang *et al.* [53] found that biomimetic spiral field is associated with a higher efficiency than radial staggered field, but the opposite for circular fields. It can be also highlighted that hybrid layouts combining both methods have a great potential. The implementation of those methods to large heliostats is already proved, however it is not tested for small heliostats that are ones of the components of next generation heliostats [50].

Nowadays, a big amount of software tools for generating, analysing and optimising heliostat fields have been or are being developed. Two basic categories can be distinguished: ray tracing software packages, also denominated statistical or Monte-Carlo software, and convolutional methods, called Hermite polynomials expansion methods too [29, 44]. In ray tracing software tools, specific and random solar rays are traced from the Sun to the target through heliostat reflection [44]. They are precise analysis tools that are suitable for computing accurate optical performance of a particular heliostat field [45]. On the other hand, convolutional methods compute solar flux distribution on the target from a mathematical perspective: the convolution of Sun shape together with mirror distribution errors [44]. They are often optimisation-orientated tools that give an optimum heliostat field configuration taking into account different objectives as deployment costs or land usage [45]. The advantage of

random ray tracing methods is its lower associated computational time, but this is also related to a lower accuracy [44]. Convolutional methods were developed before, but now ray tracing is dominant [44].

Tonatiuh is a very good example of ray tracing methods. It is open source and it is continuously being improved [45]. Nonetheless, codes like MIRVAL [54], SolTRACE [55], and more recently, SoFiA [56] and SPRAY [57] employ Monte-Carlo ray-tracing methods too [29].

With respect to convolution methods, *campo* code [58, 59] stands out because of its effort in reducing blocking and shadowing calculation time, thus it is employed for quick and precise field optimisations [45]. It is based on the regular radial staggered pattern [60] and tries to improve it, starting by the densest field since losses (except from blocking and shadowing) are small [50]. Then, the field is expanded, so blocking and shadowing are reduced, but the rest of losses grow, until the optimum is achieved [44]. Regarding annual optical efficiency, *campo* code layout and biomimetic pattern presented very similar performance [29, 61]. Heliostat field distribution simulations of this doctoral thesis are based on *campo* code method. Other examples of convolution methods are DELSOL/winDELSOL [62, 63], HFLCAL[64] and UHC/RCELL [29, 60].

Coupling between heliostat field and solar receiver is a key factor in SPTs. Multi-aiming strategies are a good alternative in order to not surpass receiver technical limits, as it can happen in single aiming [65]. Regarding this issue, several techniques have been presented, like the novel method developed by Sánchez González for receiver aiming based on the allowable flux density limit [65].

1.4.2 Solar receivers

Many efforts have been devoted to solar receivers design and optimisation since receivers are the key component that links heliostat field and power conversion cycle [30, 66]. Nevertheless, just a few receiver tests have been fully performed to date in demonstration plants [23], therefore more proof-of-concept tests should be performed under real weather conditions [67]. Innovative receiver concepts have been proposed operating at high temperatures with the aim of looking for more efficient receivers [19].

Tubular receivers, working both with gas or liquid, are the most common receiver concepts, specially the ones employing liquid as heat transfer medium [23, 30]. In fact, tubular liquid receivers constitute the only concept employed in large scale commercial plants [30]. In those cases, normally molten salts are employed, but they limit operating temperaure range since they decompose and solidify at temperatures higher than 600 ºC and lower than 220 ºC, respectively [68]. Concerning those receivers, innovative fluids have arisen in the last years,

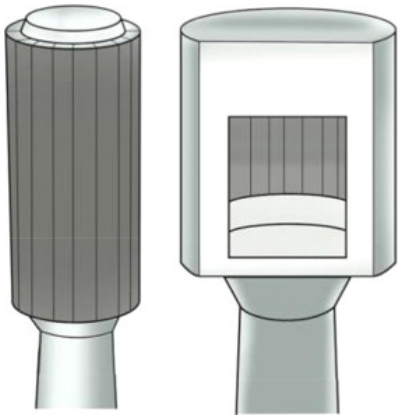

Figure 1.5: External (left scheme) and cavity (right scheme) tubular receiver concepts by Ho *et al.* [23].

namely, fluoride, chloride or cabonate salts [23]. Their performance as working fluid still have to be tested [23]. Alternatively, tubular gas receivers can withstand higher solar fluxes, which is translated to more compact receivers, and are associated with lower metal temperatures and pressure drops, but potentially higher costs [23]. Other open research area deals with tubes coatings for receivers that could improve their efficiency [66]. In an illustrative way, Figure 1.5 shows a basic scheme of both an external and a cavity tubular receiver [23] and Fig. 1.6 displays a basic diagram of different tubular receiver concept: from billboard to cylindrical and cavity [30]. *SOLUGAS* receiver, whose scheme is shown in Fig. 1.7a [27], constitutes a real example of a cavity tubular receiver. Some researchers have developed a new method for determination thermal efficiency of those cavity tubular receivers [69].

Nowadays, the best alternative to tubular receivers are volumetric receivers since volumetric effect lessens thermal radiation and reflection losses and efficiencies higher than 75% can be achieved [22, 24]. In addition, they could be simpler, cheaper and more flexible than tubular designs [24]. Lot of efforts for developing volumetric air receivers that can both operate in atmospheric pressure open cycles and in gas turbines close cycles with higher pressures have been carried out in Europe and Israel [22, 24]. According to Ávila-Marín [24], four kinds of volumetric receivers can be distinguished: open-loop with metallic (Phoebus-TSA type) or ceramic absorber (SOLAIR type), and closed-loop with metallic (REFOS type) or ceramic absorber (DIAPR type) volumetric receivers. Those efforts are being devoted because of the key advantages of air receivers, namely, non-toxic fluid, availability, highest operating temperatures, between 3 and 5 hours of TES and it is not required to trace heating [23, 24]. And they are addressed to solve main challenges associated with air as HTF: absorber durability,

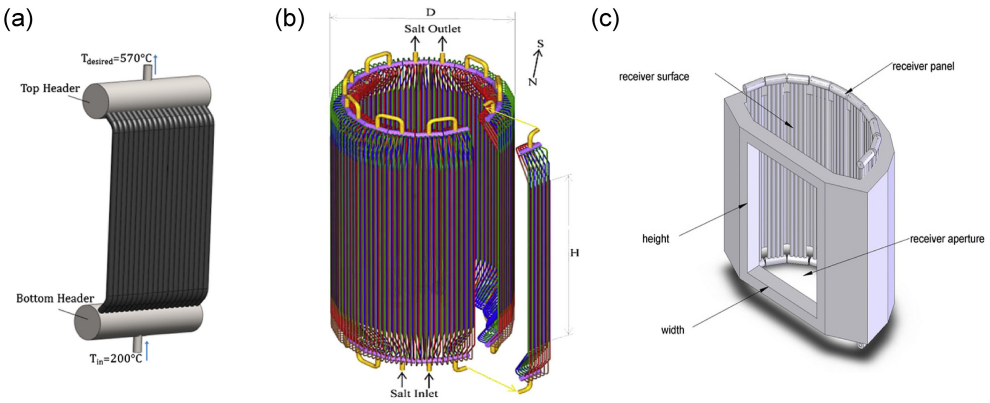

Figure 1.6: (a) Billboard, (b) cylindrical, and (c) cavity tubular receiver concepts by Conroy *et al.* [30].

efficiency, low heat capacity, potentially unstable flow and non-uniform heating, necessity of heat exchangers for TES, specific cost and windowed design for pressurised concepts [23, 24]. Those temperature dependent instabilities could be reduced if low-porosity absorber materials are employed [23]. Moreover, the usage of graded porosity materials for air volumetric absorbers has been demonstrated to have potential for reducing costs [73].

Design of a solar receiver depends on the heliostat field layout, its capacity, the HTF and its operating temperature. For instance, Brayton power cycles, the power cycle analysed in this doctoral thesis, employ very high temperatures (up to 1350 ºC) and are associated with high pressures [22]. Thus, a receiver which transmits effectively the solar heat to the pressurised air with low pressure drop is mandatory [22]. Current pressurised air receivers employ a sealed window in order to keep pressure constant, but still have some limitations [22]. In those cases, cavity receivers are proposed since external concepts are related to higher heat losses. State of the art research of those receivers have been started recently with demonstration projects like REFOS, SOLGATE or SOLTREC [70], whose receiver concepts can be observed at Fig. 1.7b). SOLTREC receiver was made by a quartz glass window, a SiSiC ceramic foams porous absorber and a second concentrator, allowing to achieve up to 1000 ºC [22, 70].

Moreover, other alternative designs denominated particle receivers comprise small particle air concepts, which can transmit heat to pressurised air for high temperature pressure cycles, and falling solid particle receivers [23]. A similar concept, but regarding liquid receivers, has been proposed: falling film receivers that account for gravity-driven fluid motion [23]. Falling solid particle receivers work with solid particles that fall meanwhile are being heated by solar radiation. Once these particles are heated, they can be stored for transmiting the energy to the

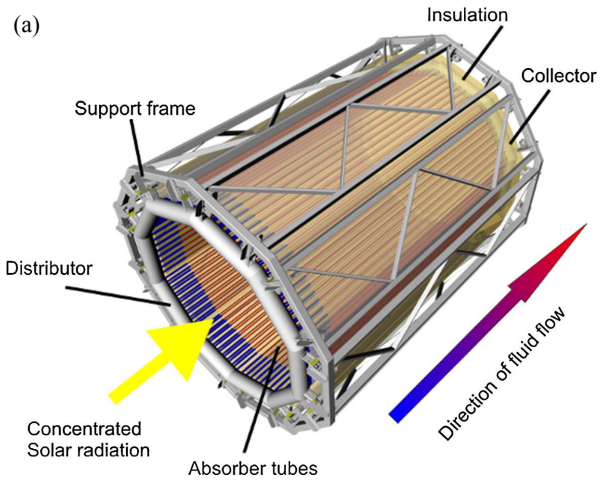

(a) *SOLUGAS* pressurised tubular air receiver by Korzynietz *et al.* [27].

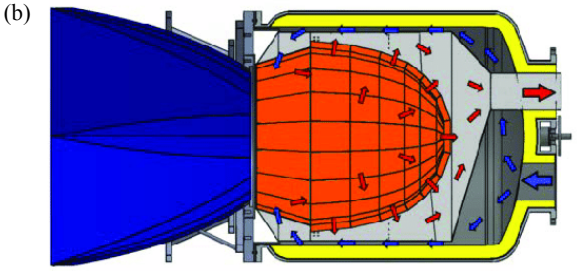

(b) SOLTREC volumetric air receiver concept by del Río *et al.* [70].

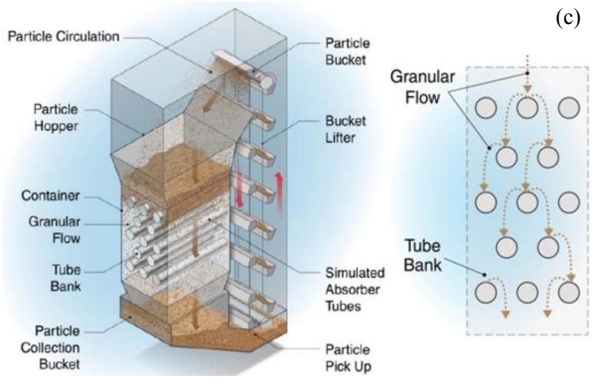

(c) Indirect solid particle receiver by Martinek *et al.* [71, 72].

Figure 1.7: Schemes of examples of different solar receivers.

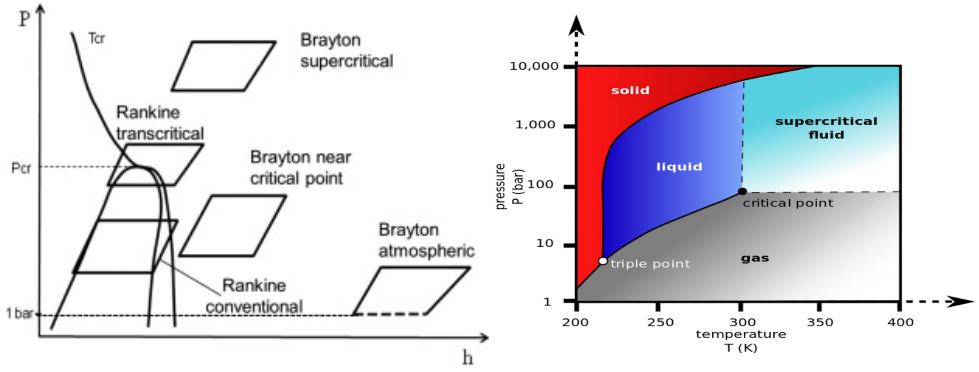

Figure 1.8: Samples of power cycles diagrams. (left) Generic pressure-enthalpy diagram for different cycles by Muñoz *et al.* [74]. (right) Pressure-temperature diagram for a CO_2 Brayton cycle by Liu *et al.* [82].

power cycle [72]. This is illustrated by Fig. 1.7c, which shows an scheme of an indirect solid particle receiver [71]. Reached temperatures are above 1000 ºC, temperature differences can be of hundreds of degrees and higher concentration ratios than in tubular concepts could be achieved and so, higher thermal efficiencies and lower costs [68, 72].

1.4.3 Thermodynamic cycles and working fluids

The next generation of high temperature receivers will allow power cycles to work with higher operating temperatures, and so, likely higher efficiency power blocks. This would lead to better overall plant efficiencies and reduced costs. In this search for better efficiency power blocks, Rankine, Brayton and combined cycles have been proposed and tested to work with several fluids such as air, carbon dioxide or helium and operating in different thermodynamic conditions (subcritical, supercritical and transcritical) for their use in Central Receiver Systems. In addition, different configurations as recompression, recuperation or partial cooling Brayton cycles have been also proposed in the literature. Some of those cycle possibilities are shown in Fig. 1.8 (left) within the framework of a pressure-enthalpy diagram [74].

In order to perform power block simulations, commercial packages [75] as TRNSYS® [76, 77], Thermoflex® [78], SAM® (System Advisor Model) [79], SolarPILOT® [80] or Ebsilon® [81] are usually employed. Nevertheless, other possibility is to develop an in-house software in some programming language with the objective of keeping control on all involved parameters, as it has been done in this doctoral thesis.

Traditional and commercial steam Rankine cycles are intended to be replaced by other innovative configurations. Reyes-Belmonte *et al.* [83] have proven that an optimised subcritical

Rankine cycle working together with a dense particle suspension solar receiver can maximize power plant efficiency, achieving values of 41% for power block efficiency. Supercritical CO_2 Rankine cycles constitute a promising technology due to their high efficiency for low-grade heat input. However, it is still necessary a deep optimisation work in order to select adequate intervals for the main plant parameters [42, 84].

Among all CSP types, the most proven technology for hybridisation with gas turbine are SPTs [85] and this interest is becoming bigger mainly because of lower water requirements and higher efficiency rates [86]. Concerning the coupling of SPTs with gas turbine power cycles, several projects have been performed. Most of those experimental plants and prototypes have been developed in Spain during the last decades. Regarding hybrid solar tower gas turbine systems, project SOLGATE [87] was the first of a series of quite interesting prototypes in Spain. It was developed between 1999 and 2003 and it showed the technical feasibility of the combination of a pressurised air volumetric solar receiver and a small scale hybrid gas turbine [87]. Afterwards, SOLHYCO project [88] was carried out from 2006 to 2010. Its main innovation was the cogeneration system based on a microturbine that could operate both with varying solar power input and fuel in parallel [88]. Finally, from 2008 to 2014, *SOLUGAS* [89] project was performed for demonstrating the solar tower hybrid gas turbine concept in a larger scale (about 5 megawatts). Expected efficiency for the open cycle was about 27% at ISO conditions [89]. Although plant operation lasted less time than expected because of different reasons, its novel hybrid gas turbine idea is one of the main basic concepts for this doctoral thesis. All those projects have a common interesting outcome: technology is feasible, however, if competitive electricity prices are desired, a bigger R&D effort is needed [90]. Other interesting projects [85] were OMSoP [91], which coupled a micro gas turbine to a parabolic dish and HYGATE [92], which deals with hybrid high solar share gas turbine systems.

Taking advantage of THEMIS facilities in France, other two interesting projects have been and are being developed at that place. First, French PEGASE project (Production of Electricity from Gas and Solar Energy) coupled hot air from a receiver directly to a gas turbine. In this context, a thermodynamic simulation model for a hybrid gas turbine system coupled with TES and a metallic cavity receiver was elaborated [75]. The stabilization of the air temperature at the inlet of the combustion chamber thanks to the integration of TES was demonstrated. Solar share was also risen due to the inclusion of TES [75]. Additionally, that TES integration allows for a higher and stable electrical production [86]. Thermodynamic efficiencies around 30% are estimated for a simple Brayton cycle [86]. After it, NEXT-CSP European project (High Temperature concentrated solar thermal power plant with particle receiver and direct thermal storage) started at 2017. This project aims to integrate a SPT with a tubular receiver, high

temperature particles as HTF and storage medium, a gas turbine and a heat exchanger able to transfer heat from the particles to pressurised air [93]. With this objective, an innovative intercooled unfired regenerative closed air Brayton cycle linked to a pressurised air receiver has been proposed [94]. It allows for a flexible electricity dispatch for solar and power demand fluctuations as a result of its pressure regulation system [94].

It has been demonstrated that CO_2 Brayton cycles are competitive against conventional cycles from efficiency and cost viewpoint [42, 95]. In Figure 1.8 (right), pressure-temperature states of CO_2 are represented together with its critical point beyond which CO_2 behaves as a supercritical fluid [82]. Supercritical carbon dioxide cycles (sCO_2) are expected to improve efficiency of gas turbines SPT systems [14], being able to reach 50% of thermodynamic efficiency [42]. The reason of these higher efficiencies lies in the behaviour of CO_2 when compressing it near its critical point. In this case, a fast variation of its properties takes place, thus compressor power consumption is decreased [42]. Furthermore, sCO_2 Brayton cycles present other advantages, as illustrated by its low molecular leakage, its stability and its non-toxicity. Additionally, it is an abundant available fluid with a low cost too and ambient temperature water could be employed as a coolant [42]. According to [96], sCO_2 has a better potential than subcritical and transcritical CO_2 for closed recuperative Brayton cycles. And it has also better higher potential than helium for Brayton cycles and superheated and supercritical steam cycles in terms of thermal efficiency [97]. Liu *et al.* [98] showed that higher overall efficiencies are found when CO_2 is employed in Brayton cycles instead of conventional steam Rankine cycles [42]. Furthermore, it has been demonstrated that sCO_2 turbomachinery can deal with short period solar fluctuations [99]. sCO_2 Brayton cycles have been researched from different perspectives, as illustrated by the energy and exergy analysis performed by Atif *et al.* [42]. From an experimental viewpoint, Solar Field (1+2) demonstration plant from CSIRO, in Australia, is testing supercritical and Brayton receiver cycles concentrating solar heat until temperatures above 1000 ºC [30, 100].

Temperature at the outlet of gas turbines coupled to SPTs are usually very high, thus trying to recover its associated exhaust heat results essential. This can be done by means of a recuperator or by coupling a bottoming cycle. The most proven combined cycle configuration is a topping Brayton cycle and a bottoming Rankine cycle. Besides water, several organic fluids can be employed in the Rankine cycle as R123, toluene, cyclohexane, isobutane or R245fa [101, 102]. A combined cycle made up by a helium closed Brayton cycle and two organic Rankine cycles was proposed by Zare *et al.*. It has been proven that its performance is better than those of Rankine and sCO_2 cycles [101]. The study also demonstrated that solar subsystem parameters are more important than power block parameters referring to the effect on overall performance [101]. At Stellenbosch University, the Stellenbosch University Solar

Power Thermodynamic cycle (SUNSPOT) was developed. Air is the HTF being heated in a CRS, then entering a gas turbine, a TES and, finally, a steam turbine [103]. A hybrid combined cycle plant based on SUNSPOT model was simulated in TRNSYS®, concluding that a reliable, stable and bankable tariff structure is a key factor for the development of solar electricity [104]. This kind of combined cycles could raise efficiency and lower cost with respect to single power block systems [22]; namely, thermal efficiency could rise from 30% to 60% [26]. In the case of *SOLUGAS* project, expected efficiency would increase from 27% to 46% ideally by implementing a bottoming cycle [89]. Additionally, combined cycles are related to better start up and shutdown performance and improved yearly records [26]. Other configurations are also possible. However, at the moment, there are no SPT commercial facilities working with combined cycles due to some technological barriers added to the gas turbines issues themselves [18, 26]. Aspects that need to be further research are techno-economy of the plant in operation and tower height influence on LCoE [26].

1.4.4 Thermal Energy Storage and hybridisation

With the objective of offsetting solar fluctuations in electric generation, different approaches can be adopted. Hybridisation with fossil or renewable fuels and Thermal Energy Storage (TES) can be used separately or combined for producing energy when there is no solar energy contribution [9]. In general and so far, 45.5 % of the operational CSP plants have TES [9]. As it was previously mentioned in Section 1.2, TES and hybridisation allow Solar Power Tower plants to work with higher capacity factors and dispatchability than other renewable energies [41]. Additionally, TES improves solar share [41]. This could be translated into 11.3 % of global electricity generated by CSP, from which 9.6 % could be associated with solar energy and 1.7 % with fuel energy, according to 2010 IEA [10]. Alternatively, the utilisation of electric storage by means of batteries is not currently a feasible option for large scale plants [41].

Thermal Energy Storage (TES)

Thermal Energy Storage systems for CSP plants have been investigated since the start of XXI century [41]. Solar Power Towers have the potential for storing much more heat than Parabolic Through Collectors [41]. Nevertheless, some key challenges must be addressed in order to become a real option for storing energy in large power capacity plants with low electricity costs in the near future [41]. In other words, some alternatives to classical temperature limits should be found, allowing the plant to work with temperatures higher than 500 ºC that could be translated into higher efficiency cycles [41]. Additionally, long term TES is required for further improving efficiency [9].

Thermal Energy Storage systems are usually divided into 3 subgroups: sensible, latent

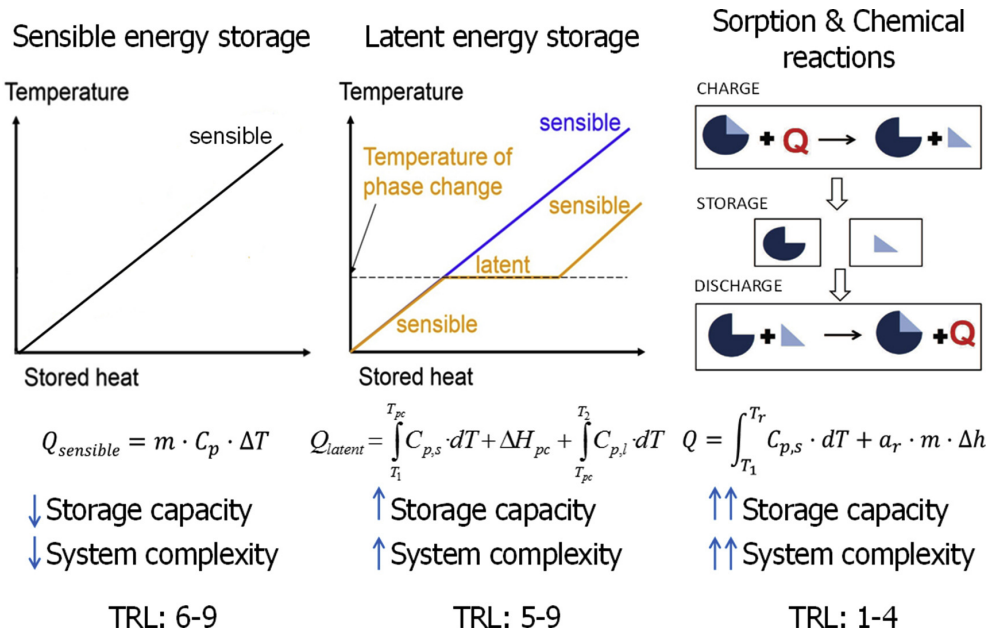

Figure 1.9: TES capacity, complexity and Technology Readiness Level (TRL) for the three main TES configurations employed in CSP plants by Palacios *et al.* [41].

and thermochemical storage. A comparison from technology complexity perspective and storage capacity is performed at Fig. 1.9. Among key desired features for TES systems, low cost, high temperatures able to couple with high efficient Brayton cycles, stability and high energy density stand out [41]. Most of commercial plants employ one tank for hot medium and another for cold medium, the so-called two tanks configuration. In order to decrease costs, some systems are intended to employ just one tank for both hot and cold storage. In this case, the separation is performed thanks to the different densities (thermocline) [105].

Storing energy by means of sensible heat is the most mature technology and it is currently commercially available as it is cost-effective and because of its simplicity from a technical viewpoint. In this case, the storing material is just heated or cooled (charge or discharge) applying a temperature gradient [41].
Sensible heat can be stored by means of liquid materials, with a share of 95.6 % of overall CSP plants employing it (and 99.8 % of installed capacity) [9], especially molten salts, which constitute the most mature TES system [41]. Molten salts are commercially available essentially since they can store high energy density during more than 20 years and 10000 cycles. This technology has a maximum limit temperature of 560 ºC imposed by the molten salts

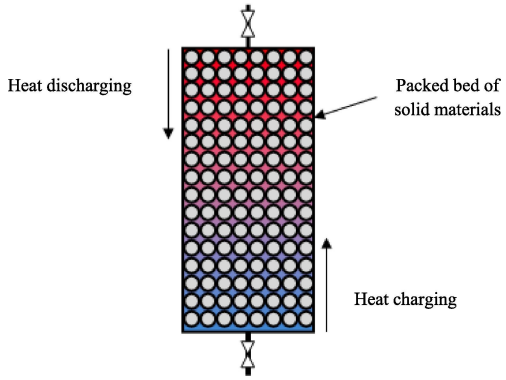

Figure 1.10: Scheme of a packed bed TES system by Achkari *et al.* [9].

theirselves. Although they have been implemented in operational plants, some aspects can be further improved as revealed by operating temperatures, optimisation and corrosion, which is currently under study through several innovative materials like ceramics or graphite [41].
In order to overcome temperature limits of molten salts, liquid metals could be a feasible alternative in the future, being able to achieve temperatures higher than 1000 ºC. However, this technology constitutes the lowest developed TES. Thus, several key issues must be addressed for a promising future. Namely, water reactivity, in particular in the case of liquid sodium, corrosivity and material costs should be coped with for a safety and feasible operation [41].
Other possibility regarding liquid sensible TES consists in adding nanoparticles to molten salts (nanofluids). Those particles increase both thermal conductivity and specific heat capacity, which implies higher energy density and lower storage volume [41, 106]. On the other hand, viscosity, instability, and pumping and material costs are also raisen. Therefore, nanofluids are not currently commercially available and need more research [41].
Nowadays, steam is the only sensible gas state system being researched and it is stored as pressurised water [41]. It is commercially available for Direct Steam Generation plants due to its high energy density, but it is attractive just for small scale generation from the economic point of view and there is no room for improvement in this area [41, 107].
Moreover, sensible heat can be also stored in solid materials as packed bed, concrete and solid particulates [41], which represent 4.4 % of operational CSP plants, being all of them demonstration plants [9]. A main feature of packed bed rocks is the possibility of employing air as HTF entering in the porous media for charging and discharging. A basic scheme for understanding packed bed sytems performance can be observed at Fig. 1.10. They stand out thanks to material stability and abundancy, and because they can be employed in a large

interval of temperatures [41, 108]. There are some commercial plants that employ this kind of TES, but there are still some open issues as its stratification problems and some pressure drops that could appear [41]. Other possibilities are supercritical beds with higher efficiency but too much higher costs than molten salts or to combine a packed bed with Phase Change Materials (latent heat) for increasing system efficiency [41, 105].
Main advantages of solid particles are their low cost, stability, low thermal losses and their high efficiencies at large temperatures [41, 109]. Nevertheless, solid particles TES has not been implemented in any commercial facility up to date due to some technical challenges like sedimentation, design of fluidized bed, material stability control and particle conveyance. If those challenges are overcome, solid particulates could become a real alternative to molten salts [41].
In the same vein, TES in concrete material could be a feasible alternative to molten salts. Within this TES features, its low cost, its performance at ambient pressure, non-toxicity and easy design can be highlighted. On the other hand, concrete can present some undesired behaviour as spalling and cracks or damage of pipes [110]. It has been already proved in some installations, but further demonstration tests regarding reliability should be performed [41].

Furthermore, storing latent heat involves phase changes of materials and has the potential for storing about eight times more energy than sensible systems [41, 111]. In the same way, technical complexity is not high [41]. Phase Change Materials (PCMs) could be organic or inorganic compounds and mixtures [112]. Currently, most mature latent systems include shell and tube PCM configurations [113]. But other layouts are being researched as cascaded, thermocline and sandwich systems [114, 115]. Nevertheless, for latent systems to be commercial there is a necessity for improving high temperature PCM encapsulation and heat transfer and to perform some parametric and optimisation analysis together with pilot tests [41].

Finally, thermochemical systems employ reversible chemical reactions for absorbing (endothermic) and releasing (exothermic) heat with the highest efficiency among mentioned systems. These systems are related to potentially high energy density and could capture atmospheric or industrial CO_2. On the contrary, they are so complex from a technical perspective that, at present times, they are not commercially available [41].

Hybridisation

As CSP plants employ conventional termodynamic cycles, other energy sources can be integrated, usually, in order to run the same power cycles. Thus, hybrid CSP plants utilize two or more energy sources: usually solar and combustion, but it could be others [116]. Hybridisation could even substitute certain degree of competition among power generation technologies by synergies. These synergies between CSP and other technologies can be light, medium and strong, depending on the degree of solar share and the importance of CSP for the

overall performance [116].

During these first stages of CSP development, to hybridise plants, especially with fuels, results essential, as a step forward before the complete deployment of CSP plants, as it has been performed with the automotive industry and hybrid cars. Apart from the already mentioned benefits, other reasons support hybrid plants: to decrease capital and electricity costs and financial and engineering risks and to enhance reliability and flexibility of operation [25, 104, 116]. In other words, key desired features of hybridised CSP plants include an increment of efficiency and a decrease of LCoE regarding single plants, larger solar shares and lower emissions than conventional fossil plants [116].

Several types of hybridisation can be implemented in SPTs since power block technology is the same as in conventional power plants. On one hand, hybridisation by means of fuel burnt is possible. Fuel can be conventional fossil like coal or natural gas, or renewable (biofuel). On the other hand, other already developed renewable technologies can be combined with CSP, namely, PV and wind [116].

Both coal and natural gas can be employed in CSP plants according to different approaches, but always producing reliable power. Nonetheless, natural gas is preferred since its combustion produces much less CO_2 and other pollutants [116]. Hybridisation with natural gas is supposed to be the most promising hybridisation technique for CSP [116], hence this strategy is followed in most of the simulations of this doctoral thesis. A Solar Hybrid Gas Turbine (SHGT) [85] could currently reach operating temperatures up to 900 ºC [117] and it has been demonstrated to be commercially and technically viable [118]. Most common layouts include open cycle gas turbines for peak power generation with efficiencies around 35-40 % and combined cycle gas turbines, which account for higher efficiencies (55-60 %) [119]. Some concepts employ both TES and hybridisation, as illustrated by the SPT air gas turbine hybridised with natural gas and employing a stone packed bed storage [120]. This system showed that an enhancement of 30 % in solar to electric efficiency could be achieved when adding hybridisation and comparing to a solar single plant [120]. A technical challenge has to be overcome when hybridising the gas turbine: the fuel air ratio has to vary in a wide interval that must be accepted by the combustion chamber [86]. Moreover, in hybrid Brayton cycles CO_2 capture mechanisms should be implemented for avoiding combustion penalties [119]. According to Peterseim *et al.* [121], SPTs seem to be the preferred option for high temperature steam systems among hybrid CSP plants. Some already mentioned interesting projects include SOLGATE [87], SOLHYCO [88], *SOLUGAS* [89] and HYGATE [92] (see Fig. 1.11 (a)), which proved that hybrid solar tower gas turbine systems are a feasible technology that requires more R&D for decreasing electricity prices [90].

Going further, fossil fuels can be replaced by biofuels from several biomass origins (as

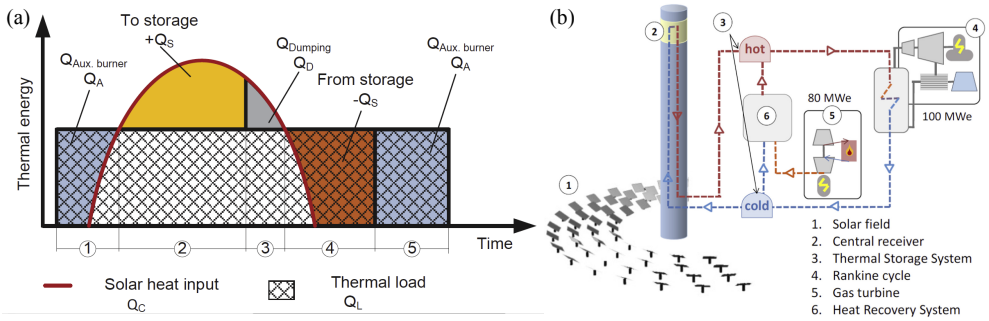

Figure 1.11: Hybridisation concepts. (a) Ideal daily performance of a solar hybrid gas turbine with TES by Puppe *et al.* [92]. (b) HYSOL plant configuration by Corona *et al.* [122].

forestry residues, wood waste or stubble) that add to the already mentioned advantages the fact that generated energy is completely renewable and sustainable [116]. Those carbon-neutral fuels are still expensive to be feasible [119]. As interesting concept, the HYSOL project [122] (see Fig. 1.11 (b)), a gas turbine hybridised with bio-derived gas, which is fully renewable can be highlighted.

Hybrid SPT plants could comprise not only fossil or renewable fuels, but also solar PV [25]. In some concepts, during solar hours, these former hybrid systems generate energy from PV and store energy to TES and then, during non-solar hours, TES is employed for generating electricity. Others employ CSP for cooling PV, which generates the electricity [116]. An interesting concept combining a hybrid SPT and PV facility together with both TES and large scale battery storage has been analysed and it was concluded that a very big reduction (around 60-90 %) of battery storage cost is needed for its integration in the hybrid plant to be feasible [123]. Hybridisation with geothermal and wind has been also proposed. Geothermal operates with low temperature, thus it has been already integrated into PTC plants, but not into SPTs [116]. Wind hybridisation with CSP is not so common and normally they are only linked at grid level, improving demand fit [116].

1.4.5 Subsystems integration

All these prototypes and studies demonstrate that there is a big amount of SPTs research projects with different perspectives. Nonetheless, most of them focus on particular subsystems of the whole Solar Power Tower plants and there are not so much research trying to analyse the overall plant as a whole and giving equal relevance to all subsystems. The importance of this subsystems integration methodology lies in the possibility of determining how certain subsystem parameters can affect other components and global plant performance in order to

look for optimum designs [86, 90, 101]. These global studies can be differentiated in three groups according to the utilization degree of commercial software codes.

From a simulation approach, some studies analyse overall plant behaviour detailing subsystems performance, which are all evaluated by means of different commercial software environments. Normally, these are very complex and realistic engineering surveys [43]. Despite being comprehensive and precise; however, this kind of approach has some disadvantages. Namely, these tools work with a big amount of parameters that are hardly managed [124]. In addition, dynamic meteorological data are not easily implemented, so just design point performance is usually evaluated [125]. Nevertheless, Barigozzi *et al.* [126] could predict dynamic performance of a SPT hybrid gas turbine by employing commercially available software tools. The solar field and the receiver were modelled using TRNSYS® [76, 77] and they were coupled to a hybrid gas turbine model implemented in Thermoflex® [78].

A mixture between those former analyses and purely academic methodologies is also carried out in the literature when some components are modelled using commercial software packages and others with the help of in-house tools. This is perfectly illustrated by Behar *et al.* [43], who modelled a hybrid SPT combined cycle with TES employing different software codes. Although, fluidized bed TES heat exchanger and gas turbine have been studied thanks to different theoretical equations, heliostat field was modelled through SolarPILOT® [80] and linked to receiver geometry employing Solstice [127], a ray-tracing code [43].

On the other hand and to the best of our knowledge, in-house simulations based on theoretical calculations and that deal with the global plant detailing each subsystem behaviour are currently scarce. This other academic methodology presents some benefits, namely, the simplicity and flexibility, the total control of all plant variables, the reduced number of input parameters and the possibility of defining global optimisation strategies [124, 128].
In this way, Grange *et al.* have emphasised the importance of models that couple TES with the rest of the plant in order to study the dynamic interaction of storage with other plant subsystems [75]. With this goal, they developed a simulation code for the overall plant, which is established via enthalply, energy and mass balances [86]. Moreover, Zare *et al.* analysed an innovative combined cycle from a thermodynamic perspective via Engineering Equation Solver® (EES) [129] and proved that the effect on overall power plant performance of solar subsystem parameters have a larger impact than those of power cycle [101]. Conversely, a study from our research group, which was also in-house programmed via Mathematica® software [130], showed that heat engine enhancements have a significant influence on overall thermal efficiency [43, 120, 125]. But an increase of solar subsystem efficiency can also diminish fuel consumption, which is followed by an operation costs decrease [125]. Therefore, there are still some discrepancies referring to which subsystem

improvement can lead to better overall performance records, which shows that this is still an open research area.

1.5 Open ongoing challenges overview. Doctoral thesis motivation

On the whole, it is clear that there is still margin for innovation in Concentrated Solar Power plants [12]. Broadly speaking, stable and reliable power production, deployment support, and expected decrease of electricity costs are the main factors that make CSP a future alternative among other renewable energies [12]. Nevertheless, current higher electricity costs of CSP regarding other more conventional technologies and unsure policies are still a big handicap for its development [12].

As it has been previously mentioned, optimal heliostats dimensions constitute presently an active research topic in SPTs since a compromise between optical and cost issues is required [29, 44, 47, 48, 49]. Most typical heliostat field layouts are radial staggered where room for improvement is not high. However, hybrid layouts mixing radial staggered and biomimetic spiral field have a great potential [50]. Another research field still open corresponds to innovative methods for calculating and analysing heliostat field performance, as revealed by the goal of lowering blocking and shadowing computational costs [45]. Additionally, heliostats aiming to solar receiver strategies are still being investigated with the goal of uniformly distributing solar flux on the receiver [30, 65, 131].

Nowadays, one of the major active research fields in SPTs are solar receivers. The search for highly efficient solar receivers that can work at high temperatures, for coupling with high efficient power cycles, is still open [19]. Even tubular receivers, the most common ones, present margin for improvement. In particular, different fluids are being tested in tubular liquid concepts [23] and different coatings are being proposed for increasing their efficiency [66]. On the other hand, volumetric receivers, which constitute the best alternative to tubular receivers, still need to cope with the main challenges related to air as Heat Transfer Fluid. Those challenges were formerly described in Section 1.4.2 and they are basically absorber durability, efficiency, low heat capacity, potentially unstable flow and non-uniform heating, necessity of heat exchangers for TES, specific cost and windowed design for pressurised concepts [24, 22, 23]. Furthermore, particle receivers have been proposed as other interesting alternative receivers that still require further investigation [23]. Moreover, more experimental tests in demonstration plants are required, in particular paying attention to real weather conditions performance [23, 67].

For power cycles, Rankine ones are highly mature, so room for improvement is scarce and research is focused on subscritical layouts [83] and supercritical CO_2 Rankine configurations [42, 84]. On the other hand, Brayton cycles can still enhance power plant performance

thanks to their higher working temperatures [86]. However, their development depends on the search of adequate solar receivers and these cycles still need to be tested. Different layouts and working fluids at different conditions, including supercritical CO_2, are being proposed [42, 95]. In this former case, sCO_2 turbomachinery should be adequately developed. Additionally, combined cycles are nowadays being researched and face the same challenges as Brayton cycles added to some others as the plant techno-economy in operation, thus there are no runnning commercial facilites [18, 26].

The other major open research challenge is the development of efficient and reliable TES systems. Lot of challenges must be dealt with for TES in order to become a real viable option in which refers to store heat at large scale for SPTs [41]. Temperature limits should be enlarged with the objective of allowing high efficient power cycles [41]. Besides low costs, stability and high energy density have to be also achieved [41]. Although being the most mature technology, molten salts can still be improved regarding operating temperatures, optimisation and corrosion [41]. Thus, new mixtures are being looked for with high temperature stability and smaller solidification temperatures features [132]. In general, liquid metals and nanofluids need to solve several issues, like material costs and instability, for increasing their maturity level [41]. On the contrary, there is no room for improvement regarding steam sensible TES [41, 107]. Alternatively, solid material sensible TES, such as packed bed that requires to cope with stratification issues and pressure drops, are being proposed [41]. However, solid particulates are not going to be commercially avaliable until some challenges as sedimentation and stability could be addressed and the same for concrete and its spalling and pipes damage issues [41, 110]. Regarding latent TES, high temperature PCM encapsulations and heat transfer have to be dealt with [41]. Lastly, thermochemical storage has to face technical complexity as its main handicap [41].

Regarding SPT fuel hybrid plants, a wide interval variation of the fuel air ratio that must be accepted by the combustion chamber constitutes one of their main challenges [86]. Additionally, diminishing electricity prices results also essential [90]. Alternatively, biofuels are still expensive [119]. In addition, integration of both TES and hybrid technologies can be improved for a flexible, reliable and ecological electricity dispatch [133].

In general, more experimental tests, especially for gas turbines coupled with high efficiency receivers working in hybrid mode and with TES, are required for SPTs further development. Studies coupling all plant subsystems and analysing how they are affected among them or how they influence overall plant parameters are still scarce from simulation perspective, in particular for in-house codes. Therefore, theoretical studies and simulations for global plant and particular subsystem behaviour are still mandatory for evaluating intra- and inter-influence of some subsystem and the effect of the coupling of those subsystems. In addition, optimisation

of overall plant performance could lead to the expected and required efficiency improvement and costs reduction. This is the main motivation for the development of this doctoral thesis.

1.6 Doctoral thesis objectives

The topic of this doctoral thesis is Concentrated Solar Power tower plants working with gas turbines in hybrid conditions. Therefore, the overall objetive is to develop a theoretical model for this kind of power plants; then, to implement it in an in-house code and to validate its outputs. Afterwards, to perform different simulations looking for improved designs and to highlight most significant results. Finally, the most relevant conclusions and open questions for future studies will be summarized.

Within these goals, some specific objectives are defined:

A. To develop a theoretical model, which fulfils next general features, for all subsystems integrating the plant:
   - Simplicity.
   - Reduced number of input parameters, with clear physical meaning each in order to easily handle all plant variables.
   - Analytical (or semi-analytical easy to compute) expressions for plant performance.
   - Flexibility.
   - To integrate real metereological data.
   - To allow for dynamic simulations.

   Additionally, this theoretical model is aimed to describe the performance of Solar Power Tower hybrid simple gas turbine plants, incorporating also:
   1. The possibility for both recuperative and non-recuperative layouts.
   2. Temperature dependent specific heats.
   3. The possibility for multi-stage configurations.
   4. The possibility for different working fluids.
   5. A coupled solar subsystem model (heliostat field and receiver), with precise optical efficiency calculations for the heliostat field.
   6. Different heliostat field layouts (surround and polar fields).
   7. A thermo-economic model.

B. Then, to implement the theoretical model in an in-house developed code programmed in Mathematica® language employing real meteorological and plant data.

C. Afterwards, to validate the model both with real data and with commercial software (Thermoflex® [78], *campo* code [58, 59]).

D. To address several types of simulations:
   - Dynamic simulations: daily, seasonal and annual.
   - Thermodynamic studies.
   - Losses evaluations.
   - Sensitivity analyses.
   - Pre-optimisation studies.
   - On-design and off-design analyses.

   All these results can be analysed from thermodynamic viewpoint: heat rates, temperatures, efficiencies and solar share; and from thermoe-conomic perspective: fuel consumption, pollutant emissions, capital costs, Levelised Cost of Electricity (LCoE).

E. Finally, to obtain main conclusions from doctoral thesis.

Two different sorts of gas turbine SPTs are tested in this doctoral thesis according to heliostat field type and size and to power scale. First, a small scale power output plant delivering to the grid approximately 5 MW is analysed. This gas turbine is coupled to a small polar field set up by 69 heliostats and a cavity receiver. A plant very similar to *SOLUGAS* project [89] is assumed as the base case for numerical implementation. Afterwards, a larger scale plant of around 20 MW is surveyed. This plant is fed by a surround field of about 1000 heliostats and an external receiver. In this case, a plant similar to *GEMASOLAR* is chosen [32] for the modellization. Nevertheless, gas turbine is kept instead of steam cycle developed by *GEMASOLAR* plant and number of heliostat is lower than half the original (2650).

A key objective of this doctoral thesis is the search of better thermodynamic plant records in order to improve overall efficiency, and so produced energy for the generated electricity to be more feasible and bankable. Broadly speaking, this study is intended to help in the pre-design of hybrid gas turbine Solar Power Tower plants, as a first concept and approach for paving the way for future commercial plants.

1.7 Doctoral thesis outline

Chapter 1 presents an introduction of the doctoral thesis subject: thermodynamic optimisation of solar central tower power plants working with hybrid Brayton cycles. At Chapter 2, thesis report is shown, detailing connections among related papers. In Chapter 3, all doctoral thesis papers are included with a brief summary in Spanish. Chapter 4 deals with other research articles not directly associated with the thesis. Main conclusions of doctoral thesis are summarized at Chapter 5 together with the open prospects and future work. Finally, three annexes are appended to the doctoral thesis. Appendix A shows the quality of appended publications, Appendix B details performed dissemination activities, and Appendix C accounts

for internships developed during doctoral thesis process.

Chapter 2. Doctoral thesis report

Doctoral thesis work is structured following flow diagram in Fig. 2.1, which describes the adopted work flow and some methodological elements. This summarized report is structured as follows. First, the theoretical model is developed (Section 2.1) and, then, implemented in an ownly developed code (Section 2.2). In a subsequent step, the model is validated (Section 2.3). And, finally, the main analyses, obtained results and discussions are summarized (Section 2.4).

A major part of this doctoral thesis has been compiled on [90] (*Paper 5*), thus this report is mainly based on it. Nevertheless, important contributions from other published papers are also highlighted and mentioned. As a reference guide, the most relevants points of the indexed publications relative to this doctoral work are hereby sketched:

Paper 1 [128]. Thermodynamic theoretical model is developed and applied to a *SOLUGAS*-like plant. Dynamic calculations are performed (daily and seasonal simulations).
Paper 2 [125]. Annual simulations and heat losses evaluation are conducted.
Paper 3 [124]. The theoretical model for the power unit is enhanced by considering the specific heats as temperature dependent.
Paper 4 [134]. Multi-stage layouts for the power unit are developed. Also, several fluids at sub-critical conditions are analysed.
Paper 5 [90]. Solar subsystem model is added, thus the model for the whole plant, including all subsystems, is fulfilled. The model is applied to a plant similar to *GEMASOLAR* (surround field).
Paper 6 [135]. Solar subsytem model is applied to a polar field (*SOLUGAS*-like plant).
Paper 7 [136]. Thermo-economic model is added. Numerical estimations of LCoE are performed for a *SOLUGAS*-like plant. The influence on LCoE of main plants design parameters is accomplished.

Apart from these publications, other two book chapters and a published proceeding are appended in Chapter 3. It is important to note that theoretical model has been applied to a

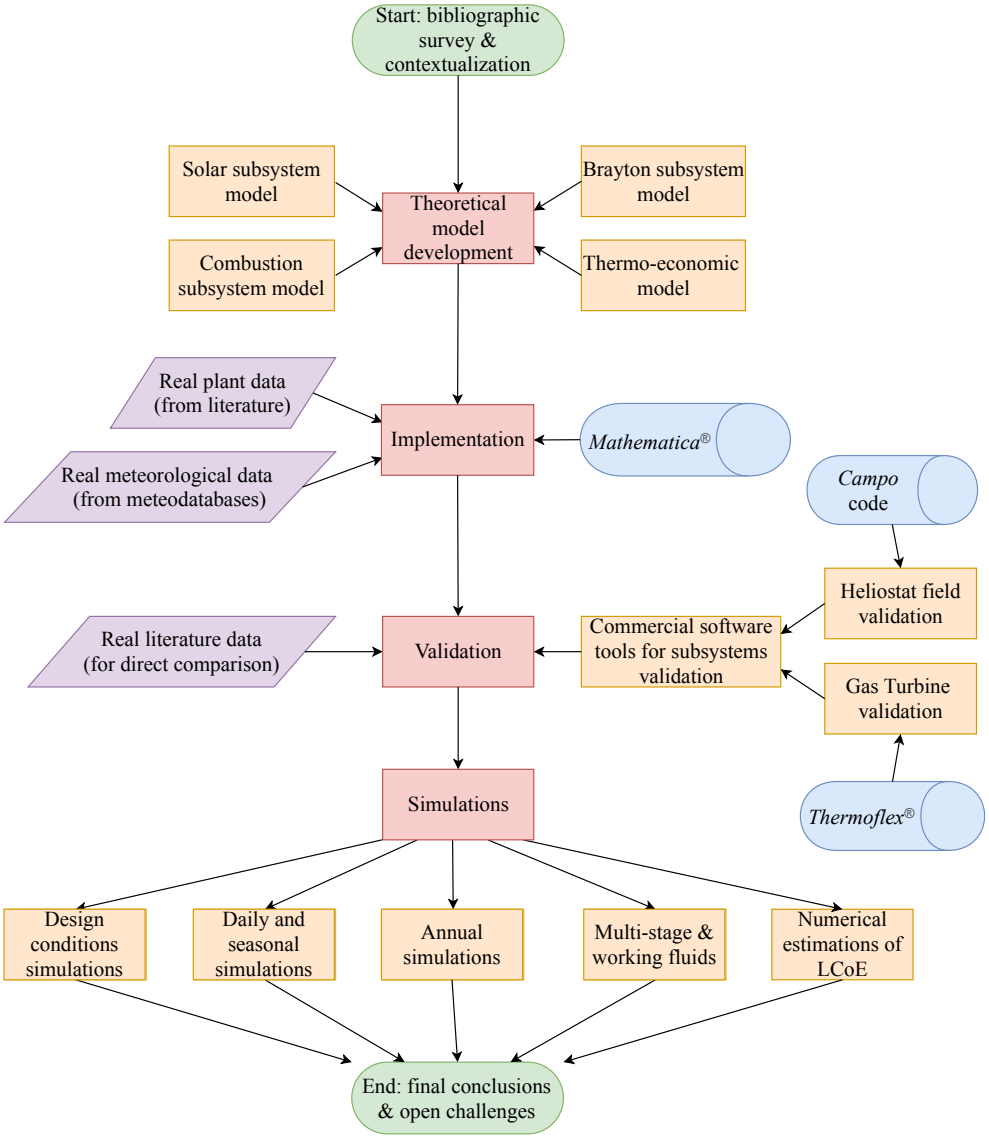

Figure 2.1: Flow diagram of the doctoral thesis work structure. Cylinders represent external software used for implementation and validation purposes and rhomboids refer to external data required for numerical computations.

SOLUGAS-like plant in all papers, with the only exception of *Paper 5*, which is devoted to a plant similar to *GEMASOLAR*. This issue is fully explained at Subsection 2.2.1.

2.1 Plant model

In this Section, the general theoretical model for a Solar Power Tower coupled with a hybrid multi-stage gas turbine developed in this doctoral work is briefly summarized. Further details of the proposed model can be found in [90] (*Paper 5*). In this model, a heliostat field is considered to concentrate solar radiation into a solar receiver atop a central tower. Then, solar high temperature heat is released by the solar receiver to a working fluid that performs a Brayton cycle. The following general assumptions are made:

- The plant is intended to operate as a baseload. Therefore, a stable power output is required and achieved by fixing turbine inlet temperature. Oscillations in solar irradiation are compensated by means of hybridisation with a combustion chamber.
- The cycle is closed, thus heat exchangers are required.
- All heat exchangers are non-ideal.
- Multi-stage configuration imposes the employment of a reheater between each pair of turbines and of an intercooler between each pair of compressors.
- Inlet temperature for all turbines is assumed the same. In a similar way, the same inlet temperature is taken for all compressors.
- Cycle components (turbomachinery) are assumed as non-ideal. Losses are internal (there are not heat transfers from compressors and turbines to the ambient) and quantified through isentropic efficiencies.
- There exist pressure drops in heat input and heat release processes.
- The working fluid developing the Brayton cycle is an ideal gas with temperature dependent specific heats.
- Combustion is not explicitly solved.
- Reflectivity, shadowing and blocking effects are considered as constant and equal for the whole heliostats set of the field.

A diagram of the considered plant is shown in Fig. 2.2, where three main subsystems can be observed: solar (heliostat field and receiver), combustion chamber and heat engine. In this model, a working fluid is considered to perform a closed multi-stage Brayton cycle composed of four main stages:

1. First of all, the working fluid is compressed via N_c compressors, increasing its temperature and, of course, its pressure.
2. Working fluid temperature is further increased in a three substages heat absorption process. First, a recuperator releases excess output turbine heat to the working

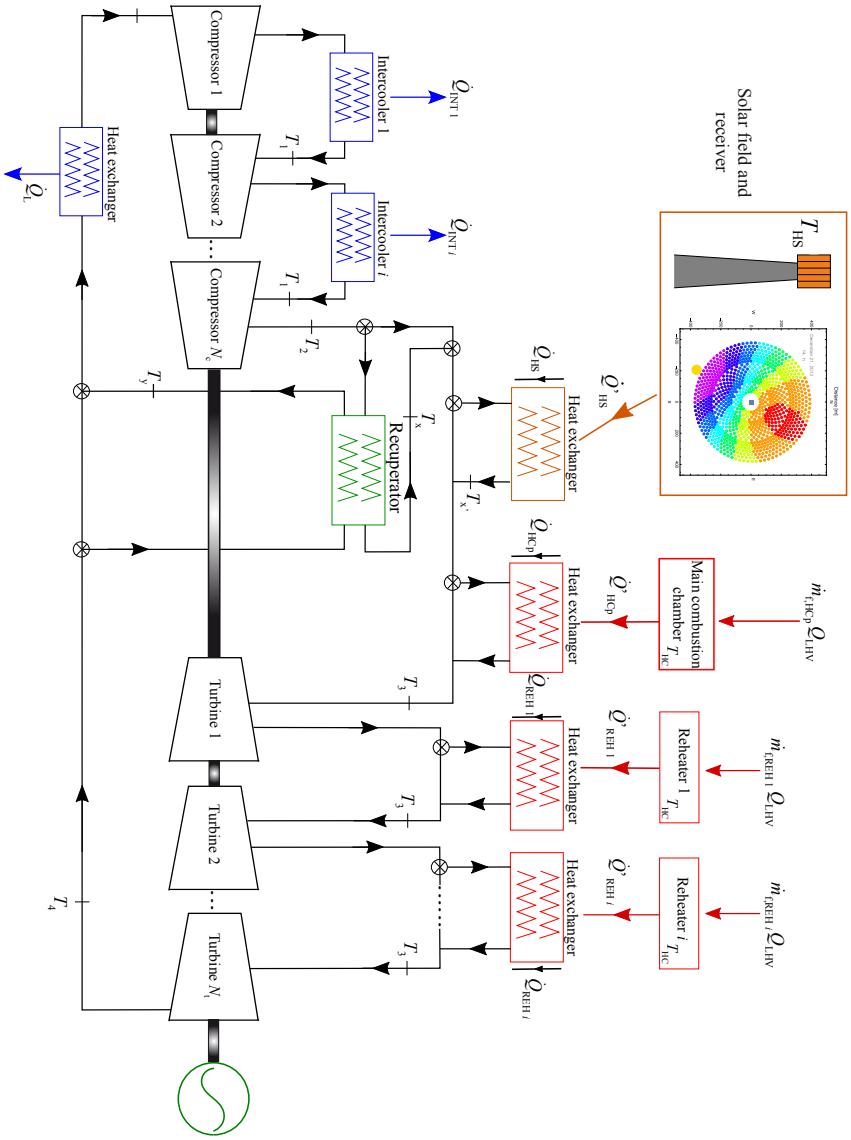

Figure 2.2: Diagram of the considered SPT hybrid gas turbine power plant model [90] (*Paper 5*). Three subsystems can be distinguished: solar field and receiver in the top left part and inside an orange rectangle; main combustion chamber and reheaters in the top right part and in red; and heat engine in the bottom part. Required heat exchangers for closing the cycle are also shown. An arbitrary number of compressors (N_c) and turbines (N_t) is displayed, with an intercooler between each two compressors and, in the same way, a reheater between each two turbines.

fluid. Then, this working fluid is heated by a solar receiver, on which heliostat field concentrates solar radiation. Lastly, if solar heat input is not enough to reach pre-fixed turbine inlet temperature, a combustion chamber exchanges heat with the fluid in order to complete and stabilize solar heat input before turbine inlet.

3. Afterwards, N_t turbines expand the fluid, thus mechanical energy is obtained.
4. Finally, excess heat is released by means of the recuperator and another heat exchanger for closing the cycle.

In this way, the general model is composed of three submodels. As it will be shown, overall plant efficiency (Subsection 2.1.1) can be obtained as a combination of subsystems efficiencies: solar (Subsection 2.1.2), combustion (Subsection 2.1.3) and heat engine (Subsection 2.1.4) subsystems models. Furthermore, to perform thermo-economic estimations, a devoted work scheme will be presented (Subsection 2.1.4).

2.1.1 Overall efficiency

For the whole system, an overall thermal efficiency (see Eq. (2.1)), η, is defined as the net mechanical output power, P, divided by the total input energy flux to the system, which has two main contributions due to the hybridisation. The solar term is characterised by the solar direct normal irradiance, G, and by the aperture area of the solar heliostat field, A_a. On the other hand, combustion heat flux depends on both the total fuel mass flow consumed in the main combustion chamber and in the reheaters, $\dot{m}_f$, and the fuel lower heating value, Q_{LHV}. Besides overall efficiency, solar share parameter (f), which accounts for the ratio of the solar to the total heat input, is included with the objective of expressing overall efficiency in terms of main involved efficiencies (see Eq. (2.1)):

$$\eta = \frac{P}{GA_a + \dot{m}_f Q_{\mathrm{LHV}}} = \eta_h \eta_s \eta_c \left[\frac{\varepsilon_{HS}\varepsilon_{HC}}{\eta_c f \varepsilon_{HC} + \eta_s (1-f)\varepsilon_{HS}} \right] \tag{2.1}$$

where η_h, η_s and η_c are the heat engine, solar and combustion subsystem efficiencies and ε_{HS} and ε_{HC} represent the solar subsystem and the combustion chamber heat exchangers effectivenesses. Intermediate equations and definitions can be found in [128] (*Paper 1*). All these contributions are considered time dependent in nature, *i.e.*, subsystem efficiencies and overall plant efficiency are fluctuating quantities. Time dependence arises from variations in the solar irradiance and in the ambient temperature.

Apart from the overall efficiency and the solar share, another general performance parameter is defined in the model: the fuel conversion rate, r_e (see Eq. (2.2)). This parameter stands for the overall performance, but taking into account just the energy input with an economical cost; that is, the fuel. For its computation, Heywood's definition [137] has been followed

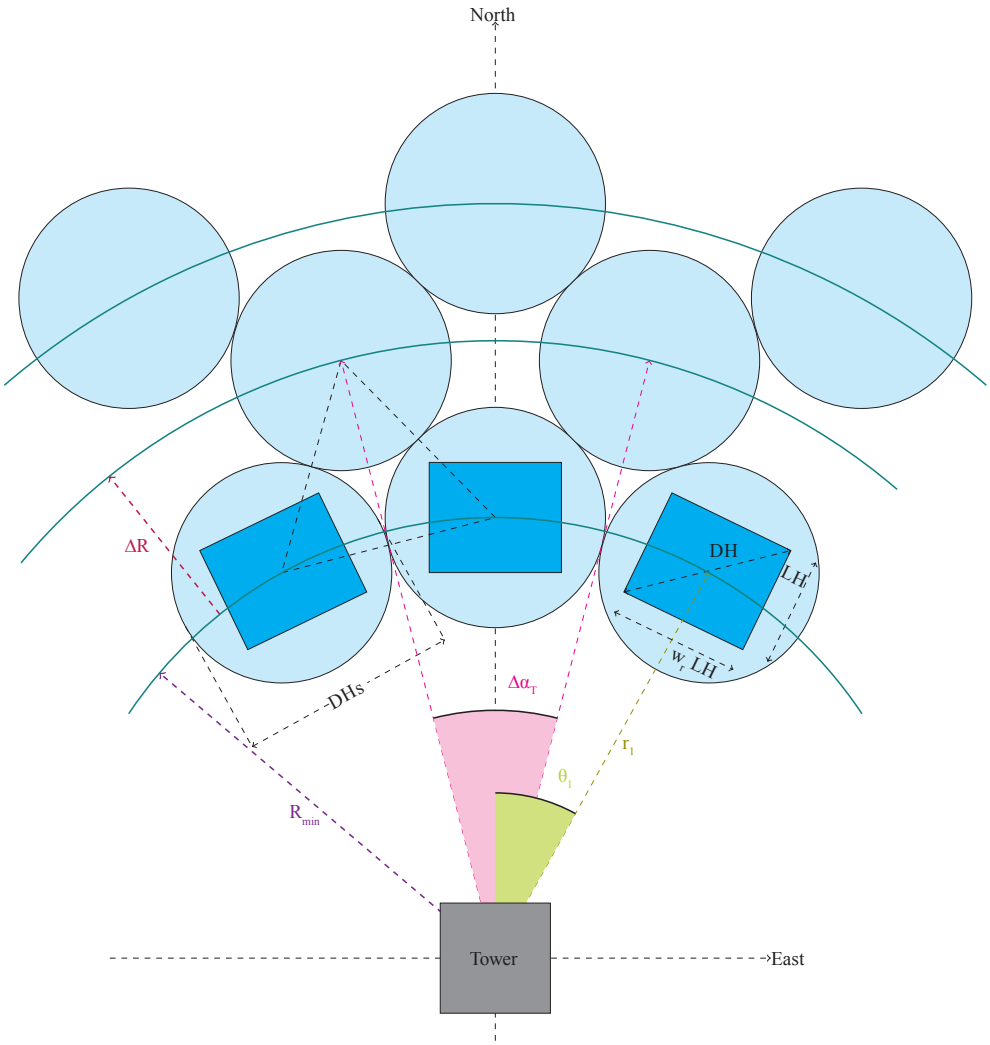

Figure 2.3: Radial staggered heliostat field distribution with some geometric parameters [90] (*Paper 5*).

(see [128], *Paper 1*).

$$r_e = \frac{\eta\,\eta_s\,\eta_h\,\varepsilon_{HS}}{\eta_s\,\eta_h\,\varepsilon_{HS} - \eta\,f} \tag{2.2}$$

which implies $r_e = \eta$ for a pure combustion operating mode ($f = 0$) and $r_e \to \infty$ in the case of only solar operating mode ($f = 1$).

2.1.2 Solar subsystem model

In this model, solar subsystem is composed of a heliostat field and a receiver. Heliostats are distributed in a radial staggered field (see Fig. 2.3). Moreover, solar receiver is supposed to be external when a surround heliostat field distribution is modelled and cavity for a polar layout. A general description of solar losses on both systems is carried out. In this way, solar subsystem efficiency, η_s (see Eq. (2.3)), accounts for the optical heliostat field efficiency, η_0, and solar receiver heat transfer energy losses due to conduction, convection and radiation [124] (*Paper 3*).

$$\eta_s = \eta_0 - \frac{1}{GC}[\alpha\sigma(T_{HS}^4 - T_L^4) + \overline{U}_L(T_{HS} - T_L)] \tag{2.3}$$

where C is the concentration ratio, α is the receiver surface emissivity, $\overline{U}_L$ is the effective overall conduction and convection heat transfer coefficient, and σ is the Stefan-Boltzmann constant. In addition, T_{HS} and T_L are solar collector and ambient temperatures, respectively.

Then, the solar subsystem model was further improved focusing on the heliostat field (see Figs. 2.3 and 2.4 (a)) by computing its efficiency [90] (*Paper 5*). In order to evaluate the average heliostat field efficiency, each heliostat efficiency, η_{hel_i}, is defined in terms of the six losses factors (see Eq. (2.4)): shadowing (f_{sh}), cosine ($cos\,\omega$), reflectivity (ρ), blocking (f_b), attenuation (f_{at}) and spillage (f_{sp}) factors (see Fig. 2.4 (b)).

$$\eta_{hel_i} = cos\,\omega \cdot f_{sh} \cdot f_b \cdot \rho \cdot f_{at} \cdot f_{sp} \tag{2.4}$$

In order to reduce computational times, shadowing and blocking factors are assumed as constant. This assumption is usually carried out in literature due to the complexity of its computation [138, 139]. In the same way, heliostats reflectivity is taken as constant. Alternatively, cosine and attenuation models and their specific equations can be found at [90] (*Paper 5*). Additionally, spillage factor is determined following Collado *et al.* methodology [140], thus spillage dependence on receiver dimensions, heliostat area and effective dispersion of sun shape on the receiver plane are taken into account. Moreover, spillage computation [58] has been further enhanced by considering heliostat tracking and surface errors too, but not astigmatic effect [135] (*Paper 6*).

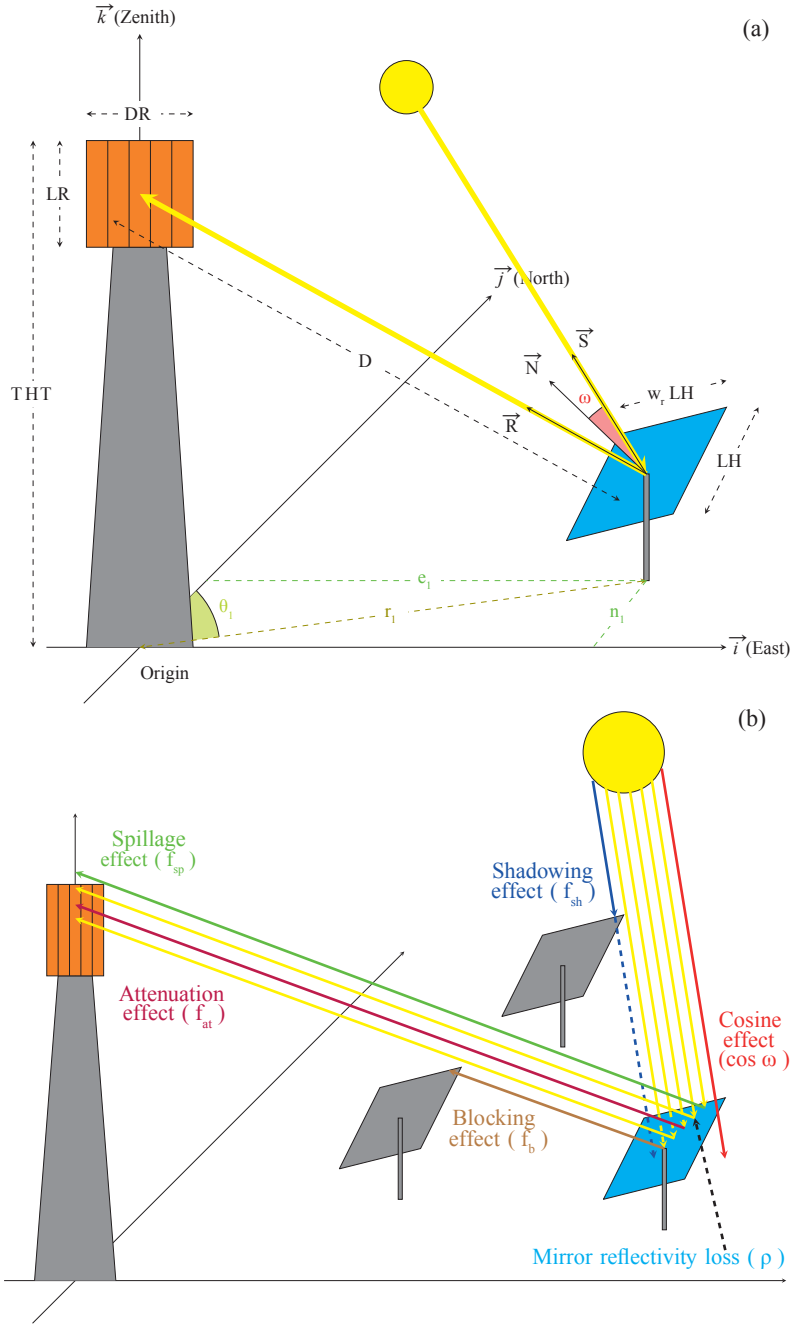

Figure 2.4: (a) Heliostat reference frame with some field geometric parameters and (b) main heliostat field energy losses factors [90] (*Paper 5*).

2.1.3 Combustion subsystem model

Fuel mass flow burned in the main combustion chamber varies with time in order to rectify solar fluctuations and to reach a stable turbine inlet temperature. Additionally, the computation of total fuel mass flow allows for the evaluation of directly emitted pollutant gases. In particular, CO_2, CH_4 and N_2O greenhouse emissions are estimated in the model.

The efficiency of both the main combustion chamber and of all reheaters, η_c, is assumed as constant and equal in both cases. This efficiency takes into account the non-ideality of the combustion and the heat losses in the combustion chamber itself. Moreover, the effectivenesses of the associated heat exchangers, ε_{HC}, are also considered as equal. A more detailed description of this subsystem is included in [90, 124] (*Paper 5* for the multi-stage model and *Paper 3* for the single model).

2.1.4 Multi-stage Brayton cycle model

Multi-stage Brayton power cycle has been introduced for the first time in [134] (*Paper 4*), but single stage heat engine model was presented in previous works too [128, 124] (*Paper 1* and *Paper 3*).

The developed model considers a working fluid performing an irreversible recuperative multi-stage Brayton cycle that behaves as an ideal gas with mass flow rate, $\dot{m}$, and temperature dependent specific heats, $c_w(T)$. The corresponding temperature-entropy diagram can be observed in Fig. 2.5. In this model, the N_c compressors and the N_t turbines are modelled via isentropic efficiencies, ε_c and ε_t, respectively. Inlet compressors temperature, T_1, is the same for all of them since an intermediate intercooler is placed in between each pair. In the same way, intermediate reheaters are employed between turbines with the aim of keeping turbine inlet temperature, T_3, constant and equal for all turbines. Additionally, a constant efficiency recuperator (ε_r) is supposed, which turns to zero in non-recuperative operating mode. Furthermore, in both heat absorption and release processes, pressure decay is modelled globally through ρ_H and ρ_L parameters, respectively, although each substage has its own pressure losses. With these ingredients, a global pressure ratio can be considered, r_p.

An essential feature of the model is that analytical and explicit equations are obtained in terms of a set of main geometric and irreversibilities parameters. These equations describe all cycle temperatures and, through them, all output plant parameters, such as heat rates, power output and heat engine efficiency.

2.1.5 Thermo-economic approach. Computation of LCoE

As it was mentioned in the Introduction (Section 1.3.4), the Levelised Cost of Electricity (LCoE) constitutes a key economic indicator that represents the minimum price at which

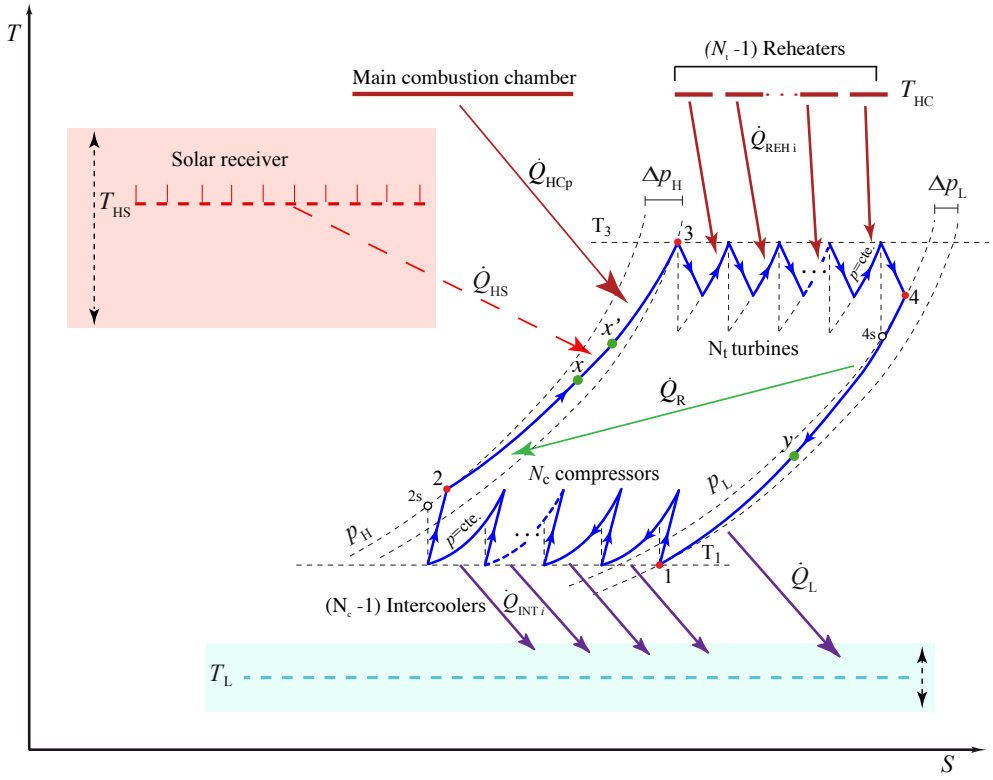

Figure 2.5: T-S diagram of the multi-stage Brayton cycle in the modelled plant [90] (*Paper 5*).

generated electricity should be sold during operational period for the power plant in order to be profitable. In this model, plant costs are divided into investment and initial installation costs (C_{inv}), also denominated capital costs, decommissioning costs (C_{dec}) and operation, maintenance and labour costs (C_{OML}), as it is illustrated by Fig. 2.6. This LCoE computation (see Eq.(2.5)) is based on Spelling's doctoral thesis [138] and it has been adapted to the particular conditions of the study, hence some modifications have been carried out. All the details are addressed at [136] (*Paper 7*).

$$\text{LCoE} = \frac{\beta_{\text{inv}} C_{\text{inv}} + \beta_{\text{dec}} C_{\text{dec}} + C_{\text{OML}}}{E_{\text{net}}} \tag{2.5}$$

where β_{inv} factor relates total capital costs to equivalent annual amount for refunding the initial credit and β_{dec} associates decommissioning costs with the equivalent yearly accumulated amount required for decommissioning. Moreover, E_{net} refers to the net energy generated in the plant during a whole year.

2.2 Model implementation

The proposed general and theoretical model has been implemented in an in-house developed code, which has been programmed in Mathematica® language. Numerical, meteorological and working fluid data sources for the model implementation are mentioned in next Subsections.

2.2.1 Numerical implementation

The proposed model has been applied to diverse situations, basically ranked by the two different kinds of heliostat fields: a polar field (*SOLUGAS*-like plant) and a surround field (similar to *GEMASOLAR* plant). Then, modications of configurations and layouts have also been performed. In both cases, natural gas is assumed as the fuel for hybridisation.

SOLUGAS-like plant

Theoretical model has been applied first to a *SOLUGAS*-like [89] plant, with a polar heliostat field pointing to a cavity receiver and at a pre-commercial power scale (4.77 MW_e). Main solar subsystem parameters implemented in the code are gathered at Table 2.1. Regarding gas turbine, *Mercury 50* turbine from Caterpillar [141] is assumed, the same as in *SOLUGAS* project. This numerical implementation is broadly presented at [128, 135, 136] (*Paper 1*, *Paper 6* and *Paper 7*), where details of input data sources from literature are given. In [136] (*Paper 7*), LCoE employed parameters and corresponding literature data are collected as well.

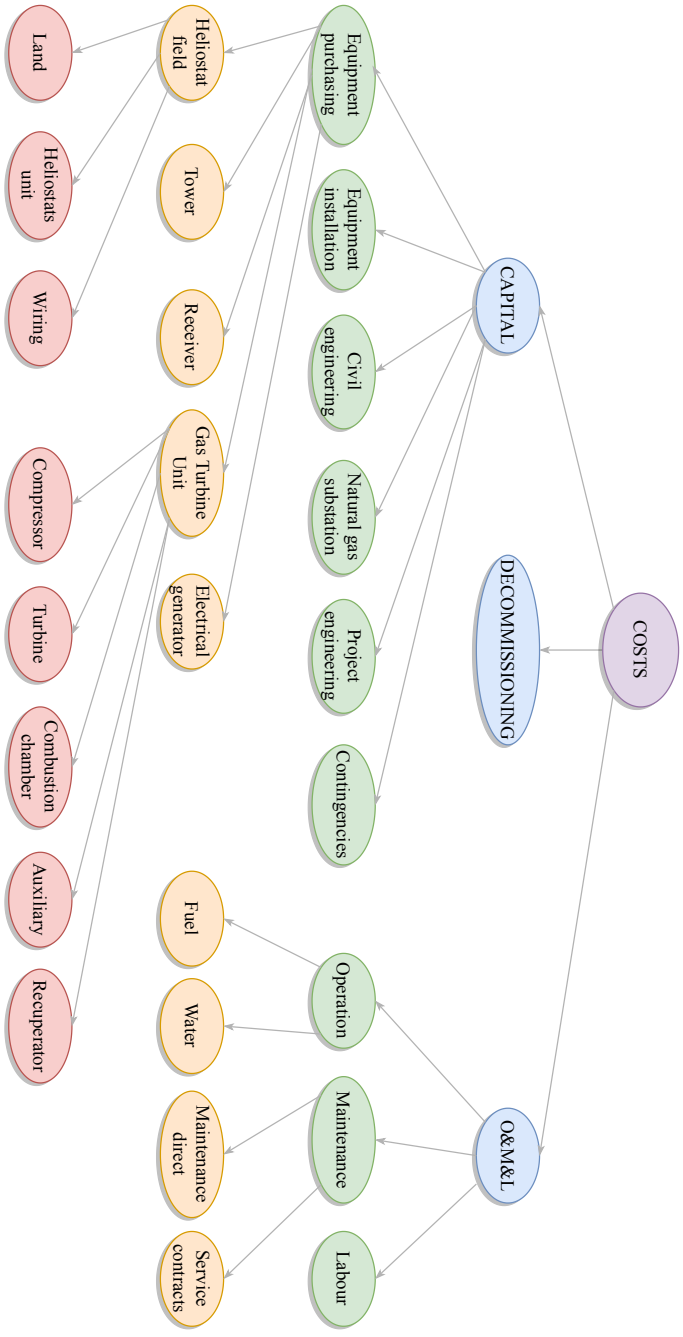

Figure 2.6: Tree structure of the costs involved in LCoE computation [136] (*Paper 7*).

	Parameter	Symbol	*SOLUGAS*-like plant	*GEMASOLAR* similar plant
Tower	Height	THT	65 m	135 m
Receiver	Diameter	DR	5 m	8.4 m
	Height	LR	-	10.5 m
	Emissivity	α	0.1	0.1
	Convection and conduction heat losses coefficient	$\overline{U}_L$	$5\,\mathrm{W/(m^2K)}$	$5\,\mathrm{W/(m^2K)}$
Heliostats	Height	LH	11.01 m	10.95 m
	Width-height ratio	w_r	1.0	1.0
Field	Separation distance between adjacent heliostats	d_s	3.303 m	3.285 m
	Minimum radius	R_{min}	64 m	65 m
	Concentration ratio	C	432.443	449.098
Efficiency	Blocking and shadowing factor	$f_{\mathrm{b}} \cdot f_{\mathrm{sh}}$	0.95	0.95
	Mirror reflectivity	ρ	0.836	0.836
	Standard deviation due to Sun shape	σ_{Sun}	2.51 mrad	2.51 mrad
	Focusing	–	Simple	Simple

Table 2.1: Table of parameters values assumed for the solar subsystem model in the Mathematica® simulations for the *SOLUGAS*-like plant [135] (*Paper 6*) and for the *GEMASOLAR* similar plant [90] (*Paper 5*). They have been adapted from *SOLUGAS* prototype plant [89] and from *GEMASOLAR* plant [58].

Plant similar to *GEMASOLAR*

Alternatively, the model has also been applied to a surround heliostat field with some features similar to *GEMASOLAR* plant [32] such as the larger power scale (20.91 MW_e) and some solar field parameters. As for *SOLUGAS*-like plant, these solar subsystem parameters employed in the simulations have been collected at Table 2.1. However, in this plant model, a Brayton cycle is performed rather than the Rankine one developed in *GEMASOLAR*. Moreover, in the case of this doctoral thesis, the stable power output is reached by hybridising the gas turbine instead of employing the *GEMASOLAR* molten salts TES system. The initial objective of this approach was to compare the performance of two different power units (Rankine and Brayton) connected to a similar heliostat field and receiver. Consequently, for the developed simulations, a gas turbine has been chosen with the help of Thermoflex® [78] commercial gas turbines database. Thus, *Solar Titan 250-30000S gas turbine* (Caterpillar) has been employed together with *Solar C85 gas compressor* [142]. Implementation details of the plant similar to *GEMASOLAR* in our code and input data sources are compiled at [90] (*Paper 5*).

2.2.2 Meteorological data

Some metereological data, basically ambient temperature (T_L) and direct normal irradiance (DNI), are required as input of the theoretical model for simulating real plant conditions. For almost all simulations, meteorological data are taken from Meteosevilla database [143] because considered plant locations are always Seville (for both *SOLUGAS* and *GEMASOLAR* similar plants). Those data (DNI and ambient temperature) daily evolutions for the four seasons are illustrated by Fig. 2.7 and they can be looked up at [128, 135] (*Paper 1* and *Paper 6*). As a general rule, they have not been smoothed nor averaged, thus they are real meteorological data. But in the case of annual analyses in Subsection 2.4.3 ([125] *Paper 2*), data were simply smoothed selecting three representative days for each season.

The only exception to that meteorological database are simulations in [136] (*Paper 7*) since a location analysis was carried out. In this case, metereological data, such as ambient temperature and ambient pressure, are obtained from Spanish Meteorological National Agency (AEMET) [144]. However, Copernicus Atmosphere Monitoring Service (CAMS) [145] was employed for getting direct normal irradiance data. Specific DNI and T_L profiles can be observed at Fig. 4 of [146].

2.2.3 Working fluids and thermodynamic diagrams

One of the reasons for considering a closed Brayton cycle is for direct comparison of different working fluids performance. Four working fluids, whose main thermodynamic properties are found at Table 2.2, are implemented in the code: air, nitrogen, helium and

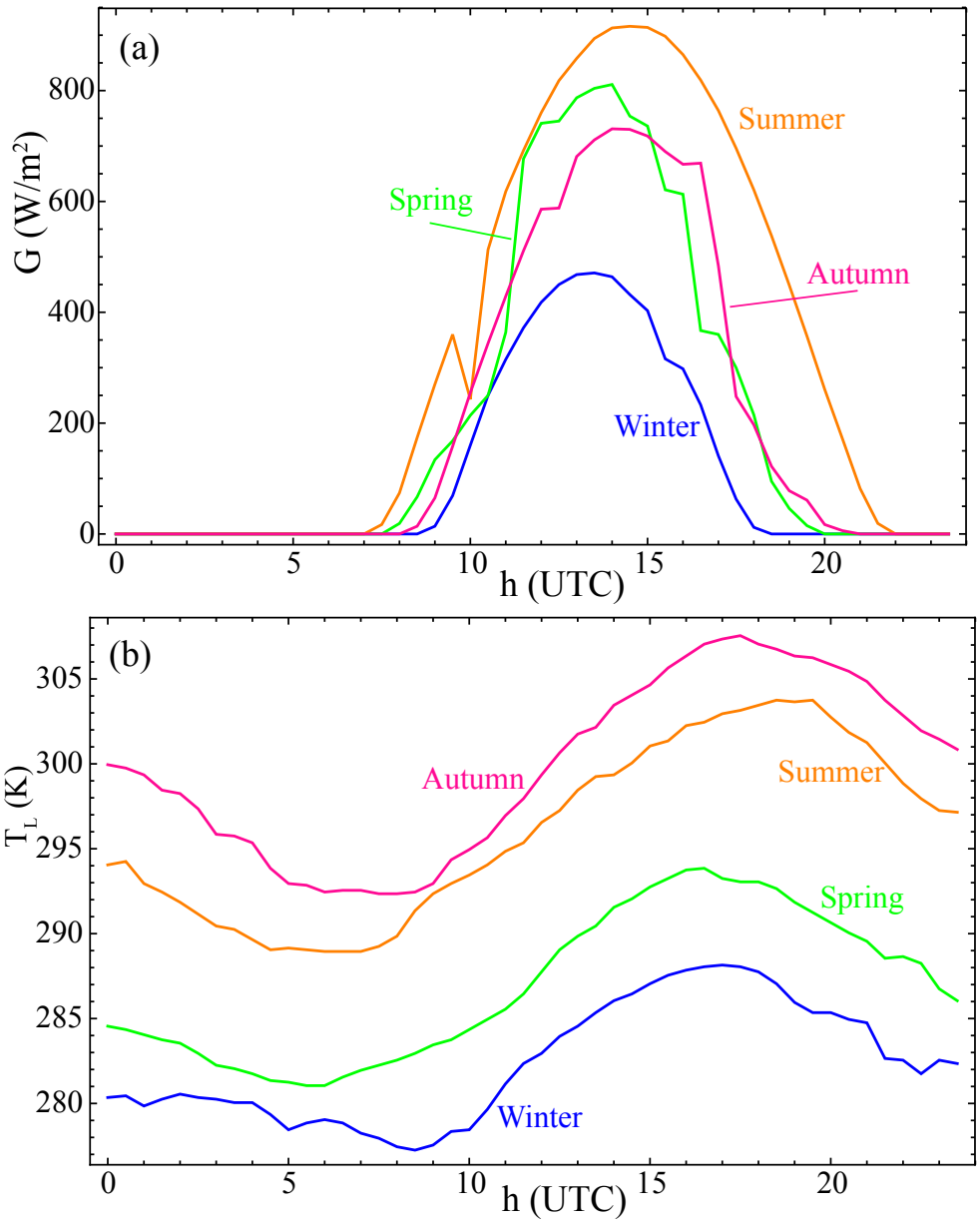

Figure 2.7: Daily curves of direct normal irradiance, G, (a) and ambient temperature, T_L, (b) for the four selected days representing each season, without any smoothing process [135] (*Paper 6*). Meteorological data are taken from Meteosevilla database [143].

	He	N_2	Dry air	CO_2
M (g/mol)	4.00	28.01	28.97	44.01
T_c (K)	5.1953	126.19	132.84	304.13
p_c (bar)	2.2761	33.958	38.501	73.773
$\bar{\gamma}$	1.6667	1.3561	1.3458	1.1986
$\bar{c}_w$ **[J/(g K)]**	5.1965	1.1354	1.1202	1.1587

Table 2.2: Main thermodynamic properties for the four considered working fluids [90] (*Paper 5*). M stands for the molecular weight. T_c and p_c are the critical temperature and pressure, respectively. $\bar{\gamma}$ refers to the mean adiabatic coefficient and $\bar{c}_w$, to the average constant pressure specific heat.

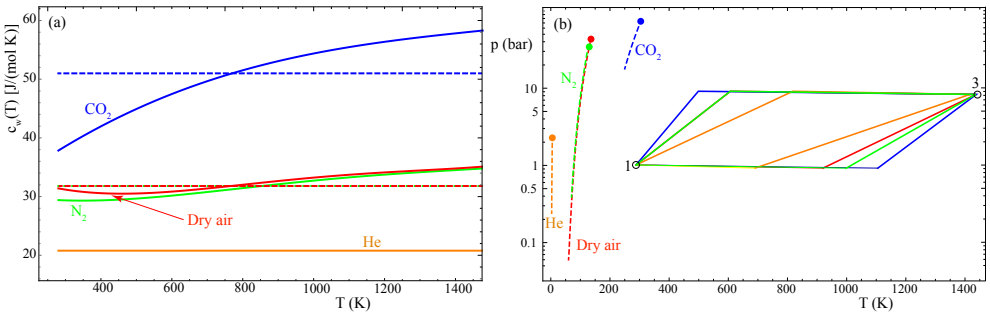

Figure 2.8: (a) Temperature dependence of the constant pressure molar heats [134] (*Paper 4*). Dashed lines represent average values. (b) Pressure-temperature diagrams of the performed Brayton cycles [134] (*Paper 4*). Filled circles refer to critical points and dashed lines, to the liquid-vapour coexistence lines.

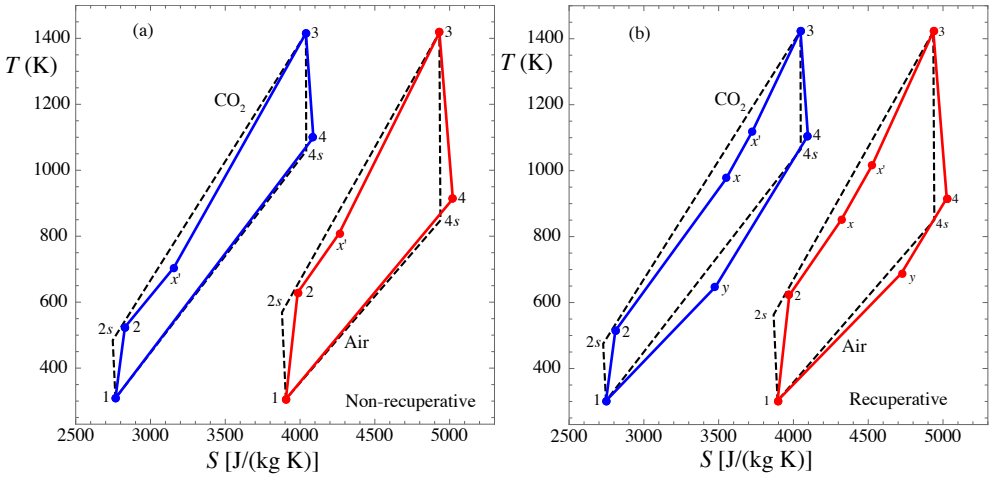

Figure 2.9: T-S diagrams for air and carbon dioxide [135] (*Paper 6*). Reversible ideal cases are associated with dashed lines and real cycles, with solid lines. (a) Non-recuperative and (b) recuperative cases are shown.

carbon dioxide. Air has been chosen since turbine design experience is broad and nitrogen for its similitude with air. Helium is inert and non-toxic, the same as CO_2, and it is also related to a good heat transfer coefficient and low pressure losses, but design experience is lower. In addition, analyses of subcritical CO_2 Brayton cycles for CSP are scarce, thus this is one of the main reasons why its performance in a SPT is evaluated in this doctoral work. Several sketches for these four fluids are displayed at Figs. 2.8 and 2.9, where constant pressure molar heats temperature dependence and pressure-temperature and temperature-entropy diagrams are shown. As suggested by Fig. 2.8 (b), air, nitrogen and carbon dioxide perform a subcritical cycle, meanwhile helium, a transcritical one. More information of the fluids implementation can be found at [134] (*Paper 4*).

2.3 Validation

The predictions of the implemented model have been validated employing different techniques: either via commercial software tools or using literature data, depending on the validated model. In addition, depending on the level of information on related published papers, a validation, a comparison or a simple contextualization have been performed. This validation process has been divided according to subsystem models. First, the gas turbine validation has been performed (Subsection 2.3.1), followed by the solar subsystem results

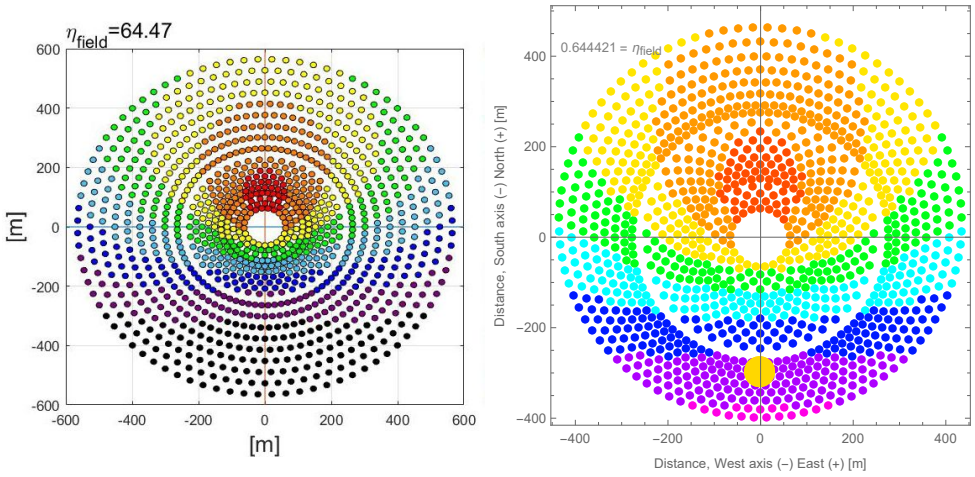

Figure 2.10: *Campo* code (left) and Mathematica® (right) heliostat field efficiency maps. Simulations correspond to the plant similar to *GEMASOLAR* during a selected day of autumn and at midday. Mathematica® efficiency map is obtained by means of the presented solar subsytem model and simulations.

comparison (Subsection 2.3.2). Then, a LCoE (Subsection 2.3.3) and overall plant records (Subsection 2.3.4) contextualization has been carried out.

2.3.1 Brayton cycle model validation

For the *SOLUGAS*-like plant and for fixed solar irradiance conditions, Brayton cycle model validation has been carried out by comparing directly *Mercury 50* turbine specifications to model outputs, in the case of air developing a single stage cycle. In this way, main performance records have been demonstrated to reach a quite good agreement with manufacturer's data. This validation has been broadly detailed on [128] (*Paper 1*).

On the other hand, for the plant similar to *GEMASOLAR*, gas turbine validation has been executed also with air as working fluid of a single stage cycle. In this case, Thermoflex® [78] gas turbines database and software has been employed and relative deviations between both commercial software and in-house code outputs have been computed. Results show small deviations, thus turbine model agreement is considered satisfactory. This information and further details can be checked in [90] (*Paper 5*), specifically at Table 6.

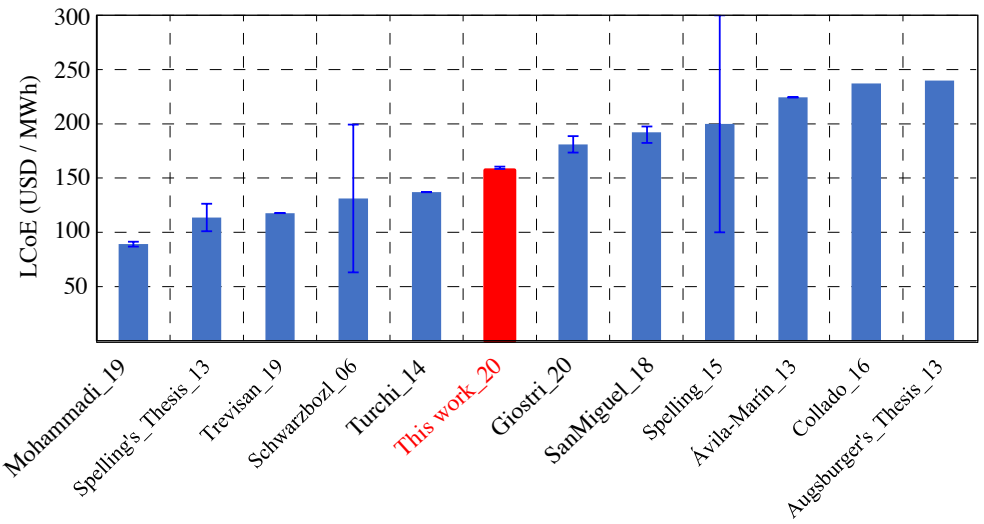

Figure 2.11: LCoE of the *SOLUGAS*-like simulated plant in the context of other values from different studies of diverse kinds of thermosolar plants [136] (*Paper 7*).

2.3.2 Solar subsystem results comparison

Solar subsystem model comparison has been directly carried out with data from literature, in particular for solar field efficiency values. In addition, a direct comparison between solar subsystem outputs and *campo* code software [58] has been made, with good agreements, as it was demonstrated in a End of Degree Project [147]. This is illustrated by Fig. 2.10 where a direct comparison of heliostat field efficiency maps between *campo* code and simulated plant similar to *GEMASOLAR* has been performed.

2.3.3 LCoE model comparison

With respect to LCoE calculation model, a comparison between the LCoE of the *SOLUGAS*-like simulated plant and other values in literature is performed. Note that these values correspond to diverse plant types, with not exactly the same features as the plant presented in this doctoral thesis since the objective of the study is just contextualizing LCoE records. It can be observed in Fig. 2.11 that LCoE of *SOLUGAS*-like simulated plant is within the interval of values of LCoE found in the literature. This analysis is included in [136] (*Paper 7*).

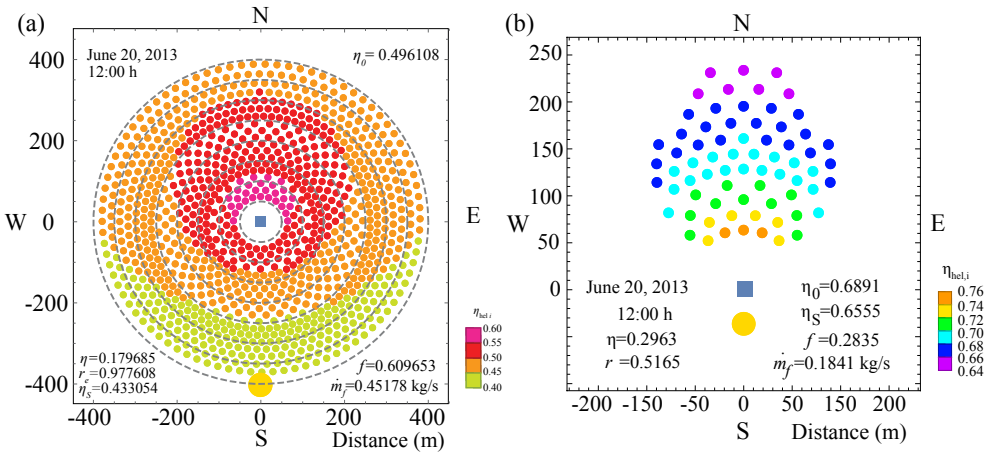

Figure 2.12: Heliostat field efficiency maps for the same day (20 June 2013) and for the same hour (12:00 h). (a) Surround field for the plant similar to *GEMASOLAR* [90] (*Paper 5*) and (b) polar field for the *SOLUGAS*-like plant [135] (*Paper 6*). Blue square represents solar tower and yellow circle refers to the Sun.

2.3.4 Overall model comparison

To conduct a direct comparison of output records for the whole plant is more complicated since there is a noticeable lack of published data. However, a general prediction of output values can be performed. In [128] (*Paper 1*), estimated outputs are gathered and demonstrated to be comparable to those published for a similar plant.

2.4 Simulations and results

Broadly speaking, performed simulations are divided into on-design (see Subsection 2.4.1) and off-design depending on particular time at which they are executed. At design conditions, different multi-stage and working fluids layouts have been tested (see Subsection 2.4.4). Within off-design analyses, daily, seasonal (see Subsection 2.4.2) and annual studies (see Subsection 2.4.3) have been carried out. Furthermore, numerical estimations of LCoE are completed in an annual basis (see Subsection 2.4.5).

2.4.1 Design conditions simulations

After the validation of the model and before dynamic analyses are carried out, simulations are performed at design conditions. These design conditions are taken at 12h, 20 June 2013 for all simulations with the only exception of [136] (*Paper 7*), where 13 June 2018 is assumed.

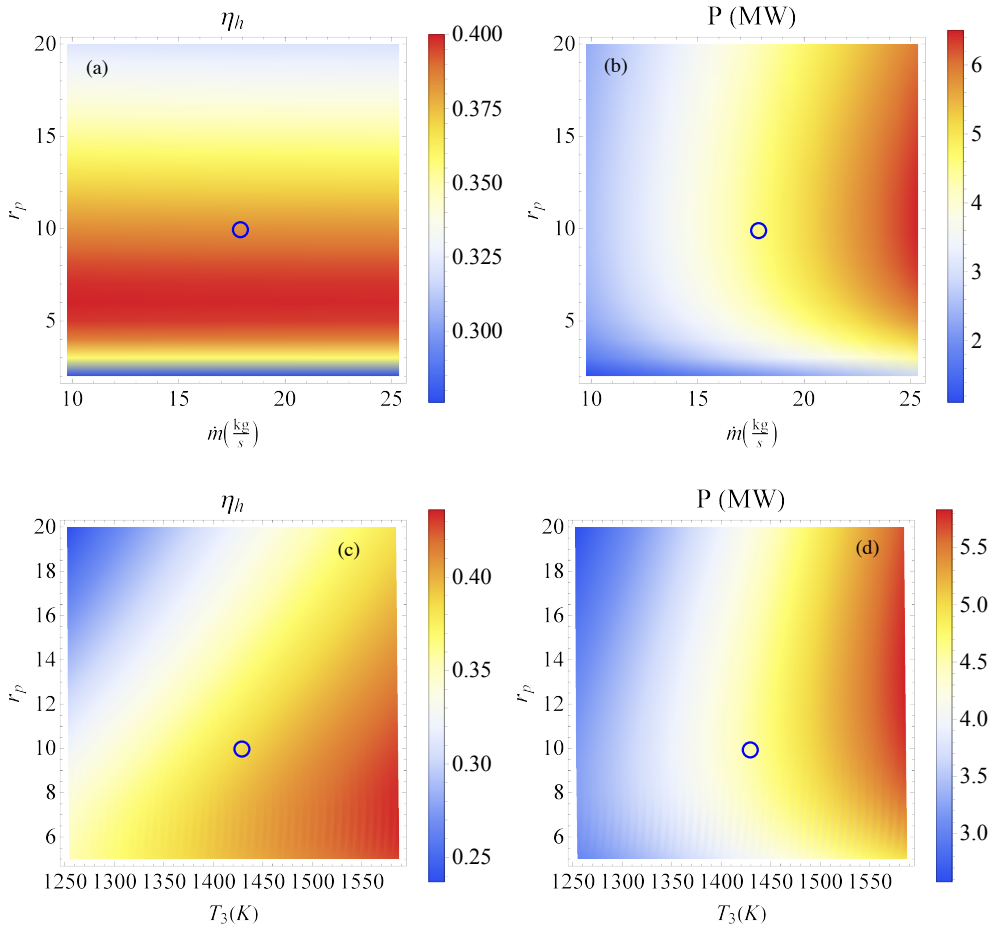

Figure 2.13: Gas turbine efficiency (η_h) and power output (P) density plots as functions of three essential design parameters: pressure ratio (r_p), working fluid mass flow ($\dot{m}$) and turbine inlet temperature (T_3) [135] (*Paper 6*). Design parameters of *Mercury 50* turbine are shown by circles.

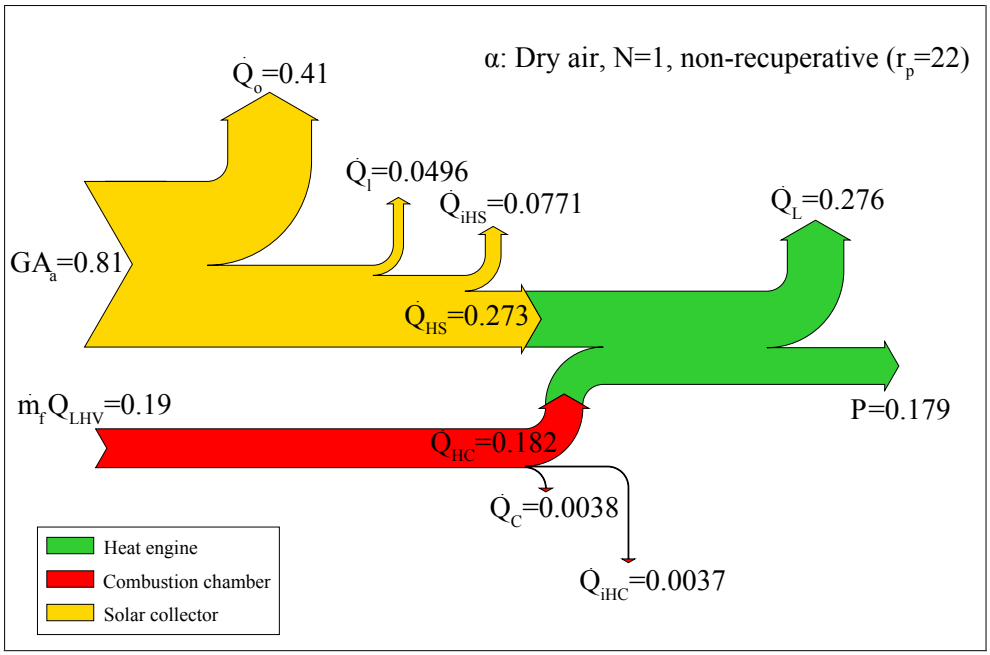

Figure 2.14: Sankey diagram for plant heat flows at the design point for dry air performing a non-recuperative and single stage cycle [90] (*Paper 5*).

Solar subsystem

Regarding solar subsystem, heliostats efficiency is computed by means of the model at design conditions and represented by efficiency maps such as Fig 2.12, where a comparison between a surround and a polar heliostat field efficiency map is shown. Main outcome is that highest efficiency is related to heliostats opposite the Sun [148]. This results discussion is gathered at [90, 135] (*Paper 5* and *Paper 6*). From now on, those design conditions heliostat field layouts are fixed in each case and different ambient conditions and subsequent modifications will be tested in next Subsections.

Brayton cycle subsystem

Gas turbine performance has also been evaluated in terms of three key design parameters: pressure ratio, mass flow of the working fluid and turbine inlet temperature, as it is shown in Fig. 2.13. Pressure ratio has a definite importance on heat engine efficiency, but not on power output. This outcome and others are broadened at [135] (*Paper 6*).

Overall system

Energy balances and main losses have been displayed as Sankey diagrams for the purpose of better visualization, as illustrated by Fig. 2.14. In this case, dry air performs a single non-recuperative Brayton cycle with an optimised pressure ratio. Main losses in each subsystem are easily identified: optical losses in the heliostat field, heat losses in the receiver, losses in the heat transfer from receiver to working fluid and losses in combustion system and in its associated heat exchanger. As the solar share is high, solar optical losses are important as well, thus overall efficiency is smaller. Further details can be found in [90] (*Paper 5*).

2.4.2 Daily and seasonal simulations

After design conditions are tested, off-design analyses are performed via dynamic simulations. The model is applied first to conduct daily and seasonal studies and, after those, to annual surveys (2.4.3). In all cases, four days corresponding to each season have been selected: 21 December, 21 March, 20 June and 21 September 2013.

Solar subsystem

Field efficiency maps are computed at any hour and any season thanks to the flexibility of the model. As a sample, Figs. 2.15 and 2.16 present seasonal variations of efficiency maps at a particular hour for both surround and polar layouts, respectively. For the surround field, highest average efficiency corresponds to summer and lowest to winter. On the contrary, highest values are found during winter and lowest in summer for the polar field. Number of heliostat within a specific efficiency range are also analysed by means of a histogram (see Fig. 2.17). Discussions on all those results are thoroughly addressed at [90, 135] (*Paper 5* and *Paper 6*).

Brayton cycle subsystem

Daily curves for the particular days representing each season have been obtained for all plant parameters. In the case of the Brayton cycle model, power output evolution has been compared to that of ambient temperature, as revealed by Fig. 2.18. Power output fluctuations are small and complementary to those of ambient temperature since just direct normal irradiance oscillations have been compensated through hybridisation. A key outcome is that power output stabilization objective has been achieved, with power fluctuations in a very small range. Additionally, gas turbine power output reduction linked to an ambient temperature increase is demonstrated. This analysis and others have been compiled at [128] (*Paper 1*).

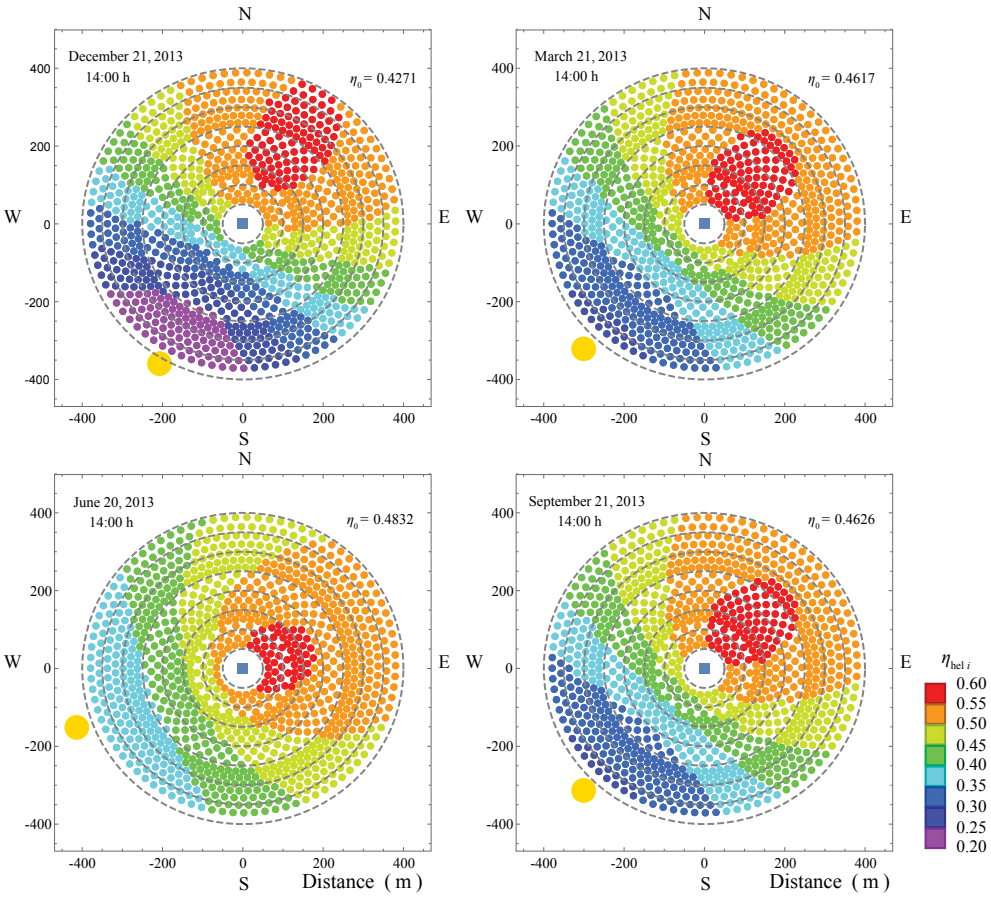

Figure 2.15: Seasonal variations of heliostat field efficiency maps for the surround field corresponding to the plant similar to *GEMASOLAR* at the same day time (14:00 h) [90] (*Paper 5*).

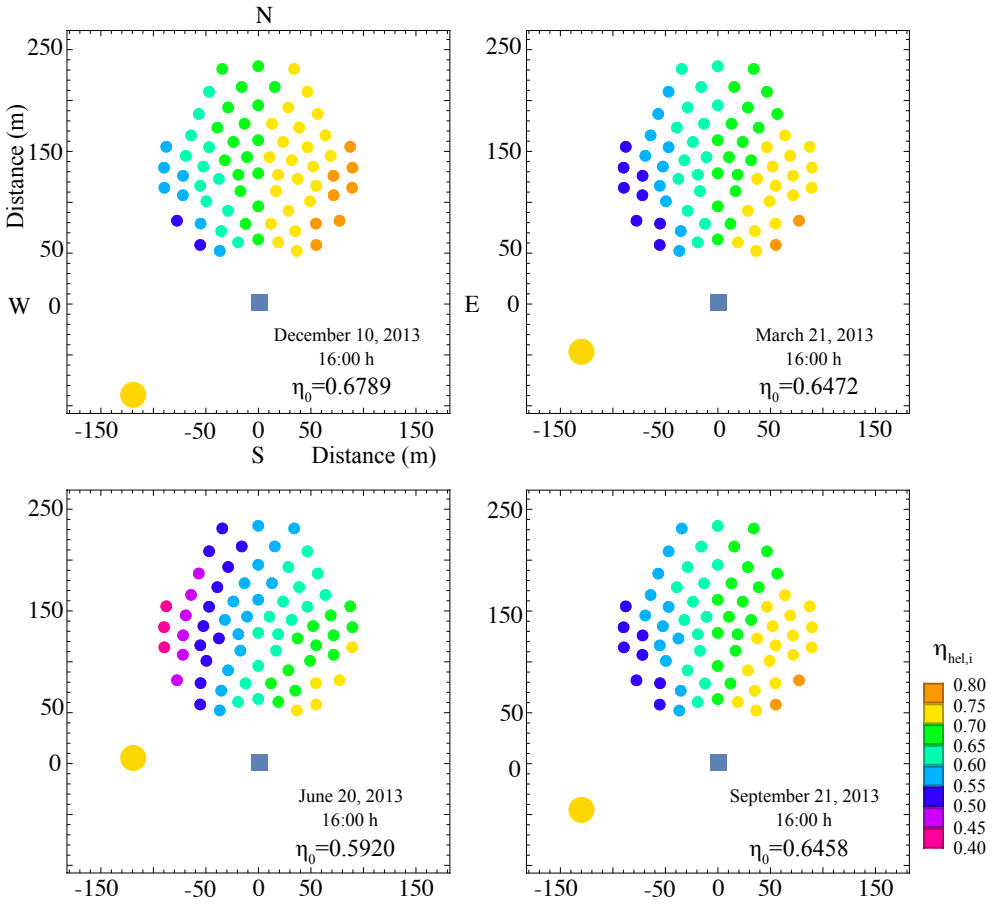

Figure 2.16: Seasonal variations of heliostat field efficiency maps for the polar field corresponding to the *SOLUGAS*-like at the same day time (16:00 h) [135] (*Paper 6*).

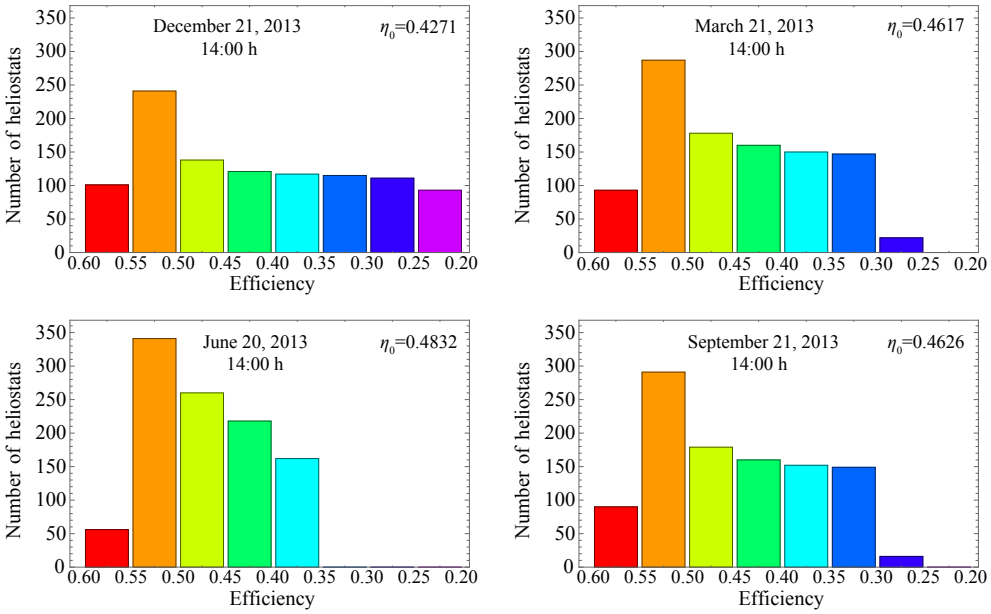

Figure 2.17: Number of heliostats and optical efficiency histogram of Fig. 2.15 [90] (*Paper 5*).

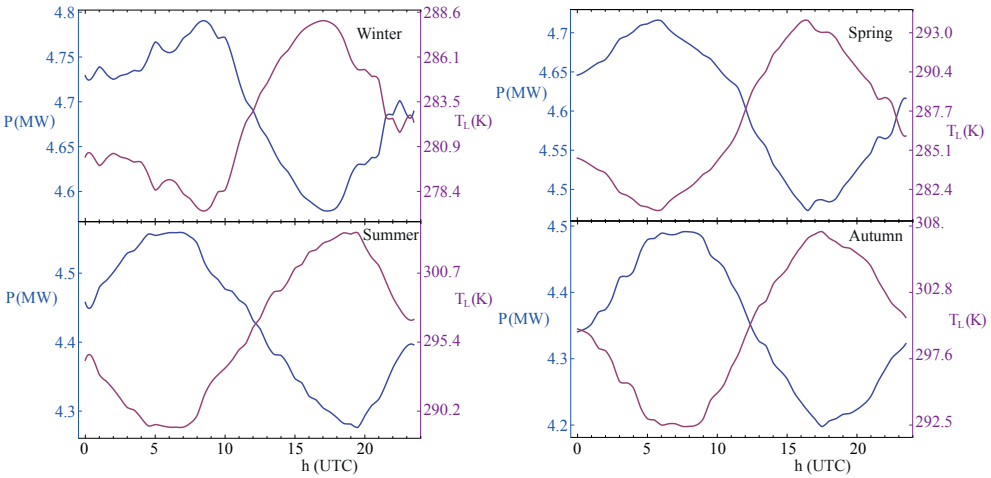

Figure 2.18: Daily evolution of power output (P) and ambient temperature (T_L) for the four seasons [128] (*Paper 1*).

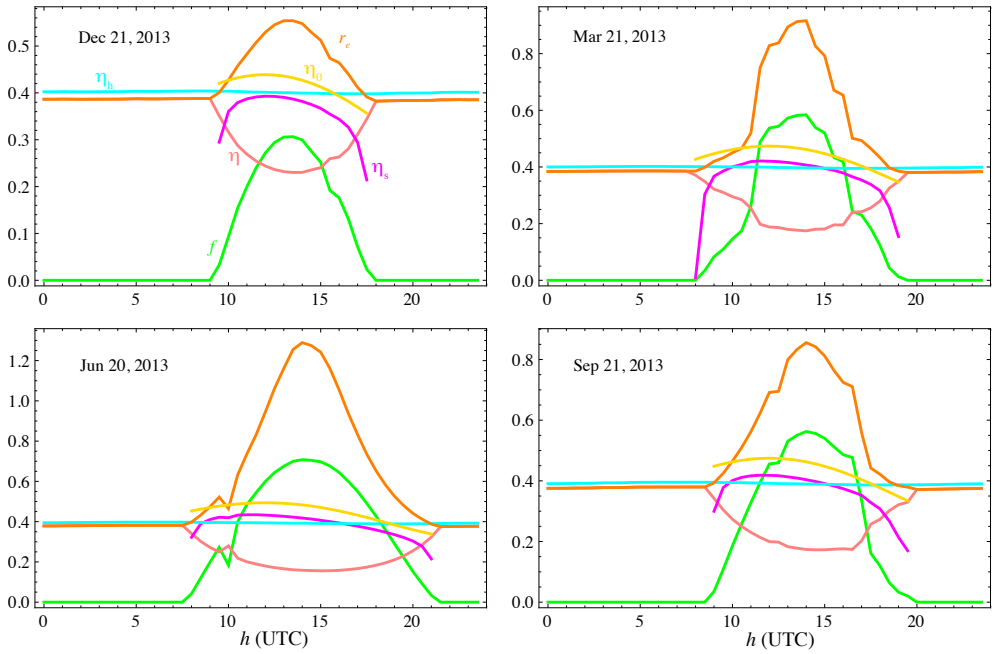

Figure 2.19: Daily evolution and seasonal variations of overall thermal efficiency (η), heat engine efficiency (η_h), heliostat field optical efficiency (η_0), solar subsystem efficiency (η_s), solar share (f) and fuel conversion rate (r_e) for air performing a single non-recuperative cycle surround field layout [90] (*Paper 5*).

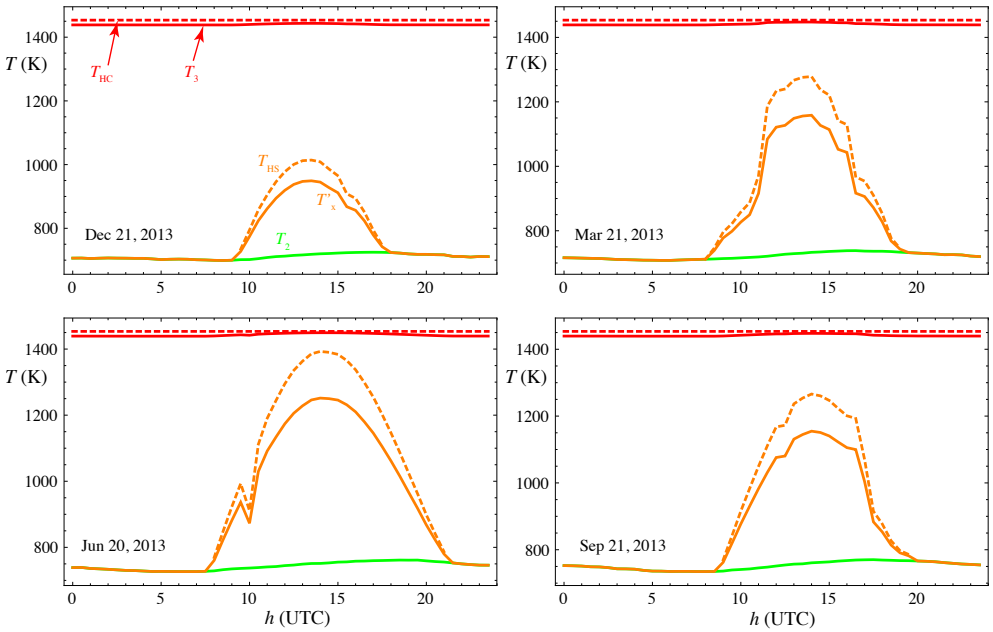

Figure 2.20: Daily evolution and seasonal variations of main heat absorption involved temperatures for dry air performing a single non-recuperative cycle surround field layout [90] (*Paper 5*). Compressor outlet temperature (T_2), solar collector outlet temperature ($T_{x'}$), solar collector temperature (T_{HS}), turbine inlet temperature (T_3) and combustion chamber temperature (T_{HC}) are displayed.

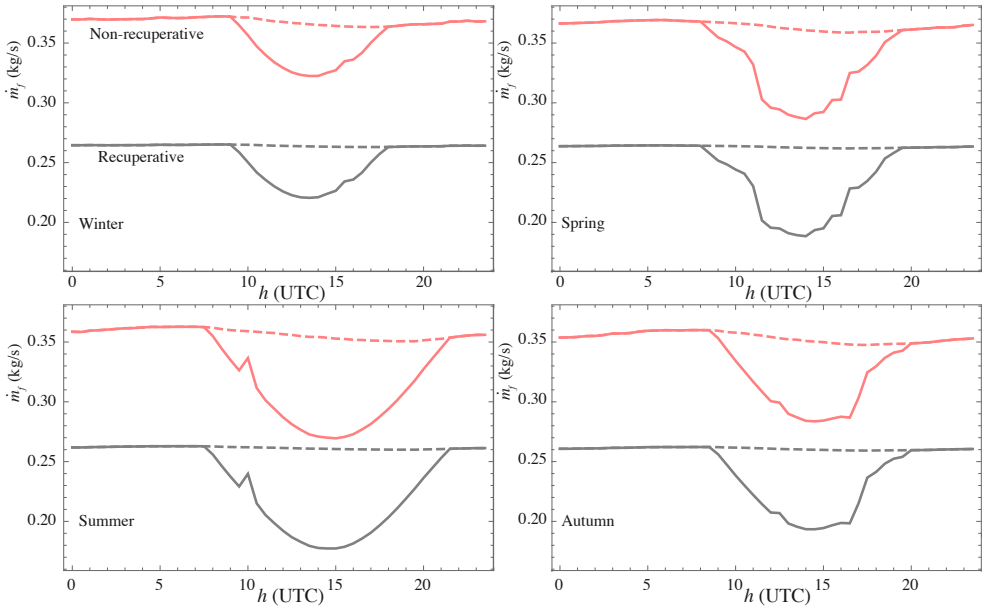

Figure 2.21: Daily evolution and seasonal variations of fuel consumption rate ($\dot{m}_f$) for recuperative and non-recuperative configurations [124] (*Paper 3*). Hybrid operation mode is represented by solid lines and pure combustion mode by dashed ones.

Overall system

In the same way, this daily and seasonal approach has been applied to different configurations for both surround and polar field layouts. As an example, Figs. 2.19 and 2.20 display involved efficiencies and temperatures in the case of the plant similar to *GEMASOLAR*. Output records show that seasonal changes are reflected on the width and on the height of parameters curves, such as efficiencies and temperatures. Overall efficiency always presents lower values during central hour of the day. The cause of this decrement is that heat losses rise during this daytime because solar subsystem is working contrary to what happens during the night. Another interesting conclusion is that, for the *GEMASOLAR* adapted dimensioning of the plant, natural gas is always being consumpted since solar receiver temperature does not reach the imposed turbine inlet temperature and, as a result, solar share reaches as maximum 0.7. The same qualitative outcome is obtained for the *SOLUGAS*-like plant. These daily and seasonal studies have been gathered at [90] (*Paper 5*) for the plant similar to *GEMASOLAR* and the surround layout and at [135] (*Paper 6*) for *SOLUGAS*-like plant and the polar field.

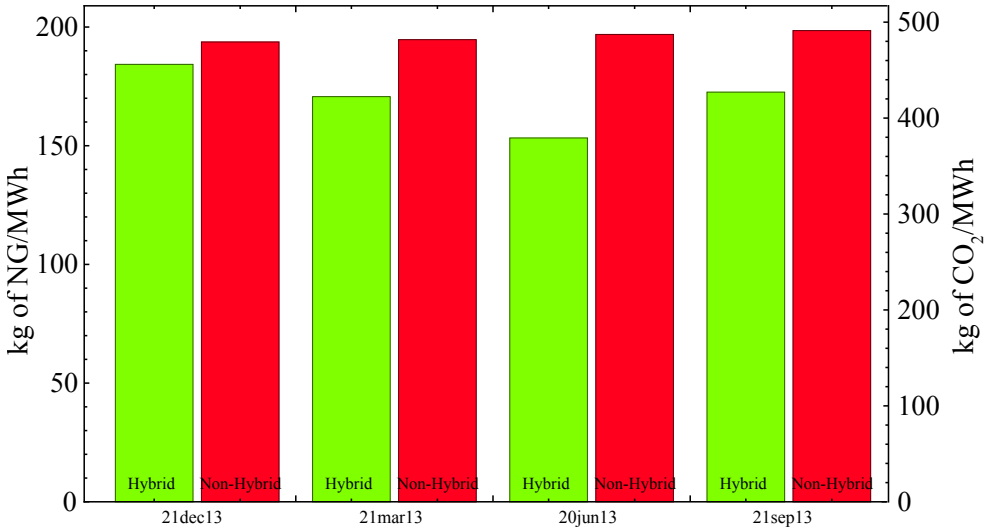

Figure 2.22: Seasonal variations of natural gas consumption (left axis) and carbon dioxide emissions (right axis) during a day in both hybrid and pure combustion operation modes [90] (*Paper 5*). Air is supposed to perform a single non-recuperative cycle coupled to a surround field layout.

Combustion subsystem

Following the same approach, fuel consumption can be analysed from a seasonal and daily perspective, as it has been performed in Fig. 2.21. Inclusion of a recuperator in plant configuration clearly reduces fuel consumption to almost the half when comparing to a non-recuperative layout. Regarding operation mode and when comparing to a non-solar plant working only by burning natural gas, fuel saving for the solar hybrid plant during a day is enclosed between the dashed and the solid lines. Moreover, the whole day fuel consumption has been computed and translated into overall daily pollutant emissions. Figure 2.22 presents these records and demonstrates that pollutant emissions saving is higher during a summer day. Fuel consumption and pollutant emissions have been widely dealt with in [128, 124, 90, 135] (*Paper 1*, *Paper 3*, *Paper 5* and *Paper 6*).

2.4.3 Annual simulations

Annual simulations have been performed with the objective of evaluating the impact of thermal losses on plant records. In this way, five different situations are considered, as revealed by Fig. 2.23: (A) real plant operating point, (B) ideal heat exchangers, (C) ideal solar subsystem, (D) ideal Brayton cycle and (E) completely ideal system. Therefore, margins for

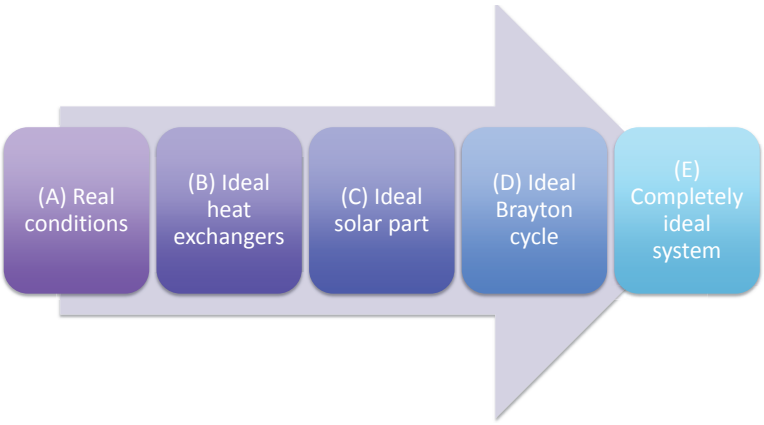

Figure 2.23: Scheme of the considered cases for the annual energy losses analysis [149] (*Chapter B*).

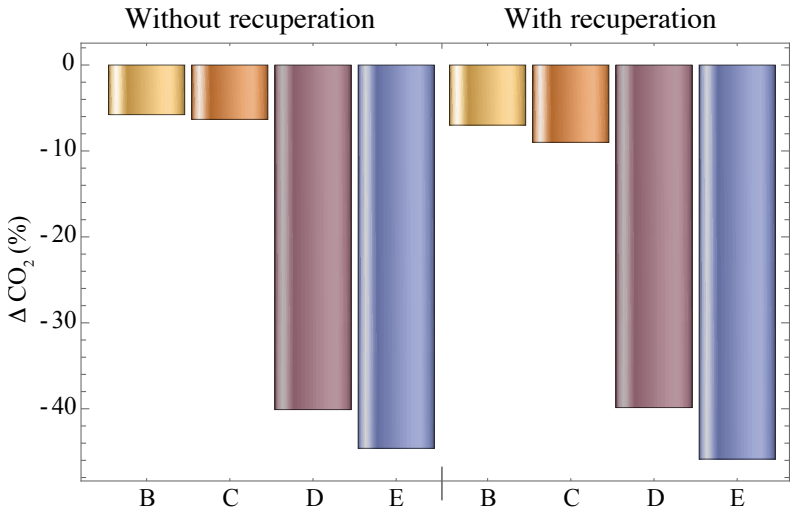

Figure 2.24: Margins for improvement of CO_2 emissions with respect to plant operating point (case A) for the recuperative and non-recuperative configurations [125] (*Paper 2*).

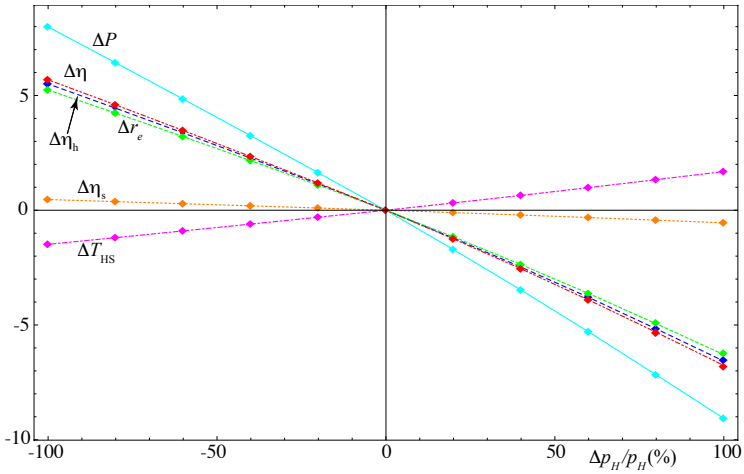

Figure 2.25: Plant performance sensitivity of power output (ΔP), overall thermal efficiency ($\Delta\eta$), Brayton cycle efficiency ($\Delta\eta_h$), fuel conversion efficiency (Δr_e), solar subsystem efficiency ($\Delta\eta_s$) and solar receiver temperature (ΔT_{HS}) to relative pressure decay in the hot side of the Brayton cycle ($\Delta p_H/p_H$) [125] (*Paper 2*). Both axis are represented in relative terms as percentages regarding yearly averaged real operating conditions.

improvement regarding real plant operating point (case (A)) are computed and depicted in Fig. 2.24. As expected, solar subsystem enhancements have no effect on power output, but they do on fuel conversion rate. Additionally, highest improvements on analysed outputs are related to better values of heat engine parameters and, of course, to the case in which the whole system is assumed as ideal. This behaviour was confirmed via a sensitivity analysis, which has also been applied to relative pressure losses in the heat absorption process. Figure 2.25 displays parabolic curves of plant performance variables for these pressure decays variations. A key outcome is that pressure losses variations have been demonstrated to have an important effect on solar subsystem through solar receiver temperature. Further discussion on those results and other thermal and pressure losses analyses of annual simulations can be accessed in [125] (*Paper 2*).

2.4.4 Different multi-stage and working fluids layouts

Within design conditions, the main purpose of next analyses is to survey pressure ratio influence on considered working fluids and plant configurations and to look for its optimum values. As reported in previously mentioned working fluids implementation (see Subsection 2.2.3), the behaviour of four working fluids is tested in this doctoral thesis. These selected

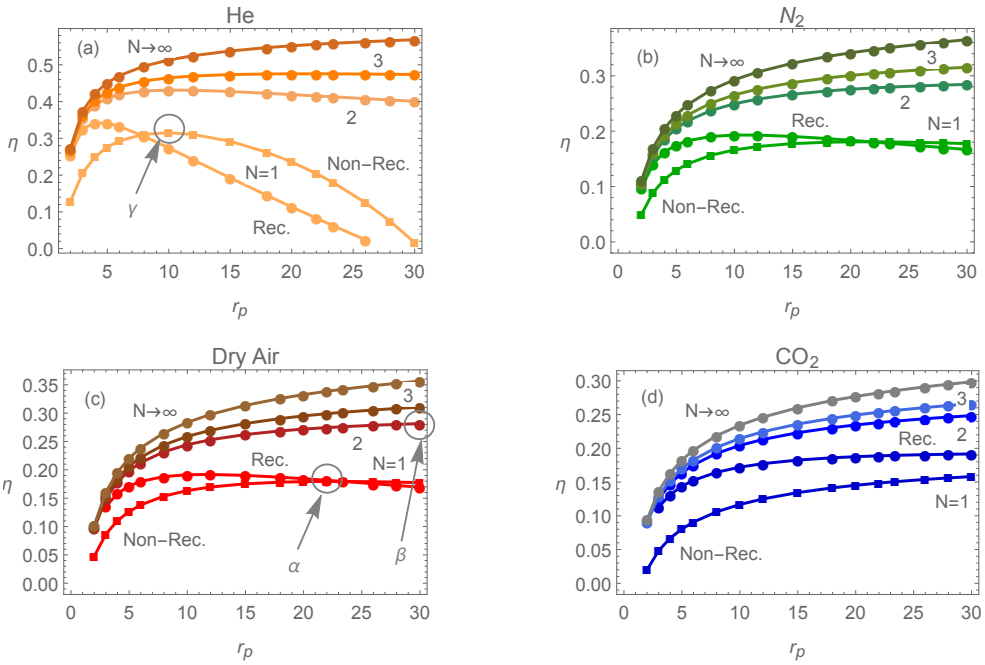

Figure 2.26: Evolution of overall thermal efficiency (η) with pressure ratio (r_p) for the four analysed working fluids: (a) helium, (b) nitrogen, (c) dry air and (d) carbon dioxide [90] (*Paper 5*). Multi-stage layouts with one, two, three and infinite compression and expansion stages are shown and recuperative (circle markers) and non-recuperative (square markers) configurations are plotted for the single stage case. For the interpretation of α, β and γ configurations, see Table 2.4.

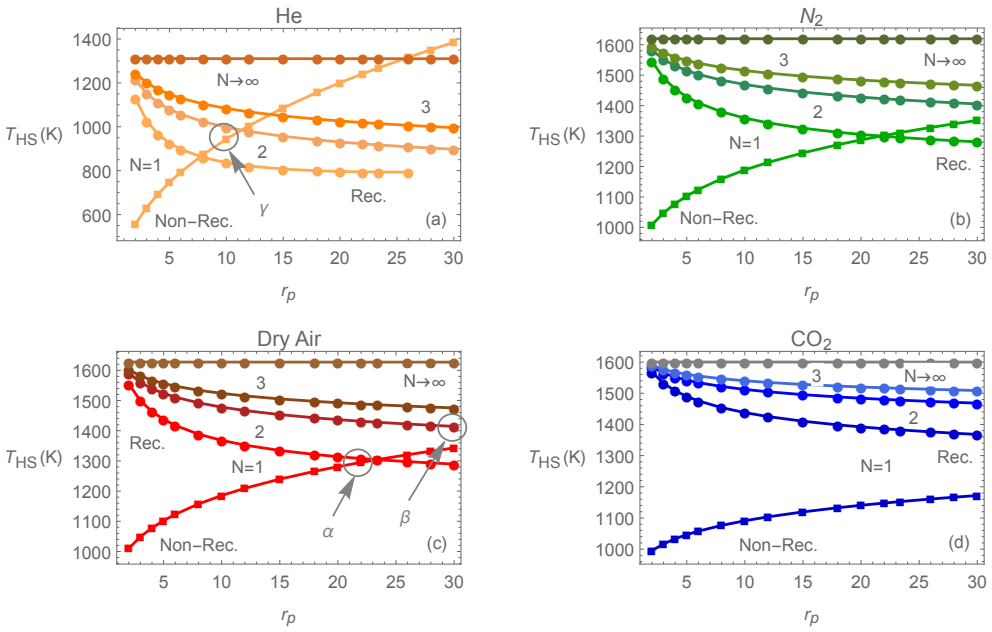

Figure 2.27: Evolution of solar receiver temperature (T_{HS}) with pressure ratio (r_p) for the four analysed working fluids: (a) helium, (b) nitrogen, (c) dry air and (d) carbon dioxide [90] (*Paper 5*). For figure interpretation, see Fig. 2.26.

Fluid	N	η_{max}	$r_{p,\eta_{max}}$	$\Delta\eta\,(\%)$	$\Delta r_e\,(\%)$	$\Delta P\,(\%)$
	1	0.191862	12	6.91837	27.3001	3.173
Dry air	2 (β)	0.28144	30	1.9495	−3.08509	4.43564
	1, NR (α)	0.179524	22	0.00645206	−2.8558	0.677957
	1	0.192919	10	8.40114	36.517	3.32931
N_2	2	0.284472	30	1.74209	−3.13519	4.2562
	1, NR	0.180737	22	0.117702	−2.94829	0.829819
	1	0.191657	30	1.07715	−5.87712	2.31038
CO_2	2	0.24847	30	3.39625	−3.25394	5.59186
	1, NR	0.15816	30	5.03173	8.85381	3.63292
	1	0.342435	4	453.512	506.163	353.99
He	2	0.4313	10	4.46969	8.90676	−11.1688
	1, NR (γ)	0.31519	10	75.7822	15.6467	194.356

Table 2.3: Relative variations of output records for the considered working fluids achieved by choosing optimum pressure ratio regarding overall thermal efficiency with respect to the design pressure ratio of the gas turbine (air, recuperative, $r_{p,DP} = 23.4$) [90] (*Paper 5*). Number of compression and expansion stages (N), maximum overall efficiency (η_{max}) with its corresponding pressure ratio ($r_{p,\eta_{max}}$), and relative improvements of overall thermal efficiency ($\Delta\eta$), fuel conversion rate (Δr_e), and power output (ΔP) are gathered. Recuperative records are shown, unless NR (non-recuperative case) is stated.

Configuration	Fluid	N	Recuperation	η	T_{HS} (K)	f	r_p
α	Dry air	1	No	0.18	1300	0.60	22
β	Dry air	2	Yes	0.28	1420	0.40	30
γ	He	1	No	0.32	925	0.16	10

Table 2.4: Three selected possible optimum pressure ratio (r_p) configurations regarding large overall thermal efficiency, low solar receiver temperature and high solar share.

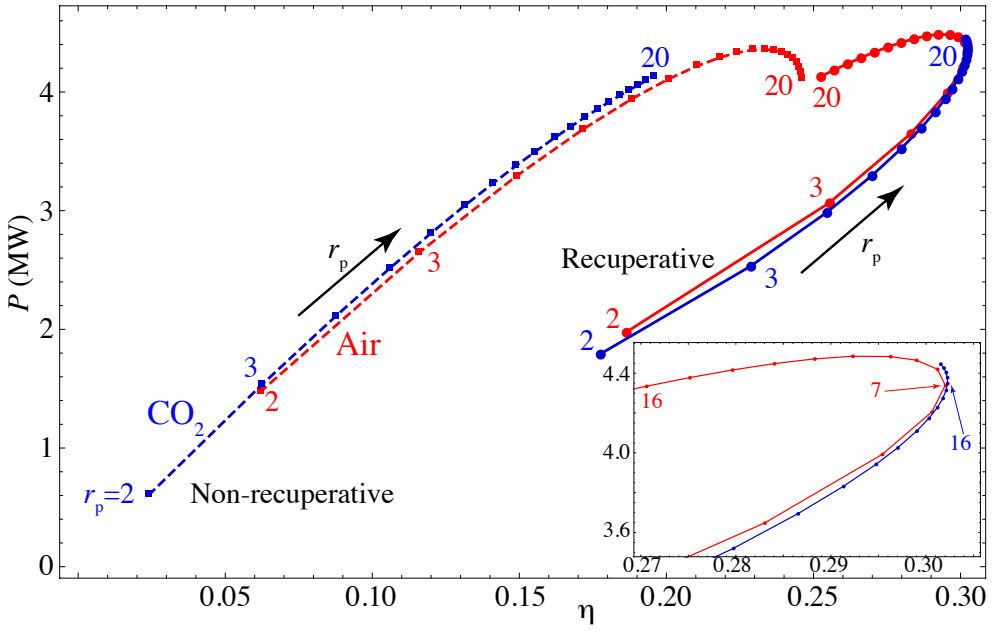

Figure 2.28: Parametric curves of overall thermal efficiency (η) and power output (P) with pressure ratio (r_p) as hidden variable for air and carbon dioxide [135] (*Paper 6*).

fluids are dry air, nitrogen, carbon dioxide working in subcritical conditions and helium. Additionally, different number of compression and expansion stages are surveyed.

Those multi-stage and different working fluids analyses were first introduced for a *SOLUGAS*-like plant in [134] (*Paper 4*). However, after that, surround fields with higher plant dimensions were also tested (plant similar to *GEMASOLAR*). With these simulations, output variables evolution with pressure ratio is analysed looking for the optimum pressure ratios according to different criteria. As a sample for the plant similar to *GEMASOLAR* with a surround field, Figs. 2.26 and 2.27 are presented, representing overall efficiency and receiver temperature, respectively. As a limit case, infinite stages represent the theoretical maximum values achievable by the variables. Scaling from a *SOLUGAS*-like plant (4.77 MW) to a plant with dimensions similar to *GEMASOLAR* (20.91 MW) makes fuel conversion rate to change its evolution with pressure ratio, except for He. Nevertheless, similar records are found for overall thermal efficiency and power output. A pre-optimisation process is carried out by analysing maximum overall thermal efficiency for different number of stages, working fluids and recuperative / non-recuperative modes. This information is gathered at Table 2.3. In this

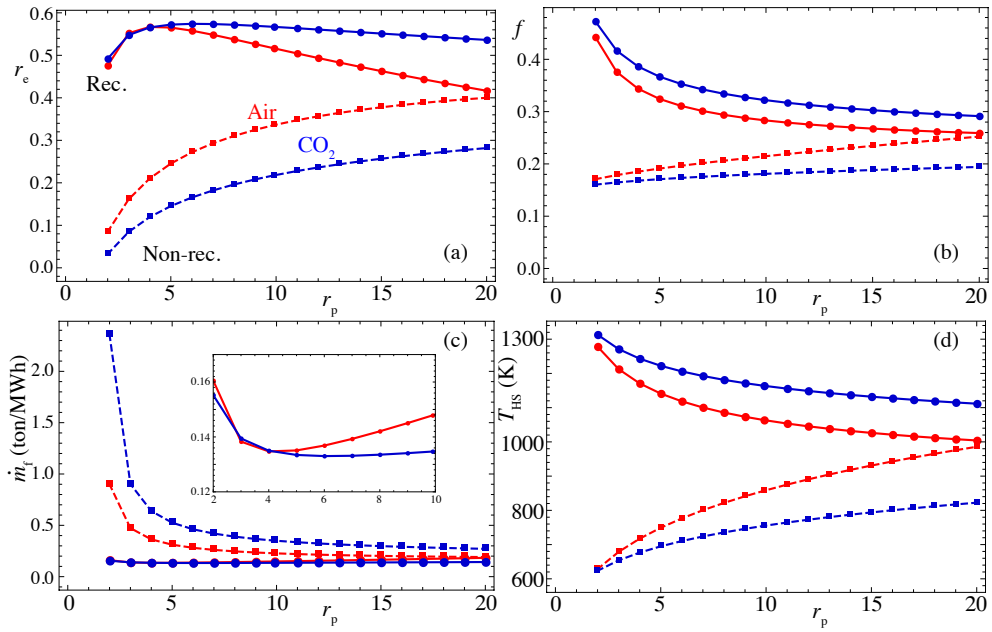

Figure 2.29: Evolution of (a) fuel conversion rate (r_e), (b) solar share (f), (c) specific fuel consumption ($\dot{m}_f$) and (d) solar receiver temperature (T_{HS}) with pressure ratio (r_p) for air (red markers) and carbon dioxide (blue markers) [135] (*Paper 6*). Recuperative configurations are represented with solid lines and circle markers, meanwhile non-recuperative layouts are plotted with dashed lines and square markers.

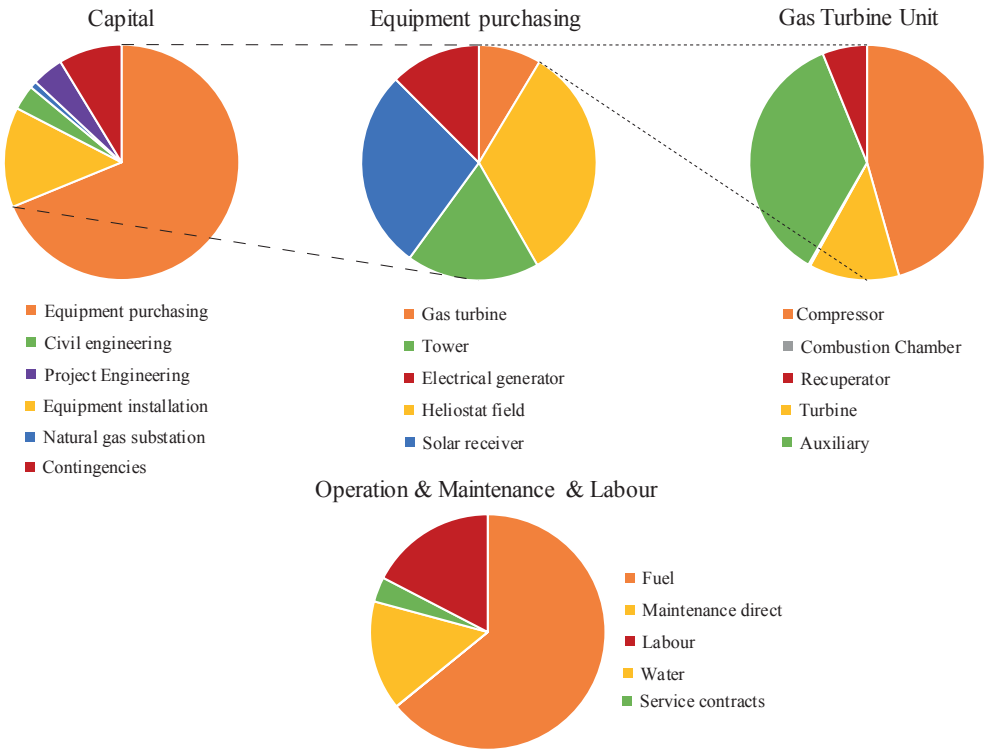

Figure 2.30: Pie charts for (top) Capital costs and some of their components such as equipment purchasing and gas turbine and for (bottom) Operation & Maintenance & Labour costs [136] (*Paper 7*).

way, for the *GEMASOLAR* dimensioning plant, three criteria are looked for in the selection of three possible optimum configurations: large overall thermal efficiency, low solar receiver temperature and high solar share (see Tables 2.3 and 2.4).

In the case of the *SOLUGAS*-like plant with a polar field, an equivalent approach with similar plots can be followed. In this way, Figs. 2.28 and 2.29 illustrate parametric behaviour of power output and overall efficiency and other output parameters evolution with pressure ratio, respectively. It has been demonstrated that power output maximum value ($r_p = 10$) is achieved for a pressure ratio very similar to *SOLUGAS* design one. Another significant outcome is that, for the same power, recuperative layouts present almost the same value of maximum achievable overall efficiency for air and CO_2, but at different pressure ratios. In addition, solar share always exhibits small numerical values, hence *SOLUGAS*-like polar field size is considered to be relatively small for the desired and fixed turbine inlet temperature and

associated mass flow.

Furthermore, an expanded presentation of the results and the corresponding discussion are carried out at [90] (*Paper 5*) for the plant similar to *GEMASOLAR* and at [134, 135] (*Paper 4* and *Paper 6*) for the *SOLUGAS*-like plant.

2.4.5 Numerical estimations of LCoE

Final performed simulations are devoted to the prediction of thermo-economic records, mainly to Levelised Cost of Electricity (LCoE) computation. In this way, following and additional analyses are thoroughly dealt with at [136] (*Paper 7*). In particular, *SOLUGAS*-like plant reaches a LCoE of about 158 USD / MWh in the base recuperative case. Costs distribution is splitted in pie charts of Fig. 2.30, where the importance of heliostat field and solar receiver in the equipment purchasing is revealed. In fact, around 80 % of total equipment costs are due to solar subsystem: heliostat field, tower, and receiver. On the other hand, gas turbine costs represent less than 10 % of equipment. The *SOLUGAS* undersized field and, therefore, its hybrid performance during the whole operation time of the plant are reflected on fuel costs, which constitute the main factor of Operation & Maintenance & Labour costs.

Recuperation influence

In order to check the influence of a recuperator on plant parameters, a direct comparison between recuperative and non-recuperative layouts for the same plant is carried out. As expected, Brayton cycle efficiency is higher when recuperation is included, but it also decreases solar subsystem efficiency. As it is illustrated by Table 2.5, LCoE increases almost 17 % when the recuperator is removed to the plant layout. Moreover, specific CO_2 emissions are about 45 % larger in the non-recuperative case. Additionally, overall efficiency for this last case is 28 % lower even though solar subsystem efficiency is higher than the recuperative one. Therefore, a key outcome is that recuperator cost and associated higher losses in the solar subsystem are not enough to decompensate its performance advantages.

Location influence

Location influence on thermo-economic parameters has also been surveyed by comparing plant records for two different locations in Spain (Seville and Salamanca). These locations present similar direct normal irradiance (DNI) values, with lightly lower values for Salamanca. Additionally, lower yearly ambient temperatures are recorded in Salamanca. Table 2.5 proves that these lower temperatures increase overall thermal efficiency about a 2 %, although not in such extent to produce better LCoE results. In this way, Salamanca displays a 3.5 % higher LCoE than Seville. As a conclusion, other latitudes different from typical ones can offer interesting thermo-economic records if acceptable solar radiation and low temperatures are

Parameter	Base case	Recuperation		Location	
	Recuperat. Seville	Non-recuperat.	Deviation (%)	Salamanca	Deviation (%)
LCoE (USD/MWh)	158.1	184.7	16.80	163.7	3.512
C_{inv} (10^6 USD)	30.74	30.49	- 0.81	30.67	- 0.24
Fuel consumpt. (10^3 ton/year)	7.31	10.24	40.05	6.89	- 5.83
CO_2 emissions (kg/MWh)	453.1	657.8	45.18	450.8	- 0.51
E_{net} (GWh/year)	39.94	38.53	- 3.54	37.80	- 5.36
η_h	0.392	0.277	- 29.30	0.398	1.54
η_0	0.658	0.658	–	0.660	0.24
η_s	0.276	0.294	6.65	0.263	- 4.56
η	0.349	0.252	- 27.96	0.356	2.01
f	0.202	0.151	- 25.19	0.175	- 13.24

Table 2.5: Main thermodynamic and thermo-economic output plant parameters for the base case (recuperative layout in Seville) [136] (*Paper 7*): Levelised Cost of Electricity (LCoE), capital cost (C_{inv}), fuel consumption, specific CO_2 emissions, net energy (E_{net}), heat engine efficiency (η_h), optical field efficiency (η_0), solar subsystem efficiency (η_s), overall efficiency (η) and solar share (f). For the recuperation and location analyses, the non-recuperative configuration and Salamanca location are tested, respectively. Relative deviations are computed regarding base case.

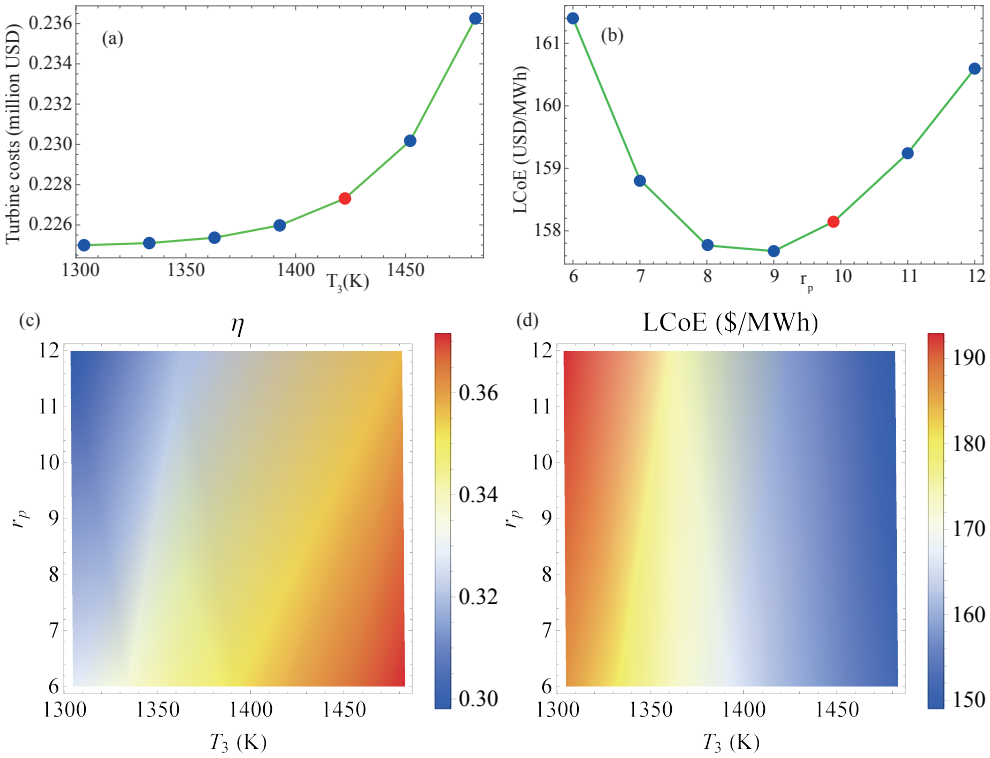

Figure 2.31: (top) (a) Evolution of gas turbine cost with turbine inlet temperature (T_3) and (b) evolution of LCoE with pressure ratio (r_p). Red dot indicates *SOLUGAS* [89] design point. (bottom) Density plots of (c) overall thermal efficiency (η) and (d) LCoE with both pressure ratio (r_p) and turbine inlet temperature (T_3). Figures are taken from [136] (*Paper 7*).

achieved.

Particular numerical results of both recuperation and location influence studies are collected at [136] (*Paper 7*).

Sensitivity analysis

The influence of several design plant input parameters is assessed through a sensitivity analysis both from thermodynamic and thermo-economic viewpoints and compiled at [136] (*Paper 7*).

With respect to power unit parameters, sensitivity analysis has been applied to pressure ratio (r_p) and turbine inlet temperature (T_3). Results are summarized in Fig. 2.31. Gas turbine cost has been assumed to increase exponentially with turbine inlet temperature. For the

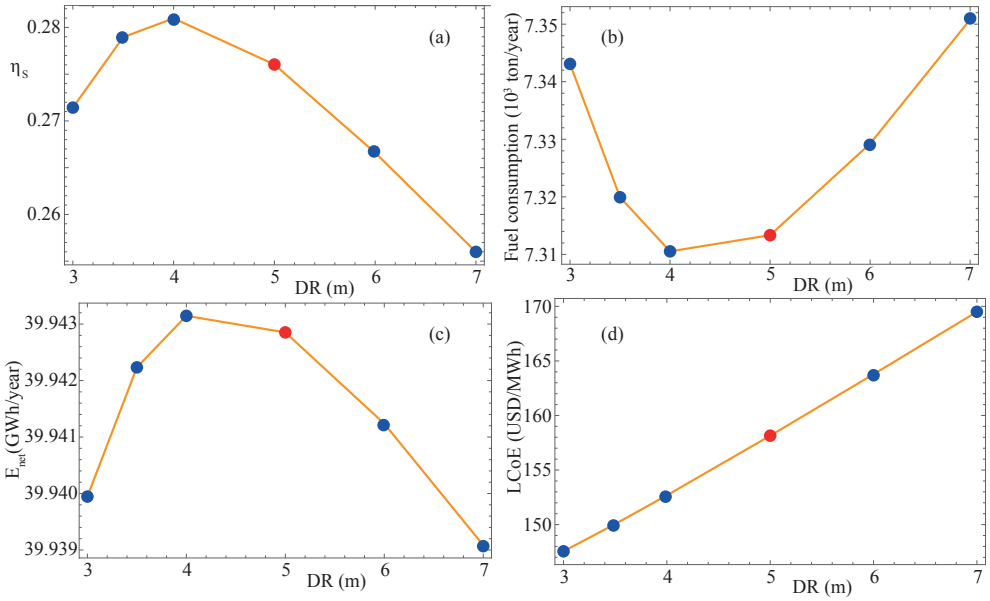

Figure 2.32: Influence of receiver diameter (*DR*) on some output records: (a) solar subsystem efficiency (solar field and receiver, η_s), (b) fuel consumption, (c) annual net energy and (d) LCoE [136] (*Paper 7*). Red dot indicates *SOLUGAS* [89] design point.

considered pressure ratio interval, LCoE curve presents a minimum at a slightly lower value of pressure ratio than *SOLUGAS* design point. Simultaneous variations of both parameters show that higher overall efficiencies are found when temperature increases for small pressure ratios. However, another significant outcome is that pressure ratio is not determining regarding LCoE minimization when high temperatures are considered.

On the other hand, heliostat field and solar receiver parameters are also analysed. A very illustrative example is related to variations regarding solar receiver aperture diameter (*DR*), represented in Fig. 2.32. Solar subsystem efficiency exhibits a maximum at lightly smaller values than *SOLUGAS* design point as a consequence of balance between optical efficiency performance and concentration ratio evolution. In addition, maximum annual net energy and minimum fuel consumption evolutions are reached for the same receiver diameters. Finally, LCoE increases almost quasi-linearly with receiver diameter since linear receiver cost evolution dominates over net energy and fuel consumption parabolic behaviour. All those results should be carefully considered since currently solar components costs have a large degree of uncertainty.

Chapter 3. Publications

In this Chapter, all publications that constitute the doctoral thesis work are appended. In the beginning, seven published papers are ordered chronologically. Afterwards, two book chapters and a published proceeding are also arranged with the same criteria, *i.e.*, taking into account chronological order.

3.1 Paper 1 – Seasonal thermodynamic prediction of the performance of a hybrid solar gas-turbine power plant

Title: "Seasonal thermodynamic prediction of the performance of a hybrid solar gas-turbine power plant"
Journal: *Energy Conversion and Management*
Authors: M.J. Santos, **R.P. Merchán**, A. Medina, A. Calvo Hernández
Year: 2016
Volume: 115
Pages: 89-102
DOI: http://dx.doi.org/10.1016/j.enconman.2016.02.019
Reference: [128]

Resumen

En este artículo se ha desarrollado un modelo teórico y termodinámico para plantas termosolares de torre central con turbinas de gas. El objetivo de la planta es producir una potencia neta constante que se pueda verter fácilmente a la red eléctrica. De esta forma, se considera una planta híbrida que emplea una cámara de combustión con gas natural para contrarrestar las fluctuaciones de la irradiancia solar y conseguir así una temperatura de entrada a la turbina aproximadamente constante. Por consiguiente, se tiene en cuenta que la planta está formada por tres susbsistemas: solar, cámara de combustión y máquina térmica, incluyéndose las principales fuentes de pérdidas en cada uno de ellos. El modelo se ha implementado en el lenguaje de programación de *Mathematica*®, desarrollando así un código propio. Para ello, se ha tomado como planta base la planta de *SOLUGAS*, en Sevilla, que sirve también para llevar a cabo la validación del modelo. Se introducen datos meteorológicos reales de irradiancia solar y temperatura ambiente en el código desarrollado, de forma que se puedan llevar a cabo simulaciones dinámicas en condiciones fuera de diseño. En consecuencia, uno de los objetivos básicos del artículo es realizar tanto simulaciones diarias como estacionales en las que se muestre la evolución con el tiempo de las principales variables de la planta, como son la eficiencia térmica global y la del subsistema solar o el *solar share*, el rendimiento económico y la potencia de salida. Se ha demostrado que, gracias a la hibridación, la potencia de salida varía en un rango muy pequeño a lo largo de un día y estas oscilaciones son debidas al perfil de la temperatura ambiente, que no se ha contrarrestado. Por otro lado, se observa que las pérdidas en el subsistema solar durante las horas de sol reducen la eficiencia térmica global por el día. Asimismo, también se ha calculado el consumo de combustible de la planta híbrida y las emisiones de gases contaminantes de efecto invernadero asociadas. El ahorro de combustible entre una planta recuperativa y una no recuperativa se estima en un 38.5 %.

Energy Conversion and Management 115 (2016) 89–102

Contents lists available at ScienceDirect

Energy Conversion and Management

journal homepage: www.elsevier.com/locate/enconman

Seasonal thermodynamic prediction of the performance of a hybrid solar gas-turbine power plant

M.J. Santos, R.P. Merchán, A. Medina *, A. Calvo Hernández

Departamento de Física Aplicada, Universidad de Salamanca, 37008 Salamanca, Spain

ARTICLE INFO

Article history:
Received 8 October 2015
Accepted 7 February 2016

Keywords:
Thermosolar gas-turbines
Hybrid plants
Thermodynamic model
Variable solar irradiance
Global plant performance
Seasonal evolution

ABSTRACT

An entirely thermodynamic model is developed for predicting the performance records of a solar hybrid gas turbine power plant with variable irradiance and ambient temperature conditions. The model considers a serial solar hybridization in those periods when solar irradiance is high enough. A combustion chamber allows to maintain an approximately constant inlet temperature in the turbine ensuring a stable power output. The overall plant thermal efficiency is written as a combination of the thermal efficiencies of the involved subsystems and the required heat exchangers. Numerical values of model input parameters are taken from a central tower installation recently developed near Seville, Spain. Real data for irradiance and external temperature are taken in hourly terms. The curves of several variables are obtained for representative days of all seasons: overall plant efficiency, solar subsystem efficiency, solar share, fuel conversion rate, and power output. The fuel consumption assuming natural gas fueling is calculated and the reduction in greenhouse emissions is discussed. The model can be applied to predict the daily and seasonal evolution of the performance of real installations in terms of a reduced set of parameters.

1. Introduction

Power generation based on gas turbine technology has experienced an enormous evolution since the first industrial gas turbines built about 1940 [1]. Directly fired coal combustion with a poor efficiency and large carbon and other emissions has evolved towards more complex, clean, and efficient techniques. Moreover, renewable energy resources have been incorporated [2–4]. Gas turbines are very versatile and can operate directly or indirectly fired [5]. This fact makes them specially suitable for their integration in concentrated central tower thermosolar plants. Another key advantage is their reduced water requirements. This is essential in regions with favorable solar irradiance conditions [6], usually linked to water shortage. These power plants can be combined with other cycles in order to improve their overall efficiency [7–11].

During the last years several experimental projects have tried to develop hybrid solar gas turbine technologies in which concentrated solar power [12–14] coming from a central receiver plant is used to heat pressurized air that performs a Brayton cycle [15–18]. The term hybrid refers to the fact that during low solar radiation periods a combustion chamber ensures a stable power release to the electricity grid and avoids the use of storage systems [19]. Several hybridization strategies have been proposed [19–22]. Hybridization can be performed by retrofitting an existing standard fossil plant or designing an original hybrid one [23]. Usually there is more flexibility in designing and optimizing a brand new one, solving the design challenges properly. It is thus required to simulate the hybrid system, taking into account technological, thermodynamic, and economic ingredients [10,20,24]. For design purposes it is usual to choose particular stationary conditions for solar irradiance and ambient temperature. Sometimes these design point conditions are too optimistic and do not properly reflect the fluctuating behavior due to daily and seasonal changes of solar irradiance at a particular place.

Apart from R+D projects, prototypes, and experimental installations several research works have been published in the last times. Some of them make use of commercial simulation environments (TRNSYS®, Thermoflex®, EES®, etc.) or in-house developed software which allows a detailed description of all plant components and specific calculations on the solar subsystem [16,25,26]. With respect to the latter, exhaustive computations for the solar efficiency including mirror area, spillage, blocking and shadowing effects, mirror tracking strategies, and so on are accomplished

* Corresponding author.
E-mail addresses: smjesus@usal.es (M.J. Santos), rpmerchan@usal.es (R.P. Merchán), amd385@usal.es (A. Medina), anca@usal.es (A. Calvo Hernández).

http://dx.doi.org/10.1016/j.enconman.2016.02.019
0196-8904/

Nomenclature

A_a	aperture area of the collector
A_r	absorber area of the collector
a_c	isentropic compressor pressure ratio
a_t	isentropic turbine pressure ratio
C	solar collector concentration ratio
c_w	specific heat of the working fluid
f	solar share
G	direct solar irradiance
h_1	radiation heat loss coefficient for the solar collector
h_2	effective convection and conduction loss coefficient for the solar collector
$\dot{m}$	mass flow rate of the working substance
$\dot{m}_f$	fuel mass flow rate
P	power output
$\lvert\dot{Q}_{\mathrm{H}}\rvert$	total heat-transfer rate absorbed from the working fluid
$\lvert\dot{Q}_{\mathrm{HC}}\rvert$	heat input from the combustion chamber
$\lvert\dot{Q}'_{\mathrm{HC}}\rvert$	heat rate transferred from the combustion chamber to the associated heat exchanger
$\lvert\dot{Q}_{\mathrm{HS}}\rvert$	heat rate input from the solar collector
$\lvert\dot{Q}'_{\mathrm{HS}}\rvert$	heat rate transferred from the solar collector to the associated heat exchanger
$\lvert\dot{Q}_{\mathrm{L}}\rvert$	heat-transfer rate between the working fluid and the ambient
Q_{LHV}	lower heating value of the fuel
r_e	fuel conversion rate
r_p	overall pressure ratio
T_{HC}	working temperature of the combustion chamber
T_{HS}	working temperature of the solar collector
T_{L}	ambient temperature (K)
T_x	working fluid temperature after the heat input from the recuperator
$T_{x'}$	working fluid temperature after heat input from the solar collector
T_y	working fluid exhaust temperature
T_3	turbine inlet temperature
U_{L}	convective losses of the solar collector
α	effective emissivity
η	overall thermal efficiency
η_C	combustion chamber efficiency
η_{H}	thermal efficiency of the Brayton heat engine
$\varepsilon_{\mathrm{HC}}$	combustion chamber heat exchanger effectiveness
$\varepsilon_{\mathrm{HS}}$	solar collector heat exchanger effectiveness
η_S	solar collector efficiency
η_0	effective transmittance–absorptance product
ε_c	isentropic efficiency of the compressor
ε_L	cold side heat exchanger effectiveness
ε_r	recuperator effectiveness
ε_t	isentropic efficiency of the turbine
γ	adiabatic coefficient of the working fluid
ρ_{H}	irreversibilities due to pressure drops in the heat input
ρ_L	irreversibilities due to pressure drops in the heat release
σ	Stefan–Boltzmann constant
τ_{HS}	temperature ratio associated to the solar collector
τ_{HC}	temperature ratio associated to the combustion chamber

[27–29]. Particular emphasis has been devoted to one of the critical points to obtain good overall performance records, the volumetric receivers that transfer the solar heat to the working fluid [30–32]. These simulations rely on the detailed model of each plant component, thus leading to a large amount of parameters to be simultaneously optimized which is a difficult task. So, it is not easy to extract direct physical information about the main losses sources in the plant and to plan global strategies for the optimization of the plant design and operation as a whole.

On the other side, there are several theoretical works starting from the Brayton ideal cycle. Thereafter refinements are included in cycle thermodynamics in order to recover realistic output records [33–37]. Usually, in these works the model for the concentrated solar subsystem, although including the main heat transfer losses, is simple. This favors to obtain closed analytical expressions for thermal efficiencies and power output, and then check the model predictions for particular design point conditions, with fixed values of solar irradiance and ambient temperature. And in a possible step forward to suggest and guide optimization strategies.

The main objectives of this work are aligned in the last *modus operandi*, but with a noticeable novelty: to develop a dynamic model that allows the incorporation of solar irradiance and ambient temperature fluctuations at a particular location. This procedure will help to predict realistic curves for plant efficiencies, avoiding the use of *a priori* design point values of solar irradiance and external temperature. The model, in which refers to the thermodynamic cycle starts from a closed Brayton cycle however incorporating the main losses sources: non-ideal turbine and compressor, pressure decays, heat exchangers, heat transfer losses in the solar collector, combustion inefficiencies, etc. The model is flexible and allows to check the performance of several plant configurations. Special emphasis will be done on recuperation because of its key influence on the plant output records [6,37,38].

The combination of the models for the solar part and the thermodynamic engine leads to expressions for the plant global efficiency and other performance data in terms of a reduced number of parameters, with clear physical meaning each. This is a basic pre-design simulation scheme in order to understand the main bottlenecks to consider in the design of this kind of facilities. It will be shown that the comparison of the model predictions with real plant data at particular conditions is good. Moreover, we shall present a complete analysis of the evolution of plant records along a year, taking real measurements for solar irradiance and ambient temperature for representative days of each season. Particularly, fuel consumption and greenhouse emissions will be estimated and analyzed.

2. Thermodynamic plant model

We consider a central tower solar installation as sketched in Fig. 1. A single step recuperative closed Brayton cycle is hybridized in order to obtain a stable power output, independent of the solar irradiance conditions. The design is flexible because the plant can work in different modes: with or without solar hybridization depending on irradiance conditions, and with or without recuperator. Next we briefly describe the main thermodynamic processes experienced by the working fluid. The working fluid at the compressor exit (temperature T_2) is heated up through a recuperator that makes use of the high temperature of the gas after the turbine, T_4. The temperature of the fluid at the recuperator exit, T_x, is elevated first by the heat released by the central tower solar subsystem if solar irradiance is enough. Afterwards, the fluid reaches a higher temperature, $T_{x'}$ and then, in the last heating step, it receives an energy input from a combustion chamber through another heat exchanger. The final temperature at the turbine inlet,

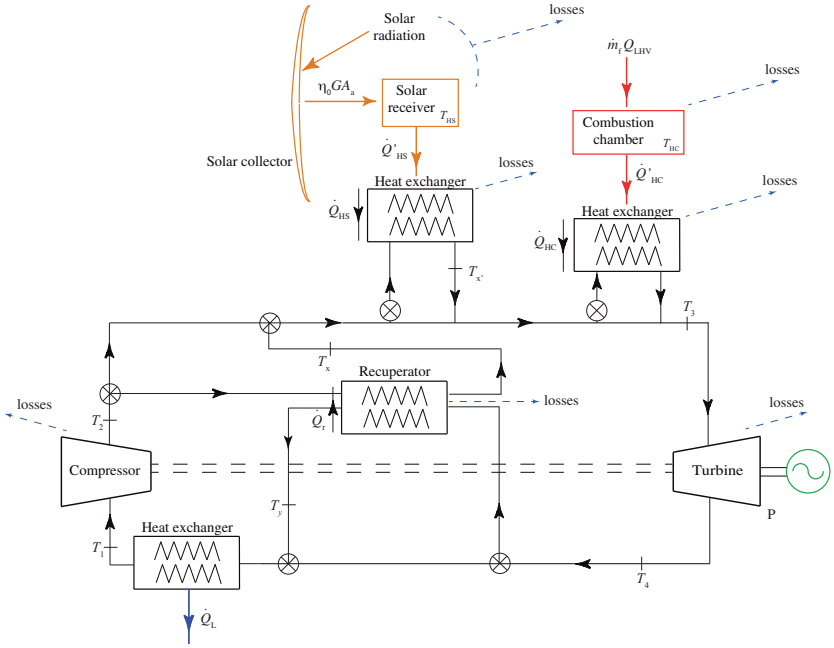

Fig. 1. Scheme of the hybrid solar gas-turbine plant considered. The main heat transfers and temperatures are depicted. Also the key losses sources considered in the model are shown.

T_3, is taken as approximately constant, so the power released by the installation to the grid is stable. In the case of insufficient irradiance a shut-off valve redirects the fluid directly to the heat exchanger below the combustion chamber.

Next we detail the nomenclature for the different heat transfers in the model. The solar subsystem receives a heat input from the sun given by GA_a where G is the direct solar irradiance and A_a the aperture area of the solar field. The solar irradiance is a function of time because it depends on the sun position during the day, weather conditions, and seasonal fluctuations. After discounting the losses, the receiver releases a useful energy to a heat exchanger, $\dot{Q}'_{HS}$, that in turn releases a final heat rate $\dot{Q}_{HS}$ to the working fluid.

A similar scheme is followed to describe the combustion chamber subsystem. The energy input in this subsystem is $\dot{m}_f Q_{LHV}$, where $\dot{m}_f$ is the fuel mass consumption rate and Q_{LHV} its corresponding lower heating value. The mass fuel rate will be also considered as time dependent, in accordance to the fluctuations of G. It should compensate variations in G in such a way that the turbine inlet temperature remains approximately constant in all conditions. In the combustion chamber losses due to incomplete combustion and heat transfers to the surroundings are accounted for. The heat rate received by the working fluid from combustion of the fuel is denoted as $\dot{Q}_{HC}$. The effectivenesses of the heat exchangers associated to the solar and the combustion subsystems are denoted as ε_{HS} and ε_{HC} respectively. The internal heat transfer associated to recuperation is called $\dot{Q}_r$. In order to close the thermodynamic cycle a cold-side heat exchanger is considered. The compressor inlet temperature, T_1, will depend on the external temperature, T_L, that will fluctuate due to daily and seasonal changes. Thus, all other temperatures in the cycle will oscillate because of the same reasons. The plant delivers a mechanical power output, P, independent of solar radiation fluctuations.

2.1. Global thermal efficiency of the plant

The thermal efficiency of the whole system, η, is the ratio between the net mechanical power output, P, and the total heat input rate,

$$\eta = \frac{P}{GA_a + \dot{m}_f Q_{LHV}} \tag{1}$$

The following objective is to express this global efficiency in terms of the efficiency of the solar collector, η_S, that of the combustion chamber, η_C, the efficiency of the Brayton heat engine, η_H, and the effectivenesses of all the required heat exchangers.

The solar collector efficiency, η_S, is the quotient between the useful energy it delivers per unit time, $|\dot{Q}'_{HS}|$ (see Fig. 1) and the solar energy rate, GA_a, *i.e.*, $\eta_S = |\dot{Q}'_{HS}|/GA_a$. The working fluid undergoing the thermal cycle receives the solar heat input in the central tower of the solar facility, which transfers a fraction of $\left|\dot{Q}'_{HS}\right|$, $|\dot{Q}_{HS}| = \varepsilon_{HS}\left|\dot{Q}'_{HS}\right|$ to the working fluid. The solar collector efficiency can be written as: $\eta_S = |\dot{Q}_{HS}|/(\varepsilon_{HS} GA_a)$.

Likewise the combustion chamber generates a heat rate, $|\dot{Q}'_{HC}|$, that is transferred to the working fluid by means of a heat exchanger with effectiveness $\varepsilon_{HC} = |\dot{Q}_{HC}|/|\dot{Q}'_{HC}|$, so the working fluid receives a heat rate $|\dot{Q}_{HC}|$ coming from combustion. Note that we are assuming an externally fired gas turbine (EFGT), so the fuel is not injected in the air itself, but the gas receives the energy input coming from combustion through a heat exchanger. The efficiency of the combustion chamber is thus given by: $\eta_C = |\dot{Q}_{HC}|/(\varepsilon_{HC}\dot{m}_f Q_{LHV})$.

The thermal efficiency of the heat engine itself is the fraction between the net power output, P, and the total heat input received by the working fluid, $\eta_H = P/(|\dot{Q}_{HS}| + |\dot{Q}_{HC}|)$. Defining a solar share fraction as the ratio of the solar heat rate that the working fluid absorbs with respect to the total heat input, $f = |\dot{Q}_{HS}|/\left(|\dot{Q}_{HS}| + |\dot{Q}_{HC}|\right)$,[1] the overall efficiency of the whole system, η, is obtained by substituting the definitions of η_S and η_C in Eq. (1):

$$\eta = \eta_S \eta_C \eta_H \left[\frac{\varepsilon_{HS}\varepsilon_{HC}}{\eta_C \varepsilon_{HC} f + \eta_S \varepsilon_{HS}(1-f)}\right] \tag{2}$$

This expression is valid for the hybrid mode when both heat sources are simultaneously releasing energy to the fluid. In the particular case in which eventually all the energy input comes from the solar collector, $f = 1$, and $\eta = \eta_S \eta_H \varepsilon_{HS}$, and when solar irradiance is null, and the turbine works only with the heat released in the combustion reactions, $f = 0$, and $\eta = \eta_C \eta_H \varepsilon_{HC}$.

It is also interesting to define a performance relative to the energy input with an economical cost, *i.e.*, to the fuel burned. It constitutes a *fuel conversion rate*, and can be defined as suggested by Heywood [39] for internal combustion engines, $r_e = P/(\dot{m}_f Q_{LHV})$. It is easy to show that:

$$r_e = \frac{\eta \eta_S \eta_H \varepsilon_{HS}}{\eta_S \eta_H \varepsilon_{HS} - \eta f} \tag{3}$$

In the particular case all the energy input comes from combustion, $f = 0$, and $r_e = \eta$. In the opposite limit, if eventually all the energy was solar, $f = 1$, and $\eta = \eta_S \eta_H \varepsilon_{HS}$, so $r_e \to \infty$. Thus, note that this rate is defined in the interval $[0, \infty]$. It does not represent a thermodynamic efficiency, it is a measure of the system performance from the viewpoint of fuel consumption costs. In a solar hybrid system as the one considered here, r_e, could get values over 1 at some point because a fraction of the energy input lacks of associated costs.

2.2. Solar subsystem and combustion process efficiencies

We consider a simple model for the concentrating solar system in order to be able to obtain analytical closed expressions for the overall plant efficiency. Of course more sophisticated representations could be considered (as those provided by commercial simulation software) but we intend to maintain a purely thermodynamic straightforward description, depending just on a few parameters. At low and intermediate working temperatures for the solar collector, T_{HS}, losses essentially comes from conduction and convection. At high temperatures radiation losses become significant and should be considered in any model. The energy collected at the aperture is GA_a, and the useful energy provided by the solar plant, $|\dot{Q}'_{HS}|$, is the difference between the energy transmitted to the receptor, $\eta_0 GA_a$ and the losses. η_0 is the effective optical efficiency considering losses coming from spillage, shadowing, blocking, sun position effects, and so on. Losses contain a linear term in temperature differences accounting for conduction and convection losses and a term on the fourth power of temperatures, linked to radiation losses. Thus, the useful heat released from the collector and its efficiency can be respectively expressed, as [40–44]:

$$|\dot{Q}'_{HS}| = \eta_0 GA_a - \alpha\sigma A_r T_L^4(\tau_{HS}^4 - 1) - U_L A_r T_L(\tau_{HS} - 1) \tag{4}$$

$$\eta_S = \frac{|\dot{Q}'_{HS}|}{GA_a} = \eta_0\left[1 - h_1 T_L^4(\tau_{HS}^4 - 1) - h_2 T_L(\tau_{HS} - 1)\right] \tag{5}$$

In Eqs. (4) and (5), $\tau_{HS} = T_{HS}/T_L$ denotes the ratio between the working temperature of the solar receiver, T_{HS}, and the surroundings, T_L. A_a and A_r are, respectively, the aperture and absorber areas, $h_1 = \alpha\sigma/(\eta_0 GC)$, $h_2 = U_L/(\eta_0 GC)$ are losses parameters, where U_L is the convective heat loss coefficient, α is the effective emissivity of the collector, $C = A_a/A_r$ is the concentration ratio, and σ the Stefan–Boltzmann constant. It will be considered in our model that the direct solar irradiance, G, and the surroundings temperature, T_L, are time functions because oscillate during a day and change with seasonal and meteorological conditions. For each particular pair of values of G and T_L at any given instant, the working temperature of the receiver, T_{HS}, is calculated by balancing the energy received from the sun and that released to the working fluid experiencing the bottoming thermal cycle [35]. The heat released by the solar subsystem to the working fluid is $|\dot{Q}_{HS}| = \varepsilon_{HS}|\dot{Q}'_{HS}|$, where $\varepsilon_{HS} = (T_{x'} - T_x)/(T_{HS} - T_x)$.

The efficiency of the combustion chamber, η_C, once elected the fuel to be burned and the fuel–air equivalence ratio, can be considered as a constant parameter. In real equipment it could slightly change with fluctuations of the fuel–air equivalence ratio, the composition of the fuel, its temperature, and several other variables, but we are more interested in an adequate qualitative description. The heat received by the working fluid from the combustion chamber, $\dot{Q}_{HC}$, can be written as:

$$|\dot{Q}_{HC}| = \varepsilon_{HC}|\dot{Q}'_{HC}| = \varepsilon_{HC}\eta_C \dot{m}_f Q_{LHV} \tag{6}$$

By expressing the effectiveness of the heat exchanger in between the combustion chamber and the thermal cycle as (see Fig. 1) $\varepsilon_{HC} = (T_3 - T_{x'})/(T_{HC} - T_{x'})$, the heat released, in terms of temperatures, is:

$$|\dot{Q}_{HC}| = \dot{m}c_w(T_3 - T_{x'}) = \dot{m}c_w\varepsilon_{HC}(T_{HC} - T_{x'}) \tag{7}$$

where $\dot{m}$ is the working fluid mass flow and c_w is its specific heat. The effective temperature in the combustion chamber is denoted as T_{HC}, and the associated temperature ratio as $\tau_{HC} = T_{HC}/T_L$. As fluctuations in G and T_L will be taken into account, the fuel mass flow to be burned in the combustion chamber will also be a time dependent function in general given by:

$$\dot{m}_f = \frac{\dot{m}c_w(T_3 - T_{x'})}{\eta_C Q_{LHV}\varepsilon_{HC}} \tag{8}$$

where $T_{x'}$ will vary with the solar irradiance and ambient conditions. The rate of fuel mass burned can be also obtained from the fuel conversion rate, r_e, as: $\dot{m}_f = P/(r_e Q_{LHV})$.

2.3. Brayton gas-turbine efficiency

In this subsection the main assumptions considered for evaluating the efficiency of the heat engine, η_H, will be briefly outlined since the model has been detailed elsewhere in previous works by our group [37,38]. It is assumed that a mass rate of an ideal gas, $\dot{m}$, undergoes an irreversible closed recuperative Brayton cycle. The T–S diagram of the cycle is depicted in Fig. 2, where it is stressed that both the working temperature of the solar receiver, T_{HS} and that of the surroundings, T_L, are fluctuating quantities. In order to obtain analytical expressions for heat transfers, a constant

[1] Note that this is not the only definition of *solar share* or *solar fraction* in the literature [16,26].

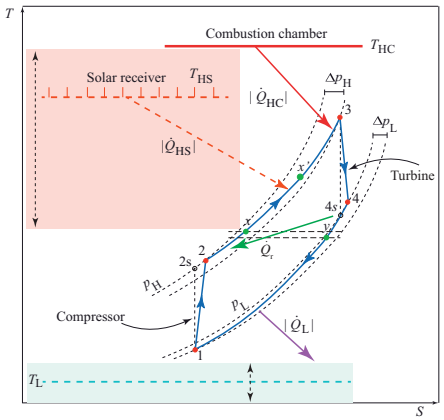

Fig. 2. T–S diagram of the irreversible Brayton cycle experienced by the working fluid. Several irreversibility sources are considered (see text). The solar receiver temperature T_{HS} and the ambient temperature T_L are considered as variable parameters.

specific heat, c_w is assumed. Although this is a debatable hypothesis, as elsewhere commented in the literature [40], it allows to get systematic expressions, and so check the influence of the most significant parameters and extract conclusions about the main physical mechanisms that lead to losses in the plant. For numerical applications, effective values for c_w or the adiabatic coefficient, γ, will be calculated by averaging the corresponding temperature dependent polynomials, $c_w(T)$, in the adequate temperature intervals.

1. As starting step the gas is compressed ($1 \rightarrow 2$) by means of a non-ideal compressor. Its isentropic efficiency is given by $\varepsilon_c = (T_{2s} - T_1)/(T_2 - T_1)$. In this equation T_{2s} represents the temperature of the working fluid after the compression process if it was adiabatic and T_2 is the actual temperature at the compressor outlet.
2. Between states 2 and 3, in the most general situation, the gas receives three energy inputs in sequence. First, the non-ideal recuperator increases the gas temperature from T_2 to T_x. Its effectiveness, ε_r, is defined as the ratio between the actual temperature $(T_x - T_2)$ increase and the maximum ideal one $(T_4 - T_2)$: $\varepsilon_r = (T_x - T_2)/(T_4 - T_2) = (T_y - T_4)/(T_2 - T_4)$. In the case of a non-recuperative cycle, $\varepsilon_r = 0$, and in the ideal limit, $\varepsilon_r = 1$.
   Secondly, the gas receives a heat flow, $|\dot{Q}_{HS}|$, from the solar subsystem (step $x \rightarrow x'$) and thus its temperature increases from T_x to $T_{x'}$. Finally, the gas receives a completing heat input from the combustion chamber ($x' \rightarrow 3$) in order to ensure an approximately constant turbine inlet temperature, T_3, independently of the solar irradiance conditions.
   In which respect to the pressure during the heat addition processes, a global parameter, ρ_H, that quantifies the pressure decrease in the process $2 \rightarrow 3$ is considered. In real plants pressure decays are associated to the particular equipment in any of the three steps of the heat input process, so the curve $2 \rightarrow 3$ would not be as smooth as it is plotted in Fig. 2. But the consideration of a unique global pressure decay parameter allows to obtain analytical equations and to numerically check the effects of pressure decays in the output parameters of the plant [26]. This parameter, ρ_H, is defined as:

$$\rho_H = \left(\frac{p_H - \Delta p_H}{p_H}\right)^{(\gamma-1)/\gamma} \tag{9}$$

   where p_H is the highest pressure of the gas and $(p_H - \Delta p_H)$ its pressure at the turbine inlet.
3. In the state 3 the working fluid has reached its maximum temperature and its is expanded by means of a non-ideal turbine performing the power stroke ($3 \rightarrow 4$). In Fig. 2 the state 4s represents the final state in the ideal case the turbine behaves isentropically, and the state 4 is the actual final state after expansion. The isentropic efficiency of the turbine, ε_t, is given by: $\varepsilon_t = (T_4 - T_3)/(T_{4s} - T_3)$.
4. Lastly, the gas recovers the conditions at the initial state 1 by releasing heat in the process $4 \rightarrow 1$ through two steps. First, by means of the recuperator (process $4 \rightarrow y$) and later by exchanging heat to the ambient through a non-ideal heat exchanger with effectiveness, ε_L (process $y \rightarrow 1$): $\varepsilon_L = (T_1 - T_y)/(T_L - T_y)$.
   The pressure loss during the whole heat release process is measured through a coefficient ρ_L given by:

$$\rho_L = \left(\frac{p_L - \Delta p_L}{p_L}\right)^{(\gamma-1)/\gamma} \tag{10}$$

   where p_L is the gas pressure at the turbine outlet and $p_L - \Delta p_L$ its lowest pressure during the cycle. It is convenient to define a global pressure ratio, r_p as: $r_p = p_H/(p_L - \Delta p_L)$.
   Provided that the processes $1 \rightarrow 2s$ and $3 \rightarrow 4s$ are adiabatic (see Fig. 2), two parameters, a_c and a_t, related to the pressure ratios of the compressor and the turbine respectively are defined:

$$a_c = \frac{T_{2s}}{T_1} = \left(\frac{p_H}{p_L - \Delta p_L}\right)^{(\gamma-1)/\gamma} = r_p^{(\gamma-1)/\gamma} \tag{11}$$

$$a_t = \frac{T_3}{T_{4s}} = \left(\frac{p_H - \Delta p_H}{p_L}\right)^{(\gamma-1)/\gamma} \tag{12}$$

   From Eqs. (9) and (10) it is easy to find a relationship between them, $a_t = a_c \rho_H \rho_L$.

Once, the main hypothesis and parameters have been made explicit, we express the temperatures of all the states in the cycle in terms of the temperature of the solar collector, T_{HS}, that of the combustion chamber, T_{HC}, and the pressure ratios of the compressor, a_c and the turbine, a_t. By using the definitions in the section above, it is possible to obtain the following set of equations:

$$T_1 = \varepsilon_L T_L + T_y(1 - \varepsilon_L) \tag{13}$$

$$T_2 = T_1 + \frac{1}{\varepsilon_c}(T_{2s} - T_1) = T_1 Z_c \tag{14}$$

$$T_3 = \varepsilon_{HC} T_{HC} + T_{x'}(1 - \varepsilon_{HC}) \tag{15}$$

$$T_4 = T_3 - \varepsilon_t(T_3 - T_{4s}) = T_3 Z_t \tag{16}$$

$$T_x = \varepsilon_r T_4 + T_2(1 - \varepsilon_r) \tag{17}$$

$$T_y = \varepsilon_r T_2 + T_4(1 - \varepsilon_r) \tag{18}$$

$$T_{x'} = \varepsilon_{HS} T_{HS} + T_x(1 - \varepsilon_{HS}) \tag{19}$$

Eqs. (14) and (16) were simplified by introducing two definitions:

$$Z_c = 1 + \frac{1}{\varepsilon_c}(a_c - 1) \tag{20}$$

$$Z_t = 1 - \varepsilon_t\left(1 - \frac{1}{a_t}\right) \tag{21}$$

By simultaneously using Eqs. (13)–(19) it is feasible to express all the temperatures in terms of the temperatures of the heat sources,

T_{HS} and T_{HC}, the ambient temperature, T_L, the pressure ratio, r_p and all the irreversibility parameters defined above. The following closed set of expressions is obtained:

$$T_2 = \frac{(1-\varepsilon_L)(1-\varepsilon_r)[\varepsilon_{HC}T_{HC} + \varepsilon_{HS}T_{HS}(1-\varepsilon_{HC})] + \varepsilon_L T_L\left[Z_t^{-1} - (1-\varepsilon_{HC})(1-\varepsilon_{HS})\varepsilon_r\right]}{\left[Z_c^{-1} - (1-\varepsilon_L)\varepsilon_r\right]\left[Z_t^{-1} - (1-\varepsilon_{HC})(1-\varepsilon_{HS})\varepsilon_r\right] - (1-\varepsilon_{HC})(1-\varepsilon_{HS})(1-\varepsilon_L)(1-\varepsilon_r)^2} \tag{22}$$

$$T_4 = \frac{[\varepsilon_{HC}T_{HC} + \varepsilon_{HS}T_{HS}(1-\varepsilon_{HC})]\left[Z_c^{-1} - (1-\varepsilon_L)\varepsilon_r\right] + \varepsilon_L T_L(1-\varepsilon_{HC})(1-\varepsilon_{HS})(1-\varepsilon_r)}{\left[Z_c^{-1} - (1-\varepsilon_L)\varepsilon_r\right]\left[Z_t^{-1} - (1-\varepsilon_{HC})(1-\varepsilon_{HS})\varepsilon_r\right] - (1-\varepsilon_{HC})(1-\varepsilon_{HS})(1-\varepsilon_L)(1-\varepsilon_r)^2} \tag{23}$$

It is easy to get the temperature of the working fluid at the recuperator exit, T_y, by substituting Eqs. (22) and (23) in Eq. (18). The total heat input rate, $|\dot{Q}_H|$, and, the heat release, $|\dot{Q}_L|$, are expressed in terms of the temperatures in the following way:

$$|\dot{Q}_H| = |\dot{Q}_{HS}| + |\dot{Q}_{HC}| = \dot{m}c_w(T_3 - T_x) \tag{24}$$

$$|\dot{Q}_L| = \dot{m}c_w(T_y - T_1) \tag{25}$$

where

$$|\dot{Q}_{HS}| = \dot{m}c_w(T_{x'} - T_x) = f|\dot{Q}_H| \tag{26}$$

$$|\dot{Q}_{HC}| = \dot{m}c_w(T_3 - T_{x'}) = (1-f)|\dot{Q}_H| \tag{27}$$

Thus, the power output released by the heat engine, $P = |\dot{Q}_H| - |\dot{Q}_L|$, and its thermal efficiency, $\eta_H = P/|\dot{Q}_H|$, have analytical expressions susceptible to be evaluated for any particular parameters arrangement. And so, from the considered models for the solar and the combustion chamber subsystems, it is possible to obtain the overall plant efficiency from Eq. (2).

It is important to stress at this point that the solar share, f, in our work does not appear as an independent parameter, but it is a function of the temperatures of the heat sources, G and solar collector details, and all the other parameters. Moreover, as a consequence of the assumptions made in this model for the sequence of heat absorption processes, the following inequalities for temperatures hold (see Fig. 2):

$$T_3 \geqslant T_{x'} \geqslant T_x \tag{28}$$

$$T_{HS} \geqslant T_x \tag{29}$$

$$T_{HC} \geqslant T_{x'} \tag{30}$$

Eq. (28) is trivially obtained from Eqs. (26) and (27). The particular case $T_3 = T_{x'}$ holds when solar radiation is capable to provide enough energy to increase gas temperature from T_x to T_3. In terms of the solar share, $f = 1$. The equality $T_{x'} = T_x$ appears in the opposite case, all the energy comes from combustion, so the solar share is zero (by night or for very poor irradiance conditions). The other relationships, Eqs. (29) and (30), arise because effectivenesses of the heat exchangers, $\varepsilon_{HS} > 0$ and $\varepsilon_{HC} > 0$. The equalities holds in the case of ideal heat exchangers with no losses, $\varepsilon_{HS} = 1$ and/or $\varepsilon_{HC} = 1$.

It is interesting to stress at this point that the model we have outlined is easy to implement. It is just necessary to consider specific numerical values for losses parameters for the main plant components and for solar irradiance, G, and ambient temperature, T_L. Particularly, fluctuations on G and T_L are effortlessly incorporated and the equilibrium working temperature of the solar receiver calculated at any time. All input parameters have a direct physical meaning and any performance variable can be estimated. So, it is feasible to check the importance of any design or irreversibility parameter in the final records of the plant. In the following sections we shall assume as working fluid for the thermal cycle pressurized air, but the model can be applied to any gas. For instance CO_2 or noble gases for which recent research demonstrate several advantages [9,45–48].

3. Numerical implementation

3.1. Numerical implementation at design point conditions

The model presented in this work was validated for fixed solar irradiance conditions in a previous paper [35]. In this section we outline the main background and conclusions of the numerical validation. As validation target it was elected the central tower concentrating collector developed by Abengoa Solar near Seville, Spain, under the project called SOLUGAS [18]. In this project, a commercial recuperative natural gas turbine (*Mercury 50*, Caterpillar) [49], was placed at the top of a 75 m high tower behind the receiver. The main objective of the installation is to check the performance and the costs estimate of this plant scheme at a pre-commercial stage. Within this aim an heliostat field consisting of 69 units of 121 m^2 reflective area each, with an innovative tracking system was built. It can produce about 5 MWth.

The validation process is divided in two steps. First, we tried to reproduce the main performance records of the turbine *Mercury 50*, for which the manufacturer provides several specifications [49]. Table 1 summarizes some data required to run our simulation as well as the measured and calculated values. The specifications give the efficiency and power output as measured as generator terminals. In our numerical calculations, generator efficiency was taken as 0.99%. We considered as working fluid air, with average values of the constant pressure specific heat, c_w and adiabatic coefficient, γ. Polynomial fits from the literature [50] were integrated over the interval $[T_1, T_3]$. The pressure losses parameters, ρ_H and ρ_L, correspond to relative pressure losses, both in heat input and heat release processes of 9.2%. The required losses parameters were assumed from standard values. Computations lead to fairly good agreement with manufacturer's measures. It is noteworthy that the relative deviations of efficiency at generator terminals, η_{He}, and power output, P_e, are below 1%. In [35] we also presented the explicit comparison of our predictions for the evolution of power output, thermal efficiency, and heat rate as functions of the ambient temperature with those provided by the manufacturer (see Fig. 4 in [35]). Also, results are quite satisfactory in spite that

Table 1
Manufacturer's specifications for the turbine *Mercury 50* (solar turbines, caterpillar) [49] and the predictions of our thermodynamic model with the irreversibility set of parameters shown.

Mercury 50 manufacturer's specifications and output records			
$\dot{m} = 17.9$ kg/s	$r_p = 9.9$	$T_L = 288$ K	
$T_3 = 1423$ K	$T_y = 647$ K	$\eta_{He} = 0.385$	$P_e = 4.6$ MW$_e$
Model: assumed losses parameters			
$\varepsilon_{HC} = 0.980$	$\rho_H = \rho_L = 0.975$	$\varepsilon_t = 0.885$	$\varepsilon_r = 0.775$
$\varepsilon_L = 0.985$		$\varepsilon_c = 0.815$	
Model: estimated output records			
$T_3 = 1418$ K	$T_y = 657$ K	$\eta_{He} = 0.384$	$P_e = 4.6$ MW$_e$
Relative deviations			
T_3	T_y	η_{He}	P_e
0.4%	1.5%	0.2%	0.6%

Table 2
Simulation predictions for the main parameters of the hybrid solar gas-turbine plant developed for the SOLUGAS project [12,18]. The elected parameters for the simulation of the combustion chamber and solar subsystems are shown. All other parameters for the gas-turbine itself are those contained in Table 1.

Solar plant parameters at design point		
$\eta_0 = 0.73$	$\varepsilon_{HS} = 0.78$	$G = 860$ W/m^2
$\alpha = 0.1$	$C = 425.2$	$U_L = 5$ W/(m^2 K)
Combustion related parameters		
$\eta_C = 0.98$	$T_{HC} = 1430$ K	$\varepsilon_{HC} = 0.98$
Thermal cycle temperatures (K)		
$T_1 = 294$	$T_2 = 590$	$T_x = 822$
$T_{x'} = 1027$	$T_3 = 1422$	$T_4 = 890$
$T_y = 657$		
Estimated output parameters		
$f = 0.341$	$\dot{m}_f = 0.172$ kg/s	$P = 4.647$ MW
Estimated efficiencies		
$\eta_H = 0.393$	$\eta_S = 0.698$	$\eta = 0.300$

the real turbine follows an open Brayton cycle and our model describes a closed one.

Second, it is more difficult to perform the same direct comparison for the whole plant working in hybrid conditions. This is due to the wariness of the companies developing R+D facilities of this type to make accessible details about the main parameters of the installations and the measured performance records. So, it is necessary to survey data for the required input parameters from different sources and present a prediction of the results of the model to check its credibility. This is done, in the case of our work, in Table 2. Input data were taken mainly from SOLUGAS (Abengoa Solar) project reports [18], the work by Romero et al. [12] but also from several other resources [40,51–53]. The design point conditions were taken from Abengoa at $G = 860$ W/m^2 and $T_L = 288$ K. The optical efficiency, $\eta_0 = 0.73$ was taken from [12] for such design point conditions. The working temperature of the solar receiver, T_{HS}, was obtained by matching the heat rate released by the solar collector, Eq. (4), and the input absorbed by the working fluid, Eq. (26). For the selected set of parameters this leads to $T_{HS} = 1085$ K that is a reasonable value. For the lower heating value of natural gas a value of $Q_{LHV} = 47.141$ MJ/kg [54] was taken. The estimated efficiencies shown at the bottom of Table 2 are in right accordance with published values for this kind of plants [12,14]. The fuel conversion rate predicted is $r_e = 0.573$.

3.2. Numerical implementation of daily variations

Direct irradiance, G, and ambient temperature, T_L, were taken from the database by Meteosevilla [55] at a location very close to the installation of the project SOLUGAS, Sanlúcar La Mayor, Seville, Spain. We took data from four regular days in 2013, each corresponding to the beginning of a season (21st): March, June, September, and December. Data were taken every 30 min. No smoothing or averaging procedures were followed. The curves for G and T_L are represented in Fig. 3. Seville has *a priori* quite favorable solar conditions. The upper panel of the figure shows that the maximum value of G reached in summer is about 875 W/m^2. The maximum of the less favorable month, December reaches about 480 W/m^2. The number of insolation hours is quite elevated. At the same time ambient temperatures are relatively high. They reach maximum values around 34 °C during the day in September (in September, at the end of summer, temperatures are higher than in June) and minimum values about 4 °C.

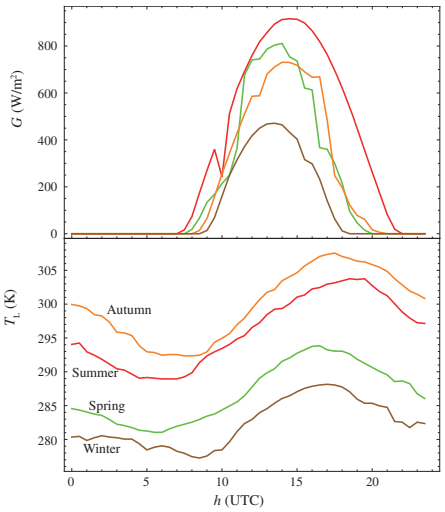

Fig. 3. Hourly direct irradiance, G, and ambient temperature, T_L, for four selected days at the beginning of each season at Seville [55]. Curves are neither smoothed nor averaged.

For each pair of values of G and T_L the working temperature of the collector, T_{HS} was calculated. It is difficult to find analytic expressions of the variations of the optical efficiency for a particular heliostat field [25], because η_0 depends on the actual concentrator and receiver geometry and optics. In consequence, trying to maintain the simplicity and analytical equations for heat transfers and efficiencies we preferred to take a realistic yearly averaged value of η_0. The numerical value was taken from the work by Romero et al. [12] for a similar facility, $\eta_0 = 0.65$.

Another important point is the one related to the pressure losses across the ducts in the plant. These losses depend of the operation regime of the plant as stressed by Barigozzi et al. [26,56]: are higher when the plant is operating in an hybrid mode and the working fluid is conducted through the solar receiver. We kept the values for ρ_H and ρ_L taken in the validation procedure (see Table 1) because they are quite pessimistic (represent pressure losses about 9%).

All the results presented in this work were obtained from our own software, developed in programming language Mathematica®. In the next sections, results with plant configurations either incorporating a recuperator or not will be shown. When no recuperator

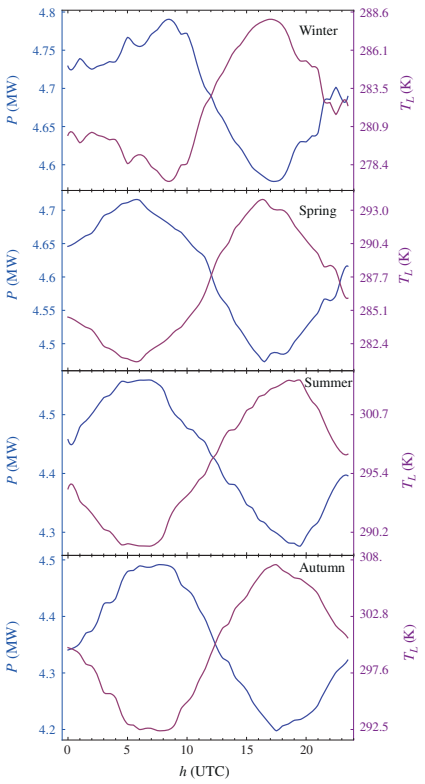

Fig. 4. Daily evolution of the power output, P, and ambient temperature, T_L, for a recuperative plant configuration. Note the small amplitude of power fluctuations.

is included, investments costs are reduced, thermal efficiency decreases, and fuel consumption is higher. But temperature of the working fluid at the exit of the expansion process is high and so, the cycle is susceptible to be combined with a bottoming cycle. In the opposite situation, when an extra investment is made in the plant and a recuperator is incorporated in the design, fuel costs decrease and thermal efficiency increases, but the temperature at the recuperator exit could make more difficult to use residual heat for bottoming cycles. Moreover, the inclusion of a recuperator will be only beneficial for not too high values of the compressor pressure ratio as discussed elsewhere in the literature [6,37,38].

4. Daily basis plant records prediction

One of the key objectives of the hybridization scheme we have followed for the plant is to guarantee a power output independent of solar irradiance fluctuations. Thus, before analyzing other output records we have evaluated the evolution of P with time for days representative of each season. In Fig. 4 the particular evolution of P during a whole day is depicted for the four seasons and a recuperative configuration. In any season power output oscillates with ambient temperature following a counterphase routine and is independent of the evolution of G. It is a well-known fact in gas turbines that an ambient temperature increase provokes a power output reduction and opposite. Barigozzi et al. [10] mention that for a temperature increase of 10 °C power output decreases about 5–13% for a simple gas turbine. Several technical procedures have been proposed in the literature in order to control and avoid if necessary these oscillations [10]. In regards to daily variations, power output increases during the night as T_L decreases, reaching a maximum around sunrise, and then decreases when T_L increases, and display a minimum when T_L is maximum. To have a quantitative idea of the amplitude of the oscillations, we have computed the relative amplitude of the oscillations defined as $(P_{max} - P_{min})/P_{min}$. It is around 4.7% in winter (for a difference between minimum and maximum values of T_L about 11 K) and around 6.8% in summer (temperature difference about 14 K). Average value of P is slightly higher in winter (4.5% higher than in summer). So, we can conclude that power output is independent of the particular conditions of solar irradiance and is only function of ambient temperature.

4.1. Plant efficiencies

We have obtained the curves for the different thermal plant efficiencies for a representative day of each season in terms of the UTC time for two plant configurations (see Fig. 1): recuperative ($\epsilon_r = 0.775$) and non-recuperative ($\epsilon_r = 0$). These efficiencies are plotted in Figs. 5 (no recuperation is considered) and 6 (including a recuperator). The efficiency of the solar subsystem, η_S, is only defined when the solar irradiance is enough to deliver an effective heat to the working fluid, so the corresponding curves are defined for a particular time interval. For any season these curves present a wide plateau during the hours with good insolation and then η_S decreases during sunrise and sunset. The shape of the functions in these periods is only indicative because a particular model for the evolution of the solar receiver temperature with G during transients should be necessary. This is out of the scope of this work. The plateaus are associated to the fact that solar efficiency are governed by the optical efficiency, η_0, that we considered as constant. The influence of heat losses is small in the shape of η_S, specially in the non-recuperative case (see Fig. 5), only the height of the plateaus is sensitive to the temperature dependent heat losses, Eq. (5). Of course the plateaus are wider during summer, because of the higher number of insolation hours. Largest values of η_S are about 0.63 for the non-recuperative case and slightly smaller for the recuperative case. As we shall comment later on this is due to the fact that working temperatures of the solar collector are higher in this case and so heat transfer losses in the solar subsystem are larger.

The efficiency of the Brayton heat engine, η_H, is almost constant, day and night. It depends on the ambient temperature for a particular day but its time dependence is small in the scale of the plots in Figs. 5 and 6. In seasonal terms, η_H, is higher for lower ambient temperatures: winter and spring. Its numerical value significantly increases when incorporating a recuperator, as it should be expected. For instance in winter, in Fig. 5, it amounts approximately 0.28 and in Fig. 6 increases up to 0.40. This represents an increase about 43% which is very significant. The relative increase is approximately the same in all seasons.

The global plant efficiency, η, appears as a combination of η_S, η_H, the efficiency of the combustion process, η_C, and the effectivenesses of heat exchangers (see Eq. (2)). In the absence of insolation, η, is almost time independent and becomes close to η_H. Numerical differences appear due to the combustion inefficiencies

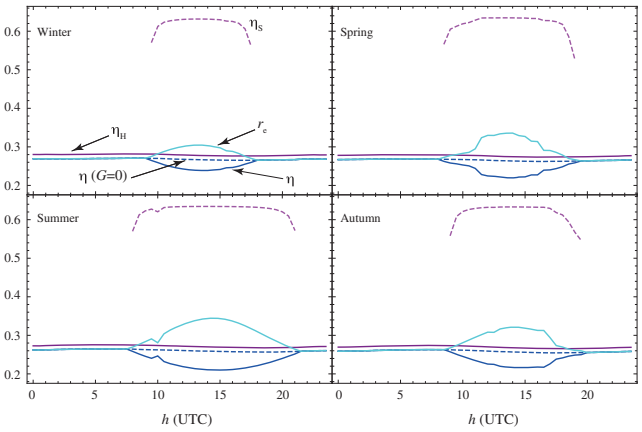

Fig. 5. Hourly evolution of plant efficiencies for representative days of each season. The plant configuration does not include recuperation ($\epsilon_r = 0$). The fuel rate conversion, r_e, although strictly not an efficiency, is also plotted (see Eq. (3)).

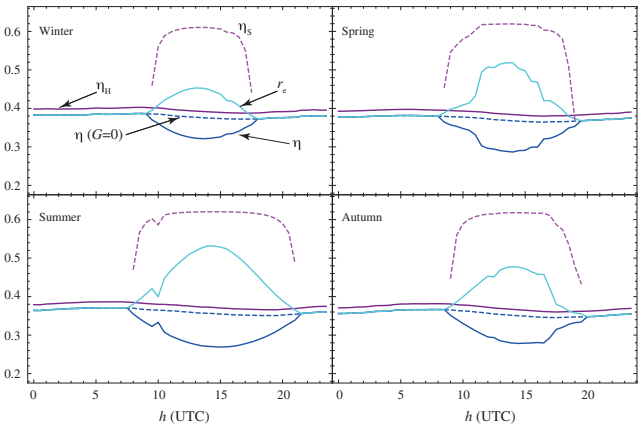

Fig. 6. Hourly evolution of plant efficiencies for representative days of each season. The plant configuration includes a recuperator with effectiveness $\epsilon_r = 0.775$.

and heat exchanger losses. When the solar receiver begins its contribution as G increases, the solar subsystem is coupled to the turbine and the combustion chamber and so, the global efficiency decreases: it presents a dip during the central hours of the day. The well width depends on the number insolation hours and its depth of the maximum values that G reaches. In the recuperative configuration, Fig. 6, of course numerical values of η are larger than for the non-recuperative, Fig. 5, one because of the important increase of η_H. For $\epsilon_r = 0$, minimum values of η change between 0.21 in summer to 0.24 in winter. For $\epsilon_r = 0.775$ the smallest value is found in summer, 0.27, and in winter is around 0.32.

Although the fuel conversion rate, r_e, thoroughly is not a thermal efficiency is also plotted in Figs. 5 and 6. It is identical to η during nights because all the heat input is associated to fuel combustion and during the day it has a parabolic shape that resembles the shape of G and qualitatively is like a mirror image of η. The maximum value of r_e appears in summer, when irradiance reaches its higher values: for $\epsilon_r = 0$. It amounts 0.34 and for $\epsilon_r = 0.775, 0.53$ which is a quite interesting value. In the less favorable season, winter, it amounts 0.30 without recuperation and 0.45 with recuperation.

The solar share, f, was defined in Section 2 as the ratio between the input heat rate from the solar collector and the total input heat rate. Its evolution with time for the considered representative days is plotted in Fig. 7. Curves for recuperative and non-recuperative configurations are shown. In all cases the shape of f for any particular season reminds that of the solar irradiance, G. Differences among seasons refer both to the number of hours with enough

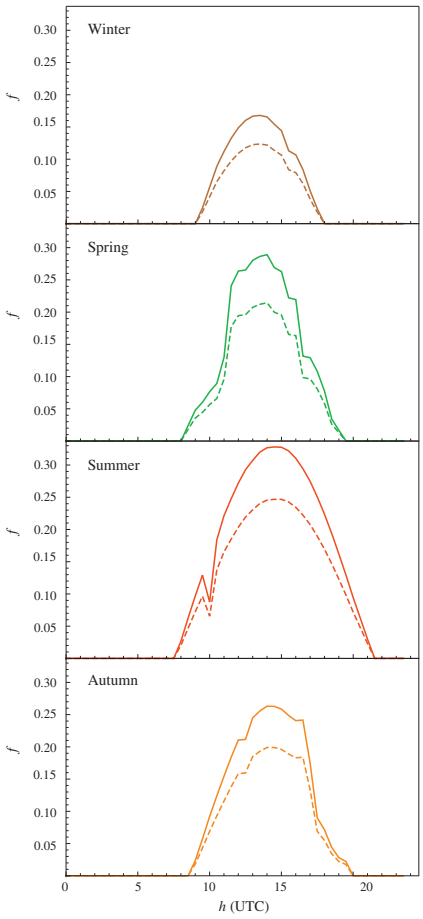

Fig. 7. Solar share, f, of the plant for each season. Solid lines correspond to the recuperative configuration and dashed lines to the non-recuperative one.

solar irradiance and to the height of the curves maxima. For instance in winter for the recuperative configuration f reaches a value slightly above 0.16 and there are 9 h of effective irradiance. At the other side, for a typical day of summer, f has a maximum around 0.34 and about 14 h of adequate solar input. When the recuperator is eliminated, for example, with the aim to take advantage of the residual heat in a bottoming cycle, the solar heat input remains the same. Nevertheless, the total heat input (in this case required to increase the temperature from T_2 to T_3 instead of from T_x to T_3) is larger, so the solar share is smaller. If we compare f in the figure for winter in both configurations, in the recuperative one the maximum is about 0.165 as mentioned above and for the non-recuperative one about 0.125. This corresponds to a decrease around 32%. At the other end, in summer the maximum with no recuperation is on 0.245, thus an increase about 39% is gained with a recuperator.

We recall that the curves for the overall efficiency, fuel conversion rate, and solar share directly reflects the oscillations in solar irradiance and ambient temperature due to the particular weather conditions of the day considered. As commented before, we deliberately did not perform smoothing or averaging procedures in the curves for G and T_L. Of course, G is more sensitive to cloudy periods, pressure depressions, storms and so on, that ambient temperature that has much slower fluctuations. So, efficiencies and other output records are directly influenced by weather and insolation conditions. The qualitative daily and seasonal evolution of all variables are in accordance with previous results in the literature, either from experimental measures [57,58] or from simulation procedures [26,59].

4.2. Cycle temperatures

The relevant temperatures in the hot side of the cycle are plotted in Fig. 8 for the recuperative and the non-recuperative configurations. The turbine inlet temperature, T_3, is almost constant in both configurations, thus providing a stable plant power output as commented at the beginning of Section 4. The compressor outlet temperature, T_2 is around 600 K and slightly oscillates following the evolution of the ambient temperature. In the non-recuperative situation and during insolation hours the solar receiver increases the temperature of the fluid from T_2 to $T_{x'}$. The latter has during these hours a parabolic shape that resembles the shape of G. During winter the maximum of $T_{x'}$ is about 700 K and during summer about 820 K. The working temperature of the solar collector, T_{HS}, as explained before is obtained, in each case, by balancing the energy rate released by the solar collector and received by the working fluid performing the Brayton cycle. It reaches maximum values above $T_{x'}$ because of the losses in the heat exchanger behind the solar receiver. The maximum values of T_{HS} in the non-recuperative situation change from 720 K in winter to 870 K in summer.

In the recuperative situation, the recuperator increases the compressor output temperature T_2 to a temperature T_x (see Fig. 1). Then, the solar collector during the day and the combustion chamber provide the heat rates to reach the turbine inlet temperature, T_3. The value of T_x does not depend neither on the time during a day nor on the season, because it is a function of the turbine outlet temperature T_4 (constant because T_3 is constant) and the recuperator effectiveness. In the plant considered T_x is around 825 K. In this case all the temperatures of the hot side (T_{HS} and $T_{x'}$) are displaced above more than 200 K. In the most favorable insolation conditions, during summer, the working temperature of the solar receiver, T_{HS} is slightly above 1000 K, similar to design point conditions of SOLUGAS project. It is important to stress here that for the intended power output in this plant $T_{x'}$ never reaches the turbine inlet temperature, T_3. This means that this plant could not work only on solar basis if the aim is to obtain a power output around 4.6 MW. A substantial combustion contribution is always required, even for the highest values of G. Some works in the literature report prototype plants working under only solar conditions, but for a power output level considerably lower than the one we consider here [30].

The temperatures of the working fluid in the cold side are depicted in Fig. 9. This plot is interesting in order to analyze the possible combination of the Brayton cycle with a bottoming one in order to take advantage of residual heat for instance through a heat recovery steam generator (HRSG) and a Rankine cycle or other possible cycles [21,22]. In the non-recuperative case the temperature of the working fluid at the turbine outlet, T_4 is season independent and is about 890 K. When a recuperator is considered,

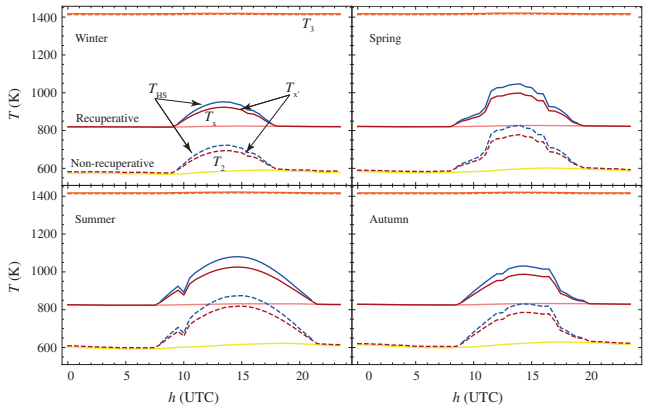

Fig. 8. Temperatures on the hot side of the plant cycle (see Figs. 1 and 2) for representative days of each season. Curves for non-recuperative and recuperative configurations are shown. The curve for T_3 is shown dashed for the non-recuperative case and solid for the recuperative.

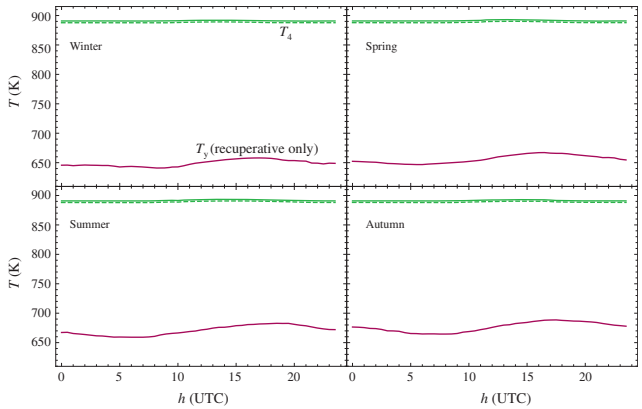

Fig. 9. Temperatures on the cold side of the plant cycle (see Figs. 1 and 2) for representative days of each season. The curve for T_4 is shown dashed for the non-recuperative case and solid for the recuperative.

the profitable temperature of the working fluid is T_y. During a day T_y oscillates as T_L and it also depends on the particular season. The smallest value is found in December, about 650 K, and the largest one in September, around 675 K. Thus, differences between seasons are scarce. Both in the non-recuperative and recuperative situations the potential use of residual heat to connect a bottoming cycle are important [9,12,14,21,60].

4.3. Fuel consumption and emissions

Numerical computation of the fuel consumption was achieved, either calculating the fuel consumption rate in hourly basis through Eq. (8) or the integrated consumption during a whole day. The mass fuel rate, $\dot{m}_f$ (see Fig. 10) has two different levels depending on the plant configuration, with or without a heat recuperator. During the night all the electricity generation comes from fuel combustion (natural gas in our case) and differences between recuperative and non-recuperative cases are around 38.5%, independently of the season. This is the difference in terms of fuel consumption rate of incorporating a recuperator to pre-heat the working fluid at the compressor exit. When the plant works on a hybrid mode because received irradiance is enough to heat the pressurized air above T_2 (without recuperation) or T_x (with recuperation), the fuel rate saving is important, and obviously depends on seasonal conditions. For each operation mode, the fuel saving for a whole day corresponds to the area of the surface between the solid lines in Fig. 10 (hybrid mode) and the corresponding dashed ones (pure combustion). The results are summarized in Table 3. The legend '*combustion mode*' corresponds to the case of

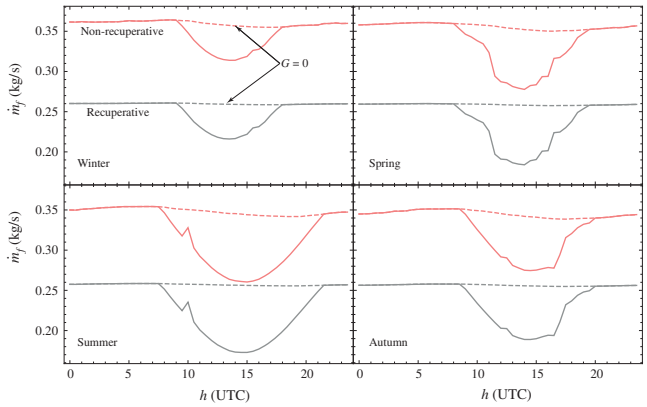

Fig. 10. Evolution with time of the fuel consumption rate, $\dot{m}_f$, supposed natural gas for representative days of each season. Solid lines refer to the hybrid operation mode and dashed ones to the pure combustion mode.

Table 3
Seasonal fuel consumption prediction on the basis of natural gas fueling.

	m_f (kg per day)	Winter	Spring	Summer	Autumn
No recuperation	Combustion mode	30,438	30,114	29,463	29,196
	Hybrid mode	29,552	28,479	26,895	27,587
Fuel saving (%)		2.9	5.4	8.7	5.5
With recuperation	Combustion mode	21,977	21,902	21,750	21,688
	Hybrid mode	21,098	20,277	19,196	20,089
Fuel saving (%)		4.0	7.4	11.7	7.4

no solar heat input and '*hybrid mode*' to the case in which solar irradiance is enough for partial heat input coming from the central tower solar plant. For the non-recuperative plant the saving varies from 2.9% in winter to 8.7% in summer. Autumn and spring behave in a similar way, the saving is about 5.5%. For the recuperative case relative differences are slightly larger: change from 4.0% in winter to 11.7% in summer. In autumn and spring, now the saving is around 7.4%.

The differences among plant configurations in fuel consumption are directly transferred to pollutant emissions. As an illustration we have plotted in Fig. 11 a bar diagram with the estimated emissions of the main greenhouse gases in real units: CO_2, CH_4, and N_2O. The data in the figure should only be taken as a guide, because each plant could have particular technologies to reduce emissions or CO_2 capture mechanisms. The data were obtained from the natural gas emission factors collected in [61,62]. The figure, in daily basis for the considered particular days of each season, allow to discern two emission levels: the associated to the non-recuperative plant and the one arising from the recuperative one. Differences are substantial as previously commented for fuel consumption. Within these two modes, the reduction associated to solar hybridization and its evolution during the year is also apparent.

5. Summary and conclusions

In this paper we have modeled a solar hybrid power plant based on a gas turbine following a closed Brayton cycle. The plant admit several configurations with or without a heat recuperator and with or without solar heat input. An assumed basic constraint of the plant operation is to keep an almost constant power output in the periods of low solar radiation. The model allows a direct calculation of the dynamic plant operation, with variable solar irradiance and variable external temperature. The hybridization scheme follows a serial or sequential heat input divided in two or three steps. In the non-recuperative configuration a heat exchanger transfers the heat received in a central tower solar collector to the working fluid at the exit of the compressor. Then, a combustion chamber completes the energy input required to have an stationary turbine inlet temperature. If a recuperator is included there exists a previous heating process by using the high temperature of the gas at the turbine exit.

The main emphasis was laid on the thermodynamic model of the Brayton cycle, where all the main irreversibility sources were considered avoiding to introduce a huge number of parameters and allowing to obtain analytical equations for all the thermal efficiencies and power output. For the solar subsystems a simple model was taken. It incorporates heat losses in the solar collector due to radiation and conduction/convection terms. The optical efficiency is an averaged effective factor. The overall plant efficiency was obtained as a combination of the efficiency of the plant subsystems (solar, combustion, and gas turbine) and the effectivenesses of the heat exchangers connecting subsystems. The SOLUGAS project [18,35] in Spain was elected as prototypical installation to compare model predictions with. Good agreement between measured values and predicted ones was found.

After the validation in stationary conditions, real seasonal data for solar irradiance and ambient temperature were incorporated to our computational scheme and taking representative days for each season, results were presented. Curves of global plant thermal efficiency, efficiencies of the subsystems, solar share, power output, and fuel conversion rate were shown in hourly basis. All the results are in agreement with other in the literature obtained both from real prototype installations and within simulation frameworks. Explicit data for fuel consumption rate and greenhouse gases inventory were presented and analyzed.

Results show that a recuperative plant working in hybrid mode has a fair potential to generate a stable power output of about

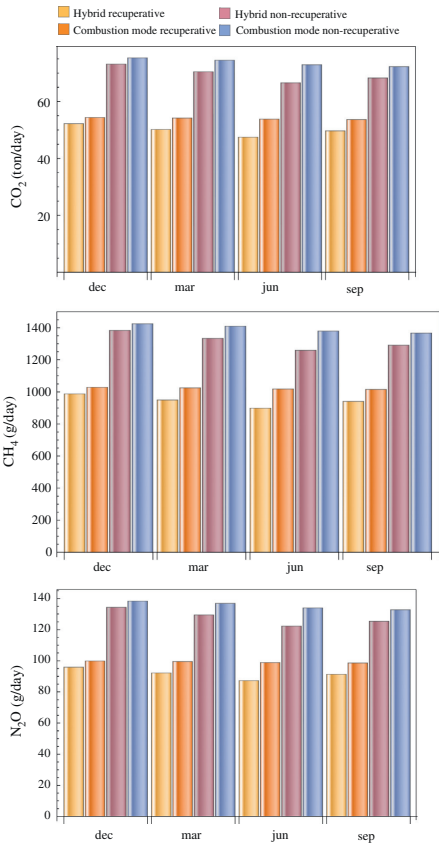

Fig. 11. Real units estimation of greenhouse emissions from the considered model.

4.6 MW with reduced fuel consumption and reduced greenhouse emissions for a location with favorable insolation conditions. Likely, the high temperature of the working gas at the recuperator exit, make these plants susceptible to be combined with a bottoming cycle, in order to increase global combined efficiency. Hybridization scheme is simple and susceptible to be used in arid regions with low water availability. The framework presented here should be considered as a starting step for the dynamic simulation of this kind of plants within thermodynamic basis. The implementation of more sophisticated models for the solar subsystem is feasible. They could include daily and seasonal variations of optical and other losses and the particularities of the solar collector field. Also more elaborated models for the involved solar receiver and other heat exchangers could be considered as well as optimization analyses based on thermoeconomic criteria for particular plants. Different working fluids for the thermal cycle are also susceptible of analysis.

Acknowledgement

The authors acknowledge financial support from MINECO of Spain, Grant ENE2013-40644-R.

References

[1] Walsh P, Fletcher P. Gas turbine performance. Blackwell Science Ltd.; 2004.
[2] le Roux W, Bello-Ochende T, Meyer J. Thermodynamic optimisation of the integrated design of a small-scale solar thermal Brayton cycle. Int J Energy Res 2012;36:1088–104.
[3] Jamel M, Abd Rahman A, Shamsuddin A. Advances in the integration of solar thermal energy with conventional and non-conventional power plants. Renew Sust Energy Rev 2013;20:71–81.
[4] Jansen E, Bello-Ochende T, Meyer J. Integrated solar thermal Brayton cycles with either one or two regenerative heat exchangers for maximum power output. Energy 2015;86:737–48. http://dx.doi.org/10.1016/j.energy.2015.04.080.
[5] Al-Attab K, Zainal Z. Externally fired gas turbine technology. Appl Energy 2015;138:474–87.
[6] Dunham M, Iverson B. High-efficiency thermodynamic power cycles for concentrated solar power systems. Renew Sust Energy Rev 2014;30:758–70.
[7] Ahmed M, Mohamed H. Performance characteristics of modified gas turbine cycles with steam injection after combustion exit. Int J Energy Res 2012;36:1346–57.
[8] Ghazikhani M, Passandideh-Fard M, Mousavi M. Two new high-performance cycles for gas turbine with air bottoming. Energy 2011;36:294–304.
[9] Chacartegui R, Muñoz de Escalona J, Sánchez D, Monje B, Sánchez T. Alternative cycles based on carbon dioxide for central receiver solar power. Appl Therm Eng 2011;31:872–9.
[10] Barigozzi G, Perdichizzi A, Gritti C, Guaiatelli I. Techno-economic analysis of gas turbine inlet air cooling for combined cycle power plant for different climatic conditions. Appl Therm Eng 2015;82:57–67.
[11] Okoroigwe E, Madhlopa A. An integrated combined cycle system driven by a solar tower: a review. Renew Sust Energy Rev 2016;57:337–50.
[12] Romero M, Buck R, Pacheco E. An update on solar central receiver systems, projects, and technologies. Trans ASME 2002;124:98.
[13] Romero M, Steinfeld A. Concentrating solar thermal power and thermochemical fuels. Energy Environ Sci 2012;5:9234–45.
[14] Behar O, Khellaf A, Mohammedi K. A review of studies on central receiver solar thermal power plants. Renew Sust Energy Rev 2013;23:12–39.
[15] SOLGATE. Solar hybrid gas turbine electric power system. Tech rep. EUR 21615, European Commission; 2005.
[16] Schwarzbözl P, Buck R, Sugarmen C, Ring A, Marcos Crespo M, Altwegg P, et al. Solar gas turbine systems: design, cost and perspectives. Sol Energy 2006;80:1231–40.
[17] Solar-hybrid power and cogeneration plants. Tech rep., European Commission; 2011. <ordis.europa.eu/publication/rcn/13318_en.html>.
[18] Korzynietz R, Quero M, Uhlig R. Solugas-future solar hybrid technology. Tech rep. SolarPaces; 2012. <http://cms.solarpaces2012.org/proceedings/paper/7ee7e32ece8f2f8e0984d5ebff9d77b>.
[19] Grange B, Dalet C, Falcoz Q, Siros F, Ferrière A. Simulation of a hybrid solar gas-turbine cycle with storage integration. Energy Proc 2014;49:1147–56.
[20] Okoroigwe E, Madhlopa A. Evaluation of the potential for hybridization of gas turbine power plants with renewable energy in South Africa. In: IEEE conference publications; 2015. http://dx.doi.org/10.1109/DUE.2015.7102985.
[21] Kribus A, Zaibel R, Carey D, Segal A, Karni J. A solar-driven combined cycle power plant. Sol Energy 1998;62:121–9.
[22] Livshits M, Kribus A. Solar hybrid steam injection gas turbine (STIG) cycle. Sol Energy 2012;86:190–9.
[23] Spelling J. Hybrid solar gas-turbine power plants. Ph.D. thesis. Stockholm, Sweden: KTH Royal Institute of Technology, Department of Energy Technology; 2013.
[24] Li Y, Liao S, Liu G. Thermo-economic multi-objective optimization for a solar-dish Brayton system using NSGA-II and decision making. Electr Power Energy Syst 2015;64:167–75.
[25] Kalogirou S. Solar thermal collectors and applications. Prog Energy Combust Sci 2004;30:231–95.
[26] Barigozzi G, Bonetti G, Franchini G, Perdichizzi A, Ravelli S. Thermal performance prediction of a solar hybrid gas turbine. Sol Energy 2012;86:2116–27.
[27] Noone C, Torrilhon M, Mitsos A. Heliostat field optimization: a new computationally efficient model and biomimetic layout. Sol Energy 2012;86:792–803.
[28] Collado F, Guallar J. A review of optimized design layouts for solar power tower plants with *campo* code. Renew Sust Energy Rev 2013;20:142–54.
[29] Soltani R, Keleshtery P, Vahdati M, Khoshgoftar Manesh M, Rosen M, Amidpour M. Multi-objective optimization of a solar-hybrid cogeneration cycle: application to CGAM problem. Energy Convers Manage 2014;81:60–71.
[30] Kribus A, Doron P, Rubin R, Reuven R, Taragan E, Duchan S, et al. Performance of the directly irradiated annular pressurized receiver (DIAPR) operating at 20 bar and 1200 °C. J Sol Energy Eng 2001;123:10–7.
[31] Kribus A, Grijnevich M, Gray Y, Caliot C. Parametric study of volumetric absorber performance. Energy Proc 2014;49:408–17.

[32] Pozivil A, Aga V, Zagorsky A, Steinfeld A. A pressurized air receiver for solar-driven gas turbines. Energy Proc 2014;49:498–503.
[33] McMahan A, Klein S, Reindl D. A finite-time thermodynamic framework for optimizing solar-thermal power plants. J Sol Energy Eng 2007;129:355–62.
[34] Le Roux W, Bello-Ochende TMJ. A review on the thermodynamic optimisation and model of the solar thermal Brayton cycle. Renew Sust Energy Rev 2013;28:677–90.
[35] Olivenza-León D, Medina A, Calvo Hernández A. Thermodynamic modeling of a hybrid solar gas-turbine power plant. Energy Convers Manage 2015;93:435–47.
[36] Sánchez-Orgaz S, Medina A, Calvo Hernández A. Maximum overall efficiency for a solar-driven gas turbine power plants. Int J Energy Res 2013;37:1580–91.
[37] Sánchez-Orgaz S, Medina A, Calvo Hernández A. Recuperative solar-driven multi-step gas turbine power plants. Energy Convers Manage 2013;67:171–8.
[38] Sánchez-Orgaz S, Pedemonte M, Ezzatti P, Curto-Risso P, Medina A, Calvo Hernández A. Multi-objective optimization of a multi-step solar-driven Brayton cycle. Energy Convers Manage 2015;99:346–58.
[39] Heywood J. Internal combustion engine fundamentals. McGraw-Hill; 1988.
[40] Wu L, Lin G, Chen J. Parametric optimization of a solar-driven Braysson heat engine with variable heat capacity of the working fluid and radiation-convection heat losses. Renew Energy 2010;35:95–100.
[41] Bejan A. Advanced engineering thermodynamics. 3rd ed. Hoboken, New Jersey: Wiley; 2006.
[42] Duffie J, Beckman W. Solar engineering of thermal processes. Hoboken, New Jersey: John Wiley and Sons; 2006.
[43] Xie W, Dai Y, Wang R. Numerical and experimental analysis of a point focus solar collector using high concentration imaging PMMA Fresnel lens. Energy Convers Manage 2011;52:2417–26.
[44] Weinstein L, Loomis J, Bhatia B, Bierman D, Wang E, Chen G. Concentrating solar power. Chem Rev 2015;115:12797–838.
[45] Tournier J-MP, El-Genk M. Properties of noble gases and binary mixtures for closed Brayton cycle applications. Energy Convers Manage 2008;49:469–92.
[46] Iverson B, Conboy T, Pasch J, Kruizenga A. Supercritical CO_2 Brayton cycles for solar-thermal energy. Appl Energy 2013;111:957–70.
[47] Al-Sulaiman F, Atif M. Performance comparison of different supercritical carbon dioxide Brayton cycles integrated with a solar power tower. Energy 2015;82:61–71.
[48] Muñoz-Antón J, Rubbia C, Rovira A, Martínez-Val J. Performance study of solar power plants with CO_2 as working fluid. A promising design window. Energy Convers Manage 2015;92:36–46.
[49] Caterpillar ST. <https://mysolar.cat.com/cda/files/126873/7/dsm50pg.pdf>.
[50] Wark K, Richards D. Thermodynamics. 6th ed. McGraw-Hill; 1998.
[51] de Mello P, Monteiro D. Thermodynamic study of an EFGT (externally fired gas-turbine) cycle with one detailed model for the ceramic heat exchanger. In: Proceedings of ECOS 2011 conference, Novi Sad, Serbia; 2011.
[52] Sunden B. High temperature heat exchangers (HTHE). In: Proceedings of the fifth international conference on enhanced, compact and ultra-compact heat exchangers: science, engineering and technology, Hoboken, NJ, USA; 2005.
[53] Zhang Y, Lin B, Chen J. Optimum performance characteristics of an irreversible solar-driven Brayton heat engine at the maximum overall efficiency. Renew Energy 2007;32:856–67.
[54] GREET. The greenhouse gases, regulated emissions and energy use in transportation model. Tech rep. Argonne (IL): Argonne National Laboratory; 2010. <http://greet.es.anl.gov>.
[55] Meteosevilla. <http://www.meteosevilla.com>.
[56] Ávila-Marín A. Volumetric receivers in solar thermal power plants with centra receiver system technology: a review. Sol Energy 2011;85:891–910.
[57] Sinai J, Sugarmen C, Fisher U. Adaptation and modification of gas turbines for solar energy applications. In: Proceedings of GT2005 ASME turbo expo 2005; 2005.
[58] Heller P, Pfänder M, Denk T, Téllez F, Valverde A, Fernández J, et al. Test and evaluation of a solar powered gas turbine system. Sol Energy 2006;80:1225–30.
[59] Spelling J, Laumert B. Thermo-economic evaluation of solar thermal and photovoltaic hybridization options for combined-cycle power plants. J Eng Gas Turb Power 2015;137:031801-1–031801-11.
[60] Sánchez D, Monje Brenes B, Muñoz de Escalona J, Chacartegui R. Non-conventional combined cycle for intermediate temperature systems. Int J Energy Res 2013;37:403–11.
[61] Direct emissions from stationary combustion sources; May 2008. <www.epa.gov/climateleaders>.
[62] Emission factors for greenhouse gas inventories; April 2014. <http://www.epa.gov/climateleadership/documents/emission-factors.pdf>.

3.2 Paper 2 – Modeling hybrid solar gas-turbine power plants: Thermodynamic projection of annual performance and emissions

Title: "Modeling hybrid solar gas-turbine power plants: Thermodynamic projection of annual performance and emissions"
Journal: *Energy Conversion and Management*
Authors: **R.P. Merchán**, M.J. Santos, I. Reyes-Ramírez, A. Medina, A. Calvo Hernández
Year: 2017
Volume: 134
Pages: 314-326
DOI: `http://dx.doi.org/10.1016/j.enconman.2016.12.044`
Reference: [125]

Resumen

En este artículo se emplea el modelo termodinámico desarrollado anteriormente como base para el estudio de plantas termosolares de torre central híbridas y de ciclo Brayton. Gracias a la nueva implementación del modelo en el código, se puedan llevar a cabo simulaciones anuales a través de días representativos de cada mes. En consecuencia, los datos meteorológicos de irradiancia solar y temperatura ambiente se promedian para tener un día típico anual. *SOLUGAS* es la planta de base de la que se extraen los valores numéricos de los principales parámetros de la planta. El objetivo principal de este artículo es realizar un análisis de sensibilidad de los principales parámetros de la planta teniendo en cuenta las pérdidas para diferentes configuraciones y desde el punto de vista anual. De este modo, se estudia cómo influyen las pérdidas de energía de los diferentes subsistemas en el sistema global y cuáles son los márgenes de mejora existentes. Asimismo, también se comparan configuraciones recuperativas y no recuperativas y modos de operación híbridos y puramente de combustión, sin aporte solar. Destaca que en el punto de operación se alcanza una eficiencia térmica global anual del 34 % para el caso híbrido recuperativo. A continuación, se considera cómo afectan a la planta las posibles mejoras en los intercambiadores de calor que cierran el ciclo, en el subsistema solar, en el ciclo Brayton y todas estas mejoras juntas. Un resultado notable es que si los intercambiadores de calor presentan menos pérdidas, los registros de salida no mejoran muy sustancialmente. Por otro lado, las mejoras en el ciclo Brayton son las que conllevan mejores valores de las variables de salida. Aparte de ello, también se ha demostrado que las pérdidas de presión tienen un efecto significativo en el subsistema solar a través de la temperatura del receptor. Sin embargo y como era de esperar, los cambios en el subsistema solar no tienen ningún efecto en la potencia, que se mantiene constante al haber sido fijada

inicialmente como objetivo una temperatura de entrada a la turbina estable, pero sí lo tienen en el rendimiento económico.

Energy Conversion and Management 134 (2017) 314–326

Contents lists available at ScienceDirect

Energy Conversion and Management

journal homepage: www.elsevier.com/locate/enconman

Modeling hybrid solar gas-turbine power plants: Thermodynamic projection of annual performance and emissions

R.P. Merchán [a], M.J. Santos [a], I. Reyes-Ramírez [b], A. Medina [a,*], A. Calvo Hernández [a]

[a] Department of Applied Physics, University of Salamanca, 37008 Salamanca, Spain
[b] UPIITA – Instituto Politécnico Nacional, México D.F., Mexico

ARTICLE INFO

Article history:
Received 19 September 2016
Received in revised form 14 December 2016
Accepted 18 December 2016

Keywords:
Thermosolar hybrid power plants
Thermodynamic simulation
Annual performance records
Yearly fuel consumption and emissions

ABSTRACT

The annual performance, fuel consumption and emissions of a hybrid thermosolar central tower Brayton plant is analyzed in yearly terms by means of a thermodynamic model. The model constitutes a step forward over a previously developed one, that was satisfactorily validated for fixed solar irradiance and ambient temperature. It is general and easily applicable to different plant configurations and power output ranges. The overall system is assumed as formed by three subsystems linked by heat exchangers: solar collector, combustion chamber, and recuperative Brayton gas-turbine. Subsystem models consider all the main irreversibility sources existing in real installations. This allows to compare the performance of a real plant with that it would have in ideal conditions, without losses. Furthermore, the improved version of the model is capable to consider fluctuating values of solar irradiance and ambient temperature. Numerical calculations are presented taking particular parameters from a real installation and actual meteorological data. Several cases are analyzed, including plant operation in hybrid or pure combustion modes, with or without recuperation. Previous studies concluded that this technology is interesting from the ecological viewpoint, but that to be compelling for commercialization, global thermal efficiency should be improved (currently yearly averaged thermal efficiency is about 30% for recuperative plants). We analyze the margin for improvement for each plant subsystem, and it is concluded that, the Brayton heat engine, by far, is the key element to improve overall thermal efficiency. Numerical estimations of achievable efficiencies are presented for a particular plant and real meteorological conditions.

1. Introduction

During the last years, extensive research and development efforts have been devoted to use concentrated solar energy as heat source (at least partially) to generate electric energy. It constitutes a promising strategy to make use of renewable resources in order to reduce fossil fuel requirements and to limit the emission of greenhouse gases. Particularly, solarized gas-turbine power plants have been developed at different scales. From small-scale solar dish units for distributed generation in the range of kW [1–4], to central tower installations capable to produce several MW to the grid [5,6]. Apart from being easily scalable, gas-turbines can be combined with Rankine or other cycles, do not require too much water for operation, and are extremely versatile [6–10].

In central tower gas-turbine plants an heliostat field collects solar energy and then focus it to a tower with a central receiver that transfers the solar power to a working fluid that performs a Brayton-like cycle. These plants can work on a hybrid configuration, a combustion chamber burning usually natural gas is incorporated in order to get a turbine inlet temperature approximately constant [11,12]. This avoids the necessity to include storing devices in the plant and the power release to the grid is independent of solar irradiation fluctuations.

Experimental projects and prototypes developed up to date show that this technology is viable [13–16] and its interest from the ecological viewpoint is undoubted. Nevertheless, thermoeconomic studies reveal that improvements in plant efficiencies are required to produce electricity at competitive prices [17–19]. Thus, active research lines on this objective are still imperative. Research objectives are being pursued at least by means of two different strategies. In the first one, detailed models for plant components and different arrangements are analyzed. This can include the design and optimization of the heliostat field, the central tower, the receiver, the thermodynamics of the diverse components of

* Corresponding author.
E-mail addresses: rpmerchan@usal.es (R.P. Merchán), smjesus@usal.es (M.J. Santos), ireyesram@hotmail.com (I. Reyes-Ramírez), amd385@usal.es (A. Medina), anca@usal.es (A. Calvo Hernández).

http://dx.doi.org/10.1016/j.enconman.2016.12.044
0196-8904/

Nomenclature

A_a	aperture area of the collector
c_w	specific heat of the working fluid
f	solar share
G	direct solar irradiance
$\dot{m}$	mass flow rate of the working substance
$\dot{m}_f$	fuel mass flow rate
P	power output
$\lvert\dot{Q}_C\rvert$	heat losses at the combustion chamber
$\lvert\dot{Q}_H\rvert$	total heat-transfer rate absorbed from the working fluid
$\lvert\dot{Q}_{iHC}\rvert$	heat losses at the heat exchanger associated to the combustion chamber
$\lvert\dot{Q}_{HC}\rvert$	heat rate input from the combustion chamber
$\lvert\dot{Q}'_{HC}\rvert$	heat rate transferred from the combustion chamber to the associated heat exchanger
$\lvert\dot{Q}_{HS}\rvert$	heat rate input from the solar collector
$\lvert\dot{Q}_{iHS}\rvert$	heat losses at the solar receiver
$\lvert\dot{Q}'_{HS}\rvert$	heat rate transferred from the solar collector to the associated heat exchanger
$\lvert\dot{Q}_I\rvert$	losses associated to heat transfers in the solar field
$\lvert\dot{Q}_L\rvert$	heat-transfer rate between the working fluid and the ambient
Q_{LHV}	lower heating value of the fuel
$\lvert\dot{Q}_o\rvert$	optical losses at the solar subsystem
r_e	fuel conversion rate
r_p	overall pressure ratio
T_{HC}	working temperature of the combustion chamber
T_{HS}	working temperature of the solar collector
T_L	ambient temperature
T_x	working fluid temperature after the heat input from the recuperator
$T_{x'}$	working fluid temperature after heat input from the solar collector
T_y	working fluid exhaust temperature
T_3	turbine inlet temperature
U_L	effective conduction-convection heat transfer parameter
α	effective emissivity
η	overall thermal efficiency
η_C	combustion chamber efficiency
η_H	thermal efficiency of the Brayton heat engine
η_S	solar collector efficiency
η_0	optical efficiency
ε_{HC}	combustion chamber heat exchanger effectiveness
ε_{HS}	solar collector heat exchanger effectiveness
ε_L	cold side heat exchanger effectiveness
ε_c	isentropic efficiency of the compressor
ε_r	recuperator effectiveness
ε_t	isentropic efficiency of the turbine
γ	adiabatic coefficient of the working fluid
ρ_H	irreversibilities due to pressure drops in the heat input
ρ_L	irreversibilities due to pressure drops in the heat release

the heat engine performing the thermal cycle and even the fluid dynamics of the gas in the turbine equipment. In this framework detailed and precise numerical calculations can be made with the help of commercial simulation tools or with software developed by the research groups [20–23]. However, it is not easy to extract direct physical information about the main losses sources in the plant and to plan global strategies for the optimization of the plant design and operation as a whole. Additionally, the consideration of fluctuating meteorological conditions it is not straightforward.

An alternative strategy is to develop a theoretical model for the overall plant, reducing the number of parameters, hence allowing a simplified and realistic picture of plant operation and to estimate its performance records. This standpoint is specially interesting for optimization, at least to provide a first order guideline for overall plant design in order to accomplish an optimum performance [24–28].

Optimization studies are divided in single-objective or multi-objective. In single-objective optimization works each objective or figure of merit is stated in terms of the model parameters and then optimized with a simple mathematical procedure. Model variables are related to the particularities of the thermodynamic cycle followed by the working fluid and to the losses or irreversibilities. Objective functions can mainly incorporate thermodynamic, ecological or thermoeconomic ingredients [25,26,29–31]. On the other side, multi-objective techniques intend to propose optimal combinations of parameters leading to a good compromise for different objectives. Specific mathematical techniques are required to generate different configurations of variables with evolutionary algorithms, non-dominated combinations for the considered objectives, and to make decisions for electing a reduced number of plausible combinations of parameters [27,32–35].

The aim of this work is to locate the bottlenecks in the overall efficiency of this kind of plants. This is, from our viewpoint, a key step in the development of future generations of efficient hybrid thermosolar central tower installations. A theoretical thermodynamical model software was previously developed by our group [24]. It is implemented in Mathematica® and has been validated at design point conditions by comparison with measures from a real installation [24,36]. The model has been enhanced to consider seasonal and meteorological fluctuations in order to analyze realistic yearly averages. In this framework, the subsystems constituting the plant are clearly identified and the main irreversibility sources modeled and quantified. The model is general and susceptible to be applied to different scale installations, and also to different locations and meteorological constraints. It can incorporate oscillations on solar irradiance and external temperature, so the curves of plant performance along a day or seasonal mean values can be estimated [36]. These points make the model specially suited for optimization purposes. A theoretical framework was previously developed for purely solar gas turbines (non-hybrid configuration) [37,38]. Special emphasis was laid on the effect of recuperation on the overall thermal efficiency. A multiobjective optimization procedure was also performed in order to provide feasible intervals for the main plant parameters for an optimum plant design [32].

In this paper, the model is applied to a particular plant recently developed near Seville, Spain. Real yearly averaged data for direct solar irradiance and ambient temperature at such particular location are considered. This gives reliable numerical information, since in several previous works fixed values for solar irradiance and ambient temperature (design point conditions) are taken, sometimes not enough close to real annual mean values. Several plant configurations (with or without recuperation) and operation modes (pure combustion mode or hybrid functioning) are surveyed. Numerical values for thermal and fuel conversion efficiencies are presented as well as for solar share (defined as the ratio between the solar heat input and the total one) and estimated fuel consumption and emissions. The importance of losses and the margins of improvement for each plant subsystem are analyzed.

2. Plant thermodynamics

The considered system is a gas-turbine power plant hybridized with a central tower solar concentration system. An sketch of the whole system is depicted in Fig. 1 and the thermodynamic model of the plant was recently proposed by the same authors in [36]. The objective of the combined system is to produce an stable power output, not relying on solar conditions. For such purpose it will be assumed that the turbine inlet temperature is kept approximately constant. During low irradiation periods and during nights, the combustion chamber ensures such temperature, and during good insolation periods, fuel inlet in the combustion chamber is reduced (or even suppressed).

The gas-turbine will be modeled as a single step recuperative closed Brayton cycle with several irreversibility losses. The $T-S$ diagram of the cycle was plotted in Fig. 2 of [36]. Pressurized air will be taken as working fluid undergoing the thermal cycle. It is first compressed through a non-ideal compressor (with an isentropic efficiency of ε_c) and then heated in three steps from two external sources: when a recuperator is included in plant design, it makes use of the high temperature of the gas after the turbine in order to heat the working fluid; then, the fluid is heated up in the solar receiver. If solar heat input does not allow to reach the (prefixed) turbine inlet temperature, the fluid receives an energy input from the combustion chamber by means of a heat exchanger. By night or in the case of low solar irradiance, a shut-off valve redirects the pressurized air directly to the combustion chamber heat exchanger. Next, the fluid at temperature T_3 is expanded at the turbine, whose isentropic efficiency is ε_t. After the regenerator exit, another heat exchanger releases a heat flux to the ambient (which temperature is T_L), in such a way that the temperature at the compressor inlet, T_1, is recovered.

The overall thermal efficiency, η, is defined as the fraction between the net mechanical power output, P, and the total heat input rate [39,40],

$$\eta = \frac{P}{GA_a + \dot{m}_f Q_{LHV}} \tag{1}$$

where G is the direct solar irradiance, depending on the seasonal fluctuations, the weather conditions, and the sun position during the day, so it is a function of time; and A_a is the aperture area of the solar field. In addition, $\dot{m}_f$ is the fuel mass consumption rate and Q_{LHV} its corresponding lower heating value. As the turbine inlet temperature must remain stable at all conditions, the fuel mass rate has to be accounted as time dependent, compensating variations in G. The thermal efficiency of the whole system is expressed as a function of the efficiency of the solar collector, η_S, the efficiency of the combustion chamber, η_C, that of the Brayton heat engine, η_H, and the effectivenesses of all the involved heat exchangers.

The solar collector efficiency, η_S, is defined as the ratio between the useful energy per unit time provided by the collector, $|\dot{Q}'_{HS}|$ (see Fig. 1), and the solar energy rate it receives, GA_a : $\eta_S = |\dot{Q}'_{HS}|/GA_a$. The solar central tower transfers a fraction of the solar heat input $|\dot{Q}'_{HS}|$, $|\dot{Q}_{HS}| = \varepsilon_{HS}|\dot{Q}'_{HS}|$, to the working fluid, representing ε_{HS} the effectiveness of the solar receiver in the heat transfer to the working fluid. Thus, the solar collector efficiency is: $\eta_S = |\dot{Q}_{HS}|/(\varepsilon_{HS}GA_a)$.

In a similar way, the combustion chamber produces a heat rate, $|\dot{Q}'_{HC}|$, transferred to the working fluid through a heat exchanger whose effectiveness is $\varepsilon_{HC} = |\dot{Q}_{HC}|/|\dot{Q}'_{HC}|$, being $|\dot{Q}_{HC}|$ the heat rate received by the working fluid from combustion. So, an externally fired gas-turbine is being considered. As a result, the combustion chamber efficiency can be written as: $\eta_C = |\dot{Q}_{HC}|/(\varepsilon_{HC}\dot{m}_f Q_{LHV})$.

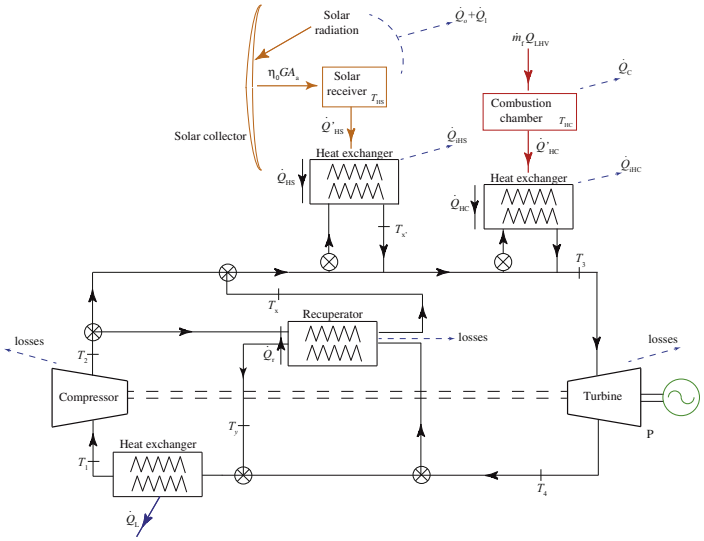

Fig. 1. Scheme of the hybrid solar gas-turbine plant considered. The main heat transfers and temperatures are depicted. Also the key losses sources considered in the model are indicated. The ambient temperature is denoted by T_l.

The Brayton heat engine thermal efficiency is the ratio between the net power output, P, and the total heat input actually received by the working fluid, $\eta_H = P/(|\dot{Q}_{HS}| + |\dot{Q}_{HC}|)$. It is convenient to define a solar share fraction as the quotient of the solar heat input with respect to the total one, $f = |\dot{Q}_{HS}|/\left(|\dot{Q}_{HS}| + |\dot{Q}_{HC}|\right)$. Thus, the overall efficiency can be obtained by the substitution of the definitions of η_S and η_C in Eq. (1):

$$\eta = \eta_S \eta_C \eta_H \left[\frac{\varepsilon_{HS}\varepsilon_{HC}}{\eta_C \varepsilon_{HC} f + \eta_S \varepsilon_{HS}(1-f)}\right] \quad (2)$$

This expression is valid for whichever solar conditions. If the energy input comes only from the solar collector, $f = 1$, and $\eta = \eta_S \eta_H \varepsilon_{HS}$, but if there is just combustion heat input, $f = 0$, and $\eta = \eta_C \eta_H \varepsilon_{HC}$.

Defining the *fuel conversion rate* as the power output relative to the heat input with associated economic costs, $r_e = P/(\dot{m}_f Q_{LHV})$, it can be followed that:

$$r_e = \frac{\eta \eta_S \eta_H \varepsilon_{HS}}{\eta_S \eta_H \varepsilon_{HS} - \eta f} \quad (3)$$

When there is just combustion heat input, $f = 0$, and $r_e = \eta$. On the contrary, if the energy input comes only from solar collector, $f = 1$, and $\eta = \eta_S \eta_H \varepsilon_{HS}$, so $r_e \to \infty$. As a result, it should be accounted that this rate is defined in the interval $[0, \infty]$, and so, strictly it is not a thermodynamic efficiency, but just an interesting measure of the system performance from the point of view of fuel consumption costs.

A more detailed development of subsystems models is included in [36] and the notation for losses terms can be seen in Fig. 1. With respect to the solar receiver, $\dot{Q}_o$ represents the optical losses, $\dot{Q}_l$ is associated to heat transfer to the surroundings, and $\dot{Q}_{iHS}$ corresponds to losses in the associated heat exchanger. On the other hand, $\dot{Q}_C$ is related to energy losses on the combustion chamber and $\dot{Q}_{iHC}$ refers to the ones on its heat exchanger. And, eventually, $\dot{Q}_L$ describes the heat-transfer rate between the working fluid and the ambient.

3. Model implementing and validation

As already mentioned, the previous thermodynamic model was developed in other works [24,36,32], and validated for design point conditions, *i.e.*, for fixed solar irradiance and ambient temperature. This was carried out by comparing model predictions against the data available in the literature for the central receiver *Solugas* Project [16,41], led by *Abengoa Solar* near Seville, Spain, in which a recuperative natural gas-turbine (*Mercury 50*, *Caterpillar*) was employed [42]. *Solugas* project aimed to check the performance of this plant scheme at a pre-commercial scale and to achieve an estimation of costs. At full load the turbine *Caterpillar Mercury 50* operates at a pressure ratio $r_p = 9.9$ with a gas flow $\dot{m} = 17.9$ kg/s. The turbine inlet temperature is $T_3 = 1423$ K and provides 4.6 MWe fueled with natural gas [36,42]. The manufacturer reports a thermal efficiency after generator, $\eta_{He} = 0.385$ for $T_L = 288$ K.

In our computations, pressurized air was assumed as working fluid and average values of the specific heat at constant pressure, c_w, and the adiabatic coefficient, γ, were supposed. For natural gas a lower heating value $Q_{LHV} = 47.141$ MJ/kg was taken [43]. Standard values were considered for the required losses parameters [5,44–48]. Particularly, global pressure losses were estimated in relative terms as 9.2%. The turbine inlet temperature, T_3, was kept fixed in the simulations in order to maintain power output approximately constant. In other words, the turbine inlet temperature is taken as a plant design parameter, and enters in the computations as a fixed parameter. It is taken as the same for all the considered plant configurations. This premise allows to compare the results for different layouts with certainty. The working temperature of the solar receiver, T_{HS}, is calculated for each case by stating and solving a non-linear equation matching the heat rate released by the solar collector, Eq. (4) in [36], and the heat input absorbed by the solar collector, Eq. (26) in the same reference. Details on the procedure can be found in [24,36].

Fairly good agreement was achieved between computations from our model and in-plant measures at fixed, design point conditions, despite the fact that actual turbine follows an open Brayton cycle and the model described in previous sections, a closed one. This hypothesis is usual in theoretical or simulation works on this kind of systems involving a Brayton cycle [49]. It allows to consider the heat input associated to combustion as an external one, avoiding to solve explicitly the chemical reaction of combustion. Detailed tables with the comparison of model predictions with experimental measures can be found in [24,36].

3.1. Yearly calculations

In this work the objective is to perform an annual analysis of the plant performance. With the aim to obtain yearly averages of plant records such as power output, thermal efficiency, fuel consumption, and emissions, we took real data at the location of the Solugas project (Sanlúcar la Mayor, Seville, Spain) for direct irradiance, G, and external temperature, T_L. Data were obtained from the database Meteosevilla [50]. A simple smoothing procedure was followed by taking three representative days of each season during the year 2013 and making an average for each season. Averaged curves for G and T_L are depicted in Fig. 2 against time. Fig. 2(a) shows that maximum irradiance during summer and spring reaches approximately 860 W/m^2 (value that in the development of the Solugas project was taken as design point irradiance) and the insolation occurs during 13 h. During autumn maximum averaged irradiance is about 615 W/m^2 and in winter it reaches about 575 W/m^2. In the worst case the width of effective irradiance curve is approximately of 9 h. The typical oscillating behavior of T_L is plotted at Fig. 2(b). Maximum temperatures in summer reach 308 K and the difference between maximum and minimum is roughly 15 K. On the other side, during winter averaged maximum temperature is 287 K and minimum 279 K, so the amplitude of the oscillations is approximately one half of that in summer.

In a subsequent step yearly averaged curves of G and T_L were obtained by weighting each season with the corresponding number of days. Final smoothed curves are also plotted in Fig. 2. Maximum solar irradiance reaches 700 W/m^2 and the mean number of useful insolation hours is about 11. Mean maximum temperature is about 297 K and the amplitude of temperature oscillations about 11 K. Yearly plant performance records were obtained by using these averaged curves for G and T_L. Averages for solar dependent parameters (solar subsystem efficiency, η_S, solar share, f, and effective working temperature of the solar receiver, T_{HS}) were done over effective insolation hours and the rest for the whole 24 h period.

Five different situations in which respect to thermal losses were considered as cases for analysis (see Table 1): (A) real plant (Solugas project) operating point,[1] (B) ideal heat exchangers (solar receiver and combustion chamber exchangers, and cold side exchanger), (C) ideal solar subsystem, (D) ideal Brayton cycle, and (E) completely ideal system (all thermodynamic subsystems are simultaneously considered without losses). The losses parameters for each of these cases are summarized in Table 1. Moreover, for any of these cases

[1] Notice that in the original project fixed values of G and T_L were considered for pre-design. We are taking yearly averaged values for both parameters.

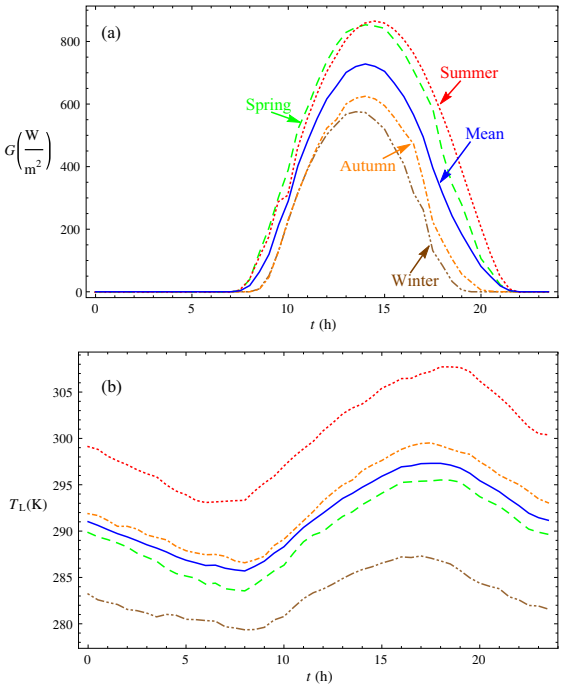

Fig. 2. (a) Seasonally averaged solar irradiance, G, and (b) ambient temperature, T_L, as a function of time (UTC hour) for a location near Seville, Spain (dashed and dotted lines). Yearly averaged curves are also shown (solid curves).

Table 1
Losses parameters for the real plant in operating conditions (A) and the other cases considered (B)–(E). In the cases (B)–(D) one of the subsystems or heat exchangers are considered as ideal, and in the case (E) all the plant subsystems and heat exchangers are ideal.

Subsystem	(A) Real (operating point)	(B) Ideal heat exchangers	(C) Ideal solar part	(D) Ideal Brayton cycle	(E) Completely ideal system
Solar subsystem	$\eta_0 = 0.650$		$\eta_0 = 1$		$\eta_0 = 1$
	$\alpha = 0.1$		$\alpha = 0$		$\alpha = 0$
	$U_L = 5$		$U_L = 0$		$U_L = 0$
	$\varepsilon_{HS} = 0.780$	$\varepsilon_{HS} = 1$	$\varepsilon_{HS} = 1$		$\varepsilon_{HS} = 1$
Combustion subsystem	$\eta_C = 0.980$				$\eta_C = 1$
	$\varepsilon_{HC} = 0.980$	$\varepsilon_{HC} = 1$		$\varepsilon_{HC} = 1$	$\varepsilon_{HC} = 1$
Brayton subsystem	$\varepsilon_t = 0.885$			$\varepsilon_t = 1$	$\varepsilon_t = 1$
	$\varepsilon_c = 0.815$			$\varepsilon_c = 1$	$\varepsilon_c = 1$
	$\varepsilon_r = 0.775$			$\varepsilon_r = 1$	$\varepsilon_r = 1$
	$\rho_H = 0.975$			$\rho_H = 1$	$\rho_H = 1$
	$\rho_L = 0.970$			$\rho_L = 1$	$\rho_L = 1$
	$\varepsilon_L = 0.985$	$\varepsilon_L = 1$		$\varepsilon_L = 1$	$\varepsilon_L = 1$

four configurations were analyzed: non-recuperative and recuperative turbine, and hybrid solar operation or pure standard natural gas fueling. A non-recuperative turbine may be interesting in the case of combining the Brayton cycle with another one because of the higher temperatures of exhaust and the recuperative one in the case of a Brayton cycle standing alone because of the associated fuel savings. In the next section we present the model predictions for power output, thermal efficiencies, fuel consumption, and emissions for all the considered cases.

4. Annual plant performance, consumption, and emissions

The yearly averages of power output, P, overall plant efficiency, η, fuel conversion rate, r_c, heat engine efficiency, η_{cc}, solar collector

efficiency, η_S, solar share, f, and solar collector working temperature, T_{HS} are collected in Tables 2–6 for the layouts in Table 1.

In the case (A) (see Table 2), real (yearly averaged) operating plant conditions the power output is approximately 4.370 MW without recuperation and 4.469 MW with recuperation, slightly below the nominal power output of the turbine *Mercury 50*. It is almost independent of using solar heat input or not, because the turbine inlet temperature was considered as fixed. Overall efficiency is larger for the plant in the absence of solar heat input, because the incorporation of the solar collector adds unavoidable thermal losses. Without recuperation η decreases 4.75% in solar hybrid operation and with recuperation the decrease is larger, 6.94%. On the contrary, fuel conversion rate, r_e is larger with solar input (see Table 2): 7.39% without recuperator and 9.54% with it. Roughly, as will be commented below, these data represents the fuel saving in annual terms, when the turbine is hybridized. The solar subsystem efficiency, η_S, is lower when recuperation is considered because the averaged temperature of the collector is larger in this case, $T_{HS} = 946.6$ K against 730.1 K. Higher temperature obviously provokes larger thermal losses and so, reduced solar efficiency. The averaged solar share in real operating conditions is between 0.123 (no-recuperation) and 0.164 (with recuperation). These small values of solar share show that the size of the heliostat field (taken from the project Solugas) is small for the intended power output. The combustion chamber is always releasing heat to the fluid to reach the turbine inlet temperature.

Table 2
Annual averages of most important plant performance records at operating point (A) in plant configurations with and without recuperation. Relative differences for each configuration are calculated with respect to the case without solar input.

Operating point (A)	Without recuperation		With recuperation	
	Without solar input	With solar input	Without solar input	With solar input
P (MW)	4.370	4.377 (+0.16%)	4.469	4.476 (+0.16%)
η	0.262	0.250 (−4.75%)	0.367	0.342 (−6.94%)
r_e	0.263	0.283 (+7.39%)	0.367	0.406 (+9.54%)
η_H	0.274	0.274 (+0.04%)	0.383	0.383 (+0.08%)
T_{HS} (K)	–	730.1	–	946.6
η_S	–	0.620	–	0.586
f	–	0.123	–	0.164

Table 3
Same that Table 2 for the case (B): all plant heat exchangers are considered ideal.

Ideal heat exchangers (B)	Without recuperation		With recuperation	
	Without solar input	With solar input	Without solar input	With solar input
P (MW)	4.668	4.668 (+0.%)	4.668	4.668 (+0.%)
η	0.275	0.265 (−3.80%)	0.386	0.365 (−5.56%)
r_e	0.275	0.301 (+9.52%)	0.386	0.441 (+14.38%)
η_H	0.281	0.281 (+0.%)	0.394	0.394 (+0.%)
T_{HS} (K)	–	712.2	–	949.0
η_S	–	0.622	–	0.585
f	–	0.152	–	0.208

Table 4
Same that Table 2 for the case (C): no losses in the solar subsystem.

Ideal solar subsystem (C)	Without recuperation		With recuperation	
	Without solar input	With solar input	Without solar input	With solar input
P (MW)	4.370	4.384 (+0.32%)	4.469	4.483 (+0.32%)
η	0.263	0.265 (+0.57%)	0.367	0.370 (+0.81%)
r_e	0.263	0.311 (+18.14%)	0.367	0.479 (+30.49%)
η_H	0.274	0.274 (+0.09%)	0.383	0.383 (+0.15%)
T_{HS} (K)	–	795.0	–	1014.2
η_S	–	1.	–	1.
f	–	0.240	–	0.327

Table 5
Same that Table 2 for the case (D): ideal Brayton cycle.

Ideal Brayton cycle (D)	Without recuperation		With recuperation	
	Without solar input	With solar input	Without solar input	With solar input
P (MW)	7.988	7.988 (+0.%)	7.988	7.988 (+0.%)
η	0.442	0.421 (−4.81%)	0.616	0.575 (−6.68%)
r_e	0.442	0.472 (+6.57%)	0.616	0.674 (+9.48%)
η_H	0.452	0.452 (+0.%)	0.628	0.628 (+0.%)
T_{HS} (K)	–	657.5	–	904.8
η_S	–	0.628	–	0.594
f	–	0.111	–	0.151

Table 6
Same that Table 2 for the case (E): the plant works under ideal conditions, no losses are considered.

Ideal plant (E)	Without recuperation		With recuperation	
	Without solar input	With solar input	Without solar input	With solar input
P (MW)	7.988	7.988 (+0.%)	7.988	7.988 (+0.%)
η	0.452	0.452 (+0.%)	0.628	0.628 (+0.%)
r_e	0.452	0.522 (+15.68%)	0.628	0.792 (+26.0%)
η_H	0.452	0.452 (+0.%)	0.628	0.628 (+0.%)
T_{HS} (K)	–	722.1	–	971.0
η_S	–	1.	–	1.
f	–	0.218	–	0.301

In the case (B) the main heat exchangers linking thermal subsystems are considered as ideal, that is, the heat transfer from the solar receiver to the working fluid is done without thermal losses ($\varepsilon_{HS} = 1$), the heat released by the combustion process is perfectly transferred to the gas ($\varepsilon_{HC} = 1$), and the gas after the turbine exit releases heat to the ambient to recover the compressor inlet temperature through another ideal heat exchanger, whose effectiveness is $\varepsilon_L = 1$. All the performance records increase with respect to case (A). But as Fig. 3 displays, the increases in overall efficiency, and fuel conversion efficiency are relatively low. This is an interesting result from our viewpoint because an investment in improving effectivenesses of heat exchangers could not lead to large improvements on overall plant records. From other perspective, the margins for improvement of the plant by incorporating heat exchangers with lower losses are substantial but not very large (compared with other losses as it will be shown below). This is depicted in Fig. 4, where we show a direct comparison with respect to case (A). For instance power output would increase about 5 % with ideal heat exchangers, and overall efficiency and fuel conversion efficiency about 8%.

Table 4 contains the results for the ideal solar system, case (C), *i.e.* no optical losses (optical efficiency, $\eta_0 = 1$) nor thermal losses (emissivity, $\alpha = 0$, effective convection and conduction losses coefficient, $U_L = 0$). In this case, (C), it is also considered that the heat transfer from the receiver to the pressurized air is ideal ($\varepsilon_{HS} = 1$). The increase of overall efficiency with respect to the case (A) is

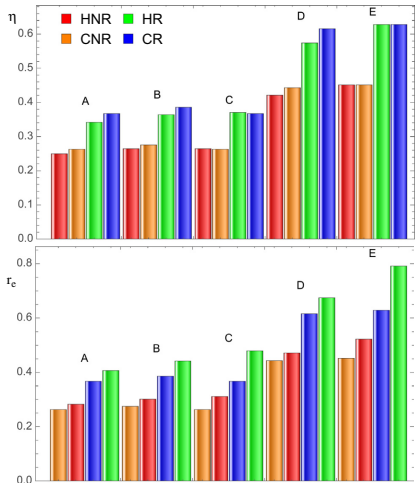

Fig. 3. Annual averages of overall plant efficiency (η) and fuel conversion efficiency (r_e) for the cases considered (A–E). Four plant configurations are analyzed: partial solar input and recuperated turbine (HR), no solar input and recuperated turbine (CR), solar input and non-recuperated turbine (HNR), and no solar input and no-recuperated turbine (CNR).

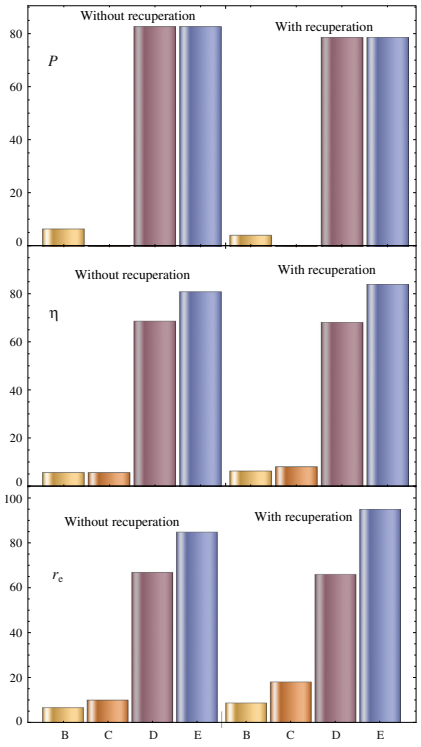

Fig. 4. Margins for improvement for power output (P), overall plant efficiency (η), and fuel conversion efficiency (r_e). They are quantified as relative increments in percentages with respect to the plant operating point (case A). In all cases solar contribution to the heat input is considered (hybrid mode). Recuperative and non-recuperative gas cycles are distinguished.

Table 7
Yearly averages of specific fuel consumption and emissions at operating point, case (A).

Operating point (A)	Without recuperation		With recuperation	
	Without solar input	With solar input	Without solar input	With solar input
m_f (kg/MWh)	283.995	266.463	203.485	186.569
CO_2 (kg/MWh)	702.758	659.374	503.534	461.674
CH_4 (g/MWh)	13.296	12.475	9.527	8.735
N_2O (g/MWh)	1.291	1.211	0.925	0.848
Relative differences	−6.173%		−8.313%	

Table 8
Annual averages of specific fuel consumption and emissions for the five cases considered. Relative differences with respect to case (A) are also shown.

With recuperation and solar input	Operating point (A)	Ideal heat exchangers (B)	Ideal solar part (C)	I-deal Brayton cycle (D)	Completely ideal plant (E)
m_f (kg/MWh)	186.569	173.516	169.781	112.204	101.019
CO_2 (kg/MWh)	461.674	429.374	420.13	277.654	249.977
CH_4 (g/MWh)	8.735	8.124	7.949	5.253	4.730
N_2O (g/MWh)	0.848	0.789	0.772	0.510	0.459
Relative differences	–	−6.996%	−8.998%	−39.859%	−45.854%

appreciable (see Figs. 3 and 4), but as it could be expected the fuel conversion rate increases in a very important way, about 10% without recuperation and 18% with recuperation. The solar share in case (C) is almost double that in the real operating point (A), $f = 0.327$ with recuperation and 0.240 without recuperation. Due to the absence of thermal losses, the working temperature of the solar receiver increases, approximately 65 K with respect to case (A), as indicated in Table 4.

The consideration of an ideal thermal cycle for the Brayton engine (case (D)) greatly improves all performance records, as shown in Table 5 and Figs. 3 and 4. To reproduce this situation the compressor and the turbines were considered isentropic ($\varepsilon_c = \varepsilon_t = 1$), the pressure losses in heat input and heat release negligible ($\rho_H = \rho_L = 1$), the recuperator effectiveness, $\varepsilon_r = 1$, and combustion chamber and cold-side heat exchangers ideal ($\varepsilon_{HC} = \varepsilon_L = 1$). The increase in power output (for the same fixed value of T_3) amounts about 78% in the recuperative case with respect to case (A) and 82% without recuperation. Overall plant efficiency increases approximately 70% and fuel conversion rate about 65%. Overall efficiencies in this situation would reach values about 0.421 without recuperation and 0.575 with recuperation and the temperatures of the solar collector would decrease (comparing with case (A)) up to 657.5 K without recuperation and 904.8 K with recuperation. The fuel conversion rate increases between 6.6% and 9.5% with respect to the standard plant without solar heat input (see Table 5).

Table 6 contains the predictions for the completely ideal plant, that is, a hybrid plant in which the solar subsystem, the heat engine, and all heat exchangers are considered as working without thermal nor pressure losses. In this case, fuel conversion efficiency in the recuperative case would reach almost 0.8 and overall plant efficiency 0.628. Solar share would be in between 21.8% and 30.1%. In summary, the margins of improvement for these plants are large and mainly associated to the development of the efficiency of the Brayton heat engine. A sensitivity analysis follows in the next section, but before we shall analyze fuel consumption and emissions for the configurations (A)-(E).

Yearly averages of specific fuel consumption (natural gas) and emissions at the operating point, case (A) are displayed in Table 7. Emissions were estimated from conversion factors for natural gas [51,52]. Fuel consumption varies from 186.569 kg/MWh for the recuperative plant working in the hybrid mode to 283.995 kg/MWh for only combustion and no-recuperation. This represents a difference of approximately 34%. In the non-recuperative plant fuel saving for the plant with partial solar heat input is about 6.173% and in the recuperative case about 8.313%. In Table 8 and Fig. 5 cases (B)–(E) are compared with the case (A), real operating conditions. The limit case with ideal heat exchangers will lead to a fuel saving of about 7% and the corresponding decrease of greenhouse emissions, a solar collector without optical and thermal losses to a saving about 9%, an ideal Brayton heat engine to 39.86% and a completely ideal plant to 45.85%. These numbers give a realistic notion about the potential of this technology to decrease fuel consumption and so emissions for plants of about a few megawatts.

5. Sensitivity of plant performance to thermal and pressure losses

The effect of the main irreversibility sources in the overall plant records is analyzed in this section. The influence of the main irreversibility sources in the solar subsystem is displayed in Fig. 6: optical efficiency (η_0), heat transfer losses parameters (α and U_L), and solar heat exchanger (ε_{HS}). The horizontal axis represents relative deviations of losses parameters with respect to yearly averaged real operating conditions and the vertical one the relative deviations for overall efficiency ($\Delta\eta$), fuel conversion rate (Δr_e), solar collector efficiency ($\Delta\eta_S$), and effective receiver working temperature (ΔT_{HS}). In all cases evolutions are almost linear. The overall efficiency, $\Delta\eta$, shows more sensitivity to optical efficiency

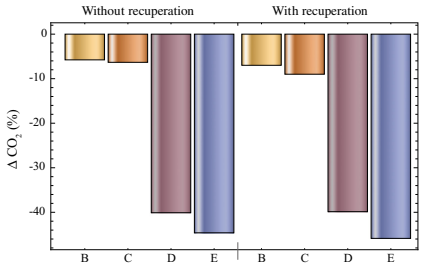

Fig. 5. Predicted decrease of CO_2 emissions for the layouts in Table 1 with respect to the operating point (case (A) in Table 1) for a gas-turbine operating in hybrid mode.

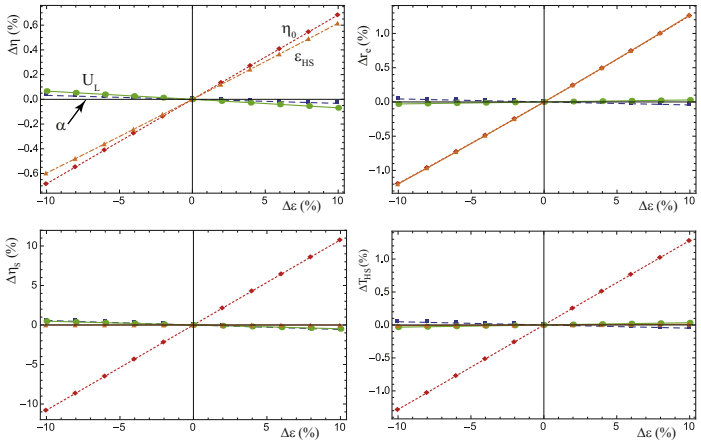

Fig. 6. Sensitivity of several output records, overall efficiency ($\Delta\eta$), fuel conversion efficiency (Δr_e), solar subsystem efficiency ($\Delta\eta_S$), and mean working temperature of the solar receiver (ΔT_{HS}), to different irreversibility parameters of the solar subsystem (denoted in general as $\Delta\varepsilon$): optical efficiency (η_0), effective emissivity (α), effective convective losses coefficient (U_L), and solar heat exchanger effectiveness (ε_{HS}). Both axis are represented in relative terms as percentages. The central point represents the yearly averages of the recuperative plant at real operating conditions, case (A).

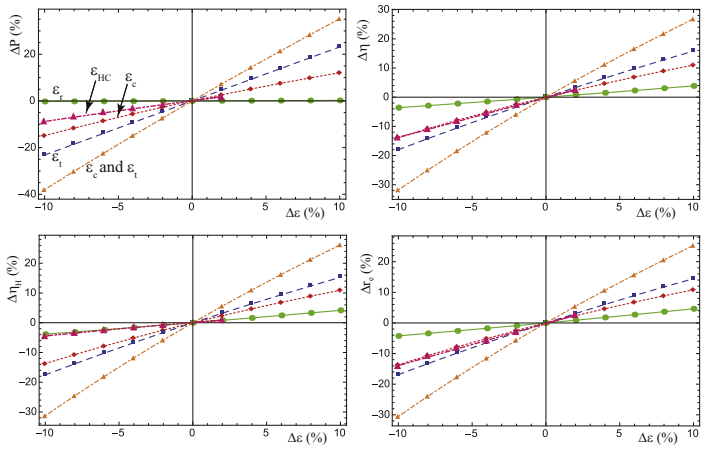

Fig. 7. Sensitivity of several output records, power output (ΔP), overall efficiency ($\Delta\eta$), Brayton cycle efficiency ($\Delta\eta_H$), and fuel conversion efficiency (Δr_e), to different irreversibility parameters of the heat engine: isentropic efficiency of the compressor (ε_c), isentropic efficiency of the turbine (ε_t), effectiveness of the heat exchanger associated to the combustion chamber, ε_{HC}, and recuperator effectiveness (ε_r). The case in which ε_c and ε_t are simultaneously changed in the same way is also considered. Both axis are represented in relative terms as percentages with respect to yearly averaged real operating conditions.

(depending on the design and operation of the solar heliostat field and receiver: shadowing effects, blocking, tracking, spillage, etc.) and heat transfer from the receiver to the working fluid than to radiation or conduction-convection heat losses, but in any case numerical variations on η are small. An improvement of about 10% on η_0 will lead to a gain of about 10% on η_S, but this only will improve 0.6% the overall efficiency, η, and 1.5% the fuel conversion rate, r_e. From our viewpoint this is one of the main conclusions of

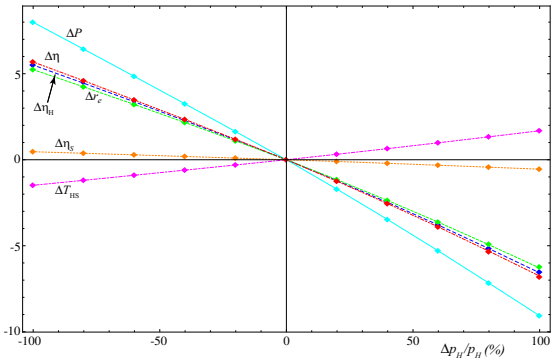

Fig. 8. Sensitivity of several output records to the relative pressure decay in the hot side of the Brayton cycle, $\Delta p_H/p_H$. Both axis are represented in relative terms as percentages with respect to yearly averaged real operating conditions.

the predictions of our model: a substantial improvement on the efficiency of the solar subsystem would be slightly reflected on the fuel conversion efficiency and poorly on the overall plant thermal efficiency, at least for the plant size considered for the numerical computations.

Nevertheless, plant performance is quite sensitivity to the losses associated to the Brayton cycle, as it is shown in Fig. 7. The evolution of all variables is also almost linear, but now the scale of the vertical axes in each plot indicates much more important changes on the performance records. For instance, with respect to power output, an improvement of about 10% on compressor isentropic efficiency, ε_c, will lead to 10% increase on power output. The same improvement on turbine isentropic efficiency, ε_t, to more than 20% on P, and an increase of both parameters simultaneously, $\varepsilon_c + \varepsilon_t$, to almost 40% on P. Of course, recuperator effectiveness variations would not affect plant power output, but other output records would be changed. Overall efficiency, η, Brayton subsystem efficiency, η_H, and fuel conversion rate, r_e, would oscillate in the interval [−30, +30]% for changes in the losses coefficients (ε_c, ε_t, and ε_{HC}) in the power unit in the interval [−10, +10]%, *i.e.*, decreases on losses would be multiplied by a factor 3 on the plant records.

Plant sensitivity to the pressure losses in the ducts the air flows during the heat absorption process is plotted in Fig. 8. Pressure drop is represented by a single parameter in spite that in real installations decays occur in different steps (ducts from the compressor to the solar receiver, solar receiver itself, ducts from the receiver to the combustion chamber, and ducts from the combustion chamber to turbine entrance). In the figure the total pressure decay is compared with that of real operating conditions by representing in the x-axis the relative pressure decays with respect to the pressure at the compressor exit, that is $\Delta p_H/p_H$ in our notation (see Fig. 2 of [36]). At real operating conditions, the decay is about 9.2%. In the limit case of no pressure decay, power output will increase 8%, and overall efficiency and fuel conversion rate about 6%. At the other side, higher pressure losses would reduce plant operation. For instance, pressure losses about 18% would worsen power output about 10% and overall efficiency about 7%. When plotted against $\Delta p_H/p_H$, performance variables do display a parabolic behavior further from linear than the shown in previous figures. It is important to emphasize that changes in pressure losses in the working fluid affect the working temperature of the solar receiver and so, the efficiency of the solar subsystem.

6. Discussion on energy fluxes and losses

Energy fluxes in the plant are represented in a visual way through Sankey's diagrams in Figs. 9 and 10 for two plant layouts, case (A) where the numerical parameters are taken from the project Solugas (although considering real averaged solar irradiance and external temperature) and case (E) where the plant eventually works in ideal conditions. In both cases energy fluxes are normalized to unity with respect to the total energy input and the width of the arrows is proportional to each energy flux. Recuperation in the Brayton cycle is considered. In Fig. 9(a) the plant is working in hybrid operation. First, it is observed that the size of the solar input is small compared with the combustion one, as consequence of the reduced dimensioning of the solar field. Nevertheless, losses in relative terms are quite larger for the solar subsystem. $\dot{Q}_o$ represents the optical losses and amount about 10% of all the energy input. Heat transfer losses in the solar field from radiation and conduction/convection is about 1%. Losses in the receiver considered as a heat exchanger that releases the solar power to the pressurized air correspond to about 4%. In the combustion equipment, losses in the combustion chamber are about 2% and in the associated heat exchanger are similar. So, the total heat input really released to the working fluid is about 82% of the total input. Then, the Brayton power unit, is capable to extract a 34% of mechanical energy but 48% is heat released to the ambient. This ratio could be improved by combining the Brayton cycle, for instance, with a Rankine cycle through a heat recovery steam generator. This is an open work line for the next future.

In the situation of pure combustion functioning, Fig. 9(b), losses from the solar subsystem are absent and the useful power output is 37%. On the other extreme, for a hypothetic ideal plant, Fig. 10, the net power output would be independent of hybridization and would amount 63% of the total energy input. These graphs are an alternative way to compare the relative dimensions of the subsystems providing the heat input to the power unit and to locate and quantify losses. Moreover, allow to analyze the thermodynamic margin for improvement for this technology as foreseen with the theoretical methodology developed in this work.

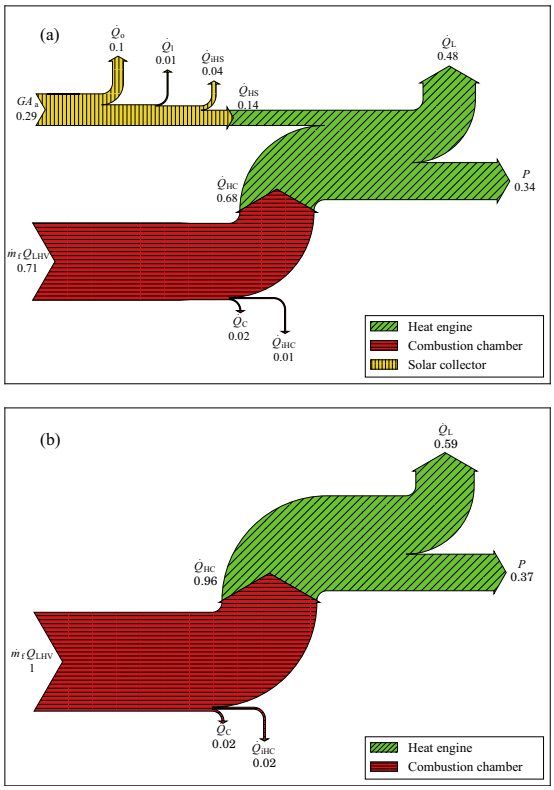

Fig. 9. Sankey's diagram of the energy fluxes in the plant for the case (A) in Table 1 with recuperation. Total energy input is normalized to unity. (a) Plant operation in hybrid mode. (b) Pure combustion mode.

7. Conclusions

The main conclusions of this work could be summarized as follows:

- A thermodynamic model was applied in order to carry out a global analysis of the performance of solarized gas-turbine power plants. Actual meteorological data were taken and annual averages of variables such as efficiencies, power output, fuel consumption, emissions, and solar share, calculated. Several plant configurations were surveyed, with or without recuperation in the Brayton cycle and hybrid or pure combustion operation. For the power output range considered, the yearly averaged solar share is small as a consequence of the size of the heliostat field. Nevertheless, fuel saving (and so, emissions) is reduced between 6% and 8% in yearly terms, depending on the plant configuration when comparing hybrid operation with pure combustion.
- Margins for improvement of the plant are large if eventually losses in the solar subsystem, Brayton engine, or heat exchangers could be diminished. Particularly, overall plant efficiency and fuel conversion efficiency are quite more sensitive to improvements on the efficiency of the power unit components (compressor, turbine, recuperator, etc.). An increase on the efficiency of the solar subsystem (especially optical losses) substantially would decrease fuel consumption and, so, operation costs.

Nowadays, the technology of gas-turbines is quite more mature than that of heliostat fields, or central tower solar receivers, so substantial efficiency improvements on the power unit should not be expected, thus the development of the central receiver solar collectors seems imperative for the future viability of this technology. In the power unit an increase on output records should be associated to combustion chambers and turbines working on higher temperatures. Also, the possible utilization of working fluids as carbon

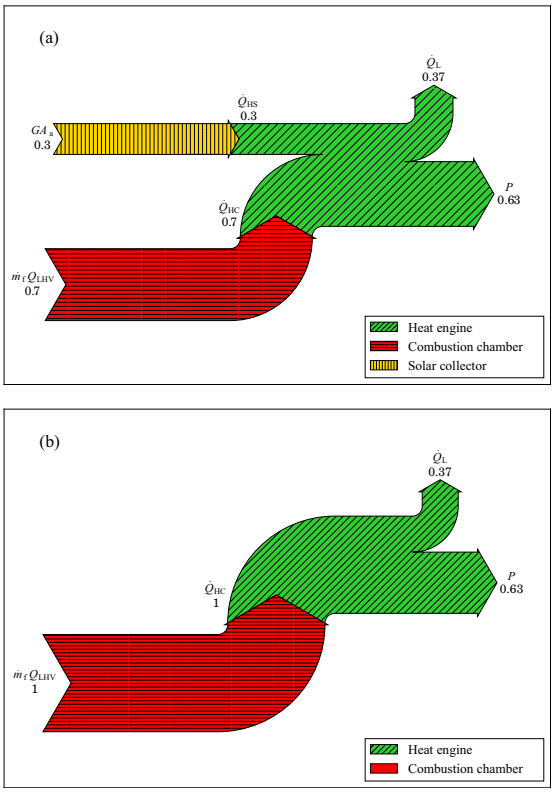

Fig. 10. Sankey's diagram of the energy fluxes in the plant for completely ideal operation, case (E). Total energy input is normalized to unity. (a) Plant operation in hybrid mode. (b) Pure combustion mode.

dioxide or others is in the scope of recent research works. In which concerns to solar collectors, optical efficiency on one hand and heat losses in the central receiver are the points to be analyzed in the future. Our work provides, for a particular installation, how these improvements in the plant equipment would affect the yearly averaged plant records.

Acknowledgements

The authors from University of Salamanca acknowledge financial support from MINECO of Spain, Grant ENE2013-40644-R and University of Salamanca. I. Reyes Ramírez acknowledges financing from COFAA-IPN, EDI-IPN, and SNI-CONACyT, México, for a sabbatical leave at Department of Applied Physics, University of Salamanca, Spain.

References

[1] Weinstein L, Loomis J, Bhatia B, Bierman D, Wang E, Chen G. Concentrating solar power. Chem Rev 2015;115:12797–838.
[2] Wang W, Ragnolo G, Aichmayer L, Strand T, Laumert B. Integrated design of a hybrid gas turbine-receiver unit for a solar dish system. Energy Proc 2015;69:583–92.
[3] Romier A. Small gas turbine technology. Appl Therm Eng 2004;24:1709–23.
[4] Daabo AM, Al Jubori A, Mahmoud S, Al-Dadah RK. Parametric study of efficient small-scale axial and radial turbines for solar powered Brayton cycle application. Energy Conv Manage 2016;128:343–60.
[5] Behar O, Khellaf A, Mohammedi K. A review of studies on central receiver solar thermal power plants. Renew Sust Energy Rev 2013;23:12–39.
[6] Okoroigwe E, Madhlopa A. An integrated combined cycle system driven by a solar tower: a review. Renew Sust Energy Rev 2016;57:337–50.
[7] Markides CN. Low-concentration solar-power systems based on organic Rankine cycles for distributed-scale applications: overview and further development. Front Energy Res 2015;3(47). http://dx.doi.org/10.3389/fenrg.2015.00047.
[8] Jansen E, Bello-Ochende T, Meyer J. Integrated solar thermal Brayton cycles with either one or two regenerative heat exchangers for maximum power output. Energy 2015;86:737–48. http://dx.doi.org/10.1016/j.energy.2015.04.080.
[9] Livshits M, Kribus A. Solar hybrid steam injection gas turbine (STIG) cycle. Sol Energy 2012;86:190–9.
[10] Kumar P, Dutta P, Srinivasa Murthy S, Srinivasan K. Solar driven carbon dioxide Brayton cycle power generation with thermal compression. Appl Therm Eng http://dx.doi.org/10.1016/j.applthermaleng.2016.06.112.

[11] Grange B, Dalet C, Falcoz Q, Siros F, Ferriére A. Simulation of a hybrid solar gas-turbine cycle with storage integration. Energy Proc 2014;49:1147–56.
[12] Okoroigwe E, Madhlopa A. Evaluation of the potential for hybridization of gas turbine power plants with renewable energy in South Africa. IEEE conference publications 2015. http://dx.doi.org/10.1109/DUE.2015.7102985.
[13] Schwarzbözl P, Buck R, Sugarmen C, Ring A, Marcos Crespo M, Altwegg P, et al. Solar gas turbine systems: design, cost and perspectives. Sol Energy 2006;80:1231–40.
[14] Solar-hybrid power and cogeneration plants. Tech. rep., European Commission; 2011. <ordis.europa.eu/publication/rcn/13318_en.html>.
[15] Korzynietz R, Quero M, Uhlig R. Solugas-future solar hybrid technology. Tech. rep., SolarPaces; 2012. <http://cms.solarpaces2012.org/proceedings/paper/7ee7e32ece8f2f8e0984d5ebff9d77b>.
[16] Korzynietz R, Brioso JA, del Río A, Quero M, Gallas M, Uhlig R, et al. Solugas – comprehensive analysis of the solar hybrid Brayton plant. Sol Energy 2016;135:578–89.
[17] Saghafifar M, Gadalla M. Thermo-economic analysis of conventional combined cycle hybridization: united arab emirates case study. Energy Conv Manage 2016;111:358–74.
[18] Spelling J, Laumert B. Thermo-economic evaluation of solar thermal and photovoltaic hybridization options for combined-cycle power plants. J Eng Gas Turb Power 2015;137:031801-1–031801-11.
[19] Siva Reddy V, Kaushik S, Tyagi SC. Exergetic analysis and economic evaluation of central tower receiver solar thermal power plant. Int J Energy Res 2014;38:1288–303. http://dx.doi.org/10.1002/er.3138.
[20] Connolly D, Lund H, Mathiesen BV, Leahy M. A review of computer tools for analysing the integration of renewable energy into various energy systems. Appl Energy 2010;87:1059–82.
[21] Collado F, Guallar J. A review of optimized design layouts for solar power tower plants with campo code. Renew Sust Energy Rev 2013;20:142–54.
[22] Barigozzi G, Bonetti G, Franchini G, Perdichizzi A, Ravelli S. Thermal performance prediction of a solar hybrid gas turbine. Sol Energy 2012;86:2116–27.
[23] Ho CK, Iverson BD. Review of high-temperature central receiver designs for concentrating solar power. Renew Sust Energy Rev 2014;29:835–46.
[24] Olivenza-León D, Medina A, Calvo Hernández A. Thermodynamic modeling of a hybrid solar gas-turbine power plant. Energy Convers Manage 2015;93:435–47.
[25] McMahan A, Klein S, Reindl D. A finite-time thermodynamic framework for optimizing solar-thermal power plants. J Sol Energy Eng 2007;129:355–62.
[26] Le Roux W, Bello-Ochende TMJ. A review on the thermodynamic optimisation and model of the solar thermal Brayton cycle. Renew Sust Energy Rev 2013;28:677–90.
[27] Li Y, Liu G, Liu X, Liao S. Thermodynamic multi-objective optimization of a solar-dish Brayton system based on maximum power output, thermal efficiency and ecological performance. Renew Energy 2016;95:465–73.
[28] Zheng H, Yu X, Su Y, Riffat S, Xiong J. Thermodynamic analysis of an ideal solar tower thermal power plant. Appl Therm Eng 2015;81:271–8.
[29] Valdes M, Duran M, Rovira A. Thermoeconomic optimization of combined cycle gas turbine power plants using genetic algorithms. Appl Therm Eng 2003;23:2169–82.
[30] Barranco-Jiménez M, Sánchez-Salas N, Angulo-Brown F. Finite-time thermoeconomic optimization of a solar-driven heat engine model. Entropy 2011;13:171–83.
[31] Barranco-Jiménez M, Sánchez-Salas N. On thermodynamic optimisation of solar collector model under maximum ecological conditions. J Energy Inst 2008;81:164–7.
[32] Sánchez-Orgaz S, Pedemonte M, Ezzatti P, Curto-Risso P, Medina A, Calvo Hernández A. Multi-objective optimization of a multi-step solar-driven Brayton cycle. Energy Convers Manage 2015;99:346–58.
[33] Soltani R, Keleshtery P, Vahdati M, Khoshgoftar Manesh M, Rosen M, Amidpour M. Multi-objective optimization of a solar-hybrid cogeneration cycle: application to CGAM problem. Energy Conv Manage 2014;81:60–71.
[34] Li Y, Liao S, Liu G. Thermo-economic multi-objective optimization for a solar-dish Brayton system using NSGA-II and decision making. Elect Power Energy Sys 2015;64:167–75.
[35] Avval H, Ahmadi P, Ghaffarizadeh A, Saidi M. Thermo-economic-environmental multiobjective optimization of a gas turbine power plant with preheater using evolutionary algorithm. Int J Energy Res 2011;35:389–403.
[36] Santos MJ, Merchán RP, Medina A, Calvo Hernández A. Seasonal thermodynamic prediction of the performance of a hybrid solar gas-turbine power plant. Energy Convers Manage 2016;115:89–102. http://dx.doi.org/10.1016/j.enconman.2016.02.019.
[37] Sánchez-Orgaz S, Medina A, Calvo Hernández A. Maximum overall efficiency for a solar-driven gas turbine power plants. Int J Energy Res 2013;37:1580–91.
[38] Sánchez-Orgaz S, Medina A, Calvo Hernández A. Recuperative solar-driven multi-step gas turbine power plants. Energy Convers Manage 2013;67:171–8.
[39] Duffie J, Beckman W. Solar engineering of thermal processes. Hoboken, New Jersey: John Wiley and Sons; 2006.
[40] Heywood J. Internal combustion engine fundamentals. McGraw-Hill; 1988.
[41] Quero M, Korzynietz R, Ebert M, Jiménez AA, del Río A, Brioso JA. Solugas – operation experience of the first solar hybrid gas turbine system at MW scale. Energy Proc 2014;49:1820–30.
[42] Caterpillar ST. <https://mysolar.cat.com/cda/files/126873/7/dsm50pg.pdf>.
[43] GREET. The greenhouse gases, regulated emissions and energy use in transportation model., Tech. rep.. Argonne, IL: Argonne National Laboratory; 2010. , <http://greet.es.anl.gov>.
[44] Wu L, Lin G, Chen J. Parametric optimization of a solar-driven Braysson heat engine with variable heat capacity of the working fluid and radiation-convection heat losses. Renew Energy 2010;35:95–100.
[45] Romero M, Buck R, Pacheco E. An update on solar central receiver systems, projects, and technologies. Trans ASME 2002;124:98.
[46] de Mello P, Monteiro D. Thermodynamic study of an EFGT (Externally fired gas-turbine) cycle with one detailed model for the ceramic heat exchanger. In: Proceedings of ECOS 2011 conference, Novi Sad, Serbia.
[47] Sunden B. High temperature heat exchangers (HTHE). In: Proceedings of the fifth international conference on enhanced, compact and ultra-compact heat exchangers: science. Hoboken, NJ, USA: Engineering and Technology; 2005.
[48] Zhang Y, Lin B, Chen J. Optimum performance characteristics of an irreversible solar-driven Brayton heat engine at the maximum overall efficiency. Renew Energy 2007;32:856–67.
[49] Horlock J. Advanced gas turbine cycles. Oxford: Pergamon; 2003.
[50] Meteosevilla. <http://www.meteosevilla.com>.
[51] Direct emissions from stationary combustion sources; May 2008. <www.epa.gov/climateleaders>.
[52] Emission factors for greenhouse gas inventories; April 2014. <http://www.epa.gov/climateleadership/documents/emission-factors.pdf>.

3.3 Paper 3 – Thermodynamic model of a hybrid Brayton thermosolar plant

Title: "Thermodynamic model of a hybrid Brayton thermosolar plant"
Journal: *Renewable Energy*
Authors: **R.P. Merchán**, M.J. Santos, A. Medina, A. Calvo Hernández
Year: 2018
Volume: 128
Pages: 473-483
DOI: `http://dx.doi.org/10.1016/j.renene.2017.05.081`
Reference: [124]

Resumen

En este artículo se presenta una mejora sustancial del modelo termodinámico desarrollado anteriormente para plantas termosolares de torre con turbinas de gas híbridas. En concreto y puesto que el rango en el que varían las temperaturas en el ciclo es grande, se ha modificado el modelo de modo que las capacidades caloríficas dependan de dichas temperaturas. Asimismo, se han implementado en el código ecuaciones semianalíticas fácilmente manejables para todas las variables de salida. De esta forma, se cumple el objetivo de simplicidad del modelo, con un número reducido de parámetros con claro significado físico. Los valores numéricos de las variables se toman similares a los del proyecto *SOLUGAS*, cuya escala de potencia es de pocos megawattios (5 MW). Gracias a las simulaciones llevadas a cabo, se estima cómo varían en el tiempo la eficiencia térmica, las eficiencias de los subsistemas, el *solar share*, la potencia, las temperaturas involucradas y el consumo de combustible, uno de los objetivos principales del artículo. También se incluye un análisis diario y estacional para estas variables. Los valores máximos de la temperatura del receptor solar varían entre 720 K en invierno y 870 K en verano cuando no hay recuperador, pero aumentan significativamente hasta valores por encima de los 1050 K en verano si en el esquema de la planta se añade un recuperador. En el caso de un ciclo Brayton recuperativo, las predicciones de ahorro de gas natural alcanzan un valor del 11.5 % en verano con respecto a una planta sin aporte solar. Además, el cálculo del consumo también se traduce en la evaluación de las emisiones contaminantes de efecto invernadero correspondientes, principalmente, dióxido de carbono, metano y óxido nitroso.

Renewable Energy 128 (2018) 473–483

Contents lists available at ScienceDirect

Renewable Energy

journal homepage: www.elsevier.com/locate/renene

Thermodynamic model of a hybrid Brayton thermosolar plant

R.P. Merchán, M.J. Santos*, A. Medina, A. Calvo Hernández

Department of Applied Physics, University of Salamanca, 37008, Salamanca, Spain

ARTICLE INFO

Article history:
Received 16 January 2017
Received in revised form
23 May 2017
Accepted 26 May 2017
Available online 31 May 2017

Keywords:
Thermosolar gas-turbines
Hybrid plants
Thermodynamic model
Variable solar irradiance
Global plant performance
Seasonal evolution

ABSTRACT

We present a thermodynamic model for the prediction of the performance records of a solar hybrid gas turbine power plant. Variable irradiance and ambient temperature conditions are considered. A serial hybridization is modeled with the aim to get an approximately constant turbine inlet temperature, and thus to deliver to the grid a stable power output. The overall thermal efficiency depends on the efficiencies of the involved subsystems and the required heat exchangers in a straightforward analytical way. Numerical values for input parameters are taken from a central tower heliostat field recently developed near Seville, Spain. Real data for irradiance and external temperature are taken in hourly terms. Curves for the evolution of plant efficiencies (solar, gas turbine, fuel conversion efficiency, overall efficiency, etc.) and solar share are presented for representative days of each season. The cases of non-recuperative and recuperative plant configurations are shown. Estimations of the hourly evolution of fuel consumption are simulated as well as savings between the hybrid solar operation model and the pure combustion mode. During summer, fuel saving can reach about 11.5% for a recuperative plant layout. In addition, plant emissions for several configurations are presented.

1. Introduction

Along the last years a number of experimental facilities based on the concept of hybrid solar gas turbines were developed. In these projects concentrated solar power [1,2] coming from a central receiver plant is used to heat pressurized air following a Brayton-like cycle [3–5]. This technology may be especially interesting for regions with advantageous solar conditions [6]. This is in turn associated to water shortage. Brayton cycles admit combinations with other cycles in order to improve overall efficiency by making use of high temperature output heat [7,8].

In this context the term *hybrid* means that during low solar radiation time spans a combustion chamber ensures a stable power release to the grid and makes not imperative the utilization of storage systems [9]. Different hybridization techniques have been proposed [10]. Hybridization can be performed starting from an existing standard fossil plant or developing an original hybrid plant sketch [11]. Usually there is more flexibility within the second option, provided that design challenges are properly worked out. Nowadays, it is necessary a rigorous simulation work considering the hybrid system as a whole. Technological, thermodynamic, and economic ingredients should be simultaneously considered in this design process [7,10,12]. In such a task it is difficult to avoid the election of particular stationary conditions for solar irradiance and ambient temperature. Nevertheless, design point conditions are usually too hopeful and do not reflect the actual fluctuating behavior due to daily and seasonal changes of solar irradiance at the elected location.

During the last years several research works on the model, analysis, and simulation of this technology have been published. A considerable amount of them make use of commercial simulation environments or software developed by research groups which allows for a detailed description and specific calculations on the solar subsystem and any plant component [3,13]. With respect to solar collectors, exhaustive computations for the solar efficiency including mirror area, spillage, blocking and shadowing effects, mirror tracking strategies, etc. have been developed [14,15]. These simulations lead to complete information for each plant component, managing a large amount of variables and parameters. In consequence, optimization procedures are not easy to apply. Furthermore, it is not straightforward to extract physical information about the main sources of thermal losses in this kind of plants and to plan global strategies for the optimization of the plant design and operation.

From another point of view, there are several theoretical works

* Corresponding author.
E-mail addresses: rpmerchan@usal.es (R.P. Merchán), smjesus@usal.es (M.J. Santos), amd385@usal.es (A. Medina), anca@usal.es (A. Calvo Hernández).

http://dx.doi.org/10.1016/j.renene.2017.05.081
0960-1481/

Nomenclature

A_a	aperture area of the collector
A_r	absorber area of the collector
a_c	isentropic compressor pressure ratio
a_t	isentropic turbine pressure ratio
C	solar collector concentration ratio
c_w	specific heat of the working fluid
f	solar share
G	direct solar irradiance
h_1	radiation heat loss coefficient for the solar collector
h_2	effective convection and conduction loss coefficient for the solar collector
$\dot{m}$	mass flow rate of the working substance
$\dot{m}_f$	fuel mass flow rate
P	power output
$\left\|\dot{Q}_{\mathrm{H}}\right\|$	total heat-transfer rate absorbed from the working fluid
$\left\|\dot{Q}_{\mathrm{HC}}\right\|$	heat input from the combustion chamber
$\left\|\dot{Q}'_{\mathrm{HC}}\right\|$	heat rate transferred from the combustion chamber to the associated heat exchanger
$\left\|\dot{Q}_{\mathrm{HS}}\right\|$	heat rate input from the solar collector
$\left\|\dot{Q}'_{\mathrm{HS}}\right\|$	heat rate transferred from the solar collector to the associated heat exchanger
$\left\|\dot{Q}_{\mathrm{L}}\right\|$	heat-transfer rate between the working fluid and the ambient
Q_{LHV}	lower heating value of the fuel
r_e	fuel conversion rate
r_p	overall pressure ratio
T_{HC}	working temperature of the combustion chamber
T_{HS}	working temperature of the solar collector
T_{L}	ambient temperature (K)
T_x	working fluid temperature after the heat input from the recuperator
$T_{x'}$	working fluid temperature after heat input from the solar collector
T_y	working fluid exhaust temperature
T_3	turbine inlet temperature
U_{L}	convective losses of the solar collector
α	effective emissivity
η	overall thermal efficiency
η_C	combustion chamber efficiency
η_{H}	thermal efficiency of the Brayton heat engine
$\varepsilon_{\mathrm{HC}}$	combustion chamber heat exchanger effectiveness
$\varepsilon_{\mathrm{HS}}$	solar collector heat exchanger effectiveness
η_S	solar collector efficiency
η_0	effective transmittance-absorptance product
ε_c	isentropic efficiency of the compressor
ε_L	cold side heat exchanger effectiveness
ε_r	recuperator effectiveness
ε_t	isentropic efficiency of the turbine
γ	adiabatic coefficient of the working fluid
ρ_{H}	irreversibilities due to pressure drops in the heat input
ρ_{L}	irreversibilities due to pressure drops in the heat release
σ	Stefan-Boltzmann constant
τ_{HS}	temperature ratio associated to the solar collector
τ_{HC}	temperature ratio associated to the combustion chamber

that model the plant starting from the ideal Brayton cycle for the power cycle and from a simple model for the solar subsystem. Then, the thermodynamic model is refined by incorporating submodels for thermal losses in order to provide more realistic output records [16–20]. This working method allows to obtain closed and general analytical expressions for thermal efficiencies and power output, and then check the model predictions for any design point conditions, with fixed values of solar irradiance and ambient temperature. This kind of models is also interesting for optimization purposes because lead to a realistic representation of real systems in terms of a reduced set of parameters.

Within the latter *modus operandi*, we present a thermodynamic cycle for the modeling of the considered solar plants that starts from a closed Brayton cycle however incorporating the main losses sources: non-ideal turbine and compressor, pressure decays, heat exchangers, heat transfer losses in the solar collector, combustion inefficiencies, etc. The model is flexible and allows to check the performance of several plant configurations. Temperature dependent specific heats for the working fluid are considered. Special emphasis will be paid on recuperation because of its key influence on the plant output records [6,21,22]. The model is dynamic in which refers to solar irradiance and ambient temperature. It allows to obtain curves for any plant output record in terms of those parameters and to analyze hourly and seasonal changes at any given location.

The model includes not too complex submodels for the solar subsystem and the power unit. This allows to get expressions for the plant global efficiency and other performance data in terms of a reduced number of parameters, with clear physical meaning. So, the proposed model constitutes a pre-design simulation scheme in order to understand the main bottlenecks to consider in the design of this kind of facilities. It will be shown that the comparison of its predictions with real plant data at particular conditions is fairly adequate. A whole analysis of plant records evolution along a year is undertaken. Real solar irradiance and ambient temperature measures for representative days of each season and a particular location are considered. Fuel consumption, pollutant, and greenhouse emissions will be evaluated.

2. Thermodynamic plant model

The layout of the hybrid solar plant considered is represented in Fig. 1 (a). A single step recuperative closed Brayton cycle is hybridized in order to obtain a stable power output, independent of the solar irradiance conditions. The design is flexible because the plant can work in different modes: with or without solar hybridization (depending on irradiance conditions), and with or without recuperator. Next we briefly describe the main thermodynamic processes experienced by the working fluid.

The working fluid at the compressor exit (temperature T_2) is heated up through a recuperator that makes use of the high temperature of the gas after the turbine, T_4. The temperature of the fluid at the recuperator exit, T_x, is elevated first by the heat released by the central tower solar subsystem if solar irradiance is enough. Afterwards, the fluid reaches a higher temperature, $T_{x'}$ and then, in the last heating step, it receives an energy input from a combustion chamber through another heat exchanger. The final temperature at the turbine inlet, T_3, is taken as approximately constant, so the

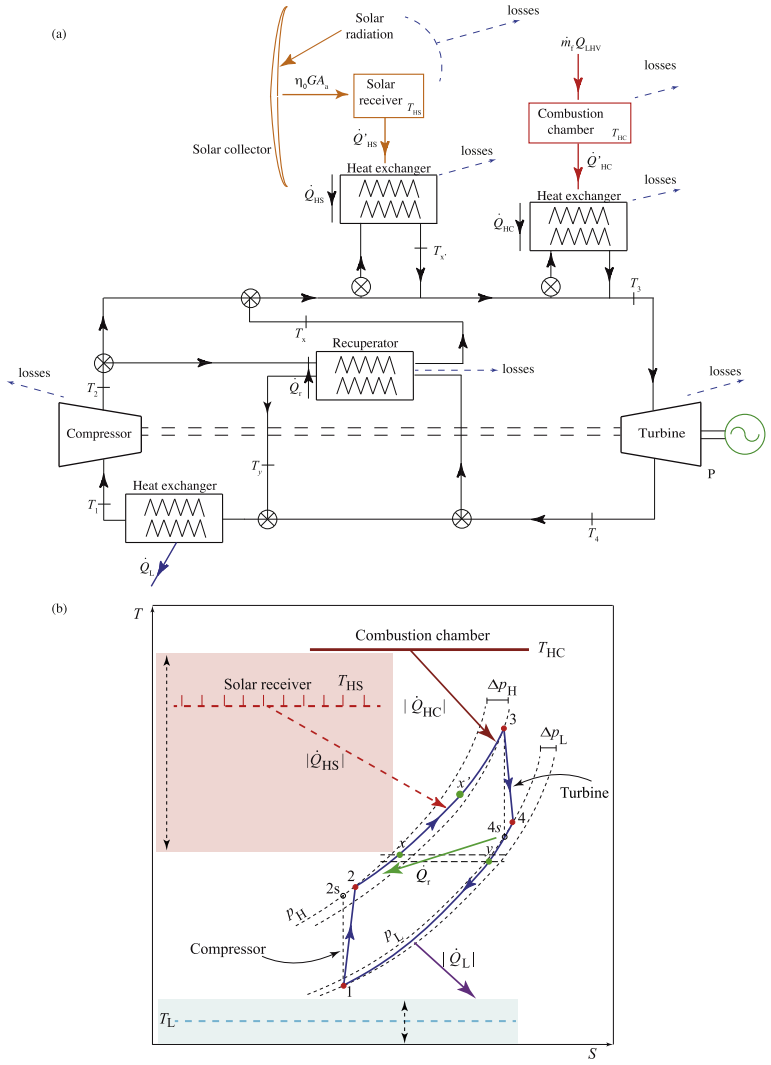

Fig. 1. (a) Scheme of the hybrid solar gas-turbine plant considered. The main heat transfers and temperatures are depicted. Also the key losses sources considered in the model are shown. (b) $T - S$ diagram of the irreversible Brayton cycle experienced by the working fluid.

power released by the installation to the grid is stable. In the case of insufficient irradiance a shut-off valve redirects the fluid directly to the heat exchanger below the combustion chamber.

From now on, the nomenclature for the different heat transfers in the model is detailed. The solar subsystem receives a heat input from the sun given by GA_a where G is the direct solar irradiance and A_a the aperture area of the solar field. The solar irradiance is a function of time because it depends on the sun position during the day, weather conditions, and seasonal fluctuations. After discounting the losses, the receiver releases a useful energy to a heat

exchanger, $\dot{Q}'_{HS}$, that in turn releases a final heat rate $\dot{Q}_{HS}$ to the working fluid.

A similar scheme is followed to describe the combustion chamber subsystem. The energy input in this subsystem is $\dot{m}_f Q_{LHV}$, where $\dot{m}_f$ is the fuel mass consumption rate and Q_{LHV} its corresponding lower heating value. The mass fuel rate will be also considered as time dependent, in accordance to the fluctuations of G. It should compensate variations in G in such a way that the turbine inlet temperature remains approximately constant in all conditions. In the combustion chamber losses due to incomplete combustion and heat transfers to the surroundings are accounted for. The heat rate received by the working fluid from combustion of the fuel is denoted as $\dot{Q}_{HC}$. The effectivenesses of the heat exchangers associated to the solar and the combustion subsystems are denoted as ε_{HS} and ε_{HC}, respectively. The internal heat transfer associated to recuperation is called $\dot{Q}_r$. In order to close the thermodynamic cycle a cold-side heat exchanger is considered. The compressor inlet temperature, T_1, depend on the external temperature, T_L, that will fluctuate due to daily and seasonal changes. Thus, all other temperatures in the cycle oscillate because of the same reasons. The plant delivers a mechanical power output, P, independent of solar radiation fluctuations.

2.1. Overall plant efficiency

The thermal efficiency of the whole system, η, is the ratio between the net mechanical power output, P, and the total heat input rate,

$$\eta = \frac{P}{GA_a + \dot{m}_f Q_{LHV}} \tag{1}$$

The following objective is to express this global efficiency in terms of the efficiency of the solar collector, η_S, that of the combustion chamber, η_C, the efficiency of the Brayton heat engine, η_H, and the effectivenesses of all the required heat exchangers. Details of the calculations can be found in Ref. [19].

The overall efficiency of the whole system, η, is obtained as:

$$\eta = \eta_S \eta_C \eta_H \left[\frac{\varepsilon_{HS}\varepsilon_{HC}}{\eta_C \varepsilon_{HC} f + \eta_S \varepsilon_{HS}(1-f)}\right] \tag{2}$$

This expression is valid for the hybrid mode when both heat sources are simultaneously releasing energy to the fluid. In the particular case in which eventually all the energy input comes from the solar collector, $f = 1$, and $\eta = \eta_S \eta_H \varepsilon_{HS}$, and when solar irradiance is null, and the turbine works only with the heat released in the combustion reactions, $f = 0$, and $\eta = \eta_C \eta_H \varepsilon_{HC}$.

It is also interesting to define a performance relative to the energy input with an economical cost, *i.e.*, to the fuel burned. It constitutes a *fuel conversion rate*, and can be defined as suggested by Heywood [23] for internal combustion engines, $r_e = P/(\dot{m}_f Q_{LHV})$. It is easy to show that:

$$r_e = \frac{\eta\, \eta_S\, \eta_H\, \varepsilon_{HS}}{\eta_S\, \eta_H\, \varepsilon_{HS} - \eta f} \tag{3}$$

In the particular case all the energy input comes from combustion, $f = 0$, and $r_e = \eta$. In the opposite limit, if eventually all the energy was solar, $f = 1$, and $\eta = \eta_S\, \eta_H \varepsilon_{HS}$, so $r_e \to \infty$.

2.2. Solar collector and combustion efficiencies

We consider a simple model for the concentrating solar system in order to be able to obtain analytical closed expressions for the overall plant efficiency. At low and intermediate working temperatures for the solar collector, T_{HS}, losses essentially comes from conduction and convection. At high temperatures radiation losses become significant and should be considered in any model. The energy collected at the aperture is GA_a, and the useful energy provided by the solar plant, $\left|\dot{Q}'_{HS}\right|$, is the difference between the energy transmitted to the receiver, $\eta_0 GA_a$, and the losses. η_0 is the effective optical efficiency considering losses coming from spillage, shadowing, blocking, sun position effects, and so on. Thus, the useful heat released from the collector and its efficiency can be respectively expressed, as [24,25]:

$$\left|\dot{Q}'_{HS}\right| = \eta_0 GA_a - \alpha\sigma A_r T_L^4\left(\tau_{HS}^4 - 1\right) - U_L A_r T_L(\tau_{HS} - 1) \tag{4}$$

$$\eta_S = \frac{\left|\dot{Q}'_{HS}\right|}{GA_a} = \eta_0\left[1 - h_1\, T_L^4\left(\tau_{HS}^4 - 1\right) - h_2\, T_L(\tau_{HS} - 1)\right] \tag{5}$$

In Eqs. (4) and (5), $\tau_{HS} = T_{HS}/T_L$ denotes the ratio between the working temperature of the solar receiver, T_{HS}, and the surroundings, T_L. A_a and A_r are, respectively, the total area of the reflectors and the area of the receiver, $h_1 = \alpha\sigma/(\eta_0 GC)$, $h_2 = U_L/(\eta_0 GC)$ are losses parameters, where U_L is the convective heat loss coefficient, α is the effective emissivity of the collector, $C = A_a/A_r$ is the concentration ratio, and σ the Stefan-Boltzmann constant. It will be considered in our model that the direct solar irradiance, G, and the surroundings temperature, T_L, are time functions because oscillate during a day and change with seasonal and meteorological conditions. For each particular pair of values of G and T_L at any given instant, the working temperature of the receiver, T_{HS}, is calculated by balancing the energy received from the sun and that released to the working fluid experiencing the bottoming thermal cycle [18]. The heat released by the solar subsystem to the working fluid is $\left|\dot{Q}_{HS}\right| = \varepsilon_{HS}\left|\dot{Q}'_{HS}\right|$, where $\varepsilon_{HS} = (T_{x'} - T_x)/(T_{HS} - T_x)$.

The efficiency of the combustion chamber, η_C, for a certain fuel and fuel-air equivalence ratio, can be considered as a constant parameter. In real equipment it could slightly change with fluctuations of the fuel-air equivalence ratio, the composition of the fuel, its temperature, and several other variables, but we are more interested in an adequate qualitative description. The heat received by the working fluid from the combustion chamber, $\dot{Q}_{HC}$, can be written as:

$$\left|\dot{Q}_{HC}\right| = \varepsilon_{HC}\left|\dot{Q}'_{HC}\right| = \varepsilon_{HC}\, \eta_C\, \dot{m}_f\, Q_{LHV} \tag{6}$$

By expressing the effectiveness of the heat exchanger in between the combustion chamber and the thermal cycle as (see Fig. 1) $\varepsilon_{HC} = (T_3 - T_{x'})/(T_{HC} - T_{x'})$, the heat released, in terms of temperatures, is:

$$\left|\dot{Q}_{HC}\right| = \dot{m}\, c_w(T_3 - T_{x'}) = \dot{m}\, c_w\, \varepsilon_{HC}(T_{HC} - T_{x'}) \tag{7}$$

where $\dot{m}$ is the working fluid mass flow and c_w is its specific heat. The effective temperature in the combustion chamber is denoted as T_{HC}, and the associated temperature ratio as $\tau_{HC} = T_{HC}/T_L$. As fluctuations in G and T_L are be taken into account, the fuel mass flow to be burned in the combustion chamber will also be a time dependent function in general given by:

$$\dot{m}_f = \frac{\dot{m}\, c_w(T_3 - T_{x'})}{\eta_C\, Q_{LHV}\, \varepsilon_{HC}} \tag{8}$$

where $T_{x'}$ will vary with the solar irradiance and ambient conditions. The rate of fuel mass burned can be also obtained from the fuel conversion rate, r_e, as: $\dot{m}_f = P/(r_e\, Q_{LHV})$.

2.3. Brayton gas-turbine efficiency

The main assumptions considered for evaluating the efficiency of the heat engine, η_H, will be briefly outlined since the model has been detailed elsewhere in previous works by our group [19,22]. It is assumed that a mass rate of an ideal gas, $\dot{m}$, undergoes an irreversible closed recuperative Brayton cycle. The specific heat of the working fluid is taken as temperature dependent, $c_w(T)$. This point constitutes a substantial improvement of this model over previous ones where an averaged, constant specific heat, was supposed [19,22]. The $T-S$ diagram of the cycle is depicted in Fig. 1(b), where it is stressed that both the working temperature of the solar receiver, T_{HS} and that of the surroundings, T_L, are fluctuating quantities.

1. As starting step the gas is compressed ($1\rightarrow 2$) by means of a non-ideal compressor. Its isentropic efficiency is given by $\varepsilon_c = (T_{2s}-T_1)/(T_2-T_1)$. In this equation T_{2s} represents the temperature of the working fluid after the compression process if it was adiabatic and T_2 is the actual temperature at the compressor outlet.
2. Between states 2 and 3, in the most general situation, the gas receives three energy inputs in sequence. First, the non-ideal recuperator increases the gas temperature from T_2 to T_x. Its effectiveness, ε_r, is defined as the ratio between the actual temperature (T_x-T_2) increase and the maximum ideal one (T_4-T_2): $\varepsilon_r = (T_x-T_2)/(T_4-T_2) = (T_y-T_4)/(T_2-T_4)$. In the case of a non-recuperative cycle, $\varepsilon_r = 0$, and in the ideal limit, $\varepsilon_r = 1$.

Secondly, the gas receives a heat flow, $\left|\dot{Q}_{HS}\right|$, from the solar subsystem (step $x\rightarrow x'$) and thus its temperature increases from T_x to $T_{x'}$. Finally, the gas receives a completing heat input from the combustion chamber ($x'\rightarrow 3$) in order to ensure an approximately constant turbine inlet temperature, T_3, independently of the solar irradiance conditions.

Pressure decrease in the process $2\rightarrow 3$ is quantified through an effective parameter, ρ_H. In real plants pressure decays are associated to the particular equipment in any of the three steps of the heat input process, so the curve $2\rightarrow 3$ would not be as smooth as it is plotted in Fig. 1(b). But the consideration of a unique global pressure decay parameter allows to obtain analytical equations and to numerically check the effects of pressure decays in the output parameters of the plant [13]. This parameter, ρ_H, is defined as:

$$\rho_H = \frac{p_H - \Delta p_H}{p_H} \tag{9}$$

where p_H is the highest pressure of the gas and $p_H - \Delta p_H$ its pressure at the turbine inlet.

3. In the state 3 the working fluid has reached its maximum temperature and it is expanded by means of a non-ideal turbine performing the power stroke ($3\rightarrow 4$). In Fig. 1(b) the state 4s represents the final state in the ideal case the turbine behaves isentropically, and the state 4 is the actual final state after expansion. The isentropic efficiency of the turbine, ε_t, is given by: $\varepsilon_t = (T_4-T_3)/(T_{4s}-T_3)$.
4. Lastly, the gas recovers the conditions at the initial state 1 by releasing heat in the process $4\rightarrow 1$ through two steps. First, by means of the recuperator (process $4\rightarrow y$) and later by exchanging heat to the ambient through a non-ideal heat exchanger with effectiveness, ε_L (process $y\rightarrow 1$): $\varepsilon_L = (T_1-T_y)/(T_L-T_y)$.

The pressure loss during the whole heat release process is measured through a coefficient ρ_L given by:

$$\rho_L = \frac{p_L - \Delta p_L}{p_L} \tag{10}$$

where p_L is the gas pressure at the turbine outlet and $p_L - \Delta p_L$ its lowest pressure during the cycle. It is convenient to define a global pressure ratio, r_p as:

$$r_p = \frac{p_H}{p_L - \Delta p_L} \tag{11}$$

Provided that the processes $1\rightarrow 2s$ and $3\rightarrow 4s$ are adiabatic (see Fig. 1(b)), two parameters, a_c and a_t, related to the pressure ratios of the compressor and the turbine respectively are defined:

$$a_c = \frac{T_{2s}}{T_1} = \left(\frac{p_H}{p_L - \Delta p_L}\right)^{(\overline{\gamma}_{12}-1)/\overline{\gamma}_{12}} = r_p^{(\overline{\gamma}_{12}-1)/\overline{\gamma}_{12}} \tag{12}$$

$$a_t = \frac{T_3}{T_{4s}} = \left(\frac{p_H - \Delta p_H}{p_L}\right)^{(\overline{\gamma}_{34}-1)/\overline{\gamma}_{34}} \tag{13}$$

where $\overline{\gamma}_{12}$ is the average adiabatic coefficient in the compression process and $\overline{\gamma}_{34}$ the corresponding one during expansion.

From Eqs. (9) and (10):

$$\frac{p_H - \Delta p_H}{p_L} = \rho_H \rho_L r_p \tag{14}$$

and so:

$$a_t = (\rho_H \rho_L r_p)^{(\overline{\gamma}_{34}-1)/\overline{\gamma}_{34}} \tag{15}$$

Both coefficients, a_t and a_c are not independent, both are related through the pressure ratio, r_p.

Once, the main hypotheses and parameters have been made explicit, we express the temperatures of all the states in the cycle in terms of the temperature of the solar collector, T_{HS}, that of the combustion chamber, T_{HC}, and the pressure ratios of the compressor, a_c and the turbine, a_t. By using the definitions in the section above, it is possible to obtain the following set of equations:

$$T_1 = \varepsilon_L T_L + T_y(1-\varepsilon_L) \tag{16}$$

$$T_2 = T_1 + \frac{1}{\varepsilon_c}(T_{2s}-T_1) = T_1 Z_c \tag{17}$$

$$T_3 = \varepsilon_{HC} T_{HC} + T_{x'}(1-\varepsilon_{HC}) \tag{18}$$

$$T_4 = T_3 - \varepsilon_t(T_3 - T_{4s}) = T_3 Z_t \tag{19}$$

$$T_x = \varepsilon_r T_4 + T_2(1-\varepsilon_r) \tag{20}$$

$$T_y = \varepsilon_r T_2 + T_4(1-\varepsilon_r) \tag{21}$$

$$T_{x'} = \varepsilon_{HS} T_{HS} + T_x(1-\varepsilon_{HS}) \tag{22}$$

The equations (17) and (19) were simplified by introducing two definitions:

$$Z_c = 1 + \frac{1}{\varepsilon_c}(a_c - 1) \tag{23}$$

$$Z_t = 1 - \varepsilon_t\left(1 - \frac{1}{a_t}\right) \tag{24}$$

By simultaneously using Eqs. (16)-(22) it is feasible to express all the temperatures in terms of the temperatures of the heat sources, T_{HS} and T_{HC}, the ambient temperature, T_L, the pressure ratio, r_p and all the irreversibility parameters defined above. The following closed set of expressions is obtained:

$$T_2 = \frac{(1-\varepsilon_L)(1-\varepsilon_r)[\varepsilon_{HC}T_{HC} + \varepsilon_{HS}T_{HS}(1-\varepsilon_{HC})] + \varepsilon_L T_L\left[Z_t^{-1} - (1-\varepsilon_{HC})(1-\varepsilon_{HS})\varepsilon_r\right]}{\left[Z_c^{-1} - (1-\varepsilon_L)\varepsilon_r\right]\left[Z_t^{-1} - (1-\varepsilon_{HC})(1-\varepsilon_{HS})\varepsilon_r\right] - (1-\varepsilon_{HC})(1-\varepsilon_{HS})(1-\varepsilon_L)(1-\varepsilon_r)^2} \tag{25}$$

$$T_4 = \frac{[\varepsilon_{HC}T_{HC} + \varepsilon_{HS}T_{HS}(1-\varepsilon_{HC})]\left[Z_c^{-1} - (1-\varepsilon_L)\varepsilon_r\right] + \varepsilon_L T_L(1-\varepsilon_{HC})(1-\varepsilon_{HS})(1-\varepsilon_r)}{\left[Z_c^{-1} - (1-\varepsilon_L)\varepsilon_r\right]\left[Z_t^{-1} - (1-\varepsilon_{HC})(1-\varepsilon_{HS})\varepsilon_r\right] - (1-\varepsilon_{HC})(1-\varepsilon_{HS})(1-\varepsilon_L)(1-\varepsilon_r)^2} \tag{26}$$

It is easy to get all the temperature of the working fluid by substituting Eqs. (25) and (26) in Eqs. (16)-(22). The total heat input rate, $|\dot{Q}_H|$, and, the heat release, $|\dot{Q}_L|$, are expressed in terms of the temperatures in the following way:

$$|\dot{Q}_H| = |\dot{Q}_{HS}| + |\dot{Q}_{HC}| \tag{27}$$

$$|\dot{Q}_L| = \dot{m}\int_{T_1}^{T_y} c_w(T)dT \tag{28}$$

where,

$$|\dot{Q}_{HS}| = \dot{m}\int_{T_x}^{T_{x'}} c_w(T)\,dT = f|\dot{Q}_H| \tag{29}$$

$$|\dot{Q}_{HC}| = \dot{m}\int_{T_{x'}}^{T_3} c_w(T)\,dT = (1-f)|\dot{Q}_H| \tag{30}$$

In these equations $c_w(T)$ represents the temperature dependent constant pressure specific heat of the working fluid. Thus, the power output released by the heat engine, $P = |\dot{Q}_H| - |\dot{Q}_L|$, and its thermal efficiency, $\eta_H = P/|\dot{Q}_H|$, have analytical expressions susceptible to be evaluated for any particular parameters arrangement. And so, from the considered models for the solar and the combustion chamber subsystems, it is possible to obtain the overall plant efficiency from Eq. (2).

3. Numerical implementation

The model presented in this work was validated for fixed solar irradiance conditions in previous works [18,19], where explicit tables containing model predictions and experimental results can be found. In this section we outline the main background and conclusions of the numerical validation. As validation target it was elected the central tower concentrating collector developed by Abengoa Solar near Seville, Spain, under the project called SOLUGAS [26]. The turbine used in the project is the model *Mercury 50* from Caterpillar, for which the manufacturer provides several specifications [27]. All the parameters required to obtain the numerical predictions can be found in Refs. [18,19]. Dry air was considered as working fluid, with polynomial fits for constant pressure specific heat taken from Ref. [28]. As highlighted before, the consideration of temperature dependent functions for working fluid specific heats constitutes a significant advance with respect to previous versions of our simulation scheme.

From now on, solar irradiance and ambient temperature are not be considered as fixed design parameters, but oscillating ones in terms of daily and seasonal conditions. This is one of the strengths of the purely thermodynamic scheme developed in this work: its capability to predict plant performance records for whichever solar and meteorological conditions.

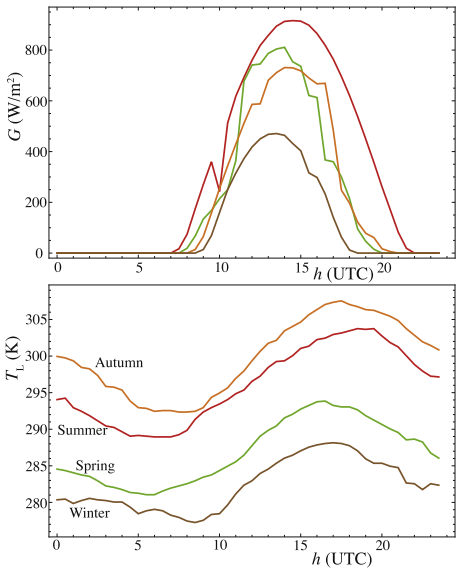

Fig. 2. Hourly direct irradiance, G, and ambient temperature, T_L, for four selected days at the beginning of each season at Seville [29]. Curves are neither smoothed nor averaged.

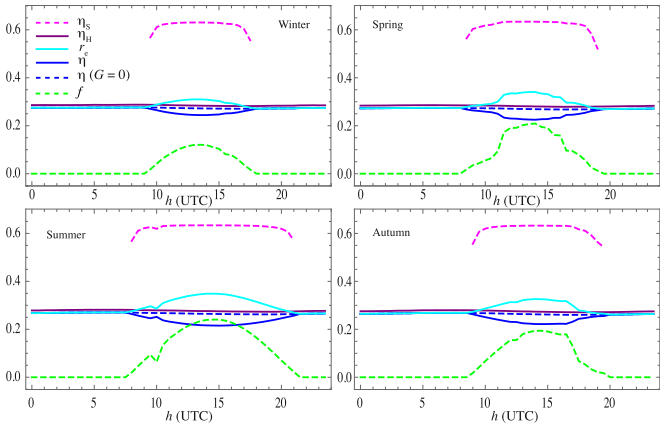

Fig. 3. Hourly evolution of plant efficiencies and solar share, f, for representative days of each season for a non-recuperative plant layout.

3.1. Daily variations and seasonal variations of solar irradiance and ambient temperature

Direct irradiance, G, and ambient temperature, T_L, were taken from a database by Meteosevilla [29] at a location very close to the installation of the project SOLUGAS, Sanlúcar La Mayor, Seville, Spain. We took data from four regular days in 2013, each corresponding to the beginning of a season (21st): March, June, September, and December. Data were taken every 30 min. No smoothing or averaging procedures were followed. The curves for G and T_L are represented in Fig. 2. Seville has *a priori* quite favorable solar conditions. The upper panel of the figure shows that the maximum value of G reached in summer is about 875 W/m^2. The maximum of the less favorable month, December reaches about 480 W/m^2. The number of insolation hours is quite elevated. At the same time ambient temperatures are relatively high. They reach maximum values around 34 °C during the day in September and minimum values about 4 °C in winter.

For each pair of values of G and T_L the working temperature of the collector, T_{HS} was calculated. All the results presented in this work were obtained from our own software, developed in programming language Mathematica®. In the next sections, results with plant configurations either incorporating a recuperator or not will be shown. When no recuperator is included, investments costs

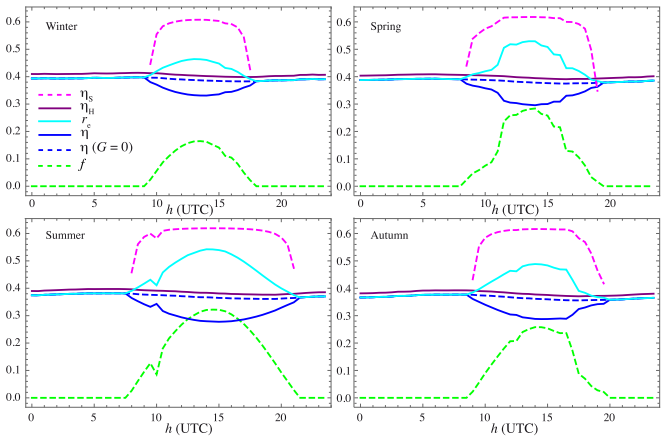

Fig. 4. Hourly evolution of plant efficiencies and solar share, f, for representative days of each season. The plant configuration includes a recuperator with effectiveness, $\varepsilon_T = 0.775$.

are reduced, thermal efficiency decreases, and fuel consumption is higher. But temperature of the working fluid at the exit of the expansion process is high and so, the cycle is susceptible to be combined with a bottoming cycle. In the opposite situation, when an extra investment is made in the plant and a recuperator is incorporated in the design, fuel costs decrease and thermal efficiency increases, but the temperature at the recuperator exit could make more difficult to use residual heat for bottoming cycles. Moreover, the inclusion of a recuperator will be only beneficial for not too high values of the compressor pressure ratio as discussed elsewhere in the literature [6,21,22].

4. Model projections

4.1. Plant efficiencies and temperatures

We have obtained the curves for the different thermal plant efficiencies and solar share for a representative day of each season in terms of the UTC time for two plant configurations (see Fig. 1): non-recuperative ($\varepsilon_r = 0$) and recuperative ($\varepsilon_r = 0.775$). These efficiencies are plotted in Fig. 3 (no recuperation is considered) and Fig. 4 (including a recuperator). The efficiency of the solar subsystem, η_S, is only defined when the solar irradiance is enough to deliver an effective heat to the working fluid, so the corresponding curves are plotted for a particular time interval. For any season these curves present a wide plateau during the hours with good insolation and then η_S decreases during sunrise and sunset. The shape of the functions in these periods is only indicative because a particular model for the evolution of the solar receiver temperature with G during transients should be necessary. This is out of the scope of this work. The plateaus are associated to the fact that solar efficiency are governed by the optical efficiency, η_0, that we considered as constant. The influence of heat losses is small in the shape of η_S, specially in the non-recuperative case (see Fig. 3), only the height of the plateaus is sensitive to the temperature dependent heat losses, Eq. (5). Of course the plateaus are wider during summer, because of the higher number of insolation hours. Largest values of η_S are about 0.63 for the non-recuperative case and slightly smaller for the recuperative case. This is due to the fact that working temperatures of the solar collector are higher in this case and so heat transfer losses in the solar subsystem are larger.

The efficiency of the Brayton heat engine, η_H, is almost constant, day and night. It depends on the ambient temperature for a particular day but its time dependence is small in the scale of the plots in Figs. 3 and 4. In seasonal terms, η_H, is higher for lower ambient temperatures: winter and spring. Its numerical value significantly increases when incorporating a recuperator, as it should be expected. For instance in winter (see Fig. 3) it amounts approximately 0.29 and with recuperation increases up to 0.41 (see Fig. 4). This represents an increase about 41% which is very significant. The relative increase is approximately the same in all seasons.

The global plant efficiency, η, appears as a combination of η_S, η_H, the efficiency of the combustion process, η_C, and the effectivenesses of heat exchangers (see Eq. (2)). In the absence of insolation, η is almost time independent and becomes close to η_H. Numerical differences appear due to the combustion inefficiencies and heat exchanger losses. When the solar receiver begins its contribution as G increases, the solar subsystem is coupled to the turbine and the combustion chamber and so, the global efficiency decreases: it presents a dip during the central hours of the day. The well width depends on the number of insolation hours and its depth of the maximum values that G reaches. In the recuperative configuration, Fig. 4, of course numerical values of η are larger than for the non-recuperative, Fig. 3, one because of the important increase of η_H. For $\varepsilon_r = 0$, minimum values of η change between 0.21 in summer to 0.24 in winter. For $\varepsilon_r = 0.775$ the smallest value is found in summer, 0.28, and in winter is around 0.33.

Although the fuel conversion rate, r_e, is not strictly a thermal efficiency is also plotted in Figs. 3 and 4. It is identical to η during nights because all the heat input is associated to fuel combustion and during the day it has a parabolic shape that resembles the shape of G and qualitatively is like a mirror image of η. The maximum value of r_e appears in summer, when irradiance reaches its higher values: for $\varepsilon_r = 0$. It amounts 0.35 and for $\varepsilon_r = 0.775$, 0.54 which is a quite interesting value. In the less favorable season, winter, it amounts 0.31 without recuperation and 0.46 with recuperation.

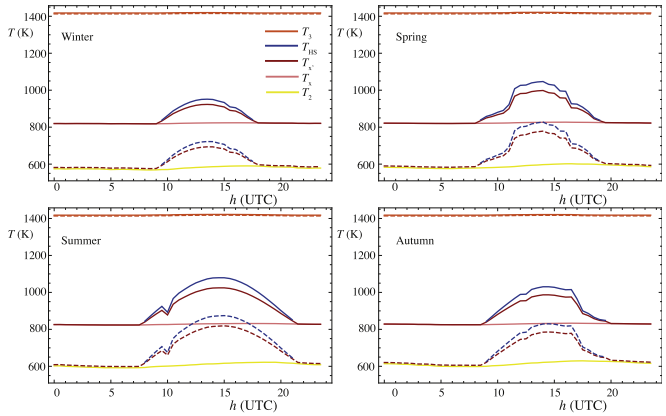

Fig. 5. Temperatures on the hot side of the plant thermodynamic cycle. The non-recuperative plant case is represented in dashed lines and the recuperative one in solid lines. Notation for temperatures corresponds to Fig. 1.

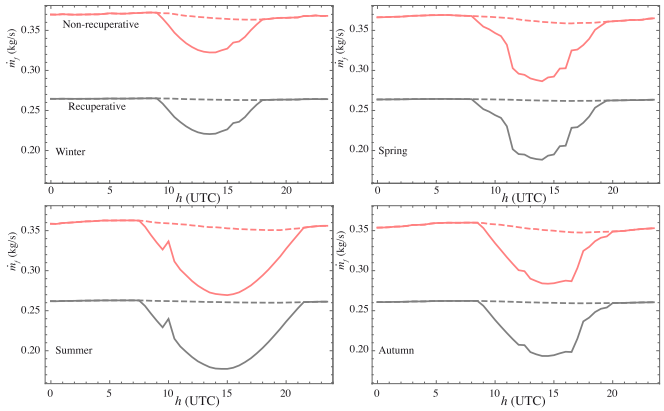

Fig. 6. Evolution with time of the fuel consumption rate, $\dot{m}_f$, supposed natural gas for representative days of each season. Solid lines refer to the hybrid operation mode and dashed ones to the pure combustion mode.

The solar share, *f*, was defined in Sec. 2 as the ratio between the input heat rate from the solar collector and the total input heat rate. Its evolution with time for the considered representative days is plotted in Fig. 3 (non-recuperative) and Fig. 4 (recuperative). In all cases the shape of *f* for any particular season reminds that of the solar irradiance, *G*. Differences among seasons refer both to the number of hours with enough solar irradiance and to the height of the curves maxima. For instance in winter for the recuperative configuration *f* reaches a value slightly above 0.16 and there are 9 h of effective irradiance. At the other side, for a typical day of summer, *f* has a maximum around 0.32 and about 14 h of adequate solar input. When the recuperator is eliminated, for example, with the aim to take advantage of the residual heat in a bottoming cycle, the solar heat input remains the same. Nevertheless, the total heat input (in this case required to increase the temperature from T_2 to T_3 instead of from T_x to T_3) is larger, so the solar share is smaller. If we compare *f* in the figure for winter in both configurations, in the recuperative one the maximum is about 0.165 as mentioned above and for the non-recuperative one about 0.121. This corresponds to a decrease around 36%. At the other end, in summer the maximum with no recuperation is on 0.241, thus an increase about 34% is gained with a recuperator.

The temperatures on the heat input steps of the thermodynamic cycle are plotted in Fig. 5. The turbine inlet temperature, T_3, is almost steady in both configurations as a design criterion, thus providing a stable plant power output. The compressor outlet temperature, T_2 is around 600 K and slightly oscillates following the evolution of the surroundings temperature, T_L. In the non-recuperative layout, during sun hours the solar receiver increases the temperature of the fluid from T_2 to $T_{x'}$. During this period, the latter has a parabolic shape resembling *G*. The working temperature of the solar collector, T_{HS}, is obtained by balancing the energy rate released by the solar collector and that received by the air performing the Brayton cycle. It reaches maximum values above $T_{x'}$ because of the losses in the solar receiver. Maximum values of T_{HS} in the non-recuperative situation change from 720 K in winter to 870 K in summer.

In the recuperative configuration, the recuperator increases the compressor output temperature T_2 to a temperature T_x. Then, the solar collector during the day and the combustion chamber provide the heat rates to reach the turbine inlet temperature, T_3. T_x is independent of time and season, because it is a function of the turbine outlet temperature T_4 (almost constant because T_3 is stable) and the recuperator effectiveness. In the plant considered T_x is around 825 K. In this case the temperatures T_{HS} $T_{x'}$ are displaced atop around 200 K. During summer, the working temperature of the solar receiver, T_{HS}, is slightly above 1000 K, similar to design point conditions of SOLUGAS project. It is important to stress that for the intended power output in this plant $T_{x'}$ never reaches the turbine inlet temperature, T_3. This means that this plant is not dimensioned to work exclusively on solar basis if the aim is to obtain a power output around 4.6 MW. A substantial combustion contribution is always required, even for the highest values of *G*. Some works in the literature report prototype plants working under only solar conditions, but for solar fields relatively larger than the considered here [30].

4.2. Fuel consumption and emissions

Numerical computation of the fuel consumption was achieved, either calculating the fuel consumption rate in hourly basis through Eq. (8) or the integrated consumption during a whole day. The mass fuel rate, $\dot{m}_f$, (see Fig. 6) has two different levels depending on the plant configuration, with or without a heat recuperator. During the night all the electricity generation comes from fuel combustion (natural gas in our case) and differences between recuperative and

Table 1
Fuel consumption for all the seasons as predicted from the simulation model, assuming natural gas fueling.

	m_f (ton per day)	Winter	Spring	Summer	Autumn
No recuperation	Combustion mode	31.1	30.8	30.2	29.9
	Hybrid mode	30.3	29.2	27.6	28.3
Fuel saving (%)		2.8	5.3	8.5	5.4
With recuperation	Combustion mode	22.3	22.3	22.1	22.1
	Hybrid mode	21.5	20.6	19.6	20.5
Fuel saving (%)		3.9	7.3	11.5	7.5

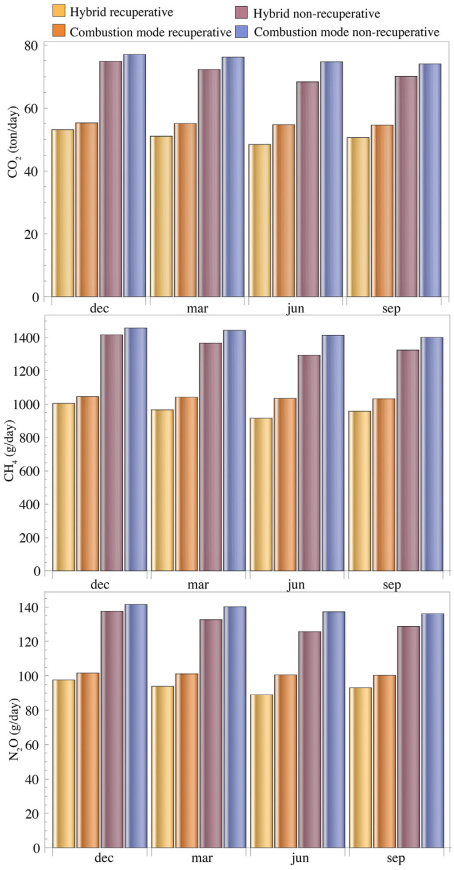

Fig. 7. Real units estimation of greenhouse emissions from the considered model.

non-recuperative cases are around 40%, independently of the season. This is the difference in terms of fuel consumption rate of incorporating a recuperator to pre-heat the working fluid at the compressor exit. When the plant works on a hybrid mode because received irradiance is enough to heat the pressurized air above T_2 (without recuperation) or T_x (with recuperation), the fuel rate saving is important, and obviously depends on seasonal conditions. For each operation mode, the fuel saving for a whole day corresponds to the area of the surface between the solid lines in Fig. 6 (hybrid mode) and the corresponding dashed ones (pure combustion). The results are summarized in Table 1. The legend '*combustion mode*' corresponds to the case of no solar heat input and '*hybrid mode*' to the case in which solar irradiance is enough for partial heat input coming from the central tower solar plant. For the non-recuperative plant the saving varies from 2.8% in winter to 8.5% in summer. Autumn and spring behave in a similar way, the saving is about 5.3%. For the recuperative case relative differences are slightly larger: change from 3.9% in winter to 11.5% in summer. In autumn and spring, now the saving is around 7.3%.

The differences among plant configurations in fuel consumption are directly transferred to pollutant emissions. As an illustration we have plotted in Fig. 7 a bar diagram with the estimated emissions of the main greenhouse gases in real units: CO_2, CH_4, and N_2O. The data in the figure should only be taken as a guide, because each plant could have particular technologies to reduce emissions or CO_2 capture mechanisms. The data were obtained from the natural gas emission factors collected in Refs. [31,32]. The figure, in daily basis for the considered particular days of each season, allow to observe two emission levels: the associated to the non-recuperative plant and the one arising from the recuperative one. Differences are substantial as previously commented for fuel consumption. For these two modes, the reduction associated to solar hybridization and its evolution during the year is also apparent.

5. Summary and conclusions

A solar hybrid power plant based on a gas turbine following a closed Brayton cycle was modeled from a thermodynamic viewpoint. Plant layout is flexible, it can work either in pure combustion mode (by night or during periods with poor solar irradiation), in a pure solar mode for good solar conditions, and also in a mixed mode with simultaneous solar and combustion heating. A basic objective for plant operation is to produce an stable power output, independent of daily and seasonal variations of solar irradiance and meteorological conditions.

The model allows a direct implementation of dynamic plant operation. The hybridization scheme follows a serial or sequential heat input divided in several steps. For instance, in the case of a recuperative plant layout and hybrid operation, the working fluid is heated up first in the recuperator by making use of the high temperatures at the turbine exit, then in the solar receiver of the central tower collector, and finally in the combustion chamber.

The thermodynamic model for the Brayton cycle incorporates the most important irreversibility sources in real facilities. But at the same time, it was avoided to introduce a huge number of parameters. This allows an entirely analytical simulation scheme where it is easy to check the influence of the most important plant design parameters. Dry air is taken as working fluid. The dependence with temperature of specific heats is explicitly considered provided that temperature variations along the cycle are large.

The solar collector was considered as an array of mirrors that collect the solar power on the top of a central tower receiver. It was modeled in an straightforward way, incorporating optical losses as well as heat losses in the solar collector due to radiation and conduction/convection terms. The optical efficiency was taken an averaged effective factor. The overall plant efficiency was obtained as a combination of the efficiency of the plant subsystems (solar, combustion, and gas turbine) and the effectivenesses of the heat exchangers connecting subsystems. The SOLUGAS project [26] in Spain was elected to take the parameters for obtaining numerical results. The model was validated in previous works by comparing with experimental measures in this installation, assuming fixed design point conditions [18].

In order to obtain representative predictions, real seasonal data for solar irradiance and ambient temperature were incorporated to our computational model. Typical days for each season were considered. The evolution of global plant thermal efficiency, efficiencies of the subsystems, solar share, power output, and fuel conversion rate was computed in hourly basis. Numerical results for fuel consumption rate and greenhouse gases inventory were presented and analyzed. The predictions of our model reveal that

the combination of a central tower solar installation in association to a closed gas turbine and a backup combustion chamber burning natural gas has a good potential to produce stable power output in the range of a few megawatts with low fuel consumption, and so considerable lower pollutant emissions compared with a standard pure combustion plant.

Acknowledgements

The authors acknowledge financial support from MINECO of Spain, Grant ENE2013-40644-R.

References

[1] M. Romero, A. Steinfeld, Concentrating solar thermal power and thermochemical fuels, Energy Environ. Sci. 5 (2012) 9234–9245.
[2] O. Behar, A. Khellaf, K. Mohammedi, A review of studies on central receiver solar thermal power plants, Rene. Sust. Energy Rev. 23 (2013) 12–39.
[3] P. Schwarzbözl, R. Buck, C. Sugarmen, A. Ring, M. Marcos Crespo, P. Altwegg, J. Enrile, Solar gas turbine systems: design, cost and perspectives, Sol. Energy 80 (2006) 1231–1240.
[4] Tech. rep., Solar-hybrid Power and Cogeneration Plants, European Commission, 2011 ordis.europa.eu/publication/rcn/13318_en.html.
[5] R. Korzynietz, M. Quero, R. Uhlig, SOLUGAS-future Solar Hybrid Technology, Tech. rep., SolarPaces, 2012, http://cms.solarpaces2012.org/proceedings/paper/7ee7e32ece8f2f8e0984d5ebff9d77b.
[6] M. Dunham, B. Iverson, High-efficiency thermodynamic power cycles for concentrated solar power systems, Renew. Sust. Energy Rev. 30 (2014) 758–770.
[7] G. Barigozzi, A. Perdichizzi, C. Gritti, I. Guaiatelli, Techno-economic analysis of gas turbine inlet air cooling for combined cycle power plant for different climatic conditions, Appl. Therm. Eng. 82 (2015) 57–67.
[8] E. Okoroigwe, A. Madhlopa, An integrated combined cycle system driven by a solar tower: a review, Renew. Sust. Energy Rev. 57 (2016) 337–350.
[9] B. Grange, C. Dalet, Q. Falcoz, F. Siros, A. Ferrière, Simulation of a hybrid solar gas-turbine cycle with storage integration, Energy Proc. 49 (2014) 1147–1156.
[10] E. Okoroigwe, A. Madhlopa, Evaluation of the Potential for Hybridization of Gas Turbine Power Plants with Renewable Energy in South Africa, IEEE Conference Publications, 2015, http://dx.doi.org/10.1109/DUE.2015.7102985.
[11] J. Spelling, Hybrid Solar Gas-turbine Power Plants, Ph.D. thesis, KTH Royal Institute of Technology, Department of Energy Technology, Stockholm, Sweden, 2013.
[12] Y. Li, S. Liao, G. Liu, Thermo-economic multi-objective optimization for a solar-dish Brayton system using NSGA-II and decision making, Elect. Power. Energy Sys 64 (2015) 167–175.
[13] G. Barigozzi, G. Bonetti, G. Franchini, A. Perdichizzi, S. Ravelli, Thermal performance prediction of a solar hybrid gas turbine, Sol. Energy 86 (2012) 2116–2127.
[14] F. Collado, J. Guallar, A review of optimized design layouts for solar power tower plants with *campo* code, Ren. Sust. Energy Rev. 20 (2013) 142–154.
[15] R. Soltani, P. Keleshtery, M. Vahdati, M. Khoshgoftar Manesh, M. Rosen, M. Amidpour, Multi-objective optimization of a solar-hybrid cogeneration cycle: application to CGAM problem, Energy Conv. Manage 81 (2014) 60–71.
[16] A. McMahan, S. Klein, D. Reindl, A finite-time thermodynamic framework for optimizing solar-thermal power plants, J. Sol. Energy Eng. 129 (2007) 355–362.
[17] W. Le Roux, T.M.J. Bello-Ochende, A review on the thermodynamic optimisation and model of the solar thermal Brayton cycle, Renew. Sust. Energy Rev. 28 (2013) 677–690.
[18] D. Olivenza-León, A. Medina, A. Calvo Hernández, Thermodynamic modeling of a hybrid solar gas-turbine power plant, Energy Convers. Manage 93 (2015) 435–447.
[19] M.J. Santos, R.P. Merchán, A. Medina, A. Calvo Hernández, Seasonal thermodynamic prediction of the performance of a hybrid solar gas-turbine power plant, Energy Convers. Manage 115 (2016) 89–102.
[20] R.P. Merchán, M.J. Santos, I. Reyes-Ramírez, A. Medina, A. Calvo Hernández, Modeling hybrid solar gas-turbine power plants: thermodynamic projection of annual performance and emissions, Ener. Conv. Manage 134 (2017) 314–326.
[21] S. Sánchez-Orgaz, A. Medina, A. Calvo Hernández, Recuperative solar-driven multi-step gas turbine power plants, Energy Convers. Manage 67 (2013) 171–178.
[22] S. Sánchez-Orgaz, M. Pedemonte, P. Ezzatti, P. Curto-Risso, A. Medina, A. Calvo Hernández, Multi-objective optimization of a multi-step solar-driven Brayton cycle, Energy Convers. Manage 99 (2015) 346–358.
[23] J. Heywood, Internal Combustion Engine Fundamentals, McGraw-Hill, 1988.
[24] J. Duffie, W. Beckman, Solar Engineering of Thermal Processes, John Wiley and Sons, Hoboken, New Jersey, 2006.
[25] L. Weinstein, J. Loomis, B. Bhatia, D. Bierman, E. Wang, G. Chen, Concentrating solar power, Chem. Rev. 115 (2015) 12797–12838.
[26] R. Korzynietz, J.A. Brioso, A. del Río, M. Quero, M. Gallas, R. Uhlig, M. Ebert, R. Buck, D. Teraji, Solugas - comprehensive analysis of the solar hybrid Brayton plant, Sol. Ener 135 (2016) 578–589.
[27] S. T. Caterpillar, https://mysolar.cat.com/cda/files/126873/7/dsm50pg.pdf. URL https://mysolar.cat.com/cda/files/126873/7/dsm50pg.pdf.
[28] E.W. Lemmon, M.L. Huber, M.O. McLinden, NIST Standard Reference Database 23: Reference Fluid Thermodynamic and Transport Properties-REFPROP, Version 9.1, National Institute of Standards and Technology, Standard Reference Data Program, Gaithersburg, 2013.
[29] Meteosevilla. http://www.meteosevilla.com. URL http://www.meteosevilla.com.
[30] A. Kribus, P. Doron, R. Rubin, R. Reuven, E. Taragan, S. Duchan, J. Karni, Performance of the directly irradiated annular pressurized receiver (DIAPR) operating at 20 bar and 1200°C, J. Sol. Energy Eng. 123 (2001) 10–17.
[31] Direct Emissions from Stationary Combustion Sources, May 2008. www.epa.gov/climateleaders.
[32] Emission Factors for Greenhouse Gas Inventories, April 2014. http://www.epa.gov/climateleadership/documents/emission-factors.pdf.

3.4 Paper 4 – Roads to improve the performance of hybrid thermosolar gas turbine power plants: Working fluids and multi-stage configurations

Title: "Roads to improve the performance of hybrid thermosolar gas turbine power plants: Working fluids and multi-stage configurations"
Journal: *Energy Conversion and Management*
Authors: M.J. Santos, C. Miguel-Barbero, **R.P. Merchán**, A. Medina, A. Calvo Hernández
Year: 2018
Volume: 165
Pages: 578-592
DOI: `https://doi.org/10.1016/j.enconman.2018.03.084`
Reference: [134]

Resumen

El modelo termodinámico desarrollado con anterioridad para plantas termosolares híbridas de ciclo Brayton ha sido adaptado para simular plantas multi-etapa. De esta forma y gracias a su flexibilidad, el modelo de la máquina térmica incluye ahora un número arbitrario de etapas de compresión y expansión. El objetivo principal de este artículo es analizar cómo influyen dicho número de etapas y el fluido de trabajo elegido en los registros de salida de los parámetros de la planta, tratando de buscar configuraciones más eficientes y/o asociadas a una mayor producción de potencia. Por consiguiente, en la implementación del modelo en el código se asumen condiciones en el punto de diseño y se consideran cuatro fluidos de trabajo diferentes. Aire, nitrógeno y dióxido de carbono están en condiciones subcríticas mientras que el helio realiza un ciclo transcrítico. Un resultado importante es que las configuraciones con dos compresores y una o dos turbinas pueden incrementar significativamente la eficiencia térmica global y reducir el consumo de combustible. Asimismo, tanto el aire como el dióxido de carbono permiten obtener eficiencias globales y de la máquina térmica de alrededor del 40 % y del 50 %, respectivamente. Del mismo modo que se predicen las eficiencias y temperaturas principales, se calcula el consumo de combustible y las emisiones de efecto invernadero asociadas. Se demuestra que para una planta con dos etapas de compresión y dióxido de carbono como fluido, el consumo de combustible específico podría llegar a alcanzar los 108 kg/(MW h) en condiciones de diseño. Por otro lado, también se lleva a cabo una búsqueda de la relación de presiones óptima para diferentes variables clave de la planta.

Energy Conversion and Management 165 (2018) 578–592

Contents lists available at ScienceDirect

Energy Conversion and Management

journal homepage: www.elsevier.com/locate/enconman

Roads to improve the performance of hybrid thermosolar gas turbine power plants: Working fluids and multi-stage configurations

M.J. Santos, C. Miguel-Barbero, R.P. Merchán, A. Medina*, A. Calvo Hernández

Department of Applied Physics, University of Salamanca, 37008 Salamanca, Spain

ARTICLE INFO

Keywords:
Thermosolar hybrid plants
Multi-stage Brayton
Overall efficiency
Improved pre-design

ABSTRACT

This paper presents a general thermodynamic model for hybrid Brayton central tower thermosolar plants. These plants have been proved to be technically feasible but research and development efforts need to be done in order to improve its commercial interest. From the thermodynamic viewpoint it is necessary to increase its performance to get larger power production with reduced fuel consumption, and so reduced emissions. A model for multi-step compression and expansion is developed with that aim. The model is flexible and allows to simulate recuperative or non-recuperative plants, with an arbitrary number of stages and working with different subcritical fluids. The results for multi-step configurations are compared with those obtained for a plant with one turbine and one compressor. Different working fluids are analyzed, including air, nitrogen, carbon dioxide, and helium. Several plant layouts and the corresponding optimal pressure ratios are analyzed. Configurations with two-stages compression with intercooling combined with one or two expansion stages can significantly improve overall plant efficiency and lower fuel consumption. Power block efficiencies can reach 0.50 and overall plant efficiency can attain values about 0.40 working with air or carbon dioxide. For instance, comparing with a single-stage plant running with air, a plant working with subcritical carbon dioxide and two compression stages with intercooling can reach an overall efficiency about 19% larger and a fuel conversion rate around 23% larger. For such configuration, the specific fuel consumption is predicted to be about 108 kg/(MW h) at design point conditions.

1. Introduction

Concentrating solar power (CSP) is one of the promising renewable energy technologies that can contribute to decrease the dependence on fossil fuels for the generation of electricity and so, the environmental impact of energy production. As mentioned by Nathan et al. [1], unlike other renewable resources this technology is suited to produce non-intermittent power with the implementation of thermal storage. Peterseim et al. [2] discuss which CSP technologies are best suited for hybridization. Powell et al. [3] have recently published an extensive work on hybridization possibilities, including geothermal and photovoltaic resources. In this work CSP plants in which solar heat input is complemented with the heat released by the combustion of natural gas in a combustion chamber are surveyed. This technology ensures an almost constant energy injection to the grid in the range of a few megawatts. These plants are not completely free of fossil fuel consumption and pollutant emissions but guarantee predictability. Olumayegun et al. [4] highlight that the plants which work following a closed Brayton-like thermal cycle require a reduced water consumption compared with those working on Rankine cycles and can reach similar efficiencies. This point is especially advantageous in arid regions with appropriate solar resources. To get those efficiencies quite high turbine inlet temperatures have to be reached in the solar receivers, about 800–1000 °C. Several experimental prototypes [5] have shown that this is feasible using ceramic materials in central tower volumetric receivers. Ho and Iverson [6] have summarized these advances. Pioneer demonstration size plants have arrived at the same conclusion: the technology is practicable but it is still necessary a R&D activity to look for ways to improve the overall plant efficiency in order to get commercially interesting levelized costs of electricity, as pointed out by Korzynietz et al. [7]. Particularly, as mentioned by Dunham and Iverson [8], thermo-economic studies show that there is still a wide margin for improvement in the power block.

Along this work line thermodynamic studies about possible refinements on the basic Brayton cycle and the effects of the working fluid are important to guide future plant designs, as stated by Osorio et al. [9]. McMahan et al. [10] modelled the plant in terms of a reduced number of parameters. Within a similar framework, Zare and Hasanzadeh [11]

* Corresponding author.
E-mail addresses: smjesus@usal.es (M.J. Santos), cesarmi@usal.es (C. Miguel-Barbero), rpmerchan@usal.es (R.P. Merchán), amd385@usal.es (A. Medina), anca@usal.es (A. Calvo Hernández).

https://doi.org/10.1016/j.enconman.2018.03.084
Received 12 December 2017; Received in revised form 20 March 2018; Accepted 26 March 2018

Nomenclature

A_a	aperture area of the solar field (m^2)
A_r	solar receiver area (m^2)
a_c	isentropic compressor pressure ratio
a_t	isentropic turbine pressure ratio
C	solar collector concentration ratio
c_w	specific heat of the working fluid [J/(mol K)]
f	solar share
G	direct solar irradiance (W/m^2)
h_1	radiation heat loss coefficient for the solar collector (K^{-4})
h_2	effective convection and conduction loss coefficient for the solar collector (K^{-1})
$\dot{m}$	mass flow rate of the working substance (kg/s)
$\dot{m}_f$	fuel mass flow rate in the main combustion chamber (kg/s)
$\dot{m}_{fi}$	fuel mass flow rate in reheaters (kg/s)
P	power output (W)
$\lvert\dot{Q}_C\rvert$	heat losses at the combustion chamber (W)
$\lvert\dot{Q}_H\rvert$	total heat-transfer rate absorbed from the working fluid (W)
$\lvert\dot{Q}_{IHC}\rvert$	heat losses at the heat exchanger associated to the combustion chamber (W)
$\lvert\dot{Q}_{HC}\rvert$	heat rate input from the combustion chamber (W)
$\lvert\dot{Q}'_{HC}\rvert$	heat rate transferred from the combustion chamber to the associated heat exchanger (W)
$\lvert\dot{Q}_{HS}\rvert$	heat rate input from the solar collector (W)
$\lvert\dot{Q}_{IHS}\rvert$	heat losses at the solar receiver (W)
$\lvert\dot{Q}'_{HS}\rvert$	heat rate transferred from the solar collector to the associated heat exchanger (W)
$\lvert\dot{Q}_I\rvert$	losses associated to heat transfers in the solar field (W)
$\lvert\dot{Q}_L\rvert$	heat-transfer rate between the working fluid and the ambient (W)
Q_{LHV}	lower heating value of the fuel (J/kg)
$\lvert\dot{Q}_{reh}\rvert$	heat rate input from the reheaters (W)
r_e	fuel conversion rate
r_p	overall pressure ratio
T_{HC}	working temperature of the combustion chamber (K)
T_{HS}	working temperature of the solar collector (K)
T_L	ambient temperature (K)
T_x	working fluid temperature after the heat input from the recuperator (K)
$T_{x'}$	working fluid temperature after heat input from the solar collector (K)
T_y	working fluid exhaust temperature (K)
T_1	compressors inlet temperature (K)
T_2	temperature after last compressor (K)
T_3	turbines inlet temperature (K)
T_4	temperature after last turbine (K)
U_L	effective conduction–convection heat transfer coefficient [$W/(m^2 K)$]
α	effective emissivity
ε_{HC}	combustion chamber heat exchanger effectiveness
ε_{HS}	solar collector heat exchanger effectiveness
ε_L	cold side heat exchanger effectiveness
ε_c	isentropic efficiency of the compressors
ε_r	recuperator effectiveness
ε_t	isentropic efficiency of the turbines
γ	adiabatic coefficient of the working fluid
η	overall energy efficiency
η_c	combustion efficiency
η_h	thermal efficiency of the Brayton heat engine
η_s	solar collector efficiency
η_0	optical efficiency
ρ_H	irreversibilities due to pressure drops in the heat input
ρ_L	irreversibilities due to pressure drops in the heat release
σ	Stefan–Boltzmann constant ($W\,m^{-2}\,K^{-4}$)

predicted realistic values for efficiencies. Thus, sensitivity studies and optimization analyses can be done in more general terms than those done, for instance, with simulation software, as performed for instance by Barigozzi et al. [12,13]. Both techniques are complementary. Probably, general thermodynamic models are to be developed first in order to select adequate plant concepts and then detailed component-to-component simulations, are required to solve technical issues as done by Milani et al. [14] and to get to very detailed predictions of plant performance as shown in the work by Kalathakis et al. [15].

One of the main drawbacks of considering Brayton cycles in CSP applications is that for the compression stage much power is required, so the net power output becomes reduced. This point is detailed by Iverson et al. [16]. One possibility to avoid this handicap is to operate at supercritical conditions as suggested by Al-Sulaiman and Atif [17]. Extensive work has been devoted to this issue, specially considering carbon dioxide as working fluid, as done by Luu et al. [18]. Near the critical region fluids show numerical values for compressibility similar to liquids. Compression work can be reduced but as critical pressure for CO_2 is about 74 bar, high pressures have to be used. Vasquez et al. [19] point out that this leads to several technical problems. Moreover, wide fluctuations of thermodynamic properties near the critical point make difficult to develop thermodynamic models relying on ideal gas approximations. With respect to the turbomachinery much scarce experience has been acquired in components working with critical or transcritical fluids. A thorough review on this point is due to Ahn et al. [20]. An alternative way to reduce compression work is by joining these concepts: recuperation and multi-stage compression with intercooling. Recent works on these issues have been developed by Reyes-Belmonte et al. [21]. Additionally, if expansion is performed in several turbines with intermediate reheaters, temperature at the exit of the last turbine is high and so the potential for recuperation, as shown in the paper by Sánchez-Orgaz et al. [22].

Even though there is a great amount of works on the possibilities of using supercritical CO_2 in CSP systems, to our knowledge there are much scarce thermodynamical investigations on subcritical fluids as CO_2 together with multi-stage compression with intercooling and multi-stage expansion with reheating. Our work deals with this point. Plant configurations for central tower hybrid CSP plants working on closed atmospheric Brayton cycles for several working fluids shall be investigated, including subcritical CO_2, helium, nitrogen, and air. Plant performance will be compared by taking similar conditions for all fluids. Although the peculiarities of heat exchangers and turbomachinery of course rely on the type of fluid, components with similar effectivenesses or isentropic efficiencies will be assumed, *i.e.*, details on the design and performance of plant components are not analyzed, but it is assumed that with the appropriate design particularities components can have similar effectivenesses or isentropic efficiencies. To get that aim it is developed a thermodynamical model that incorporates the main irreversibilities existing in all the subsystems in these plants: solar, combustion chamber, and thermal engine. A simplified model was developed and validated in previous works by our group for the case of air and single-stage compression and expansion [23,24]. In this work it is extended for an arbitrary number of compression/expansion steps, recuperation, and for subcritical fluids by explicitly considering the temperature dependence of specific heats. Although the model allows for on-design and off-design analyses as shown in the study by Santos et al. [25], in this work design point parameters summarized by Quero et al. [26] from an experimental facility will be considered as reference case to compare with. The compression ratio is a key parameter in the design of any plant involving Brayton-like cycles. In our

study, first the results for different fluids at the same compression ratio will be compared and later specific values of the pressure ratio for each working fluid leading to maximum overall plant efficiency will be calculated.

In Section 2 the thermodynamic model and the main hypotheses assumed will be detailed. Explicit equations for heat transfers, subsystem efficiencies, and overall energy efficiency will be developed. Section 3 contains information about the considered reference plant, the design parameters, and the particularities of the elected working fluids. Numerical predictions on plant performance assuming the pressure ratio of the reference plant will be compared in Section 4 for different working gases. In Section 5 a numerical analysis to maximize plant performance in terms of the pressure ratio will be performed for each fluid. Section 6 is specifically devoted to plant configurations with two compression steps and intercooling. The plant performance for this kind of plant layouts will be compared for all the fluids considered.

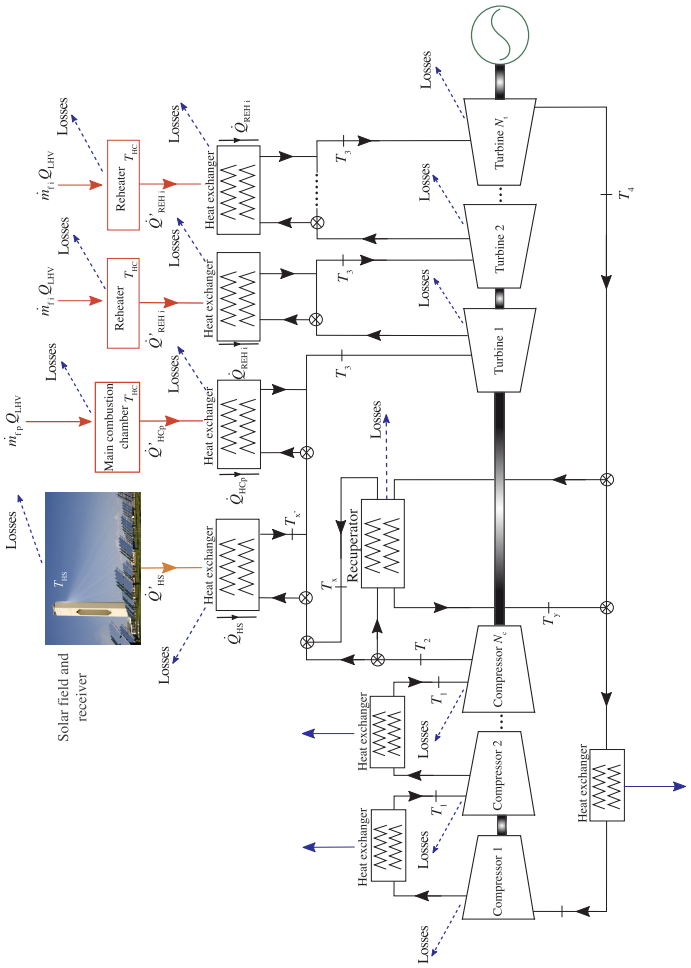

Fig. 1. Scheme of the hybrid solar gas-turbine plant considered. The plant includes a solar subsystem (solar field and central tower receiver), a main combustion chamber, an arbitrary number of compressors (N_c), and an arbitrary number of turbines (N_t). Between compressors N_c-1 intercoolers are considered and, similarly, between turbines N_t-1 intermediate reheaters. Losses in the thermodynamic model are shown in the picture. The ambient temperature, T_L, and the effective temperature of the solar receiver, T_{HS}, are fluctuating quantities, since depend on seasonal and meteorological conditions.

2. Plant thermodynamics

The considered system is a gas-turbine power plant hybridized with a central tower solar concentration system. An sketch of the whole system is depicted in Fig. 1. Briefly, the working fluid enters the first compressor at a temperature T_1, and exits the last one (N_c) at a temperature T_2. Between each pair of compressors, an intercooler is considered with the aim that the inlet temperature at each compressor is always T_1. After the last compressor the heat input in the power unit is divided in three subsequent steps:

1. A recuperator is used to take advantage of the residual heat after the last turbine. The fluid temperature at the recuperator exit is denoted as T_x.
2. When solar conditions are adequate, the fluid is redirected through the solar receiver and its temperature increases up to $T_{x'}$.
3. During night or poor insolation conditions the working fluid is conducted directly to the combustion subsystem. closed cycle is being considered, so the heat input from combustion is done through a heat exchanger associated to the main combustion chamber. Independently of solar conditions the combustion chamber ensures that the first turbine inlet temperature is stable, T_3.

The expansion stroke is performed by means of an arbitrary number of turbines, N_t. A number N_t-1 of intermediate reheaters make that for any turbine the inlet temperature is T_3. Afterwards the expansion process (temperature T_4) the fluid is redirected through the recuperator to another heat exchanger that ensures that the process is closed and cyclic, so the temperature at the compressor entrance in the following cycle is T_1. Fig. 2 contains a $T-S$ diagram of the thermodynamic cycle developed by the working fluid.

2.1. Heat fluxes, subsystem efficiencies, and overall efficiency

The overall plant energy efficiency, η, is defined as the fraction between the net mechanical power output, P, and the total heat input rate in the whole system. The latter is the sum of the heat input flows of the solar part and the combustion chamber:

$$\eta = \frac{P}{G A_a + \dot{m}_f Q_{\mathrm{LHV}}} \tag{1}$$

where G is the direct normal irradiance, A_a the aperture area of the heliostats field, Q_{LHV} the lower heating value of the fuel, and $\dot{m}_f$ is the sum of the fuel mass flows entering into the combustion chamber, $\dot{m}_{fp}$, as well as into the reheaters, $\dot{m}_{fi}$:

$$\dot{m}_f = \dot{m}_{fp} + \sum_{i=1}^{N_t-1} \dot{m}_{fi} \tag{2}$$

so, the overall efficiency is:

$$\eta = \frac{P}{G A_a + \left(\dot{m}_{fp} + \sum_{i=1}^{N_t-1} \dot{m}_{fi}\right) Q_{\mathrm{LHV}}} \tag{3}$$

Once expressed the efficiency in general terms, it will be rewritten as a function of the efficiencies of the subsystems that constitute the plant. The solar collector efficiency, η_s, is defined as the ratio between the useful energy per unit time provided by the collector, $|\dot{Q}'_{\mathrm{HS}}|$ (see Fig. 1), and the solar energy rate it receives, GA_a: $\eta_s = |\dot{Q}'_{\mathrm{HS}}|/GA_a$. The solar central tower transfers a fraction of the useful heat collected by the heliostats, $|\dot{Q}'_{\mathrm{HS}}|$, to the working fluid, that is denoted $|\dot{Q}_{\mathrm{HS}}|$. Introducing ε_{HS}, the effectiveness of the solar receiver (considered as a heat exchanger), $|\dot{Q}_{\mathrm{HS}}| = \varepsilon_{\mathrm{HS}}|\dot{Q}'_{\mathrm{HS}}|$, the solar collector efficiency can be expressed as: $\eta_s = |\dot{Q}_{\mathrm{HS}}|/(\varepsilon_{\mathrm{HS}} GA_a)$.

In a similar way the efficiency of the main combustion process, η_{cp}, is defined as the quotient between the heat flux from the combustion

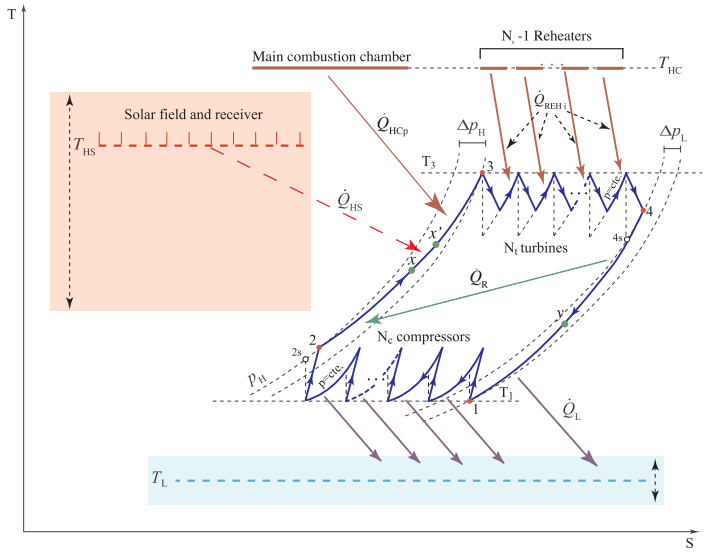

Fig. 2. Temperature-entropy diagram of the considered plant layout.

chamber and the energy contents of the entering fuel, $\dot{m}_f Q_{\mathrm{LHV}}$. The combustion chamber produces a heat rate, $|\dot{Q}'_{\mathrm{HCp}}|$, transferred to the working fluid through a heat exchanger whose effectiveness is $\varepsilon_{\mathrm{HCp}} = |\dot{Q}_{\mathrm{HCp}}|/|\dot{Q}'_{\mathrm{HCp}}|$, where $|\dot{Q}_{\mathrm{HCp}}|$ is the actual heat rate received by the working fluid from combustion. As a result, the combustion chamber efficiency can be written as:

$$\eta_{\mathrm{cp}} = \frac{|\dot{Q}_{\mathrm{HCp}}|}{\dot{m}_{fp}\,\varepsilon_{\mathrm{HCp}}\,Q_{\mathrm{LHV}}} \tag{4}$$

The combustion efficiency for each intermediate reheater, η_{ci}, is calculated alike:

$$\eta_{\mathrm{ci}} = \frac{|\dot{Q}_{\mathrm{rehi}}|}{\dot{m}_{fi}\,\varepsilon_{\mathrm{rehi}}\,Q_{\mathrm{LHV}}} \tag{5}$$

Each one has an associated heat exchanger with effectiveness, $\varepsilon_{rehi} = |\dot{Q}_{\mathrm{rehi}}|/|\dot{Q}'_{\mathrm{rehi}}|$.

The total heat input rate that the fluid absorbs from combustion is given as:

$$|\dot{Q}_{HC}| = |\dot{Q}_{HCp}| + |\dot{Q}_{reh}| \tag{6}$$

where

$$|\dot{Q}_{reh}| = \sum_{i=1}^{N_i-1} |\dot{Q}_{rehi}| \tag{7}$$

The efficiency of the thermal engine itself, η_h, is the ratio between the mechanical power output and the total heat input rate:

$$\eta_h = \frac{|\dot{W}|}{|\dot{Q}_H|} = \frac{P}{|\dot{Q}_{HS}| + |\dot{Q}_{HCp}| + |\dot{Q}_{reh}|} \tag{8}$$

Thus, the overall system efficiency, η, given by Eq. (1), is:

$$\eta = \frac{P}{\frac{|\dot{Q}_{HS}|}{\varepsilon_{HS}\eta_s} + \left[\frac{|\dot{Q}_{HCp}|}{\varepsilon_{HCp}\eta_{cp}} + \sum_{i=1}^{N_i-1}\frac{|\dot{Q}_{rehi}|}{\varepsilon_{rehi}\eta_{ci}}\right]} \tag{9}$$

Assuming identical efficiencies for the main combustion chamber and for reheaters, $\eta_{cp} = \eta_{ci} \equiv \eta_c$ and $\varepsilon_{HCp} = \varepsilon_{rehi} \equiv \varepsilon_{HC}$, the thermodynamic efficiency can be written as:

$$\eta = \frac{P}{\frac{|\dot{Q}_{HS}|}{\varepsilon_{HS}\eta_s} + \frac{|\dot{Q}_{HC}|}{\varepsilon_{HC}\eta_c}} = \eta_h\eta_s\eta_c\left(\frac{|\dot{Q}_{HS}| + |\dot{Q}_{HC}|}{\frac{\eta_c\,|\dot{Q}_{HS}|}{\varepsilon_{HS}} + \frac{\eta_s\,|\dot{Q}_{HC}|}{\varepsilon_{HC}}}\right) \tag{10}$$

It is interesting to define a solar share, f, as the ratio between the heat input rate from the sun and the total one:

$$f = \frac{|\dot{Q}_{HS}|}{|\dot{Q}_{HS}| + |\dot{Q}_{HC}|} \tag{11}$$

Depending on solar conditions, the solar share fluctuates in the interval [0,1]. $f = 1$, means that all the heat input has solar origin and $f = 0$ means that all the heat input comes from combustion, for instance by night. With this definition it is possible to express the overall plant efficiency in terms of the efficiency of the solar subsystem, η_s, that of the combustion chambers η_c, the efficiency of the Brayton heat engine η_h, the *solar share f*, and the effectivenesses of the heat exchangers between subsystems ε_{HS} and ε_{HC}:

$$\eta = \eta_h\eta_s\eta_c\left[\frac{1}{\frac{\eta_c f}{\varepsilon_{HS}} + \frac{\eta_s(1-f)}{\varepsilon_{HC}}}\right] = \eta_h\eta_s\eta_c\left[\frac{\varepsilon_{HS}\varepsilon_{HC}}{\eta_c f\varepsilon_{HC} + \eta_s(1-f)\varepsilon_{HS}}\right] \tag{12}$$

In the particular case of only solar heat input, $f = 1$, so $\eta = \eta_h\eta_s\varepsilon_{HS}$, and for only combustion $f = 0$, and $\eta = \eta_h\eta_c\varepsilon_{HC}$.

It is interesting to define an efficiency with an economic meaning, the *fuel conversion rate* as the ratio between the power output and the heat input rate with an associated cost, as proposed by Heywood [27]:

$$r_e = \frac{P}{\dot{m}_f\,Q_{LHV}} \tag{13}$$

It can be expressed in terms of the efficiency of the subsystems and the solar share as:

$$r_e = \frac{\eta\,\eta_s\eta_h\varepsilon_{HS}}{\eta_s\eta_h\varepsilon_{HS} - \eta f} \tag{14}$$

For pure solar operation ($\dot{m}_f = 0$), $f = 1$, and $r_e \to \infty$ and for only combustion operation, $f = 0$, so $r_e = \eta$.

2.2. Solar subsystem model

Next the model for the losses and efficiency for the solar subsystem is briefly summarized. An heliostat field with aperture area A_a and a central tower receiver with area A_r are considered. The solar power collected in the aperture is $|\dot{Q}_s| = GA_a$. Nevertheless, the energy flux collected at the tower is affected by optical losses associated to absorption by the heliostats, shadowing and blocking, spillage, ambient humidity, and others as stated by Collado and Turégano [28]. Details on these issues can be found in the work by López-Herráiz [29]. The most simple way to globally account for these effects is by defining an optical efficiency, η_0, so the heat input rate reaching the tower receiver is $|\dot{Q}_r| = \eta_0 GA_a$. Also there are heat transfer losses in the receiver due to convection, conduction and radiation. Heat losses can be expressed as (details can be found in the book by Duffie and Beckman [30] and the paper by Siva Reddy et al. [31]):

$$|\dot{Q}_l| = A_r\alpha\sigma(T_{HS}^4 - T_L^4) + A_r\overline{U_L}(T_{HS} - T_L) \tag{15}$$

where α is the emissivity of the receiver surface, $\overline{U_L}$ is an overall conduction and convection heat transfer coefficient, and σ the Stefan–Boltzmann constant. So, $|\dot{Q}'_{HS}| = |\dot{Q}_r - \dot{Q}_l|$, represents the effective heat flux that the receiver could transfer to the working fluid, assuming that it behaves as a heat exchanger. The energy rate finally absorbed by the working fluid considering the effectiveness of the receiver, ε_{HS} is:

$$|\dot{Q}_{HS}| = \varepsilon_{HS}\{\eta_0 GA_a - A_r[\alpha\sigma(T_{HS}^4 - T_L^4) + \overline{U_L}(T_{HS} - T_L)]\} \tag{16}$$

This energy rate, as depicted in Fig. 2 increases the working fluid temperature from T_x to $T_{x'}$. The efficiency of the solar subsystem, η_s, can be written as:

$$\eta_s = \eta_0[1 - h_1(T_{HS}^4 - T_L^4) - h_2(T_{HS} - T_L)] \tag{17}$$

where C is the concentration ratio, $C = A_a/A_r$ and h_1,h_2 are losses parameters, defined as: $h_1 = \alpha\sigma/(\eta_0 GC)$ and $h_2 = \overline{U_L}/(\eta_0 GC)$.

2.3. Combustion subsystem

The maximum energy that could be obtained from combustion is $\dot{m}_f Q_{LHV}$ considering ideal combustion and no losses in the combustion chamber. But actually the useful energy that can be transferred to the working fluid is only a fraction of that energy rate, $\eta_{cp}\dot{m}_f Q_{LHV}$. Moreover, as a closed cycle is being considered, the heat is transferred to the power unit through a heat exchanger associated to the combustion chamber with effectiveness, ε_{HCp}. Thus, the heat rate that is actually released to the working fluid can be written as: $|\dot{Q}_{HCp}| = \varepsilon_{HCp}|\dot{Q}'_{HCp}| = \varepsilon_{HCp}\eta_{cp}\dot{m}_{fp}Q_{LHV}$. In a similar way, for the intermediate reheaters:

$$|\dot{Q}_{reh}| = \sum_{i=1}^{N_i-1}\varepsilon_{rehi}|\dot{Q}'_{rehi}| = \sum_{i=1}^{N_i-1}\varepsilon_{rehi}\eta_{ci}\dot{m}_{fi}Q_{LHV} \tag{18}$$

Assuming that combustion efficiencies are the same for all the reheaters and equal to that of the main combustion and also that all the associated heat exchangers are similar:

$$|\dot{Q}_{reh}| = \varepsilon_{HC}\eta_c Q_{LHV}\sum_{i=1}^{N_i-1}\dot{m}_{fi} \tag{19}$$

Table 1
Thermodynamic properties of the considered working fluids: molecular weight (M), critical temperature and pressure (T_c and p_c respectively) and mean values of the constant pressure specific heat ($\bar{c}_w$) and adiabatic coefficient ($\bar{\gamma}$), in the temperature interval [288,1430] K. The coefficients of the fits of $c_w(T)$ [in units of J/(mol K)] correspond to the function: $c_w(T) = a + b\,T + c\,T^2 + d\,T^3 + e\,T^4$. Data for the fits were taken from [33] at a pressure $p = 5$ bar.

	He	N_2	Dry air	CO_2
M (g/mol)	4.00	28.01	28.97	44.01
T_c (K)	5.1953	126.19	132.84	304.13
p_c (bar)	2.2761	33.958	38.501	73.773
a	20.7862	32.3518	38.6449	25.4812
b	–	−0.02031	−0.044282	0.051549
c	–	4.2182×10^{-5}	7.9699×10^{-5}	-2.7778×10^{-5}
d	–	-2.7814×10^{-8}	-5.3556×10^{-8}	4.6551×10^{-9}
e	–	6.3098×10^{-12}	1.2726×10^{-11}	4.81185×10^{-13}
$\bar{\gamma}$	1.6667	1.3561	1.3458	1.1986
$\bar{c}_w$ [J/(g K)]	5.1965	1.1354	1.1202	1.1587

2.4. Multi-stage Brayton power unit model

In this section a model for the multi-stage Brayton cycle is proposed and its thermal efficiency, η_h, evaluated. The working fluid is considered as an ideal gas with temperature dependent specific heats, $c_w(T)$, following an irreversible recuperative Brayton cycle with multiple compression and expansion steps. The temperature-entropy diagram of the cycle is depicted in Fig. 2. In the following the main cycle stages are modeled together with the main irreversibility sources associated to each:

- In the first process (1 → 2), the working fluid is compressed through an arbitrary number, N_c, of compressors. They are considered identical, so the isentropic efficiency of any of them is: $\varepsilon_c = (T_{2s}-T_1)/(T_2-T_1)$, where T_{2s} would be temperature after compressions if they were isentropic (see Fig. 2). Between each pair of compressors, it is considered an intercooler, so the inlet temperature of all compressors is the same, T_1.
- Between states 2 and 3, three subsequent heat inputs increase the fluid temperature. First, a non-ideal recuperator increases temperature from T_2 up to T_x. Its effectiveness is defined as: $\varepsilon_r = (T_x-T_2)/(T_4-T_2) = (T_y-T_4)/(T_2-T_4)$. A non-recuperative plant is easily simulated by taking $\varepsilon_r = 0$. Second, if solar conditions are good enough, the fluid receives a solar heat input rate, $|\dot{Q}_{HS}|$, that rises up the temperature from T_x to $T_{x'}$. And third, the main combustion chamber provides the required energy to reach the turbines inlet temperature, T_3, that is assumed as a fixed input parameter. So, in principle (apart from fluctuations of the ambient temperature), the only oscillating temperature during heat input due to irradiance oscillations is $T_{x'}$. Although each subprocess during heat input has its own pressure losses, for simplicity a parameter that globally measures the whole pressure losses in the fluid during the heating process is assumed, $\rho_H = (p_H-\Delta p_H)/p_H$, where p_H is the highest pressure (compressor exit) and $p_H-\Delta p_H$ is the pressure at the first turbine inlet.
- At the state 3 the working fluid attains its maximum temperature and it is expanded by N_t subsequent gas turbines. Any of them is characterized by an isentropic efficiency $\varepsilon_t = (T_4-T_3)/(T_{4s}-T_3)$. To ensure that the temperature at any turbine inlet is T_3,N_t-1 intermediate reheaters are required. After the last turbine, the fluid reaches state 4.
- Finally, the fluid recovers the conditions of state 1 by means of a heat release that is split in two processes. The first associated to recuperation that ends at temperature T_y and the second through a heat exchanger that cools the fluid up to T_1. Its effectiveness is defined as: $\varepsilon_L = (T_1-T_y)/(T_L-T_y)$. The global pressure decay in 4 → 1 is measured by introducing a parameter: $\rho_L = (p_L-\Delta p_L)/p_L$ where p_L is the fluid pressure after the last turbine and $p_L-\Delta p_L$ the lowest pressure. It is convenient to define an overall pressure ratio as $r_p = p_H/(p_L-\Delta p_L)$.

Next, the objective is to obtain cycle temperatures and heat rates in terms of the parameters associated to cycle size and geometry, and thermal losses. By convenience, two parameters, a_c and a_t, related to pressure ratios of compressors and turbines are defined:

$$a_c = \frac{T_{2s}}{T_1} = \left(\frac{p_H}{p_L-\Delta p_L}\right)^{(\bar{\gamma}_{12}-1)/\bar{\gamma}_{12}} = r_p^{(\bar{\gamma}_{12}-1)/\bar{\gamma}_{12}} \tag{20}$$

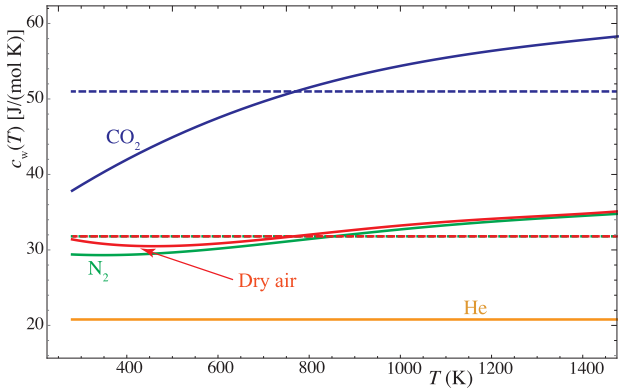

Fig. 3. Evolution with temperature of the constant pressure molar heats of the working fluids considered in the work. Average values are shown in dashed lines. Data were taken from [33] at a pressure $p = 5$ bar.

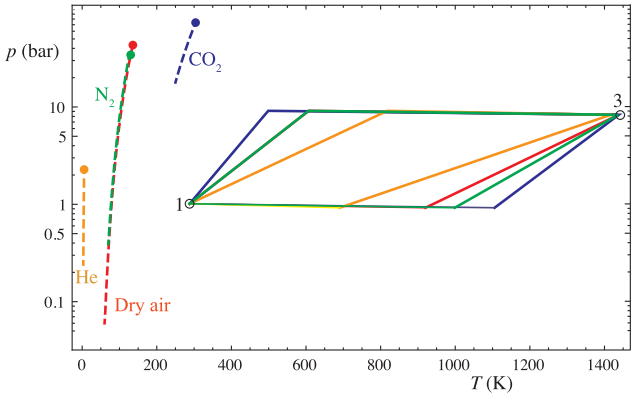

Fig. 4. $p-T$ approximate diagrams of the Brayton cycles followed by the considered working fluids. The vertical axis is represented in logarithmic scale. Dashed lines represent the liquid–vapor coexistence lines. Critical points for each fluid are shown as filled circles.

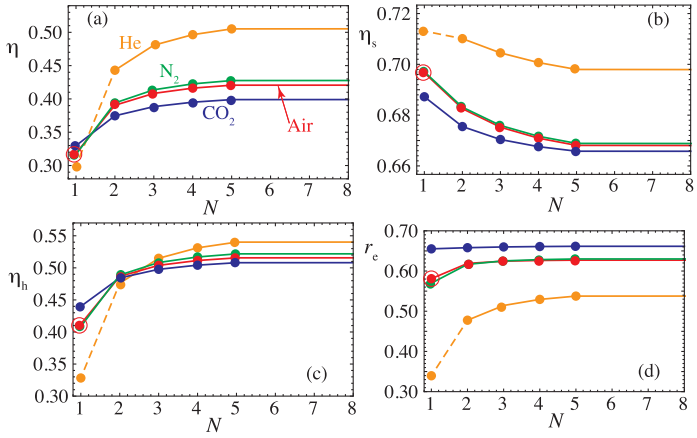

Fig. 5. Evolution of plant efficiencies (η, overall plant efficiency; η_s, solar subsystem efficiency; η_h, heat engine efficiency; and r_e, fuel conversion rate) with the number of compression/expansion stages assumed identical, $N_t = N_c \equiv N$, for all the fluids considered. The reference values corresponding to the Solugas project are marked with an open circle. Lines between points are just a guide for the eye. Lines are dashed for He between N = 1 and the other cases because for N = 1 no regeneration is considered. The input data are those in Section 3.

Table 2
Percentage relative variations of the estimated efficiencies with respect to the reference values of the Solugas project (points marked with an open circle in Fig. 5). In the case of He and N = 1, no regeneration is considered (NR). The pressure ratio was taken in all cases as in the gas turbine of the Solugas project, $r_p = 9.9$. The case of a large number of compression/expansion stages is represented as $N \to \infty$.

Working fluid	Dry Air		N_2			He			CO_2		
N	2	$N \to \infty$	1	2	$N \to \infty$	1(NR)	2	$N \to \infty$	1	2	$N \to \infty$
η	22.623	36.956	−0.560	23.713	39.868	−5.894	39.132	67.745	3.577	17.656	29.970
η_h	17.967	28.476	−0.985	18.489	30.611	−20.427	15.373	38.138	6.655	17.388	26.674
η_s	−2.026	−6.030	0.0593	−1.941	−5.894	2.359	1.932	−1.986	−1.352	−3.037	−5.563
r_e	6.531	8.119	−1.921	6.139	9.180	−41.557	−17.778	−2.833	12.768	13.262	14.245

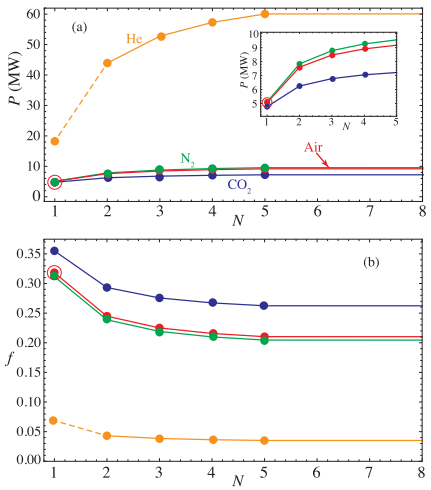

Fig. 6. Evolution of the power output, P, and the solar share, f, with N. Open circles show the values corresponding to the reference Solugas plant. The inset shows a zoom with the behavior of air, N_2, and CO_2 with changing values of N.

$$a_t = \frac{T_3}{T_{4s}} = \left(\frac{p_H - \Delta p_H}{p_L}\right)^{(\bar{\gamma}_{34}-1)/\bar{\gamma}_{34}} \tag{21}$$

In these definitions it was considered that processes $1 \rightarrow 2s$ and $3 \rightarrow 4s$ are isentropic. $\bar{\gamma}_{12}$ is the mean value of the adiabatic constant in the temperature interval $[T_1, T_2]$ and similarly for $\bar{\gamma}_{34}$. Those temperature intervals are not large, so it is reasonable to work on average values instead of temperature dependent parameters. From the definitions of ρ_H and ρ_L it is easy to show that the overall pressure ratio, r_p, and a_t are related by:

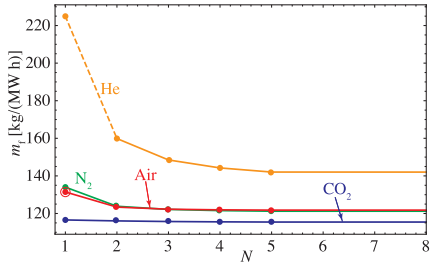

Fig. 8. Specific fuel consumption as a function of N. The open circle shows the value corresponding to the reference Solugas plant.

$$a_t = (\rho_H \rho_L r_p)^{(\bar{\gamma}_{34}-1)/\bar{\gamma}_{34}} \tag{22}$$

Thus, considering all the assumptions and definitions explained before, it is possible (after some algebraic calculations) to obtain analytical expressions for all cycle temperatures:

$$T_1 = \varepsilon_L T_L + T_y(1-\varepsilon_L) \tag{23}$$

$$T_2 = T_1 + \frac{1}{\varepsilon_c}(T_{2s} - T_1) = T_1 Z_c \tag{24}$$

$$T_3 = \varepsilon_{HC} T_{HC} + T_{x'}(1-\varepsilon_{HC}) \tag{25}$$

$$T_4 = T_3 - \varepsilon_t (T_3 - T_{4s}) = T_3 Z_t \tag{26}$$

$$T_x = \varepsilon_r T_4 + T_2(1-\varepsilon_r) \tag{27}$$

$$T_y = \varepsilon_r T_2 + T_4(1-\varepsilon_r) \tag{28}$$

$$T_{x'} = \varepsilon_{HS} T_{HS} + T_x(1-\varepsilon_{HS}) \tag{29}$$

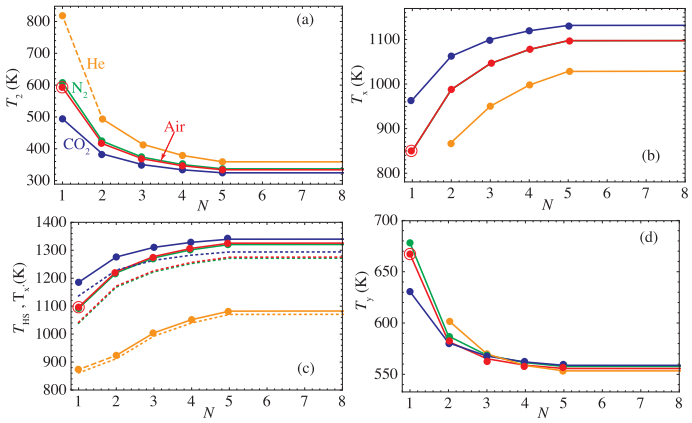

Fig. 7. Sensitivity of some plant temperatures to N: (a) T_2, compressors outlet temperature; (b) T_x, fluid temperature after regeneration; (c) T_{HS}, solar collector working temperature and $T_{x'}$, temperature of the fluid after absorbing the solar heat (shown in dotted lines in the bottom left plot); and (d) T_y, gas temperature at the output of the regeneration hot stream. Open circles show the values corresponding to the reference Solugas plant. In the case of He and N = 1 no regeneration is considered so the corresponding points for T_x and T_y does not appear in the plots.

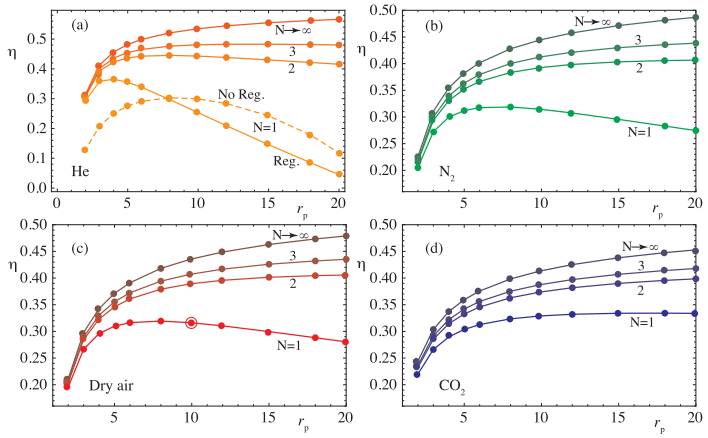

Fig. 9. Overall plant efficiency plotted against the pressure ratio for the considered working fluids: (a) He, (b) N_2, (c) air, and (d) CO_2. Several multi-step configurations are considered. In the case of He and $N = 1$ (top left figure) regenerative (solid line) and non-regenerative plant configurations are plotted (dashed line). The reference efficiency of the Solugas plant is shown for air as an open circle.

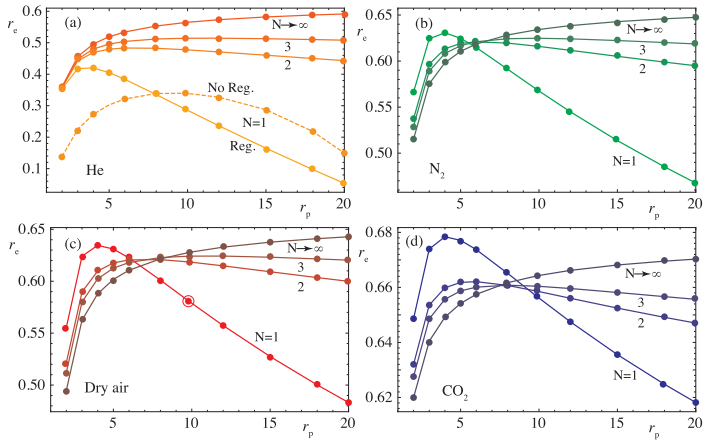

Fig. 10. Fuel conversion rate, r_e, against the pressure ratio, r_p for the considered working fluids: (a) He, (b) N_2, (c) air, and (d) CO_2. In the case of He and $N = 1$ (top left figure) regenerative (solid line) and non-regenerative plant configurations are plotted (dashed line).

where other two definitions were included:

$$Z_c = 1 + \frac{1}{\varepsilon_c}\left(a_c^{1/N_c} - 1\right) \tag{30}$$

$$Z_t = 1 - \varepsilon_t\left(1 - \frac{1}{a_t^{1/N_t}}\right) \tag{31}$$

By using all these equations, temperatures T_2 and T_4 can be written as functions of the temperatures of the heat sources, T_{HS} and T_{HC}, the ambient temperature, T_L, the overall pressure ratio, r_p and the irreversibility parameters. This leads to:

$$\frac{T_2}{T_{HC}} = \frac{(1-\varepsilon_L)(1-\varepsilon_r)[\varepsilon_{HC}T_{HC} + \varepsilon_{HS}T_{HS}(1-\varepsilon_{HC})] + \varepsilon_L T_L\left[Z_t^{-1} - (1-\varepsilon_{HC})(1-\varepsilon_{HS})\varepsilon_r\right]}{\left[Z_c^{-1} - (1-\varepsilon_L)\varepsilon_r\right]\left[Z_t^{-1} - (1-\varepsilon_{HC})(1-\varepsilon_{HS})\varepsilon_r\right] - (1-\varepsilon_{HC})(1-\varepsilon_{HS})(1-\varepsilon_L)(1-\varepsilon_r)^2} \tag{32}$$

$$\frac{T_4}{T_{HC}} = \frac{\left[\varepsilon_{HC}T_{HC} + \varepsilon_{HS}T_{HS}(1-\varepsilon_{HC})\right]\left[Z_c^{-1} - (1-\varepsilon_L)\varepsilon_r\right] + \varepsilon_L T_L(1-\varepsilon_{HC})(1-\varepsilon_{HS})(1-\varepsilon_r)}{\left[Z_c^{-1} - (1-\varepsilon_L)\varepsilon_r\right]\left[Z_t^{-1} - (1-\varepsilon_{HC})(1-\varepsilon_{HS})\varepsilon_r\right] - (1-\varepsilon_{HC})(1-\varepsilon_{HS})(1-\varepsilon_L)(1-\varepsilon_r)^2} \tag{33}$$

Any other temperature can be obtained in the same terms by

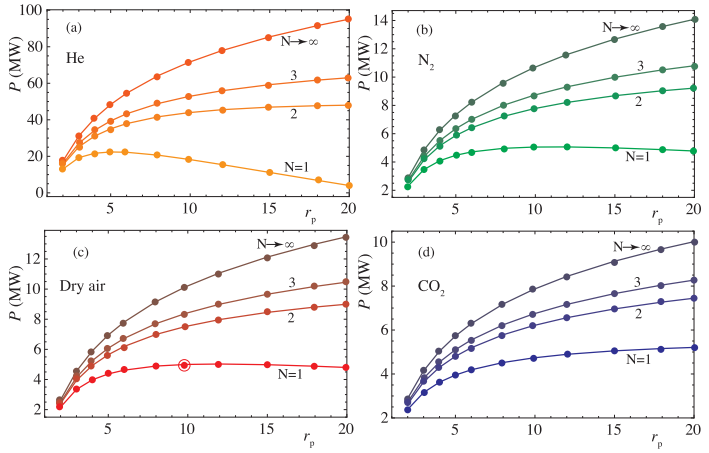

Fig. 11. Power output, P, against the pressure ratio, r_p for the considered working fluids: (a) He, (b) N_2, (c) air, and (d) CO_2.

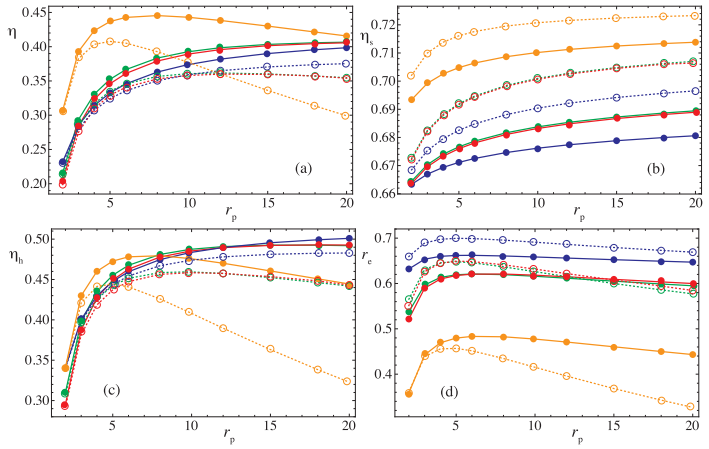

Fig. 12. Plant efficiencies as functions of the pressure ratio for different working fluids (helium, orange; dry air, red; nitrogen, green, and carbon dioxide, blue) and two particular configurations: $N_t = N_c = 2$ (solid lines) and $N_t = 1$;$N_c = 2$ (dashed). (For interpretation of the references to colour in this figure legend, the reader is referred to the web version of this article.)

substituting Eqs. (32) and (33) in Eqs. (23)–(29).

Now it is feasible to calculate all the components of the heat input rate, $|\dot{Q}_H| = |\dot{Q}_{HS}| + |\dot{Q}_{HCp}| + |\dot{Q}_{reh}|$, by using temperature equations and Eqs. (6) and (7):

$$|\dot{Q}_{HS}| = \dot{m} \int_{T_x}^{T_{x'}} c_w(T)dT = f|\dot{Q}_H| \tag{34}$$

$$|\dot{Q}_{HCp}| = \dot{m} \int_{T_{x'}}^{T_3} c_w(T)dT \tag{35}$$

$$|\dot{Q}_{reh}| = \dot{m} \sum_{j=1}^{N_t-1} \int_{T_j}^{T_3} c_w(T)dT \tag{36}$$

where T_j is the temperature at the exit of turbine j. In order to obtain an analytical expression for the last equation it will be assumed that the difference between T_3 and the temperatures at turbines exit, T_j, is not large, so a mean value for $c_w(T)$,$\bar{c}_{w,34}$ is considered. This hypothesis allows to write:

Table 3
Maximum values of overall efficiency (η_{max}), fuel conversion efficiency ($r_{e,max}$), maximum power output (P_{max}), and minimum specific fuel consumption ($m_{f,min}$). The corresponding pressure ratios, r_p, for cycles with $N_c = N_t = 2$ and $N_c = 2, N_t = 1$ are also shown. The reference values of the Solugas project, denoted as (Ref.), are included for comparison.

	η_{max}	r_p	$r_{e,max}$	r_p	P_{max} (MW)	r_p	$m_{f,min}$ [kg/(MWh)]	r_p
Ref.	0.32	9.9	0.58	9.9	5.06	9.9	132	9.9
				$N_c = N_t = 2$				
Dry air	0.41	20	0.62	6	9.0	20	121	6
N_2	0.41	20	0.62	6	9.2	20	121	6
He	0.45	8	0.48	6	48.0	20	158	6
CO_2	0.40	20	0.66	6	7.4	20	118	6
				$N_c = 2, N_t = 1$				
Dry air	0.36	12	0.65	5	6.4	20	118	5
N_2	0.37	12	0.65	5	6.6	20	118	5
He	0.41	5	0.45	5	29.3	8	170	5
CO_2	0.38	20	0.70	5	6.1	20	108	5

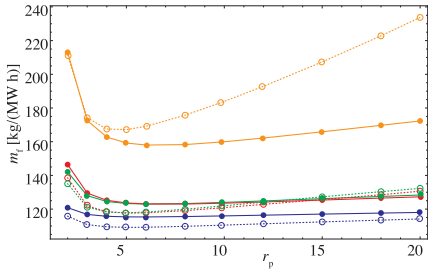

Fig. 13. Specific fuel consumption in terms of the pressure ratio for different working fluids (helium, orange; dry air, red; nitrogen, green, and carbon dioxide, blue) and two particular configurations: $N_t = N_c = 2$ (solid lines) and $N_t = 1; N_c = 2$ (dashed). (For interpretation of the references to colour in this figure legend, the reader is referred to the web version of this article.)

$$|\dot{Q}_{rek}| = \dot{m}\sum_{j=1}^{N_t-1}\int_{T_{j_s}}^{T_3} c_w(T)dT \simeq \dot{m}\,\varepsilon_t\,\bar{c}_{w,34}\sum_{j=1}^{N_t-1}(T_3 - T_{j_s}) = \dot{m}\,\bar{c}_{w,34}\,\varepsilon_t\,(N_t-1)(1-a_t^{-1/N_t})T_3 \quad (37)$$

The heat released by the working fluid to the cold source in the closed cycle can be expressed as:

$$|\dot{Q}_L| = \dot{m}\int_{T_1}^{T_y} c_w(T)dT + \dot{m}\sum_{k=1}^{N_c-1}\int_{T_1}^{T_k} c_w(T)dT \quad (38)$$

Assuming that the difference between T_1 and the temperature at any compressor exit is not large, a mean value of the specific heat, $\bar{c}_{w,12}$, is taken in order to calculate the total heat release rate:

$$|\dot{Q}_L| = \dot{m}\int_{T_1}^{T_y} c_w(T)dT + \dot{m}\frac{\bar{c}_{w,12}}{\varepsilon_c}\sum_{s=1}^{N_c-1}(T_{k_s} - T_1) \quad (39)$$

The second term at the right side can be calculated as:

$$\dot{m}\frac{\bar{c}_{w,12}}{\varepsilon_c}\sum_{s=1}^{N_c-1}(T_{k_s} - T_1) = \dot{m}\frac{\bar{c}_{w,12}}{\varepsilon_c}(N_c-1)(a_c^{1/N_c}-1)T_1 \quad (40)$$

and finally,

$$|\dot{Q}_L| = \dot{m}\int_{T_1}^{T_y} c_w(T)dT + \dot{m}\frac{\bar{c}_{w,12}}{\varepsilon_c}(N_c-1)(a_c^{1/N_c}-1)T_1 \quad (41)$$

The power output provided by the plant is then calculated as:

$$P = |\dot{Q}_H| - |\dot{Q}_L| \quad (42)$$

and its thermal efficiency through:

$$\eta_h = \frac{P}{|\dot{Q}_H|} \quad (43)$$

Before finishing this section it is convenient to recall that from the assumed plant scheme (see Fig. 2), the following conditions for the temperatures at the hot side hold:

$$T_3 \geqslant T_{x'} \geqslant T_x \quad (44)$$

$$T_{HS} \geqslant T_x \quad (45)$$

$$T_{HC} \geqslant T_{x'} \quad (46)$$

Also, in summary, its worth to note that with respect to the dependence of specific heats with temperature it was assumed that temperature changes in compression (1 → 2) and expansion (3 → 4) processes are small so mean values were taken ($\bar{c}_{w,12}$ and $\bar{c}_{w,34}$, respectively). Nevertheless, during heat input and release, of course changes could be large so explicit polynomials for $c_w(T)$ will be taken. These assumptions allow to obtain straightforward analytical expressions for all the temperatures in the cycle and so, to analyze the sensitivity of the performance of the whole plant to any design or irreversibility parameter. Accounted irreversibilities for the thermodynamic engine are external (arising from the coupling of the heat engine to the external heat sources, ε_{HS} and ε_{HC}) and internal (associated to compressors, ε_c, turbines, ε_t, recuperator, ε_r, and pressure losses, ρ_H and ρ_L).

3. Numerical computations

In this section details about the numerical implementation of the model previously developed will be presented. Particularly, the data concerning the plant sizing and operation, model validation, and particularities of the considered working fluids are exposed.

3.1. Design point conditions and model validation

The thermodynamic model presented in this work in the particular case of single-stage compression and expansion was applied in previous works by our group in order to predict the performance records of a project developed by *Abengoa Solar* near Seville, Spain, called *Solugas Project* [7]. In this project a natural gas commercial single-stage gas turbine (*Caterpillar Mercury 50*) was modified in order to be hybridized with a central tower solar receiver [26].

First, the model was validated for the turbine working at full load on an only combustion mode. This turbine operates at a pressure ratio $r_p = 9.9$ with an air gas flow $\dot{m} = 17.9$ kg/s. The turbine inlet temperature is $T_3 = 1423$ K and provides 4.6 MWe fueled with natural gas [25]. The manufacturer reports a thermal efficiency after generator, $\eta_{h,e} = 0.385$ for $T_L = 288$ K [32]. Our model is capable to reproduce the thermal efficiency of the turbine with a deviation below 0.5% and the power output below 1.5%. The following parameters were assumed in the model: $\varepsilon_{HC} = 0.98, \varepsilon_{HS} = 0.78, \varepsilon_L = 1, \rho_H = \rho_L = 0.97$ (relative global pressure losses about 9.2%), $\varepsilon_c = 0.885, \varepsilon_t = 0.815$, and $\varepsilon_r = 0.775$. Details on the calculations and explicit tables with the parameters can be found in a previous work by Santos et al. [25].

The plant developed for the Solugas project was also simulated operating in hybrid conditions at design point solar irradiance ($G = 860$ W/m^2) and ambient temperature ($T_L = 288$ K). The parameters considered for the solar subsystem are: $\eta_0 = 0.73, \alpha = 0.1, \varepsilon_{HS} = 0.95, C = 425.2$, and $\overline{U}_L = 5$ W/(m^2 K). In these conditions the model (considering dry air with temperature dependent specific heat) predicts an overall plant efficiency, $\eta = 0.32$, a fuel conversion efficiency, $r_e = 0.58$, a solar share $f = 0.32$, a specific fuel

consumption, $m_f = 132$ kg/(MWh), and a mechanical power output $P = 5.06$ MW. The objective of this work is focused on the analysis of the model predictions if the single-stage gas turbine was substituted by a multi-step one, and also on the influence of other possible working fluids, different from air. In the next subsection the interest of using different working fluids in the search for improved plant performance is motivated. The basic parameters of the Solugas plant will be assumed as reference values.

3.2. Working fluids

The advantages of closed gas turbines when compared with either those working on open cycle or when compared with Rankine cycles are diverse (a recent comprehensive review is due to Olumayegun et al. [4]): closed-cycle gas turbines at high temperatures can reach efficiencies similar to steam cycles, lead to simpler plant designs (less number of heat exchangers, pumps, and piping), and have more compact components and so lower size for a fixed rated power output. Moreover, unlike open-cycle Brayton plants can use dirty fuels as biomass and other heat sources (nuclear and solar for instance). And moreover, different working fluids (depending on their thermal and transport properties, and practical issues) can be used, as analyzed by Najjar and Zaamout [34]. This work is focused on the last point.

As mentioned by Olumayegun et al. [4], among the working fluids that have been used in closed-cycle prototype or real installations, the most usual are: air, nitrogen, helium, carbon dioxide, other noble gases as argon and neon, and also gas mixtures. The experience on the design and operation of closed-cycle turbines working with air is broad. This constitutes an evident advantage. On the contrary, these plants have considerable pressure losses, require high turbine inlet temperatures that contribute to materials oxidization, and air has a low heat transfer coefficient. For nitrogen considerations are similar because the experience from air turbines can be applied and most properties are alike. One difference with air is the behavior of materials at high temperatures that in this case nitrides instead of oxidizes.

The use of helium is related with the development of nuclear reactors. No et al. [35] give a detailed historical review of several facilities of this type. Helium is inert and non-toxic, has a good heat transfer coefficient, and low pressure losses. As drawbacks it should be highlighted that turbomachinery design experience is not so broad as for air, requires high turbine inlet temperature, leakage is high, and actually more number of turbomachinery stages are required, as analyzed by McDonald [36].

Carbon dioxide has been used as working fluid for closed Brayton cycle plants from 1950, mainly partially condensed or supercritical. From late 1990s and early 2000s there have been a renewed interest because research and development work has rapidly evolved turbomachinery and heat exchangers. A recent review has been published by Crespi et al. [37]. Solar applications are being also investigated and analyzed nowadays (see for instance the work by Coco-Enríquez et al. [38]. CO_2 is non-toxic and inert, has a favorable critical point and in supercritical conditions turbomachinery is small and compact and gives good efficiencies at moderate turbine temperatures. Similarly to helium, design experience is not wide, as pointed out by Chacartegui et al. [39]. Moreover, thermodynamic properties vary considerably in the vicinity of the critical point, so detailed investigation on compressors, turbines and other machinery is required. Nevertheless, works on subcritical CO_2 with solar applications are scarce. It is worth mentioning the work by Najjar et al. [34].

In our study four working fluids are considered: air, nitrogen, helium, and carbon dioxide. Table 1 contains several thermodynamic properties relevant to the application of our model as critical point conditions and evolution with temperature of molar heat, that is plotted in Fig. 3. The figure shows that carbon dioxide has a molar heat about twice larger that a monoatomic gas like He and that its dependence with temperature in the interval from ambient temperature to the temperature at turbine inlet is large. The curves for air and N_2 are in between those for CO_2 and He. The dependence of their $c_w(T)$ with temperature is not large in the operation interval.

Fig. 4 displays a $p-T$ diagram with the liquid–vapor coexistence curve and the approximate processes experienced by the fluids in the Brayton cycle (in the single-stage case). It was assumed atmospheric pressure at compressor inlet and a pressure ratio of 9.9 as in the Solugas project. Within these hypotheses, the considered gases are in subcritical conditions except for He, that performs a transcritical cycle because pressure of states 2 and 3 are above the critical pressure. The aim of our work is to analyze the influence of the working fluid on the performance of the plant from a purely thermodynamic model. It is noteworthy to mention that technical issues related to piping and turbomachinery design are not considered in detail. Relative pressure drops in the cycle and isentropic efficiencies for compressors and turbines are assumed to be alike for all fluids. Similarly, the same inlet pressure at the compressor and the same working fluid mass flow are supposed. Although from a technical viewpoint an exhaustive study of the mentioned issues would be imperative, the objective of this work is to investigate the role played by the thermodynamic properties of the fluids, specially the influence of the molar heat, $c_w(T)$, in the heat absorption and heat release processes. In consequence conclusions about the influence of the working fluid on plant output records, for different plant layouts in terms of the number of compression/expansion processes at similar conditions, can be extracted.

4. Numerical predictions on plant performance

Model predictions within the considerations detailed in the previous section are presented hereafter. Most significant plant efficiencies are plotted in Fig. 5 in terms of the number of compression, N_c, and expansion steps, N_t, assumed identical: $N_t = N_c = N$. In all the plots the reference values corresponding to the Solugas project (air as working fluid and $N = 1$) are marked with an open circle. Table 2 displays the relative increments with respect to that case. For instance, in the case of air, when considering two compressors with intercooling and two turbines with reheating ($N = 2$), the overall plant efficiency, η, experiences an increase about 23% with respect to $N = 1$. The addition of more compression/expansion stages could increase overall efficiency up to 37% approximately.

The evolution of the global efficiency curves for all fluids are similar: a rapid increase from $N = 1$ to $N = 2$ or 3 and a subsequent slower increase up to an asymptotic value. This evolution for the overall efficiency, η (Fig. 5(a)), comes essentially from that of the Brayton heat engine, η_h, displayed in Fig. 5(b). The behavior of air and nitrogen is similar, although the curve for nitrogen is slightly above. On the contrary, CO_2 shows values for η larger than those for air or nitrogen for $N = 1$, but the increase with the number of compression/expansion stages is slower. The case of He is different. First,for N = 1 no regeneration was considered. This is because for the considered pressure ratio (assumed for all the fluids at the design point of Solugas project) is too high for regeneration to be advantageous (see the graph corresponding to He in Fig. 4). This point will be analyzed below, when presenting the plots for cycle temperatures. And second, the overall efficiencies for $N \geqslant 2$ are quite above those for air or nitrogen. For instance, for $N = 2$,η increases about 39% with respect to the reference case for He and 23% for air or nitrogen. This larger values of η for He are essentially associated to the values of the solar subsystem efficiency, η_s (Fig. 5(c)), that are larger for He (this point will be resumed when presenting the results for temperatures). The values of η_h for helium are above those for air but only slightly for $N \geqslant 3$.

The evolution of solar subsystem efficiencies, η_s (Fig. 5(b)), with N displays a monotonic decreasing behavior because the operating temperatures of the solar collector increases with N and so losses become larger. Anyway, the interval of numerical values in which η_s evolves is quite narrow (see the vertical axis in the plot for η_s). The behavior of the

fuel conversion rate, r_e (the ratio between the power output and the heat input with an economic cost), is quite diverse and interesting (Fig. 5(d)). r_e is larger for CO_2 that for the other fluids, and almost independent of N. These values are about 13% over that for the reference case (see Table 2). Nevertheless, for air, N_2 and He, r_e increases with N. The poorest values of r_e are those for helium.

The power output is much larger for He that for the other fluids as displayed in Fig. 6(a). This is an effect associated to the conditions in which the results for the different fluids are being compared. The numerical magnitude of power output is proportional to $\dot{m}c_w$. Helium has a constant pressure specific heat, c_w, about 4 times larger than the other fluids (see the mean values in Table 1). As the working fluid mass flow is assumed to be the same for all fluids, power output for He is for $N = 1$ larger than for the rest of considered fluids in the same proportion that c_w. This effect is amplified for larger values of N due to the heat input in the reheaters between turbines. For the other fluids power output increases with N up to approximately $N = 3$. For larger N power output remains almost constant. The increase is larger for air and nitrogen. The inset in the figure shows that for $N \geqslant 2$ expected power output is larger for N_2 than for air.

The solar share, f (Fig. 6(b)), decreases for all fluids with the number of compression/expansion stages. This is associated to the increase of heat input from combustion in the intermediate reheaters between turbines. Largest solar share is observed for CO_2 and $N = 1$, where $f \simeq 0.35$. On the other side, solar heat input for helium is always very small. The solar subsystem size (aperture area) in the reference plant would be undersized for He and in consequence, the fuel conversion efficiency, r_e, is low.

Several cycle temperatures are depicted in Fig. 7. The temperature at the compressors exit, T_2 (Fig. 7(a)) decreases with N and reaches very high values for He, especially for $N = 1$. This is the reason why regeneration in this case (for the considered value of the pressure ratio, $r_p = 9.9$) is meaningless. For all the fluids, as N increases, the values of T_2 decrease, because intercooling between compressors makes the temperature decrease before the fluid enters the following compressor. The effective temperature of the solar collector, T_{HS} and the temperature the fluid reaches after the solar heat input, $T_{x'}$ (Fig. 7(c)) always increase with N and are larger for CO_2. Except for He, all numerical values are above 1000 K. Lowest values are reached for He. From the viewpoint of the solar receiver, this means that helium is a good refrigerant. Temperatures of the fluids after regeneration in the cold part of the cycle, T_y (Fig. 7(d)), are relatively high in all cases, although decrease with N. This makes feasible to combine the Brayton cycle with a bottoming one as a Rankine in order to take advantage of residual heat. This conclusion is valid for any working fluid.

Specific fuel consumption, m_f, assuming natural gas fueling is shown in Fig. 8. Fuel consumption is larger for He, specially for $N = 1$, where no regeneration is assumed. For N_2 and air, the model predicts about 135 kg/(MWh) for $N = 1$ and smaller values for larger N. The main reduction is got in the change from $N = 1$ to $N = 2$. In the case of CO_2,m_f is almost constant. Its numerical value is around 115 kg/(MWh). The fact that in all cases m_f decreases with N means that in spite of the fueling required by intermediate reheaters, the cycles takes advantage of regeneration. This is shown by the increasing behavior of the temperature of the fluids after regeneration in the heat absorption process, T_x (Fig. 7(b)).

5. Optimum pressure ratios for each fluid

Up to now the same pressure ratio for all fluids was assumed, particularly the experimental one of the gas turbine employed in project Solugas was chosen, $r_p = 9.9$. The aim of this section is to analyze simultaneously three ingredients in order to seek for optimum plant designs: working fluids, number of compression/expansion steps, and overall pressure ratio. Different efficiencies have been calculated considering the pressure ratio as a variable up to $r_p = 20$.

Overall plant efficiency is displayed in Fig. 9. In the case of He (Fig. 9(a)) two configurations were checked for $N = 1$, with and without regeneration. When regeneration is considered, optimum pressure ratios leading to the highest efficiencies are around $r_p = 4$, leading to $\eta \simeq 0.37$. Values of r_p above 8 leads to worse efficiencies than for the non-regenerative configurations. The incorporation of regeneration increases overall efficiency about 20%, provided that a lower value of the pressure ratio is considered.

For air and nitrogen the curves for η monotonically increase with r_p except for the single-stage configuration, where there is a quite flat maximum between values of r_p in the interval 6–10. In the case of CO_2 (Fig. 9(d)) always an increase of the pressure ratio leads to larger values of efficiency, although for $N = 1$,η is almost constant above $r_p \simeq 10$.

Fuel conversion rate, r_e, for all the working fluids, has a narrow maximum (see Fig. 10) for low values of r_p. For He (Fig. 10(a)) this maximum is below the values of r_e for multi-stage configurations. Curves of η and r_e are very similar due to the scarce solar heat input for this fluid with the considered aperture area. On the other side, for CO_2 (Fig. 10(d)), r_e for $N = 1$ is larger than for any other configuration and any other value of the pressure ratio ($r_e = 0.68$). Air and nitrogen are intermediate cases: values of r_e for $N = 1$ and low r_p are similar than those for multi-stage configurations and larger r_p values. For configurations with $N \geqslant 2$ there is a wide interval of values of r_p leading to good fuel conversion rates. Except for He, small r_p values lead to higher values of r_e for plant layouts with N small. As r_p increases an inversion point is reached (r_p between 6 and 8, depending on the fluid) from which higher N leads to higher values of r_p, *i.e.*, the increase on power output compensates the increase of fuel consumption.

Fig. 11 contains the evolution of the power output curves. These curves are always monotonic for multi-stage configurations. For $N = 1$, air and nitrogen display a shallow maximum about $r_p \simeq 10$. This point corresponds to the design point of Solugas project. Helium (Fig. 11(a)) shows a maximum for $r_p \simeq 5$.

Figures for the specific fuel consumption, m_f, are not shown because are essentially the reversal of those for r_e. The maxima turn to be minima and the increasing behavior of most curves with r_p turns to be decreasing. To have a numerical idea, minimum m_f is got for CO_2,$N = 1$ and $r_p = 5$,$m_f = 108$ kg/(MWh). For air and nitrogen minimum fuel consumption is reached at similar conditions and is about 120 kg/(MWh).

6. Predictions for two-stages compression cycles

In the previous section was shown that there exist a considerable increase on plant output records from single-stage configurations to two-stage configurations. The subsequent improvement for a higher number of compression/expansion steps is not so noticeable. Thus, in this section particular predictions for two different plant layouts with two compressors and intercooling ($N_c = 2$) are presented: two-stages expansion with reheating ($N_t = 2$) and single-stage expansion ($N_t = 1$). As a function of the pressure ratio, the overall plant efficiency, η, for each fluid is always smaller for single expansion (see Fig. 12(a)) than for two-stages expansion, irrespectively of the working fluid. But it is noteworthy that for air and nitrogen the curves in the case of $N_t = 1$ have a maximum around $r_p = 12$, whereas for $N_t = 2$ are monotonic in all the surveyed interval for r_p. In the case $N_t = 2$, overall efficiency can reach values slightly above 0.4 for air and nitrogen at $r_p \simeq 20$. For $N_t = 1$,η_{max} can be about 0.36–0.38, depending on the fluid (see Table 3 for precise values). The power block efficiency, η_h (Fig. 12(c)), can attain values around 0.5 for $N_t = 2$ and $r_p \simeq 20$, and 0.46 for air or nitrogen for $N_t = 1$ at $r_p \simeq 10$.

Fuel conversion efficiency, r_e (see Fig. 12(d)) behaves differently that overall efficiency. It is always larger (except for He) for $N_c = 2$,$N_t = 1$ than for $N_c = N_t = 2$. Carbon dioxide leads to the best values of fuel conversion efficiencies, specially for $N_c = 2$,$N_t = 1$ at low values of r_p and also gives reasonable good values of overall efficiency

and low specific fuel consumption (see also Fig. 13): $r_{e,max} = 0.70$ and $m_{f,min} = 108$ kg/(MWh). Comparing with air and nitrogen (that give similar numbers) in the same conditions, carbon dioxide improves fuel conversion efficiency by 7.7% and decreases specific fuel consumption by 8.5%. And comparing with the reference plant, Solugas, overall efficiency increases 18.7%, fuel conversion efficiency 22.8%, and specific fuel consumption diminishes 22.2%.

With respect to helium, in spite of the probably small size of the heliostat field taken from the reference plant, overall efficiency (Fig. 12(a)) could take values about 0.45 for $N_t = N_c = 2$ and $r_p = 8$, and about 0.40 for $N_t = 1, N_c = 2$ and $r_p = 5$. Fuel conversion rate (Fig. 12(d)) is expected to be around 0.40–0.45, that are numbers considerable smaller than those for air or carbon dioxide.

7. Conclusions

A general thermodynamic model for central tower hybrid Brayton thermosolar plants has been developed. The model is capable to predict overall plant performance and other records in terms of the efficiencies of plant subsystems: solar field and receiver, Brayton heat engine, and combustion chamber. Morevover, it allows to analyze multi-stage compression and expansion, and also recuperative or non-recuperative layouts. Temperature dependent specific heats of the working fluid are taken into account. Output records depend on a not large number of parameters with clear physical meaning, so it is feasible to develop sensitivity analysis and to propose optimum plant configurations.

Numerical results are presented for several working fluids, taking the size and data from a real prototype plant of about 5 MW at design conditions (*Solugas* project, Seville, Spain). First, a fixed overall pressure ratio is considered ($r_p = 9.9$) and four (gaseous) working fluids at subcritical conditions (dry air, nitrogen, carbon dioxide, and helium) analyzed for different multi-stage configurations. Two-stage compression and expansion configurations using air, nitrogen or CO_2 as working fluids are capable to increase overall plant efficiency about 17–20 % with respect to the reference plant (Solugas). In the case of helium, overall efficiency increases up to 40%, but large increase of fuel consumption due to reheaters between turbines is observed. In this case, the predicted solar share is small probably because the solar field taken as reference is undersized. For the other fluids, the increase of power output associated to multi-stage compression and expansion balances the increase of fuel consumption and so, the fuel conversion rate improves.

Afterwards an analysis of optimum plant configurations was presented. Three ingredients were analyzed together: the working fluid, the number of compression/expansion steps, and the overall pressure ratio. For single-stage layouts, the curves of the overall plant efficiency, η, when plotted against the pressure ratio, r_p, have a maximum between $r_p = 5–8$ except for CO_2. For multi-stage configurations, η increases monotonically with r_p for all fluids. The fuel conversion rate has a maximum for single-stage configurations at low values of pressure ratio, $r_p \simeq 4–5$. These maxima values are high, especially for subcritical CO_2.

An specific analysis for two-stages compression cycles ($N_c = 2$) including single-stage expansion ($N_t = 1$) and two-stages expansion ($N_t = 2$) was done. Overall efficiency is larger for $N_t = 2$, but this is opposite for the fuel conversion rate, r_e. The fluid leading to the highest values of r_e is again CO_2 with $N_c = 2$ and $N_t = 1$, that attains $r_e \simeq 0.7$ at $r_p \simeq 5$. Comparing with the data of the reference plant (*Solugas*, single-stage, and working with air at $r_p = 9.9$), overall efficiency increases 18.7%, fuel conversion rate increases about 22.8%, and specific fuel consumption decreases about 8.5%, leading to values about 108 kg/(MWh). These numbers suggest that the use of subcritical CO_2 with two compressors, intercooling, and single-stage expansion could be an interesting option for future plant designs.

Acknowledgements

Financial support from University of Salamanca and Junta de Castilla y León (project SA017P17) is acknowledged.

References

[1] Nathan GJ, Jafarian M, Dally BB, Saw WL, Ashman PJ, Hu E, et al. Solar thermal hybrids for combustion power plant: A growing opportunity. Prog Ener Comb Sci 2017;000:1–25.
[2] Peterseim JH, White S, Tadros A, Hellwig U. Concentrated solar power hybrid plants, which technologies are best suited for hybridisation? Renew Ener 2013;57:520–32.
[3] Powell KM, Rashid K, Ellingwood K, Tuttle J, Iverson BD. Hybrid concentrated solar thermal power systems: A review. Renew Sust Ener Rev 2017;80:215–37.
[4] Olumayegun O, Wang M, Kelsall G. Closed-cycle gas turbine for power generation: a state-of-the-art review. Fuel 2016;180:694–717.
[5] del Río A, Korzynietz R, Brioso JA, Gallas M, Ordoñez I, Quero M, et al. Soltrec – Pressurized volumetric solar air receiver technology. Energ Proc 2015;69:360–8.
[6] Ho CK, Iverson BD. Review of high-temperature central receiver designs for concentrating solar power. Renew Sust Energ Rev 2014;29:835–46.
[7] Korzynietz R, Brioso JA, del Río A, Quero M, Gallas M, Uhlig R, et al. Solugas – Comprehensive analysis of the solar hybrid Brayton plant. Sol Ener 2016;135:578–89.
[8] Dunham M, Iverson B. High-efficiency thermodynamic power cycles for concentrated solar power systems. Renew Sust Energ Rev 2014;30:758–70.
[9] Osorio JD, Hovsapian R, Ordonez JC. Dynamic analysis of concentrated solar supercritical CO_2-based power generation closed-loop cycle. Appl Therm Eng 2016;93:920–34.
[10] McMahan A, Klein S, Reindl D. A finite-time thermodynamic framework for optimizing solar-thermal power plants. J Sol Energ Eng 2007;129:355–62.
[11] Zare V, Hasanzadeh M. Energy and exergy analysis of a closed Brayton cycle-based combined cycle for solar power tower plants. Ener Conv Manage 2016;128:227–37.
[12] Barigozzi G, Bonetti G, Franchini G, Perdichizzi A, Ravelli S. Thermal performance prediction of a solar hybrid gas turbine. Sol Energy 2012;86:2116–27.
[13] Barigozzi G, Perdichizzi A, Gritti C, Guaiatelli I. Techno-economic analysis of gas turbine inlet air cooling for combined cycle power plant for different climatic conditions. Appl Therm Eng 2015;82:57–67.
[14] Milani D, Tri Luu M, McNaughton R, Abbas A. A comparative study of solar heliostat assisted supercritical CO_2 recompression Brayton cycles: Dynamic modelling and control strategies. J. Supercrit Fluids 2017;120:113–24.
[15] Kalathakis C, Aretakis N, Roumeliotis I, Alexiou A, Mathioudakis K. Concentrated solar power components toolbox in an object oriented environment. Sim Model Prac Theo 2017;70:21–35.
[16] Iverson B, Conboy T, Pasch J, Kruizenga A. Supercritical CO_2 Brayton cycles for solar-thermal energy. Appl Energ 2013;111:957–70.
[17] Al-Sulaiman F, Atif M. Performance comparison of different supercritical carbon dioxide Brayton cycles integrated with a solar power tower. Energy 2015;82:61–71.
[18] Luu MT, Milani D, McNaughton R, Abbas A. Dynamic modelling and start-up operation of a solar-assisted recompression supercritical CO_2 Brayton power cycle. Appl Ener 2017;199:247–63.
[19] Vasquez Padilla R, Soo Too Y, Benito R, McNaughton R, Stein W. Thermodynamic feasibility of alternative supercritical CO_2 Brayton cycles integrated with an ejector. Appl Ener 2016;169:49–62.
[20] Ahn Y, Bae SJ, Kim M, Cho S, Baik S, Cha JE. Review of supercritical CO_2 power cycle technology and current status of research and development. Nucl Eng Technol 2015;47:647–61.
[21] Reyes-Belmonte MA, Sebastián A, Romero M, González-Aguilar J. Optimization of a recompression supercritical carbon dioxide cycle for an innovative central receiver solar power plant. Energy 2016;112:17–27.
[22] Sánchez-Orgaz S, Medina A, Calvo Hernández A. Thermodynamic model and optimization of a multi-step irreversible Brayton cycle. Energ Convers Manage 2010;51:2134–43.
[23] Olivenza-León D, Medina A, Calvo Hernández A. Thermodynamic modeling of a hybrid solar gas-turbine power plant. Energ Convers Manage 2015;93:435–47.
[24] Sánchez-Orgaz S, Medina A, Calvo Hernández A. Recuperative solar-driven multi-step gas turbine power plants. Energ Convers Manage 2013;67:171–8.
[25] Santos MJ, Merchán RP, Medina A, Calvo Hernández A. Seasonal thermodynamic prediction of the performance of a hybrid solar gas-turbine power plant. Energ Convers Manage 2016;115:89–102.
[26] Quero M, Korzynietz R, Ebert M, Jiménez AA, del Río A, Brioso JA. Solugas – operation experience of the first solar hybrid gas turbine system at MW scale. Energ Proc 2014;49:1820–30.
[27] Heywood J. Internal combustion engine fundamentals. McGraw-Hill; 1988.
[28] Collado FJ, Turégano JA. Calculation of the annual thermal energy supplied by a defined heliostat field. Sol Ener 1989;42:149–65.
[29] López-Herraiz M, Bello Fernández A, Martinez N, Gallas M. Effect of the optical properties of the coating of a concentrated solar power central receiver on its thermal efficiency. Sol Energ Mat Sol Cells 2017;159:66–72.
[30] Duffie J, Beckman W. Solar engineering of thermal processes. Hoboken, New Jersey: John Wiley and Sons; 2006.
[31] Siva Reddy V, Kaushik SC, Tyagi SK. Exergetic analysis and economic evaluation of central tower receiver solar thermal power plant. Int J Ener Res 2014;38:1288–303. http://dx.doi.org/10.1002/er.3138.

[32] Solar, Turbines, Caterpillar. [link]. URL https://mysolar.cat.com/cda/files/126873/7/dsm50pg.pdf.
[33] Lemmon EW, Huber ML, McLinden MO. NIST Standard Reference Database 23: Reference fluid thermodynamic and transport properties-REFPROP, version 9.1, National Institute of Standards and Technology, Standard Reference Data Program, Gaithersburg; 2013.
[34] Najjar Y, Zaamout M. Comparative performance of closed cycle gas turbine engine with heat recovery using different gases. Heat Recovery Syst CHP 1992;12:489–95.
[35] No HC, Kim JH, Kim HM. A review of helium gas turbine technology for high temperature gas-cooled reactors. Nucl Eng Technol 2007;39:21.
[36] McDonald CF. Helium turbomachinery operating experience from gas turbine power plants and test facilities. App Therm Eng 2012;44.
[37] Crespi F, Gavagnin G, Sánchez D, Martínez GS. Supercritical carbon dioxide cycles for power generation. Appl Ener 2017;195:152–83.
[38] Coco-Enríquez L, Muñoz Antón J, Martínez-Val JM. New text comparison between CO_2 and other supercritical working fluids (ethane, Xe, CH_4 and N_2) in line-focusing solar power plants coupled to supercritical Brayton power cycles. Int J Hydrogen Ener 2017;42:17611–31.
[39] Chacartegui R, Muñoz de Escalona J, Sánchez D, Monje B, Sánchez T. Alternative cycles based on carbon dioxide for central receiver solar power. Appl Thermal Eng 2011;31:872–9.

3.5 Paper 5 – On-design pre-optimization and off-design analysis of hybrid Brayton thermosolar tower power plants for different fluids and plant configurations

Title: "On-design pre-optimization and off-design analysis of hybrid Brayton thermosolar tower power plants for different fluids and plant configurations"
Journal: *Renewable and Sustainable Energy Reviews*
Authors: **R.P. Merchán**, M.J. Santos, I. Heras, J. González-Ayala, A. Medina, A. Calvo Hernández
Year: 2020
Volume: 119
Pages: 109590
DOI: `https://doi.org/10.1016/j.rser.2019.109590`
Reference: [90]

Resumen

En este artículo se presenta un modelo teórico completo para una planta termosolar de torre central acoplada a una turbina de gas híbrida y multi-etapa, que integra todos los subsistemas especificando sus eficiencias. El modelo del subsistema solar ha sido ampliamente mejorado, de modo que ahora se detalla la eficiencia del campo solar dependiente de cada heliostato. Se tienen en cuenta tanto pérdidas por efecto coseno, como bloqueos y sombras entre heliostatos, atenuación, *spillage* y reflectividad de los espejos. La implementación del modelo en el código se lleva a cabo en base a las dimensiones de la planta española *GEMASOLAR* (campo de heliostatos circular). Para la validación de la turbina se emplea el *software Thermoflex*®. El objetivo principal de este artículo es realizar estudios tanto en el punto de diseño como en condiciones dinámicas de las principales variables de la planta, buscando posibles relaciones de presiones óptimas y configuraciones que mejoren tanto la eficiencia térmica global como el *solar share* y que disminuyan la temperatura del receptor solar. En ambos casos (condiciones de diseño y dinámicas), se presentan mapas de eficiencia óptica para el campo de heliostatos. Por otro lado, se analizan cuatro fluidos de trabajo (aire, nitrógeno, dióxido de carbono y helio), diferentes números de etapas de compresión y expansión y configuraciones tanto recuperativas como no recuperativas para las variables de salida de la planta. Para el caso recuperativo con aire, al pasar de una configuración monoetapa a una de dos etapas, se predice un aumento de la eficiencia térmica global de un 47 %. Asimismo, las emisiones específicas de dióxido de carbono asociadas al consumo de combustible son más pequeñas cuando es helio en vez de aire seco el fluido que realiza un ciclo termodinámico simple y no recuperativo.

Renewable and Sustainable Energy Reviews 119 (2020) 109590

Contents lists available at ScienceDirect

Renewable and Sustainable Energy Reviews

journal homepage: http://www.elsevier.com/locate/rser

On-design pre-optimization and off-design analysis of hybrid Brayton thermosolar tower power plants for different fluids and plant configurations

R.P. Merchán, M.J. Santos, I. Heras, J. Gonzalez-Ayala, A. Medina *, A. Calvo Hernández

Department of Applied Physics and Institute of Fundamental Physics and Mathematics (IUFFYM), University of Salamanca, 37008, Salamanca, Spain

ARTICLE INFO

Keywords:
Thermosolar hybrid plants
Multi-stage brayton
On-design pre-optimization
Off-design analysis
Greenhouse emissions

ABSTRACT

A working fluid performs a Brayton cycle that is fed by a heat input from a solar power tower and from a combustion chamber, which burns natural gas. This hybrid system is described by a complete model that includes all the main losses and irreversibility sources (optical and thermodynamic). Numerical implementation and validation is performed based on a Spanish commercial plant. On-design computations are carried out varying the pressure ratio for four working fluids (dry air, nitrogen, carbon dioxide, and helium), for different number of stages and for recuperative and non-recuperative configurations. When adjusting the pressure ratio, an improvement of about 7 % in overall thermal efficiency is predicted for a dry air single-stage recuperative configuration with respect to a standard commercial gas turbine. A study about the main energy losses in each plant subsystem for some particular plant layouts is accomplished. A two-compression and expansion stages recuperative Brayton cycle working with air is expected to give overall thermal efficiencies about 0.29 at design conditions, which is about a 47% increase with respect to the simplest single-stage configuration. It is stressing that fuel consumption from the reheaters maybe higher than that of the main combustion chamber for multi-stage layouts. Off-design hourly curves of output records for the four seasons throughout a day are analyzed. Greenhouse emissions are also analyzed. Specific carbon dioxide emissions are smaller for helium than for dry air, when they both work in a single-stage non-recuperative configuration.

1. Introduction

Climate change together with the finite reserves of fossil resources has made necessary the transformation of the energy paradigm towards new, cleaner, and renewable ways of producing energy. Concentrating Solar Power (CSP) technology constitutes one of the best ways to fulfill these requirements, taking into account its reliability and flexibility for storing or hybrid operation [1]. Particularly, the hybridization of combustion power plants is considered as a growing opportunity in the way to cleaner energy production [2]. For the production of energy at the level of a few megawatts central tower plants are expected to be, simultaneously, highly efficient and highly flexible in which respect to the technology for producing the energy through a power block [3]. The combination with other renewables as photovoltaic is also being analyzed [4]. These plants are constituted essentially by three subsystems with different physical and engineering nature: the solar field collecting the solar power and redirecting it to the tower, the solar receiver where the energy is concentrated and transferred to the working fluid, and the power subsystem, that converts energy as heat to mechanical energy through some thermodynamic cycle [5].

The solar collector in these plants is an arrange of individually non-concentrating mirrors with a two-axis tracking system which focus light on a central receiver at the top of a tower. A common array to distribute heliostats by looking for an optimized distribution is the radial staggered [6]. The optimization process involves to calculate repeatedly the annual energy collected by the field in terms of the considered optimization variables. Most important losses should be considered, as cosine losses, shading and blocking, spillage, and atmospheric attenuation. It is also necessary to define a figure of merit, as for instance, the ratio between the cost of the field and the total thermal energy collected during a year [7]. The final aim is to reduce the levelised cost of electricity (LCOE). Different techniques have been employed during the last years, from biomimetic layouts [8], to computationally expensive Monte Carlo

* Corresponding author.
E-mail addresses: rpmerchan@usal.es (R.P. Merchán), smjesus@usal.es (M.J. Santos), iheras@usal.es (I. Heras), jgonzalezayala@usal.es (J. Gonzalez-Ayala), amd385@usal.es (A. Medina), anca@usal.es (A.C. Hernández).

https://doi.org/10.1016/j.rser.2019.109590
Received 28 December 2018; Received in revised form 16 September 2019; Accepted 12 November 2019
Available online 19 November 2019

Nomenclature

A_a	aperture area of the solar field (m^2)
C	solar collector concentration ratio
C_n	nominal cleanliness
c_w	specific heat of the working fluid [$J/(mol\,K)$]
D	distance between the centre of each heliostat and the aim point in the receiver
f	solar share
f_{at}	attenuation factor
f_b	blocking factor
f_{sh}	shadowing factor
f_{sp}	spillage factor
G	direct solar irradiance (W/m^2)
LR	height of the receiver (m)
M	molecular weight of the working fluid ($g/\,mol$)
$\dot{m}$	mass flow rate of the working substance (kg/s)
$\dot{m}_f$	fuel mass flow rate (kg/s)
N	number of compressors or turbines when they are equal
N_c/N_t	N_t number of compressors/turbines
OK	total number of heliostats
P	power output (W)
p_{amb}	ambient pressure (bar)
p_c	critical pressure (bar)
p_H	highest pressure during heat absorption (bar)
p_L	pressure at the exit of the expansion processes (bar)
$\lvert\dot{Q}_C\rvert$	heat losses at the combustion chamber (W)
$\lvert\dot{Q}_H\rvert$	total heat-transfer rate absorbed from the working fluid (W)
$\lvert\dot{Q}_{HC}\rvert$	total heat rate input from the combustion chamber and the reheaters (W)
$\lvert\dot{Q}_{HS}\rvert$	heat rate input from the solar collector (W)
$\lvert\dot{Q}_L\rvert$	heat-transfer rate between the working fluid and the ambient (W)
Q_{LHV}	lower heating value of the fuel (J/kg)
r_p	overall pressure ratio
R_{min}	minimum radius of the heliostat field (m)
T_c	critical temperature (K)
T_{HC}	working temperature of the combustion chamber (K)
T_{HS}	working temperature of the solar collector (K)
T_L	ambient temperature (K)
T_3	turbines inlet temperature (K)
THT	height of the tower supporting the receiver (m)
$\overline{U}_L$	effective conduction-convection heat transfer coefficient [$W/(m^2\,K)$]
w_r	width-height ratio of the heliostat surface
α	effective emissivity
α_S	solar altitude angle (rad)
ΔR	radial distance between two adjacent rows (m)
ε_{HC}	ε_{HS} combustion chamber/solar collector heat exchangers effectiveness
ε_c	ε_t isentropic efficiency of the compressors
$\overline{\gamma}$	mean value of the working fluid adiabatic coefficient
η	overall thermal efficiency
η_c	combustion efficiency
η_h	thermal efficiency of the Brayton heat engine
$\overline{\eta}_{heli}$	optical efficiency of each heliostat
η_s	solar collector efficiency
η_0	optical efficiency of the whole field
ρ	actual mirror reflectivity
ρ_H/ρ_L	ρ_L irreversibilities due to pressure drops in the heat input/ heat release
ρ_n	nominal reflectivity
σ	Stefan-Boltzmann constant ($W\,m^{-2}\,K^{-4}$)
ω	incidence angle of the Sun radiation onto the heliostat surface (rad)

ray-tracing tools (as SolTRACE [9]), and also analytical methods for simultaneously optimize heliostat field (heliostat locations and number) and the tower (tower height and receiver size) as HFLCAL, *Campo* Code or others [10–12].

Solar receivers are one of the crucial elements in any CSP installation, particularly central tower plants. Their design and manufacturing materials should comprise high reliability, cost-effectiveness, and a long operational lifetime [13]. Higher plant efficiencies require good light-heat conversion efficiency in the receiver [14]. This energy conversion is affected at least by four kind of losses: reflection, radiation, convection, and conduction. There are essentially two types of receiver concepts: cavity receivers and external absorption ones (for instance, a cylindrical array of tubes). The former use to have lower radiative losses than tubular, but higher convective losses [15]. Cavity receivers usually have only one aperture, so the sunlight is received only from one side, so the heliostat field should not have circular symmetry. In these receivers, outlet temperatures about 1000 $^\circ C$ have been reported using air as working fluid [16]. In any case, for temperatures from 650 to 750 $^\circ C$ radiation effects are very important. An increase in solar absorptance and a decrease in thermal emittance are key factors to improve thermal receiver efficiency. Existing paint-based coatings, as Pyromark 2500 (currently used in central towers), with a good absorptivity are not very durable because deposition techniques nowadays only allow a limited adherence [14]. So, research lines in this field are focused to improve adhesion and maintain the optical properties above 650 $^\circ C$ [17].

In which respect to the thermal power block that transforms the heat released by the solar receiver in mechanical energy, most usual thermodynamic cycles are based on Rankine and Brayton cycles, *i.e.*, steam or gas turbines, and their combination [5]. The former are usually associated to storage with molten salts in central towers, so the working fluid for the solar receiver is different to that for the power cycle itself and at least a steam generator is required. Several plants are nowadays working on this concept, not only prototype plants, but also commercial ones, as GEMASOLAR (Spain) [18], Crescent Dunes (USA) [19], and Noor III at Ouarzazate (Morocco) [20]. An interesting review on this type of plants with a summary of plants in operation and under construction is due to Behar et al. [21].

In the case of Brayton-like cycles usually the solar receiver heats air, which flows at high pressure coming from the compressor. This technology is normally linked to hybrid operation in such a way that a combustion chamber in series with the solar receiver increases, when necessary, the temperature to ensure that the turbine inlet temperature remains approximately constant. This guarantees an approximately constant power output, independently of seasonal, meteorological variations or even nighttime [22]. An increase on overall performance is obtained when a bottoming Rankine cycle is considered to take advantage of the usually high temperature of exhaust gases. The Brayton cycle can operate in both open or closed cycle schemes and a good thermal efficiency is associated to a high turbine inlet temperature. This imposes a high working temperature for the solar receiver to get also reasonably good solar shares. Usually turbine inlet temperatures are around 1100 $^\circ C$. These plants are still at the R&D&i stage. Most of prototype plant and experimental projects during the last years have been developed in Spain: SOLGATE [23], SOLHYCO [24], and SOLUGAS [25]. A major conclusion of all these projects is that the technology is feasible and interesting, but a research and development effort is still required to

get commercially competitive prices of electricity [26].

This work is focused on the last point. Particularly, on the development of thermodynamic models for the whole plant, including all subsystems, that could allow to guide the design of future plants based on this technology. A compelling review on the thermodynamic optimization of the solar Brayton cycle was written by Le Roux et al. [27]. Osorio et al. [28] as well as McMahan et al. [29] and Zare et al. [30] have tried to model the plant in terms of a reduced set of parameters. But also detailed analysis, including thermoeconomic issues, based on simulation software have also been developed [31,32].

Thermodynamic models, as the one considered in this work, allow a comprehensive description of all plant subsystems, and so, to study the interactions among subsystems. Non-complex equations can be obtained by means of some physical parameters with a clear interpretation, so sensitivity analysis, and optimization processes can be implemented. Recently, our group presented a thermodynamic model emphasizing the details and losses in the power block [33]. In this paper a more complete model is addressed, incorporating, a detailed (but at the same time comprehensive) description of the solar subsystem. Particularly, including all the details necessary to obtain precise estimations for the optical efficiency the solar field. The model is dynamic, so it allows to predict the behavior of any plant parameter along any day of any season. And also is flexible because different working fluids can be analyzed as well as different layouts for the Brayton cycle (including single- or multi-stage compression and expansion). The model is validated for a plant of a commercial size, GEMASOLAR [18], of about 20 MW. The main sources of losses are identified and quantified for several plant configurations and daily curves of the main subsystems, and the whole plant are presented. Also the predicted temperatures of all subsystems are estimated. As a global conclusion it can be said that there is a wide inventory of options to design plants with the desired level of efficiencies or temperature limits. Once a pre-design plant scheme is adopted there is still a way to estimate the corresponding economic records, that is out of the scope of this work.

A brief description of the model developed in this work, either optical for the heliostat field or themodynamic for the power block, is presented in Sec. 2 and Appendix A. Its model implementation together with its validation are shown in Sec. 3 and Appendix B. Afterwards, Sec. 4 contains an on-design analysis of the solar plant. The performance of four different working fluids (dry air, nitrogen, carbon dioxide, and helium) in several expansion and compression configurations and in both recuperative and non-recuperative cases is studied against the pressure ratio for the design point. As a consequence, three configurations are selected looking for an improved overall thermal efficiency with respect to the pressure ratio. For these three configurations, an off-design analysis is carried out in Sec. 5. Different output records are plotted throughout a day for the four seasons and carbon dioxide emissions are estimated. In addition, heliostats field efficiency is studied at the design point as well as in real fluctuating conditions.

2. Thermodynamic model

The overall system analyzed is a multi-stage gas turbine hybridized with a central solar tower in order to obtain a stable power output, independent of the solar irradiance conditions. A diagram of the considered system is shown in Fig. 1. The working fluid is first compressed by

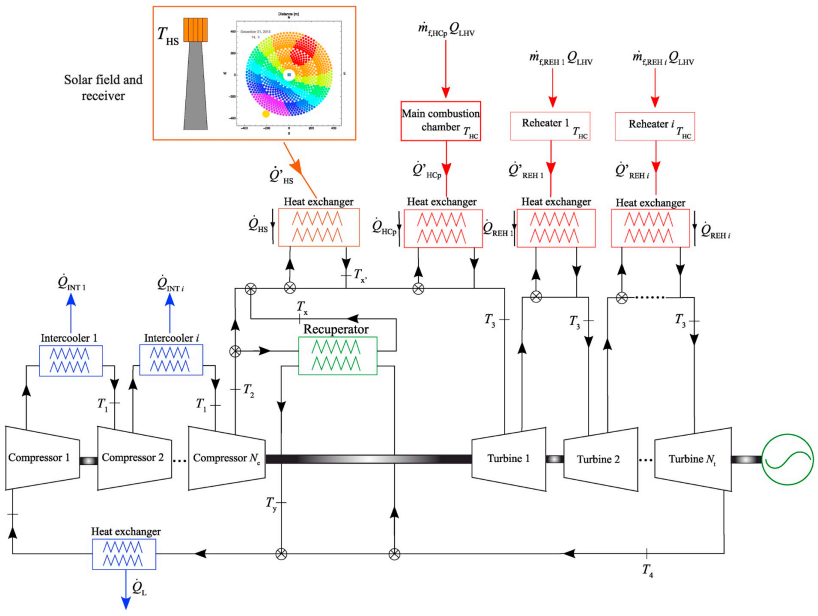

Fig. 1. Scheme of the hybrid thermosolar gas-turbine plant considered, which is composed of a solar subsystem (solar field and central tower receiver), a main combustion chamber, an arbitrary number of compressors (N_c), and an arbitrary number of turbines (N_t). Between every pair of compressors, an intercooler is considered and, similarly, between every pair of turbines, an intermediate reheater is needed.

means of a number N_c of compressors with $N_c - 1$ intercoolers between them. Inlet temperature is assumed the same for all compressors. Afterwards, the fluid is heated by means of three different heat sources: a recuperator, a solar field, and a main combustion chamber. Then, N_t expansion stages are next. It will be assumed that the inlet temperature for all turbines is the same, so $N_t - 1$ reheaters are required. And, finally, the recuperator and a subsequent heat exchanger connected to the ambient release the necessary excess heat for starting the cycle again. This last heat exchanger is necessary because the model is considered as closed. So, the overall plant is composed of three subsystems: the solar subsystem, the combustion one, and the heat engine. The proposed thermodynamic model includes all the main losses and irreversibilities sources as depicted in Fig. 2.

In this section, the thermodynamic model of the considered plant is summarized since it has been recently detailed in Ref. [33]. Then, the attention is focused on the novel model aspects of this contribution.

2.1. Overall efficiency

The overall system thermal efficiency, η, can be expressed in terms of the net mechanical power, P, of the direct normal solar irradiance, G, of the heliostats field aperture area, A_a, of the lower heating value of the fuel, Q_{LHV}, and of the total fuel mass flow, $\dot{m}_f$, which is the addition of that consumed at the main combustion chamber and at the reheaters:

$$\eta = \frac{P}{G\,A_a + \dot{m}_f\,Q_{\mathrm{LHV}}} \tag{1}$$

By defining the solar share, f, as the fraction of energy provided to the fluid that comes from the solar subsystem and by doing some thermodynamic calculations [34], the following expression for the overall thermal efficiency is achieved:

$$\eta = \eta_h\,\eta_s\,\eta_c\left[\frac{\varepsilon_{HS}\,\varepsilon_{HC}}{\eta_c f \varepsilon_{HC} + \eta_s(1-f)\varepsilon_{HS}}\right] \tag{2}$$

where η_h represents the thermal efficiency of the heat engine, η_s that of the solar subsystem (solar field and receiver), η_c the efficiency of the combustion chamber, ε_{HS} the effectiveness of the solar receiver as heat exchanger that transfers the solar heat input to the working fluid, and ε_{HC} the effectiveness of the heat exchanger associated to the combustion chamber, that it is required because a closed Brayton cycle is being assumed. All formal definitions are explicitly shown in Ref. [33].

Another important parameter is the *fuel conversion rate*, r_e, or the performance relative to the energy input with an economical cost. The definition proposed by Heywood [35], when implemented in our model [34], yields to:

$$r_e = \frac{\eta\,\eta_s\,\eta_h\,\varepsilon_{HS}}{\eta_s\,\eta_h\,\varepsilon_{HS} - \eta\,f} \tag{3}$$

For pure solar operation ($\dot{m}_f = 0$), $f = 1$, and $r_e \to \infty$ and for only combustion operation, $f = 0$, so $r_e = \eta$.

2.2. Solar subsystem model

2.2.1. Solar field geometry

The considered field is a circular heliostat field around the central tower, whose lowest part is always considered as the spacial reference origin, and its geometry is depicted at Fig. 3. The solar volumetric receiver is located atop of the tower and it is composed of several cylindrical tubes disposed symmetrically as the walls of a cylinder around a downing pipe in the centre of that cylinder.

The heliostat field is made up of several rows of heliostats and each heliostat is composed of a reflecting surface mounted on a support pedestal over the ground, with a two-axis tracking system that allows it to follow the Sun movements in the sky. The heliostat surface is a rectangular plane mirror, whose width-height ratio is $w_r = LW/LH$. Heliostats are disposed in the field taking into account that their orientation changes with Sun tracking, as it can be observed in Fig. 4. Additionally, a safety distance between heliostats, *DHs*, must be

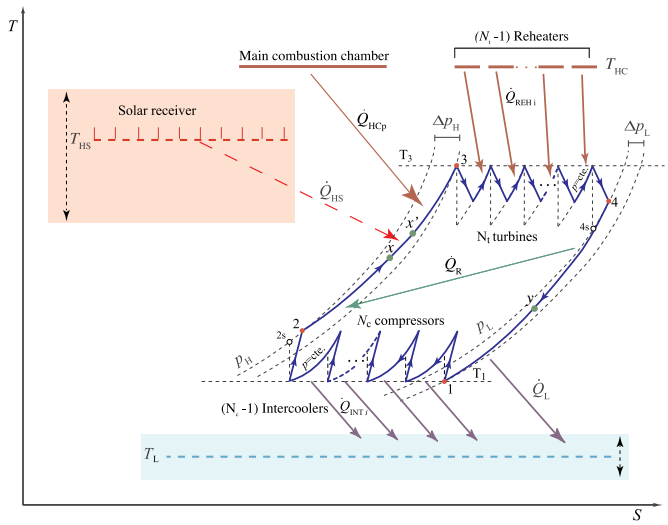

Fig. 2. Temperature-entropy diagram of the irreversible multistage Brayton cycle experienced by the working fluid in the considered plant. Solar receiver temperature, T_{HS}, and ambient temperature, T_L, are fluctuating parameters.

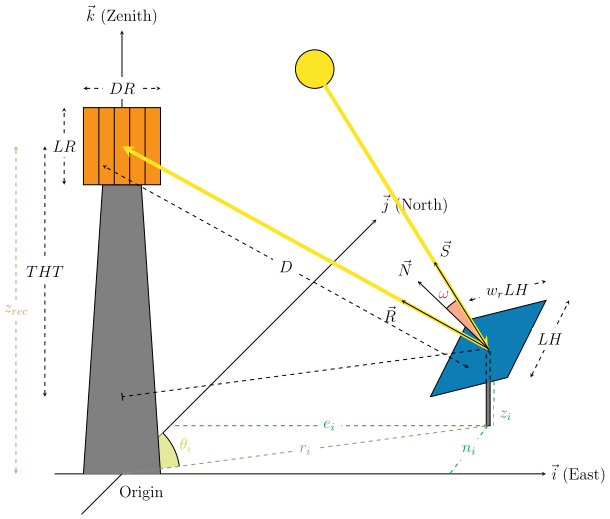

Fig. 3. Reference frame of the solar field, Sun incidence in the heliostat field, and reflection towards the solar receiver, assuming a plain ground [37].

considered [36].

Heliostats are disposed in an equidistant way over a circumference. Each one is associated to an angle θ_i (see Fig. 4). The heliostat field is divided into regions and rows. A region comprises one or more rows in which the increment of the azimuth angle, $\Delta\alpha_T$, is constant [36]. For a particular region, the farther the heliostats from the tower, the more separated they are. When this available separation is high enough for a new heliostat to be placed, then a new region starts. There are several field expansion techniques in the literature. Here, *Campo* code model was followed [11,36]. The starting point is the densest layout, that afterwards is expanded. Because of shadowing and blocking effects (explained below) there is a balance effect and optimum densities are found because field expansion advantages prevail over its disadvantages. In this work, heliostat densities were calculated as in a preliminar version of Campo code [36] with a simplified fixed blocking factor, and second, regions were completed up to find enough heliostats to approximately guarantee the desired turbine inlet temperature at design conditions.

2.2.2. Solar field efficiency

The optical efficiency of the whole field, η_0, is the average of the efficiency of each heliostat [36]:

$$\eta_0 = \overline{\eta}_{hel} = \frac{\sum_{i=1}^{NH} \eta_{heli}}{NH} \tag{4}$$

where *NH* represents the total number of heliostats in the solar field. And the optical efficiency of each heliostat is defined as a product of losses factors [36]:

$$\eta_{heli} = cos\ \omega \cdot f_b \cdot f_{sh} \cdot f_{sp} \cdot f_{at} \cdot \rho \tag{5}$$

In this equation $cos\ \omega$ stands for the cosine of the Sun radiation's incident angle, f_b represents the blocking factor, f_{sh} is associated with a shadowing factor, f_{sp} refers to a spillage factor, f_{at} is related to an attenuation factor, and ρ is the actual mirror reflectivity. These six losses parameters are represented in Fig. 5.

Cosine factor. The cosine effect constitutes the main factor of the optical efficiency [38]. In order to determine which is this incident angle of the Sun radiation in the heliostat surface, a study about the Sun-heliostat-receiver geometry should be accomplished by taking into account the law of specular reflection. This leads to an expression for ω that depends on each heliostat coordinates, receiver coordinates, and solar azimuth and altitude angles (see Fig. 3). An explicit equation for ω can be found in Ref. [36].

Blocking and shadowing factors. The blocking factor accounts for the energy loss because part of the reflected energy from a back heliostat can be stopped by an ahead one. On the other hand, the shadowing factor takes into account the energy loss when a heliostat projects a shadow on another heliostat, and then not all the surface of the last heliostat can reflect the sun radiation. The most complex elements affecting the optical efficiency are precisely these blocking and shadowing factors [38]. Therefore, it is not easy to express them in an analytical way and simulate them accurately, so it is not unusual to take these factors as constant [39,40].

Spillage factor. The power delivered by each heliostat to the receiver is the integral over the receiver contours of the corresponding flux density function. The fraction outside receiver boundaries is called spillage. In this work it is assumed the formulation by Collado [7] in which the spillage factor depends on the dimensions of the receiver, heliostat area, and the effective dispersion of the sun shape on the receiver plane. Explicit equations can be found in Ref. [7]. Other formulations as the one used in HFLCAL also consider dispersions associated to mirror surface errors and tracking errors [10,41]. This makes the spillage factor depend on each heliostat position with respect to the receiver, leading to calculations computationally more expensive. Both formulations were checked within our overall model and no significant differences found, so the analytical model from Ref. [7] was assumed.

Attenuation factor. The attenuation factor, f_{at}, takes into account the energy dissipation due to the energy absorption of the air molecules between the heliostats and the receiver. Clearly, this factor depends on

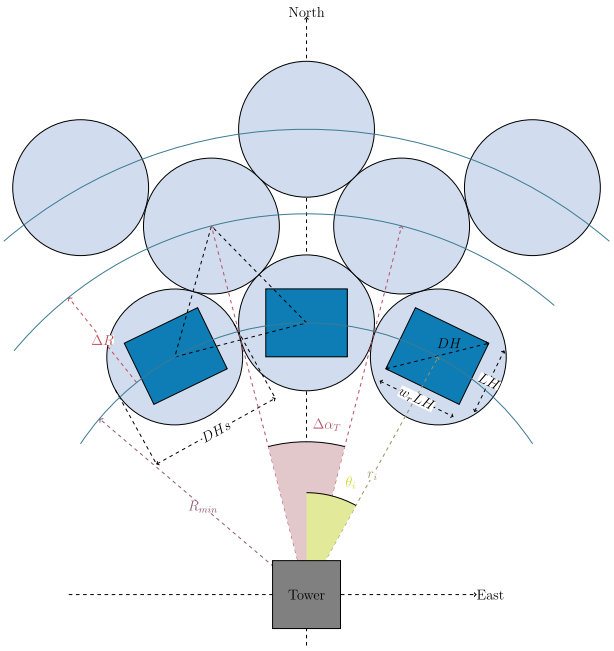

Fig. 4. Radial staggered distribution for the heliostats field [7].

the distance between the centre of the heliostat and the aim point in the receiver, D [42]. So, it varies with the particular heliostat and, thus, for great solar fields, differences in attenuation are more significant than for smaller fields. It is usual to take an empirical formula for f_{at} in terms of D. In this work the equations by Leary and Hankins [43] for distances below 1 km and Schmitz et al. [10] for longer distances are assumed.

Mirror reflectivity. The actual reflectivity, ρ, of a mirror can be modeled as the product of two factors: the nominal reflectivity, ρ_n, and the nominal cleanliness, C_n, $\rho = \rho_n \cdot C_n$ [41]. The importance of the actual reflectivity is not just related to the efficiency of the heliostat; but, in fact, it is also a function of the maintenance cost of the field since the nominal cleanliness depends on plant conservation.

As a summary, it can be noted that only the cosine factor and the attenuation factor depend on the particular heliostat, the other four factors are independent of the heliostat. So, in the average optical efficiency (see Eq. (4)), just the cosine and the attenuation factors are inside the summation, the other four terms are common factors.

2.2.3. Solar subsystem efficiency

In addition to all the aforementioned losses associated with the solar energy transfer from the heliostats to the receiver, another energy losses in the solar subsystem must be analyzed. These are the ones related to the heat transfer out of the receiver because of conduction, convection, and radiation. In this way, the solar subsystem efficiency is [33,44]:

$$\eta_s = \eta_0 - \frac{1}{GC}\left[\alpha\sigma\left(T_{HS}^4 - T_L^4\right) + \overline{U}_L\left(T_{HS} - T_L\right)\right] \quad (6)$$

where C is the concentration ratio, α refers to the emissivity of the receiver surface, σ is the Stefan-Boltzmann constant, $\overline{U}_L$ corresponds to an overall conduction and convection heat transfer coefficient, T_{HS} is the solar collector temperature and T_L, with the ambient temperature.

The heat flux actually absorbed by the working fluid is: $|\dot{Q}_{HS}| = \varepsilon_{HS} G A_a \eta_s$, where ε_{HS} refers to the effectiveness of the solar receiver, considered as a heat exchanger.

2.3. Combustion subsystem model

The model for the heat transfer from the main combustion chamber and the reheaters to the working fluid (see Fig. 1) includes the non-ideality of combustion and the losses in the combustion chamber, but also the losses in the associated heat exchanger. This applies both for the main combustion chamber and for all the reheaters. In this way, the heat rate transferred from the main combustion chamber and the reheaters to the working fluid can be expressed as:

$$\left|\dot{Q}_{\mathrm{HCp}}\right| + \left|\dot{Q}_{reh}\right| = \eta_c\, \varepsilon_{HC}\, Q_{\mathrm{LHV}} \left(\dot{m}_{HCp} + \sum_{i=1}^{N_i - 1} \dot{m}_{REHi}\right) \quad (7)$$

where $\dot{m}_{\mathrm{HCp}}$ is the fuel consumption rate at the main combustion chamber, $\dot{m}_{REHi}$ refers to the fuel mass flow entering the reheaters, ε_{HC} is the effectiveness of the heat exchangers (assumed equal), η_c combustion efficiency (also assumed the same), and Q_{LHV} the fuel lower heating value.

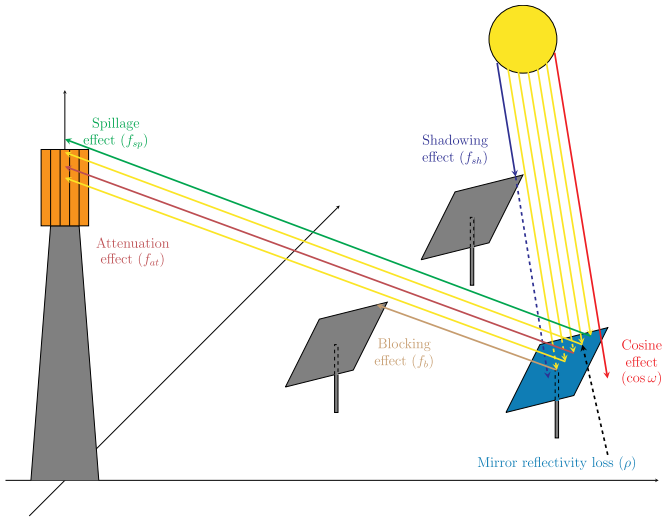

Fig. 5. Energy losses factors of the heliostat efficiency.

2.4. Multi-stage Brayton cycle model

For the multi-stage Brayton power block it is considered a working fluid behaving as an ideal gas with temperature dependent specific heats. Details on the assumptions for the losses or irreversibilities considered are summarized in Appendix A as well as the explicit equations for temperatures T_2 and T_4 in terms of the geometric and irreversibilities parameters. All other cycle temperatures can be calculated from those [33,45]. The power output provided by the plant, P, and its thermal efficiency, η_h, can be calculated through the heat rates by means of the cycle temperatures in terms of all the irreversibilities and geometric parameters: $P = |\dot{Q}_H| - |\dot{Q}_L|$ and $\eta_h = P/|\dot{Q}_H|$. The total heat input rate absorbed by the working fluid, $|\dot{Q}_H|$, can be calculated as:

$$|\dot{Q}_H| = |\dot{Q}_{HS}| + |\dot{Q}_{HCp}| + |\dot{Q}_{reh}| \begin{cases} |\dot{Q}_{\mathrm{HS}}| = \dot{m}\int_{T_x}^{T_{x'}} c_w(T)\,dT = f|\dot{Q}_H| \\ |\dot{Q}_{\mathrm{HCp}}| = \dot{m}\int_{T_{x'}}^{T_3} c_w(T)\,dT \\ |\dot{Q}_{reh}| = \dot{m}\,\overline{c}_{w,34}\,\varepsilon_t(N_t-1)\left(1-a_t^{-1/N_t}\right)T_3 \end{cases} \tag{8}$$

And the heat released by the working fluid to the ambient, $|\dot{Q}_L|$, is:

$$|\dot{Q}_L| = \dot{m}\int_{T_1}^{T_y} c_w(T)\,dT + \dot{m}\frac{\overline{c}_{w,12}}{\varepsilon_c}(N_c-1)\left(a_c^{1/N_c}-1\right)T_1 \tag{9}$$

Finally, it is important to stress that, as a consequence of the assumptions made in this model for the sequence of heat absorption processes, the following conditions for temperatures hold (see Fig. 2):

$$T_3 \geq T_{x'} \geq T_x \tag{10}$$

$$T_{HS} \geq T_x \tag{11}$$

$$T_{HC} \geq T_{x'} \tag{12}$$

3. Numerical implementation and working fluids

The thermodynamic model of the Brayton cycle was previously validated [33,34] by comparing with the SOLUGAS Project [25]. This project, developed by Abengoa Solar near Seville (Spain), tested a Brayton hybrid turbine in a pre-commercial scale of about 5 MWe. The present work is focused on the optimization and estimation of output records for a larger plant, in a commercial scale of about 20 MW. To achieve that aim the main system dimensions are taken from a commercial plant called GEMASOLAR [18] working on that power output range although within a different concept: Rankine cycle with molten salt storage. This plant includes a circular heliostat field and a cylindrical receiver. Details on the numerical parameters to run the model and its validation are contained in Appendix B.

In this work, a thermodynamic study of the plant performance for different working fluids is accomplished looking for better output records. However, the necessary study of the technical features of the devices is not carried out here. As stated by Olumayegun et al. [46], the most usual working fluids developing closed cycles in gas turbines are air, nitrogen, carbon dioxide, helium, and other noble gases and also gas mixtures. In this study, we consider the first four gases as working fluids. The widest experience in the design and operation of these cycles is associated to air cycles. However, the associated turbine inlet temperatures are high. Nitrogen has very similar characteristics than air but the curve for constant pressure specific heat is slightly different, specially for temperature between 300 and 900 K. The advantages of helium are the low pressure losses and its good heat transfer coefficient. But its design experience is smaller and its turbine inlet temperatures are also high. Finally, for the carbon dioxide, solar applications for supercritical CO_2 are being studied in order to reduce the work required by the compressor [33,47], but researches with subcritical CO_2 are still scarce.

In the particular case of the pressure and temperature intervals experienced by the fluids, three of them develop subcritical cycles: dry air, nitrogen (N_2) and carbon dioxide (CO_2); meanwhile, the other one, helium (He), develops a transcritical cycle (see Fig. 4 of [33]). Table 1

collects some thermodynamic data for these fluids, including critical pressure and temperatures. The approximate Brayton cycles developed by each fluid in $p-T$ diagrams were presented in Fig. 4 of [33]. In all cases, the specific heats are considered as temperature dependent. Polynomial fittings were taken from Ref. [48]. The explicit form of the polynomials can be found in Table 1 of [33]. It is interesting the fact that the average specific heat of the helium is four times the ones of the other fluids, as it can be seen in Table 1.

4. On design pre-optimization

In this section, numerical plant output records are analyzed for different configurations and different working fluids at the design point (see Table 4 in Appendix B). The efficiency of each heliostat is computed and represented in Fig. 6. It has been proven that the highest efficiency is related to the heliostats opposite to the Sun [42]; therefore, to the North heliostats at design point (noon). The average efficiency of the heliostats field at these conditions is 0.4961.

The evolution of the overall thermal efficiency, the fuel conversion rate, the power output, the solar collector temperature, and the solar share with the pressure ratio is depicted for the aforementioned working fluids and for different configurations in Figs. 7–11. The analyzed cases correspond to the one-turbine and one-compressor configuration ($N=1$), both recuperative and non-recuperative; and to the two ($N=2$), three ($N=3$), and infinite expansion and compression stages ($N\rightarrow\infty$) only in the recuperative mode. The cases of infinite stages are represented in order to visualize the maximum values that the variables could take, as a limit case.

The overall thermal efficiency in this study (Fig. 7) behaves in a similar way that for a smaller plant, SOLUGAS of about 5 MW [25,33] (note that in Ref. [33] heliostat field efficiency was calculated in an approximate averaged way). At the light of this figure, it can be concluded that only for some fluids (He, air, and N_2) and $N=1$ overall efficiency has a maximum in terms of r_p, *i.e.*, there is an optimum pressure ratio. In all other cases, curves increase monotonically, so larger pressure ratios lead to larger overall efficiencies. Numerical values are larger for He because of the reasons that will be detailed later on. For $N=1$ and small values of r_p overall efficiency in the recuperative case is larger than in the non-recuperative one for all fluids except CO_2. In the latter recuperation is advantageous in all the surveyed interval of pressure ratios.

In addition, curves of the fuel conversion rate, r_e (see Fig. 8), for He resemble those for SOLUGAS (see Fig. 10 in Ref. [33]). However, for the other three working fluids, these fuel conversion rate curves are quite different. Now, r_e decreases with the pressure ratio for any number of compression/expansion stages in an approximately exponential way, very fast up to values of $r_p\simeq 4-5$ (depending on the multi-stage configuration) and more slowly afterwards. This change is due to the new scaling up of the plant. Numerically, high values for r_e are found (about 4 times larger than for SOLUGAS) except for He. For $N=1$ non-recuperative layout, r_e, always increase with r_p (also except for He where there is a wide plateau in the interval $r_p\simeq 10-20$).

In the case of the power output, P, evolutions are very similar to those of overall efficiencies as it can be observed in Fig. 9. Only for He, N_2, and air and for the single stage plant configuration power output displays a (flat) maximum as a function of r_p.

Another interesting variable evolution is the solar collector temperature, depicted in Fig. 10. There is a noticeable difference between non-recuperative and recuperative configurations. In the first case, the temperature rises with the pressure ratio and, in the second one, it decreases. It should be also highlighted that the temperature increases when the number of expansion and compression stages does. It is of vital importance to control the solar collector temperature since the receiver materials themselves impose a temperature limit that could not be exceeded. Then, plant configurations associated with lower temperatures are more interesting from the viewpoint of the materials for the receiver. The lowest temperatures are predicted for He in the non-recuperative single stage case for low pressure ratios. In this case, the tubular receiver associated with the circular solar field should withstand temperatures below 1000 K for $r_p<12$. Temperatures for dry air and the other fluids in the same non-recuperative single stage case are all over 1000 K. For all multi-stage configurations smaller temperatures are required as r_p increases.

For case of He, as solar collector temperatures are smaller, the choice of a tubular receiver in a circular field could be feasible. However, when working with the other two configurations associated to higher temperatures, current tubular receivers are not the best option. Thus, the tubular receiver and circular field should be replaced by a cavity receiver with a wedge field meanwhile the limits of temperatures are surpassed [13,15,17].

Table 2 summarizes the maximum values of the overall thermal efficiencies for the four working fluids and for different numbers of turbines and compressors (assumed equal). Furthermore, the corresponding pressure ratio and the relative growth of the overall efficiency, of the fuel conversion rate, and of the power output are displayed. Comparison is always with respect to the design pressure ratio of the gas turbine ($r_{p,DP}=23.4$). For the dry air single recuperative configuration, an increase of almost 7 % in the overall thermal efficiency could be reached by reducing the pressure ratio to the half. As it can be also deduced from Fig. 7, the global efficiency for He in the single recuperative case can be highly increased if the pressure ratio is drastically reduced. Note that in some multi-stage configurations a positive increase or η corresponds to a decrease of r_e because of the corresponding increase in fuel consumption.

The behavior of solar share, Fig. 11, is easy to understand from the evolution of solar collector temperatures (see Fig. 10). Globally, the numerical values of f are smaller for He because T_{HS} are lower and so, more fuel is to be burned to achieve turbine inlet temperature. Numerical differences between numerical values for He and the other fluids are important as seen in the figure. The evolution with the number of stages is identical for all fluids. As more compression/expansion stages are considered, collector temperature decreases and so, more fuel is burned in the reheaters. So, the solar share decreases with the number of stages. In respect to the evolution with the pressure ratio, for recuperated configurations T_{HS} decreases with r_p, and similarly does f. In this case, the better configurations to take advantage of the solar input are those with small pressure ratios. For the single stage, non-recuperated configuration, both T_{HS} and f increase with r_p.

The choice of possible optimum configurations is carried out taking into account three features: high overall thermal efficiencies, low solar collector temperatures, and large solar share (although the last two ones are not independent). Three particular configurations have been selected: α, dry air single non-recuperative ($\eta=0.18$, $T_{HS}=1300$ K, $f=0.60$); β, dry air two compression and expansion stages recuperative ($\eta=0.28$, $T_{HS}=1420$ K, $f=0.40$); and γ, He single non-recuperative configuration ($\eta=0.32$, $T_{HS}=925$ K, $f=0.16$). The off-design analysis in the next section will be performed on these cases.

A Sankey diagram is represented for each of these configurations (see

Table 1
Some thermodynamic properties of the four considered working fluids: molecular weight (M), critical temperature and pressure (T_c and p_c respectively) and mean values of the constant pressure specific heat ($\overline{c}_w$) and adiabatic coefficient ($\overline{\gamma}$).

	He	N_2	Dry air	CO_2
M (g/mol)	4.00	28.01	28.97	44.01
T_c (K)	5.1953	126.19	132.84	304.13
p_c (bar)	2.2761	33.958	38.501	73.773
$\overline{\gamma}$	1.6667	1.3561	1.3458	1.1986
$\overline{c}_w$ [J/(g K)]	5.1965	1.1354	1.1202	1.1587

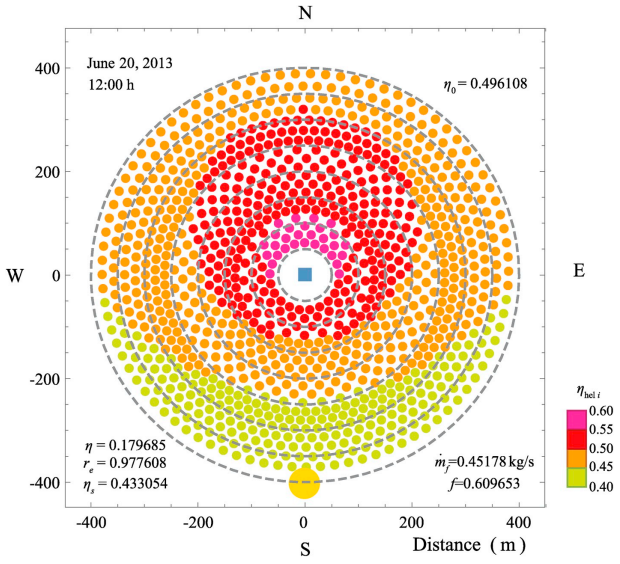

Fig. 6. Heliostat efficiencies at design conditions.

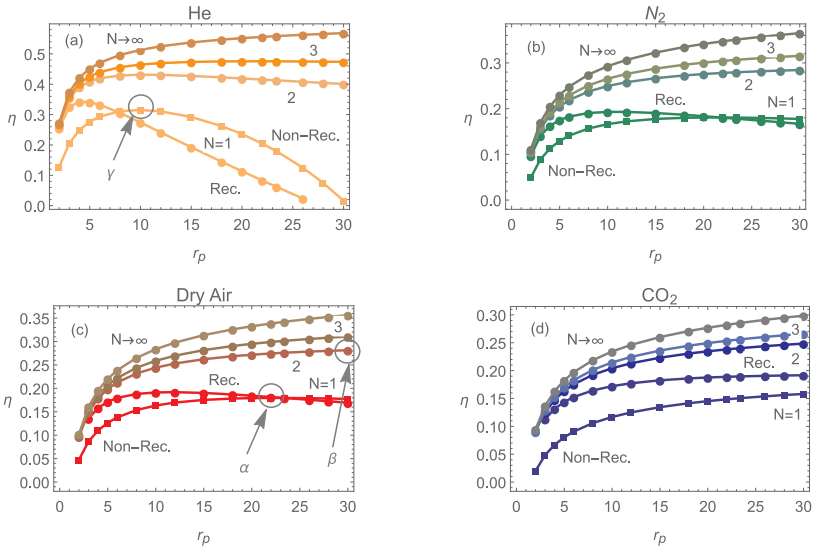

Fig. 7. Overall thermal efficiency as a function of the pressure ratio for He (a), N_2 (b), dry air (c), and CO_2 (d). One, two, three, and infinite compression and expansion stages are considered. Circle markers indicate recuperative configurations and square ones corresponds to non-recuperative case (only for N = 1). Three particular configurations, denoted α, β, and γ, are highlighted (as discussed hereinafter in the text).

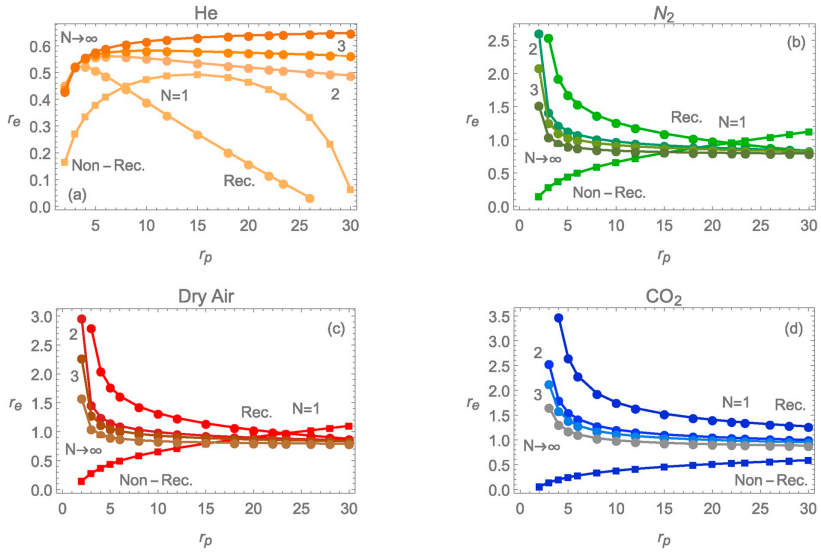

Fig. 8. Fuel conversion rate as a function of the pressure ratio for He (a), N_2 (b), dry air (c), and CO_2 (d). One, two, three, and infinite compression and expansion stages are considered.

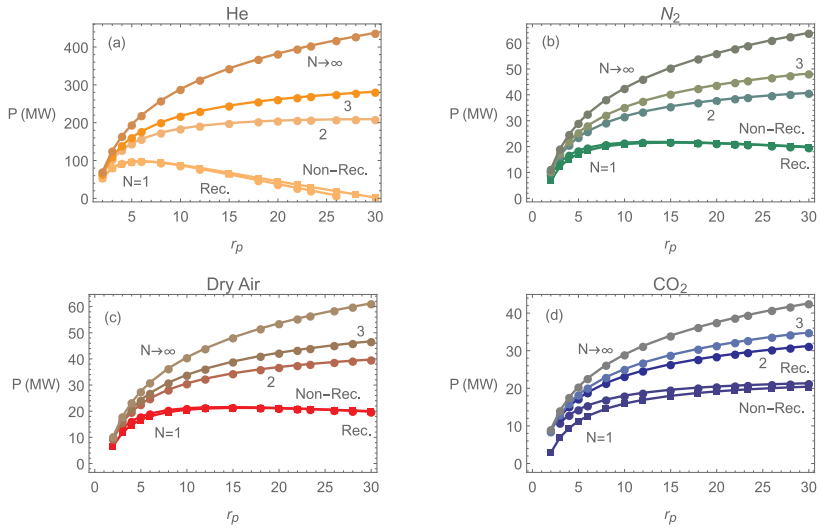

Fig. 9. Power output as a function of the pressure ratio for He (a), N_2 (b), dry air (c), and CO_2 (d).

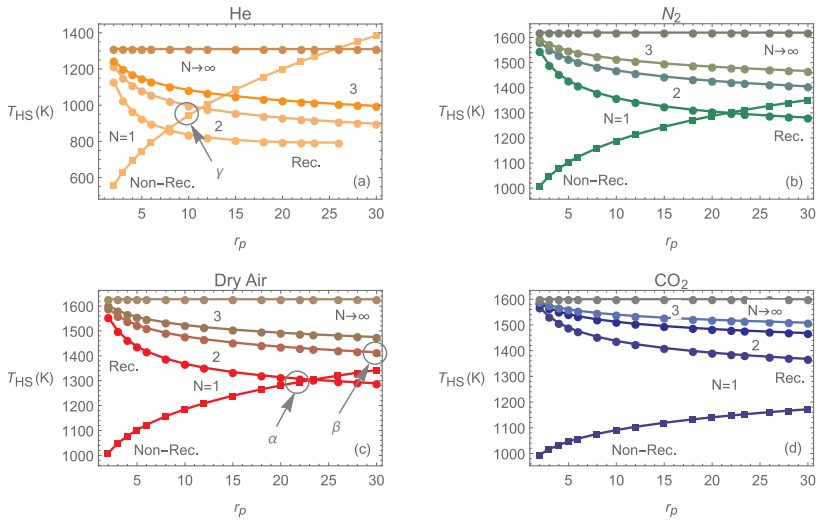

Fig. 10. Solar collector temperature as a function of the pressure ratio for He (a), N_2 (b), dry air (c), and CO_2 (d).

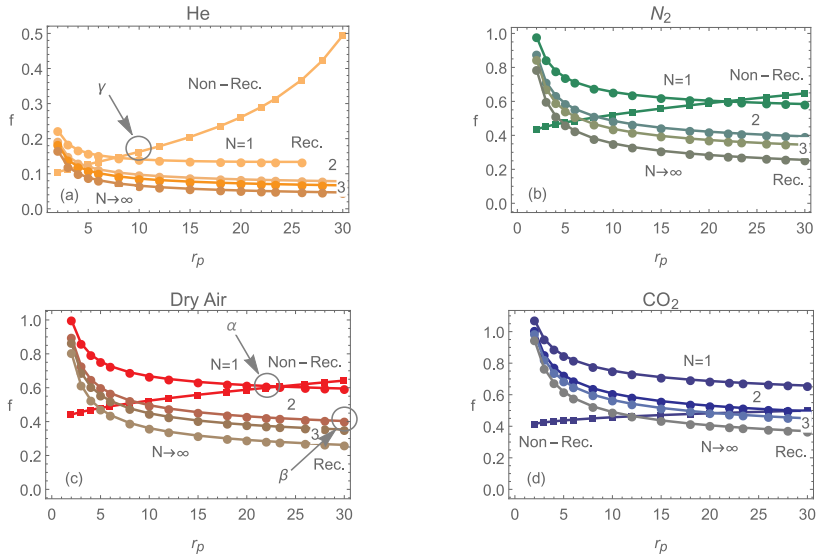

Fig. 11. Solar share as a function of the pressure ratio for He (a), N_2 (b), dry air (c), and CO_2 (d).

Table 2
Relative variations of output records achieved by choosing the optimum pressure ratio regarding overall thermal efficiency in each case with respect to the design pressure ratio of the gas turbine (dry air, $r_{p,DP} = 23.4$, recuperative) are shown. The number of compression and expansion stages (N), the maximum overall efficiency, η_{max}, its corresponding pressure ratio, $r_{p,\eta_{max}}$, and relative improvements of overall thermal efficiency, $\Delta\eta$, fuel conversion rate Δr_e, and power output, ΔP, are included.

N	η_{max}	$r_{p,\eta_{max}}$	$\Delta\eta$(%)	Δr_e(%)	ΔP(%)
Dry air					
1	0.191862	12	6.91837	27.3001	3.173
2	0.28144	30	56.8371	− 12.3100	90.98274
3	0.310565	30	73.0677	− 13.9978	124.628
1	0.192919	10	7.50699	30.0217	3.44557
2	0.284472	30	58.5266	− 13.8591	95.8396
3	0.315487	30	75.8101	− 14.9183	131.873
1	0.191657	30	6.80423	31.0573	2.50332
2	0.24847	30	38.4641	3.10643	50.1376
3	0.266093	30	48.2845	− 1.67984	67.595
He					
1	0.342435	4	90.8272	− 46.0711	349.6
2	0.4313	10	140.349	− 42.9728	786.468
3	0.475587	22	165.029	− 41.094	1182.7

Fig. 12). Energy inputs are those coming from the solar contribution and from combustion. In each plot, the total heat input rate is normalized to unity. In the two-stage example (Fig. 12(b)) two terms contribute to fuel combustion, that from the main combustion chamber, $\dot{m}_{f,HCp}Q_{LHV}$, and that from the reheater in between turbines, $\dot{m}_{f,REH}Q_{LHV}$. It is noteworthy that $\dot{m}_{f,REH}Q_{LHV}$ is larger (about 3.7 times larger). This is because the heliostat field at design conditions is capable to increase the fluid temperature to a value T_x' not far from the turbine inlet temperature, T_3 (see Fig. 2). On the other hand, the reheater has to increase the temperature from T_4 (that is quite below T_x^t) to T_3, so a comparatively larger heat input is required. Cycle temperatures will be discussed in detail below.

These diagrams include also the main losses in each subsystem with this notation: $\dot{Q}_0$ are the optical losses in the heliostat field, $\dot{Q}_l$ are the heat losses in the receiver, $\dot{Q}_{iHS}$ are the losses in the heat transfer from the receiver to the working fluid of the turbine, $\dot{Q}_C$ are the losses in the combustion chamber, and $\dot{Q}_{iHC}$ are the losses in the heat exchanger associated to the combustion chamber. In all cases it is apparent that the main losses comes from the optical losses in the heliostat field. In the case of He, solar contribution is small and so, optical losses are small. In consequence power output (and also overall efficiency because heat input is normalized) is large. On the other hand, for dry air mono-stage recuperative configuration, solar contribution represents more than 80 % of the total heat input. So, as a conclusion, in all configurations where the relative weight of the solar subsystem is large, optical losses are also large and the overall efficiency is smaller. A similar reasoning also explains the different scales in the values of the fuel conversion efficiency, r_e, displayed in Fig. 8.

5. Off-design analysis

In this section, a daily and a seasonal study is carried out by selecting four different days at the beginning of the four seasons. Solar field configuration was set at the design point (Fig. 6). Now, in off-design conditions, solar field for the four seasons is computed at any hour. For instance, Fig. 13, shows the efficiency of the heliostats and the averaged one at a particular hour (14:00 h UTC) for any season. The highest efficiency is found for summer and the smallest, for winter (relative increase in summer with respect to winter is about 13.1%) while autumn and spring lead to intermediate values. During summer no

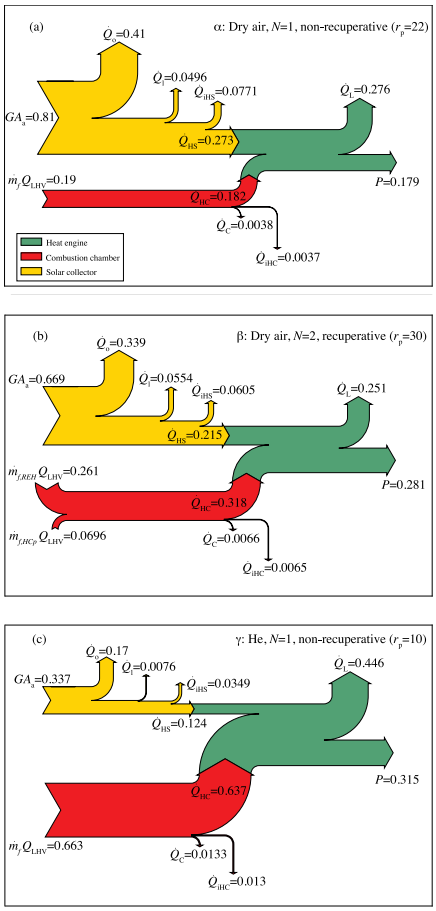

Fig. 12. Sankey diagrams for heat flows in the plant at the design point for three selected configurations, α, β, and γ. Heat input is normalized to unity in each case. (a) Dry air, non-recuperative, single stage; (b) Dry air, recuperative, N = 2; and (c) He, N = 1, non-recuperative. Notation for the losses: $\dot{Q}_0$ are the optical losses in the heliostat field, $\dot{Q}_l$ are the heat losses in the receiver, $\dot{Q}_{iHS}$ are the losses in the heat transfer from the receiver to the working fluid of the turbine, $\dot{Q}_C$ are the losses in the combustion chamber, and $\dot{Q}_{iHC}$ are the losses in the heat exchanger associated to the combustion chamber.

heliostat has efficiencies below 0.35. During winter there are more heliostats than in summer with high efficiencies (over 0.55) but at the same time there are a considerable amount of heliostats with poor efficiencies, between 0.20 and 0.25. So, the distribution of efficiencies has shorter tails to worse efficiencies in summer than in winter. These points are plotted as a bar diagram in Fig. 14.

As it was aforementioned, the off-design analysis is carried out for

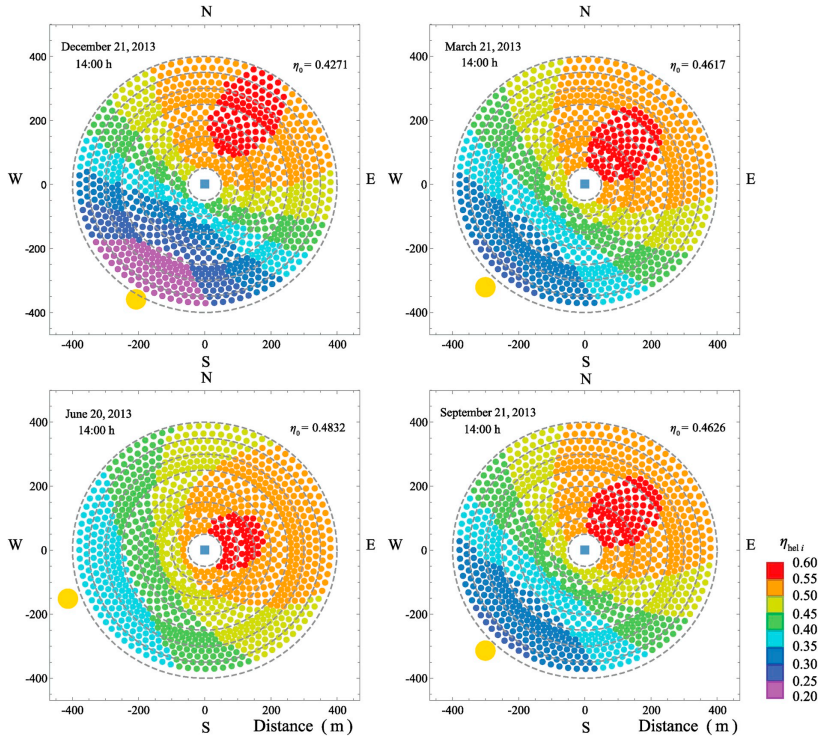

Fig. 13. Solar field efficiency plot for a representative day of each each season at the same hour.

three configurations: α, dry air single non-recuperative case; β, dry air two compression and expansion stages recuperative layout; and γ, He single non-recuperative configuration. In this way, for the three selected optimum configurations, output records as efficiencies, fuel conversion rate, and solar share have been computed and represented throughout the four seasons (Figs. 15–17). Meteorological data employed in this simulation are taken from real measures not averaged nor smoothed [49] (see Fig. 3 in Ref. [34]).

These figures present some common features and different numerical scales depending on the particular plant configuration. Among the common characteristics the following are stressed. Solar subsystem efficiency, η_s, always reaches a maximum about 10 h (UTC) and then decreases slowly during the daytime. It is slightly below the optical efficiency, η_0, of the heliostat field because η_s includes also the heat transfer losses in the receiver. The thermal efficiency of the heat engine, η_h, is approximately constant during any day and any hour, it only depends on the ambient temperature, because the turbine inlet temperature was considered as constant. Fuel conversion efficiency, r_e, increases during the daytime up to a maximum value about 14 h that corresponds with a decrease of the overall efficiency, η. During the daytime all subsystems are coupled and so, losses increase. During the night the solar subsystem is set off and all the losses come from the Brayton cycle. Solar share curves are widest and highest during summer but never reach $f = 1$, *i.e.*, for the dimensions of the heliostat field and receiver, the plant is always working on a hybrid mode. Maximum values as shown in Fig. 15, about 0.7, are reached for dry air in the case of a single stage non-recuperative configuration. On the other side, for He the solar share never goes up of about 20%. As was mentioned before for the Sankey's schemes in Fig. 12 the largest values of overall efficiency are obtained in the case of He with a single stage non-recuperative configuration because the contribution of the solar subsystem is smaller.

With respect to the temperatures of the heat absorption process (see Figs. 18–20), it is remarkable that the inclusion of a recuperator increases the working temperature of the solar collector because the temperature of the fluid at the solar receiver inlet, T_x, is higher (about 900 K, see Fig. 19). This fact makes that T_{HS} increases above 1400 K in summer. Actually, in this case (dry air, recuperative, $N = 2$), the temperature of the solar collector, T_{HS}, can be above that of the combustion chamber, T_{HC}, because losses in the heat transfer from the solar subsystem to the fluid are larger. On the other side, solar receiver temperatures are below 1000 K for He, $N = 1$, non-recuperative layout (see Fig. 20). In this case, the solar subsystem only increases the temperature of the working fluid from T_2 to T_x' about 100 K.

Fig. 21 shows the natural gas consumption and the corresponding carbon dioxide emissions during a day for the three selected configurations and both for hybrid and non-hybrid (only combustion) modes for

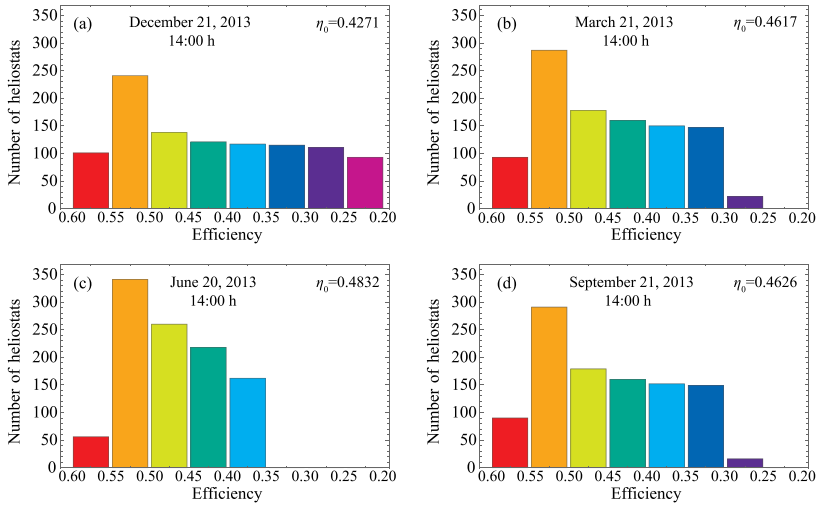

Fig. 14. Histogram corresponding to the number of heliostats with a given efficiency in the conditions of Fig. 13.

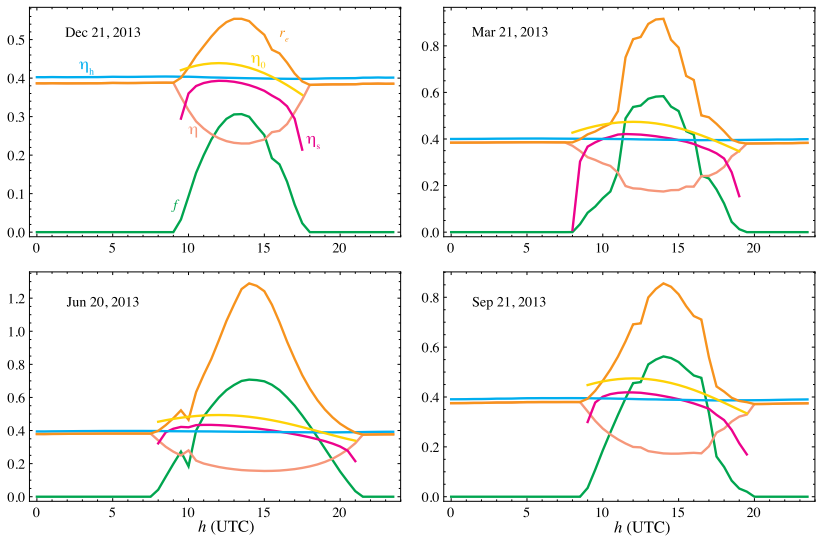

Fig. 15. Daily and seasonal evolution of overall thermal efficiency (η, pink), heat engine efficiency (η_h, cyan), solar subsystem efficiency (η_s, magenta), heliostat field optical efficiency (η_0, gold), fuel conversion rate (r_e, orange), and solar share (f, green) for configuration α. Time is represented in UTC hours. (For interpretation of the references to colour in this figure legend, the reader is referred to the Web version of this article.)

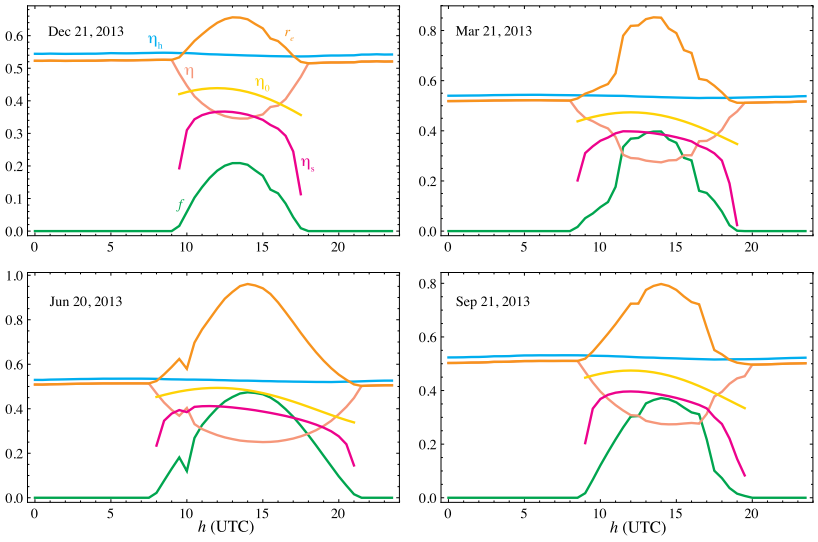

Fig. 16. Daily and seasonal evolution of solar share and efficiencies for configuration β. Notation as in Fig. 15.

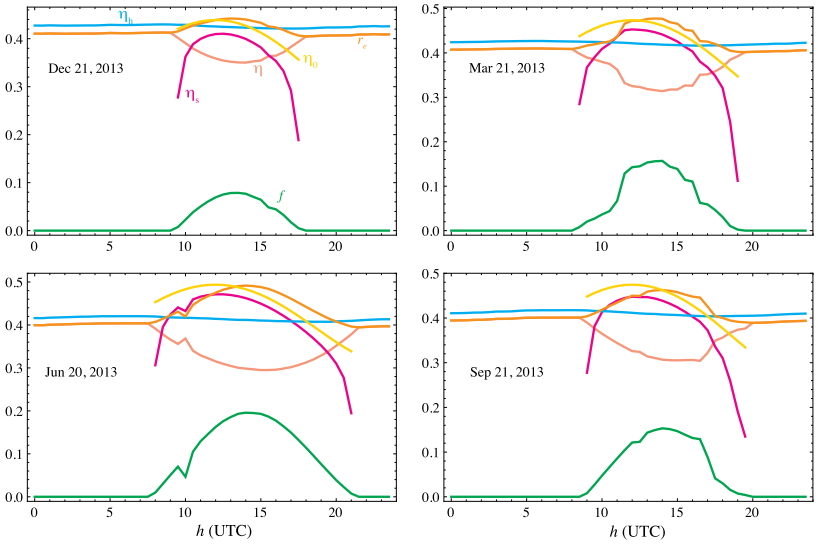

Fig. 17. Daily and seasonal evolution of solar share and efficiencies for configuration γ. Notation as in Fig. 15.

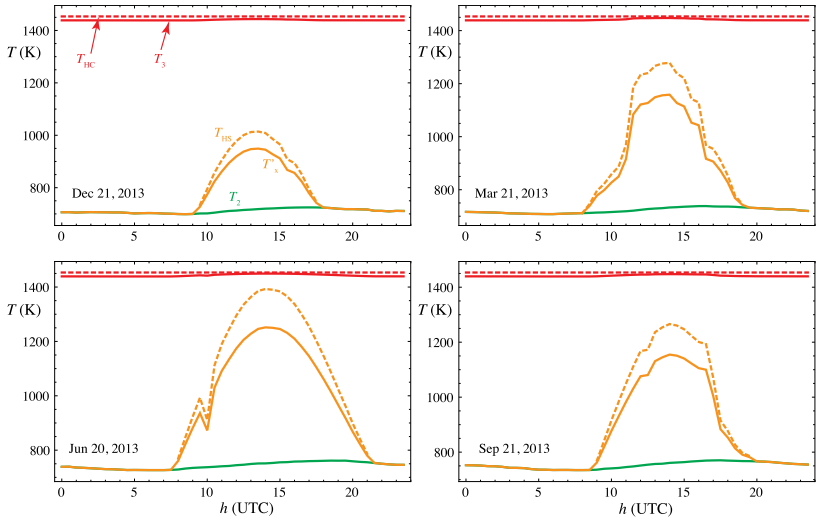

Fig. 18. Daily and seasonal evolution of compressor outlet temperature (T_2, green), solar collector outlet temperature ($T_{x'}$, solid orange), solar collector temperature (T_{HS}, dashed orange), turbine inlet temperature (T_3, solid red), and combustion chamber temperature (T_{HC}, dashed red) for configuration α. (For interpretation of the references to colour in this figure legend, the reader is referred to the Web version of this article.)

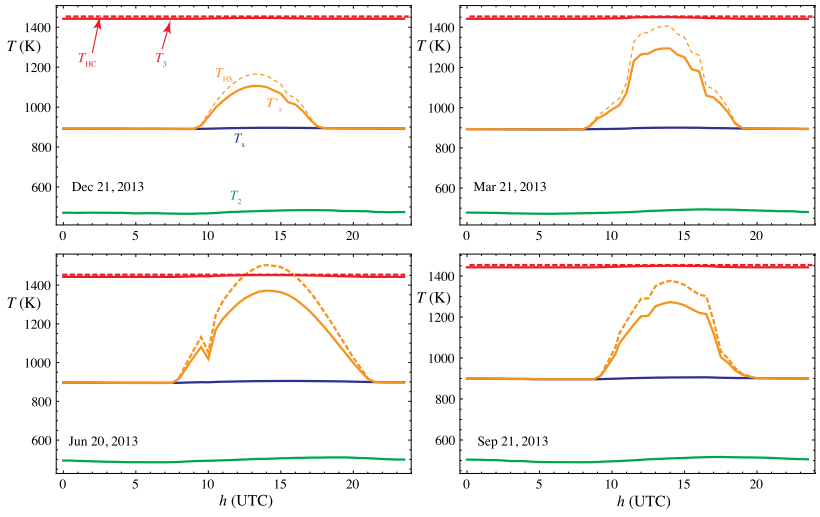

Fig. 19. Daily and seasonal evolution of temperatures for configuration β. Notation as in Fig. 18.

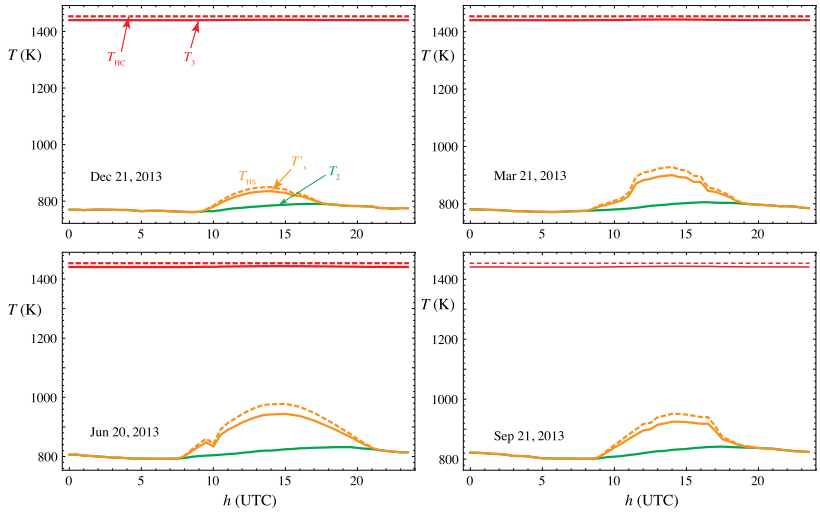

Fig. 20. Daily and seasonal evolution of temperatures for configuration γ. Notation as in Fig. 18.

comparing purposes. In the three configurations, it is clear that the difference between hybrid and non-hybrid mode is higher in summer, as a consequence of the associated higher irradiance and number of solar hours. In the case of He in single non-recuperative mode (Fig. 21(c)), differences between hybrid and non-hybrid configurations are smaller, in accordance with the lower solar share obtained before, which means that the solar contribution is relatively small. The better saving in fuel consumption and emissions is obtained for dry air, single stage, non recuperative configuration. It is about 22%. For dry air, $N = 2$, recuperative case, the savings in summer are about 13% and for the case of He, where the solar share is smaller, about 4%. In winter, the maximum savings are got for $N = 1$, dry air, non-recuperative case and amount 4%.

Finally, it should be stressed that all the results obtained in this section were computed with the optimum pressure ratio calculated at the design point in Sec. 4. At those conditions solar irradiance was taken as $G = 760$ W/m$_2$ (Table 4). The optimization process was repeated for several other values of G and approximately the same values of the optimum pressure ratios were found. So, all the results presented in this section can be considered as independent of the particular values of the pressure ratios chosen for the plant configurations considered. In other words, it was checked that the decision about the optimum pressure ratio regarding global efficiency is consistent throughout any day and any season.

6. Conclusions

In which refers to pre-design conditions, this work shows that a key point is to design the system as a whole, including ingredients from the solar field (dimensions and efficiency), the solar receiver (size and temperature level), and the gas turbine (working fluid, pressure ratio, recuperation and number of compression/expansion stages). Particularly, curves of all subsystems efficiencies as functions of the Brayton cycle pressure ratio were presented for four working fluids (dry air, nitrogen, carbon dioxide, and helium) at subcritical conditions (except for He where the cycle could be transcritical). Nitrogen and air lead to similar overall efficiencies and optimum pressure ratios although slightly better records are obtained for nitrogen. Helium causes very high power output and efficiencies (provided that the same working fluid mass rate is considered for all fluids for the sake of comparison). Subcritical CO_2 leads to a similar thermal overall efficiency that dry air but shows better fuel conversion efficiencies (at higher pressure ratios).

In all cases a substantial increase in overall efficiency is predicted when a single-stage plant configuration is substituted by a two-compressions two-expansions cycle (with a subsequent increase in fuel consumption). For larger number of compression/expansion stages, improvement is not so significant. The role played by a recuperator located in between the last turbine and the solar subsystem is also crucial. On one side, the recuperator increases overall efficiency (specially at low pressure ratios, although it depends on the peculiarities of the working fluid), but on the other it increases the temperature level of the solar receiver and so, the requirements for the materials. For all the fluids checked, solar receiver temperature decreases with higher pressure ratios for recuperative configurations and have the opposite behavior for single-stage non-recuperative layouts. In most configurations, temperatures are well above 1000 K, except single-stage configurations for He. It is noticeable that single-stage configurations for CO_2 lead to temperatures quite below those for air or nitrogen.

Numerical evaluation of losses in each plant subsystem was presented in detail. In relative terms, optical losses in the heliostat field seem to be the main bottleneck for the whole system. Thus, those configurations with larger solar share provoke worse values of overall plant thermal efficiency (but probably better values of the fuel conversion efficiency). Sankey's diagrams for losses show that there is a wide margin to set plant design for a particular solar field (by considering different working fluids, pressure ratios, number of compression/expansion stages, recuperation, etc.).

Daily and seasonal analysis have been reported for several selected plant configurations in hourly terms. For instance, dry air working on a single-stage non-recuperated cycle solar share is about 0.7 and allows

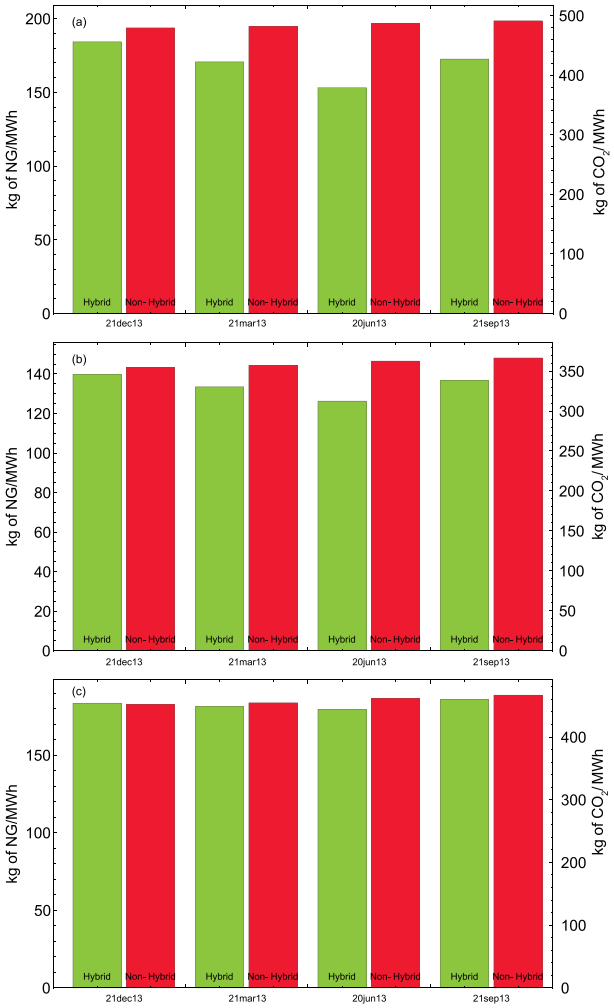

Fig. 21. Natural gas consumption (left axis) and carbon dioxide emissions (right) for the four different seasons and in both hybrid and non-hybrid configurations. (a) Configuration α; (b) configuration β; and (c) configuration γ.

fuel savings (with respect to a plant operating in a pure combustion mode with natural gas) and CO_2 emissions over 20% in summer and about 10% in winter (with solar shares about 0.3). Higher overall efficiencies (about 1.5 times larger) are obtained for dry air in a two-compression two-expansion stages with recuperation. In this case, a solar share of 0.45 in summer is predicted (in similar conditions) with a fuel saving about 13% with respect to non-hybrid operation. Finally, for helium in a single-stage non-recuperative cycle, solar share decreases to 0.2, solar receiver temperatures are considerable lower, efficiencies can reach values about 0.34, but fuel saving is poorer, about 4% in summer.

7. Summary and future work

A comprehensive model for CSP central tower power plants developing a hybrid Brayton cycle has been presented. The ultimate plant objective is to efficiently produce clean electricity at a scale of about

20 MW without intermittencies, with a reduced water consumption and with not too high investment costs. The model incorporates detailed solar field efficiency calculations and a simplified model for heat transfer losses at the tubular receiver. It also includes a flexible and realistic thermodynamic model for the gas turbine with all the main losses sources existing in real power blocks. So, the model for the overall plant encompasses rational, but at the same time comprehensive, submodels for the main plant subsystems. In this way efficiencies, solar share, power output, and other records can be obtained as combinations of the corresponding records for the plant subsystems. This approach allows, apart from obtaining realistic predictions for plant output parameters, to perform pre-design optimization studies considering the plant as a whole. And so, to propose overall plant configurations, to locate efficiency bottlenecks, and to propose optimum intervals for selected design parameters. Particularly in this work, different working fluids for the Brayton cycle developed by the gas turbine were analyzed, as well as single- or multi-stage compression and expansion plant layouts. The relevance of a recuperator in which respect to overall plant efficiency and temperatures at the solar receiver was also explored. Moreover, the model allows for numerical computations at off-design conditions for whichever plant location and seasonal or meteorological conditions. So, hourly curves can be obtained for any parameter and the influence of plant design estimated in close to reality conditions.

As reference values to size the installation, GEMASOLAR plant dimensions were adopted [50]. This commercial plant, located at the south of Spain is based on a different concept, vapor turbine with molten salt storage, but one of the objectives of this work was to analyze the possibilities of a similar size plant working on a hybrid Brayton cycle without storage. Several subcritical and transcritical working fluids for the Brayton cycle were considered. The following conclusions were extracted:

- Numerical overall efficiencies obtained for air and nitrogen are similar, as well as the optimum pressure ratios. Maximum efficiencies are slightly above for nitrogen.
- Subcritical carbon dioxide gives similar overall efficiencies but better solar share and fuel conversion efficiencies than air or nitrogen.
- Transcritical helium provokes very good overall efficiencies but lower solar share because achieved solar collector temperatures are below those for the other fluids.
- For all fluids collector temperatures for the optimized configurations are in the interval $[925, 1420]$ K.

Analyses, as the one developed here, suggest as possible lines for future research at least the following: to improve solar field design as a main restriction to enhance overall plant output records, to increase the temperature limits associated to the materials and the design of the solar receiver because most plant configurations require temperatures around or above 1000 K, to explore (simultaneously) thermodynamic plant configurations capable to produce good efficiencies at reduced maximum temperatures, and to analyze and experience the behavior of the turbomachinery (compressors and turbines) and heat exchangers with different working fluids in wide temperature and pressure intervals. The achievement of at least some of these objectives could allow to suggest plant designs and materials that make this plant concept interesting from the commercial viewpoint to companies specialized in the production of clean energy.

Acknowledgements

Financial support from University of Salamanca and Junta de Castilla y León (project SA017P17) is acknowledged. R.P. Merchán also acknowledges a pre-doctoral grant by Banco de Santander of Spain.

Appendix A. Brayton cycle model details

Next, the cycle stages developed by the working fluid, considered as an ideal gas with mass flow rate is $\dot{m}$ and with temperature dependent specific heat, $c_w(T)$, are summarized:

1. In the first stage, the working fluid is compressed by means of N_c compressors, with an isentropic efficiency $\varepsilon_c = (T_{2s} - T_1)/(T_2 - T_1)$, being T_1 the temperature at which the working fluids enters the first compressor, T_2, the exit temperature of the last compressor and T_{2s}, the hypothetical temperature after compressions if they were isentropic. It is assumed that the T_1 temperature is the same for all compressors because an intercooler is placed in between each pair of them.
2. The second stage corresponds to the heat absorption process, divided into three substages. The working fluid temperature is first increased up to T_x by means of a recuperator with efficiency $\varepsilon_r = (T_x - T_2)/(T_4 - T_2)$, where T_4 refers to the temperature after the expansion process. Then, the solar heat is provided, rising the temperature up to $T_{x'}$. And, finally, heat from the main combustion chamber is absorbed by the working fluid, reaching the temperature T_3. The global pressure decay in the total heat absorption process is quantified by the parameter $\rho_H = (p_{\mathrm{H}} - \Delta p_{\mathrm{H}})/\, p_{\mathrm{H}}$, even though each heat absorption substage has its own pressure losses. This parameter is a measure of the whole pressure decay in the heat input process. p_{H} is the highest pressure and $p_{\mathrm{H}} - \Delta p_{\mathrm{H}}$, the first turbine inlet pressure.
3. The working fluid expansion takes place in the third stage through N_t turbines that have an associated isentropic efficiency, $\varepsilon_t = (T_4 - T_3)/\,(T_{4s} - T_3)$. T_{4s} corresponds to the temperature after the expansion processes if they were isentropic. An intermediate reheater is needed between each pair of turbines for reaching the same inlet temperature, T_3, in all cases.
4. In the last stage, the working fluid releases the excess heat in two processes. First, by means of the recuperator, which decreases the temperature to T_y. And, then, with the help of a heat exchanger connected to the ambient, whose effectiveness is $\varepsilon_{\mathrm{L}} = (T_1 - T_y)/(T_L - T_y)$, recovering in this way the initial conditions of the cycle. T_L refers to the ambient temperature. In the same way as in the heat absorption process, for the heat release process, a global pressure loss parameter can be defined: $\rho_{\mathrm{L}} = (p_{\mathrm{L}} - \Delta p_{\mathrm{L}})/p_{\mathrm{L}}$, where p_{L} is the pressure at the exit of the expansion processes and $p_{\mathrm{L}} - \Delta p_{\mathrm{L}}$ is the lowest pressure.

The global pressure ratio of the whole cycle is defined as: $r_p = p_{\mathrm{H}}/(p_{\mathrm{L}} - \Delta p_{\mathrm{L}})$. One of the advantages of this model is that analytical expressions for the main cycle records can be obtained: all the temperatures involved in the cycle can be expressed in terms of a set of parameters associated with the cycle size and geometry and with the thermal irreversibilities, as our group shown in Ref. [34]. For T_2 and T_4, it is possible to obtain:

$$T_2 = \frac{(1-\varepsilon_L)(1-\varepsilon_r)[\varepsilon_{\mathrm{HC}} T_{\mathrm{HC}} + \varepsilon_{\mathrm{HS}} T_{\mathrm{HS}}(1-\varepsilon_{\mathrm{HC}})] + \varepsilon_L T_L \left[Z_t^{-1} - (1-\varepsilon_{\mathrm{HC}})(1-\varepsilon_{\mathrm{HS}})\varepsilon_r\right]}{\left[Z_c^{-1} - (1-\varepsilon_L)\varepsilon_r\right]\left[Z_t^{-1} - (1-\varepsilon_{\mathrm{HC}})(1-\varepsilon_{\mathrm{HS}})\varepsilon_r\right] - (1-\varepsilon_{\mathrm{HC}})(1-\varepsilon_{\mathrm{HS}})(1-\varepsilon_L)(1-\varepsilon_r)^2} \tag{13}$$

$$T_4 = \frac{[\varepsilon_{HC} T_{HC} + \varepsilon_{HS} T_{HS}(1-\varepsilon_{HC})]\left[Z_c^{-1} - (1-\varepsilon_L)\varepsilon_r\right] + \varepsilon_L T_L (1-\varepsilon_{HC})(1-\varepsilon_{HS})(1-\varepsilon_r)}{\left[Z_c^{-1} - (1-\varepsilon_L)\varepsilon_r\right]\left[Z_t^{-1} - (1-\varepsilon_{HC})(1-\varepsilon_{HS})\varepsilon_r\right] - (1-\varepsilon_{HC})(1-\varepsilon_{HS})(1-\varepsilon_L)(1-\varepsilon_r)^2} \quad (14)$$

Z_c refers to $Z_c = 1 + \frac{1}{\varepsilon_c}(a_c^{1/N_c} - 1)$ and Z_t to $Z_t = 1 - \varepsilon_t\left(1 - \frac{1}{a_t^{1/N_t}}\right)$. Both a_c and a_t are two parameters associated with pressure ratios of compressors and turbines: $a_c = r_p^{(\overline{\gamma}_{12}-1)/\overline{\gamma}_{12}}$ and $a_t = (\rho_H \rho_L r_p)^{(\overline{\gamma}_{34}-1)/\overline{\gamma}_{34}}$. $\overline{\gamma}_{12}$ is the average value of the adiabatic coefficient in the temperature interval $[T_1, T_2]$ and $\overline{\gamma}_{34}$, the same but in the temperature interval $[T_3, T_4]$.

Appendix B. Numerical data and validation

The main differences between GEMASOLAR plant and our model are summarized in Table 3. Regarding the power conversion system, our model employs a Brayton cycle instead of the Rankine used by GEMASOLAR because one of the objectives of this work is to compare both technologies in a similar size plant. Gas turbines consume less water than steam ones that is an additional advantage in regions with good solar conditions and (usually) scarce water resources. They are also efficient, reliable and flexible since thermal inertia is not too high [51].

Moreover, our model describes a system which gets the constant power by means of a combustion chamber rather than the molten salt storage system, that allows GEMASOLAR to produce energy up to 15 h without solar radiation [18]. This scheme is chosen because of its direct integration in gas turbine plants and because allows a very flexible plant operation avoiding an elevated number of heliostats.

As it has been already mentioned, the gas turbine has been chosen looking for a commercial turbine with a power output similar to the one of GEMASOLAR, so the difference between both of them is about 1 MW. Finally, with this model, the total number of heliostats is an output parameter, not an input one as it is usual. This happens because the number of rows is elected and the maximum number of heliostats that fit in each row are placed in the field (taking into account all the considerations in Sec. 2.2). Then, the rows number is chosen by taking into account a Thermoflex® simulation performed for the overall model validation. In addition, although GEMASOLAR employs 2650 heliostats, in our simulation 1037 heliostats are considered. A higher number of heliostats results in too much high solar collector temperatures that the materials cannot withstand.

Table 3
Main differences between GEMASOLAR plant and our model.

	Our model	Gemasolar
Thermodynamic cycle	Brayton (gas turbine)	Rankine (steam turbine)
Constant power means	Hybridization (combustion chamber)	Molten salt storage + small combustion chamber
Power output	20.91 MW	19.9 MW
Heliostats number	1037 (19 rows)	2650

Next the main parameters set to run the model previously developed and its validation are detailed. Meteorological data (direct solar irradiance, G, ambient temperature, T_L, and ambient pressure, p_L) are taken from Meteosevilla [49] and gathered in Table 4. June 20, 2013, at 12:00 h is chosen as the design point time. However, regarding the off-design analysis, four days representing the four seasons are selected [34] and all the calculations are carried out every half an hour throughout each day. The location considered for the plant is the same as GEMASOLAR, Fuentes de Andalucía (Seville, Spain) [50].

Table 4
Meteorological, date and location data at the design point for the on-design simulation.

	Date and location
φ	37°33′29.11″ *N* (Fuentes de Andalucía, Seville)
Day of the year	171
Time (h)	12
Meteorological data[49]	
T_L (K)	296.55
p_L (bar)	1.00439
G (W/m^2)	760

Heliostat field and solar receiver

Table 5
Table of parameters values employed in the Mathematica® simulation (GEMASOLAR plant [41]).

Parameter	Symbol	Value
Height of the tower supporting the receiver	*THT*	130 m
Height of the receiver	*LR*	10.5 m
Diameter of the receiver	*DR*	8.4 m
Height of each heliostat	*LH*	10.95 m
Width-height ratio of each heliostat	w_r	1.0
Focusing	–	Simple

(*continued on next page*)

Table 5 (*continued*)

Parameter	Symbol	Value
Separation distance between adjacent heliostats	d_s	3.285 m
Minimum radius of the heliostat field	R_{min}	65 m
Standard deviation due to Sun shape	σ_{Sun}	2.51 mrad
Blocking and shadowing	$f_b.f_s$	0.95
Actual mirror reflectivity	ρ	0.836

Main parameters associated to the solar subsystem are gathered in Table 5. A tubular receiver of 10.5 m height and diameter 8.4 m is placed at the top of a 140 m height tower. Every heliostat is assumed as square ($w_r = 1$), with 10.95 m of side. In this way, the heliostat area is approximately 120 m_2, the same as in GEMASOLAR [50]. With respect to the heliostats distribution, a separation distance between adjacent heliostats of 3.285 m is considered [36]. The diameter of the field is about 800 m. The minimum distance from the tower to the first heliostats row is taken as 65 m [36]. The standard deviation due to Sun shape is assumed 2.51 mrad, as in [36].

Regarding the optical efficiency of the heliostat field, the blocking factor and the shadowing factors are taken together and constant in such a way that $f_b.f_{sh} = 0.95$ as other authors use to do [36,37,40]. Also, the actual mirror reflectivity, $\rho = 0.836$, is the same for all the heliostats and it is the product of the nominal reflectivity ($\rho_n = 0.88$) by the nominal cleanliness ($C_n = 0.95$) [41].

A cylindrical receiver of height 10.5 m and of diameter 8.4 m is located at the top of the 150 m height tower. A simple focusing is supposed for simplicity, but the model can work also with double and triple focusing.

Power block validation

For the turbine choice and validation, the Thermoflex® database [52] has been employed. This database presents detailed information about different commercial gas turbines. The decision of the particular turbine has been done looking for a commercial turbine with a power output similar to the one of GEMASOLAR [18] (19.9 MW), an adequate turbine inlet temperature, and a good thermal efficiency. In this way, the ***Solar Titan 250-30000S gas turbine*** (Caterpillar) [53] was chosen. For the compressor, the ***Solar C*85 *gas compressor*** [53] was elected because it has the largest isentropic efficiency (above 89 %) from among the compatible compressors with the ***Solar Titan 250 gas turbine***.

Turbine validation data are gathered in Table 6. The first block are input data. For numerical computations, the working fluid mass flow, $\dot{m}$, and the overall pressure ratio, r_p, values are taken from Thermoflex® database [52]. The isentropic efficiencies of the turbine and compressor, ε_t and ε_c, are collected from Caterpillar® [53]. Pressure losses were assumed similar in the heat input and heat release, 9.4% in relative terms. The effectiveness of the recuperator was taken as 0.775.

The other parameters in Table 6 are output records obtained from the Brayton cycle model in Sec. 2.4. For the power output, our model predicts 20.91 ***MW***, which means a deviation of −0.89 % with respect to the Thermoflex® database. The predicted thermal efficiency deviates 2.37 % and the turbine outlet temperature, 2.95 %, which is the highest deviation. On the other hand, the smallest deviation corresponds to turbine inlet temperature, about 0.04 %.

Then, it can be concluded that the thermodynamic model of the turbine agrees very well with Thermoflex® data. It is important to note that this validation has been carried out for the mono-stage configuration and for dry air as working fluid.

Table 6
Parameters and output records values for Thermoflex® data and for the Mathematica® simulation in the turbine validation. (*) This parameter was taken directly from Caterpillar information [53].

Variable	Thermoflex® data	Mathematica® simulation (our model)	Relative deviation (%)
Input			
Working fluid mass flow ($\dot{m}$, kg/s)	67	67	–
Overall pressure ratio (r_p)	23.4	23.4	–
Compressor isentropic efficiency (ε_t)	$> 0.89^*$	0.895	–
Output			
Power output (P, MW)	21.20	20.91	− 0.89
Heat Rate (HR, kJ/kWh)	9256	9041	− 2.33
Thermal efficiency (η_h)	0.389	0.398	2.37
Turbine inlet temperature (T_3, K)	1450	1451	0.04
Turbine outlet temperature (T_4, K)	736	758	2.95

References

[1] Dunham M, Iverson B. High-efficiency thermodynamic power cycles for concentrated solar power systems. Renew Sustain Energy Rev 2014;30:758–70.

[2] Nathan GJ, Jafarian M, Dally BB, Saw WL, Ashman PJ, Hu E, Steinfeld A. Solar thermal hybrids for combustion power plant: a growing opportunity, Prog. Ener. Comb. Sci. 2018;64:4–28.

[3] Weinstein L, Loomis J, Bhatia B, Bierman D, Wang E, Chen G. Concentrating solar power. Chem Rev 2015;115:12797–838.

[4] Islam MT, Huda N, Abdullah AB, Saidur R. A comprehensive review of state-of-the-art concentrating solar power (CSP) technologies: current status and research trends. Renew. Sust. Energy Rev 2018;91:987–1018.
[5] Jamel M, Abd Rahman A, Shamsuddin A. Advances in the integration of solar thermal energy with conventional and non-conventional power plants. Rene. Sust. Energ. Rev. 2013;20:71–81.
[6] Jelley N, Smith T. Concentrated solar power: recent developments and future challenges. J. Power and Energy 2015;229:693–713.
[7] Collado FJ, Turégano JA. Calculation of the annual thermal energy supplied by a defined heliostat field. Sol Energy 1989;42:149–65.
[8] Noone C, Torrilhon M, Mitsos A. Heliostat field optimization: a new computationally efficient model and biomimetic layout. Sol Energy 2012;86:792–803.
[9] Wendelin T. SolTRACE: a new optical modeling tool for concentrating solar optics, Tech. rep., National Renewable Energy Laboratory (NREL). 2003.
[10] Schmitz M, Schwarzbozl P, Buck R, Pitz-Paal R. Assessment of the potential improvement due to multiple apertures in central receiver systems with secondary concentrators. Sol Energy 2006;80:111–20. https://doi.org/10.1016/j.solener.2005.02.012.
[11] Collado FJ, Guallar J. Campo: generation of regular heliostat fields. Renew Energy 2012;46:49–59.
[12] Carrizosa E, Domínguez-Bravo C, Fernández-Cara E, Quero M. A heuristic method for simultaneous tower and pattern-free field optimization on solar power systems. Comput Oper Res 2015;57:109–22.
[13] Ávila-Marín A. Volumetric receivers in solar thermal power plants with centra receiver system technology: a review. Sol Energy 2011;85:891–910.
[14] López-Herraiz M, Bello Fernández A, Martínez N, Gallas M. Effect of the optical properties of the coating of a concentrated solar power central receiver on its thermal efficiency. Sol. Energ. Mat. & Sol. Cells 2017;159:66–72.
[15] Uhlig R, Flesch R, Gobereit B, Giuliano S, Liedke P. Strategies enhancing the efficiency of cavity receivers. Energ. Proc. 2014;49:538–50.
[16] del Río A, Korzynietz R, Brioso JA, Gallas M, Ordoñez I, Quero M, Díaz C. Soltrec - pressurized volumetric solar air receiver technology. Energ. Proc. 2015;69:360–8.
[17] Ho CK, Iverson BD. Review of high-temperature central receiver designs for concentrating solar power. Renew Sustain Energy Rev 2014;29:835–46.
[18] Burgaleta S, Ramírez DJI. Gemasolar, the first tower thermosolar commercial plant with molten salt storage. In: Proceedings of SolarPACES; 2011. Granada, Spain.
[19] [link], https://www.solarreserve.com/en/global-projects/csp/crescent-dunes.
[20] [link], https://ec.europa.eu/europeaid/blending/noor-iii-tower-plant-ouarzazate-solar-complex_en.
[21] Behar O, Khellaf A, Mohammedi K. A review of studies on central receiver solar thermal power plants. Renew. Sust. Energy Rev 2013;23:12–39.
[22] Okoroigwe E, Madhlopa A. An integrated combined cycle system driven by a solar tower: a review. Renew Sustain Energy Rev 2016;57:337–50.
[23] Tech. rep. Solar hybrid gas turbine electric power system (SOLGATE). European Comission; 2005.
[24] Tech. rep. Solar-hybrid power and cogeneration plants. European Commission; 2011. URL ordis.europa.eu/publication/rcn/13318–en.html
[25] Korzynietz R, Brioso JA, del Río A, Quero M, Gallas M, Uhlig R, Ebert M, Buck R, Teraji D. Solugas - comprehensive analysis of the solar hybrid Brayton plant. Sol Energy 2016;135:578–89.
[26] Liu Q, Bai Z, Wang X, Lei J, Jin H. Investigation of thermodynamic performances for two solar-biomass hybrid combined cycle power generation systems. Energy Convers Manag 2016;122:252–62.
[27] Le Roux W, Bello-Ochende TMJ. A review on the thermodynamic optimisation and model of the solar thermal brayton cycle. Renew. Sust. Energy Rev 2013;28:677–90.
[28] Osorio JD, Hovsapian R, Ordonez JC. Dynamic analysis of concentrated solar supercritical CO_2-based power generation closed-loop cycle. Appl Therm Eng 2016;93:920–34.
[29] McMahan A, Klein S, Reindl D. A finite-time thermodynamic framework for optimizing solar-thermal power plants. J Sol Energy Eng 2007;129:355–62.
[30] Zare V, Hasanzadeh M. Energy and exergy analysis of a closed Brayton cycle-based combined cycle for solar power tower plants. Energy Convers Manag 2016;128:227–37.
[31] Barigozzi G, Perdichizzi A, Gritti C, Guaiatelli I. Techno-economic analysis of gas turbine inlet air cooling for combined cycle power plant for different climatic conditions. Appl Therm Eng 2015;82:57–67.
[32] Kalathakis C, Aretakis N, Roumeliotis I, Alexiou A, Mathioudakis K. Concentrated solar power components toolbox in an object oriented environment. Simul Model Pract Theory 2017;70:21–35.
[33] Santos MJ, Miguel-Barbero C, Merchán RP, Medina A, Calvo Hernández A. Roads to improve the performance of hybrid thermosolar gas turbine power plants: working fluids and multi-stage configurations. Energy Convers Manag 2018;165:578–92.
[34] Santos MJ, Merchán RP, Medina A, Calvo Hernández A. Seasonal thermodynamic prediction of the performance of a hybrid solar gas-turbine power plant. Energy Convers Manag 2016;115:89–102.
[35] Heywood J. Internal combustion engine fundamentals. McGraw-Hill; 1988.
[36] Collado FJ. Preliminary design of surrounding heliostat fields. Renew Energy 2009;34:1359–63.
[37] Collado FJ. Quick evaluation of the annual heliostat field efficiency. Sol Energy 2008;82:379–84.
[38] Zhang M, Yang L, Xu C, Du X. An efficient code to optimize the heliostat field and comparisons between the biomimetic spiral and stagerred layout. Renew Energy 2016;87:720–30.
[39] Spelling J. Hybrid solar gas-turbine power plants. Ph.D. thesis. Stockholm, Sweden: KTH Royal Institute of Technology, Department of Energy Technology; 2013.
[40] Falcone PK. A handbook for solar central receiver design. Sandia National Labs 1986;SAND 86-8009.
[41] Collado F, Guallar J. A review of optimized design layouts for solar power tower plants with *campo* code. Renew. Sust. Energy Rev 2013;20:142–54.
[42] Stine WB, Geyer M. Power from the sun. http://www.powerfromthesun.net/book.html; 2001.
[43] Leary PL, Hankins JD. A user's guide for MIRVAL– a computer code for comparing designs of heliostat-receiver optics for cenrtal receiver solar power plants. Tech. Rep., Sandia Laboratories; 1979.
[44] Duffie J, Beckman W. Solar engineering of thermal processes. Hoboken, New Jersey: John Wiley and Sons; 2006.
[45] Merchán RP, Santos MJ, Medina A, Calvo Hernández A. Thermodynamic model of a hybrid brayton thermosolar plant, Renew. Ener, vol. 128; 2018. p. 473–83. doi: doi://dx.doi.org/10.101016/j.renene.2017.05.081.
[46] Olumayegun O, Wang M, Kelsall G. Closed-cycle gas turbine for power generation: a state-of-the-art review. Fuel 2016;180:694–717.
[47] Coco-Enríquez L, Muñoz Antón J, Martínez-Val JM. New text comparison between CO_2 and other supercritical working fluids (ethane, Xe, CH_4, and N_2) in line-focusing solar power plants coupled to supercritical Brayton power cycles. Int J Hydrogen Energy 2017;42:17611–31.
[48] Lemmon EW, Huber ML, McLinden MO. NIST standard reference database 23: reference fluid thermodynamic and transport properties-REFPROP, version 9.1, national institute of standards and technology. Gaithersburg: Standard Reference Data Program; 2013.
[49] Meteosevilla. http://www.meteosevilla.com. http://www.meteosevilla.com.
[50] Relloso E, García E. Tower technology cost reduction approach after Gemasolar experience. Sol. Proc. 2015;69:1660–6.
[51] Peterseim JH, White S, Tadros A, Hellwig U. Concentrated solar power hybrid plants, which technologies are best suited for hybridisation? Renew Energy 2013;57:520–32.
[52] [link], https://www.thermoflow.com.
[53] [link], https://www.solarturbines.com.

3.6 Paper 6 – On- and off-design thermodynamic analysis of a hybrid polar solar thermal tower power plant

Title: "On- and off-design thermodynamic analysis of a hybrid polar solar thermal tower power plant"
Journal: *International Journal of Energy Research*
Authors: **R.P. Merchán**, M.J. Santos, A. Medina, A. Calvo Hernández
Year: 2020
Pages: 1-17
DOI: `https://onlinelibrary.wiley.com/doi/full/10.1002/er.5854`
Reference: [135]

Resumen

En este artículo se modela una turbina de gas hibridada con gas natural y acoplada a un campo de heliostatos polar con un receptor de cavidad en una planta termosolar de torre central. Para llevar a cabo la implementación del modelo al código, se consideran los valores de los principales parámetros del proyecto *SOLUGAS* (campo de heliostatos polar). Se analiza el funcionamiento de la turbina de gas en función de tres parámetros de diseño claves: la relación de presiones, el flujo de masa y la temperatura de entrada a la turbina. Este trabajo se ha orientado con el objetivo de analizar las principales variables de salida de la planta desde el punto de vista de las condiciones de diseño, pero también con un enfoque dinámico fuera de diseño. Las simulaciones se han llevado a cabo tanto para aire seco como para dióxido de carbono como fluidos de trabajo y para configuraciones recuperativas y no recuperativas. Asimismo, se realiza una pre-optimización en función de la relación de presiones, de modo que la eficiencia máxima es de alrededor del 30 % para ambos fluidos en el caso recuperativo. Esta eficiencia se consigue con una relación de presiones de 7 para el aire seco y de 16 para el dióxido de carbono.

Received: 4 March 2020 | Revised: 13 July 2020 | Accepted: 18 July 2020
DOI: 10.1002/er.5854

RESEARCH ARTICLE

INTERNATIONAL JOURNAL OF ENERGY RESEARCH WILEY

On- and off-design thermodynamic analysis of a hybrid polar solar thermal tower power plant

Rosa P. Merchán | María J. Santos | Alejandro Medina | Antonio Calvo Hernández

Department of Applied Physics and IUFFYM, University of Salamanca, Salamanca, Spain

Correspondence
Alejandro Medina, Department of Applied Physics and IUFFYM, University of Salamanca, Salamanca, Spain.
Email: amd385@usal.es

Funding information
Banco Santander; Consejería de Educación, Junta de Castilla y León, Grant/Award Number: SA017P17; University of Salamanca

Summary

Concentrated solar power (CSP) is one challenging renewable technology for the production of electricity. Within this concept central receiver solar plants combined with gas turbines are being investigated because of their promising efficiencies and reduced water consumption. Hybrid plants incorporate a combustion chamber in such a way that in periods of low solar irradiance power output can be kept approximately constant and so, electricity production is predictable. An integrated, non-complex solar thermodynamic model of a hybrid gas turbine solar plant is developed employing a reduced number of parameters with a clear physical meaning. The solar subsystem is modeled in detail, taking into account the main heliostats field losses factors as cosine effect, blocking and shadowing, or attenuation. An heliostat field with polar symmetry together with a cavity receiver are considered. The model is implemented in our own software, developed in Mathematica language, considering as reference SOLUGAS solar field (Seville, Spain). Heliostats field configuration is determined for the design point and its associated efficiency is computed. First, an on-design analysis is performed for two different working fluids (dry air and carbon dioxide), for recuperative and non-recuperative modes. A pre-optimization process is carried out regarding the pressure ratio of the gas turbine for different configurations. Some significant efficiency and power rises can be obtained when pressure ratio is adapted for each specific configuration and working fluid. Maximum achievable plant overall efficiency is 0.302 for both fluids in the recuperative mode, taking a pressure ratio of 7 for dry air and 16 for carbon dioxide. In non-recuperative configurations maximum overall efficiency is obtained for dry air, about 0.246. Moreover, a dynamic study is performed for four representative days of each season. Then, efficiencies and solar share are plotted against time. In addition, fuel consumption and greenhouse emissions are computed for all seasons.

KEYWORDS
concentrated solar power, dynamic analysis, gas turbines, overall plant efficiency, solar field efficiency, tower power plants

1 | INTRODUCTION

The current energetic paradigm for the planet presents lots of challenges worldwide. On one side, the climate change hazard related to pollutant greenhouse emissions produced in combustion of fossil fuels together with the finitude of these fossil resources make necessary a real change in energy paradigm towards cleaner and more reliable energy sources. On the other side, population and energy demand growth emphasize the necessity of new power production means.

Concentrated solar power (CSP) plants could fulfill to a good extent these requirements. These systems concentrate solar energy for heating a fluid, which develops a thermodynamic cycle.[1] Within these systems, plants working under Brayton cycles present all the advantages of gas turbines. Namely, they require reduced amounts of water, which is important for locations with high solar resources, and efficiency rates are high due to large working temperatures. Moreover, they stand out due to their flexibility, reliability, and scalability.[2] Another key factor is the possibility to guarantee an approximately constant power output through hybridization.[3] Hybrid plants incorporate a combustion chamber and a control system that allows a constant turbine inlet temperature. This in turn leads to a stable power production, removing solar irradiance fluctuations and affording correct night performance.[4] However, these systems are not totally emissions free, usually natural gas or biogas are burnt. Hybridization is thus an alternative to thermal storage with molten salt tanks, as several commercial plants, mostly running a Rankine cycle do.[5,6] In this case upper temperatures are smaller than in gas turbines. In the last years, several research projects and some prototypes of hybrid thermosolar Brayton plants have been carried out. A key outcome is that the technology is feasible, but competitive prices must be reached.[7] Therefore, a search for better output records as power output and efficiency results essential. This is the main objective of the present work.

During the last few years considerable efforts have been devoted to analyze the possibilities of supercritical CO_2 as working fluid for such thermosolar Brayton plants[8] or in other applications of gas turbines.[9] This is because of expected high efficiencies, compactness, and capital cost reduction.[10] Although several thermodynamical and technical studies were conducted,[11,12] there is still uncertainty on the design and efficiencies of turbomachinery components working at supercritical conditions.[13] On the contrary, there are scarce studies on CO_2 or other working fluids, different from air, working at subcritical conditions.[14] Particularly, looking for optimum design pressure ratios adequate for the typical turbine inlet temperatures of thermosolar plants is a field that deserves investigation. The work will be focused on the performance of the whole thermosolar plant, including all the subsystems that constitute it. Plant performance analysis will include, not only thermodynamic efficiency, but also solar share, fuel conversion efficiency, and a survey on the working temperature of the solar receiver, which is substantially influenced by the working fluid.

In this paper it is presented a framework to calculate the output parameters for the whole plant including a model for each subsystem (solar and power unit).[14] On one hand it is detailed enough to obtain precise numerical results but, on the other hand, it is not too intricate and the number of parameters for the whole system is not too high. This makes easier to identify the main losses in the system and to get hints about the ways with more room for optimization. A novel issue in the model is that it allows for the analysis of heliostat fields with polar symmetry, suitable for central towers with cavity receivers.[15,16] It is more usual to find in the literature studies about central towers with cylindrical receivers and so, approximately circular symmetry for the field (surround fields).[17] In this work we are interested in plants with cavity receivers, able to operate at very high temperatures. This is specially interesting for Brayton-like thermodynamic cycles where temperatures above 1000 K ensure good efficiencies. To the best of our knowledge there is only one pre-commercial scale plant of this type (cavity receiver and hybrid Brayton cycle). It is called SOLUGAS project and was developed by the company Abengoa Solar, near Seville (Spain).[18,19] Basic dimensions and design parameters will be assumed from this prototype plant and an optimization analysis considering different working fluids, plant configurations, and pressure ratios for the turbine will be analyzed. The analysis is divided into two parts: first, a pre-optimization is performed at on-design conditions, and second, an off-design analysis for particular days of any season is developed.

2 | OVERALL PLANT MODEL

A solar central tower plant hybridized with a combustion chamber and linked to a closed gas turbine is considered as system under study. The combustion chamber allows for a stable production of power output. The system is depicted in Figure 1, where the three subsystems composing the overall system can be observed: solar part, combustion chamber, and heat engine. Sun radiation is collected by a polar heliostat field, which concentrates and reflects it into a cavity receiver atop the tower. Then, the working fluid takes advantage of the solar heat and it is also heated by the combustion chamber until the desired turbine inlet temperature if necessary. Turbine

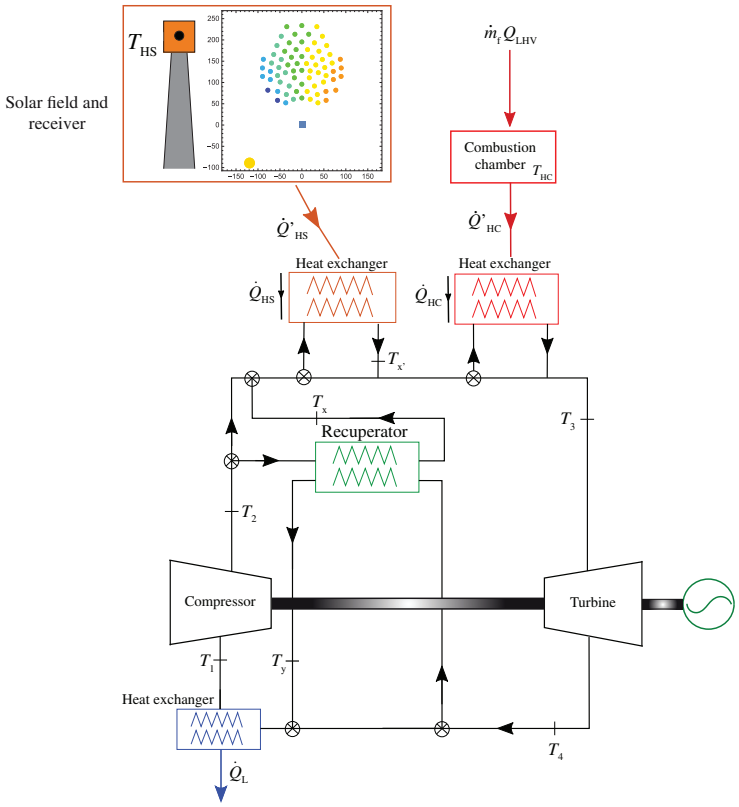

FIGURE 1 Scheme of the considered thermosolar plant, constituted by three different subsystems: solar subsystem, combustion chamber, and heat engine itself [Colour figure can be viewed at wileyonlinelibrary.com]

inlet temperature, T_3, is considered as a fixed input parameter.

The overall thermal efficiency of the system, η, is defined in the usual thermodynamic way as the quotient between the power output, P, and the total energy input into the system, $\eta = P/(GA_a + \dot{m}_f Q_{LHV})$, where G represents the direct normal irradiance; A_a, the aperture area; $\dot{m}_f$, the fuel mass flow in the combustion chamber; and Q_{LHV}, the fuel lower heating value. It is feasible to write η as a combination of the efficiencies of all the subsystems: η_h, heat engine efficiency, η_s, solar subsystem efficiency (including heliostat field and receiver), η_c, combustion efficiency, and the effectivenesses of the heat exchangers between them, ε_{HS} and ε_{HC}. In the equation it appears also the solar share or fraction of energy input coming from the solar resource, f. Definitions and explicit calculations to obtain η can be found in recent works by our group.[14,20,21]

$$\eta = \eta_h \eta_s \eta_c \left[\frac{\varepsilon_{HS}\varepsilon_{HC}}{\eta_c f \varepsilon_{HC} + \eta_s (1-f)\varepsilon_{HS}} \right] \quad (1)$$

Overall plant efficiency is thus obtained as the result of the integration of main plant subsystems in a clear way. This approach is devoted to identify main efficiency bottlenecks and, so, to propose improvements for new plant designs. Next the submodels for each component efficiency are summarized.

The thermodynamic model for the closed Brayton-like cycle in order to obtain η_h considers a working gas

with temperature dependent specific heats and mass flow $\dot{m}$. For modeling purposes the cycle is considered as closed although in real applications (when air is the working fluid) the cycle uses to be open. But one of the objectives of this work is the performance comparison between air and subcritical CO_2 and for the latter the cycle should be closed. Thus, the comparison between both fluids, to obtain meaningful results, has to be done from a closed cycle scheme.

The working fluid mass flow enters the compressor at a temperature T_1 (following the notation of Figure 1). The compressor is considered as non-ideal and its isentropic efficiency is denoted as ε_c. Then, it is heated up in three steps. First by means of a recuperator with effectiveness ε_r. The temperature of the gas at the recuperator exit is denoted as T_x. In the case of a non-recuperative layout $T_x = T_2$. Second, by the solar heat received at the solar field and transferred to the fluid in the receiver (thermodynamically the receiver is assumed as a heat exchanger with effectiveness ε_{HS}). At the receiver exit gas temperature is $T_{x'}$. If necessary (by night or when direct normal irradiance is poor) a combustion chamber ensures that the temperature of the fluid at turbine inlet is always T_3. The combustion chamber, as the solar receiver, it is also considered as a non-ideal heat exchanger with effectiveness ε_{HC}. Also losses in the combustion chamber itself associated to non-perfect combustion are accounted for. Combustion efficiency is denoted as η_c. The expander is taken as non-isentropic and it is characterized by its isentropic efficiency, ε_t. The temperature at the turbine exit is called T_4. Then, the hot gas releases heat through the recuperator to the fluid at the compressor exit. Finally, the cycle is closed by releasing heat to the ambient at temperature T_L in order to keep the compressor inlet temperature at T_1. The corresponding heat exchanger has an effectiveness ε_L. It is feasible to express all cycle temperatures in terms of those of the solar receiver, T_{HS}, and the combustion chamber, T_{HC}, the compressor pressure ratio, r_p, and all the parameters referred to cycle irreversibilities. Then, heat inputs from the solar collector, $\dot{Q}_{HS}$, and the combustion chamber, $\dot{Q}_{HC}$, are expressed in terms of the (temperature dependent) constant pressure specific heat of the working gas, $c_p(T)$, as:

$$|\dot{Q}_{HS}| = \int_{T_x}^{T_{x'}} c_p(T)\,dT \tag{2}$$

$$|\dot{Q}_{HC}| = \int_{T_{x'}}^{T_3} c_p(T)\,dT \tag{3}$$

The total heat input is $|\dot{Q}_H| = |\dot{Q}_{HS}| + |\dot{Q}_{HC}|$ and the heat released to the ambient is

$$|\dot{Q}_L| = \int_{T_1}^{T_y} c_p(T)\,dT \tag{4}$$

and so, $P = |\dot{Q}_H| - |\dot{Q}_L|$ and $\eta_h = P/|\dot{Q}_H|$. Further details on the calculations can be found in Ref.[14] This model for the Brayton cycle allows to estimate the corresponding efficiency, η_h, power output and any other parameter as cycle temperatures in a precise but not computationally expensive way, as will be shown in Sec. 3.

To calculate the efficiency of the solar subsystem, η_s, two kinds of losses have to be taken into account: the optical losses in the reflection of solar energy from the heliostats to the receiver at the top of the tower, η_0, and the thermal losses in the receiver. The second are calculated as in,[14,22] including convective, conductive, and radiation losses:

$$\eta_s = \eta_0 - \frac{1}{GC}\left[\alpha\sigma\left(T_{HS}^4 - T_L^4\right) + \overline{U}_L\left(T_{HS} - T_L\right)\right] \tag{5}$$

where C is the concentration ratio, α refers to the emissivity of the receiver surface, σ is the Stefan-Boltzmann constant, $\overline{U}_L$ corresponds to an overall conduction and convection heat transfer coefficient, T_{HS} is the solar collector temperature, and T_L represents the ambient temperature.

The optical efficiency of the heliostat field, η_0, is computed in detail. Hence, solar field is divided into different rows and, in each row, heliostats are placed considering the space they can occupy during the solar tracking together with a safety distance.[23] Each heliostat has a different efficiency, which also varies with the solar hour and the season of the year, because of its particular location. This efficiency of each heliostat is considered as a product of different losses factors, as it is shown in Equation (6).

$$\eta_{\mathrm{hel,i}} = \cos\omega \cdot f_{\mathrm{b,sh}} \cdot f_{\mathrm{sp}} \cdot f_{\mathrm{at}} \cdot \rho \tag{6}$$

The primary contribution to this optical efficiency is the cosine effect, $\cos\omega$[24] which accounts for the cosine of the incident angle of the Sun radiation in the heliostat surface. It is computed by means of a study of the Sun-heliostat-receiver geometry.[25] Blocking effect measures the amount of lost energy when a fraction of the radiation coming from a back heliostat reflects in an ahead one. In a similar way, shadowing effect comprehends lost energy due to the shadow projected by a heliostat on another one. Both effects are included in the blocking and shadowing factor, $f_{\mathrm{b,sh}}$, which is assumed as a constant factor to avoid a high computational cost, following the works by Collado et al.[25,26] The factor, ρ, defines the amount of solar radiation that each heliostat can reflect towards the receiver depending on the materials, coating,

cleanliness, and curvature.[26] When solar radiation travels towards the receiver, ambient air molecules absorb a fraction. Such attenuation factor, f_{at}, results in another energy loss[26] depending on the distance of a particular heliostat to the receiver. And, the last important energy loss source is the spillage factor, f_{sp}, related to solar radiation not aiming the absorption area of the receiver, but closer zones. The model by Collado et al. is assumed.[26] In this model spillage factor depends on the receiver dimensions, heliostat area, the effective dispersion of the sun shape on the receiver plane, heliostat tracking, and surface errors. So, the spillage factor depends on each heliostat. With all these assumptions, the efficiency of each heliostat is calculated and then, that of the whole field, η_0, as the simple averaged efficiency of all heliostats. The thermodynamic and optical models were implemented in Mathematica.

3 | NUMERICAL CONSIDERATIONS

SOLUGAS project (Seville, Spain)[18,19] is the first prototype at a pre-commercial scale where a standard gas turbine is hybridized with a polar heliostat field through a cavity receiver. It incorporates a standard gas turbine, Caterpillar Mercury 50, but with extensive modifications.[27] The standard Mercury 50 gas turbine is recuperated and single shaft, with an axial compressor and an ultra lean premix combustion system. It guarantees NOx emissions below 5 ppm and CO and UHC below 10 ppm. It was designed for combined heat and power applications and also for intermediate peaking applications. In the SOLUGAS project the turbine was modified to operate driven by solar energy. Details on the modifications were not made explicit but at least the recuperator was substituted by the solar receiver, a by-pass between the receiver inlet and outlet pipes was placed (to control receiver air mass flow and to allow directing the pressurized air directly from the compressor to the combustion chamber) and control systems modified. Also higher temperatures in the combustion system were surveyed and protections re-designed. Because of the absence of specific data for the modified turbine, the validation of the gas turbine model developed in this work was done on the original turbine design. Details can be found in previous publications[14,28] and so, only a brief summary is sketched here. Table 1 contains the main model parameters taken in order to validate the gas turbine Mercury 50 by comparing our model predictions with the measures at the real turbine. Ambient temperature at design conditions was set at 288 K, pressure ratio is 9.9 and air mas flow is 17.9 kg/s.[27] Assumed isentropic efficiencies of the compressor and turbine, heat exchangers effectivenesses and pressure losses parameters are shown in the table. Relative deviations among model outputs and real measures barely exceed 4%. Main temperatures of the gas during the cycle are also in the table. Predicted efficiency is 0.398, about 3.27% over measured efficiency and predicted power output is 4.77, about 3.66% over measured power. More details about validation can be found in.[14,28] As the focus of this work is placed on the performance of the overall thermosolar plant, those differences are assumed as reasonable.

After validation, gas turbine performance is analyzed in Figure 2 in terms of three essential design parameters: pressure ratio, r_p, working gas mass flow, $\dot{m}$, and turbine inlet temperature, T_3. From panel (a) it is concluded that power unit efficiency does not depend on the mass flow (turbine size), but pressure ratio has a definite importance. Efficiencies about 0.4 could be achieved for pressure ratios roughly between 4 and 9 and are, as expected, independent of the working fluid mass flow. Comparing with the design parameters of the turbine Mercury 50 (see the circle in Figure 2A) larger efficiencies could be obtained by reducing the experimental pressure ratio,

TABLE 1 Main irreversibility parameters considered to validate the gas turbine Caterpillar Mercury 50 used in the project SOLUGAS at design conditions.[27] Ambient temperature was set at 288 K, pressure ratio is 9.9 and air mas flow is 17.9 kg/s[27]

Model input parameters								
ε_t	ε_c	ε_r	$\Delta p_H/p_H$ (%)	$\Delta p_L/p_L$ (%)	ε_{HC}	ε_{HS}	ε_L	η_c
0.885	0.815	0.775	9.4	9.4	0.980	0.780	0.985	0.980

GT validation summary									
	T_1	T_2	T_x	$T_{x'}$	T_3	T_4	T_y	η_h	P (MWe)
Mercury 50 GT	–	–	–	–	1423	–	647	0.385	4.60
Our model	294	604	846	1009	1422	916	674	0.398	4.77
Relative deviations (%)	–	–	–	–	0.07	–	4.01	3.27	3.66

Note: All temperatures are expressed in K.

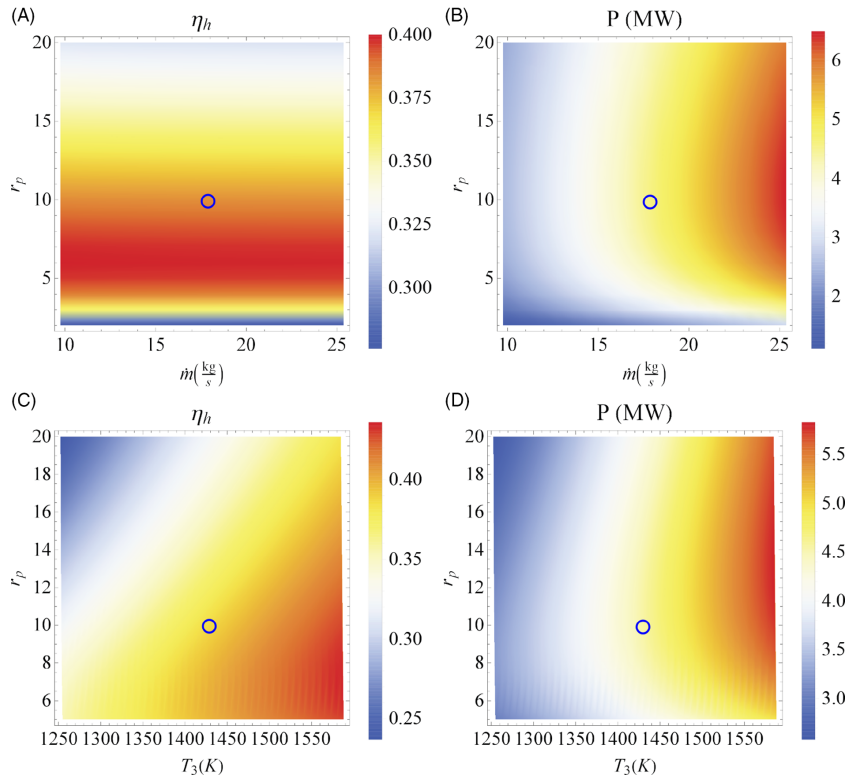

FIGURE 2 Density plots of the efficiency of the gas turbine as calculated from the developed model, η_h, and the corresponding power output, P, as functions of three key design parameters: pressure ratio, r_p; working fluid mass flow, $\dot{m}$; and turbine inlet temperature, T_3. Circles correspond to the design parameters of the turbine Mercury 50[27] [Colour figure can be viewed at wileyonlinelibrary.com]

9.9, to slightly lower values (if other parameters keep constant). Power output (see Figure 2B) linearly increases with $\dot{m}$ and there is a wide interval for r_p leading to alike power. In Figure 2C it is analyzed the evolution of η_h simultaneously with r_p and the turbine inlet temperature, T_3. Small values of pressure ratio and large values of T_3 lead to the best efficiencies. Nevertheless, T_3 is limited from a practical viewpoint because of metallurgical and cost reasons. Finally, power output (see Figure 2D) also increases with T_3 and the election of r_p is not critical, for each value of T_3 there is a wide interval of pressure ratios with similar power outputs.

The most important parameters of the solar field size and those used to estimate the efficiency of the solar subsystem are contained in Table 2. Design point with respect to solar conditions is taken as June 20th, 2013, with a direct solar irradiance G = 760 W/m^2, and ambient temperature T_L = 296.5 K. For off-design conditions meteorological data were taken from Meteosevilla database for the location of SOLUGAS[29,30] (37° 26′ 23″ North latitude, 6° 17′ 4″ West longitude). Figure 3 contains the daily evolution of direct normal irradiance, G, and ambient temperature, T_L, at SOLUGAS location. Comparing the limit cases, winter and summer, the picture shows that maximum G in summer reaches almost 900 W/m^2 and there are about 12 hours with acceptable irradiance. On the opposite, maximum G in winter is approximately 500 W/m^2 and sun hours about 8. The oscillatory profiles of ambient temperature are shown in the bottom of Figure 3. Globally, summer days are hot and winter days

TABLE 2 Table of parameters values employed in the simulations (adapted from SOLUGAS prototype plant[19])

Parameter	Value
Height of the tower supporting the receiver	65 m
Diameter of the receiver	5 m
Number of heliostats	70
Height of each heliostat	11.01 m
Width-height ratio of each heliostat	1.0
Concentration ratio (C)	432.443
Focusing	Simple (receiver center)
Separation distance between adjacent heliostats	3.303 m
Minimum radius of the heliostat field	64 m
Blocking and shadowing factor ($f_{b,sh}$)	0.95
Actual mirror reflectivity (ρ)	0.836
SD due to Sun shape	2.51 mrad
SD due to surface errors	0.94 mrad
SD due to tracking errors	0.63 mrad
Receiver emissivity (α)	0.1
Overall convection and conduction heat transfer losses ($\overline{U}_L$)	5 W/(m^{2}K)

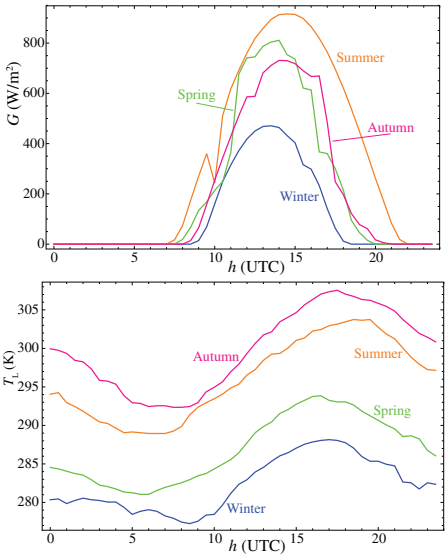

FIGURE 3 Evolution with time of direct normal irradiance, G, and ambient temperature, T_L, at Seville, Spain, for four representative days of each season during 2013: Winter (21st, December), Spring (21st, March), Summer (20th, June), and Autumn (21st, September). Curves are direct experimental data taken each 30 minutes, they are neither smoothed nor averaged[29] [Colour figure can be viewed at wileyonlinelibrary.com]

are warm, not too cool temperatures are reached. Afternoon temperature in summer is quite high, around 305 K and 20 K below in winter. Minimum temperatures in winter are about 275 and in summer 15 K above.

Two operation modes are considered, non-recuperative and recuperative (in the recuperative case, recuperator effectiveness is taken as 0.775[30]). Also two working fluids at subcritical conditions are analyzed, air and carbon dioxide. The same mass flow was considered for both. Their specific heats were considered temperature dependent and taken from database Refprop.[31] In the case of carbon dioxide an important effort has been devoted during the last years in the literature to analyze its possibilities in this kind of plants at supercritical conditions.[32-34] It is expected a decrease of the compression work, and so, an increase of power output for a fixed heat input. Nevertheless, there is still a considerable uncertainty about the operation of the turbomachinery (compressors and turbines) at such supercritical conditions. Here, a comparison of carbon dioxide with air (both at subcritical conditions) in what refers to optimum pressure ratios, temperature levels, overall plant efficiencies, and other records is developed. The aim is to look for windows where, at the working temperatures of this type of thermosolar plants, optimized pressure ratios can lead to good output records for the whole plant. As it will be seen next, the temperatures of the gas at the turbine outlet greatly depend on the gas characteristics, and so the role of recuperation is important from the viewpoint of the working fluid. A schematic $p - T$ diagram of the Brayton cycles developed for both fluids is shown in Figure 4.

Figure 5 displays the Brayton cycles developed by the power unit for both fluids in the recuperative and non-recuperative cases at the design point. Utmost temperatures (ambient temperature, T_1, and turbine inlet temperature, T_3) were fixed for all cases. As a brief summary from the figures, it should be remarked that temperatures after compression, T_2, are in both modes larger for air. This is the temperature at the entrance of the solar receiver in non-recuperative configurations (see Figure 5A). The temperature of the fluid at the receiver exit is $T_{x'}$, that it is also quite larger for air. This suggests that the operation temperature of the solar receiver for air is larger than for subcritical CO_2. This point is

important from the viewpoint of the design and materials of the solar receiver. If its temperature is considered as a key design parameter (and actually it is because of economical reasons and also because losses at the receiver increase with its temperature) the influence of the working fluid should be checked from the perspective of the whole plant and not only from the viewpoint of the thermodynamic cycle developed by the power unit.

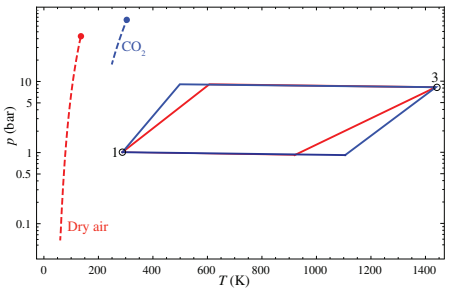

FIGURE 4 Semi-log $p - T$ plot of the base Brayton (subcritical) cycles for dry air and CO_2 considered. Liquid–vapor coexistence lines for both fluids are represented as dashed lines and the critical points as filled circles. Compressor and turbine inlet states are shown as open circles [Colour figure can be viewed at wileyonlinelibrary.com]

From Figure 5B it is observed that the recuperator greatly increases the temperature of the gas entering the solar receiver, T_x and so, its operating temperature for both fluids. Recuperative configurations require much higher temperatures for the receiver. Potential of CO_2 for recuperation is larger than for air, because the temperature at the exit of the turbine, T_4, is higher for CO_2. So, probably recuperated configurations increase the efficiency of the power unit itself but introduce undesired effects as the increase of the solar receiver operation temperatures (thus costs and heat transfer losses). With these considerations in mind, the next section is devoted to analyze simulations results, both at design conditions and also for off-design situations.

4 | RESULTS

4.1 | On-design analysis and pre-optimization

Design point fixes heliostat field configuration. Figure 6 shows the efficiency of each heliostat at the design point by a colour map. It can be observed that heliostats opposite to the Sun (marked as a yellow circle in Figure 6) present higher efficiencies, as stated by Stine and Geyer.[35] Average heliostats efficiency at design conditions is $\eta_0 = 0.6891$ and overall plant efficiency, considering air as working fluid, is $\eta = 0.2963$. The relatively low solar

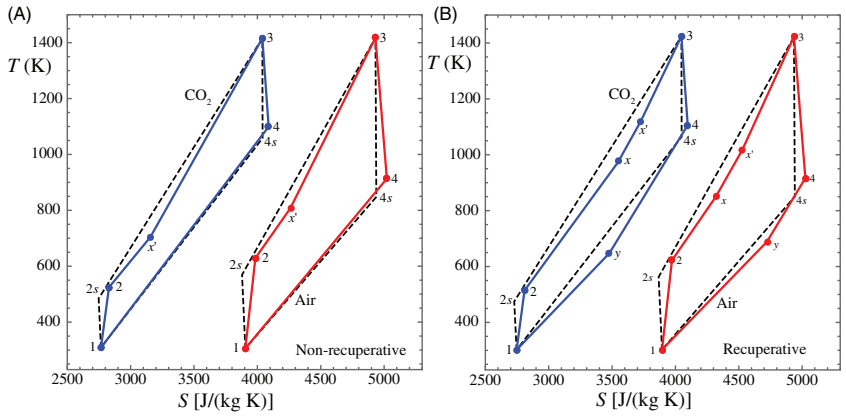

FIGURE 5 $T - S$ diagrams of the thermodynamic cycle developed by the power unit. Dashed lines represent the reversible ideal cases and solid ones the real cycles. Two working gases are considered: red color stands for air and blue for carbon dioxide. A, Non-recuperative cycles and B, recuperative ones. Notation corresponds to that of Figure 1. Without recuperation solar heat input corresponds to $2 \rightarrow x'$ and with recuperation to $x \rightarrow x'$ [Colour figure can be viewed at wileyonlinelibrary.com]

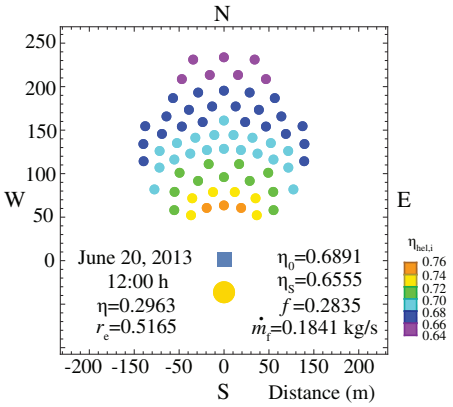

FIGURE 6 Heliostats efficiencies in the field at design conditions. Some overall plant records are also shown: η, overall thermal efficiency; r_e, fuel conversion efficiency (net power output over heat input from the combustion chamber); η_0, field optical efficiency; η_s, solar subsystem efficiency (solar field and receiver); f, solar share, and $\dot{m}_f$, fuel consumption. Tower (blue square) and sun positions (yellow circle) are also depicted as a guide [Colour figure can be viewed at wileyonlinelibrary.com]

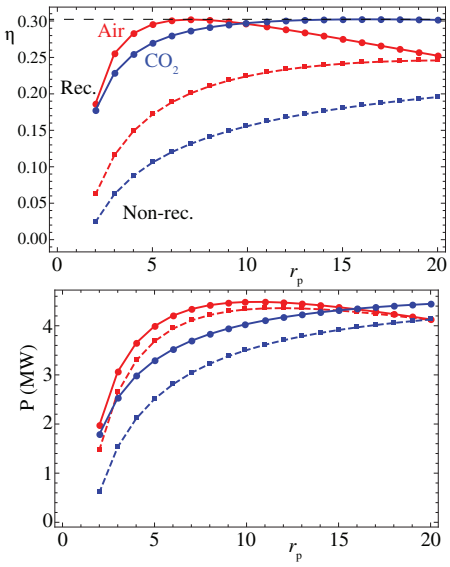

FIGURE 7 Overall plant efficiency, η, and net power output, P, at design conditions as functions of the pressure ratio, r_p. Two working fluids for the gas turbine (air, red color and CO_2, blue color) and recuperative (solid lines) and non-recuperative plant configurations (dashed) are considered [Colour figure can be viewed at wileyonlinelibrary.com]

share, $f = 0.2835$, indicates that field dimensions are small, so combustion is necessary to reach the target turbine inlet temperature.

From now on design conditions are considered, but the role played by the pressure ratio is analyzed in order to find optimum values for the considered fluids (subcritical air and carbon dioxide) and plant configurations (recuperative or non-recuperative). Overall plant efficiency, η, and power output, P, in terms of the pressure ratio are depicted in Figure 7. Overall efficiency is larger for recuperative configurations. When air is the working fluid η displays a maximum around $r_p \simeq 7$ that leads to an efficiency about 0.30, which is a remarkable value. For CO_2, η increases monotonically up to an asymptotic value similar to the maximum efficiency for air, 0.30. CO_2 allows to reach efficiencies around 0.30 only for high pressure ratios (above 10). For non-recuperative configurations, air provides considerable larger efficiencies that increase up to $\eta \simeq 0.25$ for pressure ratios above 15. For CO_2 it is difficult to reach efficiencies around 0.20, even for high pressure ratios.

The power output, P (Figure 7, bottom), presents a maximum for air in both recuperative and non-recuperative plant layouts. Maximum is located around $r_p \simeq 10$ (SOLUGAS design point). In the case of CO_2 power increases monotonically with r_p and does not reach a maximum in the surveyed interval. Power output is larger for the recuperative cases. Differences are larger for carbon dioxide. It is noteworthy that from a theoretical viewpoint, in the case of a reversible Brayton cycle developed by a gas with approximately constant specific heats, the power output (or work output) should be identical for recuperative and non-recuperative layouts. This is because recuperation implies an internal heat transfer, and the net difference between the heat input and heat release is not affected by the recuperator. But this is not true for irreversible Brayton cycles, where the intermediate temperatures T_2 and T_4 depend on cycle losses (explicit equations for those temperatures are written in the Appendix A of[21]). In the cases analyzed here, differences between the power output in recuperative and non-recuperative layouts are more important for CO_2.

Parametric $\eta - P$ curves, obtained by eliminating r_p between the curves $\eta = \eta(r_p)$ and $P = P(r_p)$, are represented in Figure 8. In the non-recuperative cases (dashed curves in the figure), curves are covered clockwise as pressure ratio increases. In the analyzed interval,

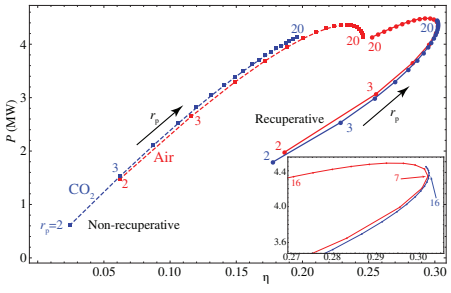

FIGURE 8 Parametric $\eta - P$ curves obtained by eliminating r_p between the curves $\eta = \eta(r_p)$ and $P = P(r_p)$. The interval considered for r_p is the same as in Figure 7, $r_p \in [2, 20]$. Left curves (dashed) correspond to non-recuperative layouts. As r_p increases the curve is covered clockwise. Right curves (recuperative) are covered in the opposite direction. Some numerical values of r_p are shown as a guide. The inset shows a zoom of the recuperative curves. Maximum η for air corresponds to $r_{p,\ max} = 7$ and to 16 for CO_2 [Colour figure can be viewed at wileyonlinelibrary.com]

$r_p \in [2, 20]$, maximum power output and maximum efficiency are reached for air but not for CO_2. In recuperative layouts curves are covered in the opposite direction. There is a clear displacement between the values $r_{p,\ max}$ that maximize overall efficiency for both gases: maximum η for air corresponds to $r_{p,\ max} = 7$ and to 16 for CO_2 (see the inset in the figure). Thus, incorporating recuperation, maximum reachable efficiency is numerically very similar for both working fluids but at considerable lower pressure ratio values for air.

The fuel conversion efficiency, r_e, is defined as the ratio between the power output and the heat input from the combustion chamber (so with an economic cost). It is much larger for recuperative configurations (see Figure 9A). The maximum value is similar for air and CO_2 (about 0.58 in both cases), but in the case of air it is more sensitive to the pressure ratio. As r_p increases over approximately 5, r_e decreases more quickly for air than CO_2. The solar share, f, is the fraction of heat input coming from the sun. For all the cases considered its numerical value is small (see Figure 9B). This means that the size of the heliostat field is relatively small for the

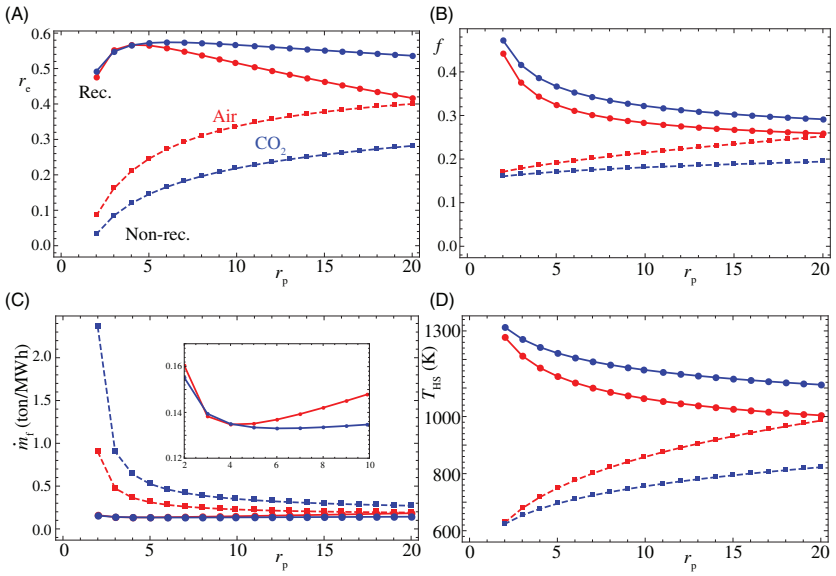

FIGURE 9 A, Fuel conversion efficiency, r_e. B, solar share, f. C, specific fuel consumption, $\dot{m}_f$ (the inset shows a zoom of the recuperative configurations), and D, solar receiver temperature, T_{HS}, as functions of the pressure ratio, r_p [Colour figure can be viewed at wileyonlinelibrary.com]

TABLE 3 Relative variations of some output records with respect to the reference case, η_{DP} (gas turbine Caterpillar Mercury 50 with or without recuperator, $r_p = 9.9$, project SOLUGAS)

	η_{DP}	$r_{p,max}$	η_{max}	$\Delta\eta$	Δr_e	ΔP	Δf
Dry air (rec.)	0.296	7	0.302	1.946	6.152	−3.213	6.319
Dry air (non-rec.)	0.224	20	0.246	9.890	19.160	−4.898	17.670
CO_2 (rec.)	0.297	16	0.302	1.764	−3.329	8.025	−6.934
CO_2 (non-rec.)	0.155	20	0.196	26.060	29.553	18.133	7.355

Note: $r_{p,\,max}$ is the pressure ratio leading to the maximum overall efficiency, η_{max} in each case. Relative variations are shown as percentages.

working fluid mass flow and the target turbine inlet temperature. Solar share is higher for the recuperative cases. For these layouts it decreases with r_p. On the contrary, when no recuperation is considered, f linearly increases with r_p (faster for air than for CO_2). Numerical values of the specific fuel consumption in the combustion chamber are displayed in Figure 9C. Of course fuel consumption is larger for non-recuperative configurations, specially at low pressure ratios. For recuperative configurations, numerical values and qualitative behavior is similar for air and CO_2. In both cases there is a quite flat minimum about $r_p \simeq 4-6$ where $\dot{m}_f$ is below 0.14ton/MWh (see the inset in Figure 9C).

The picture of the solar receiver working temperature, T_{HS}, is very interesting (see Figure 9D). Temperatures are much larger for recuperative layouts. They are between 1000 K (air at $r_p \simeq 20$) and 1300 K (CO_2 at small pressure ratios). On the contrary, the interval in the non-recuperative cases starts slightly above 600 K and goes up to 1000 K (air, non-recuperative). In recuperative layouts T_{HS} decreases with r_p, and in non-recuperative ones, the behavior is opposite.

Table 3 summarizes the variations of some output records with respect to the reference case (gas turbine Caterpillar Mercury 50 with or without recuperator, $r_p = 9.9$, project SOLUGAS) for the optimum pressure ratio. Overall plant efficiency was taken as objective function for optimization. It is remarkable the gain simultaneously in all parameters in the case of a power unit working with CO_2 in a non-recuperative configuration.

4.2 | Off-design records

The model stated in Sec. 2 can be applied to off-design conditions in a straightforward way. Ambient temperature, T_L, and direct normal irradiance, G, are now time dependent parameters. At any time, the working temperature of the solar receiver is calculated by balancing the solar power received from the heliostat field and the heat transferred to the fluid. This leads to time dependent values for the heats, $\dot{Q}_H$ and $\dot{Q}_L$, and so, to a time dependent efficiency for the heat engine, η_h. With respect to the solar subsystem, optical efficiency associated with the field, η_0, depends on time because of the cosine factor and spillage, that are calculated for each sun position during a day. Heat transfer losses, Equation (5), also evolve with time through the temperatures and G. With these elements, overall efficiency or any other thermodynamic parameter result as functions of solar irradiance and ambient temperature, and can be estimated at any hour during a day, at any season. Also yearly averages can be performed.

Off-design analysis is performed for four different days corresponding to the start of each season. Solar field layout was fixed at on-design conditions and computer simulations allow for calculating heliostats efficiency at whichever hour and season. Then, the seasonal variation of heliostats efficiency can be shown in Figure 10 at 16:00 hour (UTC). Particular days were elected without performing any smoothing or averaging. Average field efficiency is largest for winter and smallest for summer, having intermediate values for autumn and spring. Best heliostats in winter have efficiencies between 0.75 and 0.80 and the worst in summer between 0.40 and 0.45. One should be careful to generalize these results because the meteorological particularities of the selected days were not averaged out.

In Figure 11 hourly evolution of the most representative plant efficiencies for non-recuperative configurations is displayed. Pressure ratios correspond to the best overall efficiencies, as contained in Table 3. Optical efficiency, η_0 and the efficiency of the solar subsystem η_s (heliostat field and receiver) are similar for both fluids at any season. All other efficiencies are better for air. Heat engine efficiency, η_h, is approximately constant along a day, provided that turbine inlet temperature is fixed and, so, it is mainly influenced by ambient temperature evolution. Nevertheless, overall efficiency, η, presents a different behavior because it depends on the coupling of the efficiencies of all subsystems, as Equation (1) displays. Particularly, it depends on the efficiencies of the heat engine, η_h, and the solar subsystem, η_s (heliostat field and receiver with the corresponding optical and heat transfer losses, Equation (5)) because combustion efficiency, η_c, is taken as constant. Overall thermal efficiency, η, decreases

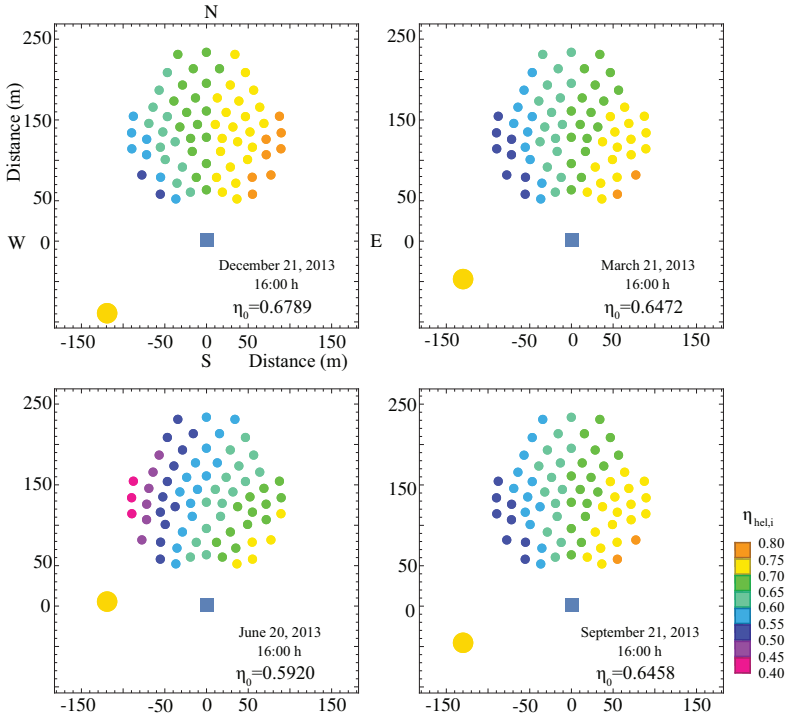

FIGURE 10 Heliostat efficiencies distribution for representative days of all seasons at 16:00 hour (UTC). Averaged field efficiency, η_0, is displayed in each plot [Colour figure can be viewed at wileyonlinelibrary.com]

during sun hours because the losses coming from the solar subsystem are added to those of the power unit. On the contrary, fuel conversion rate, r_e and solar share, f, increase. Solar share is always small because of the size of the heliostat field and is always slightly better for air than for CO_2. Maximum values are around 0.3 for air during summer.

Daily evolution for the recuperative plant is analyzed through Figure 12 for representative days of each season. All efficiencies and solar share are larger than for the non-recuperative case. Power unit efficiencies, η_h, reach remarkable values, about 0.4. It is noteworthy that curves for both fluids are very similar. This is because optimum pressure ratios in this case ($r_{p,\ max} = 7$ for air and 16 for CO_2) lead to almost identical output records (see Table 3 and the dashed horizontal line in Figure 7).

Finally, specific fuel consumption and CO_2 emissions (or any other greenhouse emission) can be calculated for any day. Several results are depicted as bar diagrams in Figure 13 for the pressure ratios optimized at design conditions. Of course consumption and emissions are larger for the non-recuperative cases. Approximately, for air emissions are 1.3 times larger in the non-recuperative case and for CO_2 the ratio increases up to 1.8. As it happened for the most significant efficiencies, consumption and emissions in recuperative layouts are very similar for both gases. In the absence of recuperation, consumption and emissions are larger for CO_2 as consequence of the worse efficiencies of the heat engine (see Figure 11). The small differences between the hybrid mode results and those for the plant working in an only combustion mode result from the relatively undersized dimensions of the solar field.

Note that all off-design calculations have been performed considering the aforementioned optimum

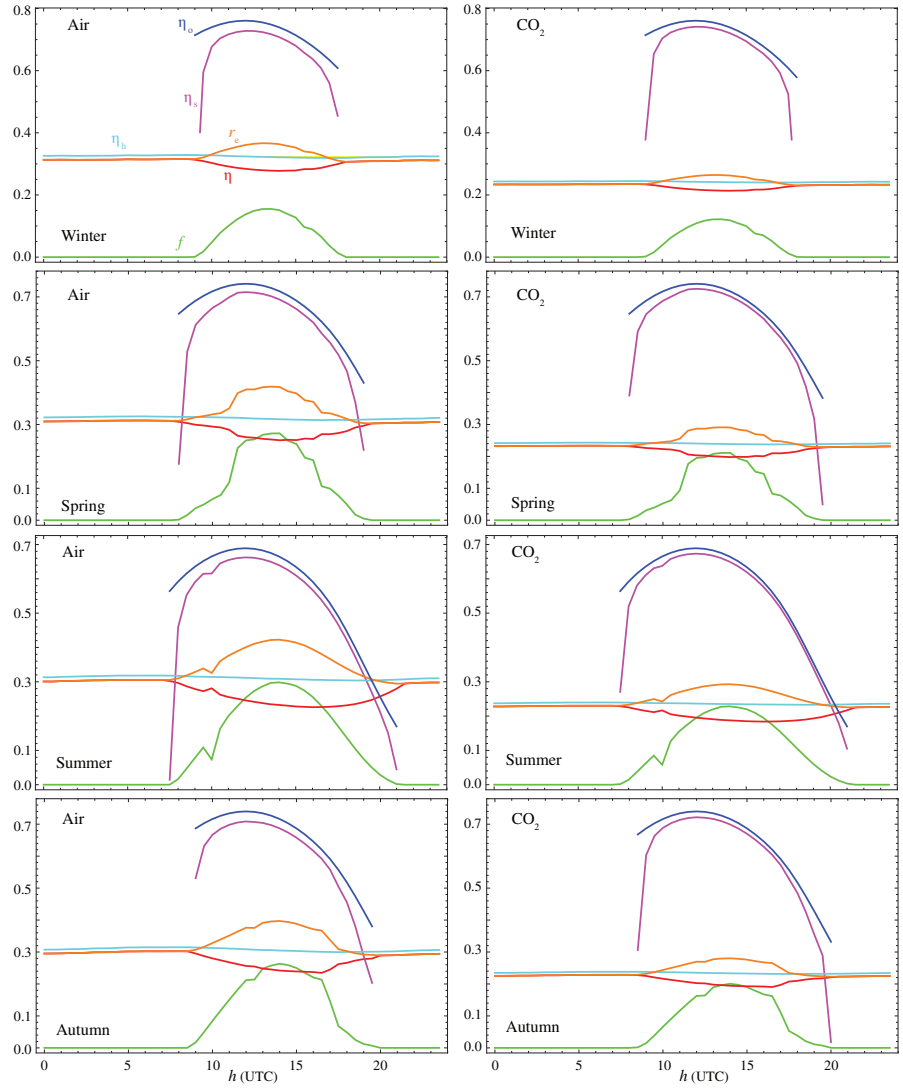

FIGURE 11 Hourly evolution of the main plant efficiencies and solar share, f, for all seasons without recuperation. Working fluids are air (left column) and CO_2 (right column). Notation is as follows: solar field optical efficiency, η_o; solar subsystem efficiency (field and receiver), η_s; fuel conversion rate, r_e; power unit efficiency, η_h; and plant overall efficiency, η. Pressure ratios were taken from those in Table 3 [Colour figure can be viewed at wileyonlinelibrary.com]

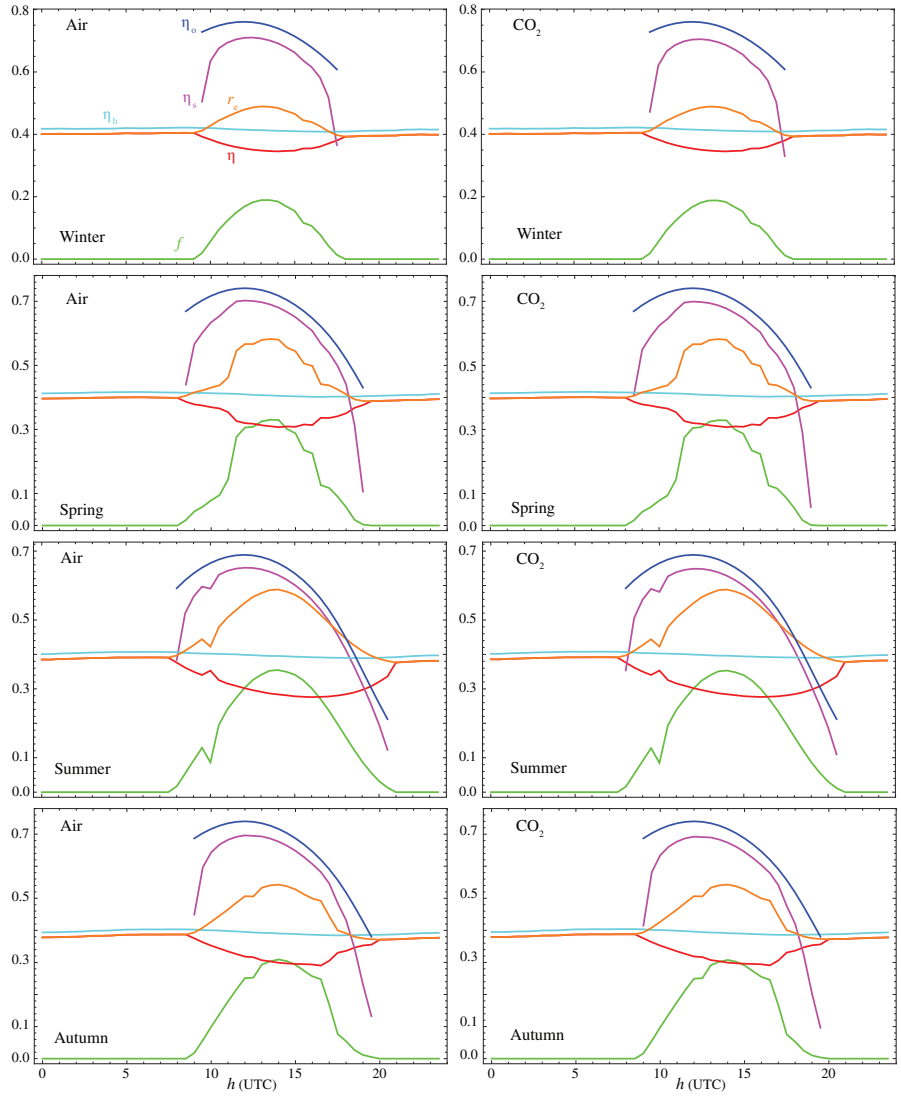

FIGURE 12 Hourly evolution of the main plant efficiencies and solar share, f, for all seasons with recuperation. Working fluids are air (left column) and CO_2 (right column). Notation is as follows: solar field optical efficiency, η_o; solar subsystem efficiency (field and receiver), η_s; fuel conversion rate, r_e; power unit efficiency, η_h; and plant overall efficiency, η. Pressure ratios were taken from those in Table 3 [Colour figure can be viewed at wileyonlinelibrary.com]

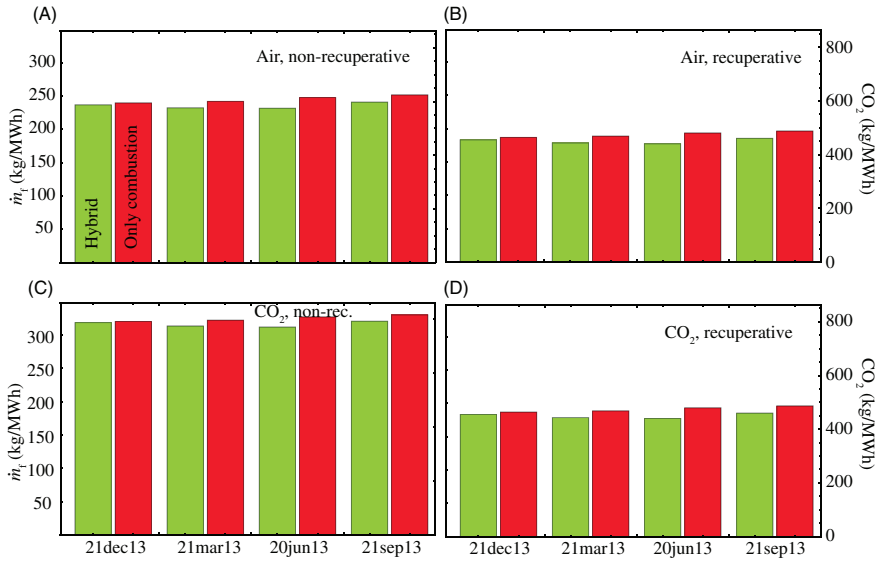

FIGURE 13 Natural gas consumption and CO_2 emissions for the configurations considered for the plant operating in hybrid mode (green bars) or in standard operation, burning natural gas without solar heat input (red ones). A, Working fluid is air and no recuperation is considered. B, air with a recuperator (effectiveness 0.775). C, CO_2 without recuperation and D, CO_2 with recuperation [Colour figure can be viewed at wileyonlinelibrary.com]

pressure ratios. The consistency of this election throughout any season and day has been checked. It was concluded that the election of the pressure ratio at on-design conditions is an acceptable choice. Notice that the fuel consumption in Figure 13 is larger than the data contained in Figure 9 because in Figure 13, $\dot{m}_f$ is averaged over the whole particular day selected and in the former figure on-design conditions at fixed solar irradiance were considered.

One interesting issue is the influence of the solar field size and shape (small and polar in the case analyzed here) in overall plant efficiency and other records. Recently, our group published another paper for a very much larger field, about 1000 heliostats and a circular field.[21] Very briefly it could be said that qualitative behavior of efficiencies with the pressure ratio at on-design conditions, and daily curves at off-design ones are similar in both cases. But numerical differences are important because field optical efficiency is quite larger for fields like the one considered in this paper (compare, for instance, Figure 12 with fig. 15 in[21]), and so, overall plant efficiency is fairly higher.

5 | CONCLUSIONS

A previously developed thermodynamic model for a gas turbine hybridized with a central tower heliostat field has been completed with a comprehensive, but at the same time, reliable solar field submodel, valid for surround (circular symmetry) or polar fields. This model takes into account losses factors as spillage, heliostats blocking and shadowing, and atmospheric attenuation and allows any off-design investigation. Numerical implementation and analysis has been made by taking the dimensions of the solar field and receiver, and the gas turbine parameters from the first prototype pre-commercial plant, called SOLUGAS project (polar field and cavity receiver).

An analysis of plant output variables at design point has been carried out for different working fluids (dry air and carbon dioxide), and for recuperative or non-recuperative plant layouts. The optimum pressure ratio was estimated for each case taking as objective function the overall plant thermal efficiency. Main subsystems efficiencies were analyzed as a function of the turbine pressure ratio. Maximum achieved overall efficiencies

were found for air and CO_2 when a recuperator is included in plant design (about 0.30), but the pressure ratios for both working fluids are different and also the behavior of different plant records with the pressure ratio as fuel conversion efficiency, solar share, and specific fuel consumption. The latter is, of course, considerable smaller for recuperated configurations. But it is important to notice that the working temperature of the solar receiver is quite higher for those configurations. At optimum pressure ratios temperatures are between 1100-1200 K. These temperatures decrease to 700-900 K when no recuperator is included in design. The consideration of subcritical CO_2 as working fluid has some interesting features: potential for recuperation is higher than for air because turbine outlet temperature is quite higher for CO_2, overall efficiency and fuel conversion efficiency have a wider maximum for CO_2 when plotted in terms of the pressure ratio (so, the election of the optimum one is less critical), and the solar share is always higher for CO_2 in recuperative layouts.

After fixing the optimum pressure ratio at design conditions, an analysis of plant records for any plant subsystem (optical and thermal) was performed for representative days of all seasons. Real meteorological and direct solar irradiance data from SOLUGAS location (south of Spain) were considered, no filtering nor smoothing were done. It is interesting that heliostat field average optical efficiency gets its largest values in winter and the smallest in summer. In the assumed conditions, numerical values fluctuate between approximately 0.59 and 0.68. Overall plant efficiency decreases during sunlight hours because the heliostat field and the receiver add inefficiencies to the whole plant. But at the same time solar share different from zero increases fuel conversion rate and decreases fuel consumption. For all the checked days and seasons heliostat field dimensions of SOLUGAS (about 70 heliostats of 121 m^2 each) only allows a small solar share, so the combustion chamber is always burning natural gas to achieve the pre-fixed turbine inlet temperature (about 1420 K). The model also allows a detailed calculation of fuel consumption, savings from the non-hybridized plant, and the estimation of any greenhouse or pollutant emissions. For those field dimensions and target turbine inlet temperature specific natural gas consumption (averaged over one representative day) is about 180 kg/MWh and CO_2 emissions are below 500 kg/MWh.

The analysis performed in this work reflects the necessity of at least three key actions in order to improve the performance of this technology for commercialization in the next future: (a) to enhance solar field design and efficiency together, (b) to widen the working temperature intervals for the receivers, and (c) to select the most important parameters of the power unit (as the turbine pressure ratio, the working fluid or the consideration of a recuperator) from an overall plant perspective. System versatility is enough to obtain good performance ratios with an appropriate plant design.

ACKNOWLEDGEMENTS

Financial support from University of Salamanca, Banco Santander, and Junta de Castilla y León of Spain (project SA017P17) is acknowledged.

ORCID

Alejandro Medina https://orcid.org/0000-0001-9797-4909

REFERENCES

1. Weinstein L, Loomis J, Bhatia B, Bierman D, Wang E, Chen G. Concentrating solar power. *Chem Rev*. 2015;115:12797-12838.
2. Olumayegun O, Wang M, Kelsall G. Closed-cycle gas turbine for power generation: a state-of-the-art review. *Fuel*. 2016;180:694-717.
3. Rashid K, Mohammadi K, Powell K. Dynamic simulation and techno-economic analysis of a concentrated solar power plant hybridized with both thermal energy storage and natural gas. *J Clean Prod*. 2020;248:119193.
4. Okoroigwe E, Madhlopa A. An integrated combined cycle system driven by a solar tower: a review. *Renew Sustain Energy Rev*. 2016;57:337-350.
5. Burgaleta S, Ramírez DJI. *Gemasolar, the First Tower Thermosolar Commercial Plant with Molten Salt Storage*. Spain: Granada; 2011.
6. Relloso S, Gutiérrez Y. SENER Molten Salt Tower Technology. Ouarzazate NOOR III Case. Paper presented at: AIP Conference Proceedings, SolarPACES 2016, Abu Dhabi, UAE, Vol 1850. Abu Dhabi, UAE: American Institute of Physics; 2017:030041.
7. Liu Q, Bai Z, Wang X, Lei J, Jin H. Investigation of thermodynamic performances for two solar-biomass hybrid combined cycle power generation systems. *Ener Conv Manage*. 2016;122:252-262.
8. Wang K, Li MJ, Guo JQ, Li P, Liu ZB. A systematic comparison of different S-CO_2 cycle layouts based on multi-objective optimization of applications in solar power tower plants. *Appl Ener*. 2020;212:109-121.
9. Linares JI, Cantizano A, Moratilla BY, Martín-Palacios V, Batet L. Supercritical CO_2 Brayton power cycles for DEMO (demonstration power plant) fusion reactor based on dual coolant lithium lead blanket. *Energy*. 2016;98:271-283.
10. Wang X, Li X, Li Q, Liu L, Liu C. Performance of a solar thermal power plant with direct air-cooled supercritical carbon dioxide Brayton cycle under off-design conditions. *Appl Energy*. 2020;261:114359.
11. de la Calle A, Bayon A, Soo Too Y. Impact of ambient temperature on supercritical CO_2 recompression Brayton cycle in arids locations: finding the optimal design conditions. *Energy*. 2018;153:1016-1027.
12. Ma Y, Morosuk T, Luo J, Liu M, Liu J. Superstructure design and optimization on supercritical carbon dioxide cycle for

application in concentrated solar power plant. *Ener Conv Manage*. 2020;206:112290.
13. Novales D, Erkoreka A, de la Peña C, Herrazti B. Sensitivity analysis of supercritical CO_2 power cycle energy and exergy efficiencies regarding cycle component efficiencies for concentrating solar power. *Ener Conv Manage*. 2019;182:430-450.
14. Santos MJ, Miguel-Barbero C, Merchán RP, Medina A, Calvo Hernández A. Roads to improve the performance of hybrid thermosolar gas turbine power plants: working fluids and multi-stage configurations. *Ener Conv Manage*. 2018;165: 578-592.
15. He YL, Cui FQ, Cheng ZD, Zeng-Yao L, Tao WQ. Numerical simulation of solar radiation transmission process for thesolar tower power plant: from the heliostat field to the pressurized volumetric receiver. *Appl Therm Eng*. 2013;61:583-595.
16. Uhlig R, Flesch R, Gobereit B, Giuliano S, Liedke P. Strategies enhancing the efficiency of cavity receivers. *Energ Proc*. 2014; 49:538-550.
17. Asselineau C. Geometrical Optimisation of Receivers for Concentrating Solar Thermal Systems [PhD thesis]. Canberra: The Australian National University; 2017.
18. Quero M, Korzynietz R, Ebert M, Jiménez AA, Río dA, Brioso JA. Solugas - operation experience of the first solar hybrid gas turbine system at MW scale. *Energ Proc*. 2014;49:1820-1830.
19. Korzynietz R, Brioso JA, del Río A, et al. Solugas - comprehensive analysis of the solar hybrid Brayton plant. *Sol Ener*. 2016; 135:578-589.
20. Merchán RP, Santos MJ, Medina A, Calvo Hernández A. Thermodynamic model of a hybrid Brayton thermosolar plant. *Renew Ener*. 2018;128:473-483.
21. Merchán RP, Santos MJ, Heras I, Gonzalez-Ayala J, Medina A, Calvo Hernández A. On-design pre-optimization and off-design analysis of hybrid Brayton thermosolar tower power plants for different fluids and plant configurations. *Renew Sust Energy Rev*. 2020;109590:119. https://doi.org/10.1016/j.rser.2019.109590.
22. Duffie J, Beckman W. *Solar Engineering of Thermal Processes*. Hoboken, New Jersey: John Wiley and Sons; 2006.
23. Li C, Zhai R, Liu H, Yang Y, Wu H. Optimization of a heliostat field layout using hybrid PSO-GA algorithm. 2018; 128: 33–41.
24. Zhang M, Yang L, Xu C, Du X. An efficient code to optimize the heliostat field and comparisons between the biomimetic spiral and stagerred layout. *Renew Ener*. 2016;87:720-730.
25. Collado FJ. Preliminary design of surrounding heliostat fields. *Renew Ener*. 2009;34:1359-1363.
26. Collado FJ, Guallar J. A review of optimized design layouts for solar power tower plants with *campo* code. *Renew Sustain Energy Rev*. 2013;20:142-154.
27. Solar, Turbines, Caterpillar.
28. Olivenza-León D, Medina A, Calvo Hernández A. Thermodynamic modeling of a hybrid solar gas-turbine power plant. *Energ Conv Manage*. 2015;93:435-447.
29. Meteosevilla. http://www.meteosevilla.com. Accessed August 1, 2020.
30. Santos MJ, Merchán RP, Medina A, Calvo Hernández A. Seasonal thermodynamic prediction of the performance of a hybrid solar gas-turbine power plant. *Ener Conv Manage*. 2016; 115:89-102.
31. Lemmon EW, Huber ML, McLinden MO. *NIST Standard Reference Database 23: Reference Fluid Thermodynamic and Transport Properties-REFPROP, Version 9.1*. Gaithersburg: National Institute of Standards and Technology, Standard Reference Data Program; 2013.
32. Luu MT, Milani D, McNaughton R, Abbas A. Dynamic modelling and start-up operation of a solar-assisted recompression supercritical CO_2 Brayton power cycle. *Appl Ener*. 2017;199: 247-263.
33. Crespi F, Gavagnin G, Sánchez D, Martínez GS. Supercritical carbon dioxide cycles for power generation. *Appl Ener*. 2017; 195:152-183.
34. Coco-Enríquez L, Muñoz-Antón J, Martínez-Val JM. New text comparison between CO_2 and other supercritical working fluids (ethane, Xe, CH_4, and N_2) in line-focusing solar power plants coupled to supercritical Brayton power cycles. *Int J Hydrogen Ener*. 2017;42:17611-17631.
35. Stine WB, Geyer M. Power from The Sun. 2001.

How to cite this article: Merchán RP, Santos MJ, Medina A, Hernández AC. On- and off-design thermodynamic analysis of a hybrid polar solar thermal tower power plant. *Int J Energy Res*. 2020; 1–17. https://doi.org/10.1002/er.5854

3.7 Paper 7 – Thermo-economic analysis of a central tower hybrid Brayton thermo-solar plant: sensitivity to main design parameters

Title: "Thermo-economic analysis of a central tower hybrid Brayton thermo-solar plant: sensitivity to main design parameters"
Journal: Submitted to *Applied Thermal Engineering*
Authors: **R.P. Merchán**, M.J. Santos, J. García-Ferrero, A. Medina, A. Calvo Hernández
Year: 2020
Reference: [136]

Resumen

Se presenta un modelo teórico que describe el funcionamiento de una planta termosolar de torre central acoplada a un ciclo Brayton híbrido. Se tienen en cuenta las características básicas de la planta sevillana *SOLUGAS* (campo de heliostatos polar) para llevar a cabo la implementación del modelo. El objetivo principal de este trabajo es realizar un estudio termo-económico de la planta mediante el cálculo del Coste Normalizado de la Electricidad (*LCoE*) para diferentes configuraciones posibles y analizando la influencia de los principales parámetros de diseño. Para el caso base, se estima un Coste Normalizado de la Electricidad de 158 USD/MWh. Asimismo, se realiza un estudio sobre los efectos de la inclusión de un recuperador en el esquema de la planta. Se demuestra que la configuración recuperativa es la mejor opción desde el punto de vista termo-económico puesto que el Coste Normalizado de la Electricidad disminuye en casi un 17 % y las emisiones específicas de CO_2 en un 45 %. Además, aumenta la eficiencia en casi un 28 % y el *solar share* en un 25 %. Por otro lado, se comparan los registros de salida para dos localizaciones de la planta diferentes: Sevilla y Salamanca. Se obtiene que el Coste Normalizado de la Electricidad es un 3.5 % mayor en Salamanca; sin embargo, su eficiencia es un 2 % mayor que en Sevilla. Finalmente, se efectúan análisis de sensibilidad tanto para parámetros del receptor solar y del campo de heliostatos como para parámetros de la turbina de gas. De dichos análisis, se deduce que la temperatura de entrada a la turbina y el tamaño de apertura del receptor solar son dos de los parámetros cuya influencia en el Coste Normalizado de la Electricidad es más destacable.

Thermo-economic analysis of a central tower hybrid Brayton thermo-solar plant: sensitivity to main design parameters

R.P. Merchán[a], M.J. Santos[a], J. García-Ferrero[a], A. Medina[a], A. Calvo Hernández[a]

[a]*Department of Applied Physics and IUFFYM, University of Salamanca, Salamanca, Spain*

Abstract

A hybrid central tower thermo-solar plant working with a gas turbine is simulated by means of an in-house developed model and software. The model considers the integration of all plant subsystems. The calculation of the heliostat solar field efficiency includes the main losses factors as blocking, shadowing, attenuation, interception, and cosine effect. The simulation considers a Brayton cycle for the power unit with irreversibilities in the compressor and turbine, and pressure drops in the heat absorption and extraction processes. A combustion chamber burning natural gas ensures an approximately constant power output. The model is flexible and precise. At the same time it is fast enough to perform sensitivity studies on the efficiency of any subsystem and the overall plant. Thus, it allows for performing a thermo-economic analysis of the plant checking the influence of the main plant design parameters. The focal objective is to analyze the importance on the levelized cost of electricity (LCoE) of the key plant design parameters. The direct influence of parameters from the heliostat field and receiver (as tower height, distance to the first row of heliostats, heliostats size, receiver size and heat losses, etc.) on final LCoE is surveyed. Similarly, parameters from the turbine as pressure ratio, turbine inlet temperature, influence of recuperation and others, are also analyzed. The dimensions of the plant are taken from SOLUGAS

Email addresses: rpmerchan@usal.es (R.P. Merchán), smjesus@usal.es (M.J. Santos), jgferrero@usal.es (J. García-Ferrero), amd385@usal.es (A. Medina), anca@usal.es (A. Calvo Hernández)

Preprint submitted to Applied Thermal Engineering *July 28, 2020*

prototype near Seville, Spain, although another location with quite different solar conditions in Spain is also considered. LCoE values predicted are about 158 USD/MWh. The analysis concludes that among several parameters surveyed, two of them are key in LCoE predicted values: turbine inlet temperature and solar receiver aperture size.

Keywords: Thermo-solar hybrid power plants, Overall plant model, Thermo-economic analysis, Sensitivity of levelized cost of electricity, Subsystems integration
PACS: 05.70.Ln, 07.20.Pe, 84.60.-h

Nomenclature

A_a (m^2) aperture area of the field

AH (m^2) heliostats area

C concentration ratio

C_{dec} (USD) decommissioning costs

C_{inv} (USD) investment and initial installation costs

C_{OML} (USD/year) operation, maintenance and labour costs

$\cos\omega$ cosine of Sun radiation angle of incidence

c_w (J/kg.K) specific heat of the working fluid

DR (m) receiver diameter

DS (m) safety distance between heliostats

E_{net} (GWh/year) net energy produced in a year

f solar share

f_{at} attenuation factor

f_b blocking factor

f_{sh} shadowing factor

f_{sp} spillage factor

G (W/m^2) direct normal irradiance

i (%) interest rate

$\dot{m}$ (kg/s) mass flow rate of the working substance

$\dot{m}_f$ (kg/s) fuel mass flow rate

n_{con} (year) number of years expended in plant construction

n_{dec} (year) number of years expended in plant decommissioning

n_{op} (year) number of years of plant operation

NH number of heliostats in the field

P (MW) power output

$|\dot{Q}_{\text{H}}|$ (J/s) total heat transfer rate absorbed by the working fluid

$|\dot{Q}_{\text{HC}}|(J/s)$ heat rate input from the combustion chamber

$|\dot{Q}_{\text{HS}}|(J/s)$ heat rate input from the solar collector

$|\dot{Q}_{\text{L}}|(J/s)$ heat-transfer rate between the working fluid and the ambient

Q_{LHV} (J/kg) lower heating value of the fuel

R_{min} (m) distance from first heliostats to the tower

r_p overall pressure ratio

T_{HC} (K) working temperature of the combustion chamber

T_{HS} (K) working temperature of the solar collector

THT (m) tower height

T_{L} (K) ambient temperature

T_x (K) working fluid temperature after the heat input from the recuperator

$T_{x'}$ (K) working fluid temperature after heat input from the solar collector

T_3 (K) turbine inlet temperature

$\overline{U}_{\text{L}}$ (W/m^{2}K) effective conduction-convection heat transfer parameter

α effective emissivity of the receiver

$\varepsilon_{\mathrm{HC}}$ combustion chamber heat exchanger effectiveness

$\varepsilon_{\mathrm{HS}}$ solar collector heat exchanger effectiveness

ε_c isentropic efficiency of the compressor

ε_r recuperator effectiveness

ε_t isentropic efficiency of the turbine

η overall thermal efficiency

η_C combustion chamber efficiency

η_{gen} electrical generator efficiency

η_{hel_i} efficiency of heliostat i

η_{H} thermal efficiency of the Brayton heat engine

η_S solar subsystem efficiency (field and receiver)

η_0 heliostat field optical efficiency

ρ mirrors reflectivity

σ ($\mathrm{W/m^2K^4}$) Stefan-Boltzmann constant

Acronyms

CSP Concentrated Solar Power

DNI Direct Normal Irradiance

LCoE Levelized Cost of Electricity

OML Operation, Maintenance and Labour

1. Introduction

Thermo-solar power plants constitute, among renewable energies, one of the best alternatives to lead the global energy transition from carbonized to decarbonized energy sources [1, 2]. Solar central tower systems stand out because of their promising high efficiencies and concentration ratios. In these systems, a heliostat field reflects and concentrates the solar radiation onto a solar receiver, located at the top of a central tower. Nowadays, most commercial projects employ a Rankine cycle in order to transform the concentrated solar heat into electricity [3]. Nevertheless, Brayton cycles can make use of air or other gas instead of water to move a turbine. Therefore, they seem interesting in areas with good insolation ratios that almost always bring about scarce hydric resources [4]. These plants are flexible to operate because thermal energy storage [5] or hybridization can be implemented, reducing the undesirable impacts of solar energy fluctuations. A recent review on this point is due to Achkari and El Fadar [6].

In the research literature there are quite a lot works on central tower thermosolar plants but many of them are specialized in any of the subsystems. There are many accurate softwares to estimate and optimize solar field efficiencies either from theoretical assumptions or from MonteCarlo simulations as Campo Code [7], HFLCAL [8], SolTrace [9], and Tonatiuth [10]. A recent compilation and comparison among those models is due to Jafrancesco *et al.* [11]. Solar receivers technology, specially at the high temperatures required by Brayton cycles, is an open research field, both from the experimental viewpoint [12, 13] or from computational fluid dynamics or materials perspectives [14]. There are also different tools to predict the performance of the power units producing the electricity from the thermosolar input as TRNSYS [15], Thermoflex [16], EBSILON Professional [17], EES [18], etc., that have been used by many authors.

Nevertheless, our approach is different: to build a precise but not too intricate model for the whole plant, controlling at any moment the physical meaning of the parameters and the main assumptions to perform. In this way, it is possible to have a broad outlook of the overall installation and to locate the main bottlenecks in efficiencies or thermo-economic indicators. And thus, to suggest improved plant layouts for better performance, reduced consumption, and reduced costs, with the final aim to produce clean electricity at affordable prices.

This study proposes to analyze a central tower thermosolar plant pow-

ered by a hybrid Brayton cycle. A first prototype plant at pre-commercial scale (about 5 MW) was developed at the south of Spain in the last years. The project was called SOLUGAS and was led by the company Abengoa Solar [19]. This project has served as a reference to test several theoretical and simulation models. It will be taken also in this study as a reference to size the simulated plant for numerical computations.

As operation objective of the plant, it will be taken to deliver an approximately constant electric power to the grid. To get this aim, a hybridization strategy is followed: the turbine inlet temperature is assumed as constant and a combustion chamber burning natural gas releases the heat necessary to reach that temperature even by night or in periods of poor insolation [20].

During the last years our research group has developed from scratch a simulation model for this kind of plants. The model considers the plant as a whole, incorporating its main subsystems. First, a thermodynamic model for a gas turbine was established. It starts from a closed irreversible Brayton-like cycle, which includes the most significant losses in this kind of power units as non-isentropic compressors and turbines, pressure drops in heat input and heat release, and non-ideal recuperation [21]. The model relies on a relatively reduced number of parameters with a clear physical meaning and was validated by comparing with different real engines [22, 23]. The model was also extended for multi-stage gas turbines with an arbitrary number of compression or/and expansion steps and different working fluids [24].

Second, more recently a detailed model for the solar subsystem, including heliostat field and receiver was developed [23]. This model is capable to predict the optical efficiency of the heliostat field at any time and any meteorological condition. The solar sub-model was tested against the heliostat field GEMASOLAR, located near Seville, Spain [25]. Shadowing and blocking effects were assumed as a constant factor in order to speed up computational calculations, because the aim of the sub-model is to be integrated with that of the power unit and thus, to make predictions for the whole plant. It was checked that this assumption does not lead to appreciable errors by comparing with the software Campo Code developed by Collado *et al.* [26, 27].

The model for the overall plant integrates all sub-models and allow precise and computationally fast estimations of plant performance under different conditions. Thus, the specific objectives of this work can be summarized as follows: (i) To analyze the influence over the whole plant of recuperation in the Brayton cycle from a thermo-economic viewpoint; (ii) To analyze plant

performance and LCoE values for two different locations in Spain, one of them well-known from the viewpoint of thermosolar installations and other at a northern latitude with slightly worse solar records but with smaller ambient average temperatures; and (iii) To perform a sensitivity analysis of the effect on thermo-economic records of the main plant design parameters. These include variables from the heliostat field, the receiver and the power unit itself.

2. Model layout

The involved thermosolar hybrid power plant has three main subsystems: solar field and receiver, combustion chamber, and heat engine; as it can be observed in Fig. 1. A central tower surrounded by a polar (or north) heliostat field together with a solar receiver constitute the first subsystem. The solar subsystem provides heat input to a gas turbine that is coupled to a combustion chamber which ensures to reach a fixed turbine inlet temperature by night or during cloudy periods or other bad meteorological conditions. Proceeding in this way, the power output is approximately constant, which is the operation aim of the installation.

The overall thermal efficiency of the system, η, is defined as the net power output divided by the total heat input [35]:

$$\eta = \frac{P}{GA_a + \dot{m}_f Q_{\mathrm{LHV}}} \tag{1}$$

Total heat input is made up of the solar heat (GA_a where G is the direct normal irradiance and A_a the aperture area) and the heat from fuel combustion ($\dot{m}_f Q_{\mathrm{LHV}}$ where $\dot{m}_f$ is the instantaneous fuel mass flow and Q_{LHV} the lower heating value of the fuel). Overall efficiency can be expressed as a function of the subsystems efficiencies. This means: in terms of the heat engine efficiency, η_H; solar subsystem efficiency, η_S; combustion efficiency, η_C; the effectivenesses of the heat exchangers associated with the solar collector, ε_{HS}, and to the combustion chamber, ε_{HC}; and finally, the solar share, f (ratio of solar heat input over the total heat input) [21]. Explicit calculations can be found in that paper. The relationship among overall efficiency and subsystems efficiencies can be expressed as [21]:

$$\eta = \eta_{\mathrm{S}}\eta_C\eta_{\mathrm{H}}\left[\frac{\varepsilon_{\mathrm{HS}}\varepsilon_{\mathrm{HC}}}{\eta_C\varepsilon_{\mathrm{HC}}f + \eta_{\mathrm{S}}\varepsilon_{\mathrm{HS}}(1-f)}\right] \tag{2}$$

In the next subsections the models for subsystems efficiencies are detailed.

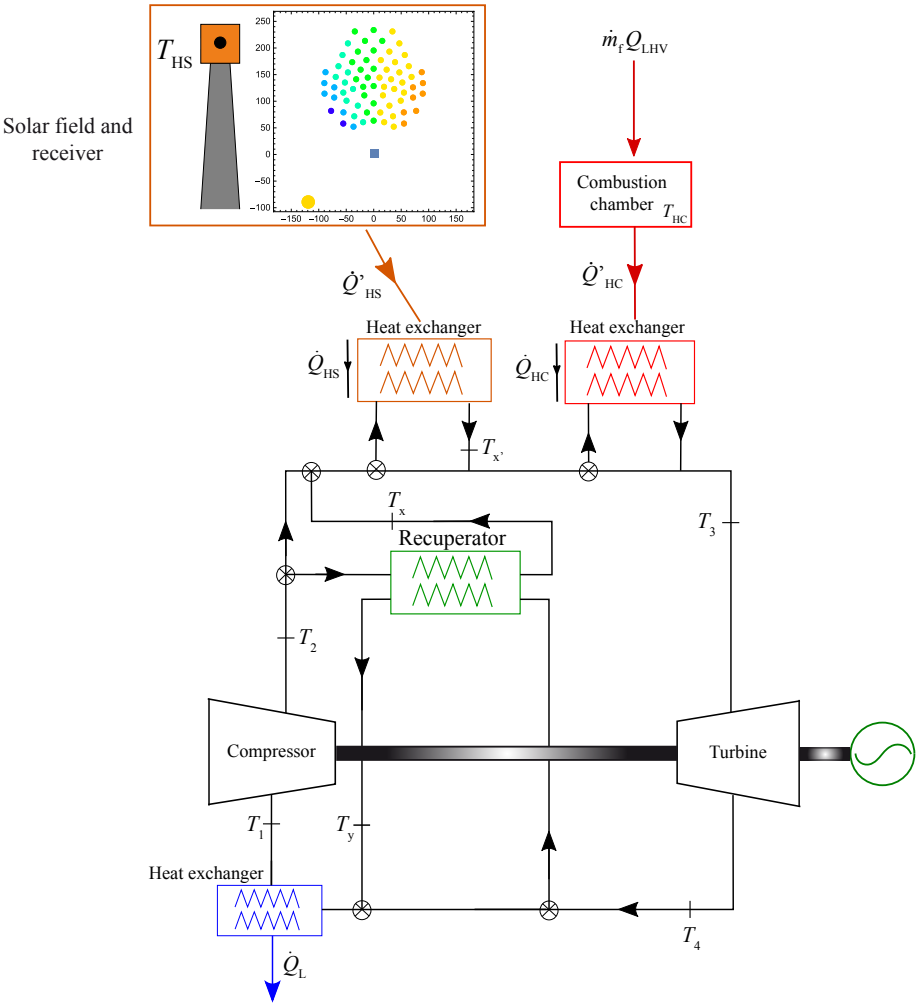

Figure 1: Plant diagram with the main subsystems: solar field and receiver, combustion chamber, and heat engine (gas turbine).

2.1. Thermodynamic model for the power unit

The thermodynamic model for the power unit, a Brayton-like gas turbine was developed by our group in previous works, so only a brief summary with the main assumptions is reported here [21, 28]. It is assumed that a mass rate of an ideal gas, $\dot{m}$, with temperature dependent specific heat, $c_w(T)$,

develops an irreversible closed Brayton cycle. Recuperation can be included in the cycle. The working temperature of the solar receiver, T_{HS}, and that of the surroundings, T_L, are fluctuating quantities.

1. First, the gas is compressed by means of a non-ideal compressor. Its isentropic efficiency is given by ε_c and measures how far is the compressor from ideal adiabatic operation. Temperature at compressor inlet is denoted T_1 and at the exit, T_2. An explicit $T-S$ scheme of the cycle with the same notation can be found in [28].

2. After compression, the gas sequentially receives three energy inputs. First, the non-ideal recuperator, when considered in plant layout, increases the gas temperature from T_2 to T_x. Its effectiveness, ε_r, is defined as the ratio between the actual temperature increase and the maximum ideal one. In the case of a non-recuperative cycle, $\varepsilon_r = 0$, and in the ideal limit, $\varepsilon_r = 1$.

   Secondly, the gas receives a heat flow, $|\dot{Q}_{\mathrm{HS}}|$, from the solar subsystem and thus, its temperature increases from T_x to $T_{x'}$. The latter is the working fluid temperature at the solar receiver outlet. From the viewpoint of the heat engine, the solar receiver acts as a heat exchanger with effectiveness, ε_{HS}. If $T_{x'}$ is below the target turbine inlet temperature, denoted as T_3, the gas receives a final heat input from the combustion chamber in order to ensure an approximately constant, T_3, independently of the value of direct irradiance, G. Similarly, as a closed cycle is being considered, the combustion chamber is represented as a heat exchanger with effectiveness, ε_{HC}.

   In which respect to the pressure during the heat addition processes, a global parameter quantifies the pressure decrease in the whole heat input process. In real plants, pressure decays are associated with the particular equipment in any of the three steps of the heat input process, but the consideration of a unique global pressure decay parameter allows to obtain analytical equations and to numerically check the effects of pressure decays in the output parameters of the plant [29].

3. At the turbine inlet, the working fluid has reached its maximum temperature and it is expanded by means of a non-ideal turbine characterized by an isentropic efficiency, ε_t. Temperature at the outlet is denoted T_4.

4. The final heat release to recover compressor inlet conditions is divided into two steps. First, through recuperation and later on by exchanging heat to the ambient through a non-ideal heat exchanger with effectiveness, ε_L. The pressure loss during the whole heat release process is measured through a unique coefficient that accounts for the relative pressure decay.

   It is convenient to define a global pressure ratio, r_p as:

$$r_p = \frac{p_{\mathrm{H}}}{p_{\mathrm{L}} - \Delta p_{\mathrm{L}}} \tag{3}$$

   where p_{H} is the highest pressure in the cycle (at compressor exit) and $p_{\mathrm{L}} - \Delta p_{\mathrm{L}}$ is the lowest one, at compressor entrance. In this equation, p_{L} represents pressure at turbine exit.

Once the main hypotheses and parameters have been established, the temperatures of all the states in the cycle can be expressed in terms of the temperature of the solar collector, T_{HS}, that of the combustion chamber, T_{HC}, the pressure ratios of the compressor, and the parameters that characterize the non-ideality of the components. The explicit set of equations can be found in [28]. The total heat input rate, $|\dot{Q}_{\mathrm{H}}|$, and, the heat release, $|\dot{Q}_L|$, are expressed in terms of the temperatures as:

$$|\dot{Q}_H| = |\dot{Q}_{\mathrm{HS}}| + |\dot{Q}_{\mathrm{HC}}| \tag{4}$$

$$|\dot{Q}_L| = \dot{m} \int_{T_1}^{T_y} c_w(T)\, dT \tag{5}$$

where,

$$|\dot{Q}_{\mathrm{HS}}| = \dot{m} \int_{T_x}^{T_{x'}} c_w(T)\, dT = f|\dot{Q}_H| \tag{6}$$

$$|\dot{Q}_{\mathrm{HC}}| = \dot{m} \int_{T_{x'}}^{T_3} c_w(T)\, dT = (1-f)|\dot{Q}_H| \tag{7}$$

Thus, the power output released by the heat engine is, $P = |\dot{Q}_{\mathrm{H}}| - |\dot{Q}_L|$, and its thermal efficiency, $\eta_{\mathrm{H}} = P/|\dot{Q}_{\mathrm{H}}|$. This sub-model for the power unit efficiency is incorporated then to calculate the overall efficiency through Eq. (2).

2.2. Heliostat field and receiver models

The considered heliostat field can be circular or polar around the central tower. The numerical application in the next sections would be developed for a polar one but the approach is similar. The heliostat field is made up of several rows of heliostats, each with a two-axis tracking to improve irradiance receiving and reflection towards the tower. The heliostat surface is a rectangular plane mirror. A safety distance between heliostats, DS, is considered [30].

Heliostats are placed uniformly over a circumference. The heliostat field is divided into regions and rows. A region comprises one or more rows in which the increment of the azimuth angle is constant [30]. For a particular region, distance between adjacent heliostats increases with the distance to the tower. A new region begins if separation between two heliostats is large enough to set one more heliostat. There are several field expansion techniques in the literature. In this work, Campo Code model was followed [30, 31]. Particular details on our model can be found in [23]. As in most models, heliostats locations arise from decreasing the heliostat density from an initial dense layout. Because of shadowing and blocking effects (explained below) there is a balance effect and optimum densities are found because field expansion advantages prevail over its disadvantages. In this work, heliostat densities were calculated as in a preliminar version of Campo Code [30].

The optical efficiency of the whole field, η_0, is the average of the efficiency of each heliostat:

$$\eta_0 = \bar{\eta}_{hel} = \frac{\sum_{i=1}^{NH} \eta_{hel_i}}{NH} \tag{8}$$

where NH represents the total number of heliostats in the solar field. The optical efficiency of each one is a product of losses factors:

$$\eta_{hel_i} = cos\,\omega_i \cdot f_{sp,i} \cdot f_{at,i} \cdot f_b \cdot f_{sh} \cdot \rho \tag{9}$$

In this equation $cos\,\omega$ denotes the cosine of Sun radiation angle of incidence, f_{sp} comes from spillage, f_{at} is the attenuation factor, f_b represents the blocking factor, f_{sh} is the shadowing factor, and ρ represents mirrors reflectivity. A subindex i has been added in those terms that actually depend on each heliostat in our framework. This is explained below.

1. *Cosine factor*

It is the main factor governing optical efficiency. An analytical study on Sun-heliostat-receiver geometry is done on the basis of optical reflection law. This leads to an expression for ω that depends on each heliostat coordinates, receiver coordinates, and solar azimuth and altitude angles. An explicit equation for ω can be found in [30].

2. *Spillage factor*

   The fraction of reflected radiation outside the receiver limits is the origin of spillage losses factor The power delivered by each heliostat to the receiver is the integral over the receiver aperture area of the corresponding flux density function. In this work it is assumed the spillage calculation model by HFLCAL [8]. Spillage is considered as dependent on the dimensions of the receiver, heliostat area, the effective dispersion of the sun shape on the receiver plane, heliostat tracking, and surface errors. Our formulation is the same that the one proposed by Collado and Guallar in [27], but without taking into account the astigmatic effect. This makes the spillage factor depend on each heliostat position with respect to the receiver.

3. *Attenuation factor*

   This factor arises from the energy dissipation due to absorption of air molecules in the region between the heliostats and the receiver. So, it depends on the distance between the centre of each heliostat and the aiming point in the receiver [32]. Therefore, it depends on each particular heliostat. For large solar fields, differences in attenuation among heliostats are larger than in small ones. It is usual to take an empirical formula for f_{at} in terms of the distance.

4. *Blocking and shadowing factors*

   The blocking factor measures the energy loss because a fraction of the reflected energy from a back heliostat can be stopped by one ahead. Besides, the shadowing factor takes into account the energy loss when a heliostat projects a shadow onto another one. Thus, only a fraction of the surface of the last heliostat reflects sun radiation. The most complex and time consuming components in the numerical evaluation of optical efficiency are these factors [33]. They can be calculated one by one, for each heliostat, with different techniques or, in order to avoid extensive calculations [34], to take them as constant for certain

purposes. As the main objective of this work is to analyze the plant as a whole, including all subsystems, these factors will be taken as constant. *A posteriori* sensitivity analysis will justify this assumption.

5. *Mirror reflectivity*

   The actual reflectivity, ρ, is usually taken as the simple product of two factors: the nominal reflectivity and the nominal cleanliness [27]. The importance of the actual reflectivity is not just related to the efficiency of the heliostat, indeed, it is also a function of the maintenance cost of the field since the nominal cleanliness depends on plant maintenance works.

As a summary, it should be noted that cosine factor, spillage, and attenuation depend on the particular heliostat. The other factors (blocking, shadowing, and reflectivity) are independent and so, are common factors in the average optical efficiency (see Eq. (8)).

All the losses above are optical in nature and arise from the collection of the solar power from the heliostats and its transfer through specular reflection to the receiver aperture. Nevertheless, the receiver as any body at high temperature has losses due to heat transfer to the surroundings because of conduction, convection, and radiation. In this way, it is usual to express the joint solar subsystem efficiency, η_S, as [24, 35]:

$$\eta_S = \eta_0 - \frac{1}{GC}[\alpha\sigma(T_{HS}^4 - T_L^4) + \overline{U}_L(T_{HS} - T_L)] \tag{10}$$

where C is the concentration ratio, α the emissivity of the receiver surface, σ the Stefan-Boltzmann constant, and $\overline{U}_L$ the overall conduction and convection heat transfer coefficient. As stated before, T_{HS} is the solar collector operation temperature and T_L the ambient temperature. From the thermodynamic viewpoint T_{HS} is an equilibrium temperature between the heat input in the receiver from the solar field and the heat release from the receiver to the working fluid. Within this scheme, the heat flux actually absorbed by the working fluid is: $|\dot{Q}_{HS}| = \varepsilon_{HS} G A_a \eta_S$.

In an analogous way, in those periods where the combustion chamber is required to guarantee an stable turbine inlet temperature, the heat flow from combustion is expressed as $|\dot{Q}_{HC}| = \varepsilon_{HC} \dot{m}_f Q_{LHV} \eta_C$. In this expression ε_{HC} is the effectiveness of the heat exchanger associated with the combustion chamber (because the thermodynamic cycle is closed and, so, combustion is

external) and η_C arises from combustion inefficiencies. It is usual to take it as a constant factor. This avoids the consideration of specific combustion and chemical reactions models.

3. Thermo-economic performance

A thermo-economic model has been implemented in our simulations with the purpose of analyzing system viability. The *levelized cost of electricity* (LCoE), represents the minimum sale price at which the electricity should be sold for the plant to be profitable during a specified length of time. It is probably the simplest and most common economic indicator. As commented by Dowling *et al.* [36], it can be criticized because it does not capture the time-varying value of electricity. Particularly, LCoE comparison within different concentrating solar power (CSP) technologies maybe subtle. Certain design modifications can, *a priori*, increase LCoE, but at the same time can lead to short pay-off periods when time varying electricity prices are considered. In any case, it is difficult to make precise estimations on costs and adequate sale prices for technologies that are still under development. Absolute numerical estimations should be taken with care, however comparison between different plant designs and sensitivity analysis under the same assumptions can certainly lead to robust conclusions. A detailed review on these issues in the case of PV and CSP systems is due to Hernández-Moro *et al.* [37].

In this work the formulation of Spelling [38] for the estimation of LCoE will be assumed. Its definition can be written as:

$$\mathrm{LCoE} = \frac{\beta_{\mathrm{inv}} C_{\mathrm{inv}} + \beta_{\mathrm{dec}} C_{\mathrm{dec}} + C_{\mathrm{OML}}}{E_{\mathrm{net}}} \tag{11}$$

where C_{inv} represents the investment and initial installation costs, C_{dec} the decommissioning costs, and C_{OML} the operation, maintenance and labour costs (OML), that include fuel consumption in the case of hybrid plants as the one considered here. All these terms are yearly costs. The denominator, E_{net}, stands for the annual net energy output of the plant. The weight β_{inv} relates the total capital investment costs to the equivalent annual payments over a fixed period of years. Similarly, β_{dec} represents the yearly equivalent

cost of decommissioning. These factors can be written as [38]:

$$\beta_{\text{inv}} = \frac{(1+i)^{n_{\text{con}}} - 1}{i \cdot n_{\text{con}}} \frac{i\,(1+i)^{n_{\text{op}}}}{(1+i)^{n_{\text{op}}} - 1} + k_{\text{ins}} \tag{12}$$

$$\beta_{\text{dec}} = \frac{(1+i)^{n_{\text{dec}}} - 1}{i \cdot n_{\text{dec}}(1+i)^{n_{\text{dec}}-1}} \frac{i}{(1+i)^{n_{\text{op}}} - 1} \tag{13}$$

In these equations i is the real interest rate and k_{ins}, the annual plant insurance rate. The number of years expended in plant construction, operation, and decommissioning are denoted, n_{con}, n_{op}, and n_{dec}, respectively. Thus, this formulation of LCoE explicitly considers the time spent during construction and decommissioning. In other formulations these times are considered as one year, but in this case these times could be longer. Figure 2 depicts in a tree shape all the terms considered for LCoE computation.

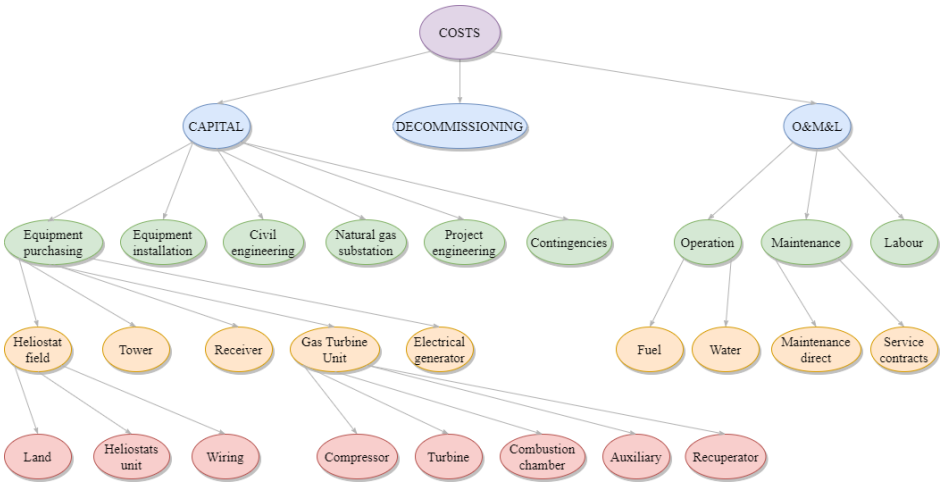

Figure 2: Tree structure of all the costs considered for the calculation of LCoE.

4. Model Implementation

The theoretical model summarized in the last section has been implemented in our own software, developed in programming language Mathematica Values of solar and gas turbine parameters are very similar to SOLUGAS plant features [19]. This project was developed by Abengoa Solar in Sanlúcar

Table 1: Parameters for the solar field and receiver were taken from SOLUGAS project data [19] and those for the Brayton cycle correspond to the turbine Mercury 50 [39]. Those marked with * were assumed from [40] where the numerical model for the gas turbine was validated.

Subsystem	Parameter	Symbol	Value	Unit
Heliostat field and receiver	Tower height	THT	65	m
	Heliostats number	NH	70	–
	Heliostat height	LH	11.01	m
	Safety distance	DS	0.3	LH
	Heliostat area	AH	121.3	m^2
	Adjacent heliostats separation	–	3.285	m
	First row distance from tower	$R_{\min}$	64	m
	Concentration ratio	C	432	–
	Blocking and shadowing factor	$f_b \cdot f_{sh}$	0.95	–
	Actual mirrors reflectivity	ρ	0.836	–
	Sun shape deviation	–	2.51	mrad
	Surface errors deviation	–	0.94	mrad
	Tracking errors deviation	–	0.63	mrad
	Receiver diameter	DR	5	m
	Receiver emissivity*	α	0.1	–
	Conduction and convection losses factor*	$\overline{U}_L$	5	$W/(m^2K)$
	Receiver effectiveness*	ε_{HS}	0.78	–
Combustion system	Combustion chamber efficiency*	η_C	0.98	–
	Heat exchanger efficiency*	ε_{HC}	0.98	–
Brayton cycle	Pressure ratio	r_p	9.9	
	Air mass flow	$\dot{m}$	17.9	kg/s
	Turbine isentropic efficiency*	ε_t	0.885	–
	Compressor isentropic efficiency*	ε_c	0.77	–
	Turbine inlet temperature*	T_3	1423	K
	Recuperator effectiveness*	ε_r	0.775	–
	Heat input pressure drop*	$\Delta p_H/p_H$	9.2	%
	Generator efficiency*	η_{gen}	0.99	–

la Mayor, near Seville (Spain). As in our simulation, the plant is made up of a polar heliostats field focusing on a cavity receiver atop a central tower, where pressurized air develops a recuperated Brayton cycle.

4.1. Heliostat field and power unit data

The most significant data from the heliostats field are collected in Table 1. SOLUGAS field is made up of 70 square heliostats of 121.3 m^2 area. They are placed with polar symmetry with respect to the receiver, located on the

central tower at a height of 65 m at the south of the field. The distances of all heliostats to the receiver are below 1 km and the formula by Leary and Hankins [41] for the attenuation factor, f_{at}, is assumed.

Meteorological data are taken from Spanish Meteorological National Agenc (AEMET) [42], except for solar irradiance which has been obtained from Copernicus Atmosphere Monitoring Service (CAMS) [43]. Annual averages of ambient temperatures and direct normal irradiance were made by taking one representative day of each season (taking real data for that day) and weighting each one with the number of days corresponding to each season.

Our code for heliostat field efficiency calculation has been validated by comparing against Campo Code software [27, 30], not only at design conditions but also seasonally. Deviations in average optical efficiency, η_0, and all its components are always below 1%. The power unit used in SOLUGAS is the Mercury 50 gas turbine by Caterpillar [39]. It delivers 4.6 MW of nominal power output, with a pressure ratio of 9.9 and an air mass flow of 17.9 kg/s. Further details on Brayton cycle numerical features and its validation are gathered in [40] (see tables 1 and 2 of that paper), [24] (Sec. 3.1), and [23] (see Appendix B). Numerical data for all the subsystems in the particular case of the SOLUGAS project are compiled in Table 1. The particular value of the effective convective heat transfer coefficient $\overline{U}_L$ for the receiver was taken from [35].

4.2. Data for the computation of LCoE

As commented before, the operation aim of the plant is to produce an approximately constant power output during all the year independently of solar conditions. This strategy, on one side, allows for a high capacity factor and a high yearly energy production, but, on the other side, requires a considerable amount of fuel, to keep electricity production by night or during bad solar conditions.

For the thermo-economic analysis, the solar plant is assumed to be operating 25 years with a real interest rate of 7% and an annual plant insurance rate of 1%. These parameters and other employed in the calculation of LCoE are shown in Tables 2 and 3. Most correlations and numerical data were taken from Spelling's work [38]. Of course, all costs correlations have been adapted as close as possible to the conditions of the particular plant chosen to perform calculations, *i.e.*, SOLUGAS project plant. Capital, decommissioning, and OML costs have been computed following Spelling's work [38]. However, regarding equipment costs, some differences with respect to Spelling

work are considered for a more reasonable implementation in our thermodynamic model: the solar receiver cost computation [44] and the addition of the recuperator cost [45]. All equipment purchasing costs have been updated according to Marshall and Swift indexes for taking into account inflation [46].

Table 2: Interest and time parameters assumed for the calculation of LCoE [38].

Parameter	Symbol	Value	Unit
Real interest rate	i	7	(%)
Insurance interest rate	k_{ins}	1	(%)
Construction time	n_{con}	2	year
Operation time	n_{op}	25	year
Decommissioning time	n_{dec}	2	year

In order to survey different cost scenarios, pessimistic and optimistic, costs from different works were analyzed. Particularly, it was found that most spread out costs among different studies correspond to prices of receiver and recuperator. Three different scenarios are analyzed in this work: optimistic (both with the cheapest costs [45, 47]), pessimistic (both with the most expensive costs [44, 48]) and intermediate scenario (most expensive receiver [44] and cheapest recuperator [45]). For the sake of conciseness, costs results from our calculations with the data taken in the mentioned references and applied for the case of the SOLUGAS base case are broken down in Table 3 for the intermediate scenario.

Capital costs reach more than 30 Million USD, meanwhile decommissioning and OML take values about 1.3 Million USD and 3.3 Million USD per year, respectively. Equipment requires about 69% of all investment costs. And, within equipment purchasing, the solar subsystem (heliostat field, tower and receiver) amounts near 80%. In the case of SOLUGAS, the heliostat field is small (70 heliostats) and so, land investment is also reduced. Land costs are 22.2% with respect to heliostat field cost. With reference to the gas turbine, it constitutes 8.7% of all equipment purchasing. Several pie charts with the distribution of costs are shown in Fig. 3. Within OML, fuel expenses are the main factor since the plant works in a hybrid mode the whole time. This is also a consequence of the undersized heliostat field. Here it should be noticed that it was probed before that SOLUGAS solar field is not sized enough for achieving selected turbine inlet temperature even for very good direct normal irradiance (see Fig. 7 in [40]). And so, combustion of natural

Table 3: Costs obtained in the calculation of LCoE. All of them are expressed in Million US dollars except those from OML that are accounted in yearly terms. The numerical values were obtained for the SOLUGAS plant with the costs data commented in the text.

			Cost (Million USD)
Capital costs			30.74
Equipment purchasing			21.19
	Gas turbine unit		1.837
		Compressor	0.834
		Turbine	0.227
		Combustion chamber	$5.086\,10^{-3}$
		Auxiliary	0.650
		Recuperator	0.120
	Heliostat field		7.044
		Land	1.562
		Heliostat units	5.423
		Wiring	$5.825\,10^{-2}$
	Tower		3.882
	Receiver		5.844
	Electrical generator		2.578
Equipment installation			4.237
Civil engineering			1.021
Natural gas substation			0.287
Project engineering			1.337
Contingencies			2.673
Decommissioning			1.337
Operation, maintenance and labour			3.259 (Million USD/year)
Operation			2.069
	Fuel		2.068
	Water		$1.089\,10^{-3}$
Maintenance			0.613
	Direct maintenance		0.500
	Service contracts		0.113
Labour			0.577

gas is always required. Therefore, this solar field should be increased in size in order to reach a larger solar share at least at design point [23]. Explicit values of solar share will be shown below.

5. Numerical estimations of LCoE

All these ingredients allow to determine the LCoE for the intermediate scenario, which is around 158 USD/MWh for a recuperated gas turbine. With the purpose of contextualizing this number, a comparison among LCoE values from some papers for different systems has been performed in Fig. 4.

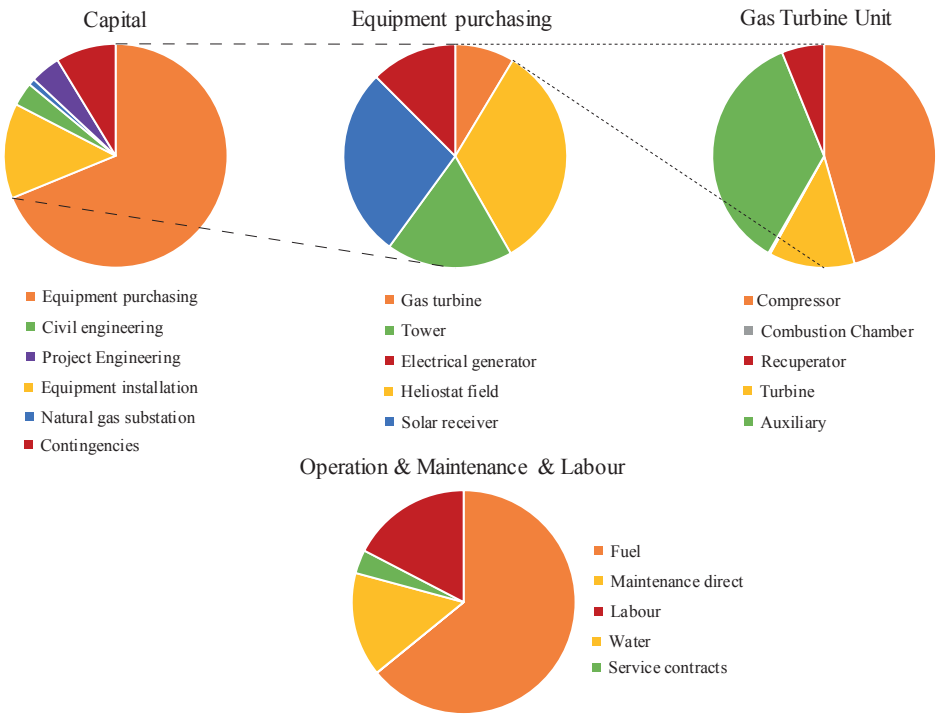

Figure 3: Pie charts for spared costs distributions for the intermediate scenario. Top: capital, equipment purchasing, and gas turbine unit costs. Bottom image: operation, maintenance, and labour costs.

Our plant simulation leads to a LCoE that is in the middle region of the interval that can be found in the literature.

It is interesting to comment some of the values shown in Fig. 4. Mohammadi *et al.* [45] have recently developed a thermo-economic analysis of several multi-stage configurations for a recuperative Brayton power cycle hybridized with a solar tower. The project SOLGATE [57], located at Almería, south of Spain, with a power output about 30 MWe was taken as reference. For the single-stage case an average thermal efficiency of 0.404 and LCoE of 89.53 USD/MWh were predicted. It was also predicted that increasing the number of compression-expansion stages to 4, LCoE could decrease to 80.82 USD/MWh. These values are the lowest found in the literature in our survey. They are quite far, by cheaper, from our calculations. Giostri

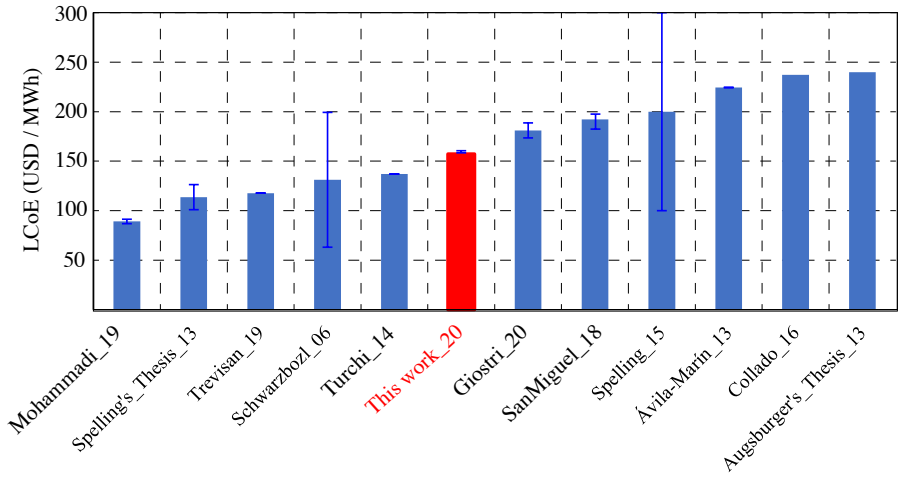

Figure 4: Comparison of the LCoE obtained in this work (red bar) with other values in the literature [38, 44, 45, 49, 50, 51, 52, 53, 54, 55, 56]. Error bars are shown when the mentioned references include them.

et al. [53] very recently have presented another survey for a different power output scale: a micro gas turbine operating in the range 100-200 kWe. The plant was also supposed to be located at Almería, Spain. An interval between 161 and 173 USD/MWh was estimated. The plant design included a recuperator. This interval is quite close to the values obtained in this work. It is also interesting to compare the LCoE of this technology (hybrid central tower with a gas turbine) with a widely commercial one. For instance, in Fig. 4 it is included also a recent study for a plant located in Spain based on parabolic trough with Rankine cycle, thermal storage and natural gas back-up unit for maintenance and start-up operations (in Fig. 4 it is denoted as SanMiguel_18) [52]. Cycle efficiency was estimated about 36.8% and LCoE interval (depending on natural gas input) between 184 and 200 USD/MW. The interval is slightly over the values found here, in spite of the different technologies and commercial maturity.

5.1. Influence of recuperation

A key point in the pre-design of any type of plant based on a gas turbine power unit is the inclusion or not of a recuperator. The main, *a priori*, positive feature is that recuperation increases cycle thermal efficiency. But

Table 4: Main parameters and indicators of the plant both for the recuperative and for the non-recuperative configurations in Seville (SOLUGAS location). Specific CO_2 emissions, net energy, overall thermal efficiency (η), heliostats field efficiency (η_0), and solar share (f) calculated in annual values. Relative deviations refer to the non-recuperative case with respect to the recuperative one.

Parameter	Recuperative	Non-recuperative	Deviation (%)
LCoE (USD/MWh)	158.1	184.7	16.8
Capital cost (Million USD)	30.74	30.49	-0.81
Annual fuel consumption (10^3 ton/year)	7.31	10.24	40.05
Specific CO_2 emissions (kg/MWh)	453.1	657.8	45.18
E_{net} (GWh/year)	39.94	38.53	-3.54
η_H	0.392	0.277	-29.30
η_0	0.658	0.658	–
η_S	0.276	0.294	6.65
η	0.349	0.252	-27.96
f	0.202	0.151	-25.19

from the perspective of the solar subsystem, recuperation increases the mean working temperature of the solar receiver and so, its thermal losses (see, for instance, Fig. 10 in [23]). Moreover, it is evident from the viewpoint of equipment investment, that the recuperator, depending on system size, is an expensive component. Thus, it is interesting to check its influence on LCoE.

Table 4 contains the data for a direct comparison between recuperated and non-recuperated plant layouts. The recuperated plant displays an overall thermal efficiency 0.349 that is almost 28% over that of the non-recuperated one. This is a consequence of the balance between two facts. Thermal engine efficiency, η_H, is quite larger for the recuperative case, but, on the contrary, the whole solar subsystem efficiency, η_S, that includes heat transfer losses at the receiver, is higher for the non-recuperative case (as commented above, because the lower receiver operating temperatures in the non-recuperative case). But η_S is only 6.65% above for the non-recuperative layout. As global consequence overall thermal efficiency, η, is, as mentioned above, 28% better in the recuperative case.

Nevertheless, annual net energy output is similar. It is only 3.54% above for the recuperative case. These similar values are a consequence of the elected plant operation strategy. It is considered that hybridization is used to keep approximately constant turbine inlet temperature, and so power output. Another important difference is solar share. It is 25.19% larger for the recuperated plant, because fuel consumption is smaller. Specific CO_2 emis-

sions are 45% larger for the non-recuperative case, which is an important factor. From the economic perspective, the recuperator increases capital costs about 1% and reduces annual fuel consumption (OML costs) about 40.05%. Final LCoE is 16.8% lower for the recuperative plant, it changes from 158.1 in the recuperated turbine to 184.7 USD/MWh when recuperation is not considered.

5.2. LCoE at two different locations in Spain

Values of levelized costs of electricity for technologies still not fully developed from the commercial point of view can always have some uncertainty. Nevertheless, the comparison between numerical values calculated within the same scheme at different conditions is interesting. In this section, the aim is to compare LCoE values at two locations of Spain with different climatological conditions: globally similar direct normal irradiance (DNI) annual records but quite different average ambient temperatures.

In the previous computations, the location of the SOLUGAS project was elected. Seville is a well-known location for thermosolar installations because of its good solar records. It is at the south of Spain at a latitude 37.4°N. Annual DNI is about 1975 kWh/m^2. Peak values of DNI above 800 W/m^2 are usual at any season. Weather is mediterranean: dry and warm, with many sunny days at any season. Rain is concentrated in winter (approximately 50 rainy days per year), and temperatures are quite hot in summer and warm in winter. Yearly average is about 18.6°C. Altitude above sea level is small, below 10 m in several sites.

It was chosen another location about 500 km to the north of Seville to compare with, Salamanca. Latitude is 40.4° N. But altitude is quite different (it is located on a plateau about 800 m above see level) and so, climatological conditions. DNI is slightly below Seville, but values are acceptable, around 1834 kWh/m^2. Weather is continental and dry. There are only about 64 days per year with more than 1 mm rainfall. But, probably, the most important difference comparing with Seville is ambient temperature. Summers are warm and winters cold, in such a way that yearly averaged temperature is 12.1°C (about six degrees below Seville). Our main interest in the comparison between these two locations is to check the influence of this difference in temperature. *A priori*, lower temperatures should favor the increase of the thermal efficiency of the power unit, but also would affect the heat transfer losses at the receiver.

Table 5: Thermodynamic and thermo-economic indicators at two different locations in Spain with quite different climatological conditions, Seville and Salamanca. Relative deviations are calculated for Salamanca with respect to Seville.

Parameter	Seville	Salamanca	Deviation (%)
LCoE (USD/MWh)	158.1	163.7	3.512
Capital cost (Million USD)	30.74	30.67	-0.24
Annual fuel consumption (10^3 ton/year)	7.31	6.89	-5.83
Specific CO_2 emissions (kg/MWh)	453.1	450.8	-0.51
E_{net} (GWh/year)	39.94	37.80	-5.36
η_H	0.392	0.398	1.54
η_0	0.658	0.660	0.24
η_S	0.276	0.263	-4.56
η	0.349	0.356	2.01
f	0.202	0.175	-13.24

Table 5 contains the data for the two locations. Globally, records are quite similar for both sites. Solar share is higher in Seville, about 13%. Heliostat field efficiency is similar, but slightly above for Salamanca. Power unit efficiency, η_H is 1.54% above for Salamanca because average ambient temperature is lower. The largest difference comes from η_S. It is 4.56% larger at Seville. Probably this is due to the larger mean ambient temperature, that provokes a lower temperature gradient between the solar receiver and its surroundings, so lower heat transfer losses. Overall efficiency is about 2.01% larger in Salamanca. This is likely due to two facts: on one hand, thermodynamic cycle efficiency is larger in Salamanca because mean ambient temperature is smaller. On the other hand, solar share in Salamanca is lower, so the plant is working on pure combustion mode during more time and this operation is always associated to larger overall efficiency because the solar subsystem (and the corresponding loss) is disconnected.

Fuel consumption and, so, emissions are very similar and final LCoE is only 3.5% worse for Salamanca. It is 163.7 USD/MWh against 158.1 USD/MWh for Seville. There results suggest that locations with higher latitudes than most usual in thermosolar plants, but with acceptable insolation records and relatively low average temperatures deserve to be studied as feasible places for this kind of concentrated solar power plants.

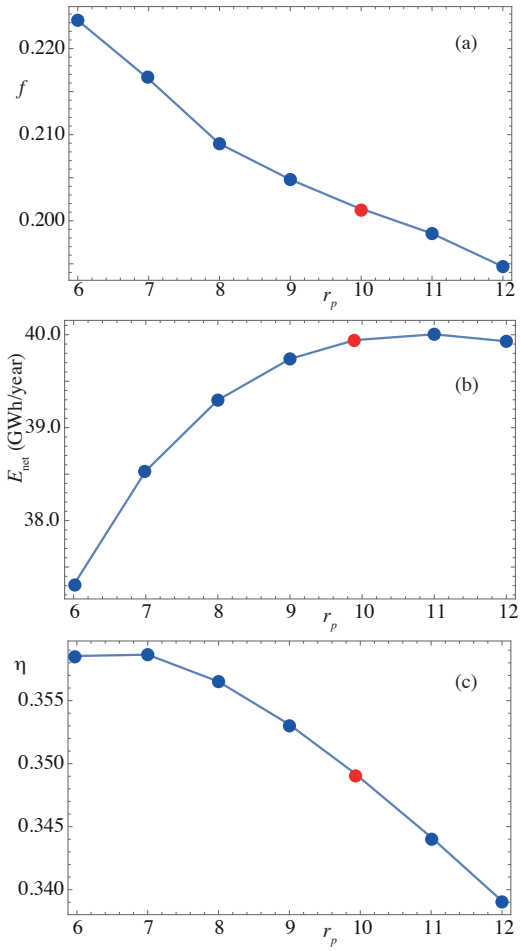

Figure 5: Evolution of some thermodynamic parameters with the pressure ratio of the compressor in the power unit: (a) f, solar share; (b) E_{net}, net energy produced in a year; and (c) η, overall plant thermal efficiency. The red dot corresponds to the design point of SOLUGAS project [19].

6. Sensitivity analysis of plant efficiencies and LCoE

The aim of this section is to analyze how several design inputs affect thermodynamic and thermo-economic output values. One of the key strong points of the developed model is that it allows to survey the main param-

eters of any of the plant subsystems (power unit, heliostat field, and solar receiver) in a realistic and precise way, but without an excessive computational cost. The next subsections present some interesting results on the analysis performed, but other alike ones could be done.

6.1. Power unit parameters

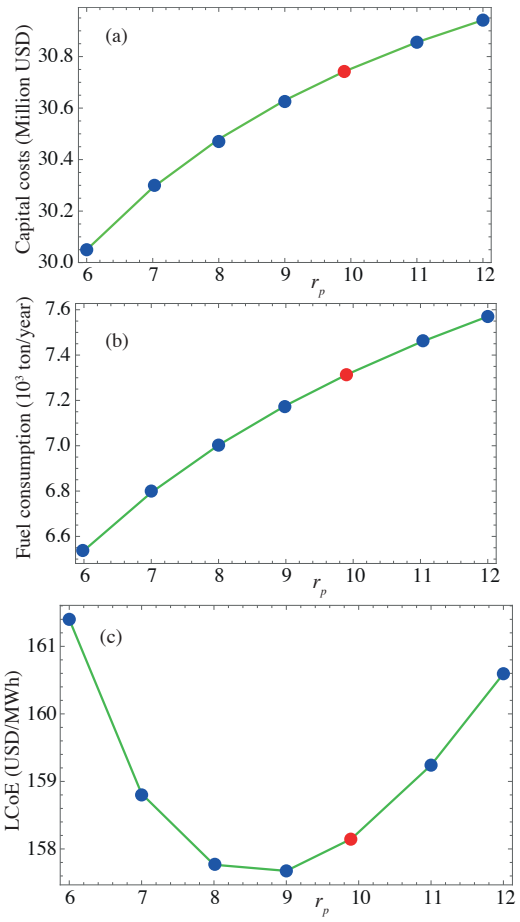

Figure 6: Evolution with the pressure ratio of the compressor in the power unit of: (a), total investment capital costs; (b), fuel consumption; and (c), LCoE.

Two essential design parameters of the Brayton-like power unit have been

selected for analysis: the compressor pressure ratio, r_p, and the turbine inlet temperature, T_3. Beginning with the pressure ratio, Fig. 5 shows the evolution with r_p of some variables with a thermodynamic meaning. Solar share, f (see Fig. 5(a)) decreases with r_p in the interval displayed because the operating temperature of the solar receiver (and the one reached by the working fluid after the heating from the receiver) decreases in a similar way, and, thus, an increasing amount of fuel is burned when r_p increases to meet the fixed value of T_3. The net energy obtained per year, E_{net}, behaves as the power output with the pressure ratio. It increases from small r_p, reaches a maximum about $r_p \simeq 11$ and decreases again. Pressure ratio, in our scheme, affects the plant overall thermal efficiency, η, through the heat engine efficiency, η_H. It was shown in previous works that, for a system with similar dimensions as the one considered here, η_H displays a maximum for pressure ratios about 4 - 6, and then decreases almost linearly for higher pressure ratios [24]. This is displayed in overall efficiency, η, as shown in Fig. 5(c). In all the plots of this figure and the following ones, the red dot refers to the SOLUGAS project design point.

The behavior of capital costs, fuel consumption, and LCoE with r_p is shown in Fig. 6. Capital costs increase in a parabolic shape with r_p because, both, compressor and turbine costs increase in a similar way. With the correlations considered in this work [38], in the pressure ratio interval between 6 and 12, compressor costs increase from 6.0×10^5 USD dollars to 9.5×10^5 (that is about 58% of relative increment) and turbine costs increase is similar. This is reflected in whole capital costs as an increment about 3%. Fuel consumption along a year (see Fig. 6(b)) increases about 1000 ton with the corresponding increase in OML costs. This increase is due to the decrease of solar share as commented in the paragraph before.

LCoE behavior is plotted against r_p in Fig. 6(c). It has a parabolic shape and displays a minimum about $r_p \simeq 9$, *i.e.*, at slightly higher values that the maximum displayed by the plant overall efficiency, η. This evolution is a consequence that LCoE is the ratio between costs and net annual energy produced. The numerator (capital and OML costs) increases with r_p (see Fig. 6(a)), and also E_{net} increases, but at a different rate as shown in Fig. 5(b). Consequently, LCoE displays a minimum in the surveyed interval. However, although the existence of a minimum is qualitatively interesting, the numerical variation of LCoE in the considered pressure ratio interval is not large. Difference among minimum value and the highest in the interval is about 4.0 USD/MWh (2% in relative terms).

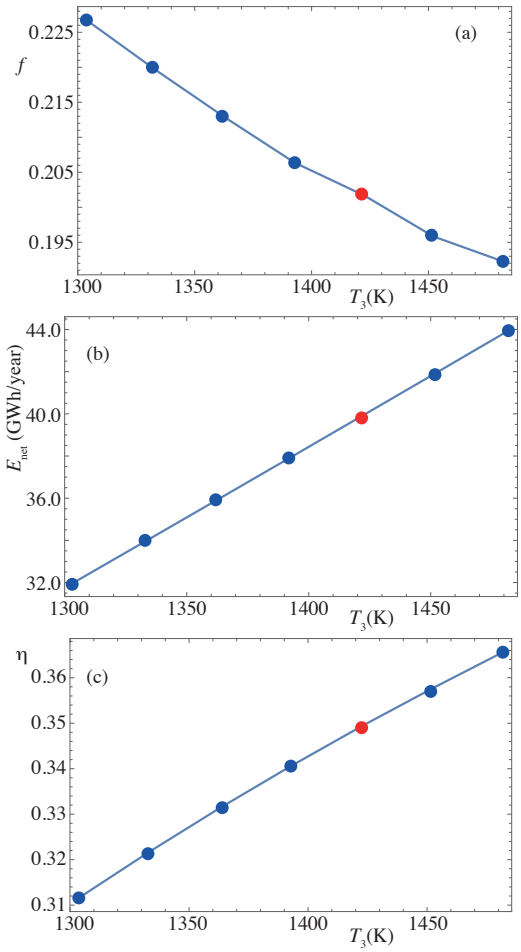

Figure 7: Evolution of some thermodynamic parameters with the turbine inlet temperature, T_3: (a) f, solar share; (b) E_{net}, net energy produced in a year; and (c) η, overall plant thermal efficiency. The red dot corresponds to the design point of SOLUGAS project [19].

Another essential factor at the design level of any gas turbine power unit is the turbine inlet temperature, T_3. Larger values of T_3 ensure better thermodynamic efficiencies on the power unit cycle, but also increase production costs of the turbine components because very specific alloys or ceramic coatings are required to withstand high temperatures. Thus, it has both

consequences, purely thermodynamic and also economic. Figure 7 shows the rapid increase of overall efficiency with larger T_3 values. The relative increase in the temperatures interval $[1300, 1500]$ is about 20%. Nevertheless, the increase in T_3 also provokes an increase in net power output and so, in the net annual energy, which increases 37.5% in the interval (see Fig. 7(b)). Solar share decreases because as T_3 increases more fuel is needed to reach the required temperature.

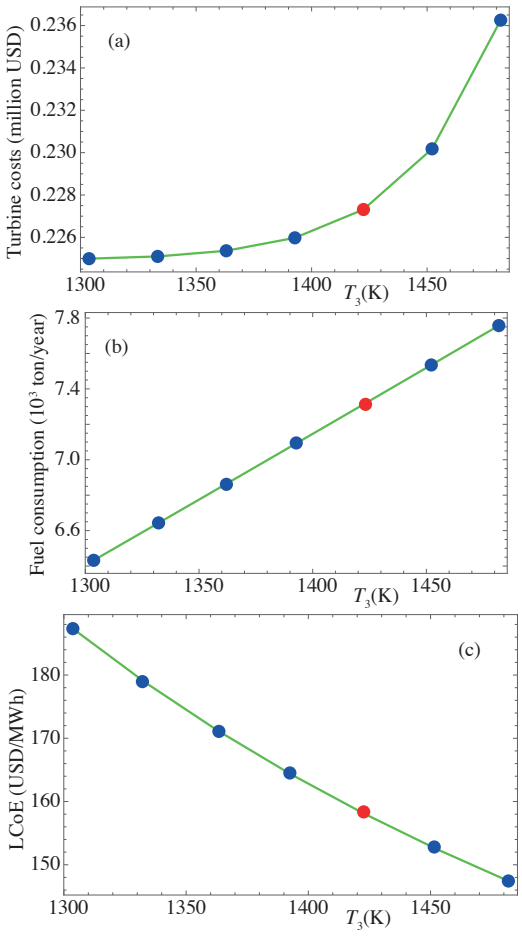

Figure 8: Evolution with the turbine inlet temperature, T_3 of: (a), gas turbine costs; (b), fuel consumption; and (c), LCoE.

Gas turbine costs rapidly increase for temperatures above 1400 K approximately. This is depicted in Fig. 8(a). The evolution of the gas turbine costs with temperature was taken from [38]. Fuel consumption linearly increases with T_3. To have an approximate numerical reference, it increases from 6400 to 7800 ton/year in the basis of natural gas. As a consequence of the balance between increasing investment and OML costs on one hand and net yearly energy production on the other hand, LCoE presents an almost linear decrease with increasing T_3, *i.e.*, net energy production increases more rapidly than costs, which is an interesting conclusion. Particularly, the lowest LCoE is got at 1500 K and is 148 USD/MWh. The highest is reached at $T_3 = 1300K$ and is about 188 USD/MWh, which is 27% higher.

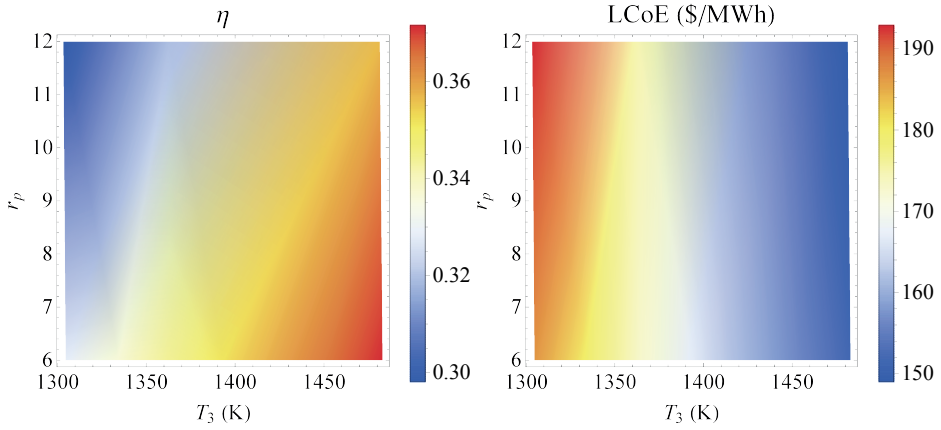

Figure 9: Density plots showing the evolution of plant overall thermal efficiency (left) and LCoE (right) with simultaneous changes on pressure ratio, r_p, and turbine inlet temperature, T_3.

The sensitivity of overall plant efficiency and LCoE to simultaneous changes in r_p and T_3 has been also studied. Figure 9 shows these analyses as density plots. Larger thermal efficiencies are observed as turbine inlet temperature increases and pressure ratio decreases (left panel of Fig. 9). In the considered intervals, η reaches its largest values for temperatures above 1450 K and r_p between 6 and 8. Nevertheless, as temperature increases LCoE is almost independent of the pressure ratio, which is a significant result. In other words, for high temperatures, pressure ratio is not a critical variable to minimize LCoE values. For temperatures above 1400 K, LCoE values around 150 USD/MWh are got for whichever value of r_p (see right panel of Fig. 9).

6.2. Heliostat field parameters

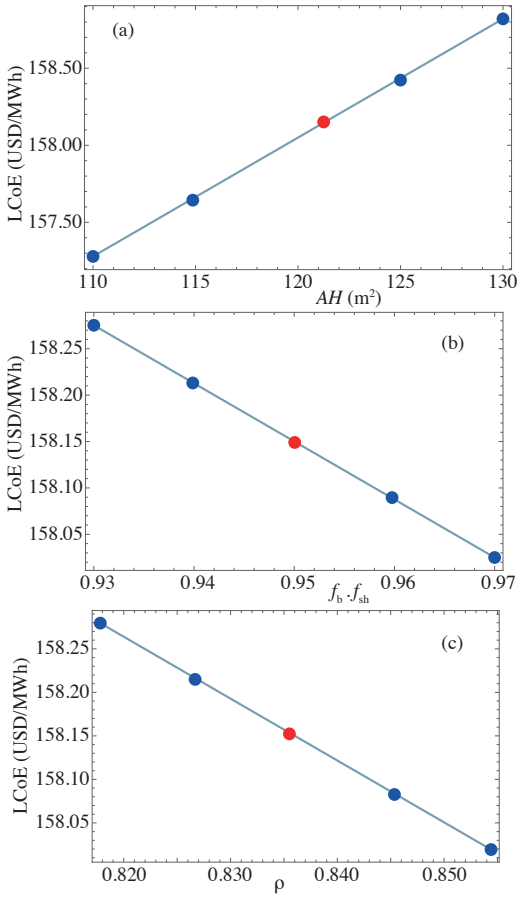

Figure 10: LCoE sensitivity to some key parameters of the heliostat field: (a), AH, mirrors area; $f_b \cdot f_{sh}$, blocking and shadowing efficiency factor; and (c), ρ, mirrors reflectivity. The red dot corresponds to SOLUGAS design point [19].

The sensitivity of main efficiencies (thermal and optical) and economical parameters (investment costs, OML costs, and LCoE) as functions of several key parameters of the heliostat field has been surveyed. Parameters have been checked one by one. In the following paragraphs the main conclusions are condensed:

- Mirrors area, AH. Starting from the design point mirror area of SOLUGAS project, $AH = 121.3$ m^2, an interval $[110, 130]$ m^2 has been surveyed (considering square mirrors). In this interval mean optical efficiency of the field linearly decreases with larger mirrors areas. For $AH = 110$ m^2, $\eta_0 = 0.661$ and for $AH = 130$ m^2, $\eta_0 = 0.655$, which corresponds to a decrease of 0.92%. It was checked that this decrease is associated with a reduction in all the main factors of the field optical efficiency: $\cos\omega$, spillage, and attenuation. This is reflected in plant overall efficiency in a decrease of about 1.15%. Moreover, heliostat units costs increase with AH and consequently LCoE increases from 157.30 to 158.80, as it is displayed in Fig. 10(a). This corresponds to an increase in LCoE of about 0.95%.

- Safety distance between adjacent heliostats, DS. At design point, this required safety distance is taken as 0.3 in units given by mirrors length, LH (see Table 1). An interval $[0, 1]$ has been studied. As this distance is increased, η_0 and η monotonically decrease and, at the same time, field costs increase, provoking an slight increase of LCoE. In the limit case $DS = 0$, LCoE would eventually be 157.5 USD/MWh and at the other side, for $DS = 1$ it would be 159.3 USD/MWh. This increase is about 1.14 in percentile terms.

- Blocking and shadowing factors, $f_b \cdot f_{\mathrm{sh}}$. As the developed model considers both factors independent of each mirror, they have been analyzed together. Design point value is $f_b \cdot f_{sh} = 0.95$ and the investigated interval is $[0.93, 0.97]$. Of course, optical efficiency grows with the increase of this factor. For $f_b \cdot f_{sh} = 0.95$, $\eta_0 = 0.644$ and for $f_b \cdot f_{sh} = 0.97$ it is 0.672. This represents a gain of 3.35% that leads to a much smaller increase of overall efficiency, 0.30%. LCoE drops when blocking and shadowing losses decrease, but in numerical terms, the decrease is small, 0.16%. This fall is shown in Fig. 10(b).

- Reflectivity, ρ. It plays the same role that blocking and shadowing factors, appears in the optical efficiency, η_0, as a multiplicative factor. For design point, it was assumed to be $\rho = 0.836$ and a wide realistic interval $[0.818, 0.854]$ is analyzed. When ρ is covered in this interval, η_0 increases from 0.643 to 0.673, and correspondingly overall efficiency grows up from 0.349 to 0.350, *i.e.*, η increases 0.31%. LCoE (see Fig. 10(c)) decreases 0.16%. This numerical decrease is almost

identical to the one associated with a reduction in blocking and shadowing losses and would represent the margin of improvement in LCoE with respect to an improvement on mirrors surface reflection of solar energy towards the receiver.

- First row distance to the tower, $R_{\min}$. This is the minimum distance from the first heliostats in the field to the central tower. It is also a main parameter in the design of any heliostat field. SOLUGAS field takes $R_{\min} = 64$ m. Our model has been applied to study a wide interval $[35, 75]$ m. Optical and overall efficiencies decrease with increasing $R_{\min}$, but numerical differences are small. Moreover, land area and so, land investment costs increase with $R_{\min}$. The whole consequence is that LCoE increases, about 0.18% in the considered interval.

- Finally, the tower height, THT is analyzed. It is a key parameter in which respect to investment costs and solar subsystem efficiencies. Design point value is $THT = 65$ m and the interval considered for analysis 45-75 m. Results for some indicators are shown in Fig. 11. From the figure is clear that THT provokes an increase of efficiencies (optical and thermal), but also capital costs are larger because of tower costs. In the analyzed interval tower costs grow from 3.25 to 4.25 Million USD. This is a substantial increase of about 30.77%. Nevertheless, it is partially subsumed by the gain in thermal efficiency and LCoE is not so sensitive to changes in THT. It increases in that interval from about 156.0 to 159.5 USD/MWh, that is 2.24%. It is also noticeable that the behavior of all output parameters with respect to THT is monotonic (slightly parabolic), there are neither maxima nor minima.

6.3. Solar receiver main parameters

This subsection is devoted to analyze the role played by the basic solar receiver parameters in final overall plant outputs and LCoE. Next, the main conclusions of the analysis are enumerated.

- Receiver emissivity, α. The global emissivity of the receiver accounts for the heat transfer losses associated with radiation as shown in Eq. (10). Larger values of α provoke larger radiation losses, and thus, smaller solar subsystem efficiency, η_S, and smaller overall efficiency, η. Sensitivity

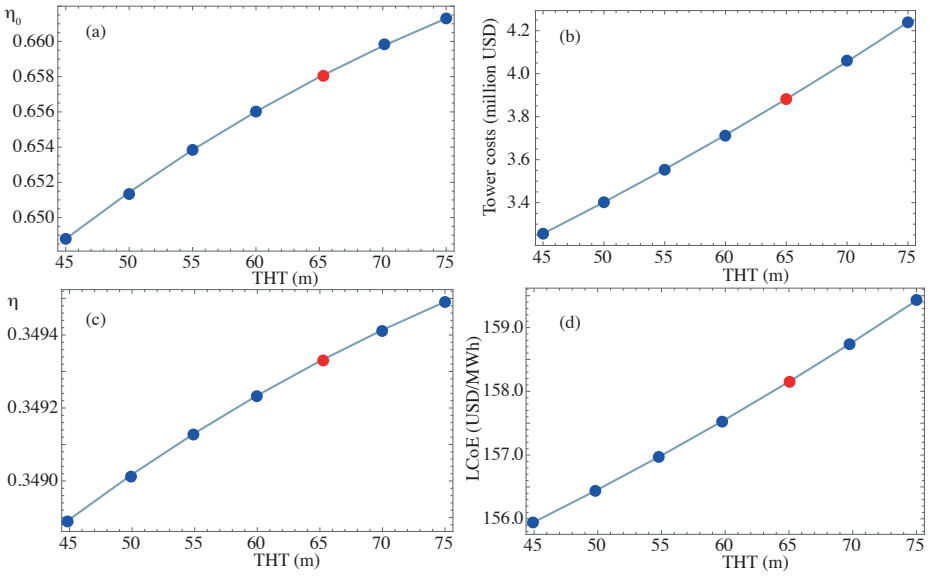

Figure 11: Influence of tower height (THT) on some parameters: (a), η_0, optical efficiency of the heliostat field; (b), tower costs; (c), η, overall plant efficiency; and (d) LCoE.

of efficiencies and LCoE were surveyed in a realistic interval around design point value, that is $\alpha = 0.10$. The interval chosen was $[0.05, 0.30]$. As α increases, radiation losses do, and so, overall plant efficiency decreases and LCoE increases. All the curves are approximately linear, as, for example LCoE, depicted in Fig. 12(a). In numerical terms, sensitivity of η and LCoE is small. In the referred interval η decreases from 0.350 to 0.348, that is only 0.01%. LCoE increase in that interval is larger, about 0.33%. As limit case, for an hypothetical perfect cavity receiver from the viewpoint of radiation losses, $\alpha \simeq 0$, LCoE would decrease to 157.94 USD/MWh. As design point LCoE is 158.15 USD/MWh, this eventual decrease could amount at best 0.13%.

- Effective conduction and convection heat transfer coefficient, $\overline{U}_L$. This coefficient plays an identical role as α for effective conduction and convection heat transfer losses. Its limit $\overline{U}_L \to 0$ would correspond to a receiver without heat transfer losses through the tower itself to the ground, nor through the surrounding air. The interval analyzed is $[3.0, 7.0]$ W/(m^{2}K) (at the design point, $\overline{U}_L = 5$ W/(m^{2}K)). The in-

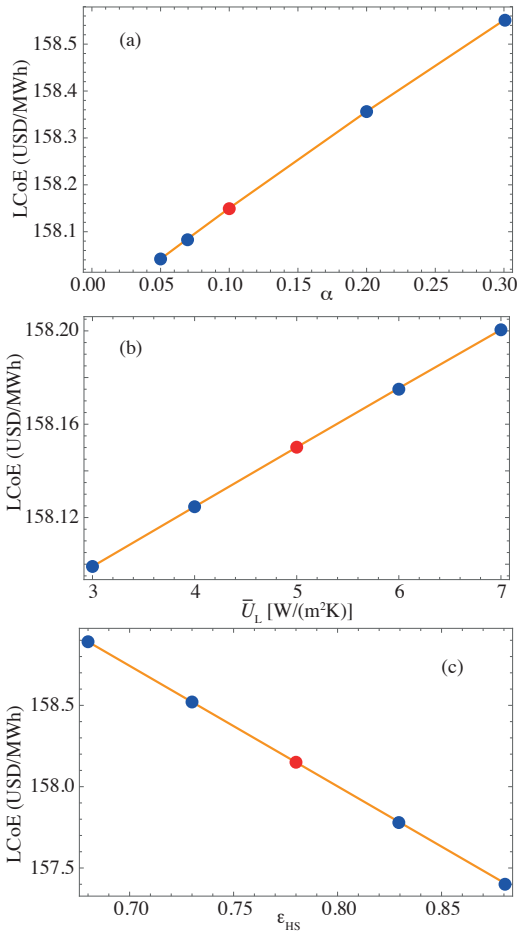

Figure 12: LCoE dependence on some receiver parameters: (a), α, receiver emissivity; (b), $\overline{U}_L$, effective conduction-convection heat transfer coefficient; and (c), ε_{HS}, receiver effectiveness as heat exchanger.

crease of LCoE with $\overline{U}_L$ is linear (see Fig. 12(b)). The relative increase in the surveyed interval is around 0.063%. Total elimination of these losses, as limit speculative case, would lead to an LCoE about 158.025 USD/MWh.

- Effectiveness of the receiver as heat exchanger, ε_{HS}. This coefficient measures the ratio between the solar heat input in the receiver (once

heat transfer losses has been discounted) and the solar heat input in the working fluid performing the thermodynamic cycle. It depends on the heat transfer materials properties, size, and geometry (for instance of the ceramic sponge at the back of the receiver for high temperature receivers). The limit case $\varepsilon_{HS} \rightarrow 1$ would represent an ideal heat exchange. A realistic interval to analyze the weight of this parameter is $[0.68, 0.88]$. As ε_{HS} increases, overall efficiency increases (from 0.346 to 0.353) and LCoE decreases (from 158.9 to 157.4 USD/MWh). In the case of an ideal heat transfer from the receiver to the fluid, LCoE could decrease to 156.5 USD/MWh, *i.e.*, from the design point ($\varepsilon_{HS} = 0.78$) LCoE could decrease as best 1.28%.

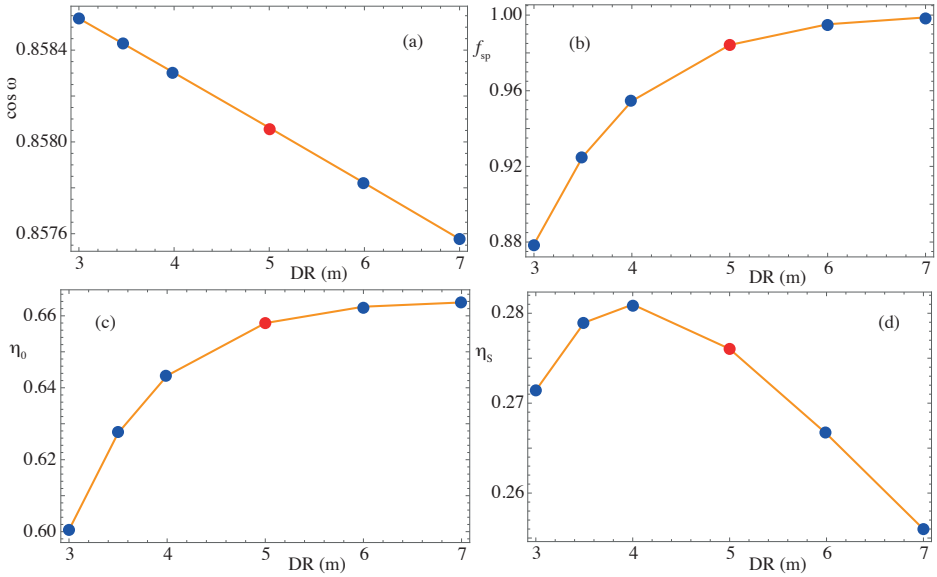

Figure 13: Influence of the receiver diameter, DR, on some parameters of the field: (a), $\cos\omega$ factor; (b), spillage factor, f_{sp}; (c), solar field optical efficiency, η_0; and solar subsystem efficiency, η_s (field and receiver).

- Solar receiver aperture diameter, DR. This parameter is essential because influences the plant efficiencies and thermo-economic records at several levels. SOLUGAS project makes use of a cavity receiver with a diameter of 5 m. An analysis of a wide interval $[3.0, 7.0]$ m has been performed in order to get into its influence from both qualitative and

quantitative perspectives. Figure 13 displays the evolution of some efficiencies with DR. It slightly affects the factor $\cos\omega$. As seen in the figure, $\cos\omega$ decreases as DR increases. It does in a linear way, but with relatively low numerical differences. Nevertheless, spillage factor, f_{sp}, is greatly associated with DR. As DR increases, f_{sp} approaches $f_{\text{sp}} \simeq 1$ (see Fig. 13(b)). For values of DR around $DR \simeq 7$ this is accomplished, *i.e.*, spillage losses almost disappear. In consequence, the field optical efficiency, η_0, resembles the behavior of f_{sp} with respect to DR (see Fig. 13(c)). In the span considered, η_0 increases from 0.60 to 0.66, which is a noteworthy numerical increment, about 10%. Moreover, the thermal efficiency of the whole solar subsystem, η_S, apart from depending on DR through η_0 it also depends on the concentration ratio, C, and so, on DR, in the heat transfer losses term (see Eq. (10)). As DR increases, heat transfer losses also increase. Thus, the balance between optical losses and heat transfer losses makes that η_S has a maximum as displayed in Fig. 13(d). For the reference plant considered, maximum η_S is achieved at $DR \simeq 4$, and is about 0.28.

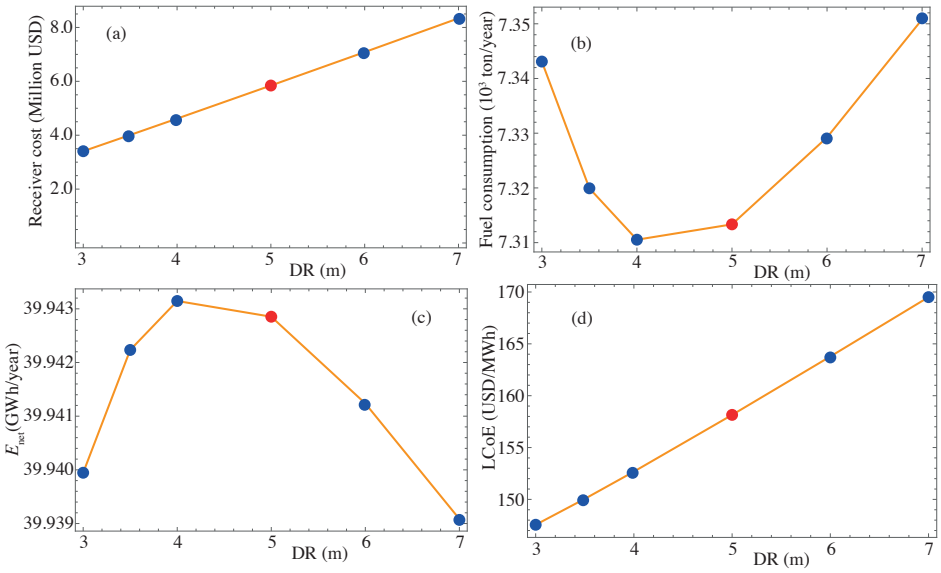

Figure 14: Influence of the receiver diameter, DR, on some thermo-economic parameters: (a), receiver cost; (b), annual fuel consumption; (c), net annual energy production; (d), and LCoE.

From the thermo-economic viewpoint, receiver size and design particularities have a deep impact. Its cost has a large degree of uncertainty, specially in the case of high temperature cavity receivers as the case considered here. Up-to-date receiver designs are non-standard prototypes, designed for particular projects, mass production seems still distant. As suggested by Augsburger [44], in this work receiver costs are estimated from a reference base case as a function of receiver area, progress ratio, and price index. The evolution with DR of receiver costs is shown in Fig. 14(a). Evolution is linear and the slope is very high, about 1.3 Million USD/m. This means that in the interval considered for DR, receiver cost increases 157.6%. This is reflected in total capital costs as an increase from 27.2 to 34.2 Million USD, which in porcentual terms represents about 25.7%. The dependence of fuel consumption and net annual energy with DR are represented in Figs. 14(b) and (c). Net yearly energy presents a maximum about $DR \simeq 4$ and fuel consumption a minimum about the same value. Both evolutions are due to the behavior of the thermal solar subsystem efficiency, η_S (see Fig. 13(d)), as commented before. Thus, LCoE evolves as displayed in Fig. 14(d). It rapidly increases with DR, in an almost quasilinear way. No relative maximum or minimum are found. This is because the linear increase in costs is more important than the parabolic behavior of net energy or OML costs associated with fuel consumption. The slope of the increase of LCoE with DR is about 5.75 USD/(MWh.m). This represents an increase of LCoE in the interval from $DR = 3$ to $DR = 7$ of about 15.6%, which is really noticeable.

7. Discussion

The model developed in this work is focused to perform a thermo-economic analysis of a hybrid Brayton central tower thermosolar plant. It includes the following ingredients. A detailed design and description of the solar field which incorporates optical efficiency terms depending on each heliostat as $\cos\omega$ factor, spillage, and attenuation, and other taken as independent as blocking, shadowing, and reflectivity. The assumption of the last ones as constant allows to speed up numerical calculations and does not affect final conclusions for the whole plant. For the solar receiver, a simple scheme valid for cavity receivers operating at high temperatures is assumed. Heat transfer losses coming from radiation, conduction, and convection are considered.

The power unit is supposed to operate as a closed Brayton-like thermodynamic cycle that includes the most significant losses in these systems. The connection between solar receiver and the thermodynamic cycle is associated with a non-ideal heat exchanger.

For numerical implementation and analysis, a prototype plant at a pre-commercial scale (about 5 MWe) was considered, the SOLUGAS project developed at the south of Spain. Heliostat field and gas turbine parameters, and thermo-economic correlation were adapted to get closer to that prototype plant. Considering a recuperative gas turbine power unit, thermal overall plant efficiency is predicted to be about 0.349. Solar share is relatively low because of the undersized heliostat field due to the pioneer essence of SOLUGAS project. This means that the combustion chamber burning natural gas is required most of the time in order to ensure that the air flow rate developing the thermal cycle reaches the pre-fixed turbine inlet temperature. Resulting specific CO_2 emissions are about 453.1 kg/MWh. Estimated LCoE in these conditions is 158.1 USD/MWh. It was compared with several referenced values in the literature, for systems alike, but also for different solar technologies, and the predicted values are perfectly in accordance with them. It was checked a plant design eliminating recuperation in the gas turbine. Overall efficiency decreases about 28% and LCoE increases 16.8%. The main advantage of a non-recuperated layout is that the average operating temperature of the solar receiver is quite lower, and so the efficiency of the solar subsystem (field and receiver) is slightly larger than in the recuperated case.

Another issue was analyzed, the possibility to locate a similar plant at a northern latitude (about 450 kms to the north of the original location of SOLUGAS, Seville, Spain) with not bad solar conditions and average temperatures about six degrees below Seville. The conclusion is that yearly averaged thermal efficiency is larger (about 2%), nevertheless LCoE increases about 3.5%. In any case, differences are not so large and probably detailed thermo-economic analysis at those latitudes (and depending of particular climatological conditions) could be interesting.

8. Conclusions

In this work it was intended to highlight the importance of global models at the design stage of concentrated solar power plants, particularly in the case of central tower heliostat fields combined with a hybrid gas turbine

power unit. These models should include the main particularities of each subsystem (heliostat field, solar receiver, power unit, and heat exchangers) and their interdependence. At a pre-design stage, an overall plant description, depending on a reduced parametrical modeling, is essential in order to achieve the required design or operation objectives. Once the main plant parameters are set, an specific analysis of each subsystem would be demanded in order to guarantee the stated requirements.

The model developed is specially adequate to fulfill a sensitivity analysis of plant outputs with respect to the main variables of any subsystem. This allows to perform a reduction in system dimensionality and to put the focus on those critical design variables. Next, main conclusion of the analysis are summarized:

- The evolution of thermal overall plant efficiency, η, and LCoE with the pressure ratio of the compressor in the power unit is not linear: η shows a maximum at low pressure ratios and LCoE a minimum for slightly larger values. This means that this variable is susceptible of optimization for pre-design, nevertheless numerical changes on those objective functions are not large.

- The turbine inlet temperature is a key parameter in plant costs and operation. An interval of inlet temperatures from 1300 to 1500 K was surveyed. Capital investment costs greatly increase in that interval, but net annual energy also does, even more rapidly. Thus, LCoE decreases in that temperature span, from 188 to 150 USD/MWh. This is a noticeable reduction, so turbine inlet temperature would be a crucial parameter in plant design.

- Several parameters relative to the heliostat field were analyzed: mirrors area, security distance between them, first region distance to the tower, shadowing and blocking factors, reflectivity, and tower height, THT. The one with a larger weight in plant outputs is tower height. Optical field efficiency and thermal overall plant efficiency increase with THT. But investment costs associated with tower construction also increase, actually faster. Thus, LCoE monotonically increases in the surveyed interval.

- With respect to the receiver, variations on the the following parameters were studied: emissivity, conduction-convection effective heat transfer

coefficient, heat exchanger effectiveness, and aperture diameter. All of them, except aperture diameter, lead to monotonic evolutions for efficiencies or economic parameters. Moreover, their influence in final plant numerical values is relatively small. Nevertheless, the influence of receiver aperture diameter is essential. As it increases, spillage factor does and so, field optical efficiency grows up to an asymptotic limit. This provokes a maximum of the solar subsystem global efficiency, but at the same time, investment costs increase with receiver diameter. The increase is so quick that dominates over the other considerations and LCoE linearly increases with the diameter.

All these conclusions allow to point out at least two key variables in order to go on the research and development of plants based on this technology for a future profitability and commercial expansion. First, the capacity to work on higher concentration ratios that allow on one hand higher turbine inlet temperatures and, on the other hand, relatively smaller aperture size for the solar receiver. This is associated with operating gas turbines at very high temperatures, finding the appropriate materials with prices quite lower than nowadays. And also, to seek for standardized high temperature solar receivers geometries and materials that also could lead to reduced investment costs. Second, and probably not so significant, to adapt tower height and costs to field and receiver design.

All the findings in this work could be extrapolated for plants with power outputs in an interval close to 10 MWe. Other system scales, as smaller towers operating together with micro gas turbines for distributed energy production (in the scale of tens or a few hundreds of kWe), or larger plants about several hundreds of megawatts, should be investigated. Models like the one developed in this paper can be elucidating guides in this research.

Acknowledgements

Financial support from University of Salamanca, Banco Santander, and Junta de Castilla y León of Spain (project SA017P17) is acknowledged.

[1] G. J. Nathan, M. Jafarian, B. B. Dally, W. L. Saw, P. J. Ashman, E. Hu, A. Steinfeld, Solar thermal hybrids for combustion power plant: A growing opportunity, Prog. Ener. Comb. Sci. 64 (2018) 4–28.

[2] L. Weinstein, J. Loomis, B. Bhatia, D. Bierman, E. Wang, G. Chen, Concentrating solar power, Chem. Rev. 115 (2015) 12797–12838.

[3] S. Relloso, Y. Gutiérrez, SENER molten salt tower technology. ouarzazate NOOR III case, in: AIP Conference Proceedings, Vol. 1850, American Institute of Physics, 2017, p. 030041. doi:10.1063/1.4984384.

[4] O. Olumayegun, M. Wang, G. Kelsall, Closed-cycle gas turbine for power generation: A state-of-the-art review, Fuel 180 (2016) 694–717.

[5] S. Bazri, I. A. Badruddin, M. S. Naghavi, M. Bahirei, A review of numerical studies on solar collectors integrated with latent heat storage systems employing fins or nanoparticles, Renew. Ener. 118 (2018) 761–778.

[6] O. Achkari, A. El Fadar, Latest developments on TES and CSP technologies - Energy and environmental issues, applications and research trends, Appl. Therm. Eng. 167 (2020) 114806.

[7] F. J. Collado, J. Guallar, Quick design of regular heliostat fields for commercial solar tower power plants, Energy 178 (2019) 115–125. doi:10.1016/j.energy.2019.04.117.

[8] M. Schmitz, P. Schwarzbozl, R. Buck, R. Pitz-Paal, Assessment of the potential improvement due to multiple apertures in central receiver systems with secondary concentrators, Sol. Ener. 80 (2006) 111–120. doi:10.1016/j.solener.2005.02.012.

[9] T. Wendelin, SolTRACE: a new optical modeling tool for concentrating solar optics, Tech. rep., National Renewable Energy Laboratory (NREL) (2003).

[10] M. J. Blanco, J. M. Amieva, A. Mancillas, The TONATIUH software development project: An open source approach to the simulation of solar concentrating systems, Comput. Inf. Eng. 2005 (2005) 157–164.

[11] D. Jafrancesco, J. Cardoso, A. Mutuberria, E. Leonardi, I. Les, P. Sansoni, F. Francini, D. Fontani, Optical simulation of a central receiver system: Comparison of different software tools, Renew. Sust. Energy Rev. 94 (2018) 792 – 803.

[12] M. Ebert, D. Benitez, M. Röger, R. Korzynietz, J. A. Brioso, Efficiency determination of tubular solar receivers in central receiver systems, Sol. Ener. 139 (2016) 179–189.

[13] A. L. Ávila Marín, M. Álvarez de Lara, J. Fernández-Reche, Experimental results of gradual porosity volumetric air receivers with wire meshes, Renew. Ener. 122 (2018) 339–353.

[14] J. Kim, J.-S. Kim, W. Stein, Simplified heat loss model for central tower solar receiver, Solar Energy 116 (2015) 314–322. doi:10.1016/j.solener.2015.02.022.

[15] P. J. Harper, T. W. von Backström, T. P. Fluri, D. G. Kröger, TRNSYS modeling of a 100 MWe hybrid combined cycle concentrating solar power plant, 2012.

[16] G. Barigozzi, A. Perdichizzi, C. Gritti, I. Guaiatelli, Techno-economic analysis of gas turbine inlet air cooling for combined cycle power plant for different climatic conditions, Appl. Therm. Eng. 82 (2015) 57–67.

[17] F. Petrakopoulou, S. Sánchez-Delgado, C. Marúgan-Cruz, D. Santana, Improving the efficiency of gas turbine systems with volumetric solar receivers, Ener. Conv. Manage. 149 (2017) 579–592.

[18] J. Muñoz-Antón, C. Rubbia, A. Rovira, J. M. Martínez-Val, Performance study of solar power plants with CO_2 as working fluid. A promising design window, Energ. Conv. Manage. 92 (2015) 36–46.

[19] R. Korzynietz, J. A. Brioso, A. del Río, M. Quero, M. Gallas, R. Uhlig, M. Ebert, R. Buck, D. Teraji, Solugas - Comprehensive analysis of the solar hybrid Brayton plant, Sol. Ener. 135 (2016) 578–589.

[20] E. Okoroigwe, A. Madhlopa, An integrated combined cycle system driven by a solar tower: a review, Renew. Sust. Energ. Rev. 57 (2016) 337–350.

[21] D. Olivenza-León, A. Medina, A. Calvo Hernández, Thermodynamic modeling of a hybrid solar gas-turbine power plant, Energ. Conv. Manage. 93 (2015) 435–447.

[22] R. P. Merchán, M. J. Santos, I. Reyes-Ramírez, A. Medina, A. Calvo Hernández, Modeling hybrid solar gas-turbine power plants: Thermodynamic projection of annual performance and emissions, Ener. Conv. Manage. 134 (2017) 314–326.

[23] R. P. Merchán, M. J. Santos, I. Heras, J. Gonzalez-Ayala, A. Medina, A. Calvo Hernández, On-design pre-optimization and off-design analysis of hybrid Brayton thermosolar tower power plants for different fluids and plant configurations, Renew. Sust. Energy Rev. 119 (2020) 109590. doi:j.rser.2019.109590.

[24] M. J. Santos, C. Miguel-Barbero, R. P. Merchán, A. Medina, A. Calvo Hernández, Roads to improve the performance of hybrid thermosolar gas turbine power plants: Working fluids and multi-stage configurations, Ener. Conv. Manage. 165 (2018) 578–592.

[25] S. Burgaleta, D. J. I. Ramírez, Gemasolar, the first tower thermosolar commercial plant with molten salt storage, in: Proceedings of SolarPACES, Granada, Spain, 2011.

[26] F. J. Collado, Quick evaluation of the annual heliostat field efficiency, Sol. Ener. 82 (2008) 379–384.

[27] F. J. Collado, J. Guallar, A review of optimized design layouts for solar power tower plants with *campo* code, Renew. Sust. Energ. Rev. 20 (2013) 142–154.

[28] R. P. Merchán, M. J. Santos, A. Medina, A. Calvo Hernández, Thermodynamic model of a hybrid brayton thermosolar plant, Renew. Ener. 128 (2018) 473–483.

[29] G. Barigozzi, G. Bonetti, G. Franchini, A. Perdichizzi, S. Ravelli, Thermal performance prediction of a solar hybrid gas turbine, Sol. Energy 86 (2012) 2116–2127.

[30] F. J. Collado, Preliminary design of surrounding heliostat fields, Renew. Ener. 34 (2009) 1359–1363.

[31] F. J. Collado, J. Guallar, Campo: Generation of regular heliostat fields, Renew. Ener. 46 (2012) 49–59.

[32] W. B. Stine, M. Geyer, Power from the Sun (2001).
URL http://www.powerfromthesun.net/book.html

[33] M. Zhang, L. Yang, C. Xu, X. Du, An efficient code to optimize the heliostat field and comparisons between the biomimetic spiral and stagerred layout, Renew. Ener. 87 (2016) 720–730.

[34] C. Noone, M. Torrilhon, A. Mitsos, Heliostat field optimization: a new computationally efficient model and biomimetic layout, Sol. Energ. 86 (2012) 792–803.

[35] J. Duffie, W. Beckman, Solar Engineering of Thermal Processes, John Wiley and Sons, Hoboken, New Jersey, 2006.

[36] A. W. Dowling, T. Zheng, M. Zavala, Victor, Economic assesssment of concentrated solar power technologies: A review, Renew. Sust. Ener. Rev. 72 (2017) 1019–1032.

[37] J. Hernández-Moro, J. M. Martínez-Duart, Analytical model for solar PV and CSP electricity costs present LCOE values and their future evolution, Renew. Sust. Ener. Rev. 20 (2013) 119–132.

[38] J. Spelling, Hybrid solar gas-turbine power plants, Ph.D. thesis, KTH Royal Institute of Technology, Department of Energy Technology, Stockholm, Sweden (2013).

[39] Solar, Turbines, Caterpillar. [link].
URL https://mysolar.cat.com/cda/files/126873/7/dsm50pg.pdf

[40] M. J. Santos, R. P. Merchán, A. Medina, A. Calvo Hernández, Seasonal thermodynamic prediction of the performance of a hybrid solar gas-turbine power plant, Ener. Conv. Manage. 115 (2016) 89–102.

[41] P. L. Leary, J. D. Hankins, A user's guide for MIRVAL– a computer code for comparing designs of heliostat-receiver optics for cenrtal receiver solar power plants, Tech. rep., Sandia Laboratories (1979).

[42] AEMET, http://www.aemet.es.
URL http://www.aemet.es

[43] http://www.soda-pro.com/web-services/radiation/cams-radiation-service, Copernicus atmosphere monitoring service (ECMWF) (2019).
URL http://www.soda-pro.com/web-services/radiation/cams-radi

[44] G. Augsburger, Thermo-economic optimisation of large solar tower power plants, Ph.D. thesis (2013).

[45] K. Mohammadi, J. G. McGowan, M. Saghafifar, Thermoeconomic analysis of multi-stage recuperative Brayton power cycles: Part I- hybridization with a solar power tower system, Ener. Conv. Manage. 185 (2019) 898–919.

[46] Swift, Marshall, Marshall & Swift Valuation Services. Inventory Index Factors (2018).
URL https://www.corelogic.com/products/marshall-swift-valuat

[47] C. Turchi, G. Heath, Molten salt power tower cost model for the System Advisory Model (SAM) (2013).

[48] S. A. Wright, C. S. Davidson, W. O. Scamell, Thermo-economic analysis of four sCO_2 waste heat recovery power systems, in: 5th Int Symp. Supercrit. CO_2 Power Cycle, 2016, pp. 1–16.

[49] S. Trevisan, R. P. Merchán, R. Guedéz, A. Medina, B. Laumert, A. Calvo Hernández, Techno-economic analysis of a solar hybrid combined cycle power plant integrated with a packed bed storage at gas turbine exhaust, in: SolarPACES19, 2019.

[50] P. Schwarzbözl, R. Buck, C. Sugarmen, A. Ring, M. Marcos Crespo, P. Altwegg, J. Enrile, Solar gas turbine systems: design, cost and perspectives, Sol. Energy 80 (2006) 1231–1240.

[51] C. S. Turchi, Z. Ma, Co-located gas turbine/solar thermal hybrid designs for power production, Renew. Ener. 64 (2014) 172–179.

[52] G. San Miguel, B. Corona, Economic viability of concentrated solar power under different regulatory frameworks in spain, Renew. Sust. Ener. Rev. 91 (2018) 205–218.

[53] A. Giostri, M. Binotti, C. Sterpos, G. Lozza, Small scale solar tower coupled with micro gas turbine, Renew. Ener. 147 (2020) 570–583.

[54] J. Spelling, B. Laumert, Thermo-economic evaluation of solar thermal and photovoltaic hybridization options for combined-cycle power plants, J. Eng. Gas Turb. Power 137 (2015) 031801–1,–11.

[55] A. L. Avila-Marin, J. Fernandez-Reche, F. M. Tellez, Evaluation of the potential of central receiver solar power plants:configuration, optimization and trends, Appl. Ener. 112 (2013) 274–288.

[56] F. J. Collado, J. Guallar, Two-stages optimised design of the collector field of solar power tower plants, Sol. Ener. 135 (2016) 884–896.

[57] SOLGATE. Solar hybrid gas turbine electric power system, Tech. Rep. EUR 21615, European Commission (2005).

3.8 Chapter A – Simulación termodinámica de una planta termosolar híbrida tipo Brayton

Title: "Simulación termodinámica de una planta termosolar híbrida tipo Brayton"
Book: *Current Trends in Energy and Sustainability. 2015 Edition*
Authors: Santos Sánchez, María Jesús; **Merchán Corral, Rosa Pilar**; Medina Domínguez, Alejandro; Calvo Hernández, Antonio
Year: 2015
Chapter: XVII
Pages: 267-284
ISBN: 978-84-608-5438-8
Reference: [150]

Current Trends in Energy and Sustainability 2015 Edition

Invited Editors: Roberto Gómez-Calvet
José M. Martínez-Duart

Symposium on Energy and Sustainability. XXXV Biennial.
Spanish Royal Physical Society
Gijón (Spain), July 13-17. 2015

Book title: Current Trends in Energy and Sustainability. 2015 Edition
Invited Editors: Roberto Gómez-Calvet , José M. Martínez-Duart.
(roberto.gomezcalvet@universidadeuropea.es - martinez.duart@uam.es)

ISBN: 978-84-608-5438-8
Depósito Legal: M-4058-2016

Current Trends in Energy and Sustainability 2015 Edition

Symposium on Energy and Sustainability. XXXV Biennial.

Spanish Royal Physical Society

Gijón (Spain), July 13-17. 2015

CONTENTS

"SIMULACIÓN TERMODINÁMICA DE UNA PLANTA TERMOSOLAR HÍBRIDA TIPO BRAYTON"

Santos Sánchez, María Jesús [1], Merchán Corral, Rosa Pilar [2], Medina Domínguez, Alejandro[3], Calvo Hernández, Antonio[4].

1: Departamento Física Aplicada, Facultad de Ciencias, Universidad de Salamanca
Plaza de la Merced, s/n. 37071 Salamanca. e-mail: smjesus@usal.es

2: Departamento Física Aplicada, Facultad de Ciencias, Universidad de Salamanca
Plaza de la Merced, s/n. 37071 Salamanca. e-mail: rpmerchan@usal.es

3: Departamento Física Aplicada, Facultad de Ciencias, Universidad de Salamanca
Plaza de la Merced, s/n. 37071 Salamanca. e-mail: amd385@usal.es

4: Departamento Física Aplicada, Facultad de Ciencias, Universidad de Salamanca
Plaza de la Merced, s/n. 37071 Salamanca. e-mail: anca@usal.es

Resumen. *Desde el punto de vista termodinámico, se realiza el estudio dinámico de una planta termosolar híbrida de tipo Brayton: un tipo de plantas de generación de energía eléctrica con las que se pretende reducir el consumo de combustible y la emisión de contaminantes, así como conseguir una potencia neta constante. Lo más característico de estas plantas híbridas es que emplean dos fuentes principales de energía para su funcionamiento: la energía termosolar, proveniente de un campo de heliostatos que recoge y concentra la radiación solar recibida dirigiéndola hacia una torre central; y la energía que se origina en la oxidación de combustibles fósiles dentro de la cámara de combustión. Con `dinámico' se indica que se realiza un análisis de los parámetros de salida de la planta con la hora solar y con la estación del año. En primer lugar se expone brevemente en qué consiste una planta termosolar de receptor central (o planta CRS), además de especificar los objetivos del trabajo. Posteriormente se presenta el modelo termodinámico que se ha desarrollado, así como su validación. Finalmente se presentan y analizan los resultados de la simulación y las conclusiones obtenidas.*

Palabras clave: planta termosolar híbrida, ciclo Brayton, estudio dinámico.

1. INTRODUCCIÓN

1.1. Planta CRS

La tecnología termosolar constituye una de las formas básicas de aprovechamiento de la energía solar. Consiste en el calentamiento de un fluido que realiza un ciclo termodinámico (en este caso, de tipo Brayton), generando así energía eléctrica indirectamente.
Sus principales ventajas son: menor consumo de combustibles fósiles, reducción de emisiones contaminantes (que son la principal causa del efecto invernadero) y menor consumo de agua asociado a los ciclos Brayton (comparativamente con otros ciclos, como los Rankine, en los que se necesitan mayor cantidad de agua). Estas plantas se instalan en regiones donde la irradiación solar es alta, que suelen corresponderse con zonas áridas, donde la disponibilidad de agua es escasa, por lo que los ciclos Brayton resultan *a priori* una buena opción.

Chapter XVII

Dentro de la generación termosolar nos restringimos a las Centrales de Concentración y, más concretamente, a los sistemas con torre de concentración central (CRS, *Central Receiver System*), aunque también existen otros tipos, como los concentradores parabólicos lineales, los lineales de tipo Fresnel y los sistemas de discos parabólicos.
Estas plantas constan de tres elementos principales: el campo de heliostatos, formado por muchos espejos que reflejan y concentran la radiación solar hacia el receptor, que es el segundo elemento, situado en la parte superior de la torre, que convierte la radiación solar absorbida en calor a altas temperaturas. Y, por último, el sistema de conversión de potencia, también en la torre, que transforma la energía térmica en eléctrica.
España es pionera en el desarrollo de esta tecnología (Behar 2013) con las dos primeras plantas comerciales del mundo: la PS10 y la PS20, que se pueden observar en la Fig. 1, localizadas en Sanlúcar La Mayor, cerca de Sevilla, con potencias netas respectivas de 11 y 20 MW; y con la planta Gemasolar, la primera en utilizar sales fundidas como sistema de almacenamiento térmico.

Figura 1. Ejemplo de planta termosolar de torre de concentración central (plantas PS10 y PS20, Sanlúcar la Mayor, Sevilla). Foto de Abengoa Solar [http://www.abengoasolar.com].

1.2. Proyecto SOLUGAS

La misma empresa española que construyó PS10 y PS20, Abengoa Solar, está desarrollando uno de los proyectos con torre de concentración central más importantes en la actualidad: el Proyecto SOLUGAS (*http://www.abengoa.es/htmlsites/boletines/es/octubre2011*), que es un proyecto de I+D, emplazado también en Sanlúcar La Mayor, Sevilla.
La característica innovadora de esta planta es que está alimentada por dos fuentes de energía: una solar y otra fósil. Esto es lo que se denomina planta híbrida. El aporte de calor fósil proviene de la combustión de gas natural en una cámara que completa y rectifica el aporte solar, permitiendo, asimismo, que la planta genere energía por la noche y en condiciones de nula insolación.
Es la primera planta con tecnología CRS híbrida a escala comercial, con una potencia neta constante de 4,6 MW. El objetivo principal de este proyecto es demostrar la viabilidad de la tecnología CRS híbrida de tipo Brayton. Actualmente se encuentra en estado de desarrollo, por lo que no se han publicado todavía todos los resultados.

1.3. Objetivos

El primer objetivo de este trabajo es desarrollar un modelo termodinámico general para una

planta termosolar híbrida de tipo Brayton y llevar a cabo su aplicación en concreto al Proyecto SOLUGAS. Si bien este modelo es válido para cualquier otra planta de estas características.
Se debe comprobar, además, que el modelo funciona correctamente, arrojando los resultados esperados. Para ello se hará un análisis de validación comparando con datos de una planta real.
Otro objetivo importante es simular y predecir el comportamiento de la planta a lo largo del tiempo, observando la evolución estacional y las curvas diarias de los parámetros de salida. Además de obtener estimaciones sobre el consumo de combustible y la emisión de gases contaminantes a la atmósfera asociados a la producción de energía.

2. MODELO TERMODINÁMICO DE LA PLANTA

En este apartado se presenta el estudio termodinámico de la planta, basado en el modelo de Sánchez Orgaz *y col*. (Sánchez-Orgaz 2010), Sánchez-Orgaz 2015) y Olivenza *y col.* (Olivenza-León 2015).

2.1. Esquema de la planta

En la Fig. 2 se muestra el esquema de la planta termosolar que estamos analizando. La planta consta de tres subsistemas principales: el colector solar, la cámara de combustión y la máquina térmica.

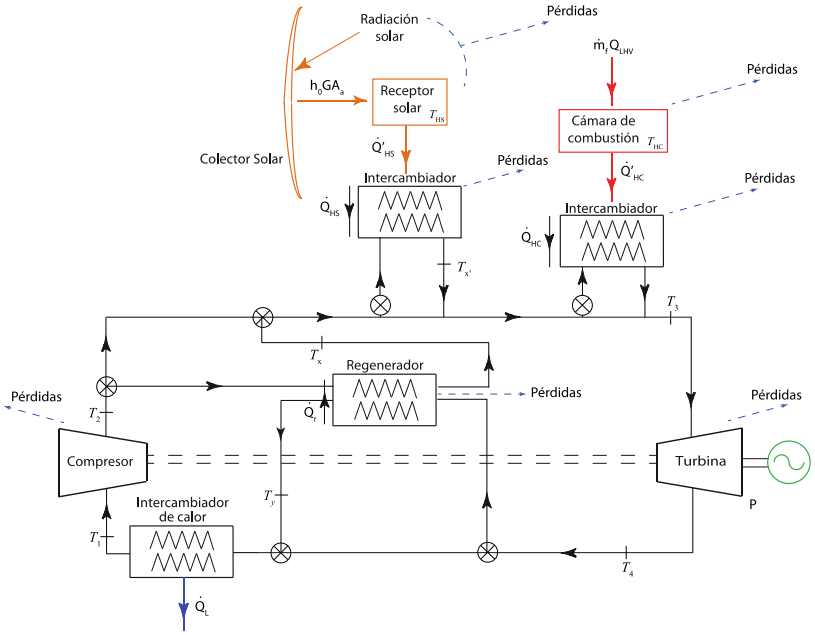

Figura 2. Esquema de la planta termosolar híbrida considerada.

En el colector solar (parte naranja Fig. 2) se recibe el flujo de energía GA_a, siendo G la irradiancia solar o energía recibida por unidad de tiempo y superficie y A_a el área de apertura del campo de heliostatos. La reflexión hacia el concentrador solar no es perfecta, sino que hay pérdidas, definidas por la eficiencia óptica, η_0, y debidas a factores como absorción del aire, humedad ambiente, suciedad en los espejos o efectos de sombras entre ellos (Duffie 2006). La temperatura que se alcanza en el receptor solar es T_{HS}. El colector cede calor al fluido de trabajo mediante un intercambiador de calor no ideal que, por tanto, presenta pérdidas.
En la cámara de combustión (parte roja, Fig. 2), se recibe un flujo de energía $\dot{m}_f Q_{LHV}$, determinado por el flujo de combustible, $\dot{m}_f$, que llega a la misma y por el poder calorífico inferior por unidad de masa, Q_{LHV} (energía por unidad de masa que aporta el combustible). El flujo de combustible necesario varía dependiendo de la hora solar, de la época del año y de las condiciones meteorológicas puesto que debe rectificar las oscilaciones de la irradiancia. En la cámara, a temperatura media, T_{HC}, hay pérdidas provocadas por la combustión incompleta del gas natural y por disipación del calor en las paredes. La cámara cede calor al fluido de trabajo a través de otro intercambiador de calor no ideal, siendo la combustión externa. En la máquina térmica, un fluido, en concreto, aire a presión con una capacidad calorífica media, c_w, y un coeficiente adiabático, γ, independiente de la temperatura, realiza el ciclo termodinámico tipo Brayton, que consta de cuatro etapas:

1. En primer lugar, los gases se comprimen en un compresor, aumentando su presión y temperatura desde T_1 hasta T_2.
2. Posteriormente se aumenta la temperatura del aire, en este caso, con varios aportes de calor: primero con el que cede un posible regenerador, que es un dispositivo intercambiador de calor utilizado para aprovechar el calor residual al finalizar el ciclo y que eleva la temperatura hasta T_x. En segundo lugar, se utiliza el calor proveniente del colector solar, con el que se alcanza una temperatura de $T_{x'}$; y, en tercer lugar, el transmitido por la cámara de combustión, que aumenta la temperatura del aire hasta T_3. Consideraremos que esta temperatura es aproximadamente constante, de modo que la potencia de salida de la planta también lo será.
3. A continuación los gases se expanden en una turbina, generando energía mecánica, que se transforma en energía eléctrica mediante un generador eléctrico. A la salida de la turbina, la temperatura del aire ha disminuido y es T_4.
4. Para finalizar el ciclo el aire debe volver a su estado inicial de temperatura T_1, por lo que se debe ceder el calor sobrante. Se puede colocar un regenerador a la salida de la turbina para aprovechar parte de esta energía térmica sobrante, destinándola a un primer aumento de la temperatura de los gases tras el compresor. Tras el regenerador la temperatura es T_y. Para llegar a T_1, se cede el resto de calor al medio exterior a través de un intercambiador de calor.

Con estos intercambiadores de calor, que conectan el fluido de trabajo con las partes externas a la máquina térmica, lo que se consigue es que el ciclo Brayton sea cerrado y de combustión externa. No son ideales por lo que siempre presentan pérdidas.
Esta planta posee varias válvulas de paso para poder conectar o desconectar ciertas partes de la misma. La cámara de combustión siempre está conectada así como el regenerador, pero el colector solar se desconecta por la noche y cuando la irradiancia es inferior a la mínima necesaria para aumentar T_x.

2.2. Transmisiones de calor

Se estudia a continuación las transmisiones de calor que tienen lugar en la planta. En la Fig. 3 el recuadro negro en línea discontinua muestra lo que se considera como sistema

termodinámico global, mientras que el círculo verde en línea discontinua representa a la máquina térmica que realiza el ciclo Brayton.

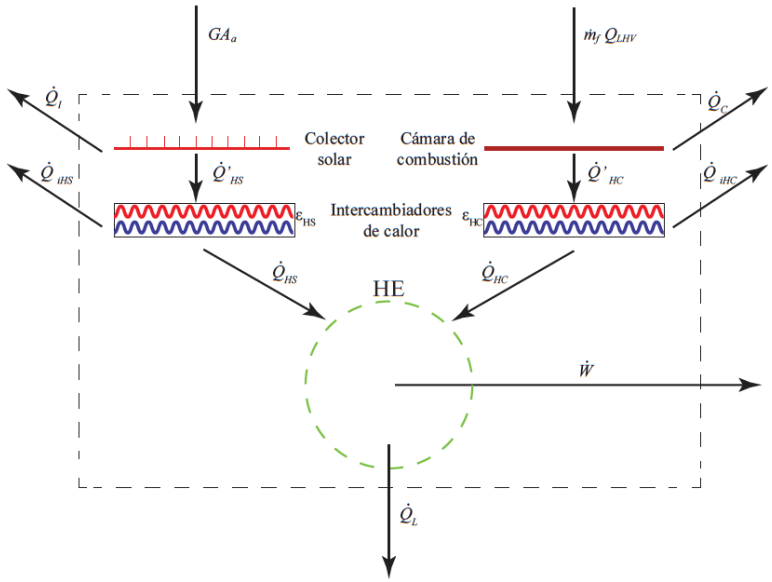

Figura 3. Diagrama de flujos de energía de la planta [Olivenza-León 2015].

Al colector solar le llega una energía GA_a, pierde un flujo de calor $\dot{Q}_l$ y transmite $\dot{Q}'_{HS}$ a su intercambiador de calor, cuyas pérdidas son $\dot{Q}_{iHS}$ con una eficiencia isoentrópica ϵ_{HS}, definida, como el cociente entre el flujo de energía transmitido y el que se transmitiría si funcionara de forma adiabática. A la máquina térmica le llega procedente de la parte solar un flujo de calor $\dot{Q}_{HS}$ que está determinado por el flujo de fluido que realiza el ciclo, $\dot{m}$, por su capacidad calorífica c_w y por el aumento de la temperatura producida

$$|\dot{Q}_{HS}| = \dot{m}c_w(T_{x'} - T_x). \quad (1)$$

La cámara de combustión recibe una energía $\dot{m}_f Q_{LHV}$, pierde un flujo de calor $\dot{Q}_C$ y transmite $\dot{Q}'_{HC}$ a su intercambiador de calor, que tiene una eficiencia isoentrópica ϵ_{HC} y cuyas pérdidas son $\dot{Q}_{iHC}$. La máquina térmica recibe procedente de la cámara de combustión un flujo de calor $\dot{Q}_{HC}$, que viene dado, de la misma forma que antes, por

$$|\dot{Q}_{HC}| = \dot{m}c_w(T_3 - T_{x'}). \quad (2)$$

El calor total recibido de las dos fuentes externas es $\dot{Q}_H$, la suma de $\dot{Q}_{HS}$ y $\dot{Q}_{HC}$, es decir

$$|\dot{Q}_H| = |\dot{Q}_{HS}| + |\dot{Q}_{HC}| = \dot{m}c_w(T_3 - T_x). \quad (3)$$

La máquina térmica cede al ambiente el calor $\dot{Q}_L$ dado por

$$|\dot{Q}_L| = \dot{m}c_w(T_y - T_1), \quad (4)$$

y produce una potencia $\dot{W}$ ó P, dada por la diferencia entre el calor que absorbe $\dot{Q}_H$ y el que cede $\dot{Q}_L$.

$$\dot{W} = P = \left|\dot{Q}_H\right| - \left|\dot{Q}_L\right|. \quad (5)$$

El *solar share (*o *fracción solar), f,* es la fracción de la energía aportada al fluido que proviene de la parte solar

$$f = \frac{|\dot{Q}_{HS}|}{|\dot{Q}_{HS}|+|\dot{Q}_{HC}|}. \quad (6)$$

El rendimiento termodinámico se define siempre como el cociente entre la energía producida y la empleada para obtenerla. De este modo el rendimiento global de la planta es la potencia neta obtenida partido por el calor total absorbido:

$$\eta = \frac{|\dot{W}|}{|\dot{Q}_{abs}|} = \frac{P}{G\,A_a+\dot{m}_f\,Q_{LHV}}. \quad (7)$$

El rendimiento del colector solar, η_s,

$$\eta_s = \frac{|\dot{Q}'_{HS}|}{G\,A_a} = \frac{|\dot{Q}_{HS}|/\epsilon_{HS}}{G\,A_a}, \quad (8)$$

el de la cámara de combustión, η_c,

$$\eta_c = \frac{|\dot{Q}'_{HC}|}{\dot{m}_f\,Q_{LHV}} = \frac{|\dot{Q}_{HC}|/\epsilon_{HC}}{\dot{m}_f\,Q_{LHV}}, \quad (9)$$

y el de la máquina térmica, η_h,

$$\eta_h = \frac{|\dot{W}|}{|\dot{Q}_H|} = \frac{P}{|\dot{Q}_{HS}|+|\dot{Q}_{HC}|}, \quad (10)$$

se hallan haciendo balance de la energía saliente y de la entrante en cada caso.
Se define también el rendimiento sobre el consumo de combustible o rendimiento económico, η_e, como el cociente entre la potencia obtenida y la cantidad de calor necesaria para obtenerla que tiene un coste económico asociado, es decir, la correspondiente a la cámara de combustión

$$\eta_e = \frac{|P|}{\dot{m}_f\,Q_{LHV}}. \quad (11)$$

No es un rendimiento termodinámico como tal, puesto que está definido de 0 a infinito y no de 0 a 1.

2.3. Rendimiento y potencia

El rendimiento global es el producto de los rendimientos de los tres subsistemas multiplicado por un factor que engloba a las eficiencias de los intercambiadores y al *solar share.* La siguiente ecuación se obtiene combinando las definiciones de rendimientos anteriores y la definición de fracción solar*, f:*

$$\eta = \eta_h\eta_s\eta_c\left[\frac{\epsilon_{HS}\,\epsilon_{HC}}{\eta_c\,f\,\epsilon_{HC}+\eta_s\,(1-f)\,\epsilon_{HS}}\right]. \quad (12)$$

El rendimiento del colector solar es la eficiencia óptica del campo de heliostatos menos dos términos de pérdidas: uno con temperaturas a la cuarta, que se corresponden con pérdidas de energía debidas a radiación y otro lineal con la temperatura, que se asocia con pérdidas debidas a la conducción en el soporte de los heliostatos y la convección del aire próxima a ellos (Duffie 2006):

$$\eta_s = \eta_O - \frac{1}{GC}\left[\alpha\,\sigma\left({T_{HS}}^4 - {T_L}^4\right) - \overline{U}_L\,(T_{HS} - T_L)\right], \quad (13)$$

donde $\overline{U}_L$ es un coeficiente efectivo de pérdidas por conducción y convección, T_L es la temperatura ambiente, C la relación de concentración o cociente entre el área de apertura y el área del receptor, α la emisividad de la superficie del colector y σ la constante de Stefan-Boltzmann.
El rendimiento de la cámara de combustión se puede considerar aproximadamente constante y, así, el flujo de combustible viene dado por:

$$\dot{m}_f = \frac{\dot{m} c_w (T_3 - T_{x'})}{\eta_c \, Q_{LHV} \, \epsilon_{HC}} \,, \tag{14}$$

en la que se ve que varía de forma inversa a como lo hace $T_{x'}$, para conseguir una T_3 constante que proporcione una potencia sin fluctuaciones.
En la Fig. 4 se presenta el diagrama *T-S* del ciclo que muestra las pérdidas e irreversibilidades que hay siempre como consecuencia de que los procesos no son ideales. El ciclo se ha representado con líneas continuas para observarlo mejor pero, de forma estricta, debería estar representado en líneas discontinuas puesto que no se trata de una sucesión de estados de equilibrio sino de procesos no reversibles.

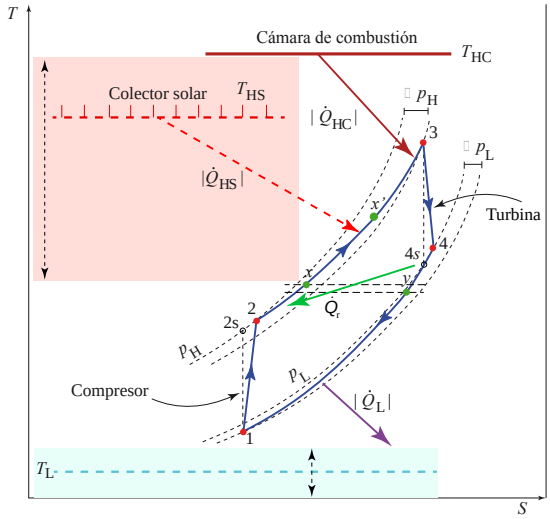

Figura 4. *Diagrama T-S del ciclo Brayton irreversible que experimenta el fluido de trabajo.*

Como se expuso anteriormente, en la etapa 1-2 el aire se comprime, pero no de forma adiabática reversible porque el compresor no es ideal. En la etapa 2-3, se produce el calentamiento del aire con el calor cedido por el regenerador, por el colector solar y por la cámara de combustión. En él hay una caída de presión desde p_H hasta $p_H - \Delta p_H$ como consecuencia de la no idealidad del proceso. En la etapa 3-4 el aire se expande en la turbina, pero tampoco de forma adiabática reversible porque la turbina tampoco es ideal. Y en la etapa 4-1 el fluido cede calor, mediante un regenerador y un intercambiador con el exterior, hasta recuperar las condiciones iniciales, habiendo también una caída de presión desde p_L hasta $p_L - \Delta p_L$.
Se definen dos relaciones de temperaturas: la del colector $\tau_{HS} = T_{HS}/T_L$ y la de la cámara con

la temperatura externa $\tau_{HC} = T_{HC}/T_L$. Las irreversibilidades se modulan con los siguientes parámetros:

- eficiencia isoentrópica del compresor, $\epsilon_C = \frac{T_{2s}-T_1}{T_2-T_1}$,
- regenerador, $\epsilon_r = \frac{T_x-T_2}{T_4-T_2} = \frac{T_y-T_4}{T_2-T_4}$,
- intercambiador solar, $\epsilon_{HS} = \frac{T_{x'}-T_x}{T_{HS}-T_x}$,
- intercambiador de la cámara, $\epsilon_{HC} = \frac{T_3-T_{x'}}{T_{HC}-T_{x'}}$,
- turbina, $\epsilon_t = \frac{T_{4s}-T_3}{T_4-T_3}$,
- intercambiador con el medio ambiente, $\epsilon_L = \frac{T_1-T_y}{T_L-T_y}$;

definidas todas ellas como cocientes de las diferencias de temperaturas involucradas (Fig. 4). Las irreversibilidades también se modulan con las caídas de presión, ρ_H y ρ_L,

$$\rho_H = \left(\frac{p_H-\Delta p_H}{p_H}\right)^{(\gamma-1)/\gamma}, \quad (15)$$

$$\rho_L = \left(\frac{p_L-\Delta p_L}{p_L}\right)^{(\gamma-1)/\gamma}, \quad (16)$$

la relación de presiones global, r_p,

$$r_p = \frac{p_H}{p_H-\Delta p_H}, \quad (17)$$

la del compresor, a_c ,

$$a_c = \frac{T_{2s}}{T_1} = r_p{}^{(\gamma-1)/\gamma}, \quad (18)$$

y la de la turbina, a_t ,

$$a_t = \frac{T_3}{T_{4s}} = \left(\frac{p_H-\Delta p_H}{p_L}\right)^{(\gamma-1)/\gamma} = a_c\rho_H\rho_L . \quad (19)$$

Se definen asimismo otros dos parámetros, Z_c y Z_t , para simplificar las ecuaciones:

$$Z_c = 1 + \frac{1}{\epsilon_c}(a_c - 1), \quad (20)$$

$$\mathrm{Z_t} = 1 - \epsilon_\mathrm{t}\left(1 - \frac{1}{\mathrm{a_t}}\right) . \quad (21)$$

Realizando una serie de cálculos (Olivenza-León 2015), se pueden determinar ecuaciones analíticas para los calores que intervienen en el ciclo, esto es, el calor recibido de la parte solar

$$\left|\dot{Q}_{HS}\right| = \dot{m}c_w T_L\epsilon_{HS}\left(\tau_{HS} - \frac{T_x}{T_L}\right) = \dot{m}c_w T_L\epsilon_{HS}\left[\tau_{HS} - Z_t\epsilon_r\frac{T_3}{T_L} - Z_c(1-\epsilon_r)\frac{T_1}{T_L}\right], \quad (22)$$

el recibido de la cámara de combustión

$$\left|\dot{Q}_{HC}\right| = \dot{m}c_w T_L\epsilon_{HC}\left\{\tau_{HC} - \tau_{HS}\epsilon_{HS} - (1-\epsilon_{HS})\left[\frac{T_3}{T_L}Z_t\epsilon_r + \frac{T_1}{T_L}Z_c(1-\epsilon_r)\right]\right\}, \quad (23)$$

y el cedido al medio exterior,

$$\left|\dot{Q}_L\right| = \dot{m}c_w T_L\epsilon_L\left[\frac{T_3}{T_L}Z_t(1-\epsilon_r) + \frac{T_1}{T_L}Z_c\epsilon_r - 1\right], \quad (24)$$

para la eficiencia de la turbina

$$\eta_h = 1 - \frac{\epsilon_L\left[\frac{T_3}{T_L}Z_t(1-\epsilon_r) + \frac{T_1}{T_L}Z_c\epsilon_r - 1\right]}{\epsilon_{HS}\left[\tau_{HS} - Z_t\epsilon_r\frac{T_3}{T_L} - Z_c(1-\epsilon_r)\frac{T_1}{T_L}\right] + \epsilon_{HC}\left\{\tau_{HC} - \tau_{HS}\epsilon_{HS} - (1-\epsilon_{HS})\left[\frac{T_3}{T_L}Z_t\epsilon_r + \frac{T_1}{T_L}Z_c(1-\epsilon_r)\right]\right\}}, \quad (25)$$

y para la potencia neta adimensional

$$\bar{P} = \epsilon_{HS}\left[\tau_{HS} - Z_t\epsilon_r\frac{T_3}{T_L} - Z_c(1-\epsilon_r)\frac{T_1}{T_L}\right] + \epsilon_{HC}\left\{\tau_{HC} - \tau_{HS}\epsilon_{HS} - (1-\epsilon_{HS})\left[\frac{T_3}{T_L}Z_t\epsilon_r + \frac{T_1}{T_L}Z_c(1-\epsilon_r)\right]\right\} - \epsilon_L\left[\frac{T_3}{T_L}Z_t(1-\epsilon_r) + \frac{T_1}{T_L}Z_c\epsilon_r - 1\right], \quad (26)$$

en función todos ellos de los parámetros de pérdidas, de las dos relaciones de temperaturas y de las relaciones de presiones.

3. VALIDACIÓN DEL MODELO TERMODINÁMICO

Una vez descrito el modelo, se procede a su validación.

3.1. Validación de la turbina

En primer lugar se valida la turbina. Los principales parámetros se resumen en la Tabla 1. Con las especificaciones del fabricante de la turbina Mercury 50 (del fabricante Caterpillar), que es la empleada en el proyecto SOLUGAS (Korzynietz 2012), y con ciertos valores asumidos para los parámetros de pérdidas, se determinan los valores de salida de nuestro modelo, que se pueden comparar con los que ofrece el fabricante Caterpillar (*https://mysolar.cat.com/cda/files/126873/7/dsm50pg.pdf*), observándose que la desviación relativa de casi todos es menor del 1% y que en ningún caso supera el 1,4%, lo cual indica que el modelo para la turbina se ajusta muy bien a la turbina real.

Especificaciones del fabricante de la turbina Mercury 50 (Caterpillar)			
$\dot{m} = 17.9\ kg/s$	$r_p = 9.9$		$T_L = 288\ K$
Valores asumidos de los parámetros de pérdidas			
$\epsilon_{HC} = 0.98$ $\epsilon_L = 1$	$\rho_H = \rho_L = 0.97$	$\epsilon_t = 0.885$ $\epsilon_c = 0.815$	$\epsilon_r = 0.775$
Valores de salida del fabricante			
$T_3 = 1423\ K$	$T_y = 647\ K$	$\eta = 0.385$	$\lvert\dot{W}\rvert = 4.6\ MW$
Valores de salida del modelo			
$T_3 = 1418\ K$	$T_y = 650\ K$	$\eta_h = 0.387$	$\lvert\dot{W}\rvert = 4.5\ MW$
Desviación relativa			
0.4%	0.4%	0.6%	1.4%

Tabla 1. Comparación de los resultados obtenidos por el fabricante con el modelo presentado, para los valores de los parámetros de irreversibilidades indicados (Olivenza-León 2015).

3.2. Validación de la planta termosolar

No es sencillo validar la planta termosolar en sí porque, al tratarse de un proyecto de I+D, la empresa propietaria aun no ha publicado los resultados completos. Sin embargo, se puede llevar a cabo una estimación de los resultados de la planta termosolar en condiciones estáticas, asumiendo parámetros estándar de combustión y tomando los parámetros de la parte solar de la literatura (Romero 2002). Para la temperatura ambiente se toma el valor de 288K y

para la irradiancia de 860W/m^2, que son los valores en el punto de diseño que asume la empresa que lidera el proyecto. Con ellos se obtienen los parámetros de salida y las eficiencias que se muestran en la Tabla 2. Todos los números son perfectamente razonables por lo que se concluye que el modelo que describe la planta funciona muy bien. Esta validación responde a un caso estacionario en el que la irradiancia y la temperatura ambiente permanecen constantes (Olivenza-León 2015); sin embargo, el estudio posterior que presentamos es dinámico.

Parámetros de combustión			
$\boldsymbol{\eta_c = 0.98}$	$T_{HC} = 1430\ K$	$\epsilon_{HC} = 0.98$	
Parámetros solares			
$\boldsymbol{\eta_0 = 0.73}$ $\boldsymbol{\alpha = 0.1}$	$T_{HS} = 1088\ K$ $\sigma = 5.67 \times 10^{-8} \frac{W}{m^2 K^4}$	$\epsilon_{HS} = 0.95$ $C = 425.2$	$G = 860\ W/m^2$ $\bar{U}_L = 5 \frac{W}{m^2 K}$
Parámetros de salida estimados			
$\boldsymbol{T_3 = 1423\ K}$	$f = 0.42$	$\dot{m}_f = 0.151\ kg/s$	$\lvert\dot{W}\rvert = 4.2\ MW$
Eficiencias estimadas			
$\boldsymbol{\eta_h = 0.392}$	$\eta_s = 0.697$	$\eta = 0.317$	$\eta_e = 0.647$

Tabla 2. Predicciones de nuestro modelo para los principales parámetros de la planta termosolar híbrida desarrollada en el Proyecto SOLUGAS. Los demás parámetros propios de la turbina se encuentran en la Tabla 1.

4. RESULTADOS

Partiendo únicamente de dos datos de entrada, irradiancia, G, y temperatura ambiente, T_L, y todas las magnitudes anteriores, se pueden obtener todos los parámetros de salida de la planta, con ayuda de las ecuaciones desarrolladas en el modelo. Como pretendemos realizar un estudio dinámico o, lo que es lo mismo, un estudio sobre la evolución de los parámetros a lo largo de las horas del día y de las estaciones del año, necesitamos disponer de datos de entrada con una cierta frecuencia. Así seleccionamos, de una base de datos de la empresa *Meteosevilla (http://www.meteosevilla.com),* datos de irradiancia y temperatura ambiente cada 30 minutos, para 4 días diferentes del año 2013, que señalan el inicio de las 4 estaciones (el 21 de diciembre, el 21 de marzo, el 20 de junio y el 21 de septiembre). Se trata, así pues, de datos en condiciones reales, que no han sido promediados ni suavizados para observar bien el ruido debido a las inclemencias meteorológicas.

El resto de parámetros toman los valores anteriores (Tabla 2), exceptuando la eficiencia, ϵ_{HS}, que toma un valor más realista (0,78) y la eficiencia óptica, η_0, que se considera ahora como un promedio anual (0,65). Con estos datos, a partir de nuestra simulación, se puede obtener la evolución estacional de todos los parámetros de la planta. Se exponen a continuación los resultados más relevantes.

4.1. Comportamiento estacional de los parámetros de la planta

4.1.1. Irradiancia y temperatura ambiente

En primer lugar, se analiza cómo se comportan estacionalmente los parámetros de entrada de la planta: irradiancia y temperatura ambiente, cuyos resultados se muestran en la Fig. 5.

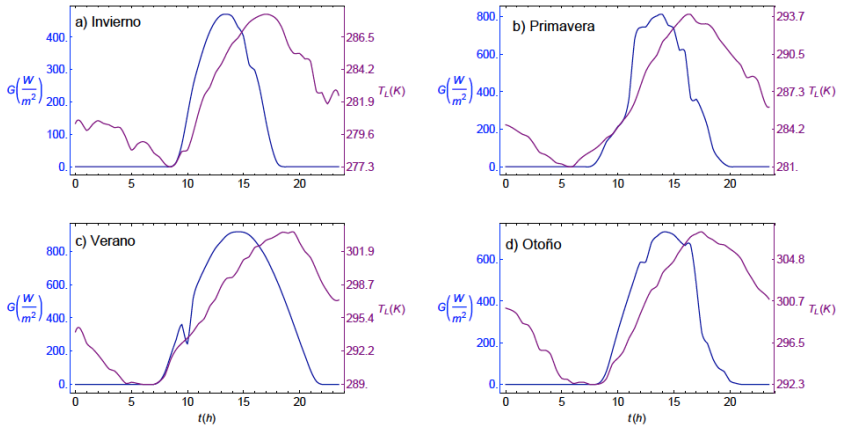

Figura 5. Irradiancia, G, (azul) y temperatura ambiente, T_L, (morado) frente al tiempo, t (UTC): a) 21 de diciembre, b) 21 de marzo, c) 20 de junio y d) 21 de septiembre.

En la Fig. 5 se representan la irradiancia, *G*, (azul, eje vertical izquierda) y la temperatura ambiente, T_L, (morado, eje vertical derecha) frente al tiempo, t, para cuatro días de distintas estaciones. Observando dicha figura es claro que la irradiancia es nula por la noche y comienza a crecer en el amanecer, alcanzando su valor máximo en las horas centrales del día. Después decrece y se anula de nuevo al anochecer.

En el comportamiento de la irradiancia destacan dos factores fundamentales:

- Por un lado la anchura de la curva o número de horas de Sol, que varía desde 10 horas en invierno hasta 15 en verano, pasando por 13 en otoño y aproximadamente 12 y media en primavera.
- Y, por otro lado, la altura de la curva o irradiancia máxima, que se recibe en las horas centrales, y oscila desde los 470 W/m^2 en invierno hasta los 910 W/m^2 del verano.

La forma de la gráfica de la temperatura ambiente es senoidal, en las primeras horas del día disminuye tomando el mínimo en el amanecer y luego crece. Las temperaturas más altas se alcanzan el 21 de septiembre y las más bajas el 21 de diciembre. En otoño y primavera, los valores de *G* y T_L son intermedios. La temperatura ambiente está desfasada respecto de la irradiancia.

4.1.2. Eficiencia y *solar share*

En la figura 6 se representan, frente al tiempo, el rendimiento global, η, (rosa claro), el rendimiento del colector solar, η_s, (fucsia), el rendimiento de la turbina, η_h, (azul claro), el rendimiento económico, η_e, (naranja) y *solar share, f,* (verde), para los cuatro días elegidos como representativos del año. Como se muestra en esta figura, el rendimiento solar, η_s, no

está definido por la noche y está dominado durante las horas de insolación por el término de la eficiencia óptica, porque los términos de pérdidas son pequeños. Por este motivo es prácticamente constante y está alrededor de 0,62, siempre menor de 0,65, que es el valor de η_0. La meseta es más ancha en verano que en inverno debido al número de horas de insolación. Este rendimiento crece durante el amanecer y decrece en el anochecer.

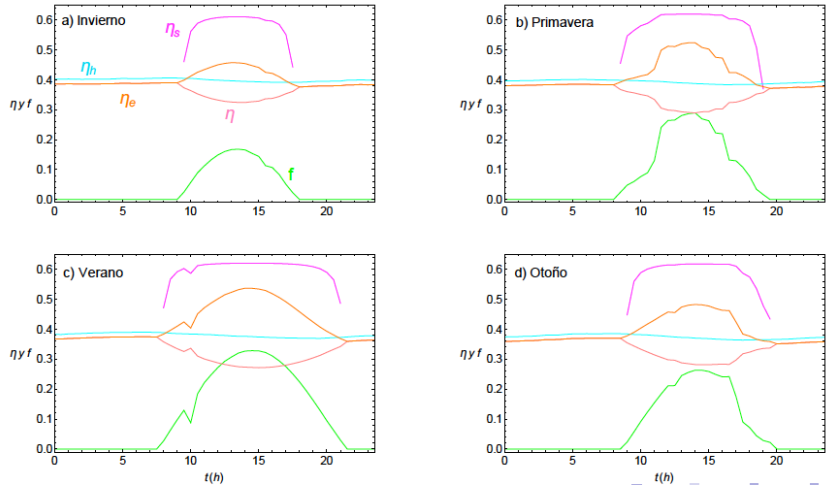

Figura 6. Rendimiento global, η (rosa claro), rendimiento del colector solar, η_s (fucsia), rendimiento de la turbina, η_h (azul claro), rendimiento económico, η_e (naranja) y fracción solar, f (verde) frente al tiempo, t (UTC): a) 21 de diciembre, b) 21 de marzo, c) 20 de junio y d) 21 de septiembre.

El rendimiento de la turbina, η_h, toma valores alrededor de 0,4 y varía muy poco porque se han conseguido rectificar las oscilaciones de la irradiancia, pero se mantienen las de la temperatura ambiente, de valor cuantitativo bastante más pequeñas (estas oscilaciones no se observan bien en la escala de todos los rendimientos).

El rendimiento global, η, se mantiene constante por la noche, cuando η_s no está definido, y disminuye durante las horas de insolación porque η_s ya está definido y porque, como se indica en la ecuación (12), es el producto de los rendimientos de los subsistemas, todos menores de 1. Toma valores mínimos de 0,27 en verano y de 0,32 en invierno.

Por la noche, el rendimiento económico, η_e, se corresponde con el global porque no hay aporte solar y cuando hay irradiancia suficiente varía de forma inversa a él. Como veremos más adelante esto se asocia al hecho de que en las horas centrales el consumo de combustible es mínimo.

El *solar share*, *f*, es 0 cuando la irradiancia es 0 y toma el máximo cuando la irradiancia es máxima, momento en el cual el rendimiento global es mínimo y el económico, máximo. *f* alcanza el valor de 0,33 en verano y la mitad, 0,17, en inverno. Primavera y otoño tienen siempre valores medios. El rendimiento solar, el económico y el *solar share* toman valores más altos en verano y más pequeños en invierno; mientras que el rendimiento global lo hace al contrario.

4.1.3. Rendimiento global y potencia

En la Fig. 7 se representa la evolución frente al tiempo del rendimiento global, η, (azul, eje vertical izquierda), y de la potencia, *P,* (morado, eje vertical derecha), para los días seleccionados. En ella se puede ver que la potencia neta no es estrictamente constante sino que oscila, pero en un intervalo pequeño, con variaciones máximas de 0,2 MW; así pues, se consigue uno de los objetivos principales de este proyecto: rectificar las oscilaciones de la irradiancia tras el colector, para obtener una potencia prácticamente constante. Sus pequeñas oscilaciones se deben a las de la temperatura ambiente, que no han sido corregidas.

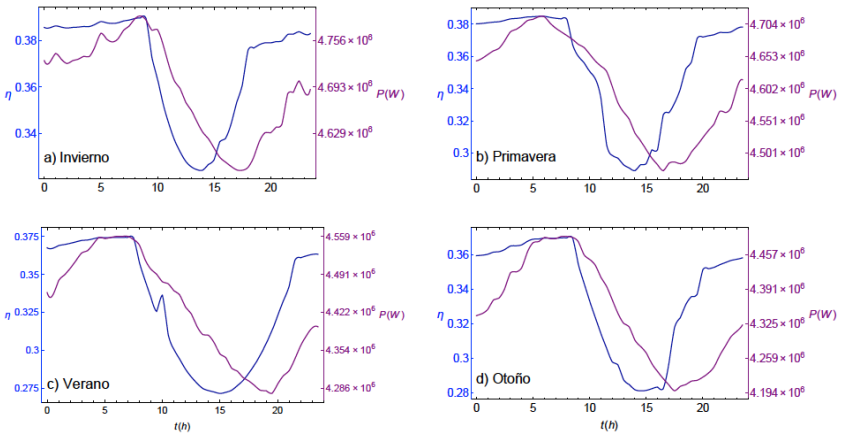

Figura 7. *Rendimiento global, η, (azul), y potencia, P, (morado) frente al tiempo, t (UTC): a) 21 de diciembre, b) 21 de marzo, c) 20 de junio y d) 21 de septiembre.*

La potencia está desfasada con respecto al rendimiento global del mismo modo que la temperatura ambiente está desfasada respecto de la irradiancia (Fig. 5). Sin embargo, las oscilaciones del rendimiento global, η, se deben tanto a aquéllas de la irradiancia como a las de la temperatura ambiente.

4.1.4. Flujo de combustible

En cuanto al flujo de combustible quemado varía de forma inversa a como lo hace la irradiancia, siendo constante por la noche, cuando toma su valor máximo debido a que la aportación solar es nula.

Esto se puede apreciar en la Fig. 8, en la que se representa el flujo de combustible quemado con aporte solar, $\dot{m}_f$ (azul, eje vertical izquierda), y sin aporte solar (línea gris) e irradiancia, *G*, (morado, eje vertical derecha) frente al tiempo, *t,* para las cuatro estaciones del año. Como era de esperar, al amanecer el consumo comienza a caer hasta tomar su valor mínimo cuando la irradiancia es máxima, en las horas centrales del día. Esta bajada en el consumo instantáneo es mínima en invierno (17%) y máxima en verano (33%). El flujo de combustible sin aporte solar es aproximadamente constante en todas las estaciones y ronda los 0,26 kg/s; mientras que con aporte solar es mínimo en verano y máximo en invierno debido a la mayor irradiancia.

Chapter XVII

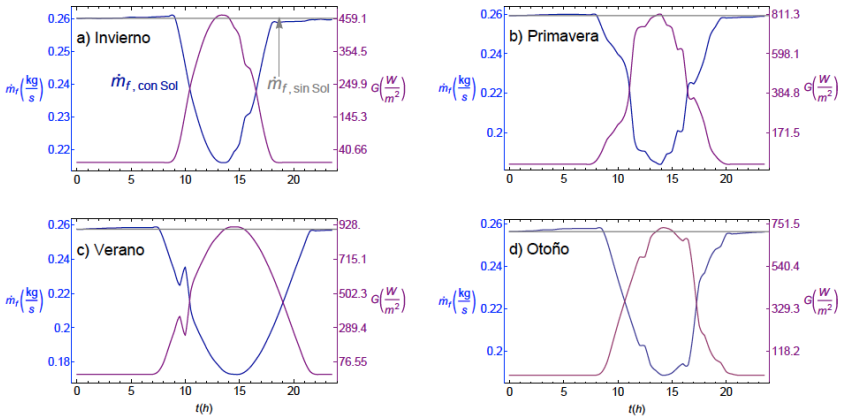

Figura 1. Flujo de combustible quemado con Sol, $\dot{m}_f$ (azul), y sin Sol (línea gris) e irradiancia, G (morado) frente al tiempo t (UTC): a) 21 de diciembre, b) 21 de marzo, c) 20 de junio y d) 21 de septiembre.

4.2. Comparación de resultados por estaciones

En este apartado se compara el consumo de combustible y las emisiones contaminantes para las diferentes estaciones.

4.2.1. Consumo de combustible

Se representa en la Fig. 9, en color gris (con línea discontinua) el flujo de combustible, $\dot{m}_f$, necesario si la planta funcionara sólo con aporte fósil y en azul, el correspondiente a la hibridación, para el 21 de septiembre de 2013. El área encerrada entre ambas curvas y que está rayada representa el ahorro en el consumo de combustible. Los resultados de las estimaciones para las cuatro estaciones se recogen en la Fig. 10, tanto numéricamente como en un diagrama de barras, en azul el consumo de la planta híbrida y en rojo sin aporte de calor solar.

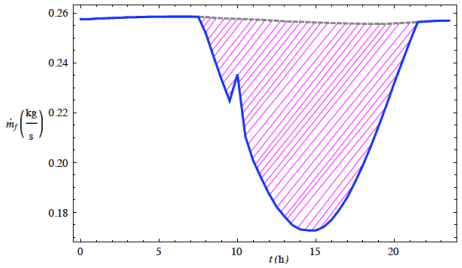

Figura 2. Flujo de combustible quemado con Sol, $\dot{m}_f$ (azul), y sin Sol (línea discontinua gris) frente al tiempo, t (UTC), para el 21 de diciembre.

Numéricamente, si la planta funcionara siempre sin aporte solar, sólo con el calor de la combustión, el consumo de combustible sería aproximadamente constante a lo largo de las estaciones, consumiéndose más de 21 toneladas de gas natural al día. Sin embargo, cuando la planta funciona de forma híbrida, el aporte solar baja significativamente el consumo de gas natural, que cae hasta las 19 toneladas al día en verano. Estos datos se ponen de manifiesto en la Tabla 3 que recoge la previsión del consumo de combustible en las diferentes estaciones, tanto con aporte de energía solar, como sin él.

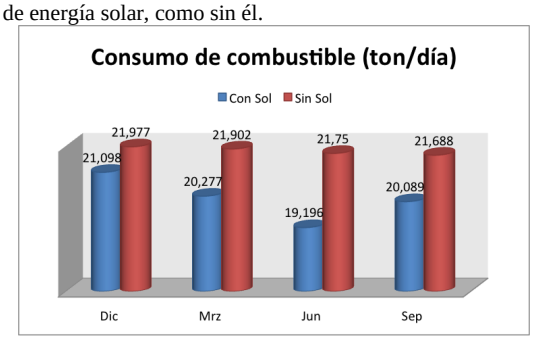

Figura 3. Diagrama de barras y valores númericos de la variación estacional del consumo de combustible: en azul el consumo de la planta híbrida y en rojo sin aporte de calor solar.

Así, el ahorro que se produce con el aporte solar varía desde el 4% en invierno hasta el 11,7% en verano, rondando el 7,4% en primavera y otoño.

	Inverno	Primavera	Verano	Otoño
Consumo sin aporte solar (ton/día)	21.9772	21.9018	21.7503	21.6883
Consumo con aporte solar (ton/día)	21.0981	20.2767	19.1960	20.0886
Ahorro (%)	4.00	7.41	11.74	7.38

Tabla 3. Tabla comparativa del consumo de combustible estimado en las diferentes estaciones con y sin aporte de la energía solar.

4.2.2. Emisiones contaminantes

Las plantas de combustibles fósiles de ciclo Brayton con gas natural son las más limpias, dentro de este tipo de plantas, ya que no emiten azufre ni derivados de él, aunque sí producen otras emisiones contaminantes, específicamente de efecto invernadero. Estudiamos en nuestro caso tres gases: dióxido de carbono CO_2, metano CH_4 y óxido nitroso N_2O, porque son los principales gases de efecto invernadero asociados a la combustión del gas natural.
En la Fig. 11 se presentan en diagramas de barras la variación estacional de las emisiones de contaminantes: a) CO_2, b) CH_4 y c) N_2O. Para calcular los resultados se ha hecho uso de factores de emisión estándar para el gas natural (*http://www.epa.gov/ghgreporting/documents/pdf/2013/documents/memo-2013-technical-revisions.pdf*). El color oscuro se corresponde a las emisiones de la planta híbrida y el color claro las emisiones sin aporte de calor solar. Como se muestra claramente en dicha figura, las emisiones de todos los gases, sin aporte solar, son similares: 54 toneladas al día para el CO_2, 1022 g para el CH_4 y casi 100 g diarios para el N_2O. El funcionamiento híbrido baja las

emisiones en todas las estaciones, especialmente en verano. La diferencia entre el verano y el inverno es la emisión de casi 5 toneladas de CO_2 más al día, de alrededor de 90 g de CH_4 y de 8,6 g diarios de N_2O.
Sin embargo, hay que tener en cuenta que las plantas pueden tener mecanismos para reducir estas emisiones, como los sistemas de atrapamiento y almacenamiento de CO_2 o los catalizadores para el óxido nitroso. Por lo que estos resultados son meramente orientativos y los valores de contaminantes emitidos dependerán de las particularidades de cada planta.

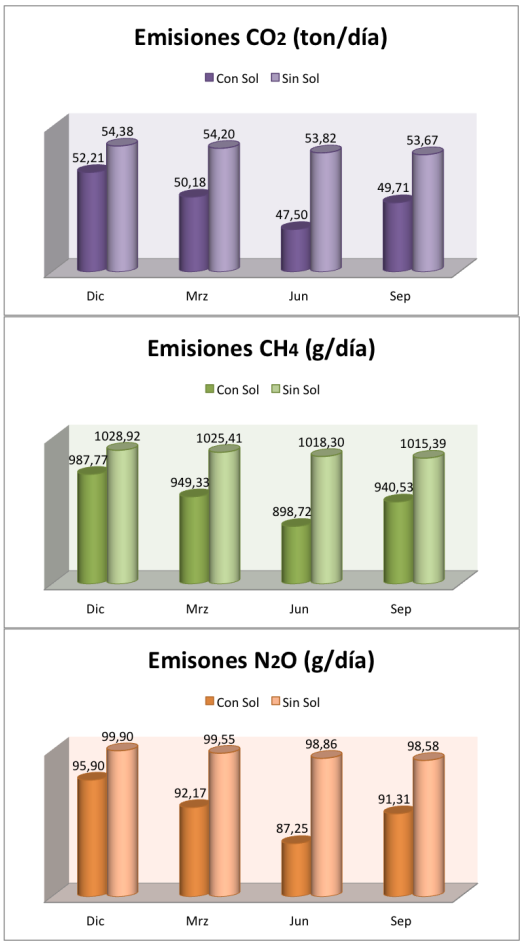

Figura 4. Diagrama de barras y valor numérico de la variación estacional de las emisiones de contaminantes: a) CO_2, b) CH_4 y c) N_2O. En oscuro las emisiones de la planta híbrida y en color claro las emisiones sin aporte de calor solar.

La reducción de emisiones viene representada por los mismos porcentajes que el ahorro de combustible (Tabla 3), puesto que para calcularlas se ha hecho uso de unos factores de conversión, que relacionan directamente el consumo de gas natural con las emisiones en masa que produce su combustión (*http://www.epa.gov/ghgreporting/documents/pdf/2013/documents/memo-2013-technical-revisions.pdf*). Así pues ambos ahorros toman valores entre el 11,7% y el 4%, que supondrían un ahorro apreciable en términos anuales para las empresas y una reducción importante de las emisiones de efecto invernadero.

5. CONCLUSIONES

Se detallan las conclusiones más importantes que se pueden obtener de este trabajo:

- Se ha desarrollado un modelo termodinámico no estacionario, con ecuaciones analíticas, para una planta de generación de energía eléctrica basada en la hibridación en serie de un campo de heliostatos con concentrador de torre central y una turbina de gas de ciclo Brayton operando en ciclo cerrado.
- El sistema se describe desde el punto de vista termodinámico con un número reducido de parámetros, cada uno de ellos de claro contenido físico.
- Las ecuaciones finales para los parámetros de salida (eficiencias, potencia, temperaturas y consumo de combustible) dependen de factores que cuantifican las pérdidas e irreversibilidades en cada uno de los subsistemas y en los intercambiadores de calor.
- Este modelo permite hacer un seguimiento en función del tiempo de cualquiera de los parámetros del sistema.
- El modelo ha quedado validado utilizando la planta del Proyecto SOLUGAS (Abengoa Solar).
- La eficiencia del subsistema solar es aproximadamente constante durante las horas de insolación.
- La eficiencia de la turbina permanece aproximadamente constante a lo largo de todo el día.
- El rendimiento global se mantiene constante por la noche y disminuye durante las horas de insolación.
- El rendimiento económico tiene forma parabólica y presenta un máximo en las horas de máxima insolación u horas centrales del día.
- El número de horas de insolación se ha demostrado determinante en la evolución estacional de las curvas de eficiencias de la planta.
- La potencia de salida de la planta permanece aproximadamente constante para condiciones estacionales y meteorológicas cualesquiera; por lo que se ha cumplido el objetivo de que el suministro de energía eléctrica no dependa de dichas condiciones.
- Este tipo de plantas termosolares resultan muy interesantes desde el punto de vista del ahorro del consumo de combustibles fósiles y de emisiones de contaminantes en regiones con alta radiación solar y poca disponibilidad de agua.

AGRADECIMIENTOS

Los autores agradecen la financiación del MINECO, proyecto ENE2013-40644-R.

Chapter XVII

REFERENCIAS

Behar, O., Khellaf, A., Mohammedi, K., (2013). A review of studies on central receiver solar termal plants. *Renew. Sust. Energ. Rev.* 23: 12-39.

Duffie, J. & Beckman, W. (2006), *Solar Engineering of Thermal Processes*, John Wiley and Sons, Hoboken, New Jersey.

Emission factors for greenhouse gas inventories: Table 1 Stationary Combustion Emission Factors. http://www.epa.gov/ghgreporting/documents/pdf/2013/documents/memo-2013-technical-revisions.pdf

Korzynietz, R., Quero, M., Uhlig, R., (2012) *SOLUGAS-future solar hybrid technology*, Tech. Rep., SolarPaces,. http://cms.solarpaces2012.org/proceedings\\/paper/7ee7e32ece8f2f8e0984d5ebff9d77b

Olivenza-León, D., Medina, A., Calvo, A., (2015), Thermodynamic modeling of a hybrid solar-turbine power plant. *Energ. Conv. Manage.* 93: 435-447.

Romero, M.; Buck, R. & Pacheco, .E. (2002), An Update on Solar Central Receiver Systems, Projects, and Technologies. *Transactions of the ASME, 124*: 98

Sánchez-Orgaz, S.; Medina, A. & Calvo Hernández, A. (2010), Thermodynamic model and optimization of a multi-step irreversible Brayton cycle. *Energ. Convers. Manage., 51*, 2134-43

Sánchez-Orgaz, S.; Pedemonte, M.; Ezzatti, P.; Curto-Risso, P.; Medina, A. & Calvo Hernández, A. (2015). Multi-objective optimization of a multi-step solar-driven Brayton cycle. *Energ. Conv. Manage, 99*: 346-358

3.9 Chapter B – Hybrid Brayton thermosolar systems: thermodynamic prediction of annual efficiencies and emissions

Title: "Hybrid Brayton thermosolar systems: thermodynamic prediction of annual efficiencies and emissions"
Book: *Current Trends in Energy and Sustainability. 2017 Edition*
Authors: **R.P. Merchán**, M.J. Santos, A. Medina, A. Calvo Hernández
Year: 2017
Chapter: IV
Pages: 47-60
ISBN: 978-84-0903541-0
Reference: [149]

Resumen

En este trabajo se presenta un modelo termodinámico válido para plantas termosolares híbridas, de ciclo Brayton y de torre de concentración solar. El modelo se implementa en un código propio desarrollado en el lenguaje de programación de *Mathematica*® empleando para este fin los valores de las variables de diseño propios de la planta *SOLUGAS*, ubicada en Sevilla. Además, se introducen datos meteorológicos reales que después son promediados anualmente. Por otro lado, se analiza la influencia de la temperatura en el calor específico. Para ello, se comparan los registros de las principales variables de la planta para calor específico tanto constante como dependiente de la temperatura. Se demuestra que ambos modelos ofrecen resultados muy similares en el caso anual. Mediante este capítulo de libro se pretenden evaluar los límites teóricos de la planta llevando a cabo estudios anuales. Las principales pérdidas de energía de la planta se representan mediante diagramas de Sankey que muestran que el tamaño del campo solar es demasiado pequeño para la potencia fijada, por lo que la planta funciona siempre en modo híbrido. Asimismo, los análisis de sensibilidad efectuados concluyen que los parámetros de pérdidas de la máquina térmica influyen significativamente en el funcionamiento global de la planta. Finalmente, se hace hincapié en cuáles son las posibles líneas de trabajo futuro a partir de esta contribución.

Current Trends in Energy and Sustainability 2017 Edition

Invited Editors: Roberto Gómez-Calvet (Univ. Europea de Valencia)
José M. Martínez-Duart (Univ. Autónoma de Madrid)

Symposium on Energy and Sustainability. XXXVI Biennial.
Spanish Royal Physics Society
Santiago de Compostela (Spain), July 17-21. 2017

Book title: Current Trends in Energy and Sustainability. 2017 Edition
Invited Editors: Roberto Gómez-Calvet (Universidad Europea de Valencia) and José M. Martínez-Duart (Universidad Autónoma de Madrid).
(roberto.gomezcalvet@universidadeuropea.es - martinez.duart2@gmail.com)

ISBN: 978-84-0903541-0
Depósito Legal: M-26519-2018

Current Trends in Energy and Sustainability 2017 Edition

Symposium on Energy and Sustainability. XXXVI Biennial.

Spanish Royal Physics Society

Santiago de Compostela (Spain), July 17-21. 2017

CONTENTS

XXXVI Biennial Meeting of the Real Sociedad Española de Física
Symposium on Energy and Sustainability

Hybrid Brayton thermosolar systems: thermodynamic prediction of annual efficiencies and emissions

R.P. Merchán[1,*], M.J. Santos[1], A. Medina[1], A. Calvo Hernández[1]

[1] Department of Applied Physics, University of Salamanca, Plaza de la Merced s/n, 37008, Salamanca, Spain

* rpmerchan@usal.es

1. Introduction

The necessity to diversify the energy sources in power generation and to look for renewable ones is undoubted. Thermosolar power plants, which constitute one of the main ways of solar energy exploitation, are competing with other renewable energy sources for generating clean electrical energy, reducing fuel consumption. Hybrid thermosolar plants combine two great advantages on electricity generation: the emissions reduction of thermosolar energy, as well as the stable supply of power output to the grid of conventional power plants, avoiding the use of storage systems. For those reasons in the last years a big effort has been done in the development of prototypes and experimental plants in order to investigate the viability of thermosolar hybrid Brayton cycle plants.

A working fluid, usually air, is preheated by concentration solar energy, before entering a combustion chamber. Then, the fluid performs a thermodynamic cycle (in this case, a Brayton cycle), generating electrical energy indirectly. In this way fossil fuel and the associated emissions are reduced. It is important to note that apart from being easily scalable, gas-turbines can be combined with other cycles like bottoming Rankine. Also they do not require too much water for operation, which makes them suitable for electrical generation in arid regions, and are extremely versatile [1].

Experimental projects and prototypes developed up to date show that this technology is viable, but they also reveal that it is necessary to improve their efficiency, in order to generate electricity at competitive prices. Apart from R+D projects, prototypes, and experimental installations, several research works have been published in the last times. Some of them make use of commercial simulation environments, which allow a detailed description of all plant components and specific calculations on the solar subsystem. However, it is not easy to extract direct physical information about the main losses sources in the plant and to perform a global optimization of the plant design. Because of this reason, in this paper the next modus operandi is followed instead of this one.

A second type of strategy is to build a theoretical model of the plant, in terms of a reduced number of parameters, allowing a simple but realistic picture of plant operation and to estimate its performance records. Thermodynamic analyses can provide an integrated point of view of all subsystems and their importance in the overall efficiency. Moreover, they help to predesign future generations of plants based in this concept because of their flexibility to survey the adequate intervals of key parameters for optimal plant operation.

There are several theoretical works that start from the ideal Brayton cycle and thereafter refinements are included in the analysis of the thermodynamics of the cycle in order to recover realistic output records. Usually, in these works, the model for the concentrated solar subsystem, although including the main heat transfer losses, is simple. This allows to obtain closed analytical expressions for thermal efficiencies and power output, and then check the model predictions for particular design point conditions, with fixed values of direct solar irradiance and ambient temperature. But also by means of this thermodynamic model, a dynamic analysis that varies solar irradiance and external temperature conditions with time can be carried out. And in a possible step forward to suggest and guide optimization strategies.

2. Plant thermodynamics

A thermodynamic model for hybrid Brayton thermosolar plants, which has been proposed recently by the same authors, is going to be presented [2-5]. These plants have three main elements: the heliostat field, the receiver, and the power conversion system. The model, in which refers to the thermodynamic cycle, starts from a closed Brayton cycle however incorporating the main losses and irreversibility sources: pressure decays, non-ideal compressor and turbine, heat transfer losses in the solar collector, combustion inefficiencies, heat exchangers, etc.

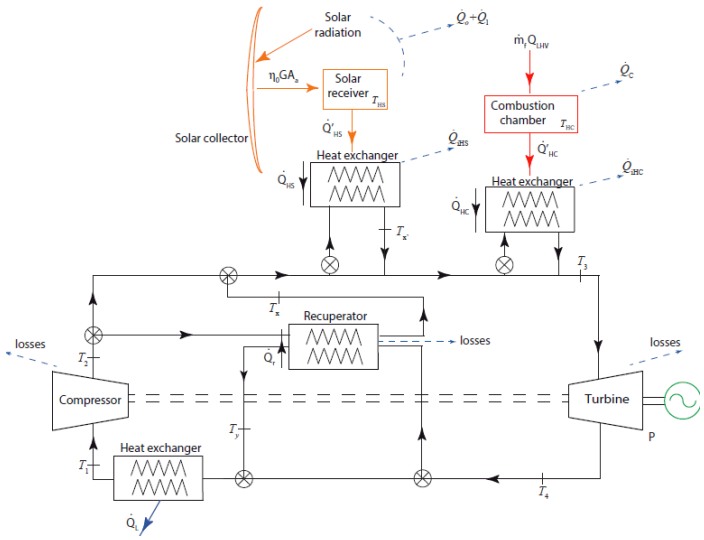

Figure 1. Scheme of the hybrid solar Brayton plant considered. The main heat transfers and temperatures are shown. Also the key losses sources considered in the model are depicted.

A central tower hybrid solar thermal installation, as depicted in Fig. 1, is considered. The whole system receives two energy inputs. On one hand, a heat input, GA_a, coming from the sun, where G is the direct solar irradiance and A_a, the aperture area of the solar field. For the solar subsystem, a simple model, which accounts for heat losses in the solar collector due to radiation and conduction/convection terms, was supposed.

$$\eta_S = \eta_0 - \frac{1}{GC}[\alpha\sigma(T_{HS}^4 - T_L^4) + U_L(T_{HS} - T_L)] \qquad (1)$$

In this equation η_S is the solar collector efficiency, η_0 the optical efficiency, C the concentration ratio, α the effective emissivity of the collector, σ the Stefan-Boltzmann constant, T_{HS} the collector working temperature, T_L the ambient temperature and U_L the conduction/convection heat loss coefficient.

On the other hand, the energy input at the combustion chamber is $\dot{m}_f Q_{LHV}$, being $\dot{m}_f$ the fuel mass flow rate and Q_{LHV}, its corresponding lower heating value. Finally, the heat engine generates a mechanical power output, P, and releases a heat flux to the ambient, $\dot{Q}_L$.

The overall thermal efficiency (η) was found as a function of the efficiency of the plant subsystems (solar η_S, combustion η_C, and gas turbine η_H), the effectivenesses of the heat exchangers linking subsystems (ε_{HS} for solar subsystem and ε_{HC} for combustion subsystem) and the solar share fraction (f).

$$\eta = \eta_S \eta_C \eta_H \left[\frac{\varepsilon_{HS}\varepsilon_{HC}}{\eta_C \varepsilon_{HC} f + \eta_S \varepsilon_{HS}(1-f)} \right] \qquad (2)$$

There is another interesting performance, denominated fuel conversion rate, that relates power output to the required heat with an associated economical cost (fuel burned). It does not represent a thermodynamic efficiency because it is defined in the range $[0, \infty]$:

$$\eta_e = \frac{P}{\dot{m}_f Q_{LHV}} = \frac{\eta \eta_S \eta_H \varepsilon_{HS}}{\eta_S \eta_H \varepsilon_{HS} - \eta f} \qquad (3)$$

A mass rate of an ideal gas (pressurized air) undergoes an irreversible recuperative closed Brayton cycle, in which the recuperator can be removed. The working gas is first compressed in a non-ideal compressor; and then it is heated up by the recuperator, the solar collector, and the combustion chamber. After the heating stage, the air is expanded and cooled irreversibly through a non-ideal turbine. And finally, the working gas recovers its initial conditions releasing heat with the recuperator and with another heat exchanger that connects the cycle to the surroundings. Turbine model includes these existing losses and irreversibilities. On the one hand, the geometric parameters related to the size of the cycle are taken into account. And, on the other hand, the heat losses irreversibilities in the compressor and turbine, in the recuperator and in all the heat exchangers and the pressure drop irreversibilities in the heat absorption and extraction processes are included. The key of the model resides in the fact that all the involved temperatures can be expressed in terms of the whole set of geometric and irreversibility parameters, so the performance of the plant is a function of these parameters [2].

3. Numerical implementation and validation

Once the thermodynamic model has been proposed, a numerical implementation is performed. This validation has been widely addressed by the same authors in [2].

Table 1. Top: output records from the manufacturer and from our model for the pure combustion mode. Bottom: estimated parameters and efficiencies from our model for the hybrid thermosolar mode.

GAS TURBINE: PURE COMBUSTION MODE			
Mercury 50 turbine: manufacturer's output records (*Caterpillar*)			
$T_3 = 1423\ K$	$T_y = 647\ K$	$\eta_h = 0.385$	$\lvert\dot{W}\rvert = 4.6\ MW$
Model: estimated output records			
$T_3 = 1418\ K$	$T_y = 650\ K$	$\eta_h = 0.387$	$\lvert\dot{W}\rvert = 4.5\ MW$
Relative deviations			
0.4 %	0.4 %	0.6 %	1.4 %
GAS TURBINE: HYBRID THERMOSOLAR MODE (at design point)			
Estimated output parameters			
$T_3 = 1423\ K$	$f = 0.42$	$\dot{m}_f = 0.151\ kg/s$	$\lvert\dot{W}\rvert = 4.2\ MW$
Estimated efficiencies			
$\eta_H = 0.393$	$\eta_S = 0.697$	$\eta = 0.317$	$\eta_e = 0.647$

In order to introduce the solar heat, researchers from SOLUGAS Project [6] have modified *Mercury 50* turbine (manufactured by *Caterpillar*). Output values of our model can be obtained and compared to the ones of manufacturer for the pure combustion mode (see Table 1). In accordance with this, relative deviations are very small, hence the turbine model agrees very well with real turbine data.

However, it is not possible to validate the thermosolar plant itself because the owner company has not published all the results, but a stationary estimation at the design point can be done. In this way, output parameters and efficiencies are estimated and all the results are perfectly reasonable, so it is concluded that the thermosolar plant model works fairly properly.

4. Results

4. 1. Temperature dependent specific heat (c_p)

Needed meteorological data (solar direct irradiance and ambient temperature) have been obtained from *Meteosevilla* database [7]. As probably Solugas design point conditions are too optimistic, average conditions are taken into account. So, an average calculation process is followed for obtaining annual mean values of these meteorological data [4]. In this way, the surrounding averaged temperature is $T_L = 291.575\ K$, while annual mean solar irradiance is $G = 457.874\ W/m^2$. This last one value can be considered a realistic value since it constitutes about half of the design point irradiance considered in Solugas project, $G = 860\ W/m^2$ [6].

As the temperature changes in this Brayton cycle are high (from about $300K$ to approximately $1400K$), the influence of the temperature on the specific heat, $c_p(T)$, may be important. The polynomial fit for this constant pressure specific heat has been determined by taking into account NIST data through RefProp software [8]. In order to analyze this influence, a comparison between the case when specific heat is supposed constant and the case when specific heat depends on the temperature has been carried out.

Table 2 shows these results together with relative deviations between the two alternatives, related to the temperature dependent case:

$$\Delta x\ (\%) = \frac{x_{c_{p(T)}} - x_{\bar{c}_p}}{x_{c_{p(T)}}} * 100 \qquad (4)$$

Table 2. Comparison of output values for temperature independent ($\bar{c}_p$) and dependent specific heat ($c_p(T)$), with relative deviations (Δx (%)).

WITH RECUPERATION	AVERAGE CONDITIONS		
	$\bar{c}_p$	$c_p(T)$	Δx (%)
η	0.323	0.324	0.475
η_e	0.449	0.450	0.267
η_S	0.610	0.609	−0.472
η_H	0.392	0.393	0.463
f	0.163	0.161	−1.023
$T_{HS}\ (K)$	948.886	971.150	2.293
$P\ (MW)$	4.621	4.677	1.207
$m_{f,spec}\ (kg/MWh)$	170.037	169.582	−0.268

In view of the results the differences between output variables with $\bar{c}_p$ and $c_p(T)$ are very small. For instance, overall thermal efficiency, solar collector efficiency, and solar share change only in the third decimal place. At the other extreme, temperatures present larger changes, although they are still small.

The main conclusion obtained from this study is that both models can be applied because results are very similar. So henceforth the model with constant specific heat will be used, since it is simpler and allows a completely analytical description. But the opposite approach, the cycle with temperature dependent specific heat, has been followed in [5]. It should be highlighted that our result contradicts conclusions from [9].

4. 2. Theoretical limits of the plant

Starting from real conditions (also called operating point), other four hypothetical configurations can be investigated with the goal of examining possible plant improvements over the real conditions of the plant: first the heat exchangers are considered as ideal, then the solar subsystem, after it is the Brayton cycle which is supposed ideal, and finally a completely ideal system is assumed. (see Fig. 2).

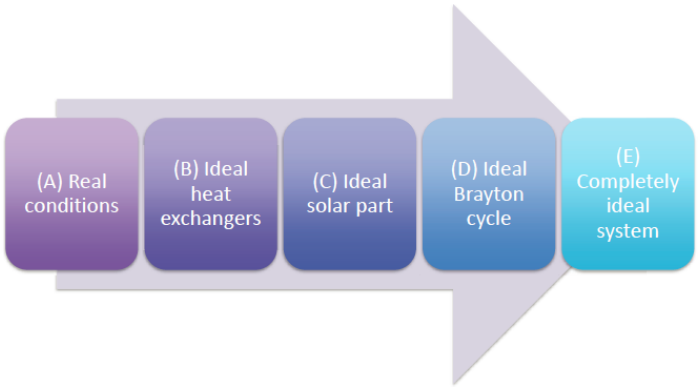

Figure 2. Scheme of the analyzed cases.

Apart from those five configurations, four operating modes are analyzed according to the existence or not existence of solar input and recuperator.

At real conditions (Table 3), a power output of 4.5 MW can be achieved, very close to that of the design point. It should be highlighted that exhaust temperature presents a high value in all cases, which is important to take advantage of residual heat with cogeneration or bottoming cycles.

Overall thermal efficiency of the recuperative plant is larger if there is no solar input: a 6.9 % higher than for hybrid operation, due to energy losses in solar subsystem associated with high temperatures. On the other hand, fuel conversion rate takes its larger value when there is solar input and recuperation. It can be confirmed that, in combustion mode, the fuel conversion rate is the overall thermal efficiency. In addition, solar collector efficiency is relatively good; however, solar share is still small.

Table 3. Annual means of most important plant performance records: (A) operating point. Relative differences are calculated with respect to the layout with no solar input.

Operating point (A)	Without recuperation		With recuperation	
	Without solar input	With solar input	Without solar input	With solar input
$P\ (MW)$	4.370	4.377 (+0.16%)	4.469	4.476 (+0.16%)
η	0.262	0.250 (−4.75%)	0.367	0.342 (−6.94%)
η_e	0.263	0.283 (+7.39%)	0.367	0.406 (+9.54%)
η_H	0.274	0.274 (+0.04%)	0.383	0.383 (+0.08%)
$T_{HS}\ (K)$	–	730.1	–	946.6
η_S	–	0.620	–	0.586
f	–	0.123	–	0.164

Table 4 is obtained when a completely ideal system is assumed. So, these are the maximum achievable values that mark the plant performance limits. A great power output can be reached: almost 8 MW. Also, an overall efficiency of 0.6, a fuel conversion rate of about 0.8, and a solar share of 0.3 (double that for the real conditions) are predicted.

Table 4. Annual means of most important plant performance records: (E) completely ideal system. Relative differences are calculated with respect to the layout with no solar input.

Completely ideal system (E)	Without recuperation		With recuperation	
	Without solar input	With solar input	Without solar input	With solar input
$P\ (MW)$	7.988	7.988 (+0.%)	7.988	7.988 (+0.%)
η	0.452	0.452 (+0.%)	0.628	0.628 (+0.%)
η_e	0.452	0.522 (+15.68%)	0.628	0.792 (+26.0%)
η_H	0.452	0.452 (+0.%)	0.628	0.628 (+0.%)
$T_{HS}\ (K)$	–	722.1	–	971.0
η_S	–	1.	–	1.
f	–	0.218	–	0.301

The intermediate configurations have been also analyzed [4], but for the sake of brevity their tables results are not exposed here. As a summary, Fig. 3 is presented, where some output records are shown for the five configurations. It is clear that configurations (D) and (E), that is to say, assuming the Brayton cycle and the whole system as ideal, is which affects more to overall efficiency, to fuel conversion rate and to power output.

When the solar subsystem is supposed ideal, the solar collector efficiency raises fairly significantly. However, these increments are not reflected on the overall thermal efficiency.

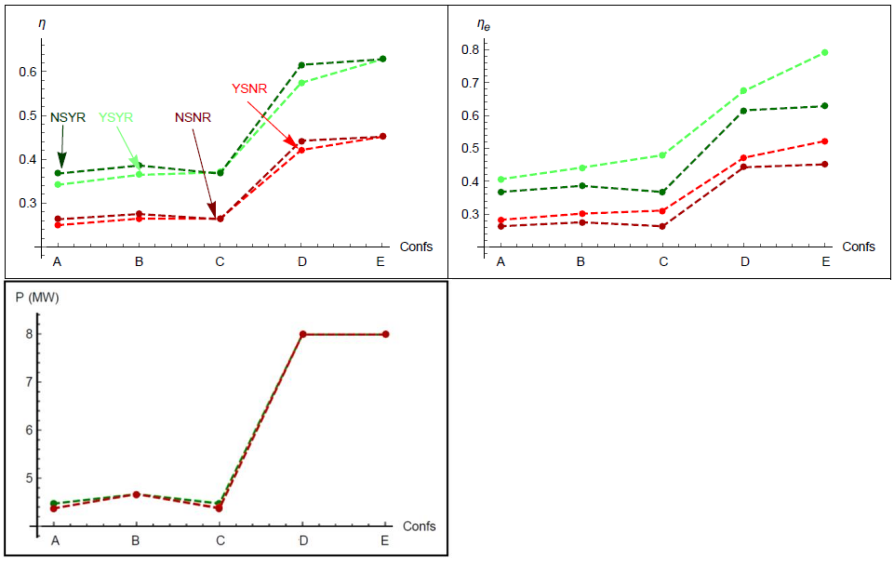

Figure 3. Some output records for the five layouts. Top left: overall thermal efficiency, η; up right: fuel conversion rate, η_e; bottom left: power output, P. The lines between dots are just a guide for the eyes. Legend: YSYR= With solar input and with recuperation, NSYR=Without solar input and with recuperation, YSNR=With solar input and without recuperation, NSNR=Without solar input and without recuperation.

In Figs. 4 and 5 two Sankey diagrams representing the main plant losses can be seen for the real conditions configuration as well as for the layout when the completely system is assumed as ideal. Looking at the solar part, $\dot{Q}_l$ and $\dot{Q}_{iHS}$ are the losses associated to the heat transfers on the solar receiver and $\dot{Q}_{HS}$ denotes the heat rate input from the solar collector. And regarding at combustion part, $\dot{Q}_C$ is related to the heat losses in combustion subsystem, $\dot{Q}_{iHC}$ refers to the heat losses at its heat exchanger and $\dot{Q}_{HC}$ is the heat rate input from combustion chamber.

These energy fluxes are normalised to unity and so, in the first case, the solar input is 26 % of the total and the combustion input constitutes the rest, 74 %. It is quite visible that the first diagram presents small energy losses both in combustion and solar subsystems; while the other does not have any heat loss.

Moreover, it must be stressed that, at real conditions, the wasted heat flux, which is released to the ambient, is higher than the one of power output; however, in the completely ideal system configuration, the power output flux is quite higher than the wasted heat, due to the high increment of heat engine efficiency. Despite Brayton cycle subsystem can achieve the highest improvements for the performance of the hybrid plant, technical feasibility and room for improvement have to be considered, since it may be easier to improve solar subsystem performance, due to the fact that thermosolar technology is considerably less mature than gas-turbine equipment.

On the other hand, the solar flux is always smaller than the combustion one, since the solar share does not exceed 30 % in any case. This fact means that the solar collector field is very small for the desired power output, and so the turbine inlet temperature required for obtaining this power is not reached only with solar subsystem. Therefore it is always necessary to burn quite fuel. This is a plant sizing problem, which is solved by reducing the power output supplied to the grid or by increasing the heliostat field size.

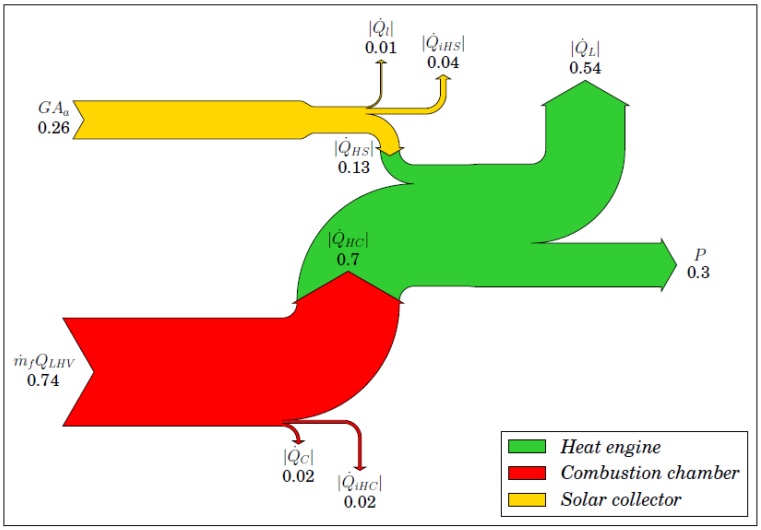

Figure 4. Sankey diagram for the real conditions configuration (A), for the hybrid recuperative case. Energy fluxes are normalised to unity.

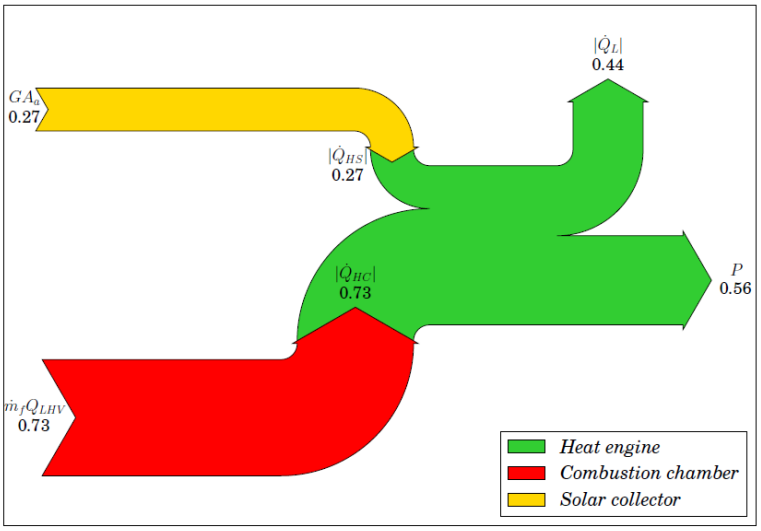

Figure 5. Sankey diagram for the completely ideal system (E), for the hybrid recuperative case. Energy fluxes are normalised to unity.

Finally, the specific natural gas consumption and the pollutant emissions can be analyzed. They are directly estimated through the natural gas emission factors. However, the calculated predictions on emissions should only be taken as a guide, because each plant could have particular technologies to reduce emissions or CO_2 capture mechanisms.

In Table 5 both specific fuel consumption and emissions are collected for the operating point case (A). In the case of recuperation and solar input, the fuel consumption is about 187 kg/MWh, value that rises until 284 kg/MWh when no recuperation and no solar input are taken. Comparing pure combustion and hybrid modes, fuel savings of 8.3 % and 6.2 % can be achieved for recuperative and non-recuperative cases, respectively. These percentages can seem relatively small, but this consumption saving can supposed important advantages for companies in annual terms.

Table 5. Annual means of fuel specific consumption and of specific emissions: (A) real conditions.

Operating point (A)	Without recuperation		With recuperation	
	Without solar input	With solar input	Without solar input	With solar input
$m_f\ (kg/MWh)$	283.995	266.463	203.485	186.569
$CO_2\ (kg/MWh)$	702.758	659.374	503.534	461.674
$CH_4\ (g/MWh)$	13.296	12.475	9.527	8.735
$N_2O\ (g/MWh)$	1.291	1.211	0.925	0.848
Relative differences	-6.173%		-8.313%	

Also, it is important to note that, comparing recuperative and non-recuperative modes, a 30 % of fuel reduction can be reached for solar input and a 28 % for no solar input.

In addition, the pollutant gases emission associated with the natural gas burning are estimated, namely, the methane, the nitrous oxide, and the carbon dioxide generation. Specific emissions of carbon dioxide at normal performance (operating point, recuperation, and solar input) are $CO_2 = 461.674\ kg/MWh$, whereas those of CH_4 and N_2O are $CH_4 = 8.735\ g/MWh$ and $N_2O = 0.848\ g/MWh$, respectively.

Table 6. Annual means of fuel specific consumption and of specific emissions in the five configurations, for the hybrid recuperative case. The increments are relative differences of the particular configuration with respect to configuration (A).

With recuperation and solar input	Operating point (A)	Ideal heat exchangers (B)	Ideal solar part (C)	Ideal Brayton cycle (D)	Completely ideal system (E)
$m_f\ (kg/MWh)$	186.569	173.516	169.781	112.204	101.019
$CO_2\ (kg/MWh)$	461.674	429.374	420.13	277.654	249.977
$CH_4\ (g/MWh)$	8.735	8.124	7.949	5.253	4.730
$N_2O\ (g/MWh)$	0.848	0.789	0.772	0.510	0.459
Relative differences	–	-6.996%	-8.998%	-39.859%	-45.854

The same variables but for the five before mentioned configurations are displayed in Table 6, where also relative differences are shown with respect to operating point. Also here it is observed that the leap occurs when approaching the ideal Brayton power unit, with almost a 40 % of decrease in fuel consumption and pollutant emissions. Ideal heat exchangers and ideal solar part models give a smaller reduction on consumption: approximately 7 % and 9 %, respectively. Of

course, the completely ideal system configuration presents the higher decrease, around 46 %. Those percentages correspond with theoretical limits for greenhouse emissions reduction. Therefore, the room for improvement is wide. If the complete system was ideal, specific carbon dioxide emission would be $CO_2 = 249.977\ kg/MWh$, which is a very promising result.

In doing the same as before, comparing the carbon dioxide production for the five configurations, Fig. 6 can be obtained, where it is clearly visible that considering the Brayton cycle or the complete system as ideal have a great effect on emissions reduction, reaching the same values of before, 40 % and 46 %, respectively.

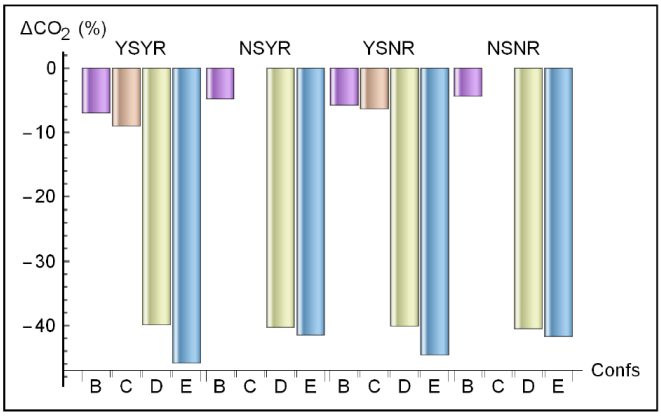

Figure 6. Relative differences of specific emissions of CO_2 between configurations (B)-(E) and configuration (A) quantified as relative increments in percentages with respect to the real conditions configuration (A). Hybrid and combustion modes and recuperative and non-recuperative configurations are considered. Legend: YSYR= With solar input and with recuperation, NSYR=Without solar input and with recuperation, YSNR=With solar input and without recuperation, NSNR=Without solar input and without recuperation.

4. 3. Sensitivity analysis

A sensitivity analysis is performed in order to study the influence of the main subsystems irreversibilities on the overall plant performance records. Heat engine losses parameters will be varied, starting from design point conditions. But also the influence of solar subsystem losses parameters and that of pressure losses in the heat absorption process, $\Delta p_H/p_H$, can be analysed [4].

Changes on the losses parameters associated to the heat engine will greatly affect plant performance, as it is surveyed in Fig. 7. The evolution of all variables is also almost linear, however the scales of the vertical axes indicate much more important variations on the performance records. For example, an increment of 10 % on compressor isentropic efficiency, ε_c, will lead to 10 % rise on power output and the same increment on turbine isentropic efficiency, ε_t, to more than 20 % on P. Great improvements are achieved when both the compressor and turbine efficiency are incremented simultaneously, almost 40 % on power output can be reached if $\varepsilon_c + \varepsilon_t$ rises up to 10 %.

As recuperation is an internal process of the heat engine, recuperator effectiveness changes would not have any influence on power output, nevertheless other output records would be affected. The other analyzed output records (overall efficiency, η, Brayton subsystem efficiency, η_H, and fuel conversion rate would, η_e) change in the interval $[-30\ \%, +30\ \%]$ for variations in the losses coefficients of the power unit in the interval $[-10\ \%, +10\ \%]$. In short, reductions on Brayton losses would be increased by a factor 3 on the plant records.

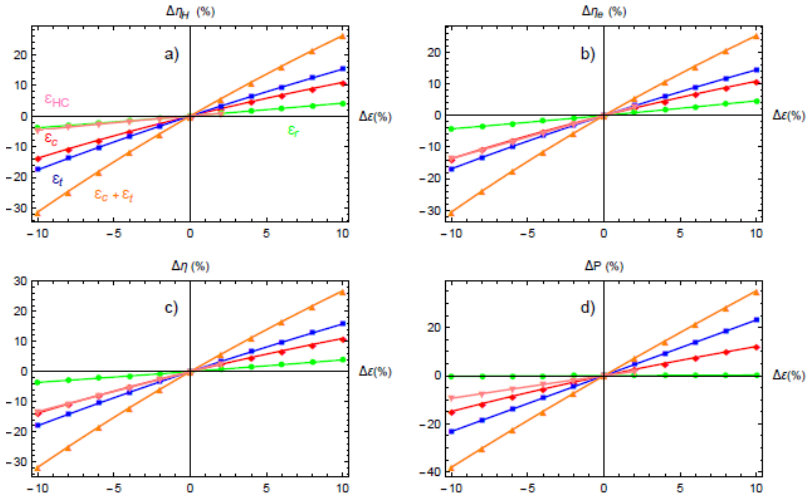

Figure 7. Sensitivity of different output records, power output (P), overall thermal efficiency (η), Brayton cycle efficiency (η_H), and fuel conversion efficiency (η_e), to several irreversibility parameters of the heat engine: isentropic efficiency of the turbine (ε_t), isentropic efficiency of the compressor (ε_c), recuperator effectiveness (ε_r), and effectiveness of the heat exchanger associated to the combustion chamber (ε_{HC}). Another case is also considered: when ε_c and ε_t are simultaneously changed in the same way. Both axis are represented in relative terms as percentages. The central point is related to the yearly averages of the recuperative plant at real operating conditions.

5. Future work

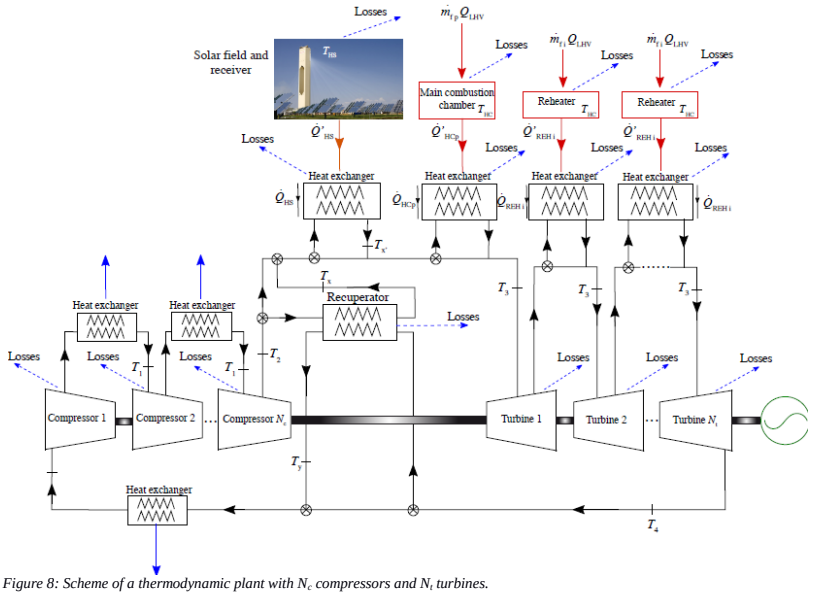

Figure 8: Scheme of a thermodynamic plant with N_c compressors and N_t turbines.

Currently this project continues with other lines of research, among them: multistage plants, different working fluids, parabolic dishes, and combined cycles.

The inclusion of several turbines and compressors in the thermodynamic plant's scheme (Fig. 8) results in an increase of the overall efficiency and of the net power, although the economic investment also rises.

Changing the working fluid from dry air to other less usual gases as nitrogen, helium or carbon dioxide can be beneficial from the viewpoint of the reduction of temperatures (CO_2) or the pressure losses (He), but it can also lead to some disadvantages like the lower experience (see Table 7) [10].

Table 7. Comparative table of some working fluids.

Working fluid	Advantages	Disadvantages
Dry air	Experience, abundant, free	High pressure losses, high temp.
N_2	Similar to air	High pressure losses, high temp.
He	Low pressure losses, inert, non-toxic	More stages, high temp., few experience, leaks
CO_2	Moderate temp., good critical point, inert, non-toxic	Fast variations of critical point, scarce experience

Another possibility for future work is to change the tower Central Receiver System by parabolic dishes, which allow an electric generation in a smaller scale, with only a few kW, thanks to the microturbines set up in their receivers. Therefore, parabolic dishes can be employed for distributed generation in isolated places without access to the electric gird or also, when lot of them are placed in fields, for releasing energy to the grid.

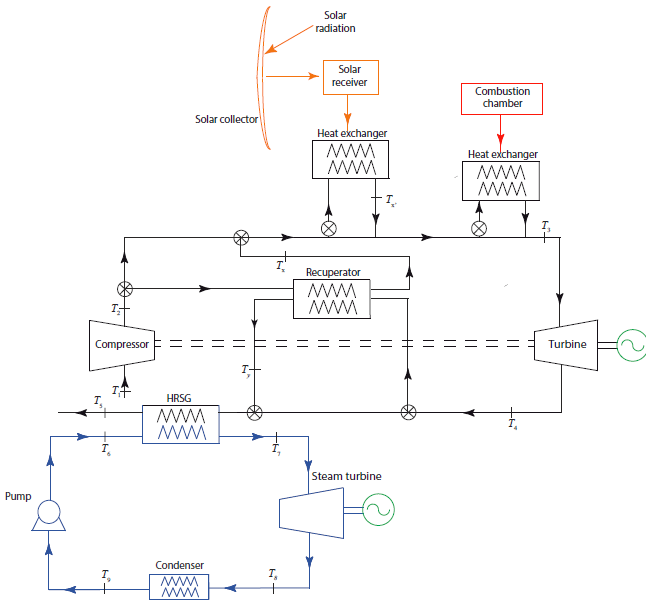

Figure 9: Scheme of a combined thermodynamic plant (Brayton cycle + Rankine bottoming cycle).

On the other hand, setting up a Rankine cycle bottoming the Brayton one (combined cycle) can lead to the use of the excess of heat after the turbine (Fig. 9) and can improve the overall efficiency and increase the power output.

6. Conclusions

Finally, the most important conclusions obtained from this study are summed up here:

- A thermodynamic model for a hybrid system composed of a solar central receiver heliostat field and a Brayton gas turbine was developed.
- Additionally, the system is described in terms of a reduced number of parameters, with clear physical meaning each.
- Furthermore, the model was validated by the consideration of the SOLUGAS Project, developed by the company Abengoa Solar, near Seville.
- Likewise, the model incorporates the main losses and irreversibility sources: non-ideality turbine and compressor, pressure decays, real heat exchangers, heat transfer losses in the solar collector, combustion inefficiencies, etc.
- It was shown that since the model is flexible, it allows to check the performance of several plant configurations.
- As summary, it can be said that the most important improvements are related to the Brayton cycle, since higher increments can be observed in all the variables.
- Also, it is interesting to stress that high increments on solar collector efficiency do not raise significantly overall thermal efficiency. Nevertheless, they can increase fuel conversion rate.
- As mentioned before, numerically, the most influential factor corresponds to improvements on Brayton cycle. On the other side, the technical possibilities have to be taken into account. This issue is outside the range of this study. However, we are aware that it has to be accounted, since Brayton cycle improvements may not be feasible nowadays, although they are the most effective ones, and perhaps the solar efficiency improvements are easier achievable.
- In conclusion, this kind of plants are especially interesting for regions with good insolation ratios and scarce hydric resources, because allow an appreciable reduction of fossil fuel consumption. There is still room for improvement in the economic issues, so further research and development are needed; but these facilities are worth the effort from the ecological point of view, since they reduce significantly pollutant emissions related to greenhouse effect, so they can help to mitigate the anthropogenic intensification of climate change.

Acknowledgments

The authors acknowledge financial support from MINECO of Spain, Grant ENE2013-40644-R and University of Salamanca.

References

[1] O. Behar, A. Khellaf, K. Mohammedi, *Rene. Sust. Energ.* **23** (2013) 12-39.
[2] D. Olivenza-León, A. Medina, A. Calvo Hernández, *Energ. Conv. Manage.* **93** (2015) 435-447.
[3] M.J. Santos, R.P. Merchán, A. Medina, A. Calvo Hernández, *Energ. Convers. Manage.* **115** (2016) 89-102.
[4] R.P. Merchán, M.J. Santos, I. Reyes-Ramírez, A. Medina, A. Calvo Hernández, *Energ. Convers. Manage.* **134** (2017) 314-326.
[5] R.P. Merchán, M.J. Santos, A. Medina, A. Calvo Hernández, *Renew. Energ.* xxx (2017) 1-11. https://doi.org/10.1016/j.renene.2017.05.081

[6] R. Korzynietz, J.A. Brioso, A. del Río, M. Quero, M. Gallas, R. Uhlig, M. Ebert, R. Buck, D. Teraji, *Sol. Energy* **135** (2016) 578-589.
[7] Meteosevilla. http://www.meteosevilla.com.
[8] E. W. Lemmon, M. L. Huber, M. O. McLinden. NIST Standard Reference Database 23: Reference fluid thermodynamic and transport properties-REFPROP, version 9.1. National Institute of Standards and Technology, Standard Reference Data Program, Gaithersburg (2013).
[9] L. Wu, G. Lin, J. Chen, *Renew. Energ.* **35** (2010) 95-100.
[10] O. Olumayegun, M. Wang, G. Kelsall, *Fuel* **180** (2016) 694-717.

3.10 Proceeding α – Towards a more efficient generation of central tower hybrid thermosolar gas turbine power plants

Title: "Towards a more efficient generation of central tower hybrid thermosolar gas turbine power plants"
Journal: *AIP Conference Proceedings*
Authors: **Rosa P. Merchán**, Alejandro Medina, María Jesús Santos, Irene Heras, José Miguel M. Roco, and Antonio Calvo Hernández
Year: 2019
Conference: SolarPACES 2018
Number: 2126
Pages: 140004
DOI: `https://doi.org/10.1063/1.5117652`
Reference: [151]

Resumen

En este trabajo se presenta un modelo teórico completo desarrollado para simular plantas de torre de concentración solar que operan con turbinas de gas híbridas. El funcionamiento global de la planta se describe en términos de tres subsistemas principales: el subsistema solar, la cámara de combustión y la máquina térmica, destacando la integración entre ellos. El ciclo Brayton simulado es multi-etapa por lo que considera varias etapas de expansión y compresión. Se toman dimensiones similares a las de la planta *GEMASOLAR* para llevar a cabo la implementación del modelo en el código desarrollado. Asimismo, se comparan los registros de salida del modelo con los del *software Thermoflex*®, de forma que los resultados obtenidos permiten validar el modelo de la turbina. Este trabajo se enfoca en el pre-diseño de este tipo de plantas, efectuando un análisis en condiciones fuera de diseño de variables de la planta como potencia, eficiencia, consumo de combustible y emisiones de gases de efecto invernadero. De este modo, se analiza el comportamiento de configuraciones multi-etapa, así como de cuatro fluidos de trabajo (aire, nitrógeno, dióxido de carbono y helio) y de la presencia del recuperador. Se emplea la relación de presiones de la turbina de gas como parámetro objetivo para analizar las variables de salida. En consecuencia, se presentan curvas de las principales variables con la relación de presiones. Destaca la importancia de considerar la planta como un todo, es decir, de elegir los principales parámetros de la turbina de gas de acuerdo a las características del subsistema solar.

AIP Conference Proceedings

Towards a more efficient generation of central tower hybrid thermosolar gas turbine power plants

Cite as: AIP Conference Proceedings **2126**, 140004 (2019); https://doi.org/10.1063/1.5117652
Published Online: 26 July 2019

Rosa P. Merchán, Alejandro Medina, María Jesús Santos, Irene Heras, José Miguel M. Roco, and Antonio Calvo Hernández

Towards a More Efficient Generation of Central Tower Hybrid Thermosolar Gas Turbine Power Plants

Rosa P. Merchán[1,2,b)], Alejandro Medina[1,2,a)], María Jesús Santos[1,2,c)], Irene Heras[1,2,d)], José Miguel M. Roco[1,2,e)], and Antonio Calvo Hernández[1,2,f)]

[1]*Department of Applied Physics, University of Salamanca, 37008 Salamanca, Spain*
[2]*IUFFYM, University of Salamanca, 37008 Salamanca, Spain*

[a)]Corresponding author: amd385@usal.es
[b)]rpmerchan@usal.es, [c)]smjesus@usal.es, [d)]iheras@usal.es, [e)]roco@usal.es, [f)]anca@usal.es

Abstract. In this communication we present a novel model for the pre-design of hybrid thermosolar Brayton plants. The plant is described as a whole allowing to predict overall performance. It is considered as composed by three subsystems: solar field and receiver, combustion chamber, and power block. Overall efficiency is obtained as a combination of subsystems efficiencies. Solar field efficiency is computed in detail for any location and any meteorological condition. Most important losses are considered, including shadowing, blocking, spillage, atmospheric attenuation, and so on. A simplified model is taken for the thermal losses in the receiver, including radiation losses. For the power block a detailed thermodynamic model based on an irreversible Brayton cycle is assumed. Multi-stage compression and expansion and regeneration are included in the model. All these ingredients allow for obtaining precise estimations of plant performance at off-design conditions as diary power and efficiency curves, consumption, emissions, and fuel conversion efficiency, in terms of a relatively reduced number of parameters with clear physical meaning, avoiding complex and over-detailed computations. Annual averages are also susceptible to be computed. And so, sensitivity analysis and optimization suggestions can be performed in the framework of the model. Model predictions for several subcritical working fluids (including air, nitrogen, carbon dioxide, and helium) and different plant configurations, are analyzed. The importance of considering the plant as a whole, *i.e.*, to choose the main parameters of the gas turbine (operation temperature, pressure ratio, number of stages, etc.) in concordance to the details of the solar subsystem (concentration ratio, operation temperature of the receiver, etc.) is highlighted.

INTRODUCTION

Hybrid thermosolar plants constitute a promising technology in the transition to diversified, clean, and efficient energy production strategies [1]. In this contribution a central tower concentrating solar power (CSP) plant is hybridized in series with a combustion chamber burning natural gas. This system allows an almost stable electric energy production in the scale of a few megawatts. Although not completely free of pollutant emissions, these plants allow for a predictable energy production (which is always attractive from the viewpoint of economic balances) with reduced emissions and remarkable performance records. In the particular case that the power unit is a Brayton gas turbine other advantages are added: very reduced water consumption (that is a definite point in arid regions with good insolation but poor hydric resources), reliability, scalability, and wide operation experience [2].

During the last times several projects have been conducted in order to check the feasibility of the hybrid thermosolar Brayton technology and the economic issues associated to the price of the produced electricity. Some prototype plants have been built and analyzed, several of them in Spain (as the recent project SOLUGAS [3]). In summary, all these developments have arrived to similar conclusions: the technology is feasible, but there are some open lines to work along in order to achieve competitive prices. Among others two lines are of greater importance. First, the development of solar receivers capable to work under very high temperatures (above 1000 K) in an

SolarPACES 2018
AIP Conf. Proc. 2126, 140004-1–140004-7; https://doi.org/10.1063/1.5117652
Published by AIP Publishing. 978-0-7354-1866-0/$30.00

efficient and unfailing way. And second, to improve the efficiency of the thermodynamic cycle the power unit follows, which greatly determines overall plant performance and so, the levelized cost of the produced electricity.

This work is focused on the last point. A mathematical simulation model that our research group developed during the last years will be aimed to search appropriate working fluids and thermodynamic configurations for the Brayton cycle the plant develops [4]. The model includes a detailed calculation of the optical efficiency of the heliostat field, estimations of the heat losses in the receiver, and a flexible thermodynamic model for the heat engine that considers all the main loss sources in this kind of plants. The plant is considered as a whole, so any subsystem (heliostat field, receiver, heat exchangers, power unit, etc.) influences the overall plant behavior. Another advantage of the framework is that dynamic calculations (for instance, curves in hourly terms) can be estimated, although in this contribution only results for design point conditions will be shown.

MATHEMATICAL MODEL AND NUMERICAL IMPLEMENTING

In this section the main assumptions of the mathematical model developed to simulate the overall plant are briefly described. The whole system is considered as an assembly of three main subsystems: the solar one (heliostat field and solar receiver), the main combustion chamber, and the power unit. The latter is considered as a multi-stage gas turbine with an arbitrary number of compressors, N_c, and an arbitrary number of turbines, N_t. The links between subsystems are the required heat exchangers. In ref. [4] detailed explanations about the mathematical formalism can be found. The overall thermal efficiency, η, can be expressed as the product of the thermal efficiencies of the subsystems and a factor coming from the heat exchangers. Explicit equations can be found in [4].

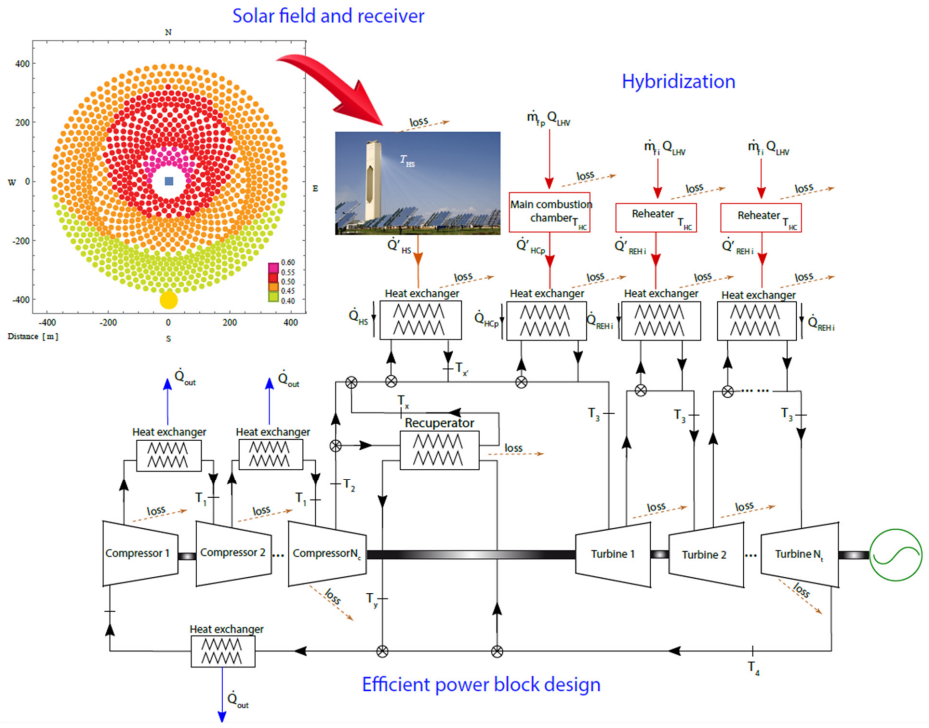

FIGURE 1. Component diagram of the whole plant including solar subsystem with solar field efficiency map, hybridization scheme and multi-step compression and expansion.

At difference with [4], where an average optical efficiency, η_0, was assumed, in this work detailed calculations in order to obtain η_0 for a particular geometry and size of the heliostat field have been developed. Heliostats have been placed in the solar field in different rows and considering all the space they can occupy during the solar tracking together with a safety distance. The optical efficiency of each heliostat is defined as a product of several losses factors. The main factor of this optical efficiency is the cosine effect ($\cos\omega$), which accounts for the cosine of the Sun radiation's incident angle in the heliostat surface and it is calculated by means of a study of the geometry of the Sun-heliostat-receiver system [5]. Blocking effect (f_b) represents the energy lost due to the reflection of some part of the radiation coming from a back heliostat in an ahead one. On the other hand, the shadowing effect (f_{sh}) corresponds to the energy loss because of the shadow projected by a heliostat on another one. Both shadowing and blocking factors are also considered in the model, in this case as constant factors [5]. It is important to note that heliostats present an actual mirror reflectivity (ρ) that determines the amount of solar radiation that they can reflect towards the receiver [6]. When this solar radiation goes from the heliostat to the receiver, some part of it is absorbed by the molecules of the ambient air, so the attenuation (f_{att}) also results in an energy loss. And, finally, another important energy loss source is the spillage (f_{sp}) of the incoming radiation in the absorption area of the receiver [6]. Then, the global heliostat optical efficiency (η_0) is calculated as the average over all heliostats.

TABLE 1. Comparison between Thermoflex® data corresponding to Solar Titan 250-30000S gas turbine [7] and records from our model simulated in Mathematica®. (I) stands for input data and (O) for output records.

Variable	Thermoflex® data	Mathematica® simulation (our model)	Relative deviation (%)
Working fluid mass flow (kg/s)(I)	67	67	0
Overall pressure ratio (I)	23.4	23.4	0
Power output (MW) (O)	21.10	20.91	-0.89
Heat Rate (kJ/kWh) (O)	9256	9041	-2.33
Thermal efficiency (O)	0.389	0.398	2.37
Turbine inlet temperature (K) (O)	1450	1451	0.04
Turbine outlet temperature (K) (O)	736	758	2.95

The power unit, as mentioned before, is taken as a multi-stage gas turbine running a closed irreversible Brayton cycle (see Fig. 1). Irreversibility sources include: non-ideal compression and expansion processes, pressure decays in heat absorption and heat release processes, non-ideal heat exchangers, and losses in combustion processes. A detailed *T-S* diagram of the cycle considered can be found in [4] as well as the main hypothesis and mathematical developments. Four subcritical working fluids are considered to be analyzed: dry air, nitrogen, helium, and carbon dioxide. For all of them temperature dependent correlations for specific heats are considered (see [4] for details). As fuel, natural gas is assumed, although it is feasible to make predictions for other fuels, such as biogas.

TABLE 2. Values of the solar field parameters employed in the simulation [6,8].

Parameter	Value
Rows number	19
Visibility	23 km
Pointing	Simple
Height of the tower supporting the receiver	150 m
Height of the receiver	10.5 m
Diameter of the receiver	8.4 m
Height of each heliostat	10.95 m
Width-height ratio of each heliostat	1
Separation distance between adjacent heliostats	3.285 m
Minimum radius of the heliostat field	65 m
Standard deviation due to sun shape	2.51 mrad
Blocking factor	0.95
Shadowing factor	1
Actual mirror reflectivity	0.836

This thermodynamic model was validated by our group for the numerical parameters of SOLUGAS project [3,4]. However, the present model is validated by comparison with another real similar plant built by Torresol Energy in Fuentes de Andalucía (Sevilla): GEMASOLAR [8]. Output records are validated for the mono-stage case and taking dry air as working fluid. The main difference between this plant and our assumptions is the thermodynamic cycle itself: the steam turbine in GEMASOLAR is replaced by a gas one. And also a combustion chamber has been added for the hybridization with natural gas instead of employing the molten salt storage of GEMASOLAR. A second validation process has been carried out by using a commercial software (Thermoflex [9]). Table 1 contains a summary of results for the validation of the power unit. The adequate number of heliostats rows in the design point and, so, number of heliostats have been chosen by comparing with Thermoflex simulation's outputs (19 rows, 1037 heliostats). Meteorological data are chosen from Meteosevilla [10] for the design point (12:00h of 20 June 2013). Receiver and heliostats geometry and also numerical values of solar field plant parameters are taken from GEMASOLAR plant [8] and from Collado [6] (see Table 2).

ANALYSIS AND RESULTS

In this section the numerical results obtained within the model outlined before are presented. Three main points of interest are surveyed in relationship with the overall plant records: the type of working fluid performing the thermodynamic cycle, the number of compression/expansion stages in the gas turbine, and its overall pressure ratio. Figure 2 displays the overall plant thermal efficiency, η, in terms of the pressure ratio, r_p, for all the fluids considered. Single stage configurations are denoted with N=1 (in this case results for recuperative and non-recuperative plants are plotted), two-stage configurations with N=2, and so on. The limit case of an arbitrary large number of steps is also shown. This particular configuration is plotted as a way to show the eventual (unachievable) upper limit for the plant overall efficiency. For some particular values of r_p, the maximum temperature in the turbine could be exceeded (in the figure this is shown with dashed lines). From the figure, it is observed that globally He leads to considerable larger overall efficiencies when comparing different fluids. For instance, with N=2 overall efficiencies about 0.45 could be obtained for pressure ratios around 10. On the other side, CO_2, would give the lowest ones, even for high pressure ratios. For air and nitrogen and N=1, the non-recuperative configuration leads to better overall efficiencies over r_p=25. In all fluids, curves for N=1 displays a maximum in terms of r_p, while for multi-stage configurations curves increase monotonically with r_p (except for He).

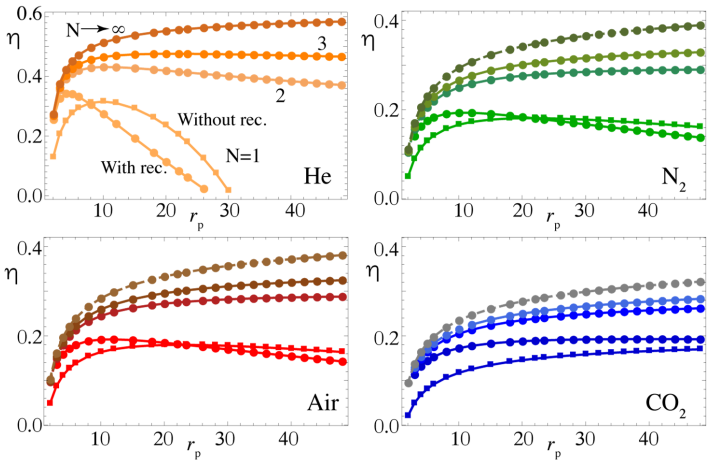

FIGURE 2. Overall thermal efficiency, η, of the hybrid thermosolar plant as a function of the overall pressure ratio, r_p. All the fluids considered are shown. Curves marked with circles correspond to recuperative plant configurations and those marked with squares to non-recuperative ones. Dashed lines between dots indicate that eventually too high temperatures in the turbine could be reached.

The fuel conversion rate, r_e, is plotted in Fig. 3. This variable is defined as the ratio between the power output and the heat input associated to fuel combustion, *i.e.*, has an economic significance in relation with the operation cost of the plant. For N_2, air, and CO_2, this parameter increases with the pressure ratio only for N=1 and a non-recuperative plant. In all other cases, curves monotonically decrease with r_p. This decrease is very rapid for low values of the pressure ratio, and then it remains almost unchanged. Largest values are found for CO_2. The case of He is different. The slope of the curves of r_e depends on the interval of pressure ratios, the number of stages and the existence or not of internal recuperation. For air and nitrogen the following conclusion could be achieved: for small pressure ratios (below approximately 25), the most interesting configuration from the viewpoint of r_e (or fuel consumption) would be a single stage recuperative one. For larger pressure ratios, improved r_e is obtained for a single stage non-recuperative layout.

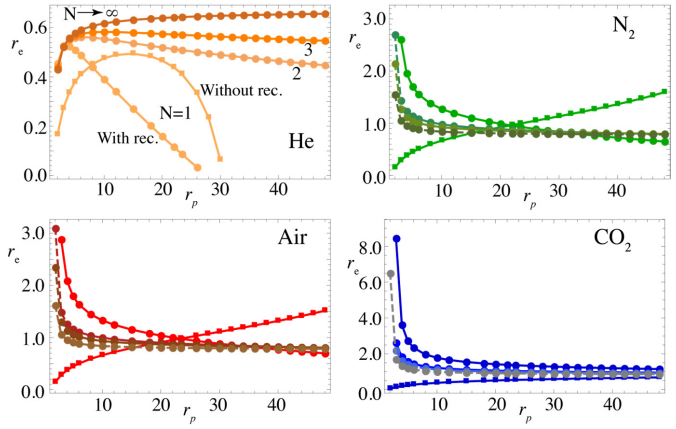

FIGURE 3. Fuel conversion efficiency, r_e, of the plant. Details as in Fig. 2.

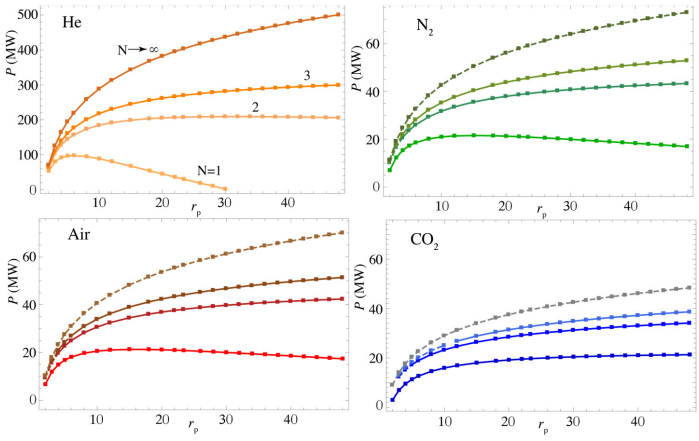

FIGURE 4. Power output, P, of the plant. Details as in Fig. 2.

The power output, P, is displayed in Fig. 4. It is much higher for He than for the other fluids, whichever value of the pressure ratio is considered. This is a consequence of the fact that the same working fluid mass flow is considered in all cases. Within this constraint, the power output is proportional to the constant pressure specific heat of the fluid, c_p. In the case of He, the average value of c_p in the temperature interval of interest is about 4.5 times higher than for the other fluids, and this is reflected in the numerical values of power output. With respect to the evolution with r_p, in all cases multi-stage configurations show an increasing power output with increasing r_p, towards an asymptotic limit at high pressure ratios. Higher power outputs are obtained with increasing number of compression/expansion stages. Compared to N_2 or air, CO_2 leads to smaller power output, provided that its average specific heat is similar to that of those fluids.

The solar share, f, *i.e.*, the fraction of heat input flow coming from solar resources is plotted in Fig. 5. It decreases with r_p for all fluids except for single stage configurations without recuperation. This means that with increasing pressure ratio more fuel consumption is required to reach the imposed turbines inlet temperature. Globally, the highest values are found for CO_2. In consequence, as commented before, the fuel conversion efficiency for this fluid is larger.

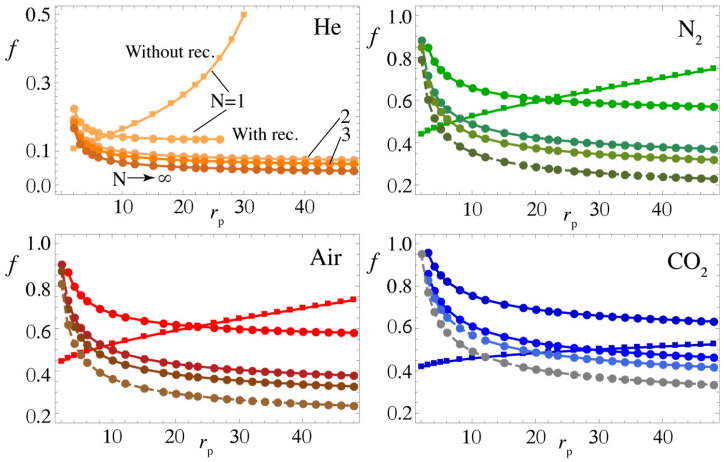

FIGURE 5. Solar share, f, of the plant. Details as in Fig. 2. In the case of He, curves are plotted in the interval or r_p leading to positive overall efficiency, η.

SUMMARY AND CONCLUSIONS

In this communication it was intended to summarize a framework developed in order to analyze the main parameters of the pre-design of future thermosolar central tower solar plants operating under hybrid gas turbine thermodynamic cycles. One of the aims of the framework is to consider the plant as a whole, avoiding an excessive number of parameters by identifying the most important ones in each subsystem. Special attention is devoted to the coupling between subsystems. These subsystems are the solar field and the receiver, the combustion chamber, and the thermodynamic power unit. The solar subsystem is considered in detail. The main optical losses for each heliostat are modelled in terms of the field size and geometry, its location, the heat losses in the receiver, and the particular solar and ambient conditions. Optical efficiency can be predicted at off-design conditions as a time dependent parameter. On the other side, a complete thermodynamic model for the power unit is also developed. The main irreversibility sources in closed gas turbine cycles are accounted for. The model is capable to predict the behavior of different subcritical working fluids and basic ingredients required to the pre-design of the power unit are also taken into account: recuperation possibilities and mono- or multi-stage configurations. With all these elements it is possible to simulate plant output records at on-design conditions and also at off-design ones. These output

records depend on a reasonable number of parameters, thus allowing to identify the main bottlenecks in plant performance, to check the possibilities of different configurations, to develop sensitivity analysis, and to perform optimization studies.

Numerical predictions of the model were validated by comparison with an existing plant located at the south of Spain (GEMASOLAR, Torresol Energy) at particular solar and ambient conditions. Four working fluids for the gas turbine were surveyed (dry air, nitrogen, carbon dioxide, and helium). As target variable to analyze the output records it was used the overall pressure ratio of the gas turbine. Non-recuperative and recuperative configurations were analyzed, as well as multi-stage configurations with the same number of compression and expansion stages. Variables as the overall thermal efficiency, the fuel conversion efficiency, the power output, and the solar share were calculated in terms of the plant pressure ratio. In order to achieve the desired objectives a particular pressure ratio interval should be chosen, as well as, the incorporation or not of a recuperator and the number of compression/expansion stages. So, this kind of models can be a helpful tool to determine the most significant plant variables at a pre-design stage.

ACKNOWLEDGMENTS

Financial support from University of Salamanca, Banco Santander, and Junta de Castilla y León of Spain under grant no. SA017P17 are acknowledged.

REFERENCES

1. G.J. Nathan, M. Jafarian, B.B. Dally, W.L. Saw, P.J. Ashman, E. Hu, and A. Steinfeld, Prog. Ener. Comb. Sci. **64**, 4-28 (2018).
2. O. Olumayegun, M. Wang, G. Kelsall, Fuel **180**, 694-717 (2016).
3. R. Korzynietz, J.A. Brioso, A. del Río, M. Quero, M. Gallas, R. Uhlig, M. Ebert, R. Buck, and D. Teraji, Sol. Ener. **135**, 578-589 (2016).
4. M.J. Santos, C. Miguel-Barbero, R.P. Merchán, A. Medina, and A. Calvo Hernández, Ener. Conv. Manage. **165**, 578-592 (2018).
5. F. J. Collado, Renew. Ener. **34**, 1359-1363 (2009).
6. F. J. Collado and J. Guallar, Renew. Sust. Ener. Rev. **20**, 142-154 (2013).
7. Solar® Turbines: https://www.solarturbines.com/en_US/products/gas-compressor-packages/titan-250.html.
8. J. I. Burgaleta, S. Arias, and D. Ramírez, "Gemasolar, the first tower thermosolar commercial plant with molten salt storage", in SolarPACES 2011 Conference, 11-14 (Granada, Spain, 2011).
9. Thermoflex software: https://www.thermoflow.com/
10. Meteosevilla: http://www.meteosevilla.com

Chapter 4. Other research articles

In this Chapter, other two research articles, to which the author of this doctoral thesis has contributed, are appended. None of them are directly related to this doctoral thesis. First one is devoted to the implementation of a similar, but simpler theoretical model to other type of Concentrated Solar Power plants: parabolic dish. Second article analyses the integration of Thermal Energy Storage in hybrid combined cycles by means of a different methodology for the main computation: employing commercial software tools. Besides those, all conference articles in which doctoral thesis work has been presented and others are mentioned.

4.1 Parabolic Dish

Title: "Thermodynamic and Cost Analysis of a Solar Dish Power Plant in Spain Hybridized with a Micro-Gas Turbine"
Journal: *Energies*
Authors: J. García-Ferrero, I. Heras, M.J. Santos, **R.P. Merchán**, A. Medina, A. González, A. Calvo Hernández
Year: 2020
Reference: [146]

MDPI

Article

Thermodynamic and Cost Analysis of a Solar Dish Power Plant in Spain Hybridized with a Micro-Gas Turbine

Judit García-Ferrero [1], Irene Heras [1,†], María Jesús Santos [1], Rosa Pilar Merchán [1], Alejandro Medina [1], Antonio González [1] and Antonio Calvo Hernández [1,*]

[1] Department of Applied Physics and IUFFyM, University of Salamanca, Salamanca, Spain
* Correspondence: anca@usal.es.
† Current address: Centro Avanzado de Tecnologías Aeroespaciales (Catec), Seville, Spain

Version September 29, 2020 submitted to Energies

Abstract: Small-scale hybrid parabolic dish Concentrated Solar Power systems are a promising option to obtain distributed electricity. During the day, solar energy is used to produce electricity and the absence of sunlight can be overwhelmed with fuel combustion. This study presents a thermo-economic survey for a hybridized power plant in different regions of Spain, considering the local climatic conditions. The developed model considers the instant solar irradiance and ambient temperature dynamically, providing an estimation of the power output, the associated fuel consumption, and the most relevant pollutant emissions linked to combustion. Hybrid and combustion only operating modes at selected geographical locations in Spain (with different latitudes, mean solar irradiances, and meteorological conditions) are analyzed. The levelized cost of electricity indicator is estimated as a function of investment, interest rate, maintenance, and fuel consumption actual costs in Spain. Values about 124 €/MWhe are feasible. Fuel consumption and emissions in hybrid operation can be reduced above 30% with respect to those of the same turbine working in a pure combustion model. This model shows the potential of hybrid solar dishes to become cost-competitive against non-renewable technologies from the point of view of costs and reduction in gas emission levels in regions with high solar radiation and low water resources.

Keywords: Concentrated Solar Power; Parabolic Dish; Distributed Energy Production; Brayton Cycles; Thermo-economic Analysis

PACS: 05.70.Ln; 07.20.Pe; 84.60.-h

1. Introduction

Nowadays, in which respect to the production and consumption of electrical energy, it is recognized the unavoidable future change from the traditional supply-demand model to a new scheme based on the smart grids or microgrid concept. Traditional scheme is defined on a centralized remote power generation and long transmission lines. Producer and consumer are well differentiated. On the contrary, new tendencies are characterized by distributed generation close to the consumption location, bidirectional power flows, and the integration of traditional and renewable energy sources [1,2].

Thermosolar power generation has been established as a viable and promising source of renewable energy [3]. In the last few years it has emerged as a potential solution to supply dispatchable electricity, since it can rely on hybridization or thermal energy storage [4]. The hybridization of a solar thermal power system with combustion provides a continuous supply of electricity throughout the year, with a much lower investment and maintenance costs than thermal storage [5].

Besides the full dispatchability, hybrid thermosolar plants using a Brayton thermodynamic power cycle present a wide number of advantages over other Concentrated Solar Power (CSP) systems, including the scalability and adaptability to the requirements of the location, higher global efficiencies, and low to zero water consumption. High exhaust temperature also enables the possibility of including additional services such as thermal energy supply, cooling or water purification [6]. The first generation of hybrid solar gas-turbine power plants was based on existing industrial gas-turbine units [7]. Some EU-funded test plants have demonstrated the Brayton hybrid concept, from small-scale gas-turbines up to 250 kWe [8,9] to scaled up systems such as the full operable prototype SOLUGAS project [10]. This project included a proven combustion chamber and a 4.6 MWe gas turbine. All these hybrid systems were made up of the solar components and a combustion chamber separately.

Conversely, Hybrid Solar Receiver Combustors (HSRC) are a promising technology that integrates into a single device the functions of a solar receiver and a combustor [11,12]. It has been demonstrated how this machinery reduces the overall costs and net fuel consumption relative to equivalent hybrid solar gas systems [13]. The first-of-a-kind successful demonstration of a HSRC was designed by Chinnici *et al.* [11] employing an annular solar cavity receiver with a combustor at laboratory-scale. In parallel, the EU-funded OMSoP project developed a CSP plant based on parabolic dish technology that integrates in a volumetric receiver a combustion chamber, attached to a micro-gas turbine (mGT), obtaining a nominal electrical power output of 5-10 kWe with air outlet temperatures up to 820°C [14]. Specific designs for the solar receiver have been recently proposed and validated [15–17]. These small-scale hybrid CSP plants show a clear tendency to be attractive for off-grid applications in the distributed energy generation [18,19] and nowadays can compete against non-renewable diesel generators or photovoltaic technology. The solar receiver and combustion chamber integration into the HSRC is currently the greatest technological challenge and it has not yet been commercially exploited [14].

The first aim of this study is to present a model for the estimation of the performance (both at on-design and also at off-design conditions) and thermo-economic indicators of a small-scale parabolic dish plant for distributed generation. The plant is based on the hybrid Brayton-like turbine concept. The model intends to be precise, but at the same time simple enough to allow to perform different sensitivity analysis on the influence of the main parameters of any of the subsystems (dish, receiver, gas turbine, combustion chamber, heat exchangers, etc.) on final output records. Thus, it integrates all subsystems in an straightforward way, with a reduced number of parameters. It is intended to avoid an excessive dependence of particular geometric parameters of the receiver, so the role of different receivers designs (that is a very active research field without standard solutions up-to-date [20]) can be analyzed. Comprehensive models for the whole plant, as the one proposed here, can guide the development of these installations in order to get reliability and good efficiencies at moderate costs, giving hints about the role played by each subsystem in final output records.

After an analysis of the optical subsystem and the regime conditions for the thermodynamic model based on previous developments [21,22], off-design simulations are performed for an annual evaluation in different locations. The purpose of this assessment is to analyze the subsystems efficiencies, the global efficiency, the annual energy production, the average solar share or the specific CO_2 emissions from combustion. Next aim in this paper is to estimate the equipments, manufacture, installation and other costs of the system and provide a comprehensive annual appraisal. In order to be able to compare different power plants or operation modes, the minimum electricity sale price or *levelized cost of electricity* (LCoE) is calculated and analyzed.

The presented simulated plant comprises a paraboloid dish collector and a hybrid solar receiver combustor integrated with a small scale (7 to 30 kWe) micro-gas turbine located at the focal point of the dish. The thermodynamic model algorithm is developed under Mathematica® software [23]. As first step, the parameters of the power cycle are optimized to assess the expected power output and performance, by using a reduced number of parameters of the designed power plant. Thereinafter, a dynamic simulation is carried out taking into consideration daily real environmental conditions

(temperature and solar radiation) of certain locations in Spain. Precise estimations of the hybrid plant performance at off-design conditions have been then calculated (*i.e.* net output power, global efficiency, fuel consumption, solar share, etc.) for time-dependent conditions and integrated over a year. The hybrid system working mode has been compared against pure combustion operation in three selected locations (Salamanca, Santander and Seville) of Spain at different latitudes and with quite diverse climatological conditions. This joint thermodynamic and economic assessment could help to identify the optimum design parameters and the operation mode yielding to the minimum specific cost for a selected location.

Section 2 presents the modeling framework and its main assumptions, including the economic considerations. Then, the numerical data required for computations and validation details are summarized in Sec. 3. Next sections are devoted to present the results in daily and seasonal terms (Sec. 4) and yearly ones (Sec. 5). LCoE results are presented in Sec. 6. Finally, the most relevant findings of the work and summarized in Sec. 7.

2. Modelling framework

In this section it is first described the plant configuration and the optical and thermodynamic models employed to simulate the overall plant. The different performance indicators employed for comparing different locations and plant configurations are explained below. A pictorial representation of the plant, including the components of the thermodynamic subsystem, is represented in Fig. 1.

2.1. Overall plant model

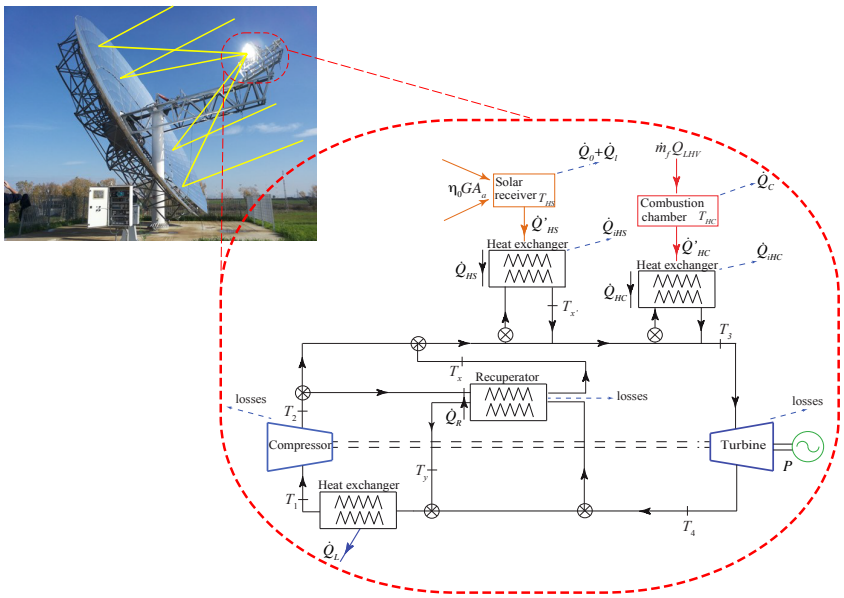

Figure 1. Schematic representation of the hybrid CSP plant composed of the parabolic dish collector and the Hybrid Solar Receiver Combustor (HSRC) which includes the solar receiver, the combustion chamber and the micro-gas turbine.

The designed hybrid CSP plant includes a parabolic dish that collects the sun radiation and heats a working fluid (dry air) flowing in the hybrid receiver situated at the focal point. According to the amount of solar irradiation quantified by the direct normal irradiance, G, and to the ambient temperature T_L, the integrated combustion chamber could release an energy flow in order to increase the fluid temperature up to a pre-fixed turbine inlet temperature, T_3. So, plant power output is approximately constant along the day, it oscillates only as a consequence of T_L variations. The HSRC includes a volumetric solar receiver, a combustion chamber, and a micro-gas turbine (mGT) operating on a recuperative Brayton cycle. Overall plant model includes mathematical submodels for all subsystems.

A thermodynamic representation of the overall system components is depicted in Fig.2. All heat transfers and losses included in the model are schematically represented. Details on all definitions, calculations, and equations can be found in previous works [21,22]. Overall plant thermal efficiency, η, is defined as the ratio between the net power output and the total energy input per unit time:

$$\eta = \frac{P}{GA_a + \dot{m}_f Q_{\mathrm{LHV}}} \tag{1}$$

where A_a is the aperture area, $\dot{m}_f$ the fuel mass flow entering in the combustion chamber at any time and Q_{LHV} the lower heating value of the fuel. Overall efficiency can be expressed as a combination of the efficiencies of the subsystems (η_s, solar collector and receiver; η_c, combustion chamber; and η_h, heat engine efficiencies), the solar share, f (fraction of the total heat input due to sun irradiance), and the effectiveness of the heat exchanges from the receiver and the combustion chamber to the fluid (ε_{HS} and ε_{HC}, respectively):

$$\eta = \eta_s \, \eta_c \, \eta_h \left[\frac{\varepsilon_{HS} \, \varepsilon_{HC}}{\eta_c \, f \varepsilon_{HC} + \eta_s (1-f) \varepsilon_{HS}} \right]. \tag{2}$$

Explicit calculations to obtain this equation can be found in [21,22]. In the case of a purely solar operation $f = 1$ and $\eta = \eta_s \eta_h \varepsilon_{HS}$ and for pure combustion $f = 0$ and $\eta = \eta_c \eta_h \varepsilon_{HC}$.

2.2. Optical model

The solar collector consists of a paraboloid shape dish with aperture diameter D_{col} and focal distance f_{col} that focuses the solar irradiation to a flat receiver. The receiver diameter D_{rcv} is determined as function of the concentration factor C, which is defined as $C = A_a / A_r$. A_a stands for the irradiated aperture area of the collector and A_r for the receiver area. The closed Brayton cycle employed in the plant requires high upper temperature and a pressurized volumetric receiver. Thus, it becomes necessary to furnish the receiver with a transparent window with minimized reflection, radiation, and convection losses [24].

The energy delivered from the receiver to the working fluid depends not only on the optical losses but also on the undesired heat transfer from the receiver to the surroundings. The latter are calculated as in [22,25], including convective, conductive, and radiation losses. Thus, the whole efficiency of the solar subsystem, η_s, is:

$$\eta_s = \eta_0 - \frac{1}{GC} [\alpha \sigma (T_{HS}^4 - T_L^4) + \overline{U}_L (T_{HS} - T_L)], \tag{3}$$

where η_0 stands for the optical efficiency, α refers to the emissivity of the receiver surface, σ is the Stefan-Boltzmann constant, $\overline{U}_L$ is the overall conduction and convection heat transfer coefficient, and T_{HS} is the solar collector temperature (see [21,22] for explicit definitions).

2.3. Power unit model

The gas turbine is considered to develop an irreversible recuperative Brayton-like cycle. The associated T-S diagram and main losses locations are depicted in Fig. 2. The thermodynamic model

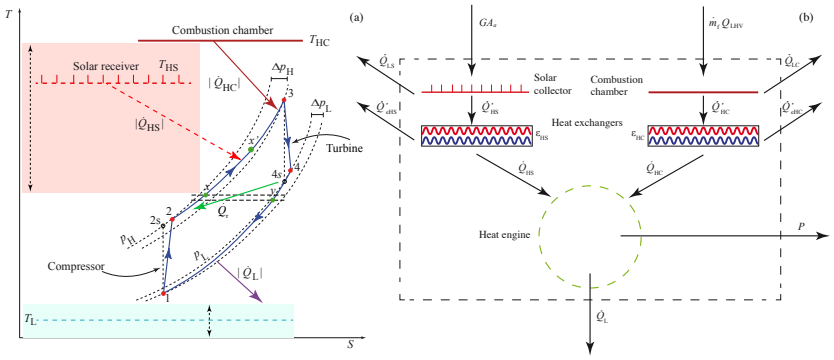

Figure 2. (a) $T-S$ diagram of the Brayton cycle developed by the gas turbine. Solar receiver temperature, T_{HS}, and ambient temperature, T_L, are fluctuating quantities. (b) Graphical scheme of the energy flows in the whole system: solar and combustion heat inputs, heat transfers and losses in solar and combustion subsystems, and main loss sources considered in the model. Details on the thermodynamic model can be found in [21,22].

has been previously detailed and validated by our research group for central tower plants [22,26]. The model intends to be comprehensive and analytical to facilitate sensitivity and optimization analyses. Furthermore, it was developed to be applied to different working fluids (He, carbon dioxide, etc.) [22] and so, it relies on the assumption of a closed cycle. Validation results showed that their results compare favorably with those of standard open cycle gas turbines [27].

Thus, the thermal efficiency of the micro-gas turbine, η_h, is calculated on the basis of a closed irreversible Brayton cycle considering non-isentropic compressor and turbine, pressure losses in heat absorption and heat release processes, and a non-ideal recuperator. The working fluid is dry air, considered as an ideal gas with temperature-dependent specific heats. Following the T-S diagram in Fig. 2(a), the gas is compressed from state 1 to state 2. Then, a first temperature rise up to T_x is due to the recuperator connected to the turbine exit. Subsequently, during sunlight hours, the receiver releases heat to increase the temperature up to $T_{x'}$. If this temperature is below the fixed turbine inlet temperature, T_3, a combustion chamber contributes with the corresponding heat. After state 3, the fluid is expanded in the turbine. Finally, the cycle is closed by means of a heat transfer to the recuperator and to the ambient through a heat exchanger. All those temperatures can be analytically expressed in terms of the compressor pressure ratio and parameters quantifying the considered irreversibilities. Explicit equations can be found in [22,26].

The micro-gas turbine efficiency is defined as $\eta_h = P/|\dot{Q}_H|$, where $|\dot{Q}_H|$ is the total heat input rate.

$$|\dot{Q}_H| = |\dot{Q}_{HS}| + |\dot{Q}_{HC}| \tag{4}$$

where $|\dot{Q}_{HS}|$ represents the heat rate input from the solar collector and $|\dot{Q}_{HC}|$ from the combustion chamber. The ratio between the solar heat input and the total one is the solar share, $f = |\dot{Q}_{HS}|/|\dot{Q}_H|$.

$$|\dot{Q}_{HS}| = \dot{m} \int_{T_x}^{T_{x'}} c_w(T)\, dT = f|\dot{Q}_H| \tag{5}$$

$$|\dot{Q}_{HC}| = \dot{m} \int_{T_{x'}}^{T_3} c_w(T)\, dT = (1-f)|\dot{Q}_H| \tag{6}$$

The heat release to the ambient is expressed as:

$$|\dot{Q}_L| = \dot{m} \int_{T_1}^{T_y} c_w(T)\, dT \tag{7}$$

In these equations $c_w(T)$ represents the temperature dependent constant pressure specific heat of the working fluid. Thus, the power output released by the heat engine, $P = |\dot{Q}_H| - |\dot{Q}_L|$.

2.4. Hybridization model

It is assumed that the operation objective of the solar dish is to provide a constant power output, independently of the solar and meteorological conditions, all year around. Thus, a combustion chamber is incorporated in such a way that it releases a variable heat rate that complements solar input to guarantee a constant turbine inlet temperature. This means that the theoretical capacity factor of the plant is 100%.

The efficiency of the combustion chamber, η_c, once elected the fuel to be burned and the fuel-air equivalence ratio, can be considered as a constant parameter. In real equipment it could slightly change with fluctuations of the fuel-air equivalence ratio, the composition of the fuel, its temperature, and several other variables. The heat received by the working fluid from the combustion chamber, $\dot{Q}_{HC}$, can be written as:

$$|\dot{Q}_{HC}| = \varepsilon_{HC} |\dot{Q'}_{HC}| = \varepsilon_{HC}\, \eta_C\, \dot{m}_f\, Q_{LHV} \tag{8}$$

By expressing the effectiveness of the heat exchanger in between the combustion chamber and the thermal cycle as $\varepsilon_{HC} = (T_3 - T_{x'})/(T_{HC} - T_{x'})$ (see Fig. 1), the heat released, in terms of temperatures, is:

$$|\dot{Q}_{HC}| = \dot{m}\, c_w\, (T_3 - T_{x'}) = \dot{m}\, c_w\, \varepsilon_{HC}\, (T_{HC} - T_{x'}) \tag{9}$$

The effective temperature in the combustion chamber is denoted as T_{HC}. As fluctuations in G and T_L will be taken into account, the fuel mass flow to be burned in the combustion chamber will also be a time dependent function in general given by:

$$\dot{m}_f = \frac{\dot{m}\, c_w (T_3 - T_{x'})}{\eta_C\, Q_{LHV}\, \varepsilon_{HC}} \tag{10}$$

where $T_{x'}$ will vary with the solar irradiance and ambient conditions.

The final electrical energy produced, E_{elec}, allows to quantify the actual electricity output. It can be calculated from the net mechanical power output, P, the efficiencies of generator and alternator systems (η_{gen} and η_{alt}), and the mechanical efficiency, which represents the ratio between the shaft power and the gas turbine rotor power, η_{mec}. Thus, the net electrical energy output can be written as:

$$E_{elec} = \eta_{gen} \cdot \eta_{alt} \cdot \eta_{mec} \cdot P. \tag{11}$$

2.5. Economic performance indicators

Nowadays, it is necessary to evaluate not only the thermodynamic and technical aspects of a power plant, but also to assign costs and to identify the intensity of harmful emissions. Therefore, once the thermodynamic performance of the plant is established, the second stage is to assign costs: investment and initial installation costs, CI_0, costs incurred during operation (indirect and maintenance costs $C_{O\&M}$, such as labor to operate the plant or water for cleaning the mirrors), and fuel costs in the case of hybrid plants, C_{fuel}. The *levelized cost of electricity* is an economic indicator commonly employed to compare power plants with different sizes and it serves to determine the minimum electricity sale price needed to recover investment and operation costs over the expected lifetime of the plant [28]. Equation (12) describes the LCoE calculation following the International Energy Agency (IEA) definition [29,30]. It is the ratio between the sum of the total costs and the sum of the electrical

energy production, EE, over the expected lifetime which is usually assumed to be $n = 25$ years for solar plants. Both sums are discounted at a constant rate r over the lifetime of the plant.

$$\mathrm{LCoE} = \frac{\sum_{i=1}^{n} \left(CI_0 + C_{O\&M_i} + C_{\mathrm{fuel}_i}\right)(1+r)^{-i}}{\sum_{i=1}^{n} EE_i (1+r)^{-i}}. \tag{12}$$

Neither the decommissioning costs nor the interest accrued during the construction are considered, as the construction time for these parabolic dishes is considered lower than 1 year.

- In this paper, the total investment costs, CI_0, are derived from the sum of the equipment cost, C_{eqp}, the cost of equipment installation, C_{inst}, civil engineering costs, C_{civil}, and contingencies, C_{cont}. C_{civil} summarizes the costs from the system engineering, tracking, basement, cabling, and assembly. C_{cont} is a purely financial cost associated to the risk and uncertainty of the project, based on previous experience regarding similar technologies.

$$CI_0 = \sum C_{\mathrm{eqp}} + C_{\mathrm{inst}} + C_{\mathrm{civil}} + C_{\mathrm{cont}}. \tag{13}$$

  In turn, the equipment is considered as formed by the HSRC (C_{HSRC}), comprising the micro-gas turbine, the compressor, the solar receiver (control system, absorber, and pressure resistant glass window) and combustion chamber, as well as other auxiliary items as insulation and housing. Also, the equipment includes the dish itself (C_{dish}), that incorporates the parabolic mirror, facets, tracking system, and installation pedestal. Finally, generator costs (C_{gen}) arises from the electrical generator costs (with power electronics and control system).

$$C_{\mathrm{eqp}} = C_{\mathrm{HSRC}} + C_{\mathrm{dish}} + C_{\mathrm{gen}}. \tag{14}$$

- The term $C_{O\&M_i}$ in Eq. (12) represents the annual cost from operation and maintenance in year i. It comprises cleaning labors, water, and an annual share of equipment costs, C_{eqp}.
- C_{fuel_i} is a strongly uncertain component of costs. It is the annual fuel cost in year i associated with hybridization. Not only fuel price variations can be found of course among different countries, but also it is likely to suffer fluctuations during the year, even in the same region.
- EE_i is the electrical energy produced in year i. It is directly associated with the plant thermal efficiency. An optimized design from the optical and thermodynamic viewpoints makes the denominator of LCoE increase and, so, reduce LCoE values.
- Finally, r is the discount rate, considered as the sum of the inflation rate and the interest. A standard fixed value is usually taken for numerical estimations.

3. Numerical data for computations and validation

In order to perform numerical computations and analysis, dish sizes and power output levels were taken from Semprini *et al.* [31]. Particularly, two power levels were chosen, 7 and 30 kWe. Aperture and receiver areas, and so, concentration factors were taken from that paper as well as the optical efficiency of the dishes. Independent simulations of optical efficiency were made in our group by using the software Tonatiuth [32]. Discrepancies from the values obtained by Semprini *et al.* [31] were very small (below 0.5%), so those values were assumed for calculations. All the optical parameters, as well as those from the combustion system and for the Brayton cycle developed by the micro-gas turbine are collected in Table 1.

On-design direct normal irradiance was taken as $G = 780$ W/m^2 and ambient temperature $T_L = 298.15$ K. The data used to simulate the micro-gas turbine were adapted to reproduce the turbine Capstone C30 [33], the same analyzed by Semprini *et al.* [31]. Generator and alternator efficiencies (η_{gen} and η_{alt}) were set at 96% and the mechanical efficiency, η_{mec}, at 98% [34]. For the case of 30

Subsystem			Study Cases	
			$P = 30$ kWe	$P = 7$ kWe
Solar system	Collector Area*	A_a (m^2)	211.8	52.80
	Diameter Receiver*	A_r (m)	0.3879	0.1941
	Concentration factor*	C	1792	1784
	Optical efficiency*	η_0	0.9083	0.9086
	Heat exchanger efficiency	ε_{HS}	0.7951	0.7923
	Emissivity coefficient	α	0.1	0.1
	Convection & Conduction effective coefficient	$\overline{U}_L$ [W/(m^{2}K)]	5	5
Combustion system	Combustion chamber efficiency	η_c	0.97	0.97
	Heat exchanger efficiency	ε_{HC}	0.97	0.97
Brayton cycle micro-gas turbine	Turbine efficiency*	ε_t	0.76	0.74
	Compressor efficiency*	ε_c	0.77	0.76
	Turbine inlet temperature*	T_3 (K)	1173.15	1173.15
	Pressure ratio*	r_p	3.84	3.65
	Air mass flow*	$\dot{m}$ (g/s)	337.9	88.1
	Recuperator effectiveness	ε_r	0.85	0.85
	Pressure drop (Process 2→3)	$\Delta p_H / p_H$ (%)	12.5	12.5

Table 1. Parameters extracted from Semprini *et al.* [31] (*) and those taken to validate our model. Validation target is the micro gas-turbine Capstone C30 [33].

kWe, the deviation of our calculations for the thermal efficiency and the power output are below 3.5% and 0.4%, respectively. For the lowest power output, 7 kWe, differences are below 4.7% for thermal efficiency and 2.2% for power output. These results for validation were obtained by taking polynomial fits for the specific heat of air from RefProp 9.1 [35]. The same model for the gas turbine was validated for other thermosolar systems (central towers) at higher power levels (megawatts scale) in previous works [22,26,27].

Assembling a wide variety of information sources including literature and direct personal communications, specific cost functions have been determined to calculate the final purchasing costs of each element, based on the size and operating conditions. This hybrid solar power plant with an specific HSRC is still not currently marketed, however, to draw price comparisons, a prototype of integrated combustion chamber and mGT based on Ragnolo *et al.* [36,37] is employed. Many factors will affect the final purchasing costs such as the number of units ordered or the state of the market. Therefore, the data provided here is useful for comparison between locations and operations modes, but it could not be deemed as an exact cost prediction of a hybrid solar gas turbine dish. The purchased equipment costs are estimated assuming a production rate of 1000 modules year, as described in [38].

Following recommendations from Peters and Timmerhaus [39], the cost of equipment installation C_{inst} is equal to 20% of the initial equipment purchasing costs. Likewise, civil cost C_{civil}, including project engineering costs, is calculated by 8 to 23% of the total C_{eqp} (the most pessimistic was taken [30]). For the unforeseen regulatory of technical problems during the construction or operations, the IEA estimates a total contingency cost, C_{cont}, equal to the 10% of the total initial investment cost. Contrary to initial investment costs, operation and maintenance costs $C_{O\&M}$ are incurred during the power plant lifetime, such as water consumption for occasional mirror facets cleaning (50 l/m^2 per year) and costs related to reparation or replacement of damaged components, calculated as a percentage of the initial equipment cost (*i.e.*, 2%/yr for the mGT and receiver, 3%/yr for the elements of the parabolic dish, and 4%/yr for the control system). Due to the small plant size, no specific operation labor costs are considered, and the technician or operator is included within the maintenance costs detailed above.

Fuel costs strongly depend on system location. Policies of each country establish taxes that greatly rely on financial or economic cycles and particular conditions. IEA defines international prices for the fuel industry in order to perform global statistics. For Spain, fuel cost data were taken from 2018 and was set to 26.41 €/MWht [40] for natural gas. This price was chosen in a quite pessimistic

Cost type		Specific cost (€/ kWe)	Source
C_{eqp}	C_{HSRC}	480	[42]
	C_{dish}	1550	[42]
	C_{gen}	226.8	[43]
C_{inst}		20 % C_{eqp}	[39]
C_{civil}		23 % C_{eqp}	[30]
C_{cont}		10 % (C_{eqp}+ C_{inst}+ C_{civil})	[30]
$C_{O\&M}$		2 % C_{HSRC}+ 3 % C_{dish}+ 4 % C_{gen}	[6,28]
C_{fuel}		26.41 €/ MWh	[40]

Table 2. Cost parameters used to estimate LCoE and the corresponding sources. Total costs appearing in Eq. (12) are obtained as the simple product of specific costs by the plant nominal power output, except for fuel costs that are already expressed in €/MWh.

scenario, including taxes, transport and commercialization expenses. Lower heating value for natural gas considered is 47.146×10^6 J/kg [41]. The discount rate, r, is assumed to be 9% [42]. All the data considered for LCoE calculations are compiled in Table 2.

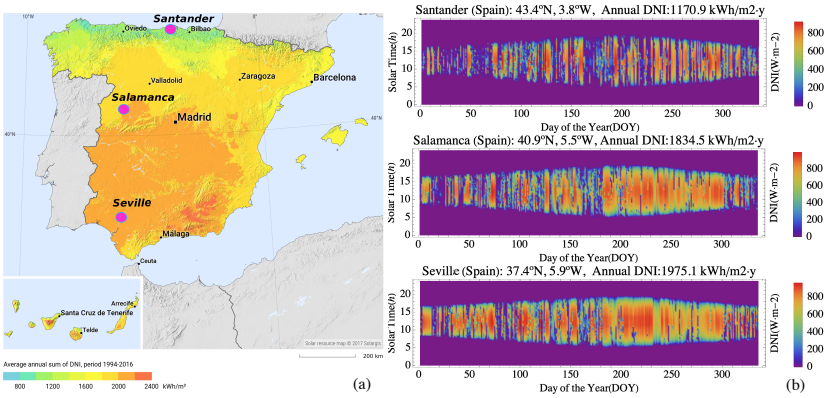

Figure 3. (a) Map of the average annual sum of the Direct Normal Irradiation (DNI) in kWh/m^2 in Spain in the period 1994-2016 [44]. The location of the selected cities is indicated on the map. (b) Annual DNI map from December 2017 until November 2018 in Salamanca, Santander, and Seville [45]. The annual DNI accumulated during this period is indicated above the figure for each city.

After validation, seasonal and annual analysis were made for the mentioned power outputs, for recuperative and non-recuperative micro-gas turbines, and for three locations in Spain with quite different latitudes and meteorological conditions. The locations of the three cities considered in Spain are shown in Fig. 3(a).

- Santander is located at the north of Spain, with latitude 43.4°N, in the Atlantic coast, at sea level. In principle, solar conditions are not favorable, climate is oceanic and humid, plenty of cloudy days [see Fig. 3(b)] and with mild temperatures (mean annual temperature is 14.1°C). Averaged annual DNI is about 1170 kWh/m^2. This location was elected to numerically evaluate the differences with other two, *a priori*, more interesting locations.
- On the other side, Seville is located in Andalusia, at the south of Spain (latitude 37.4°N). Averaged annual DNI is almost twice that of Santander, about 1975 kWh/m^2. Several CSP commercial and prototype installations have been developed in the last years around Seville. Weather is dry and

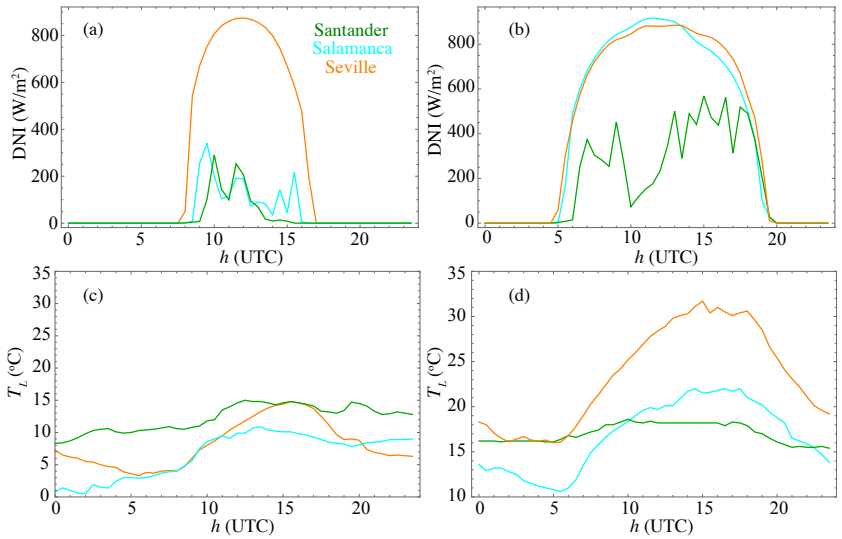

Figure 4. Samples of DNI and ambient temperature, T_L, for the considered locations at particular days in winter and summer: (a), (c) correspond to December 13th, 2017 and (b), (d) to June 13th, 2018. DNI data were obtained from CAMS [45] and temperatures from AEMET [46].

warm and sunny days are usual at any season. It has a typical mediterranean climate: dry and hot summers, and mild temperatures in winter, when rain is concentrated. Temperatures during daytime in summer can reach values above 30°C (see a sample day in Fig. 4) and are rarely below 5°C in winter. Yearly averaged temperature is 18.6 °C. Peak DNI can be quite above 800 W/m^2 at any season (see also the days taken for Fig. 4). Altitude above sea level is small, about 7 m. In average, there are about 50 rainy days per year (above 1 mm rainfall).

- Salamanca is located in between Santander and Seville, over a plateau at about 800 m above sea level. It has a dry continental climate. Summers are dry and hot and winters cold and not too rainy. DNI is only slightly below that of Seville, about 1834 kWh/m^2. Annual precipitations are about 373 mm and there are only 64 days per year with more than 1 mm rainfall. During winter months daily averaged temperatures could be around 5°C (from December to March). Annual mean temperature in Salamanca is 12.1 °C.

Ambient temperatures were taken from the Spanish Meteorological National Agency (AEMET) [46]. Temperatures are averaged each 30 minutes. Nevertheless, the absence of several DNI data for some locations from AEMET made necessary to take data from Copernicus Atmosphere Monitoring Service (CAMS) [45], also each 30 minutes. With this time lapse, the working temperature of the solar receiver [T_{HS} in Fig. 2(a)] is dynamically obtained by balancing the solar energy input in the receiver and the heat extracted by the working fluid. The sample curves of DNI and ambient temperature in Fig. 4 for particular days of winter and summer in the three locations have not been smoothed nor averaged to visualize the differences at the same particular days among the three locations. It is particularly interesting, for instance, that in summer it is possible, as shown in Figs. 4 (b) and (d), that Seville and Salamanca reach the same peak DNI values. Temperature curves are roughly parallel but displaced. Always T_L values for Salamanca are between 5 and 10°C below.

Version September 29, 2020 submitted to *Energies*

All the greenhouse emissions that will be shown below were calculated from standard emission factors for greenhouse gases [47].

4. Daily and seasonal behavior of plant records

The evolution of main plant output records as efficiencies, power output, solar share (the fraction of heat input to the working fluid from the sun with respect to the total), and main temperatures have been estimated from the model for the three locations and particular days representative of each season.

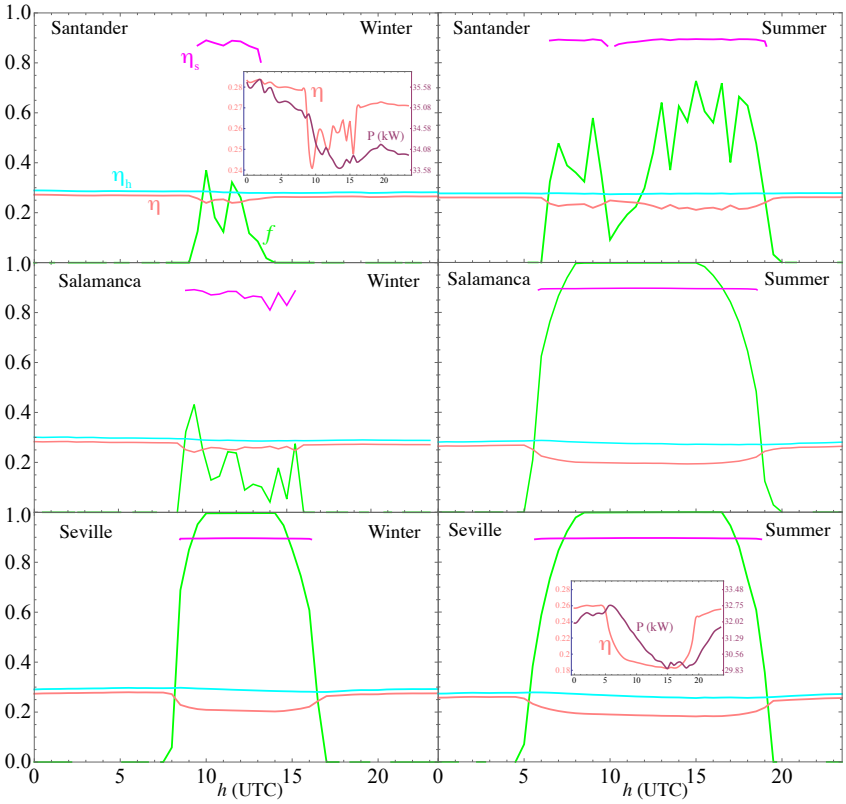

Figure 5. Overall efficiency, η, subsystems efficiency (η_s, solar and η_h, heat engine), and solar share (f) for the locations analyzed during particular days of winter (December 13th, 2017) and summer (June 13th, 2018). The insets show examples of the hourly evolution of overall efficiency, η, and power output P.

Figure 5 shows the evolution of main efficiencies and solar share for two particular days, in winter and summer. These days are December 13th, 2017 and June 13th, 2018. The shape of DNI and ambient temperature for these days is shown in Fig. 4. Some of the curves correspond to cloudy days, but have not been smoothed nor averaged, in order to analyze the behavior of the dish in conditions so close to reality as possible. Annual averages will be shown in the next section. The curves correspond to

the power output level of 30 kWe and include recuperation. Solar subsystem efficiency, η_s, is really high and almost constant during daytime, always around 0.9. Heat engine efficiency, η_h, is stable because turbine inlet temperature is a fixed input parameter. Overall efficiency, η, is regular by night and slightly below η_h (the difference is associated with combustion efficiency), and decreases when the solar dish is operating because its losses are added to those of the heat engine. Solar share is also depicted in Figure 5. It has a behavior in concordance with DNI evolution (see Fig. 4). In some situations it reaches its maximum attainable value (in the cases considered for DNI approximately over 750 W/m^2), so for the considered dish dimensions, a defocusing system should be designed to avoid overheating and damage.

The insets in Figure 5 show for two different cases the amplitude of the fluctuations of overall efficiency and power output. The latter are essentially associated to ambient temperature evolution and very small in relative terms. Nevertheless, fluctuations of overall efficiency are appreciable, in the pictures shown reach 15% in Santander during the considered winter day and almost 30% for Seville in summer (see Fig. 5 bottom right). These fluctuations arise, apart from meteorological oscillations, from having or not the solar subsystem operating, *i.e.*, when the plant works with solar heat input, solar collector and receiver losses decrease overall efficiency up to 30% in the cases shown. It is important here to recall that a factor $\epsilon_{HS} \simeq 0.79$ (see Table 1) is considered as effectiveness of the solar receiver acting as a heat exchanger.

The hourly evolution of air temperatures in main thermodynamic cycle states are depicted in Fig. 6. Notation for those states is shown in Figs. 1 and 2(a). As commented before, turbine inlet temperature, T_3, is considered as a fixed input parameter (about 1173 K). Thus, the gas temperature before entering into the recuperator, T_x, is also fixed (about 850 K), although it depends on ambient temperature. $T_{x'}$ is the temperature after the solar receiver, that depends on DNI. When the solar share is above $f = 1$, $T_{x'} = T_3$. Solar receiver operating temperature, T_{HS}, also fluctuate with DNI and ambient temperature and need to be controlled to avoid engine damage in periods with good solar conditions. So, at very good conditions the solar receiver increases gas temperature about 300 K.

The simulations of plant records have been also performed without recuperation in order to analyze efficiencies and temperatures. A particular case is shown in Fig. 7. It corresponds to Salamanca during a summer day. Curves should be compared with those on the right middle panels in Figs. 5 and 6. On one hand, engine efficiency, η_h, and overall efficiency, η, decrease to about a half of the recuperative configuration. Maximum solar share decrease is similar. On the other hand, temperature of the fluid after the solar receiver, $T_{x'}$, does not reach fixed turbine inlet temperature, so the dish is always operating within a partial combustion mode. In this case, defocusing would not be necessary. The difference between instantaneous fuel consumption with or without recuperation for the same conditions is shown in Fig. 8 (Salamanca, summer, and $P = 30$ kWe).

5. Monthly and annual plant estimations

In this section it is intended to provide a monthly evolution of dish output records and also the annually averaged ones, comparing among the three elected locations and power outputs. The effects of recuperation from this perspective also deserve an analysis.

As it can be observed in Fig. 9 for the lowest level of power output, η oscillates between 0.20 and 0.25 for a recuperated plant. During summer months, from approximately June to October, it shows a dip for any location because of the average increase of ambient temperature. For $P = 30$ kWe, monthly evolution is similar but numerical values of overall efficiency are larger for all places. It is important to have in mind here (looking at Table 1) which are the main differences between both power levels with respect to model input parameters. Although the size of the dish in both cases is different, concentration factor, optical efficiency, and other parameters from the solar subsystem are similar. Combustion system and losses parameters in the Brayton cycle are also analogous, pressure ratios are slightly different and air mass flows are quite different. The combination of these factors leads to the minimum efficiency in Seville (for $P = 30$ kWe) during September. It is about 0.21. Maximum is

Version September 29, 2020 submitted to *Energies*

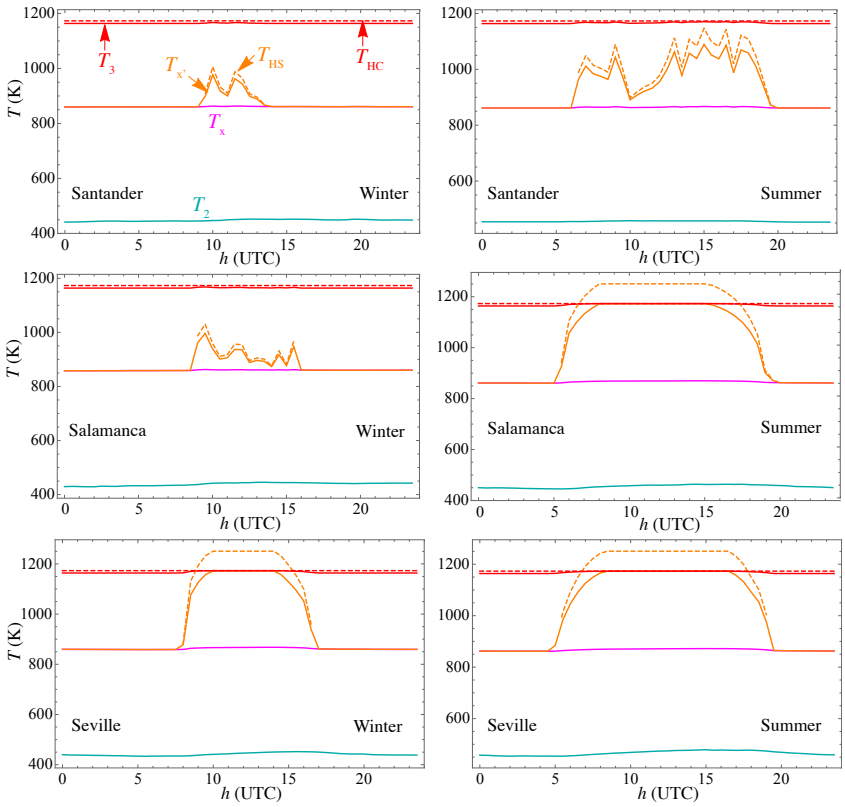

Figure 6. Daily evolution of the working fluid temperatures for the same places and particular days that Fig. 5. Notation for temperatures corresponds to the thermodynamic states in Fig. 2(a).

achieved in the coldest location, Salamanca, in February, approximately 0.28. This suggests that at this modeling level, the most important factor for the monthly evolution of overall efficiency is the average ambient temperature. This fact can be corroborated by looking at the temperatures profile shown in the inset of Fig. 9. Almost without exception, for any month, lowest average ambient temperature corresponds with the highest overall thermal efficiency.

Table 3 contains the yearly averaged global efficiencies. For all locations, averaged η is slightly larger for the highest power output. Differences among locations are also small. Santander has the best records. This is associated with a lower solar share: larger solar share means that the solar subsystem (and its losses) is coupled during more time to the power unit, decreasing overall efficiency. Yearly solar shares are largest for Seville, about 41%, and smallest for Santander, about 21%.

The energy produced by month is outlined in Fig. 10. It is approximately constant for both power levels, although oscillations are smaller for 7 kWe. The stability of the produced energy means that the objective of the plant is fulfilled: to guarantee steady output records by means of hybridization. Table 3 contains annual averages of the energy generated, both in hybrid operation mode and for pure combustion. For the same level of power output, energy produced is similar in all locations.

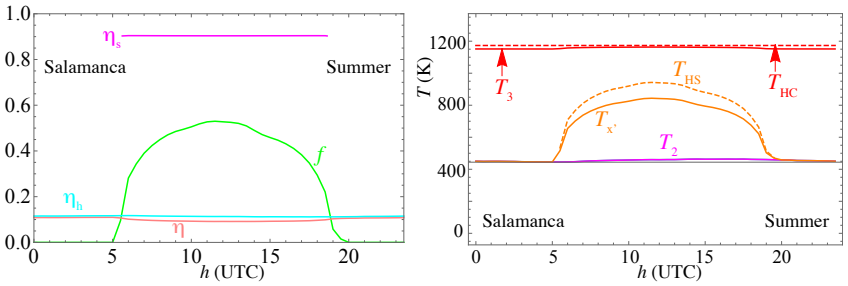

Figure 7. Plant efficiencies and temperatures without recuperation for the location at Salamanca during a summer day (June 13th, 2018). This figure should be compared with the right middle panels in Figs. 5 and 6.

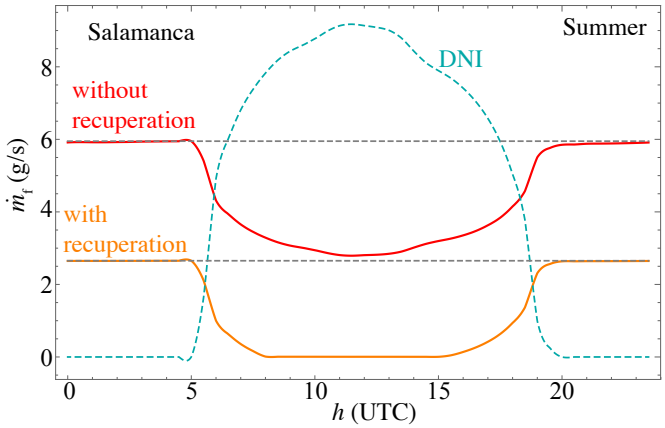

Figure 8. Instantaneous fuel consumption for plant configurations with or without recuperation. The particular case of Salamanca during a summer day for the power output level of $P = 30$ kWe is shown. The corresponding DNI is shown just as a guide.

The evolution during the year of fuel consumption on the basis of natural gas is depicted in Fig. 11, where the shaded areas represent the fuel savings along the year. Numerical values are also included in Table 3 as well as yearly emissions in real units. The decrease of fuel consumption is perfectly clear around summer months. More evident in Seville, but even in Salamanca, savings are also noteworthy in other seasons. Fuel savings are largest in Seville and amount about 31%. The lowest correspond to Santander, because of its worse irradiance data. There fuel consumption is almost double compared with Seville. Salamanca, at an intermediate latitude, but also with lower mean temperatures, leads to savings about 24%. This is smaller than Seville, but they are remarkable numbers anyway. All the data in Fig. 11 and Table 3 refer to a plant layout that incorporates a recuperator. Of course, it increases thermodynamic efficiency, decreases fuel consumption but conversely greatly increase operating temperatures (as explained before from Figs. 5 - 7).

Monthly produced energy, overall efficiency and solar share for $P = 30$ kWe and Salamanca as example are depicted in Fig. 12 for two plant layouts: with and without recuperation. The energy

Version September 29, 2020 submitted to *Energies*

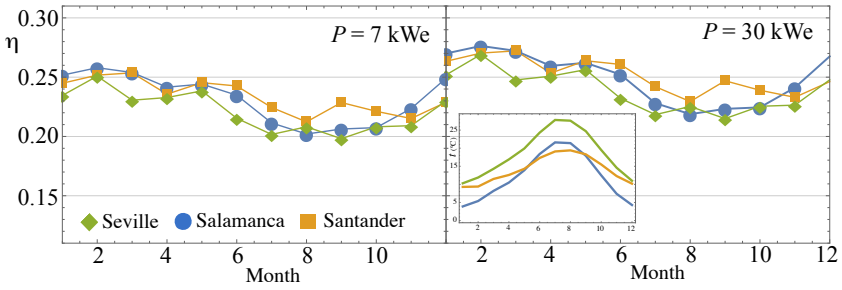

Figure 9. Monthly evolution of overall efficiency for the three locations considered and two power levels (recuperated layout). The inset displays the monthly average temperature profile in each location.

Location	Seville		Salamanca		Santander	
Power output	7 kWe	30 kWe	7 kWe	30 kWe	7 kWe	30 kWe
Hybrid Operation Mode						
Overall Efficiency (%)	22.14	23.88	23.18	24.95	23.35	25.16
Averaged solar share, f (%)	41.12	41.35	30.42	30.59	20.99	21.18
Energy generated (MWh_e)	58.49	251.06	60.14	257.54	59.22	253.89
Fuel consumption (t)	14.00	55.63	15.67	62.29	17.39	69.12
Combustion operation mode						
Energy generated (MWh_e)	60.52	259.141	62.26	265.96	60.32	258.29
Fuel consumption (t)	20.56	81.83	20.63	82.11	20.56	81.83
Mode Comparison						
Fuel savings (t)	6.56	26.20	4.96	19.82	3.17	12.71
Fuel savings (%)	31.91	32.02	24.04	24.14	15.42	15.53
Net reduction of CO_2 (t)	16.23	64.83	12.28	49.04	7.84	31.45
Net reduction of CH_4 (kg)	306.99	1226.69	232.26	927.77	148.25	595.09
Net reduction of N_2O (kg)	29.81	119.09	22.55	90.08	14.39	57.78

Table 3. Comparison of the annual results for different locations for hybrid and pure combustion modes.

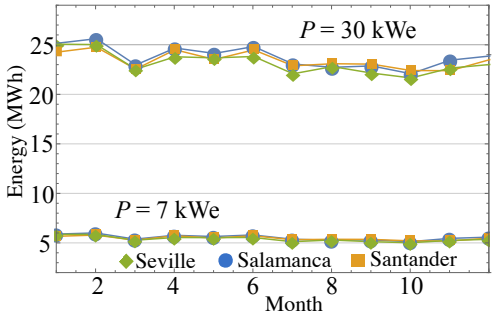

Figure 10. Monthly evolution of produced energy (recuperated layout) for the two levels of power output considered.

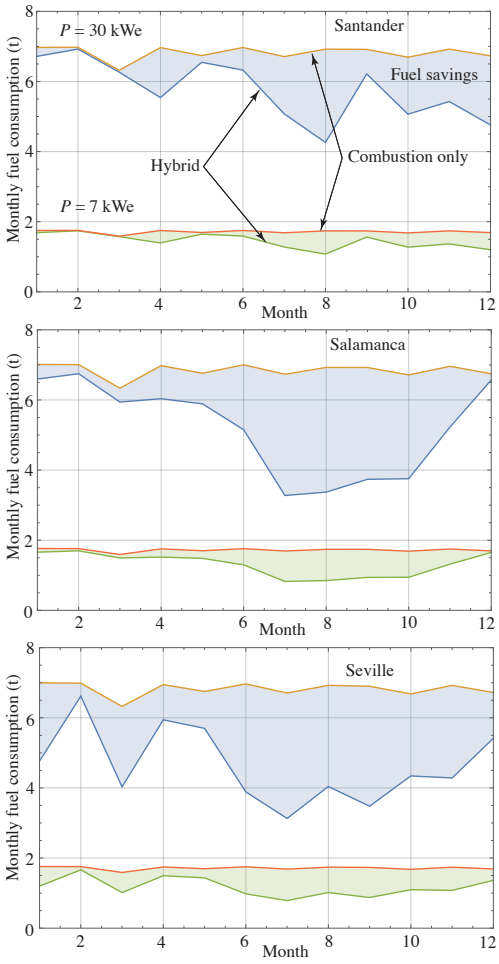

Figure 11. Monthly fuel consumption on the basis of natural gas fueling. Shaded areas represent the total annual savings when comparing between a purely fuel combustion mode (natural gas burning) and the hybrid mode. All cases are recuperative.

produced [see Fig. 12(a)] is similar in both configurations because the same turbine inlet temperature is fixed in both cases. Differences between lines representing overall efficiency are substantial [see Fig. 12(b)]. Efficiency for the recuperated plant is, in all months, above twice the non-recuperated one. Although, fixing the same scale for both, seasonal decrease during summer is less evident for the non-recuperated plant. This is explained in Fig. 12(c) that contains a plot of solar share. During summer solar share is quite larger for the recuperated plant: the solar subsystem is contributing to a larger extent, so the losses it incorporates to the whole system decrease thermal efficiency.

Version September 29, 2020 submitted to *Energies*

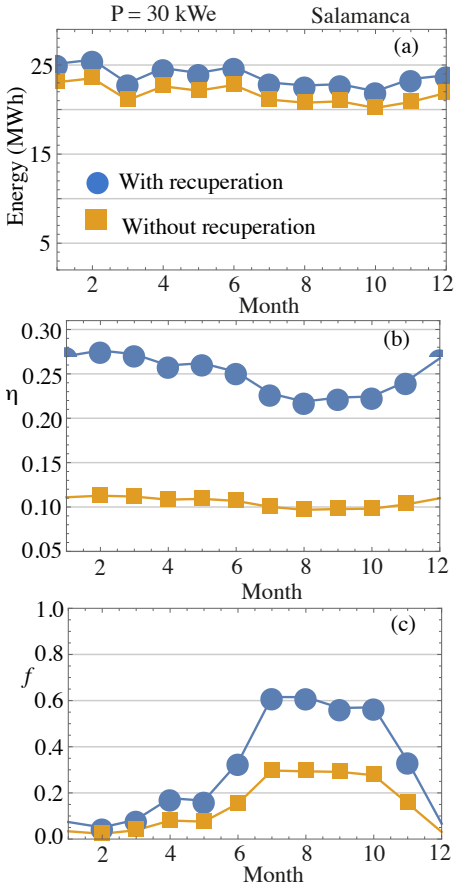

Figure 12. Monthly comparison between recuperated and non-recuperated plant layouts for an example case: plant located at Salamanca, with an objective power output of 30 kWe. (a) Monthly energy production; (b) overall plant efficiency; and (c) solar share.

Fuel consumption and savings are also plotted, Fig. 13, at the same scale to visualize the differences between those two modes. Lines are parallel but displaced (approximately, monthly consumption is 2.5 times larger without recuperation), so savings are similar in a yearly average.

6. Levelized cost of electricity

As explained in Sec. 2 the levelized cost of electricity is the economic indicator selected to analyze the performance of the hybrid solar dish from the perspective of the price of the electricity produced. It is always difficult to assign costs to the components and operation of a system that is still under development, obtained net values can have an appreciable uncertainty. Nevertheless, the comparison between different locations, different weather conditions, different plant layouts, etc. within the same

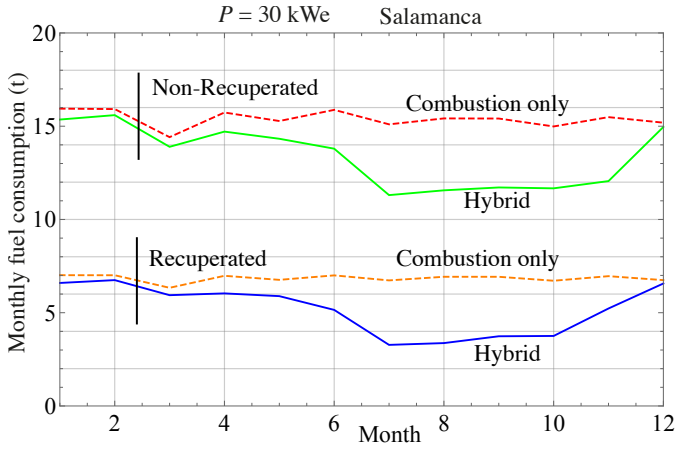

Figure 13. Fuel consumption per month at Salamanca, $P = 30$ kWe, in recuperative (bottom lines) and non-recuperative (top lines) cases. Plant operation in a pure combustion mode is shown with dashed lines and in hybrid solar mode with solid lines.

scheme, can reveal interesting aspects. All the estimations were performed with the data considered in Sec. 3. The three locations chosen were analyzed for the turbine working in a standard only combustion model (assuming natural gas fueling and recuperation) and in a hybrid solar mode on annual basis. To survey the values of LCoE in the aim interval of power output levels, four values of power output, between 7 and 30 kW_e, were analyzed.

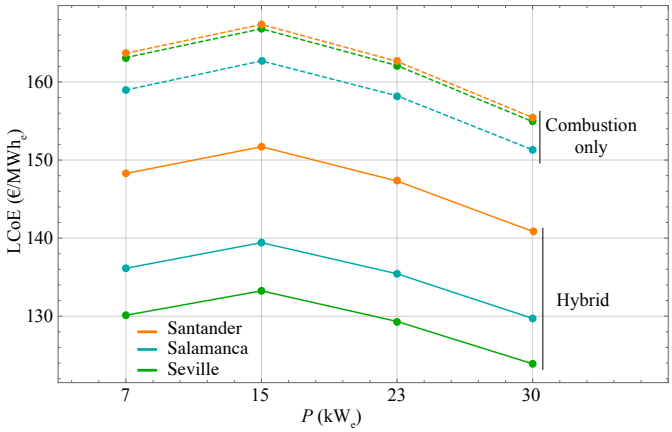

Figure 14. Levelized cost of electricity for two operating modes of the hybrid solar dish: combustion only (dashed lines) and hybrid mode (solid lines). Four power output levels are considered, between 7 and 30 kW_e.

Version September 29, 2020 submitted to *Energies*

Figure 14 collects the evolution of LCoE with the power output and Table 4 contains the particular numerical results. Figure 14 shows a non-linear evolution of LCoE with the power output level. It increases from 7 kW_e up to 15 kW_e where it presents a maximum, and then it decreases up to a minimum value at the highest power output analyzed, 30 kW_e. Values of LCoE for combustion only are always above the hybrid mode, and differences are substantial. In only combustion mode, LCoE is smallest for Salamanca, probably due to its lower mean ambient temperatures, the only parameter influencing the thermodynamics of the system associated with site location in this mode. Roughly, Salamanca mean annual temperature is 12.1°C, Seville's is 18.6°C, and Santander is in between, 14.1°C. LCoE for only combustion is in the interval $[152 - 168]$ €/MWh_e.

In hybrid operation, LCoE has a similar evolution with the power output, but the saving in operation costs because of the reduced fuel consumption displaces curves to lower values. It is important to have in mind here that the same equipment costs were considered to perform these calculations, *i.e.*, costs of the HSRC and dish were considered the same in both modes. In hybrid mode Santander reaches the highest values of LCoE due to its worse DNI records and Seville gives the lowest LCoE values. However, values of LCoE for Salamanca are close to those of Seville. Its lower DNI values are compensated with its also lower mean ambient temperatures. In numerical terms, the best record (see Table 4) is obtained in Seville for 30 kW_e and is about 124 €/MWh_e. In relative terms this value is about 18% lower than the analogue for the pure combustion mode.

Power output		7 kW_e	15 kW_e	23 kW_e	30 kW_e
LCoE (€/MWh_e)					
Seville		130.12	133.24	129.33	123.90
Salamanca		136.14	139.42	135.44	129.71
Santander		148.28	151.70	147.32	140.86
Hybrid Mode Specific Emissions (kg/MWh_e)					
Seville	CO_2	592	600	584	548
	CH_4	11.21	11.35	11.06	10.37
	N_2O	1.09	1.10	1.07	1.01
Salamanca	CO_2	645	654	637	598
	CH_4	12.20	12.37	12.06	11.32
	N_2O	1.18	1.20	1.17	1.10
Santander	CO_2	727	737	718	674
	CH_4	13.75	13.94	13.58	12.74
	N_2O	1.45	1.35	1.32	1.24

Table 4. Summary of LCoE and specific emissions for different power output and locations.

Of course a key (and uncertain) factor in the particular values of estimated LCoE is the cost of fuel. For the calculations shown in Fig. 14 it was taken $C_{fuel} = 26.41$ €/MWh [40] that is a realistic (and pessimistic) price in Spain for 2018. To deepen in the influence of fuel costs, Fig. 15 shows the slope of the dependence of LCoE with fuel costs in a wide interval of prices. In hybrid operation, of course, the increase of LCoE with the price of natural gas is largest at Santander and smallest at Seville.

The final purpose of this section is to present a brief comparison of LCoE results obtained within our model with other estimations for the same type of systems and for other renewable systems for electricity production. As commented by Giostri *et al.* [34] a LCoE equal to approximately 160 €/MWh_e could guarantee competitiveness with reference CSP technologies, for instance parabolic trough or solar towers located in Mojave desert, USA. In the study by Giostri *et al.* it is presented an evolution of LCoE with receiver specific cost. This is motivated by the prototypal stage of high temperature solar receiver technologies. For a specific cost for the receiver similar to that assumed by us in Table 2, Giostri *et al.* obtain a LCoE about 180 €/MWh_e for a 33 kW_e solar dish located at Las Vegas, slightly

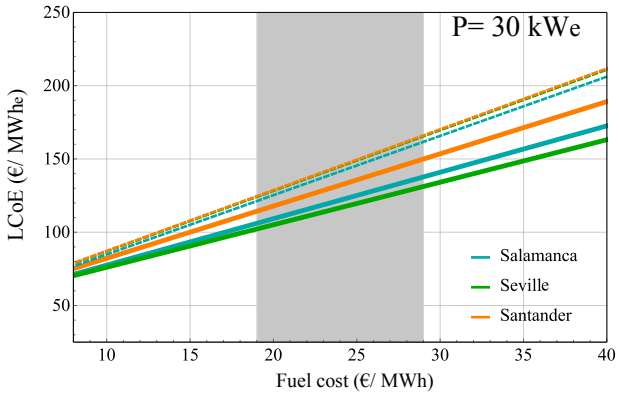

Figure 15. Evolution of the LCoE for the considered solar dish and the locations considered in a wide interval of natural gas price. The shaded area corresponds to realistic actual prices in Spain, 2018 (around 26.41 €/MWh). The case shown corresponds to the power output of 30 kW_e. Dashed lines refer to the only combustion mode and solid to solar hybrid.

over our results, but entirely comparable (see Fig. 16 in [34]). In the last years, a prototype parabolic dish with hybrid Brayton technology was developed with funding from the European Commission (2013-2017), the so-called OMSoP project [14]. The prototype dish, capable to support a micro-gas turbine up to 15 kWe, was built in Italy (Casaccia, Rome). Probably, the experimental period for data acquisition after complete installation was not sufficiently long to extract robust conclusions, but it was argued that LCoE values between 100 and 150 €/MWh_e could be achieved in a location with mild solar conditions [48]. This interval is slightly below the one obtained in this work, but also comparable.

Figures 16 and 17 allow to compare our results with those of the International Renewable Energy Agency published in 2018 [49]. The figures were obtained just by adding our estimations to the data in that report. In Fig. 16 a timeline of LCoE evolution from 2010 - 2022 is represented, attending at the geographical location of CSP plants. And in Fig. 17 different renewable technologies are analyzed in the period 2016 - 2017. From both figures, the results obtained in this work are reasonable. In any case, it should be not forgotten that LCoE strongly fluctuates depending on each country pricing policies, the state of the market, the estimated number of manufactured units, and fuel costs. The fact that an increasing number of research works, with different perspectives and approaches, lead to comparable economic indicators makes more robust the confidence on realistic electricity sale prices from this technology.

7. Summary and conclusions

In this work it was presented a complete model to analyze the performance of a solar dish working on a hybrid Brayton thermodynamic cycle. The model is simple enough to incorporate in an attainable way all the main subsystems that form the global plant, including the most relevant sources of losses, optical, mechanical, and thermodynamic. The micro-gas turbine is considered as integrated with the receiver, *i.e.*, it is taken as a hybrid solar receiver combustor. The model is capable to predict, with good precision (as it is shown in the validation process), the main output records of the plant, not only at on-design conditions, but also at any time for any particular location and meteorological condition. Thermodynamic parameters as efficiencies and temperatures at any thermodynamic cycle

Version September 29, 2020 submitted to *Energies*

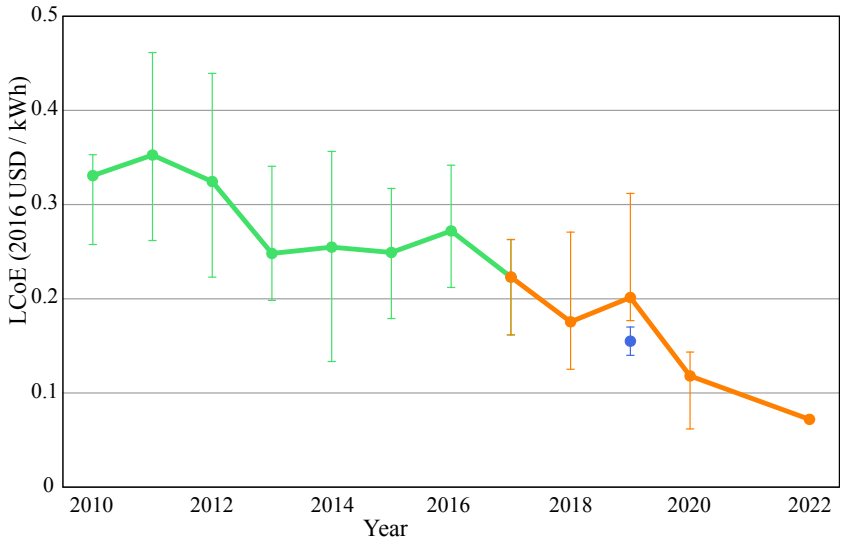

Figure 16. Levelised cost of electricity and auction price trend for CSP in the period 2010-2022. The figure is taken from IRENA [49]. Blue line showing the tendency corresponds to actual data and the orange one to estimations. Error bars are estimated by considering different locations. LCoE estimated for the solar Brayton dish in this work is displayed in blue.

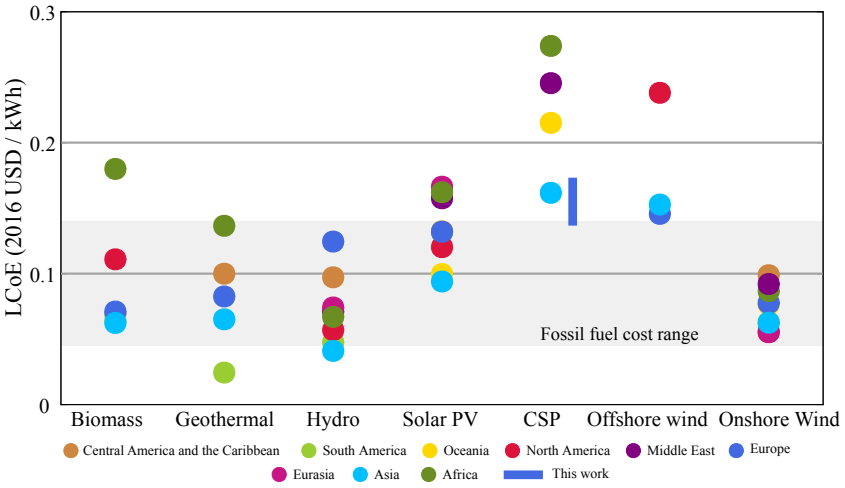

Figure 17. Regional weighted average LCoE for different renewable power generation technologies [49]. Data correspond to 2016 and 2017. The results obtained for the solar Brayton dish in this work are shown as a blue bar. The shaded area indicates fossil fuel cost interval.

step can be estimated dynamically. And also key indicators to analyze the marketing possibilities of this technology as LCoE or specific emissions can be estimated.

The model was applied to analyze the possibilities of this solar dish in a power output level from 7 to 30 kW_e in three locations in Spain with quite different latitudes (south, middle, and north), DNI levels, and mean temperatures. The daily fluctuations of all subsystems efficiency were analyzed for particular days at any season. It was shown how hybridization allows to obtain an almost constant power output, if that is the aim of the plant. Overall efficiencies about 0.30 are achievable when the plant design includes a recuperator for all the surveyed locations and seasons. Non-recuperated plant layouts are also feasible, but two consequences are straightforward. First, overall plant thermal efficiency greatly decreases (up to one half of the recuperated plant) and the operating temperature of the solar receiver also decreases. For a recuperated turbine it can reach values above 1200 K if solar conditions are good and for non-recuperated receiver temperatures are about 200 K below. This, of course, would affect the type of materials necessary to build the receiver and its costs. Influence of recuperation is alto important from the viewpoint of solar share. When the micro-gas turbine incorporates a recuperator, it is actually possible that for DNI values over 800 W/m^2, solar share reaches 1, and so some security system is necessary to avoid damages in the turbine. On the other side, when no recuperation is considered, solar share barely reaches 0.6. This means that the combustion of a fuel is imperative to reach turbine inlet temperature (that was considered as a fixed design input, about 1173 K).

A monthly analysis allowed to conclude that thermal efficiency oscillates along the year, reaching its highest values during coldest months. Maximum values are slightly larger for the highest power output level, 30 kW_e. The smallest are predicted during summer for the lowest power output. It was also shown that the monthly energy production is almost constant. Emissions and fuel savings were also analyzed, from monthly and yearly perspectives. By comparing a pure combustion operation mode with a solar hybrid one it is demonstrated that fuel savings can amount between 15% for a location with poor solar conditions to 32% at Seville, south of Spain. Specific emissions of CO_2 are estimated to be about 0.548 t/MWh_e in the best case (Seville and 30 kW_e). In a location at the center of Spain with relatively good solar conditions and lower annual mean temperature, Salamanca, specific emissions are also below 0.6 t/MWh_e (see Table 4).

The levelized cost of electricity was also computed for several power outputs and the same locations. A previous survey was performed to select actual and realistic costs parameters. A non-linear behavior for LCoE as a function of power output level has been reported in the surveyed interval of power outputs. In the range between 7 and 30 kW_e, LCoE increases up to 15 kW_e and then decreases. At 30 kW_e reaches its minimum value for wherever considered location. For a realistic natural gas price in Spain, LCoE ranges from 123.9 €/kWh_e as best (Seville and 30 kW_e) to 151.7 €/kWh_e as worst (Santander and 15 kW_e) values. Salamanca, a location with considerable smaller average temperatures and slightly lower DNI levels compared with Seville reaches values of LCoE only slightly worse than Seville. All the numerical values obtained for LCoE, when compared with other renewable technologies, are positive.

The model exposed in the work can be applied to any location and any climatological or meteorological condition. Direct normal irradiance and ambient temperature are input data, and the model can be used for whichever curves at any time moment. Thus, this technology, with the required investment on R&D, could be competitive at the mid term for the distributed generation of clean electric energy at the micro-scale, and thus play a significant role in the development of future smart microgrids. Probably, before mass production the main issue to solve is to integrate the solar receiver and the gas turbine itself with concepts like HSRC or similar and to check its reliability under different operation conditions. Once designs and materials are standardized, costs could even significantly decrease and the technology will be ready to compete with others like PV or small wind turbines.

Author Contributions: Conceptualization, M.J.S. and A.M.; software, J.G.F., I.H. and R.P.M.; validation, M.J.S. and A.M.; formal analysis, J.G.F.; investigation, J.G.F.; writing–original draft preparation, A.M.; writing–review

and editing, A.C.H.; visualization, J.G.F. and A.G.; supervision, A.C.; funding acquisition, M.J.S. and A.C. All authors have read and agreed to the published version of the manuscript.

Funding: This research was funded by University of Salamanca grant number PC-TCUE18-20-002, Banco Santander, and Junta de Castilla y León of Spain grant number SA017P17.

Conflicts of Interest: The authors declare no conflict of interest. The funders had no role in the design of the study; in the collection, analyses, or interpretation of data; in the writing of the manuscript, or in the decision to publish the results.

References

1. Kazerani, M.; Tehrani, K. Grid of hybrid AC/DC microgrids: a new paradigm for smart city of tomorrow. IEEE 15th International Conference on System of Systems Engineering (SoSE 20. IEEE, 2020, pp. 000175–000180.
2. Solano, J.; Jimenez, D.; Ilinca, A. A Modular Simulation Testbed for EnergyManagement in AC/DC Microgrids. *Energies* **2020**, *13*, 4049.
3. Köberle, A.C.; Gernanat, D.E.H.J.; van Vuuren, D.P. Assessing current and future techno-economic potential of concentrated solar power and photovoltaic electricity generation. *Energy* **2015**, *89*, 739–756.
4. Powell, K.M.; Rashid, K.; Ellingwood, K.; Tuttle, J.; Iverson, B.D. Hybrid concentrated solar thermal power systems: A review. *Renew. Sust. Ener. Rev.* **2017**, *80*, 215–237.
5. Giuliano, S.; Buck, R.; Eguiguren, S. Analysis of Solar-Thermal Power Plants With Thermal Energy Storage and Solar-Hybrid Operation Strategy. *J. Sol. Energy Eng.* **2011**, *133*, 031007.
6. Aichmayer, L.; Spelling, J.; Laumert, B.; Fransson, T. Micro gas-turbine design for small-scale hybrid solar power plants. *Journal of Engineering for Gas Turbines and Power* **2013**, *135*, 113001–1.
7. Quero, M.; Korzynietz, R.; Ebert, M.; Jiménez, A.A.; del Río, A.; Brioso, J.A. Solugas - Operation experience of the first solar hybrid gas turbine system at MW scale. *Energ. Proc.* **2014**, *49*, 1820–1830.
8. SOLGATE. Solar hybrid gas turbine electric power system. Technical Report EUR 21615, European Commission, 2005.
9. Solar-Hybrid Power and Cogeneration Plants (SOLHYCO). Technical Report 13318, European Commission, 2011.
10. Korzynietz, R.; Brioso, J.A.; del Río, A.; Quero, M.; Gallas, M.; Uhlig, R.; Ebert, M.; Buck, R.; Teraji, D. Solugas - Comprehensive analysis of the solar hybrid Brayton plant. *Sol. Ener.* **2016**, *135*, 578–589.
11. Lim, J.H.; Chinnici, A.; Dally, B.B.; Nathan, G.J. Assessment of the potential benefits and constraints of a hybrid solarreceiver and combustor operated in the MILD combustion regi. *Energy* **2016**, *116*, 735 – 745.
12. Chinnici, A.; Nathan, G.; Dally, B.B. Experimental demonstration of the hybrid solar receiver combustor. *Appl. Energy* **2018**, *224*, 426 – 437.
13. Nathan, G.J.; Battye, D.L.; Ashman, P.J. Economic evaluation of a novel fuel-saver hybrid combining a solar receiver with a combustor for a solar power tower. *Appl. Energy* **2014**, *113*, 1235 – 1243.
14. Lanchi, M.; Montecchi, M.; Crescenzi, T.; Mele, D.; Miliozzi, A.; Russo, V.; Mazzei, D.; Misceo, M.; Falchetta, M.; Mancini, R. Investigation into the coupling of Micro Gas Turbines with CSP technology: OMSoP project. *Energ. Proc.* **2015**, *69*, 1317–1326.
15. Aichmayer, L.; Garrido, J.; Wang, W.; Laumert, B. Experimental evaluation of a novel solar receiver for a micro-gas turbine based solar dish system in the KTH high-flux solar simulator. *Energy* **2018**, *159*, 184–195.
16. Bashir, M.A.; Giovanelli, A.; Ali, H.M. Design of high-temperature solar receiver integrated with short-term thermal storage for Dish-Micro Gas Turbine systems. *Sol. Ener.* **2019**, *190*, 156–166.
17. Aichmayer, L.; Garrido, J.; Laumert, B. Thermo-mechanical solar receiver design and validation for a micro-gas turbine based solar dish system. *Energy* **2020**, *196*, 116929.
18. Aichmayer, L.; Spelling, J.; Laumert, B. Preliminary design and analysis of a novel solar receiver for a micro gas-turbine based solar dish system. *Sol. Ener.* **2015**, *114*, 378–396.
19. Ssebabi, B.; Dinter, F.; van der Spuy, J.; Schatz, M. Predicting the performance of a micro-gas turbine under solar-hybrid operation. *Energy* **2019**, *177*, 121–135.
20. Aichmayer, L. Solar receiver development forgas-turbine based solar dish systems. PhD thesis, 2018.
21. Merchán, R.P.; Santos, M.J.; Reyes-Ramírez, I.; Medina, A.; Calvo Hernández, A. Modeling hybrid solar gas-turbine power plants: Thermodynamic projection of annual performance and emissions. *Ener. Conv. Manage.* **2017**, *134*, 314–326.
22. Santos, M.J.; Miguel-Barbero, C.; Merchán, R.P.; Medina, A.; Calvo Hernández, A. Roads to improve the performance of hybrid thermosolar gas turbine power plants: Working fluids and multi-stage configurations. *Ener. Conv. Manage.* **2018**, *165*, 578–592.
23. Wolfram. Mathematica Package. https://www.wolfram.com/mathematica/, accessed on 2020.
24. Ávila-Marín, A. Volumetric receivers in solar thermal power plants with centra receiver system technology: a review. *Sol. Energy* **2011**, *85*, 891–910.

25. Duffie, J.; Beckman, W. *Solar Engineering of Thermal Processes*; John Wiley and Sons: Hoboken, New Jersey, 2006.
26. Merchán, R.P.; Santos, M.J.; Heras, I.; Gonzalez-Ayala, J.; Medina, A.; Calvo Hernández, A. On-design pre-optimization and off-design analysis of hybrid Brayton thermosolar tower power plants for different fluids and plant configurations. *Renew. Sust. Energy Rev.* **2020**, *119*, 109590. doi:j.rser.2019.109590.
27. Olivenza-León, D.; Medina, A.; Calvo Hernández, A. Thermodynamic modeling of a hybrid solar gas-turbine power plant. *Energ. Conv. Manage.* **2015**, *93*, 435–447.
28. Spelling, J. Hybrid Solar Gas-Turbine Power Plants. PhD thesis, KTH Royal Institute of Technology, Department of Energy Technology, Stockholm, Sweden, 2013.
29. Dowling, A.W.; Zheng, T.; Zavala, Victor, M. Economic assesssment of concentrated solar power technologies: A review. *Renew. Sust. Ener. Rev.* **2017**, *72*, 1019–1032.
30. van der Hoeven, M. Technology Roadmap Solar Thermal Electricity. Technical Report 52, Int. Energy Agency (IEA), 2014.
31. Semprini, S.; Sánchez, D.; De Pascale, A. Performance analysis of a micro gas turbine and solar dish integrated system under different solar-only and hybrid operating conditions. *Sol. Ener.* **2016**, *132*, 279–293.
32. Blanco, M.J.; Amieva, J.M.; Mancillas, A. The TONATIUH Software Development Project: An Open Source Approach to the Simulation of Solar Concentrating Systems. *Comput. Inf. Eng.* **2005**, *2005*, 157–164.
33. https://www.capstoneturbine.com/products/c30. Capstone Turbine Corporation, Capstone C30 Turbine. https://www.capstoneturbine.com/products/c30, accessed on 2019-11-29.
34. Giostri, A.; Macchi, E. An advanced solution to boost sun-to-electricity efficiency of parabolic dish. *Sol. Ener.* **2016**, *139*, 337–354.
35. Lemmon, E.W.; Huber, M.L.; McLinden, M.O. NIST Standard Reference Database 23: Reference Fluid Thermodynamic and Transport Properties-REFPROP, Version 9.1. National Institute of Standards and Technology, Standard Reference Data Program, Gaithersburg, 2013.
36. Wang, W.; Ragnolo, G.; Aichmayer, L.; Strand, T.; Laumert, B. Integrated design of a hybrid gas turbine-receiver unit for a solar dish system. *Energ. Proc.* **2015**, *69*, 583–592.
37. Ragnolo, G.; Aichmayer, L.; Wang, W.; Strand, T.; Laumert, B. Techonoeconomic design of a micro gas-turbine for a solar dish system. *Ener. Proc.* **2015**, *69*, 1133–1142.
38. Gavagnin, G.; Sánchez, D.; Martínez, G.S.; Rodríguez, J.M.; Muñoz, A. Cost analysis of solar thermal power generators based on parabolic dish and micro gas turbine: Manufacturing, transportation and installation. *App. Ener.* **2017**, *194*, 108–122.
39. Peters, M.S.; Timmerhaus, K.; E., W.R. *Plant design and economics for chemical engineers*, 5th ed.; McGraw-Hill, 2002.
40. Informe de Supervisión del Mercado de Gas Natural en España. Technical Report IS/DE/007/19, Comisión Nacional de los Mercados y la Competencia (CNMC).
41. GREET. The Greenhouse Gases, Regulated Emissions and Energy Use in Transportation Model. Technical report, Argonne National Laboratory, Argonne, IL, 2010.
42. Ragnolo, G. A techno-economic comparison of a micro gas-turbine and a Stirling engine for solar dish application. PhD thesis, KTH School of Industrial Engineering and Management, Energy Technology Department, Stockholm, Sweden, 2013.
43. Lozza, G. *Turbine a gas e cicli combinati*; Esculapio, 2016.
44. https://solargis.com/es/maps-and-gis-data/download/spain. SOLARGIS Solar Resource Maps and GIS data. https://solargis.com/es/maps-and-gis-data/download/spain, accessed on 2019-06-10.
45. http://www.soda-pro.com/web-services/radiation/cams-radiation-service. Copernicus atmosphere monitoring service (ECMWF). http://www.soda-pro.com/web-services/radiation/cams-radiation-service, accessed on 2019-03-01.
46. https://opendata.aemet.es/centrodedescargas/inicio. AEMET OpenData. https://opendata.aemet.es/centrodedescargas/inicio, accessed on 2019-03-01.
47. Emission Factors for Greenhouse Gases. http://www.epa.gov/climateleadership/documents/emission-factors.pdf, accessed on 2020.
48. https://cordis.europa.eu/project/id/308952. OMSoP Report Summary. https://cordis.europa.eu/project/id/308952.

572 49. Ilas, A.; Ralon, P.; Rodriguez, A.; Taylor, M. Renewable Power Generation Costs in 2017. Techreport
573 978-92-9260-040-2, IRENA (International Renewable Energy Agency).

4.2 Thermal Energy Storage

Title: "Techno-Economic Analysis of a Solar Hybrid Combined Cycle Power Plant Integrated with a Packed Bed Storage at Gas Turbine Exhaust"
Journal: *AIP Conference Proceedings*
Authors: Silvia Trevisan, **Rosa P. Merchán**, Rafael Guédez, María J. Santos, Alejandro Medina, Björn Laumert, Antonio Calvo-Hernández
Year: 2020
Conference: SolarPACES 2019
Reference: [133]

Techno-Economic Analysis of a Solar Hybrid Combined Cycle Power Plant Integrated with a Packed Bed Storage at Gas Turbine Exhaust

Silvia Trevisan[1, a)], Rosa P. Merchán[2, 3, b)], Rafael Guédez[1], María J. Santos[2, 3], Alejandro Medina[2, 3], Björn Laumert[1], Antonio Calvo-Hernández[2, 3]

[1]*Department of Energy Technology, KTH Royal Institute of Technology, 100 44 Stockholm, Sweden.*
[2]*Department of Applied Physics, University of Salamanca, 37008 Salamanca, Spain.*
[3]*IUFFYM, University of Salamanca, 37008 Salamanca, Spain.*

[a)] Corresponding author: trevisan@kth.se
[b)] rpmerchan@usal.es

Abstract. The present work performs a techno-economic analysis of an innovative solar-hybrid combined cycle composed of a topping gas turbine coupled to a bottoming packed bed thermal energy storage at the gas turbine exhaust, which runs in parallel to a bottoming steam cycle. Plant performances have been evaluated in terms of the capacity factor, the specific CO_2 emissions, the capital expenditure, and the Levelised Cost of Electricity. The influence of the combustion chamber outlet temperature, solar multiple and energy storage capacity has been assessed by means of a sensitivity analysis. The present study also compares the previously listed performance against that of conventional molten salt tower Concentrating Solar Power plants and traditional combined cycle gas turbine power plants with equivalent installed capacities and load factors. The results show that it is worth hybridizing the system, particularly at high combustion chamber outlet temperature, large storage size and solar multiple. Furthermore, plant configurations leading to a Levelised Cost of Electricity lower than 110 $/MWh can be achieved for a capacity factor of about 60%. Under these working conditions, the proposed configuration would be only 1.66 times more costly than an equivalent size CCGT. At the same time, it would yield less than half of the emissions of the latter. Simultaneously, the proposed layout is considerably cheaper than an equivalent molten salt Concentrating Solar Power plant.

INTRODUCTION

The introduction of more advanced power cycles with higher conversion efficiencies has been identified as one of the key alternatives for enhancing the economic viability, and the flexibility, of Concentrated Solar Power (CSP) plants. This paper performs a techno-economic assessment of an innovative solar-hybrid combined cycle composed of a topping solar-hybrid gas turbine (GT) coupled to a bottoming packed bed TES at the GT exhaust, which runs in parallel also to a traditional bottoming steam cycle. The plant layout itself is shown in Fig. 1 and is similar to the Sunspot cycle introduced by Harper et al. [1], but in this study the focus is placed on larger installed capacities (300MWe instead of 120MWe). Furthermore, a sensitivity analysis of key design variables such as the temperature at the outlet of the combustion chamber (TCC), the Thermal Energy Storage (TES) size, the Solar Multiple (SM), and the nominal power ratio between the gas and steam cycle (γ) is performed. In this first assessment, the selected indicators for evaluating the performance have been the Levelized Cost of Electricity (LCoE), the specific CO_2 emissions, the Capacity Factor (CF), net electrical energy produced and the thermal wasted energy. The study also compares such performance against that of conventional molten salt tower CSP plants (STCSP) and traditional combined cycle gas turbine (CCGT) power plants with equivalent installed capacities and load factors. As expected, it is shown that despite being more costly than conventional CCGTs, and less environmentally friendly than purely solar driven tower CSP plants, best configurations of the proposed layout can result in an attractive compromise of

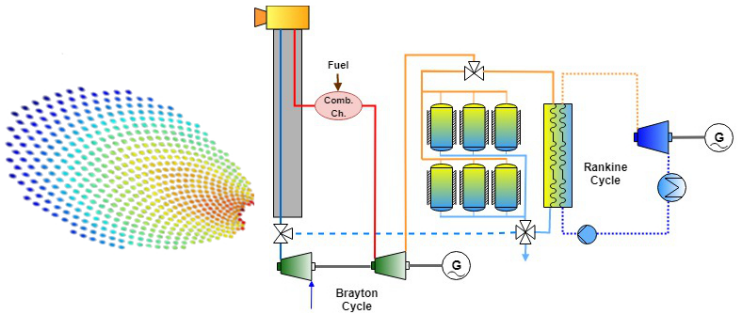

FIGURE 1. Scheme of the studied hybrid solar combined cycle plant.

both. Ultimately, the authors consider that the value of decoupling the topping and bottoming cycles through an intermediate TES would be more appreciated in techno-economic optimization studies coupled to TES dispatch optimization algorithms under hourly price variations or load profile demands. The flexibility of the proposed layout is expected to lead to attractive solutions for flexible energy generation at a reduced environmental cost, ahead of equivalent STCSPs or CCGTs plants. This work intends to be a stepping stone in such comparative analysis. Although it is focused towards a stable electricity production during the central hours of the day and a baseline smaller production during the rest of the day, results could be extrapolated to other particular dispatch objectives.

SYSTEM CONFIGURATION

The present work introduces a 300 MWe solar-hybrid combined cycle composed of a topping solar-hybrid gas turbine (GT) coupled to a traditional bottoming steam cycle and a packed bed TES at the GT exhaust. The plant scheme is shown in Fig.1. During the day, when the incoming solar radiation is higher than a minimum value, the air entering the system at ambient conditions is compressed up to 15 bar in the Brayton cycle compressor and heated up to 800°C in the receiver (REC). As Direct Normal Irradiance (DNI) changes in each time step, GT mass flow in the receiver varies accordingly in order to reach that 800°C temperature. To fully exploit the Brayton cycle, the air temperature is raised by means of a combustion chamber up to 1200°C, design GT inlet temperature. The air is then expanded in the GT and exits at approximately 580°C and ambient pressure. At GT exhaust, the air is partially sent to the heat recovery steam generator (HRSG), where superheated steam is produced (at nominal load conditions), and to a parallel set of packed bed TES units where heat is stored in order to extend the bottoming cycle production after sun hours or during cloudy periods. Therefore, during night time, air is ventilated through the TES unit and then sent to the HRSG where superheated steam is generated. Hence, ST mass flow is kept constant when DNI is higher than the minimum value and it slowly decreases during discharge of TES.

Control Logic

In order to operate the CSP plant, a control logic has been built considering a deterministic operating regime, also identified as one of the limitations to further investigate by means of introducing a dispatch optimizer in a subsequent study. Thus, the control of the plant has been designed such as to allow the GT to produce whenever there is enough energy from the solar field, and to let the bottoming cycle operate continuously – as long as there is energy in the TES. Depending on the actual Direct Normal Irradiance (DNI) and TES State of the Charge (SoC), evaluated at each time step, five different operation modes (OMs) can be identified. The control logic associated flow chart is shown in Fig. 2, while Table 1 defines the main implications of each operational mode in the plant control. During daylight, when the solar input alone is sufficiently high to cover the steam cycle design heat load ($DNI > DNI_{min_{ST}}$), the GT runs at a load that mirrors the DNI trend. Furthermore, if the TES SoC is lower than SoC_{max}, the mass flow at GT outlet is divided into two streams: one constant mass flow performs the Rankine cycle at on-design conditions; meanwhile, the other one, which inherits the time variation, charges the TES (OM1). If the TES units are already full, the excess of thermal power at the GT outlet is wasted and the Steam Turbine (ST) continues working at design conditions (OM2).

On the other side, when the solar input is not sufficient for running the ST, the TES units are discharged extending the CSP plant power production as long as the SoC remains above a minimum level (SOC_{min}). Specifically, the design air stream goes through the TES increasing its temperature and, then, it performs the Rankine cycle at off-design conditions since the TES outflow temperature and consequently the ST inlet temperature decreases as the storage units are being discharged (OM3). When SoC falls below the minimum level, TES is considered as empty, so there is no power production at all (OM4). It can also occur that during the early mornings the DNI is lower than the minimum threshold and the TES empty, in such a situation the GT works a low partial load from solar energy, while the ST is still shut off as the solar irradiance is not high enough for its ST start-up (OM 5). Instead, when a similar DNI pattern occurs during the late evening, with the TES at least partially charged, OM3 is preferred in order to operate the ST and limits the GT operation at low load conditions. The whole control strategy has been implemented together with plant layout in TRNSYS® software with the objective of performing dynamic simulations, as it is explained in Methodology section.

TABLE 1. Operational Modes (OM) main implications in CSP plant control

OM	GT	ST	REC	TES
1	ON	ON: Design	ON	Charge
2	ON	ON: Design	ON	Full
3	OFF	ON: Off-Design	OFF	Discharge
4	OFF	OFF	OFF	Empty
5	ON	OFF	ON	Empty

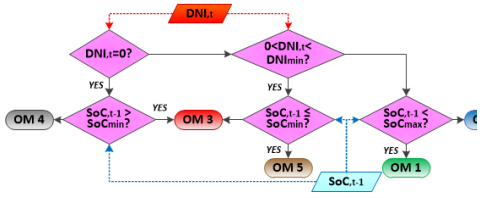

FIGURE 2. Control strategy flowchart of the proposed layou

Economic Model

In the present work the capital investment (CAPEX) and the LCoE have been chosen as the main economic indicators in order to measure both the investment and the relative profitability of the studied hybrid CSP plant. The CAPEX has been calculated by adding the direct cost for all the main specific components (Brayton and Rankine cycle turbomachinery, combustion chamber, HRSG, condenser, electrical generators, heliostat field and land, tower, receiver, TES, and auxiliaries) and indirect cost (engineering, procurement and construction, taxes and decommissioning). The cost of the Brayton and Rankine cycle components and relative auxiliaries have been calculated according to the scaling function presented in [2]. In order to consider the effects of inflation, all scaling functions have been multiplied by the ratio between the reference Marshall & Swift index for 2018 and the one for the year of the publication when the cost function was proposed, $f_{infl}^{ref} = M\&S_{2018}/M\&S_{ref}$. The reference Marshall & Swift indexes have been gathered from [3]. The cost for the heliostat field has been evaluated by means of the cost functions proposed in [4], while the tower cost has been calculated based on the functions proposed in [2]. The air receiver cost (C_{REC}) has been based on the values proposed by Schwarzbözl *et al.* [5], the specific costs suggested for low, medium and high temperature receiver have been linearly fitted obtaining Eq. (1), where A_{REC} and T_{REC} account for the receiver area and temperature, respectively.

$$C_{REC} = f_{infl}^{2006}\left[A_{REC}[m^2]\left(79\left[\frac{USD}{m^2{}^{\circ}C}\right]T_{REC}[^{\circ}C] - 20833\left[\frac{USD}{m^2}\right]\right)\right] \quad (1)$$

A more detailed approach has been followed to evaluate the cost of the storage units. Indeed, the overall TES cost has been calculated by adding the cost of the filler material (natural rocks), high and low temperature insulation, TES tank main material (MA253 Steel) and foundation accordingly to the specific prices reported in Table 2. The remaining cost components have been evaluated thanks to the data and approach presented in [2].

TABLE 2. Specific costs of TES main components.

Rocks [$/m^3]	66
High Temperature Insulation [$/m^3]	4’269
Low Temperature Insulation [$/m^3]	616
MA253 Steel [$/m^3]	42’354
Foundation [$/m^2]	1’210

Furthermore, the operational cost (OPEX) has been evaluated including the cost of required fuel assumed as natural gas (NG), CO_2 emissions, O&M, contracts and administration. For the NG, a fixed price has been assumed, equal to 0.142 \$/kg_{NG}; while for the CO_2 emissions an allowance of 0.0284 \$/kg_{CO2} has been considered. Finally, the LCoE is calculated by means of Eq. (2) as function of the annualized CAPEX and decommissioning cost, annual OPEX and net annual energy production E_{NET}. The initial investment, CAPEX, and the decommissioning cost, C_{Decom}, are translated into equivalent annual payments thanks to the two factors α and β, which are defined in Eq. (3) and (4), where i is the real debt interest rate, k_{ins} is the annual insurance rate, assumed equal to 7% and 1% respectively. While, n_{op} is the plant lifetime, n_{con} is the plant construction time and n_{cdec} is the plant decommissioning time, equal to 30, 2 and 2 years respectively.

$$LCoE = \frac{\alpha \cdot CAPEX + \beta \cdot C_{Decom} + OPEX}{E_{NET}} \tag{2}$$

$$\alpha = \frac{(1+i)^{n_{con}} - 1}{n_{con} \cdot i} \cdot \frac{i \cdot (1+i)^{n_{op}}}{(1+i)^{n_{op}} - 1} + k_{ins} \tag{3}$$

$$\beta = \frac{(1+i)^{n_{dec}} - 1}{n_{dec} \cdot i(1+i)^{n_{dec}-1}} \cdot \frac{i}{(1+i)^{n_{op}} - 1} \tag{4}$$

METHODOLOGY

In order to study the thermo-economic performance of the proposed hybrid CSP plant, different interconnected models have been built:

- A steady state thermodynamic CSP plant model to evaluate design working conditions and some design input value for the different components
- A System Advisor Model (SAM) model for simulating the heliostats solar field and for obtaining the solar field efficiency matrixes at different SM
- A transient TRNSYS model, with integrated control logic and meteorological data gathered from Meteonorm database, where annual simulations have been performed
- An economic model, in MatLab scripts, to evaluate all costs functions and overall plant Key Performance Indicators (KPIs)

At last, sensitivity analysis with regards to the desired outlet temperature from the combustion chamber (TCC), the TES size, the SM, and the nominal power ratio between the gas and steam cycle (γ) were performed. This last power ratio is defined just as the proportion of GT power (P_{GT}) over ST power (P_{ST}) at design: $\gamma = \frac{P_{GT}}{P_{ST}}$. Besides the LCoE, other indicators considered were the specific emissions, the net energy production, the wasted or defocused energy and the capacity factor (CF), evaluated as in Eq. (5), where h_{TES} corresponds to the TES size (in number of hours).

$$CF = \frac{E_{NET}}{[P_{GT} \cdot (24 - h_{TES}) + P_{ST} \cdot 24] \cdot 365} \tag{5}$$

The previously listed four input parameters were considered because they constitute the most interesting and valuable variables for the sensitivity analysis. Outlet temperature of the combustion chamber was chosen for the sensitivity analysis since it establishes inlet gas turbine temperature (so, Brayton efficiency) and also since it is directly related to the hybridization level of the plant, namely to the fuel consumption. Therefore, this parameter will be crucial for trade-off between lower hybridization level and higher efficiency. Furthermore, TES size refers to the amount of stored energy, which is one of the two heat sources for Rankine cycle. Thus, it turns out to be critical for steam turbine production and therefore to enhance the capacity factor and extend the production during night-time. The third analyzed parameter is the Solar Multiple (SM), associated with solar field size, which is decisive for the design of the plant since it determines the heliostat field size, so the collected power in the receiver and consequently the receiver air mass flow. Finally, gas turbine to steam turbine power ratio (γ) is studied, provided that total design power remains the same. The effect of this ratio is related to both design GT and ST mass flows. For the sensitivity analysis, the four aforementioned parameters were varied up and down around the base case values in the parameters ranges collected at Table 3. TCC is fixed at 1200°C for the base case. Solar receiver heats up air mass flow up to 800°C, so 800°C was also chosen as lower limit value for TCC with the purpose of reproducing plant behavior in pure solar mode, without combustion chamber necessity. The Gas Turbine to Steam Turbine power ratio (γ) is only computed for two values

around the base case for preserving feasible and realistic values while presenting significant effects on output variables.

TABLE 3. Parameters ranges for the sensitivity analysis.

Parameters	TCC	TES size	SM	γ
Base case	1200 °C	8 h	1.5	5
Range	800 °C – 1400 °C	4 h – 12 h	1 – 2	3 – 9
Step	100 °C	2 h	0.25	-

RESULTS AND DISCUSSION

CSP Plant Performance – Design Case

The studied CSP plant was located in Seville, Spain (37.39°N, -5.99°E). The evolution of main results with time is plotted for the base case as an example for the first of July in Fig. 3. Where GT and ST power represent the net electrical power produced; while the thermal wasted power is the sum of the power wasted at the TES outlet during OM1, the curtailed one during OM5 and the remaining power at the economizer hot side outlet during OM1, OM2 and OM3. GT is only working when DNI is higher than the minimum value (OM 1 and OM 2), as it was imposed in TRNSYS logic control. Nevertheless, ST is also producing electricity when Sun goes down, extending number of generating hours and so the capacity factor. During the initial hours of the day, plant is stopped (OM4), until DNI is higher than the minimum value, when OM 1 starts. Afterwards, if TES is full, OM 2 is established and, finally, when DNI becomes zero again, plant is under OM 3. There is an intermediate state between OM 4 and OM 1, when ST has not started to run, which is denominated OM 5. SOC is always between 0.1 and 0.95, it is never allowed to reach 0 or 1 for stability reasons. The emission of CO_2 is higher around central hours of the day, when DNI is maximum, since the associated air mass flow is higher and, so, the fuel consumption. It is worth noting that during the second part of

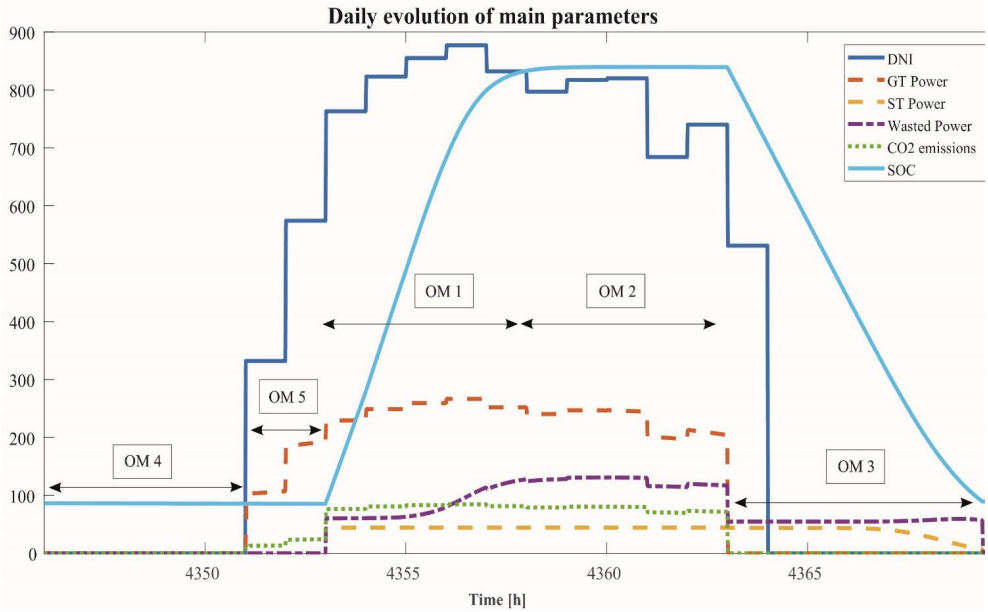

FIGURE 3. Daily evolution of main variables during 1st July (in number of hours from the start of the year) for the base case

OM 1 the wasted power gradually increases due to the increase of the TES outlet temperature when the thermocline is discharged. Similarly, during the second half of OM 3 the ST power decreases due to the partial thermocline discharge and the consequent TES outflow temperature drop.

For the year-round simulation, the net energy produced is 613.20 GWh_e, meanwhile the wasted thermal energy is 222.567 GWh_{th} (see data in Table 5). Specifically, the main component of the latter thermal energy wasted is represented by the remaining thermal power at the economizer hot side outlet. The higher the OM 1 share to the total hours, the better performance and design of the plant. According to results in Table 4, OM4 share should be reduced in order to increase CF. OM 1 share is higher than OM 2 and OM 3, so the initial design works for the whole year. With respect to CAPEX and OPEX, Fig. 4 shows the distribution of costs. For the capital investment, the field costs are the major ones, although plant installation and civil engineering represent together a big part of expenditure too. Meanwhile, in the OPEX case, the maintenance is the most expensive factor, followed by the fuel costs, since it includes costs associated with maintenance of the receiver and gas piping, mirror breakage, field control systems, ground keeping or mirror washing. In addition, expenses related to CO_2 emissions have been also taken into account and result to be the third ones in order of importance.

TABLE 4. Operating Modes shares for the annual simulation and for the base case.

OM	OM 1	OM 2	OM 3	OM 4	OM 5
Share (%)	18.32	6.36	10.01	45.36	19.96

TABLE 5. Net annual energy and wasted energy for the sensitivity analysis. * Base case for SM. ** Regular base case.

SM [-]	Net Energy [GWh_e]	Wasted Energy [GWh_{th}]	TES size [h]	Net Energy [GWh_e]	Wasted Energy [GWh_{th}]
1	546.588	174.584	4	593.407	290.395
1.25	665.725	199.976	6	602.012	240.264
1.5 *	788.224	225.444	8 **	613.197	222.567
1.75	906.222	249.712	10	618.680	219.668
2	1042.897	275.200	12	625.336	221.290
TCC [°C]	**Net Energy [GWh_e]**	**Wasted Energy [GWh_{th}]**	**γ [-]**	**Net Energy [GWh_e]**	**Wasted Energy [GWh_{th}]**
800	436.762	308.384	3	643.873	266.750
900	433.823	215.020	5 **	613.197	222.567
1000	433.335	300.268	9	658.410	199.945
1100	501.952	324.685			
1200 **	613.197	222.567			
1300	723.407	361.302			
1400	838.168	383.061			

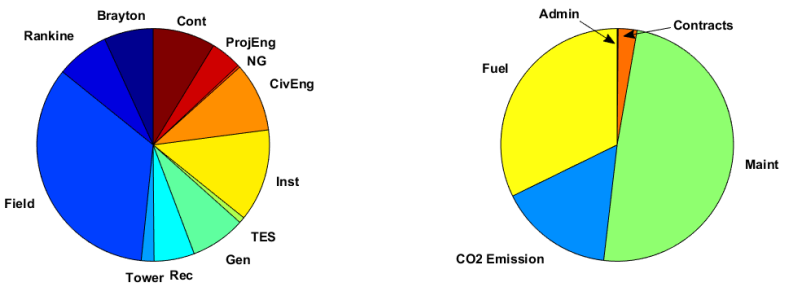

FIGURE 4. CAPEX (left) and OPEX (right) share for the base case

Sensitivity Analysis

The main results for the sensitivity analysis are reported in Fig. 5 and Table 5. The results show that an increase of TCC will lead to an increase of the Capacity Factor in the analyzed temperature range (Fig. 5 top left). Specifically, the CF remains almost constant for a TCC up to 1000°C, while for higher TCC a clear enhancement of the CF can be achieved. Thus, hybridization would be interesting for high TCC though this leads to higher CO_2 emissions. On the other hand, the LCoE trend displays a maximum for a TCC of 1000°C and a minimum for a TCC of 1300°C, showing that for assumed gas costs it is worth hybridizing the system. The variation of the TES size has a pretty clear relative influence on the final plant KPIs. With increasing TES size, the LCoE decreases, while the CF increases, as it was expected, and as it can observed in Fig. 5 (top right). This capacity factor increment is related also to a net energy rise. In addition, bigger TES leads to positive results in terms of reduction of wasted energy and CO_2 emissions. The results show that an increase of SM will lead to an increase of the Capacity Factor and a decrease of the LCoE in the analyzed range (Fig. 5 bottom left). As expected, a larger SM enables to store more energy in the TES during daytime and consequently to extend longer the power production during night, achieving higher CF. In this case, the improvement in the net electrical energy production is well enough to compensate for the increase in the required initial expenditure, leading to lower LCoE. A different trend can be identified considered the specific emissions, indeed a maximum is recorded for SM equal to 1.25, while for larger SM a decrease in the specific CO_2 emission is achieved. As a last input (Fig. 5 bottom right), increasing power ratio between the gas and steam cycle (γ) leads to higher specific emissions and CF. Indeed, a larger GT would require more fuel but it will also increase the power production during daytime.

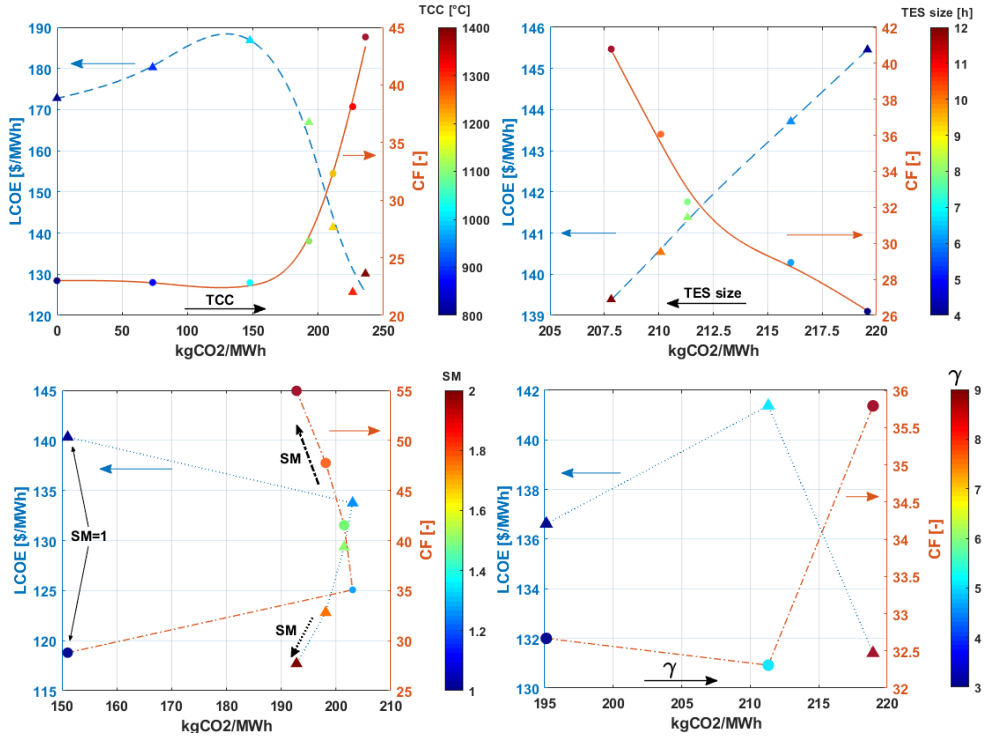

FIGURE 5. LCoE and Capacity Factor vs specific CO_2 emissions for a variable TCC (top left), for a variable TES size (top right), for variable SM (bottom left), and for a variable GT-ST power ratio, γ (bottom right)

Instead a maximum trend can be recorded for the LCoE, indeed both studied GT to ST ratios enable lower LCoE and higher net energy production. The study shows that LCoE figures lower than 120 $/MWh and capacity factors of about 55% can be achieved. Interestingly, the comparative analysis shown in Table 6 reveals that at such capacity factor the proposed configuration is only about two times more costly than an equivalent size CCGT, but at the same time yielding less than half of the emissions of the latter. Simultaneously, the proposed layout is considerably cheaper than an equivalent molten salt CSP plant. The analysis performed thus far reveals that the cycle is then worth continuing to explore, especially when considering the value of generation in time and when integrating a dispatch optimizer.

TABLE 6. Comparison between different electricity plants at 55% Capacity Factor.

	Hybrid TES CSP	**Molten salts CSP [6]**	**Conventional CCGT**
Emissions ($kgCO_2/MWh$)	192.78	0	464.91
LCoE ($/MWh)	117.69	137	54.01

CONCLUSIONS

In this work a techno-economic assessment of an innovative solar-hybrid combined cycle has been performed. The studied plant is composed of a topping solar-hybrid gas turbine coupled to a bottoming packed bed thermal energy storage at the gas turbine exhaust, which runs in parallel also to a traditional bottoming steam cycle. In order to evaluate the plant performances, the following KPIs have been analyzed: capacity factor, specific CO_2 emissions, capital expenditure, and Levelised Cost of Electricity. The combustion chamber outlet temperature, solar multiple and energy storage capacity has been considered as decisional variables in the performed sensitivity analysis. The techno-economic performance of the proposed plant has been compared against that of more conventional molten salt tower CSP plants and traditional combined cycle gas turbine power plants with equivalent installed capacities and load factors. The results show that capacity factor enhancement and consequent LCoE reduction would be enabled by high TCC, large TES size and large SM. Higher storage capacity and wider heliostat field seem to be a viable design choice as they lead to specific CO_2 emission reduction. Conversely, a trade-off can be identified between improvements in CF and LCoE and specific emissions while looking at the TCC. Moreover, for a capacity factor of about 55%, proposed plant configurations are associated with a Levelised Cost of Electricity lower than 120 $/MWh. Under these working conditions, the suggested layout would be only about two times more costly than an equivalent size CCGT, although it will produce less than half of the emissions of the latter. At the same time, the proposed configuration is considerably cheaper than an equivalent molten salt CSP plant. Finally, the analysis performed thus far reveals that the cycle is worth continuing to explore, especially when considering the value of generation in time and when integrating a dispatch optimizer. Therefore, the authors would like to remark the value of decoupling the topping and bottoming cycles through an intermediate TES, which could be important in the framework of techno-economic optimization studies focused to flexible energy production and dispatch. Its capability even to account for hourly price variations or load profile demands is a suggesting work for the future.

ACKNOWLEDGMENTS

Financial support from University of Salamanca, Junta de Castilla y León of Spain under grant no. SA017P17, Banco Santander and Swedish Energy Agency and Azelio AB through the Energy Agency program Electricity from the Sun, project P43284-1 are acknowledged.

REFERENCES

1. P. J. Harper, T. W. Von Backström, T. P. Fluri and D. G. Kröger, “TRNSYS modeling of a 100 MWe hybrid combined cycle concentrating solar power plant”, 1st Southern African Solar Energy Conference (SASEC, 2012).
2. J. D. Spelling, “Hybrid Solar Gas-Turbine Power Plants. A Thermoeconomic Analysis”, Ph.D. thesis, KTH Royal Institute of Technology, 2013. ISBN 978-91-7501-704-4.
3. Marshall Swift Valuation Services, “Report-Inventory Index Factors” (January 2018).
4. J. B. Blackmon, Conc. Sol. Power Technol. Princ. Dev. Appl., 536–576 (2012). “Heliostat size optimization for central receiver solar power plants”, doi:10.1016/B978-1-84569-769-3.50017-0.
5. P. Schwarzbözl, R. Buck, C. Sugarmen, A. Ring, M. J. Marcos Crespo, P. Altwegg and J. Enrile, Sol. Energy 80, 1231-1240 (2005). “Solar gas turbine systems: Design, cost and perspectives”, doi:10.1016/j.solener.2005.09.007.
C. Turchi, M. Mebos, C. K. Ho and G. J. Kolb, “Current and Future Costs for Parabolic Trough and Power Systems in the US Market”, presented at SolarPACES2010, (Perpignan, France, October 2010).

4.3 Conference articles

Other conference articles related and unrelated to the doctoral thesis are outlined here. Bold letters are employed for highlighting doctoral thesis author's contribution and underlined ones for standing out presenter.

- *XXXV Reunión Bienal de la Real Sociedad Española de Física* (Gijón, Spain, 13/07/2015-17/07/2015). ISBN 978-84-606-9611-7.
  - M. J. Santos, **R.P. Merchán**, A. Medina, A. Calvo. "Simulación termodinámica de una planta termosolar híbrida tipo Brayton". Oral presentation.
- *The International Conference on Renewable Energies and Power Quality (ICREPQ16)* (Madrid, Spain, 04/05/2016-06/05/2016). ISBN 978-84-608-5473-9.
  - **R.P. Merchán**, M.J. Santos, A. Medina and A. Calvo. "Thermodynamic Simulation of a Hybrid Brayton Thermosolar Plant". Oral presentation.
- *29th International Conference on Efficiency, Cost, Optimization, Simulation and Environmental Impact on Energy Systems (ECOS 2016)* (Portorož, Slovenia, 19/06/2016-23/06/2016). ISBN 978-961-6980-15-9.
  - **R.P. Merchán**, M.J. Santos, A. Medina and A. Calvo Hernández. "Thermodynamic Model of a Hybrid Brayton Thermosolar Plant". Oral presentation.
- *12th International Conference on Heat Transfer, Fluid Mechanics and Thermodynamics (HEFAT16)* (Málaga, Spain, 11/07/2016-13/07/2016).
  - **R.P. Merchán**, M.J. Santos, A. Medina and A. Calvo Hernández. "Annual Performance Prediction of a Hybrid Brayton Thermosolar Plant". Oral presentation.
- *The International Conference on Renewable Energies and Power Quality (ICREPQ17)* (Málaga, Spain, 04/04/2017-06/04/2017). ISBN 978-84-617-8076-1.
  - **R.P. Merchán**, M.J. Santos, A. Medina and A. Calvo Hernández. "Parametric analysis of thermal losses on hybrid solar gas-turbine power plants". Poster.
  - C. Miguel, **R.P. Merchán**, M.J. Santos, A. Calvo Hernández, and A. Medina. "Multistage configurations for hybrid thermosolar gas turbine power plants". Poster.
- *10th Congreso Internacional de Ingeniería Termodinámica (10CNIT)* (Lleida, Spain, 28/06/2017-30/06/2017).
  - César Miguel, **Rosa P. Merchán**, María Jesús Santos, Antonio Calvo Hernández, and Alejandro Medina. "A thermodynamic model for a hybrid multistage Brayton thermosolar plant". Oral presentation.
- *30th International Conference on Efficiency, Cost, Optimization, Simulation and Environmental Impact on Energy Systems (ECOS 2017)* (San Diego, USA, 02/07/2017-06/07/2017).

- **R.P. Merchán**, M.J. Santos, A. Medina and A. Calvo Hernández. "Thermodynamic Modelling of the Annual Performance of a Hybrid Thermosolar Brayton Plant". Oral presentation.

- *XXXVI Reunión Bienal de la Real Sociedad Española de Física* (Santiago de Compostela, Spain, 17/07/2017-21/07/2017). ISBN 13 978-84-09-01780-5.
  - **R.P. Merchán**, M.J. Santos, A. Medina, A. Calvo Hernández. "Centrales termosolares Brayton híbridas: predicción termodinámica de eficiencias anuales y emisiones". Oral presentation.
- *The International Conference on Renewable Energies and Power Quality (ICREPQ18)* (Salamanca, Spain, 21/03/2018-23/03/2018).
  - M.J. Santos, C. Miguel-Barbero, **R.P. Merchán**, A. Medina, and A. Calvo Hernández. "Working fluid effects on the performance of hybrid Brayton thermosolar plants". Oral presentation.
  - M.J. Santos, E. Vega-Lozano, **R.P. Merchán**, J. García-Ferrero, A. Medina and A. Calvo Hernández. "Micro Gas Turbine and Solar Parabolic Dish for distributed generation". Oral presentation.
- *I Jornadas de Jóvenes Investigadores INNOVA Salamanca* (Salamanca, Spain, 04/05/2018-05/05/2018).
  - **R.P. Merchán**, M.J. Santos, A. Medina and A. Calvo Hernández. "Pressure ratio analysis of a hybrid Brayton solar thermal plant". Oral presentation.
- *31st International Conference on Efficiency, Cost, Optimization, Simulation and Environmental Impact on Energy Systems (ECOS 2018)* (Guimarães, Portugal, 17/06/2018-21/06/2018).
  - **R.P. Merchán**, M.J. Santos, A. Medina and A. Calvo. "Multistage Configurations for Central Receiver Hybrid Gas-Turbine Thermosolar Plants". Oral presentation.
  - María Jesús Santos, Judit García-Ferrero, **Rosa Merchán**, Alejandro Medina and Antonio Calvo-Hernández. "Distributed generation: Thermodynamic model for a solar-dish micro-gas turbine system". Oral presentation.
- *XVI Congreso Ibérico* and *XII Congreso Iberoamericano de Energía Solar (CIES 2018)* (Madrid, Spain, 20/06/2018-22/06/2018).
  - Irene Heras, María Jesús Santos, **Rosa Merchán**, Judit García-Ferrero, Alejandro Medina and Antonio Calvo-Hernández. "Evaluación del rendimiento de una planta híbrida de concentración termosolar de disco parabólico con ciclo Brayton para generación distribuida". Poster.
- *XVI Encuentro Inter-Bienal del Grupo Especializado de Termodinámica (GET) (TERMO 2018)* (Oleiros, Spain, 16/09/2018-18/09/2018).

- A. Calvo Hernández, **R. P. Merchán**, M. J. Santos, C. Miguel and A. Medina. "Configuraciones multietapa para diferentes fluidos de trabajo en plantas termosolares híbridas". Oral presentation.

- *Solar Power and Chemical Energy Systems Conference 2018 (SolarPACES18)* (Casablanca, Morocco, 02/10/2018-05/10/2018).
  - **Rosa P. Merchán**, Alejandro Medina, María Jesús Santos, Irene Heras, José Miguel M. Roco and Antonio Calvo-Hernández. "Towards a more efficient generation of central tower hybrid thermosolar gas turbine power plants". Oral presentation. AIP Conference Proceedings 2126, 140004 (2019).
  - I. Heras, M. J. Santos, **R. P. Merchán**, J. García-Ferrero, A. Medina, and A. Calvo-Hernández. "Hybrid thermosolar and micro gas turbine power plant for distributed generation: thermoeconomic evaluation". Oral presentation.
- *15th Joint European Thermodynamics Conference (JET 2019)* (Barcelona, Spain, 20/05/2019-24/05/2019).
  - Julián González-Ayala, **Rosa Merchán**, Irene Heras, Juncheng Guo, J.M.M Roco, Alejandro Medina, Antonio Calvo Hernández. "Thermodynamic self-improvement in the stability of a low dissipative refrigerator engine". Oral presentation.
- *32nd International Conference on Efficiency, Cost, Optimization, Simulation and Environmental Impact of Energy Systems (ECOS 2019)* (Wroclaw, Poland, 23/06/2019-28/06/2019).
  - **R. P. Merchán**, M. J. Santos, A. Medina, I. Heras, and A. Calvo Hernández. "On-design and off-design thermodynamic analysis of a hybrid multi-stage solar thermal tower power plant". Oral presentation.
  - Irene Heras, Judit García-Ferrero, María Jesús Santos, **Rosa Pilar Merchán**, Alejandro Medina, and Antonio Calvo-Hernández. "Thermo-economic study of hybrid parabolic dish solar power plants in different regions of Spain". Oral presentation.
- *XXXVII Reunión Bienal de la Real Sociedad Española de Física* (Zaragoza, Spain, 15/07/2019-19/07/2019).
  - **R. P. Merchán**, M. J. Santos, A. Medina, I. Heras, J. González-Ayala, and A. Calvo Hernández. "Towards more efficient central tower gas turbine thermosolar plant". Oral presentation.
  - J. García-Ferrero, I. Heras, **R. P. Merchán**, M. J. Santos, A. Medina, J. González-Ayala, and A. Calvo Hernández. "Distributed energy: the challenge of solar parabolic dishes". Oral presentation.
- *II Jornadas de Jóvenes Investigadores INNOVA-Salamanca* (Salamanca, Spain, 26/09/

2019-27/09/2019).

- **Rosa Pilar Merchán Corral**, María Jesús Santos Sánchez, Alejandro Medina Domínguez, Irene Heras Pérez, and Antonio Calvo Hernández. "Heliostats field for a hybrid Brayton concentrated solar power plant". Oral presentation.
- J. García-Ferrero, I. Heras, **R.P. Merchán**, M.J. Santos, A. Medina, J. González-Ayala, A. Calvo Hernández. "Distributed energy: the challenge of solar parabolic dishes". Oral presentation.

- *Solar Power and Chemical Energy Systems Conference 2019 (SolarPACES19)* (Daegu, South Korea, 01/10/2019-04/10/2019).
  - Silvia Trevisan, **Rosa P. Merchán**, Rafael Guédez, María J. Santos, Alejandro Medina, Björn Laumert, Antonio Calvo-Hernández. "Techno-Economic Analysis of a Solar Hybrid Combined Cycle Power Plant Integrated with a Packed Bed Storage at Gas Turbine Exhaust". Oral presentation.
  - Irene Heras, Judit García-Ferrero, María J. Santos, **Rosa P. Merchán**, Alejandro Medina, and Antonio Calvo-Hernández. "Hybrid parabolic-type thermosolar gas-turbine power plants: working fluid analysis". Oral presentation.
- *33rd International Conference on Efficiency, Cost, Optimization, Simulation and Environmental Impact of Energy Systems (ECOS 2020)* (Osaka, Japan, 29/06/2020-03/07/2020).
  - **R. P. Merchán**, M. J. Santos, J. García-Ferrero, A. Medina and A. Calvo Hernández. "Thermo-economic analysis of a central tower hybrid Brayton thermosolar plant". Accepted oral presentation, but cancelled in-situ conference due to Covid-19 pandemic.
  - Judit García-Ferrero, **Rosa P. Merchán**, María Jesús Santos, Alejandro Medina, and Antonio Calvo Hernández. "Thermosolar hybrid parabolic dishes running a Brayton-like cycle and fueled with biogas". Accepted oral presentation, but cancelled in-situ conference due to Covid-19 pandemic.

Chapter 5. Conclusions

In this final Chapter, main general conclusions obtained from the accomplishment of this doctoral thesis are presented. Afterwards, some open prospects for future work are also mentioned.

5.1 Conclusions

In this doctoral thesis, a comprehensive study of a Solar Power Tower coupled to a hybrid Brayton cycle has been accomplished. The literature review performed in the Introduction showed that there is a certain lack of studies coupling all plant subsystems and evaluating intra- and inter-influence among them. Therefore, analyses of this kind of plant focusing on subsystems integration have been conducted.

1. First, a theoretical model for a Solar Power Tower coupled to a hybrid gas turbine has been developed:
   - Theoretical model includes submodels for three main subsystems (solar field and receiver, combustion chamber and heat engine) and a general description integrating all of them. Thermo-economic approach has been addressed too.
   - Optical heliostat field efficiency has been computed in detail.
   - Heat engine model includes multi-stage and recuperative / non-recuperative layouts feature. Temperature dependent specific heats were considered.
   - Model is simple, flexible and described by means of a reduced number of input parameters, with a clear physical meaning.
   - Model allows for an easy handling of plant output variables.
2. After model development, its implementation in an in-house developed code, which has been programmed in Mathematica® language, has been succesfully caried out.
   - Proposed model has been applied to two different kinds of plants. First, to a

SOLUGAS-like plant with a power scale of about 5 MW and a polar field. And afterwards, to a plant similar to *GEMASOLAR* with a larger power scale of about 20 MW and a surround field.

- Real meteorological data of the considered location, such as direct normal irradiance and ambient temperature, were employed.
- Four different working fluids were implemented in the code: dry air, nitrogen and carbon dioxide working at subcritical conditions and helium performing a transcritical cycle.

3. Proposed implemented model has been validated within a mixed framework.
    - Gas turbine model has been validated both by employing a commercial software (Thermoflex®) and by comparing model outputs with literature data. Data agreement demonstrated a proper gas turbine validation.
    - Next, solar subsystem model comparison has been conducted employing literature data and via *campo* code software.
    - Levelised Cost of Electricity (LCoE) estimations were contextualized within literature data from different sorts of plants.
    - Lastly, predictions for the overall model were addressed and were shown to be comparable to published data for a similar plant.
4. Finally, significant results have been obtained from performed simulations. Input parameters like pressure ratio, fixed turbine inlet temperature or solar design parameters have been assessed. On the other hand, output variables such as overall efficiency, subsystems efficiencies, solar share, power output, fuel consumption and greenhouse effect emissions, cycle temperatures and Levelised Cost of Electricity have been surveyed.
    - First, simulations at design conditions were carried out. Pressure ratio has been demonstrated to have a significant influence on heat engine efficiency and on overall plant efficiency.
    - Due to the flexibility of the model, dynamic simulations at off-design conditions were also performed with daily, seasonal and annual approaches. Daily analyses showed that direct normal irradiance fluctuations are counteracted thanks to gas turbine hybridisation, which is translated into a stable power output, one of the main desired plant objectives. Additionally, an ambient temperature rise has been proven to be followed by a decrement in power output. Regarding average heliostat field efficiency, a different seasonal behaviour has been found for the *SOLUGAS*-like plant than for the plant similar to *GEMASOLAR*. Moreover, seasonal variations were reflected on the width and on the height of output variables daily curves, such as efficiencies and temperatures. A reduction in fuel consumption of about

the half has been accomplished when a recuperator is included in plant layout. Furthermore, annual losses evaluation assessed energy losses impact on overall plant and subsystems, in other words, it allowed to locate main plant efficiency bottlenecks. Along these lines, a significant outcome was that lower losses on heat engine led to the highest improvements on studied output records.

- Several working fluids, different number of compresion and expansion stages, and recuperative / non-recuperative layouts were tested. The curves of fuel conversion rate with pressure ratio changed their evolution when scaling up from *SOLUGAS*-like plant dimensions to the size of the plant similar to *GEMASOLAR* (except for helium). Another relevant outcome is that maximum power output has been proven to be reached for a pressure ratio very similar to *SOLUGAS* one. Moreover, configurations with optimum pressure ratios according to different criteria were selected.
- Lastly, thermo-economic estimations, mainly Levelised Cost of Electricity computations, were conducted. According to results obtained, the recuperative configuration is favoured from both thermo-economic and thermodynamic perspective. In addition, interesting thermo-economic records could be achieved if other latitudes different from typical ones were tested provided that acceptable solar radiation and low temperatures are reached. Finally, design plant parameters were surveyed from the thermo-economic viewpoint. For the *SOLUGAS*-like plant analysis, LCoE has been demonstrated to have still potential for reduction regarding pressure ratio.
- Broadly speaking, in both simulated plants (*SOLUGAS*-like and similar to *GEMASOLAR*), solar heliostat field has been shown to be too small for achieving desired fixed turbine inlet temperature (and so, power output) and for its associated mass flow. Then, hybridisation is always required and natural gas is constantly being consumpted. As a consequence, solar share records never reach 1 in any case. This plant sizing issue could be solved by reducing the power output supplied to the grid or by increasing the heliostat field scale.
- Energy fluxes and losses studies through Sankey diagrams have been performed for different situations: for the *SOLUGAS*-like and similar to *GEMASOLAR* plants, in an annual basis and at design conditions, for dry air and for the other three working fluids, for recuperative and non-recuperative configurations, and for single and multi-stage layouts. These analyses have conducted to several conclusions. A key common outcome of all carried out analyses is that, even though solar field was under size for all situations, losses in relative terms were higher in the solar subsystem than in the combustion chamber. Within solar

subsystem, heliostat field losses were the highest ones, followed by solar receiver ones. When examining the *SOLUGAS*-like plant in an annual basis, it was found that despite Brayton cycle subsystem is shown as the subsystem that can achieve the highest improvements for the performance of the global hybrid plant, the technical feasibility and the room for improvement of all components have to be considered. As gas turbine turbomachinery is a highly mature technology, the solar subsystem (heliostat field and receiver) could be brought into focus and, in a similar way, all componentes with a lower technology readiness. Paying attention to the proper integration of all subsystems is considered as other key action. For the plant similar to *GEMASOLAR*, a significant difference was found between dry air and helium performance at design point. Main energy source for the dry air was the concentrated solar heat, while for the helium the fuel heat contribution was more relevant. Following this trend, for dry air (when solar contribution was large), solar losses were higher in relative terms than those of the heat engine.

As general conclusions, the following can be sketched:

- The importance of pressure ratio on overall plant performance has been revealed.
- Carried out analyses have pointed out the importance of considering all subsystems in the global plant design through their integration in the developed model. The consideration of how they affect global and particular subsystems parameters; *i.e.*, their intra- and inter-relationships, results essential for input variables selection in the overall system design.
- Nowadays, these plants are not economically profitable, but likely they will be in the near future if some improvements are accomplished. One of the fulfilled goals of this doctoral thesis is to locate existing energy losses and, also, to suggest configurations that lead to enhanced efficiency and lowered costs. In other words, several configurations that improve plant output records, like overall efficiency, power output and Levelised Cost of Electricity, have been proposed for the generated electricity to be more feasible and bankable.
- A significant reduction of fossil fuel consumption and pollutant emissions, specially greenhouse gases, has been demonstrated for this kind of plants. Therefore, they are important from the ecological perspective and especially interesting for regions with good insolation ratios and scarce hydric resources. In this way, they can help to mitigate the anthropogenic intensification of climate change.

On the whole, this doctoral thesis could guide the pre-design of hybrid gas turbine Solar Power Tower plants, as an initial concept and approach. It could constitute a step forward for future commercial plants working on this concept. As a consequence of the further

development of hybrid gas turbines integrated into Solar Power Tower systems, Concentrated Solar Power technology is expected to become more feasible and bankable, as it has been demonstrated in this doctoral thesis. Therefore it could present a relative relevance on the new energy generation paradigm being able to produce energy in a cleaner, efficient, safe and reliable way.

5.2 Open Prospects

Although the main objectives of this doctoral thesis have been fulfilled, some prospects are open for further development of hybrid gas turbine Solar Power Tower plants. Analyses both related to specific subsystems and corresponding to a more general scope are suggested as possible future work on this topic.

- With respect to the combustion chamber, the employment of biogas instead of natural gas could be interesting since it constitutes a renewable fuel, which is considered to produce zero greenhouse effect emissions, like CO_2. An analysis of key plant variables in this case is mandatory.
- Regarding heat engine, supercritical CO_2 cycles could be studied within a non-analytical framework looking for better output records. Future objective metrics to consider in this task will include thermo- and techno-economic analyses of the overall plant performance.
- Additionally, combined cycles could be tested with the objective of taking advantage from turbine excess output heat. In this way, a bottoming Rankine cycle can be added to the topping Brayton one. For the Rankine cycle, several fluids can be tested including Organic ones (Organic Rankine Cycles, ORC). It can also be checked the suitability of a recuperator in this new plant scheme.
- In the light of the thermo-economic results obtained, the examination of configurations that do not require so high turbine inlet temperatures could be relevant for the reduction of receiver costs even though thermodynamic efficiency would be decreased too.
- From a solar subsystem perspective, solar receiver model could be improved by further detailing main losses and parameters and by taking into account dynamic behaviour and transients.
- When performing dynamic simulations, transients could be further analysed by studying in detail both sunrise and dusk times effect on the overall plant. Additionally, a small Thermal Energy Storage system could be integrated in the plant layout so that small solar fluctuations due to cloudy periods could be rectified.
- A special focus should be placed on the consideration of other operation frameworks rather than the baseload one. With this purpose, adding a Thermal Energy Storage

system to the plant layout could enhance solar share and other output parameters. In particular, a packed bed storage can be implemented to the model.

- In the field of hybridisation, non-combustion techniques can also be tested as coupling the plant to a photovoltaic system. This could allow the hybrid plant to combine advantages of both main solar energy generation technologies.
- In order to assess solar irradiance and ambient temperature joint influence on thermodynamic and economic parameters, it would be interesting to perform a thermo-economic study regarding diverse geographic plant locations.
- From a broader viewpoint, multiobjective optimisation could lead to better output records when looking for optimum design parameters. Objective functions should be carefully chosen in order to obtain significative results.
- If smaller power scales are desired for distributed generation and smart grids, a parabolic dish could be modelled rather than a central tower. When comparing to this doctoral thesis, development and implementation of the model can be addressed in a similar way, but with some modifications. Actually, as it was mentioned in Chapter 4 and Section 4.2, this is already a parallel work line from the Research Group, which is not directly devoted to this doctoral thesis.

All these proposed research analyses constitute ones of the next steps towards the deployment of Solar Power Tower plants coupled to hybrid gas turbines.

Appendix A. Quality of appended publications

Paper	Journal	Year of publication	Impact Factor (year)	Quartile (year)	Reference
Paper 1	*Energy Conversion and Management*	2016	5.589 (2016)	Q1 (2016)	[128]
Paper 2	*Energy Conversion and Management*	2017	6.377 (2017)	Q1 (2017)	[125]
Paper 3	*Renewable Energy*	2018	5.439 (2018)	Q1 (2018)	[124]
Paper 4	*Energy Conversion and Management*	2018	7.181 (2018)	Q1 (2018)	[134]
Paper 5	*Renewable and Sustainable Energy Reviews*	2020	12.110 (2019)	Q1 (2019)	[90]
Paper 6	*International Journal of Energy Research*	2020	3.741 (2019)	Q1 (2019)	[135]
Paper 7	*Applied Thermal Engineering* (submitted)	Submitted in 2020	4.725 (2019)	Q1 (2019)	[136]

Table A.1: Quality of appended publications. All data were taken from Web of Science (Clarivate Analytics, 2020).

Appendix B. Dissemination

Within this doctoral thesis, the dissemination of the research topic and progress to diverse audiences has been considered highly relevant and necessary. These audiences have varied from school to university students and general public unconnected to this kind of topic. In this way, the following activities have been performed:

- *"Seeing alpha particles" ("Viendo partículas alfa")* activity organised by the Applied Physics Department of the University of Salamanca at the European Researchers' Night [Salamanca, Spain, 30/09/2016].
- *"Locating an innovative thermosolar plant" ("Ubicando una innovadora planta termosolar")* video report performed by DiCYT [Salamanca, Spain, 25/11/2016]. `https://www.youtube.com/watch?v=t5837QyDo9U`
- *"Through a more efficient and less pollutant energy" ("Por una energía más eficiente y menos contaminante")* newspaper report at *'La Gaceta de Salamanca'* [Salamanca, Spain, 25/03/2018].
- *"Sustainable energy generation through thermosolar plants" ("Generación sostenible de energía mediante plantas termsolares")* talk at the "PechaKucha Night Salamanca Vol.16" organised by *MEDIALAB USAL* and devoted to STEM [Salamanca, Spain, 24/05/2018].
- *"New approaches for optimising solar energy" ("Nuevas estrategias para optimizar la energía del Sol")* newspaper report at *'El Mundo' (Castilla y León Edition) Suplemento Innovadores* [05/02/2019]. `http://www.diariodevalladolid.es/noticias/innovadores/nuevas-estrategias-optimizar-energia-sol_142261.html`
- *"Sustainable energy generation through solar concentration plants" ("Generación sostenible de energía mediante plantas de concentración solar") +Physics* talk organised by the Salamanca Local Section of the Spanish Royal Physics Society at the

University of Salamanca [Salamanca, Spain, 05/11/2019].

- *"USAL researchers design a thermosolar plants model for generating electricity in a clean and efficient way" ("Investigadores de la USAL diseñan un modelo de plantas termosolares para generar electricidad de forma limpia y eficiente")* newspaper reports [10/12/2019].
  `https://www.20minutos.es/noticia/4083104/0/la-usal-disena-un-modelo-de-plantas-termosolares-para-generar-electricidad-de-forma-limpia-y-eficiente/`
- Video report for the Castilla y León regional news program by Spanish Radio and Television Corporation [Salamanca, Spain, 11/12/2019].
  `https://twitter.com/RTVEcyl/status/1205083624942559232`
- *"The 'socket' of the clean electricity" ("El 'enchufe' de la electricidad limpia")* newspaper report at *'El Mundo' (Castilla y León), Suplemento Innovadores* [14/01/2020].
  `https://diariodevalladolid.elmundo.es/articulo/innovadores/enchufe-electricidad-limpia/20200114130051370920.html`
- M.J. Santos, **R.P. Merchán** and J. García Ferrero. *"Clean and efficient electric energy generation at small scale: thermosolar parabolic dishes" ("Generación limpia y eficiente de energía eléctrica a pequeña escala: discos parabólicos termosolares")* poster at the *"Climatic change female researchers. International Day of Women and Girls in Science" ("Investigadoras del Cambio Climático. Día Internacional de la mujer y la niña en la ciencia")* exhibition at the University of Salamanca [Salamanca, Spain, 10/02/2020-14/02/2020].
- *"Simulation model for thermosolar plants (University of Salamanca)" ("Modelo de simulación para plantas termosolares (Universidad de Salamanca)")* talk at the *Plataforma Tecnológica de la Energía Solar de Concentración (Solar Concentra)* [online, 09/07/2020].

Appendix C. Research internships

During the development of this doctoral thesis, several collaborations with different international research groups and internships have been carried out. Key research internships are outlined here:

- Research internship at the *Termodinámica Aplicada a la Ingeniería Industrial* research group from the *Department of Ingeniería Eléctrica* from the *Escuela Técnica Superior de Ingenieros Industriales de Madrid (ETSII-UPM)* (Madrid, Spain, 7/11/2016 - 11/11/2016). The objective of this internship was to perform thermodynamic analyses of Solar Power Tower plants via Thermoflex® software.
- Research internship at *Concentrating Solar Power and Techno-Economic Analysis Group* from the *Division of Heat and Power Technology*, in the *Department of Energy Technology*, at *KTH Royal Institute of Technology* (Stockholm, Sweden, 11/02/2019 - 10/05/2019). The objective of this internship was to perform dynamic simulations via TRNSYS® software and to perform a thermo-economic study of Solar Power Tower plants coupled to combined cycles that are hybridised and employ Thermal Energy Storage.
- Research internship at the *Concentrating Solar Power group* from *Centre for Renewable Energy Systems* at *Cranfield University* (Cranfield, United Kingdom, 13/01/2020 - 28/01/2020). The objective of this internship was to exchange information about the heliostat fields of Solar Central Receiver plants and their efficiency computation techniques and about the gas turbines coupled to them.

Bibliography

[1] A. Calvo Hernández, A. Medina, and J.M. M. Roco. Power and efficiency in a regenerative gas turbine. *Journal of Physics D: Applied Physics*, 28:2020–23, 1995.

[2] S. Sánchez-Orgaz. *Modelización, análisis y optimización termodinámica de plantas de potencia multietapa tipo Brayton. Aplicación a centrales termosolares*. PhD thesis, ETSII de Béjar, Universidad de Salamanca, 2012.

[3] S. Sánchez-Orgaz, A. Medina, and A. Calvo Hernández. Thermodynamic model and optimization of a multi-step irreversible Brayton cycle. *Energy Conversion and Management*, 51:2134–43, 2010.

[4] S. Sánchez-Orgaz, A. Medina, and A. Calvo Hernández. Maximum overall efficiency for a solar-driven gas turbine power plants. *International Journal of Energy Research*, 37:1580–1591, 2013.

[5] S. Sánchez-Orgaz, A. Medina, and A. Calvo Hernández. Recuperative solar-driven multi-step gas turbine power plants. *Energy Conversion and Management*, 67:171–178, 2013.

[6] S. Sánchez-Orgaz, M. Pedemonte, P. Ezzatti, P.L. Curto-Risso, A. Medina, and A. Calvo Hernández. Multi-objective optimization of a multi-step solar-driven Brayton cycle. *Energy Conversion and Management*, 99:346–358, 2015.

[7] D. Olivenza-León, A. Medina, and A. Calvo Hernández. Thermodynamic modeling of a hybrid solar gas-turbine power plant. *Energy Conversion and Management*, 93:435–447, 2015.

[8] A.G. Fernández, J. Gómez-Vidal, E. Oró, A. Kruizenga, A. Solé, and L.F. Cabeza. Mainstreaming commercial CSP systems: A technology review. *Renewable Energy*, 140:152–176, 2019.

[9] O. Achkari and A. El Fadar. Latest developments on TES and CSP technologies - Energy and environmental issues, applications and research trends. *Applied Thermal Engineering*, 167:114806, 2020.

[10] IEA Technology Roadmaps. Concentrating Solar Power, 2010.

[11] M. van der Hoeven. Technology Roadmap Solar Thermal Electricity. Technical Report 52, International Energy Agency (IEA), 2014.

[12] P. del Río, C. Peñasco, and P. Mir-Artigues. An overview of drivers and barriers to concentrated solar power in the European Union. *Renewable and Sustainable Energy Reviews*, 81:1019–1029, 2018.

[13] P. Gauché, J. Rudman, M. Mabaso, W.A. Landman, T.W. von Backström, and A.C. Brent. System value and progress of CSP. *Solar Energy*, 152:106–139, 2017.

[14] O. Behar, A. Khellaf, and K. Mohammedi. A review of studies on central receiver solar thermal power plants. *Renewable and Sustainable Energy Reviews*, 23:12–39, 2013.

[15] A. Ilas, P. Ralon, A. Rodriguez, and M. Taylor. Renewable power generation costs in 2017. Techreport 978-92-9260-040-2, IRENA (International Renewable Energy Agency).

[16] M. Taylor, P. Ralon, H. Anuta, and S. Al-Zoghoul. Renewable Power Generation Costs in 2019. techreport 978-92-9260-244-4, IRENA (International Renewable Energy Agency), 2020.

[17] B. Belgasim, Y. Aldali, M.J.R. Abdunnabi, G. Hashem, and K. Hossin. The potential of concentrating solar power (CSP) for electricity generation in Libya. *Renewable and Sustainable Energy Reviews*, 90:1–15, 2018.

[18] NREL. Concentrating Solar Power Projects. `https://solarpaces.nrel.gov/`. Accessed on 19-05-2020.

[19] M. Romero and A. Steinfeld. Concentrating solar thermal power and thermochemical fuels. *Energy and Environmental Science*, 5:9234–9245, 2012.

[20] M. Romero-Alvarez and E. Zarza. *Concentrating Solar Thermal Power*, chapter 21, pages 1–98. Taylor and Francis, 2007.

[21] N.C. Thirumalai, M.A. Ramaswamy, G. Srilakshmi, V. Venkatesh, and B.S. Rao. Global Review of Solar Tower Technology. Technical report, Indo-US collaborative research platform - Solar Energy Research Institute for India and the United States (SERIIUS), 2014.

[22] M. Lubkoll, T.W. von Backström, and D.G. Kröger. Survey on pressurized air receiver development. Technical report, SolarPACES.

[23] C.K. Ho and B.D. Iverson. Review of high-temperature central receiver designs for concentrating solar power. *Renewable and Sustainable Energy Reviews*, 29:835–846, 2014.

[24] A.L. Ávila-Marín. Volumetric receivers in solar thermal power plants with central receiver system technology: a review. *Solar Energy*, 85:891–910, 2011.

[25] Md.T. Islam, N. Huda, A.B. Abdullah, and R. Saidur. A comprehensive review of state-of-the-art concentrating solar power (CSP) technologies: Current status and research trends. *Renewable and Sustainable Energy Reviews*, 91:987–1018, 2018.

[26] E. Okoroigwe and A. Madhlopa. An integrated combined cycle system driven by a solar tower: a review. *Renewable and Sustainable Energy Reviews*, 57:337–350, 2016.

[27] R. Korzynietz, M. Quero, and R. Uhlig. SOLUGAS-Future solar hybrid technology. Technical report, SolarPaces, 2012.

[28] BrightSource energy. `http://www.brightsourceenergy.com`. Accessed on 10-06-2020.

[29] L. Li, J. Coventry, R. Bader, J. Pye, and W. Lipiński. Optics of solar central receiver systems: a review. *Optics Express*, 24(14), 2016. 2016 Optical Society of America.

[30] T. Conroy, M.N. Collins, and R. Grimes. A review of steady-state thermal and mechanical modelling on tubular solar receivers. *Renewable and Sustainable Energy Reviews*, 119:109591, 2020.

[31] Asociación Española de la Energía Termosolar. `http://www.protermosolar.com`. Accessed on 08-06-2020.

[32] S. Burgaleta and D.J.I. Ramírez. Gemasolar, the first tower thermosolar commercial plant with molten salt storage. In *Proceedings of SolarPACES*, Granada, Spain, 2011.

[33] Solar Quotes. `https://www.solarquotes.com.au/blog/aurora-solar-storage-mb1528/`. Accessed on 09-06-2020.

[34] S&P Global Platts. https://www.spglobal.com/platts/en/market-insights/latest-news/electric-power/080219-solarreserves-csp-technology-with-storage-struggles-to-stay-online. Accessed on 09-06-2020.

[35] Cerro Dominador. https://cerrodominador.com/. Accessed on 02-06-2020.

[36] Helios CSP. http://helioscsp.com/. Accessed on 08-06-2020.

[37] PV magazine Australia. https://www.pv-magazine-australia.com/. Accessed on 08-06-2020.

[38] R.O. González-Aguilar. PS 10 and PS 20 Power Towers in Seville, Spain. Technical report, NREL CSP Technology Workshop, 2007.

[39] U.S. Energy Information Administration. Levelized Cost and Levelized Avoided Cost of New Generation Resources in the Annual Energy Outlook 2020. Technical report, 2020.

[40] H. Anuta, P. Ralon, and M. Taylor. Renewable Power Generation Costs in 2018. Techreport 978-92-9260-126-3, IRENA (International Renewable Energy Agency), 2019.

[41] A. Palacios, C. Barreneche, M.E. Navarro, and Y. Ding. Thermal energy storage technologies for concentrated solar power - a review from a materials perspective. *Renewable Energy*, 156:1244–1265, 2020.

[42] M. Atif and F. Al-Sulaiman. Energy and exergy analyses of solar tower power plant driven supercritial carbon dioxide recompression cycles for six different locations. *Renewable and Sustainable Energy Reviews*, 68:153–167, 2017.

[43] O. Behar, B. Grange, and G. Flamant. Design and performance of a modular combined cycle solar power plant using the fluidized particle solar receiver technology. *Energy Conversion and Management*, 220:113108, 2020.

[44] A. Pfahl, J. Coventry, M. Röger, F. Wolfertstetter, J.F. Vásquez-Arango, F. Gross, M. Arjomandi, P. Schwarzbözl, M. Geiger, and P. Liedke. Progress in heliostat development. *Solar Energy*, 152:3–37, 2017.

[45] N.C. Cruz, J.L. Redondo, M. Berenguel, J.D. Álvarez, and P.M Ortigosa. Review of software for optical analyzing and optimizing heliostat fields. *Renewable and Sustainable Energy Reviews*, 72:1001–1018, 2017.

[46] J. Coventry, J. Campbell, Y.P. Xue, C. Hall, J.S. Kim, J. Pye, G. Burgess, D. Lewis, G. Nathan, M. Arjomandi, W. Stein, M. Blanco, J. Barry, M. Doolan, W. Lipiński, and A. Beath. Heliostat Cost Down Scoping Study - Final Report. Technical report, ANU - ASTRI, 2016.

[47] K.R. Bhargav, F. Gross, and P. Schramek. Life cycle cost optimized heliostat size for power towers. In *Energy Procedia*, volume 49, pages 40–49, 2014.

[48] J. Coventry and J. Pye. Heliostat cost reduction-where to now? In *Energy Procedia*, volume 49, pages 60–70, 2014.

[49] A. Pfahl. Survey of heliostat concepts for cost reduction. *Journal of Solar Energy Engineering - Transactions of the ASME*, 136(1):014501, 2013.

[50] J.G. Barberena, A. Mutuberria Larrayoz, M. Sánchez, and A. Bernardos. State-of-the-art of heliostat field layout algorithms and their comparison. In *Energy Procedia*, volume 93, pages 31–38, 2016.

[51] C.J. Noone, M. Torrilhon, and A. Mitsos. Heliostat field optimization: a new computationally efficient model and biomimetic layout. *Solar Energy*, 86:792–803, 2012.

[52] F.J. Collado and J. Guallar. Campo: Generation of regular heliostat fields. *Renewable Energy*, 46:49–59, 2012.

[53] M. Zhang, L. Yang, C. Xu, and X. Du. An efficient code to optimize the heliostat field and comparisons between the biomimetic spiral and stagerred layout. *Renewable Energy*, 87:720–730, 2016.

[54] P.L. Leary and J.D. Hankins. User's guide for MIRVAL: a computer code for comparing designs of heliostat receiver optics for central receiver solar power plants. Technical report, Sandia National Laboratories, 1977.

[55] T. Wendelin. SolTRACE: a new optical modeling tool for concentrating solar optics. In *ISEC 2003: International Solar Energy Conference*, pages 253–260. National Renewable Energy Laboratory (NREL).

[56] C. Gertig, A. Delgado, C. Hidalgo, and R. Ron. SoFiA - A novel simulation tool for central receiver systems. In *Energy Procedia*, volume 49, pages 1361–1370, 2014.

[57] R. Buck. Solar Power Raytracing Tool SPRAY User Manual. Technical report, German Aerospace Center (DLR), 2011.

[58] F.J. Collado and J. Guallar. A review of optimized design layouts for solar power tower plants with *campo* code. *Renewable and Sustainable Energy Reviews*, 20:142–154, 2013.

[59] F.J. Collado and J. Guallar. Quick design of regular heliostat fields for commercial solar tower power plants. *Energy*, 178:115–125, jul 2019.

[60] F. Lipps and L. Vant-Hull. A cellwise method for the optimization of large central receiver systems. *Solar Energy*, 20(6):505–516, 1978.

[61] A. Mutuberria, J. Pascual, M. Guisado, and F. Mallor. Comparison of heliostat field layout design methodologies and impact on power plant efficiency. In *20th SolarPACES International Symposium on Concentrating Solar Power and Chemical Energy*, 2014.

[62] T.A. Dellin and M.J. Fish. User's manual for DELSOL: A computer code for calculating the optical performance, field layout and optimal system design for solar central receiver plants. Technical report, Sandia National Laboratories, 1979.

[63] B.L. Kistler. A user's manual for DELSOL3: a computer code for calculating the optical performance and optimal system design for solar thermal central receiver plants. Technical report, Sandia National Laboratories, 1986.

[64] P. Schwarzbözl, R. Pitz-Paal, and M. Schmitz. Visual HFLCAL - a software tool for layout and optimisation of heliostat fields. In *15th SolarPACES International Symposium on Concentrating Solar Power and Chemical Energy*, 2009.

[65] A. Sánchez González. *Heliostat field aiming strategies for solar central receivers*. PhD thesis, Universidad Carlos III de Madrid, 2016.

[66] M. López-Herraiz, A. Bello Fernández, N. Martínez, and M. Gallas. Effect of the optical properties of the coating of a concentrated solar power central receiver on its thermal efficiency. *Solar Energy Materials & Solar Cells*, 159:66–72, 2017.

[67] M. Sedighi, R. Vasquez Padilla, R.A. Taylor, M. Lake, I. Izadgoshasb, and A. Rose. High-temperature, point-focus, pressurised gas-phase solar receivers: A comprehensive review. *Energy Conversion and Management*, 185:678–717, 2019.

[68] K. Jiang, X Du, Y. Kong, C. Xu, and X. Ju. A comprehensive review on solid particle receivers of concentrated solar power. *Renewable and Sustainable Energy Reviews*, 116:109463, 2019.

[69] M. Ebert, D. Benitez, M. Röger, R. Korzynietz, and J.A. Brioso. Efficiency determination of tubular solar receivers in central receiver systems. *Solar Energy*, 139:179–189, 2016.

[70] A. del Río, R. Korzynietz, J.A. Brioso, M. Gallas, I. Ordoñez, M. Quero, and C. Díaz. Soltrec - Pressurized volumetric solar air receiver technology. *Energy Procedia*, 69:360–368, 2015.

[71] J. Martinek and Z. Ma. Granular flow and heat-transfer study in a near-blackbody enclosed particle receiver. *Journal of Solar Energy Engineering - Transactions of the ASME*, 137:051008–051008, 2015.

[72] C.K. Ho. A review of high-temperature particle receivers for concentrating solar power. *Applied Thermal Engineering*, 109:958–969, 2016.

[73] A.L. Ávila-Marín, M. Álvarez de Lara, and J. Fernández-Reche. Experimental results of gradual porosity volumetric air receivers with wire meshes. *Renewable Energy*, 122:339–353, 2018.

[74] J. Muñoz Antón, C. Rubbia, A. Rovira, and J.M. Martínez-Val. Performance study of solar power plants with CO_2 as working fluid. A promising design window. *Energy Conversion and Management*, 92:36–46, 2015.

[75] B. Grange, C. Dalet, Q. Falcoz, F. Siros, and A. Ferrière. Simulation of a hybrid solar gas-turbine cycle with storage integration. *Energy Procedia*, 49:1147–1156, 2014.

[76] S. Klein. TRNSYS A transient system simulation program, 2000.

[77] R. Pitz-Paal and S.A. Jones. *A TRNSYS Model Library for Solar Thermal Electric Components (STEC)*, Task III: Solar Technologies and Applications edition, 1998.

[78] Thermoflow. Thermoflex - Spotlight on solar thermal modeling, 2012.

[79] M.J. Wagner and G. Zhu. A Generic CSP Performance Model for NREL's System Advisor Model. 2011.

[80] NREL. Solar PILOT. `https://www.nrel.gov/csp/solarpilot.html`. Accessed on 22-06-2020.

[81] Ebsilon. `https://www.ebsilon.com/en/`. Accessed on 22-06-2020.

[82] Y. Liu, Y. Wang, and D. Huang. Supercritical CO_2 Brayton cycle: A state-of-the-art review. *Energy*, 189:115900, 2019.

[83] M.A. Reyes-Belmonte, A. Sebastián, J. Spelling, M. Romero, and J. González-Aguilar. Annual performance of subcritical Rankine cycle coupled to an innovative particle receiver solar power plant. *Renewable Energy*, 130:786–795, 2019.

[84] J. Sarkar. Review and future trends of supercritical CO_2 Rankine cycle for low-grade heat conversion. *Renewable and Sustainable Energy Reviews*, 48:434–51, 2015.

[85] O. Behar. A novel hybrid solar preheating gas turbine. *Energy Conversion and Management*, 158:120–132, 2018.

[86] B. Grange, C. Dalet, Q. Falcoz, A. Ferrière, and G. Flamant. Impact of thermal energy storage integration on the performance of a hybrid solar gas-turbine power plant. *Applied Thermal Engineering*, 105:266–275, 2016.

[87] SOLGATE. Solar hybrid gas turbine electric power system. Technical Report EUR 21615, European Commission, 2005.

[88] Solar-Hybrid Power and Cogeneration Plants (SOLHYCO). Technical Report 13318, European Commission, 2011.

[89] R. Korzynietz, J.A. Brioso, A. del Río, M. Quero, M. Gallas, R. Uhlig, M. Ebert, R. Buck, and D. Teraji. Solugas - Comprehensive analysis of the solar hybrid Brayton plant. *Solar Energy*, 135:578–589, 2016.

[90] R.P. Merchán, M.J. Santos, I. Heras, J. Gonzalez-Ayala, A. Medina, and A. Calvo Hernández. On-design pre-optimization and off-design analysis of hybrid Brayton thermosolar tower power plants for different fluids and plant configurations. *Renewable and Sustainable Energy Reviews*, 119:109590, 2020.

[91] M. Lanchi, M. Montecchi, T. Crescenzi, D. Mele, A. Miliozzi, V. Russo, D. Mazzei, M. Misceo, M. Falchetta, and R. Mancini. Investigation into the coupling of Micro Gas Turbines with CSP technology: OMSoP project. In *Energy Procedia*, volume 69, pages 1317–1326, 2015.

[92] M. Puppe, S. Giuliano, M. Krüger, O. Lammel, R. Buck, S. Boje, K. Saidi, U. Gampe, C. Felsmann, M. Freimark, and U. Langnickel. Hybrid high solar share gas turbine systems with innovative gas turbine cycles. In *Energy Procedia*, volume 69, pages 1393–1403, 2015.

[93] next csp. `http://next-csp.eu/`. Accessed on 19-06-2020.

[94] F. Rovense, M.A. Reyes-Belmonte, J. González-Aguilar, M. Amelio, S. Bova, and M. Romero. Flexible electricity dispatch for CSP plant using un-fired closed air Brayton cycle with particles based thermal energy storage system. *Energy*, 173:971–984, 2019.

[95] R. Chacartegui, J.M. Muñoz de Escalona, D. Sánchez, B. Monje, and T. Sánchez. Alternative cycles based on carbon dioxide for central receiver solar power. *Applied Thermal Engineering*, 31:872–879, 2011.

[96] P. Garg, P. Kumar, and K. Srinivasan. Supercritical carbon dioxide Brayton cycle for concentrated solar power. *Journal of Supercritical Fluids*, 76:54–60, 2013.

[97] C.S. Turchi. Supercritical CO_2 for Application in Concentrating Solar Power Systems. 2009.

[98] J. Liu, H. Chen, Y. Xu, L. Wang, and C. Tan. A solar energy storage and power generation system based on supercritical carbon dioxide. *Renewable Energy*, 64:43–51, 2014.

[99] B.D. Iverson, T.M. Conboy, J.J. Pasch, and A.M. Kruizenga. Supercritical CO_2 Brayton cycles for solar-thermal energy. *Applied Energy*, 111:957–70, 2013.

[100] CSIRO. `https://www.csiro.au/en`. Accessed on 22-06-2020.

[101] V. Zare and M. Hasanzadeh. Energy and exergy analysis of a closed Brayton cycle-based combined cycle for solar power tower plants. *Energy Conversion and Management*, 128:227–237, 2016.

[102] I. García-Sáez, J. Méndez, C. Ortiz, D. Loncar, J.A. Becerra, and R. Chacartegui. Energy and economic assessment of solar Organic Rankine Cycle for combined heat and power generation in residential applications. *Renewable Energy*, 140:461–476, 2019.

[103] D.G. Kröger. SUNSPOT - The Stellenbosch UNiversity Solar POwer Thermodynamic cycle, 2011.

[104] P.J. Harper, T.W. von Backström, T.P. Fluri, and D.G. Kröger. TRNSYS modeling of a 100 MWe hybrid combined cycle concentrating solar power plant. 2012.

[105] L. Heller. Literature Review on Heat Transfer Fluids and Thermal Energy Storage Systems in CSP Plants, 2013.

[106] M. Chieruzzi, G.F. Cerritelli, A. Miliozzi, J.M. Kenny, and L. Torre. Heat capacity of nanofluids for solar energy storage produced by dispersing oxide nanoparticles in nitrate salt mixture directly at high temperature. *Solar Energy Materials and Solar Cells*, 167:60–69, 2017.

[107] K. Lovegrove and W. Stein. *Concentrating Solar Power Technology: Principles, Developments and Applications*. Woodhead Publishing, 2012.

[108] G. Zanganeh, A. Pedretti, S. Zavattoni, M. Barbato, and A. Steinfeld. Packed-bed thermal storage for concentrated solar power - pilot-scale demonstration and industrial-scale design. *Solar Energy*, 86:3084–3098, 2012.

[109] Z. Ma, G.C. Glatzmaier, and M. Mehos. Development of solid particle thermal energy storage for concentrating solar power plants that use fluidized bed technology. In *Energy Procedia*, volume 49, pages 898–907, 2014.

[110] G. Alva, L. Liu, X. Huang, and G. Fang. Thermal energy storage materials and systems for solar energy applications. *Renewable and Sustainable Energy Reviews*, 68:693–706, 2017.

[111] P. Tatsidjodoung, N. Le Pierres, and L. Luo. A review of potential materials for thermal energy storage in building applications. *Renewable and Sustainable Energy Reviews*, 18:327–349, 2013.

[112] A. Sharma, V.V. Tyagi, C.R. Chen, and D. Buddhi. Review on thermal energy storage with phase change materials and applications. *Renewable and Sustainable Energy Reviews*, 13:318–345, 2009.

[113] F. Agyenim, I. Knight, and M. Rhodes. Design and experimental testing of the performance of an outdoor $LiBr/H_2O$ solar thermal absorption cooling system with a cold store. *Solar Energy*, 84:735–744, 2010.

[114] Z. Yang and S.V. Garimella. Molten-salt thermal energy storage in thermoclines under different environmental boundary conditions. *Applied Energy*, 87:3322–3329, 2010.

[115] D. Laing, C. Bahl, T. Bauer, D. Lehmann, and W.D. Steinmann. Thermal energy storage for direct steam generation. *Solar Energy*, 85:627–633, 2011.

[116] K.M. Powell, K. Rashid, K. Ellingwood, J. Tuttle, and B.D. Iverson. Hybrid concentrated solar thermal power systems: A review. *Renewable and Sustainable Energy Reviews*, 80:215–237, 2017.

[117] P. Heller, M. Pfänder, T. Denk, F. Téllez, A. Valverde, J. Fernández, and A. Ring. Test and evaluation of a solar powered gas turbine system. *Solar Energy*, 80:1225–1230, 2006.

[118] U. Fisher, C. Sugarmen, A. Ring, and J. Sinai. Gas turbine solarization-modifications for solar/fuel hybrid operation. *Journal of Solar Energy Engineering - Transactions of the ASME*, 126:872–8, 2004.

[119] G.J. Nathan, M. Jafarian, B.B. Dally, W.L. Saw, P.J. Ashman, E. Hu, and A. Steinfeld. Solar thermal hybrids for combustion power plant: A growing opportunity. *Progress in Energy and Combustion Science*, 64:4–28, 2018.

[120] K. Ellingwood, S.M. Safdarnejad, H. Kovacs, J.F. Tuttle, and K. Powell. Analysing the benefits of hybridisation and storage in a hybrid solar gas turbine plant. *International Journal of Sustainable Energy*, 2019.

[121] J.H. Peterseim, S. White, A. Tadros, and U. Hellwig. Concentrated solar power hybrid plants, which technologies are best suited for hybridisation? *Renewable Energy*, 57:520–532, 2013.

[122] B. Corona, D. Ruiz, and G.S. Miguel. Environmental assessment of a HYSOL CSP plant compared to a conventional tower CSP Plant. In *Procedia Comput Sci*, volume 83, pages 1110–7, 2016.

[123] A. Zurita, C. Mata-Torres, C. Valenzuela, C. Felbol, J.M. Cardemil, A.M. Guzmán, and R.A. Escobar. Techno-economic evaluation of a hybrid CSP+PV plant integrated with thermal energy storage and a large-scale battery energy storage system for base generation. *Solar Energy*, 173:1262–1277, 2018.

[124] R.P. Merchán, M.J. Santos, A. Medina, and A. Calvo Hernández. Thermodynamic model of a hybrid Brayton thermosolar plant. *Renewable Energy*, 128:473–483, 2018.

[125] R.P. Merchán, M.J. Santos, I. Reyes-Ramírez, A. Medina, and A. Calvo Hernández. Modeling hybrid solar gas-turbine power plants: Thermodynamic projection of annual performance and emissions. *Energy Conversion and Management*, 134:314–326, 2017.

[126] G. Barigozzi, G. Bonetti, G. Franchini, A. Perdichizzi, and S. Ravelli. Thermal performance prediction of a solar hybrid gas turbine. *Solar Energy*, 86:2116–2127, 2012.

[127] SOLar Simulation Tool In ConcEntrating optics SOLSTICE. `https://www.labex-solstice.fr/solstice-software/`. Accessed on 02-07-2020.

[128] M.J. Santos, R.P. Merchán, A. Medina, and A. Calvo Hernández. Seasonal thermodynamic prediction of the performance of a hybrid solar gas-turbine power plant. *Energy Conversion and Management*, 115:89–102, 2016.

[129] Engineering Equation SOLVER (EES). `http://fchartsoftware.com/ees/`. Accessed on 02-07-2020.

[130] WolframAlpha. Mathematica. `https://www.wolfram.com/mathematica/`. Accessed on 03-07-2020.

[131] S.M. Besarati, D.Y. Goswami, and E.K. Stefanakos. Optimal heliostat aiming strategy for uniform distribution of heat flux on the receiver of a solar power tower plant. *Energy Conversion and Management*, 84:234–243, 2014.

[132] C.A. Asselineau. *Geometrical optimisation of receivers for concentrating solar thermal systems*. PhD thesis, The Australian National University, 2017.

[133] S. Trevisan, R.P. Merchán, R. Guédez, M.J. Santos, A. Medina, B. Laumert, and A. Calvo Hernández. Techno-Economic Analysis of a Solar Hybrid Combined Cycle Power Plant Integrated with a Packed Bed Storage at Gas Turbine Exhaust. *AIP Conference Proceedings (SolarPACES2019)*, 2020.

[134] M.J. Santos, C. Miguel-Barbero, R.P. Merchán, A. Medina, and A. Calvo Hernández. Roads to improve the performance of hybrid thermosolar gas turbine power plants: Working fluids and multi-stage configurations. *Energy Conversion and Management*, 165:578–592, 2018.

[135] R.P. Merchán, M.J. Santos, A. Medina, and A. Calvo Hernández. On- and off-design thermodynamic analysis of a hybrid polar solar thermal tower power plant. *International Journal of Energy Research*, pages 1–17, 2020.

[136] R.P. Merchán, M.J. Santos, J. García-Ferrero, A. Medina, and A. Calvo Hernández. Thermo-economic analysis of a central tower hybrid Brayton thermo-solar plant: sensitivity of LCoE to main design parameters. *Applied Thermal Engineering - Submitted for publication*, 2020.

[137] J.B. Heywood. *Internal Combustion Engine Fundamentals*. McGraw-Hill, 1988.

[138] J.D. Spelling. *Hybrid Solar Gas-Turbine Power Plants*. PhD thesis, KTH Royal Institute of Technology, Department of Energy Technology, Stockholm, Sweden, 2013.

[139] P. K. Falcone. *A Handbook for Solar Central Receiver Design*. Sandia National Labs, SAND 86-8009 edition, 1986.

[140] F.J. Collado and J.A. Turégano. Calculation of the annual thermal energy supplied by a defined heliostat field. *Solar Energy*, 42:149–165, 1989.

[141] Solar Turbines - Caterpillar.

[142] Solar Turbines. `https://www.solarturbines.com`. Accessed on 09-06-2020.

[143] Meteosevilla. `http://www.meteosevilla.com`. Accessed on 09-06-2020.

[144] AEMET. `http://www.aemet.es`. Accessed on 09-06-2020.

[145] Copernicus atmosphere monitoring service (ECMWF). `http://www.soda-pro.com/web-services/radiation/cams-radiation-service`, 2019. Accessed on 09-06-2020.

[146] J. García-Ferrero, I. Heras, M.J. Santos, R.P. Merchán, A. Medina, A. González, and A. Calvo Hernández. Thermodynamic and Cost Analysis of a Solar Dish Power Plant in Spain Hybridized with a Micro-Gas Turbine. *Energies*, 2020.

[147] J. Estévez Del Corral. *Evaluación de la eficiencia del campo de heliostatos en una planta termosolar de torre central*, End of Degree Project, University of Salamanca, 2019.

[148] W.B. Stine and M. Geyer. Power from the Sun, 2001.

[149] R.P. Merchán, M.J. Santos, A. Medina, and A. Calvo Hernández. *Hybrid Brayton thermosolar systems: thermodynamic prediction of annual efficiencies and emissions*, chapter IV, pages 47–60. Symposium on Energy and Sustainability. XXXVI Biennial. Spanish Royal Physics Society, 2017 Edition edition, 2018.

[150] M.J. Santos, R.P. Merchán, A. Medina, and A. Calvo Hernández. *Simulación Termodinámica de una planta termosolar híbrida tipo Brayton*, chapter XVII, pages 267–284. Symposium on Energy and Sustainability. XXXV Biennial. Spanish Royal Physical Society, 2015 Edition edition, 2016.

[151] R.P. Merchán, A. Medina, M.J. Santos, J.M. M. Roco, and Calvo Hernández. Towards a more efficient generation of central tower hybrid thermosolar gas turbine power plants. *AIP Conference Proceedings (SolarPACES2018)*, 2126:140004, 2019.

Nomenclature

Abbreviations and acronyms

AEMET	Spanish *Agencia Estatal de Meteorología* / Spanish Meteorological National Agency
ASTRI	Australian Solar Thermal Research Initiative
CAMS	Copernicus Atmosphere Monitoring Service
CRS	Central Receiver System
CSIRO	Commonwealth Scientific and Industrial Research Organisation
CSP	Concentrated Solar Power
DLR	German Aerospace Center
DNI	Direct Normal Irradiance
EES	Engineering Equation Solver
GT	Gas Turbine
HTF	Heat Transfer Fluid
HYGATE	Hybrid High Solar Share Gas Turbine Systems
IEA	International Energy Agency
IRENA	International Renewable Energy Agency
ISO	International Organization for Standardization
KTH	Royal Institute of Technology
LCoE	Levelised Cost of Electricity
LFR	Linear Fresnel Reflector
MENA	Middle East and North Africa
MS	Molten Salts
NR	Non-Recuperator
NREL	US National Renewable Energy Laboratory

OML	Operation, Maintenance and Labour
OMSoP	Optimised Microturbine Solar Power system
ORC	Organic Rankine Cycles
PCM	Phase Change Material
PDC	Parabolic Dish Collector
PEGASE	Production of Electricity from Gas and Solar Energy
PPA	Power Purchase Agreement
PTC	Parabolic Trough Collector
PV	Photovoltaic
R&D	Research & Development
SAM	System Advisor Model
sCO_2	Supercritical CO_2
SHGT	Solar Hybrid Gas Turbine
SOLGATE	Solar Hybrid Gas Turbine Electric Power System
SOLHYCO	SoLar Hybrid Power and Cogeneration plants
SOLUGAS	Solar Up-scale Gas Turbine System
SPT	Solar Power Tower
SS	Saturated Steam
SUNSPOT	Stellenbosch University Solar Power Thermodynamic cycle
TES	Thermal Energy Storage
TRL	Technology Readiness Level
TRNSYS	Transient System Simulation Tool
UC	Under Construction
UD	Under Development
USA	United States of America
USD	USA Dollar

Symbols

A_a	Aperture area of the heliostat field	m^2
AH	Heliostat area	m^2
C	Solar concentration ratio	-
C_{dec}	Decommissioning costs	USD
C_{inv}	Investment and initial installation costs	USD
C_{OML}	Operation, Maintenance and Labour costs	USD/year
c_w	Specific heat of the working fluid	J/(mol K)
D	Distance between the centre of each heliostat and the aim point in the receiver	m
DHs	Separation diameter between heliostats	m
DR	Receiver diameter	m
d_s	Separation distance between adjacent heliostats	m
d_{safe}	Safety distance between heliostats	units of LH
e_i	East coordinate of each heliostat	m
E_{net}	Net energy produced in a year	MWh/year
f	Solar share	-
f_{at}	Attenuation factor	-
f_b	Blocking factor	-
f_{sh}	Shadowing factor	-
f_{sp}	Spillage factor	-
G	Direct solar irradiance	W/m^2
i	Interest rate	%
LH	Heliostat height	m
LR	Height of the receiver	m
LW	Heliostat width	m
M	Molecular weight of the working fluid	g/mol
$\dot{m}$	Mass flow rate of the working fluid	kg/s
$\dot{m}_f$	Total fuel mass flow rate	kg/s
$\dot{m}_{fi}$	Fuel mass flow rate in reheaters	kg/s
$\dot{m}_{fp}$	Fuel mass flow rate in the main combustion chamber	kg/s
n_i	North coordinate of each heliostat	m
n_{con}	Number of years expended in plant construction	-
n_{dec}	Number of years expended in plant decommissioning	-
n_{op}	Number of years of plant operation	-
N	Number of compressors or turbines when they are equal	-

N_c	Number of compressors	-
N_t	Number of turbines	-
NH	Total number of heliostats	
P	Power output	W
p_c	Critical pressure	bar
p_H	Highest pressure during heat absorption	bar
p_H-Δp_H	First turbine inlet pressure	bar
p_L	Pressure at the exit of the expansion processes	bar
p_L-Δp_L	Lowest pressure during heat release	bar
$\lvert\dot{Q}_{\mathrm{C}}\rvert$	Heat losses at the combustion chamber	W
$\lvert\dot{Q}_{\mathrm{H}}\rvert$	Total heat transfer rate absorbed by the working fluid	W
$\lvert\dot{Q}_{\mathrm{HC}}\rvert$	Total heat rate input from the combustion chamber and the reheaters	W
$\lvert\dot{Q}_{\mathrm{HC}_p}\rvert$	Heat rate transferred from the main combustion chamber to the associated heat exchanger	W
$\lvert\dot{Q}_{\mathrm{HS}}\rvert$	Heat rate input from the solar collector	W
$\lvert\dot{Q}_{\mathrm{iHC}}\rvert$	Heat losses at the heat exchanger associated with the combustion chamber	W
$\lvert\dot{Q}_{\mathrm{iHS}}\rvert$	Heat losses at the solar receiver	W
$\lvert\dot{Q}_l\rvert$	Losses associated with heat transfers in the solar field	W
$\lvert\dot{Q}_{\mathrm{L}}\rvert$	Heat transfer rate between the working fluid and the ambient	W
Q_{LHV}	Lower heating value of the fuel	J/kg
$\lvert\dot{Q}_{reh}\rvert$	Heat rate input from the reheaters	W
$\lvert\dot{Q}_0\rvert$	Optical losses at the solar subsystem	W
r_i	Horizontal distance (North-East plane) between each heliostat and the centre of the tower	m
r_e	Fuel conversion rate	-
r_p	Overall pressure ratio	-
R_{min}	Distance from first heliostats row to the tower	m
R_{zone}	Zonal radius	m
T_c	Critical temperature	K
T_{HC}	Working temperature of the combustion chamber	K
T_{HS}	Working temperature of the solar receiver	K
T_{L}	Ambient temperature	K
T_x	Working fluid temperature after the heat input from the recuperator	K

$T_{x'}$	Working fluid temperature after heat input from the solar collector	K
T_y	Working fluid exhaust temperature	K
T_1	Compressors inlet temperature	K
T_2	Temperature after last compressor	K
T_{2s}	Hypothetical temperature after isentropic compressions	K
T_3	Turbines inlet temperature	K
T_4	Temperature after last turbine	K
T_{4s}	Hypothetical temperature after isentropic expansions	K
THT	Height of the tower supporting the receiver	m
$\overline{U}_L$	Effective conduction-convection heat transfer coefficient	W/(m^2 K)
w_r	Width-height ratio of the heliostat surface	-
z_{rec}	Zenith coordinate of the receiver	m
z_i	Zenith coordinate of each heliostat	m

Greek symbols

α	Effective emissivity	-
β_{inv}	Total capital costs to equivalent annual amount for refunding the initial credit factor	-
β_{dec}	Decommissioning costs to equivalent yearly accumulated amount required for decommissioning factor	-
Δ R	Radial distance between two adjacent rows	m
Δ R_{min}	Minimum increment of radial distance	m
$\Delta\alpha_T$	Increment of the azimuth angle	rad
$\varepsilon_{\mathrm{HC}}$	Combustion chamber heat exchanger effectiveness	-
$\varepsilon_{\mathrm{HS}}$	Solar collector heat exchanger effectiveness	-
ε_L	Cold side heat exchanger effectiveness	-
ε_c	Isentropic efficiency of the compressors	-
ε_r	Recuperator effectiveness	-
ε_t	Isentropic efficiency of the turbines	-
ε_T	Elevation angle of the tower unit vector focusing from the centre of the heliostat to the receiver	rad
$\bar{\gamma}$	Mean value of the working fluid adiabatic coefficient	-
η	Overall thermal efficiency	-
η_c	Combustion efficiency of main combustion chamber and reheaters	-
η_{gen}	Electrical generator efficiency	-
η_h	Thermal efficiency of the Brayton heat engine	-
η_{hel_i}	Efficiency of heliostat i	-
$\bar{\eta}_{hel_i}$	Optical efficiency of each heliostat	-
η_s	Solar subsystem efficiency (field and receiver)	-
η_0	Optical efficiency of the whole field	-
θ_i	Angle of each heliostat	rad
ρ	Actual mirrors reflectivity	-
ρ_{H}	Irreversibilities due to pressure drops in the heat input	-
ρ_{L}	Irreversibilities due to pressure drops in the heat release	-
σ	Stefan-Boltzmann constant	$\mathrm{W\ m^{-2}\,K^{-4}}$
σ_{Sun}	Dispersion of the effective Sun shape on the receiver plane	rad
ω	Incident angle of the Sun radiation onto the heliostat surface	rad

List of Figures

List of Tables

VNiVERSiDAD D SALAMANCA

CAMPUS OF INTERNATIONAL EXCELLENCE

Thermodynamic optimisation of thermosolar hybrid Brayton cycle plants

Rosa Pilar Merchán Corral - Doctoral thesis

UNIVERSITY OF SALAMANCA / UNIVERSIDAD DE SALAMANCA

Department of Applied Physics / Departamento de Física Aplicada

Salamanca (Spain), September 2020